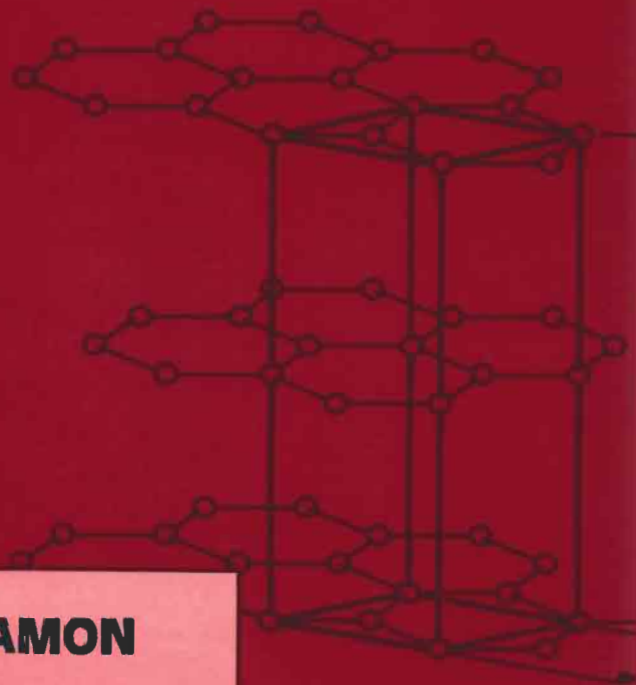


Carbon Materials for Advanced Technologies

Edited by
Timothy D. Burchell



PERGAMON

Carbon Materials for Advanced Technologies

Carbon Materials for Advanced Technologies

Edited by

Timothy D. Burchell

Oak Ridge, National Laboratory
Oak Ridge, TN 37831-6088 U.S.A.

1999



PERGAMON

An Imprint of Elsevier Science

Amsterdam - Lausanne - New York - Oxford - Shannon - Singapore - Tokyo

ELSEVIER SCIENCE Ltd
The Boulevard, Langford Lane
Kidlington, Oxford OX5 1GB, UK

© 1999 Elsevier Science Ltd. All rights reserved.

This work is protected under copyright by Elsevier Science, and the following terms and conditions apply to its use:

Photocopying

Single photocopies of single chapters may be made for personal use as allowed by national copyright laws. Permission of the Publisher and payment of a fee is required for all other photocopying, including multiple or systematic copying, copying for advertising or promotional purposes, resale, and all forms of document delivery. Special rates are available for educational institutions that wish to make photocopies for non-profit educational classroom use.

Permissions may be sought directly from Elsevier Science Rights & Permissions Department, PO Box 800, Oxford OX5 1DX, UK; phone: (+44) 1865 843830, fax: (+44) 1865 853333, e-mail: permissions@elsevier.co.uk. You may also contact Rights & Permissions directly through Elsevier's home page (<http://www.elsevier.nl>), selecting first 'Customer Support', then 'General Information', then 'Permissions Query Form'.

In the USA, users may clear permissions and make payments through the Copyright Clearance Center, Inc., 222 Rosewood Drive, Danvers, MA 01923, USA; phone: (978) 7508400, fax: (978) 7504744, and in the UK through the Copyright Licensing Agency Rapid Clearance Service (CLARCS), 90 Tottenham Court Road, London W1P 0LP, UK; phone: (+44) 171 631 5555; fax: (+44) 171 631 5500. Other countries may have a local reprographic rights agency for payments.

Derivative Works

Tables of contents may be reproduced for internal circulation, but permission of Elsevier Science is required for external resale or distribution of such material.

Permission of the Publisher is required for all other derivative works, including compilations and translations.

Electronic Storage or Usage

Permission of the Publisher is required to store or use electronically any material contained in this work, including any chapter or part of a chapter.

Except as outlined above, no part of this work may be reproduced, stored in a retrieval system or transmitted in any form or by any means, electronic, mechanical, photocopying, recording or otherwise, without prior written permission of the Publisher.

Address permissions requests to: Elsevier Science Rights & Permissions Department, at the mail, fax and e-mail addresses noted above.

Notice

No responsibility is assumed by the Publisher for any injury and/or damage to persons or property as a matter of products liability, negligence or otherwise, or from any use or operation of any methods, products, instructions or ideas contained in the material herein. Because of rapid advances in the medical sciences, in particular, independent verification of diagnoses and drug dosages should be made.

First edition 1999

Library of Congress Cataloging in Publication Data

A catalog record from the Library of Congress has been applied for.

British Library Cataloguing in Publication Data

A catalogue record from the British Library has been applied for.

ISBN 0-08-042683-2

∞ The paper used in this publication meets the requirements of ANSI/NISO Z39.48-1992 (Permanence of Paper).
Printed in The Netherlands.

Contents

<i>Contributors</i>	<i>xi</i>
<i>Acknowledgments</i>	<i>xiii</i>
<i>Preface</i>	<i>xv</i>
1 Structure and Bonding in Carbon Materials	1
<i>Brian McEnaney</i>	
1 Introduction	1
2 Crystalline Forms of Carbon	3
3 The Phase and Transition Diagram for Carbon	12
4 Carbon Films	14
5 Carbon Nanoparticles	18
6 Engineering Carbons	20
7 Concluding Remarks	28
8 Acknowledgments	29
9 References	29
2 Fullerenes and Nanotubes	35
<i>Mildred S. Dresselhaus, Peter C. Eklund and Gene Dresselhaus</i>	
1 Introduction	35
2 Fullerenes and Fullerene-based Solids	37
3 Carbon Nanotubes	61
4 Applications	84
5 Acknowledgments	87
6 References	87
3 Active Carbon Fibers	95
<i>Timothy J. Mays</i>	
1 Introduction	95
2 Background	96
3 Applications of Active Carbon Fibers	101
4 Concluding Remarks	110
5 Acknowledgments	111
6 References	111

4	High Performance Carbon Fibers	119
	<i>Dan D. Edie and John J. McHugh</i>	
1	Introduction	119
2	Processing Carbon Fibers from Polyacrylonitrile	119
3	Carbon Fibers from Mesophase Pitch	123
4	High Performance Carbon Fibers from Novel Precursors	133
5	Carbon Fiber Property Comparison	133
6	Current Areas for High Performance Carbon Fiber Research	134
7	Summary and Conclusions	135
8	References	135
5	Vapor Grown Carbon Fiber Composites	139
	<i>Max L. Lake and Jyh-Ming Ting</i>	
1	Introduction	139
2	Current Forms	142
3	Fiber Properties	144
4	Composite Properties	146
5	Potential Applications	158
6	Manufacturing Issues	160
7	Conclusions	164
8	References	165
6	Porous Carbon Fiber-Carbon Binder Composites	169
	<i>Timothy D. Burchell</i>	
1	Introduction	169
2	Manufacture	169
3	Carbon Bonded Carbon Fiber	173
4	Damage Tolerant Light Absorbing Materials	181
5	Carbon Fiber Composite Molecular Sieves	183
6	Summary and Conclusions	200
7	Acknowledgments	201
8	References	201

7	Coal-Derived Carbons	205
	<i>Peter G. Stansberry, John W. Zondlo and Alfred H. Stiller</i>	
1	Review of Coal Derived Carbons	205
2	Solvent Extraction of Coal	211
3	Preparation and Characteristics of Cokes Produced from Solvent Extraction	223
4	Preparation and Evaluation of Graphite from Coal-Derived Feedstocks	229
5	Summary	233
6	Acknowledgments	233
7	References	233
8	Activated Carbon for Automotive Applications	235
	<i>Philip J. Johnson, David J. Setsuda and Roger S. Williams</i>	
1	Background	235
2	Activated Carbon	239
3	Vehicle Fuel Vapor Systems	244
4	Adsorption	246
5	Carbon Canister Design	252
6	Application of Canisters in Running Loss Emission Control	257
7	Application of Canisters in ORVR Control	263
8	Summary and Conclusions	265
9	References	266
9	Adsorbent Storage for Natural Gas Vehicles	269
	<i>Terry L. Cook, Costa Komodromos, David F. Quinn and Steve Ragan</i>	
1	Introduction	269
2	Storage of Natural Gas	274
3	Adsorbents	280
4	Adsorbent Fill-Empty Testing	293
5	Guard Beds	294
6	Summary	298
7	References	299

10	Adsorption Refrigerators and Heat Pumps	303
	<i>Robert E. Critoph</i>	
1	Why Adsorption Cycles?	303
2	The Basic Adsorption Cycle	306
3	Basic Cycle Analysis and Results	313
4	Choice of Refrigerant - Adsorbent Pairs	319
5	Improving Cost Effectiveness	322
6	Summary and Conclusions	339
7	References	339
11	Applications of Carbon in Lithium-Ion Batteries	341
	<i>Tao Zheng and Jeff Dahn</i>	
1.	Introduction	341
2.	Useful Characterization Methods	347
3.	Graphitic Carbons	353
4.	Hydrogen-Containing Carbons from Pyrolyzed Organic Precursors	358
5.	Microporous Carbons from Pyrolyzed Hard-Carbon Precursors	375
6.	Carbons Used in Commercial Applications	384
7.	References	385
12	Fusion Energy Applications	389
	<i>Lance L. Snead</i>	
1.	Introduction	389
2.	The Advantages of Carbon as a Plasma-Facing Component	394
3.	Irradiation Effects on Thermophysical Properties of Graphite and Carbon Fiber Composites	400
4.	Plasma Wall Interactions	412
5.	Tritium Retention in Graphite	420
6.	Summary and Conclusions	424
7.	Acknowledgments	424
8.	References	425

13 Fission Reactor Applications of Carbon	429
<i>Timothy D. Burchell</i>	
1. The Role of Carbon Materials in Fission Reactors	429
2. Graphite Moderated Power Producing Reactors	438
3. Radiation Damage in Graphite	458
4. Radiolytic Oxidation	469
5. Other Applications of Carbon in Fission Reactors	473
6. Summary and Conclusions	477
7. Acknowledgments	478
8. References	478
14 Fracture in Graphite	485
<i>Glenn R. Romanoski and Timothy D. Burchell</i>	
1. Introduction	485
2. Studies and Models of Fracture Processes in Graphite	486
3. Linear Elastic Fracture Mechanics Behavior of Graphite	491
4. Elastic-plastic Fracture Mechanics Behavior of Graphite	497
5. Fracture Behavior of Small Flaws in Nuclear Graphites	503
6. The Burchell Fracture Model	515
7. Summary and Conclusions	530
8. Acknowledgments	531
9. References	532
Index	535

Contributors

Timothy D. Burchell, *Metals and Ceramics Division, Oak Ridge National Laboratory, Oak Ridge, Tennessee 37831, USA*

Terry L. Cook, *Atlanta Gas Light Company, P.O. Box 4569, Atlanta, Georgia 30302, USA*

Robert E. Critoph, *Department of Engineering, University of Warwick, Coventry CV4 7AL, United Kingdom*

Jeff Dahn, *Department of Physics, Dalhousie University, Halifax, Nova Scotia B3H 3J5, Canada*

Gene Dresselhaus, *Francis Bitter Magnet Laboratory, Massachusetts Institute of Technology, Cambridge, Massachusetts 02139, USA*

Mildred S. Dresselhaus, *Department of Electrical Engineering and Computer Science and Department of Physics, Massachusetts Institute of Technology, Cambridge, Massachusetts 02139, USA*

Dan D. Edie, *Department of Chemical Engineering, Clemson University, Clemson, South Carolina 29634, USA*

Peter C. Eklund, *Department of Physics and Astronomy and Center for Applied Energy Research, University of Kentucky, Lexington, Kentucky 40506, USA*

Philip J. Johnson, *Ford Motor Company, Automotive Components Division, Schaefer Court II, 14555 Rotunda Drive, Dearborn, Michigan 48120, USA*

Costa Komodromos, *Gas Research Centre, British Gas, Ashby Road, Loughborough, Leicestershire LE11 36U, United Kingdom*

Max L. Lake, *Applied Sciences, Inc. 141 West Xenia Avenue, Cederville, Ohio 45314, USA*

Timothy J. Mays, *School of Materials Science and Engineering, University of Bath, Bath BA2 7AY, United Kingdom*

Brian McEnaney, *School of Materials Science and Engineering, University of Bath, Bath BA2 7AY, United Kingdom*

John J. McHugh, *Hexcel Corporation, Hercules Research Center, Wilmington, Delaware 19808, USA*

David F. Quinn, *Royal Military College, Kingston, Ontario K7K 5L0, Canada*

Steve Ragan, *Sutcliffe Speakman Carbons Ltd., Lockett Road, Ashton in*

Makerfield, Lancashire WN4 8DE, United Kingdom

Glenn R. Romanoski, *Metals and Ceramics Division, Oak Ridge National Laboratory, Oak Ridge, Tennessee 37831, USA*

David J. Setsuda, *Ford Motor Company, Automotive Components Division, Schaefer Court II, 14555 Rotunda Drive, Dearborn, Michigan 48120, USA*

Lance L. Snead, *Metals and Ceramics Division, Oak Ridge National Laboratory, Oak Ridge, Tennessee 37831, USA*

Peter G. Stansberry, *Department of Chemical Engineering, West Virginia University, Morgantown, West Virginia 26502, USA*

Alfred H. Stiller, *Department of Chemical Engineering, West Virginia University, Morgantown, West Virginia 26502, USA*

Jyh-Ming Ting, *Department of Materials Science and Engineering, National Cheng Kung University, Tainan, Taiwan*

Roger S. Williams, *Westvaco Corporation, Washington Street, Covington, Virginia 24426, USA*

Tao Zheng, *Department of Physics, Simon Fraser University, Burnaby, British Columbia V5A 1S6, Canada*

John W. Zondlo, *Department of Chemical Engineering, West Virginia University, Morgantown, West Virginia 26502, USA*

Acknowledgments

I wish to acknowledge the cooperation and patience of the contributing authors, the assistance of my colleagues with the task of refereeing the chapter manuscripts, the forbearance and understanding of the book's publishers, and the contribution of Dr. Frederick S. Baker in soliciting chapters in the area of activated carbons.

Finally, it is appropriate that I acknowledge my wife Lynne, whose support and encouragement were essential ingredients in the completion of this book.

Timothy D. Burchell.

Preface

In 1994 the Oak Ridge National Laboratory hosted an American Carbon Society Workshop entitled "Carbon Materials for Advanced Technologies". The inspiration for this book came from that workshop. By late 1995 a suitable group of contributors had been identified such that the scope of this book would be sufficiently broad to make a useful contribution to the literature.

Carbon is a truly remarkable element which can exist as one of several allotropes. It is found abundantly in nature as coal or as natural graphite, and much less abundantly as diamond. Moreover, it is readily obtained from the pyrolysis of hydrocarbons such as resins and pitches, and can be deposited from the vapor phase by cracking hydrocarbon rich gases. In its various allotropic forms carbon has quite remarkable properties. Diamond possesses the highest thermal conductivity known to man and is prized as a gem stone. Both of these attributes result from the high degree of crystal perfection and bond strength in the diamond lattice. Graphite possesses extreme anisotropy in the bond energies of its crystal lattice, resulting in highly anisotropic physical properties. The most recently discovered allotrope of carbon, C_{60} or Buckminsterfullerene, has been the subject of extensive research, as have the related carbon nanotubes and nanostructures.

Engineered carbons take many forms. For example, cokes, graphites, carbon and graphite fibers, carbon fiber - carbon matrix composites, adsorbent carbons and monoliths, glassy carbons, carbon blacks, carbon films and diamond like films. Many of these engineered carbon forms are discussed in this book, especially with respect to their applications in technologically advanced systems. Moreover, this book contains accounts of research into the uses of novel carbons. Modern day applications of carbon materials are numerous. Indeed, the diversity of carbon applications are truly astounding, and range from the mundane (*e.g.*, commodity adsorbent carbons or carbon black), to the exotic (*e.g.*, high modulus carbon fibers that enable the lightweight stiff composite structures used in airframes and spacecraft).

Chapter 1 contains a review of carbon materials, and emphasizes the structure and chemical bonding in the various forms of carbon, including the four allotropes diamond, graphite, carbynes, and the fullerenes. In addition, amorphous carbon and diamond films, carbon nanoparticles, and engineered carbons are discussed. The most recently discovered allotrope of carbon, *i.e.*, the fullerenes, along with carbon nanotubes, are more fully discussed in Chapter 2, where their structure-property relations are reviewed in the context of advanced technologies for carbon based materials. The synthesis, structure, and properties of the fullerenes and

nanotubes, and modification of the structure and properties through doping, are also reviewed. Potential applications of this new family of carbon materials are considered.

Detailed accounts of fibers and carbon-carbon composites can be found in several recently published books [1-5]. Here, details of novel carbon fibers and their composites are reported. The manufacture and applications of adsorbent carbon fibers are discussed in Chapter 3. Active carbon fibers are an attractive adsorbent because their small diameters (typically 6-20 μm) offer a kinetic advantage over granular activated carbons whose dimensions are typically 1-5 mm. Moreover, active carbon fibers contain a large volume of mesopores and micropores. Current and emerging applications of active carbon fibers are discussed. The manufacture, structure and properties of high performance fibers are reviewed in Chapter 4, whereas the manufacture and properties of vapor grown fibers and their composites are reported in Chapter 5. Low density (porous) carbon fiber composites have novel properties that make them uniquely suited for certain applications. The properties and applications of novel low density composites developed at Oak Ridge National Laboratory are reported in Chapter 6.

Coal is an important source of energy and an abundant source of carbon. The production of engineering carbons and graphite from coal via a solvent extraction route is described in Chapter 7. Coal derived carbons and graphites are first reviewed and the solvent extraction of coal using N-methyl pyrrolidone is described. The characteristics of cokes and graphites derived from solvent extracted pitches and feedstocks are reported. The modification of the calcined cokes by blending the extracted pitches, and/or by hydrogenation of the pitch, and subsequent control of graphite artifact properties are discussed.

Applications of activated carbons are discussed in Chapters 8-10, including their use in the automotive arena as evaporative loss emission traps (Chapter 8), and in vehicle natural gas storage tanks (Chapter 9). The use of evaporative loss emission traps has been federally mandated in the U.S. and Europe. Consequently, a significant effort has been expended to develop a carbon adsorbent properly optimized for evaporative loss control, and to design the on board vapor collection and disposal system. The manufacture of activated carbons, and their preferred characteristics for fuel emissions control are discussed in Chapter 8, along with the essential features of a vehicle evaporative loss emission control system.

The use of activated carbons as a natural gas storage medium for vehicles is attractive because the gas may be stored at significantly lower pressures in the adsorbed state (3.5 - 4.0 MPa) compared to pressurized natural gas (20 MPa), but with comparable storage densities. The development of an adsorbed natural gas storage system, and suitable adsorbent carbons, including novel adsorbent carbon

monoliths capable of storing >150 V/V of natural gas, are reported in Chapter 9. Moreover, the function and use of a guard bed to prevent deterioration of the carbon adsorbent with repeated fill-empty cycling is discussed.

The application of activated carbons in adsorption heat pumps and refrigerators is discussed in Chapter 10. Such arrangements offer the potential for increased efficiency because they utilize a primary fuel source for heat, rather than use electricity, which must first be generated and transmitted to a device to provide mechanical energy. The basic adsorption cycle is analyzed and reviewed, and the choice of refrigerant-adsorbent pairs discussed. Potential improvements in cost effectiveness are detailed, including the use of improved adsorbent carbons, advanced cycles, and improved heat transfer in the granular adsorbent carbon beds.

Chapter 11 reports the use of carbon materials in the fast growing consumer electronics application of lithium-ion batteries. The principles of operation of a lithium-ion battery and the mechanism of Li insertion are reviewed. The influence of the structure of carbon materials on anode performance is described. An extensive study of the behavior of various carbons as anodes in Li-ion batteries is reported. Carbons used in commercial Li-ion batteries are briefly reviewed.

The role of carbon materials in nuclear systems is discussed in Chapters 12 and 13, where fusion device and fission reactor applications, respectively, are reviewed. In Chapter 12 the major technological issues for the utilization of carbon as a plasma facing material are discussed in the context of current and future fusion tokamak devices. Problems such as surface sputtering, erosion, radiation enhanced sublimation, radiation damage, and tritium retention are addressed. Carbon materials have been used in fission reactors for >50 years. Indeed the first nuclear reactor was a graphite "pile" [6]. The essential design features of graphite moderated reactors, (including gas-, water- and molten salt-cooled systems) are reviewed in Chapter 13, and reactor environmental effects such as radiation damage and radiolytic corrosion are discussed. The forms of carbon used in fission reactors (graphite, adsorbent carbon, carbon-carbon composites, pyrolytic graphite, etc.) are reviewed and their functions described.

Graphite is a widely used commodity. In addition to its nuclear role, graphite is used in large quantities by the steel industry as arc electrodes in remelting furnaces, for metal casting molds by the foundry industry, and in the semi-conductor industry for furnace parts and boats. Graphite is a brittle ceramic, thus its fracture behavior and the prediction of failure are important in technological applications. The fracture behavior of graphite is discussed in qualitative and quantitative terms in Chapter 14. The applications of Linear Elastic Fracture Mechanics and Elastic-Plastic Fracture Mechanics to graphite are reviewed and a study of the role of small flaws in nuclear graphites is reported. Moreover, a mathematical model of fracture

is reported and its performance discussed.

Clearly, not all forms of carbon material, nor all the possible applications thereof, are discussed in this book. However, the application of carbon materials in many advanced technologies are reported here. Carbon has played an important role in mankind's technological and social development. In the form of *charcoal* it was an essential ingredient of gunpowder! The industrial revolution of the 18th and 19th centuries was powered by steam raised from the burning of coal! New applications of carbon materials will surely be developed in the future. For example, the recently discovered carbon nanostructures based on C₆₀ (closed cage molecules, tubes and tube bundles), may be the foundation of a new and significant applications area based on their superior mechanical properties, and novel electronic properties.

Researching carbon materials, and developing new applications, has proven to be a complex and exciting topic that will no doubt continue to engage scientists and engineers for many years to come.

References.

1. Donnet, J-B. and Bansal, R.C. *Carbon Fibers*, 2nd Edition, Marcel Dekker, Inc., New York. 1990.
2. Thomas, C.R., ed. *Essentials of Carbon-Carbon Composites*, Royal Society of Chemistry, UK. 1993
3. Buckley, J.D. and Edie, D.D. *Carbon-Carbon Materials and Composites*, Noyes Publications, Park Ridge, NJ. 1993.
4. Savage, G. *Carbon-Carbon Composites*, Chapman & Hall, London, 1993.
5. D.L. Chung, *Carbon Fiber Composites*, Pub. Butterworth-Heinemann, Newton, MA. 1994.
6. E. Fermi, Experimental production of a divergent chain reaction, *Am. J. Phys.*, 1952, 20(9), 536 538.

Timothy. D. Burchell

CHAPTER 1

Structure and Bonding in Carbon Materials

BRIAN McENANEY

*Department of Materials Science & Engineering
University of Bath
Bath, BA2 7AY
United Kingdom*

1 Introduction

The extraordinary ability of the chemical element carbon to combine with itself and other chemical elements in different ways is the basis of organic chemistry and of life. This chemical versatility also gives rise to a rich diversity of structural forms of solid carbon. This introductory chapter is an attempt to survey the very wide range of carbon materials that is now available with emphasis on chemical bonding and microstructure. The materials reviewed include: (i) crystalline forms of carbon: diamond, graphite, Fullerenes and carbynes; (ii) amorphous carbon films and diamond films; (iii) carbon nanoparticles, including carbon nanotubes; (iv) engineering carbons with more-or-less disordered microstructures based on that of graphite that are the main focus of this book.

1.1 Bonding between carbon atoms

Here, the bonding between carbon atoms is briefly reviewed; fuller accounts can be found in many standard chemistry textbooks, e.g., [1]. The carbon atom [ground state electronic configuration $(1s^2)(2s^2 2p_x 2p_y)$] can form sp^3 , sp^2 and sp hybrid bonds as a result of promotion and hybridisation. There are four equivalent $2sp^3$ hybrid orbitals that are tetrahedrally oriented about the carbon atom and can form four equivalent tetrahedral σ bonds by overlap with orbitals of other atoms. An example is the molecule ethane, C_2H_6 , where a Csp^3 - Csp^3 (or C-C) σ bond is formed between two C atoms by overlap of sp^3 orbitals, and three Csp^3 -H1s σ bonds are formed on each C atom, Fig. 1, A1.

A second type of hybridisation of the valence electrons in the carbon atom can occur to form three $2sp^2$ hybrid orbitals leaving one unhybridised $2p$ orbital.

The sp^2 orbitals are equivalent, coplanar and oriented at 120° to each other and form σ bonds by overlap with orbitals of neighbouring atoms, as in the molecule ethene, C_2H_4 , Fig. 1, A2. The remaining p orbital on each C atom forms a π bond by overlap with the p orbital from the neighbouring C atom; the bonds formed between two C atoms in this way are represented as $Csp^2=Csp^2$, or simply as $C=C$.

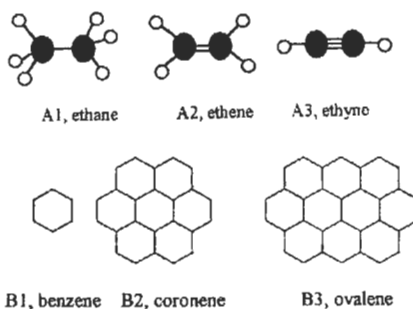


Fig. 1. Some molecules with different C-C bonds. A1, ethane, C_2H_6 (sp^3); A2, ethene, C_2H_4 (sp^2); A3, ethyne, C_2H_2 (sp^1); B1, benzene, C_6H_6 (aromatic); B2, coronene, $C_{24}H_{12}$; B3, ovalene, $C_{32}H_{14}$.

In the third type of hybridisation of the valence electrons of carbon, two linear $2sp^1$ orbitals are formed leaving two unhybridised $2p$ orbitals. Linear σ bonds are formed by overlap of the sp hybrid orbitals with orbitals of neighbouring atoms, as in the molecule ethyne (acetylene) C_2H_2 , Fig. 1, A3. The unhybridised p orbitals of the carbon atoms overlap to form two π bonds; the bonds formed between two C atoms in this way are represented as $Csp\equiv Csp$, or simply as $C\equiv C$.

It is also useful to consider the aromatic carbon-carbon bond exemplified by the prototypical aromatic molecule benzene, C_6H_6 . Here, the carbon atoms are arranged in a regular hexagon which is ideal for the formation of strain-free sp^2 σ bonds. A conventional representation of the benzene molecule as a regular hexagon is in Fig. 1, B1. The ground state π orbitals in benzene are all bonding orbitals and are fully occupied and there is a large delocalisation energy that contributes to the stability of the compound. The aromatic carbon-carbon bond is denoted as $Car\sim Car$. Polynuclear aromatic hydrocarbons consist of a number, n , of fused benzene rings; examples are coronene, $C_{24}H_{12}$, ($n = 7$) and ovalene, $C_{32}H_{14}$, ($n = 10$), Fig. 1 B2, B3, where delocalisation of π electrons extends over the entire molecule. Note that the C:H atomic ratio in polynuclear aromatic hydrocarbons increases with increasing n . Dehydrogenative condensation of polynuclear aromatic compounds is a feature of the carbonisation process and eventually leads to an extended hexagonal network of carbon atoms, as in the basal plane of graphite (see Sections 2.2 and 6.1).

For carbon-carbon bonds the mean bond enthalpy increases and bond length decreases with increasing bond order, Table 1. When considering bond lengths in disordered carbon materials, particularly those containing significant amounts of heteroelements, it is useful to note that the values in Table 1 are mean, overall values. Carbon-carbon bond lengths depend upon the local molecular environment. Table 2 lists some values of carbon-carbon bond lengths obtained from crystals of organic compounds. In general, bond length decreases as the bond order of adjacent carbon-carbon bonds increases.

Table 1. Some properties of carbon-carbon bonds

Bond	Bond order	Bond length /pm	Mean bond enthalpy /(kJ mol^{-1})
$\text{Csp}^3\text{-Csp}^3$	1	153.0	348
$\text{Car}\text{-}\text{Car}$	1.5	138.4	518
$\text{Csp}^2\text{=Csp}^2$	2	132.2	612
$\text{Csp}\equiv\text{Csp}$	3	118.1	838

Table 2. Carbon-carbon bond lengths in organic compounds [2].

Carbon-carbon bond	Sub-structure	Bond length/pm
<i>Single bonds</i>		
	\downarrow^a	
$\text{Csp}^3\text{-Csp}^3$	$\text{-C}^*\text{-C}^*\text{-}$	153.0 ^b
$\text{Csp}^3\text{-Car}$	$\text{-C}^*\text{-Car}\text{-}$	151.3 ^b
$\text{Csp}^3\text{-Csp}^2$	$\text{-C}^*\text{-C=C-}$	150.7 ^b
$\text{Csp}^3\text{-Csp}^1$	$\text{-C}^*\text{-C}\equiv\text{C-}$	149.0
$\text{Csp}^2\text{-Car}$	$\text{C=C-Car}\text{-}$	148.3 ^b
$\text{Csp}^2\text{-Csp}^2$	C=C-C=C	146.0 ^b
$\text{Csp}^2\text{-Csp}^1$	$\text{C=C-C}\equiv\text{C}$	143.1
<i>Multiple bonds</i>		
$\text{Car}\text{-}\text{Car}$ (phenyl)	$\text{C}^*\text{-C}\text{-}\text{C}\text{-}\text{C}^*$	139.7 ^b
$\text{Csp}^2\text{=Csp}^2$	$\text{C}^*\text{-C=C-C}^*$	131.6
$\text{Csp}^1\equiv\text{Csp}^1$	$\text{C}^*\text{-C}\equiv\text{C-C}^*$	118.1 ^b

a, points to the relevant carbon-carbon bond; b. overall value

2 Crystalline Forms of Carbon

The commonest crystalline forms of carbon, cubic diamond and hexagonal graphite, are classical examples of allotropy that are found in every chemistry textbook. Both diamond and graphite also exist in two minor crystallographic forms: hexagonal diamond and rhombohedral graphite. To these must be added carbynes and Fullerenes, both of which are crystalline carbon forms. Fullerenes are sometimes referred to as the third allotrope of carbon. However, since Fullerenes were discovered more recently than carbynes, they are

chronologically the fourth crystalline allotrope of carbon. Crystalline Fullerenes are now commercially-available chemicals and their crystal structures and properties have been extensively studied. By contrast, convenient methods for mass production of pure carbynes have not yet been discovered. Consequently, carbynes have not been as extensively characterised as other forms of carbon. The structures and chemical bonding of these crystalline forms of carbon are reviewed in this section.

2.1 Diamond

Diamond is an important commodity as a gemstone and as an industrial material and there are several excellent monographs on the science and technology of this material [3-5]. Diamond is most frequently found in a cubic form in which each carbon atom is linked to four other carbon atoms by sp^3 σ bonds in a strain-free tetrahedral array, Fig. 2A. The crystal structure is zinc blende type and the C-C bond length is 154 pm. Diamond also exists in an hexagonal form (Lonsdaleite) with a wurtzite crystal structure and a C-C bond length of 152 pm. The crystal density of both types of diamond is $3.52 \text{ g}\cdot\text{cm}^{-3}$.

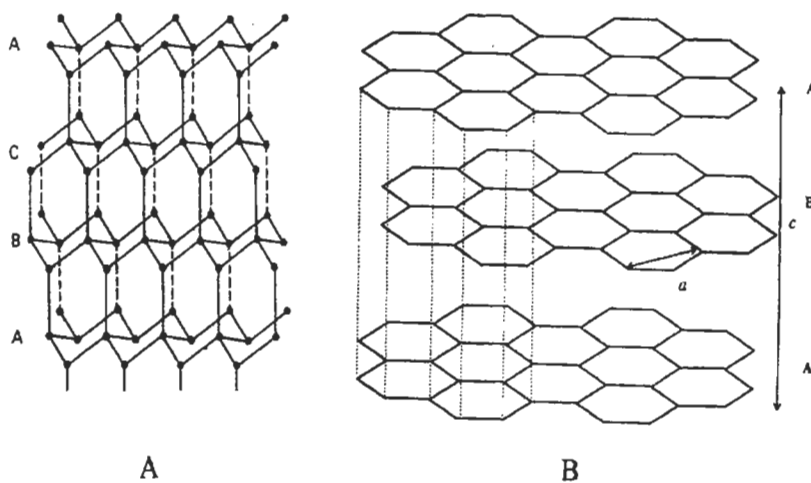


Fig. 2. The crystal structures of: A, cubic diamond; B, hexagonal graphite

Natural diamonds used for jewellery and for industrial purposes have been mined for centuries. The principal diamond mining centres are in Zaire, Russia, The Republic of South Africa, and Botswana. Synthetic diamonds are made by dissolving graphite in metals and crystallising diamonds at high pressure (12-15 GPa) and temperatures in the range 1500-2000 K [6]; see section 3. More recently, polycrystalline diamond films have been made at low pressures by

carbon deposition from hydrocarbon-containing gas mixtures that are rich in hydrogen [7]; see section 4.2.

Natural and synthetic diamonds contain various impurities. Nitrogen and boron are found as substitutional impurity atoms in the crystal lattice. Diamonds are classified as Types I and II with subtypes [5]. Most natural diamonds are Type Ia containing up to 0.5% of nitrogen in small aggregates, since this concentration is considerably in excess of the solubility limit for nitrogen in the diamond lattice. Type Ib diamonds are rare in nature, but most synthetic diamonds produced by the high pressure method are of this type. Type Ib diamonds contain up to 500 ppm of substitutional nitrogen. Type IIa diamonds are very rare in nature and contain barely detectable amounts of nitrogen. Type IIb diamonds are even rarer in nature and are p-type semi-conductors, since the nitrogen content is insufficient to compensate for the substitutional boron present. Significant quantities of hydrogen and oxygen are found in diamonds, especially at surfaces where they stabilise dangling bonds. Metallic inclusions are found in diamonds, typically aluminium in natural diamonds and nickel and iron in synthetic diamonds produced at high temperatures and pressures by the catalytic method.

2.2 Graphite

As a well-established allotrope of carbon the crystal structure of graphite is fully documented [8]. The graphite crystal was an early subject for application of X-ray diffraction [9]. Subsequent studies [e.g., 10, 11] confirmed the well-known hexagonal crystal structure of graphite. The basis of the crystal structure of graphite is the graphene plane or carbon layer plane, i.e., an extended hexagonal array of carbon atoms with sp^2 σ bonding and delocalised π bonding. The commonest crystal form of graphite is hexagonal and consists of a stack of layer planes in the stacking sequence ABABAB..., Fig. 2B.

The rhombohedral form of graphite with a stacking sequence ABCABC... is a minor component of well-crystallised graphites. The proportion of rhombohedral graphite can be increased substantially (typically from a few percent to ~ 20%) by deformation processes, such as grinding [12]. Conversely, the proportion of rhombohedral graphite can be reduced by high temperature heat-treatment, showing that the hexagonal form is more stable. The density of both forms of graphite is $2.26 \text{ g}\cdot\text{cm}^{-3}$.

For both forms of graphite the in-plane C-C distance is 142 pm, i.e., intermediate between Csp^3-Csp^3 and $Csp^2=Csp^2$ bond lengths, 153 and 132 pm respectively, Table 1. Consideration of the resonance structures between carbon atoms in the plane show that each C-C bond in the carbon layer plane has about one third double bond character. Carbon layer planes (of various dimensions

and with different degrees of perfection) are a very important microstructural element in most engineering carbons and graphites (see Section 6).

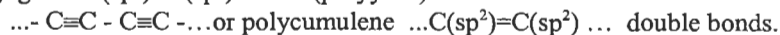
There is a large difference between the in-plane C-C distance, 142 pm, and the interlayer distance, 335 pm, in graphite that results from different types of chemical bonding. Within planes the C-C bonds are trigonal sp^2 hybrid σ bonds with delocalised π bonds. The large interlayer spacing suggests that the contribution to interlayer bonding from π bond overlap is negligible. The usual assumption has been that interlayer potentials are of the van der Waals type and there have been many attempts to calculate interplanar properties starting from Lennard-Jones and Buckingham pair potentials. This work has been reviewed in detail by Kelly [8] who concluded that there is no entirely satisfactory treatment of interlayer forces in graphite. More recent evidence from scanning probe microscopical images of a graphite surface suggest that there may be some π orbital interaction between planes [13].

Natural graphites occur widely around the world, although the quality of the ores varies widely. High purity graphite ores with up to 100% carbon contents are mined in Sri Lanka; lower grade ores which must be concentrated are mined in Russia, China, Germany, Norway, Korea, Mexico and Austria. Ticonderoga in the USA has been used as a source of high quality natural graphite flakes for fundamental studies. Principal uses of natural graphites are in the foundry and steel industries and in the refractory and electrical industries.

Most synthetic graphites used for engineering applications are granular composites consisting of a filler (usually a coke) and a binder carbon formed from pitch. The graphitic order in most engineering grade synthetic graphites is less well-developed than in natural graphite; see section 6. Well-graphitised synthetic graphites are produced by hot-pressing pyrolytic graphite (HOPG grade); recently, well-graphitised carbons have been formed by heat-treatment of compacted polyimide films [15].

2.3 Carbynes

Carbynes are a form of carbon with chains of carbon atoms formed from conjugated $C(sp^1)\equiv C(sp^1)$ bonds (polyynes):



From X-ray diffraction studies of short chain (C_4 - C_8) polyynes [16] $C\equiv C$ bond lengths ranged from 119-121 pm while C-C bond lengths ranged from 132-138 pm, depending upon the local molecular environment, cf. Table 2.

In the late 1960s El Goresy and Donnay [17] discovered a new form of carbon which they called white carbon or Chaoite in a carbon-rich gneiss in the Ries meteorite crater in Bavaria. Chaoite has an hexagonal crystal structure and it

was proposed that it consisted of polyynes or polycumulene carbon chains lying parallel to the hexagonal axis. At about the same time other carbyne forms with hexagonal structures were obtained in Russia [18, 19] by dehydropolymerisation of acetylene: α -carbyne and β -carbyne and by Whittaker and his group in the USA [20-22] (Carbons VI, VIII, and IX). Lattice parameters for some of these carbyne forms are summarised in Table 3.

Table 3. Crystal structure data for some carbynes

Carbyne	Chaoite	α -carbyne	β -carbyne	carbon VI	Carbolite I
Structure ^a	hex.	hex.	hex.	rhomb.	hex.
a_0 /pm	895	894	824	923	1192
c_0 /pm	1408	1536	768	1224	1062
Density ^b	3.43	2.68	3.13	2.90	1.46
Ref.	[17]	[18,19]	[18,19]	[20-22]	[24]

a- hex. = hexagonal, rhomb. = rhombohedral; b, $\text{g}\cdot\text{cm}^{-3}$.

The different forms of carbynes were assumed to be polytypes with different numbers of carbon atoms in the chains lying parallel to the hexagonal axis and different packing arrangements of the chains within the crystallite. Heimann *et al* [23] proposed that the sizes of the unit cells were determined by the spacing between kinks in extended carbon chains, Fig. 3A. They were able to correlate the c_0 value for the different carbyne forms with assumed numbers of carbon atoms, n (in the range $n = 6$ to 12), in the linear parts of the chains.

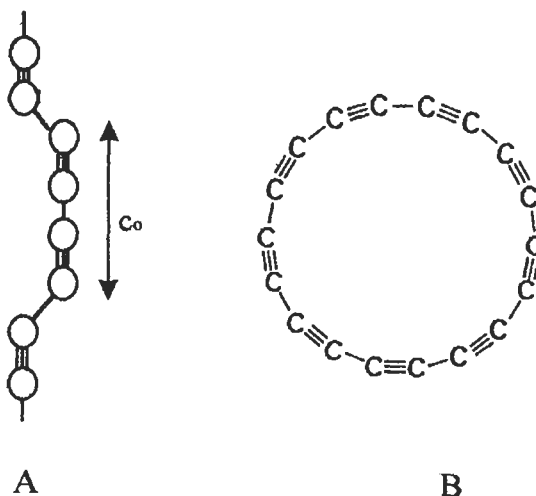


Fig. 3. A, A kinked polyyn chain model for linear carbynes (after [23]); B, cyclo C-18 carbyne [25].

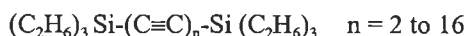
Recently, Tanuma and Palnichenko [24] have reported a new form of carbon which they call 'Carbolite' formed by quenching high temperature carbon vapour onto a metal substrate. Hexagonal Carbolite I was formed from an Ar-rich gas; a rhombohedral form, Carbolite II, was formed from an Ar-H₂ gas mixture.

X-ray diffraction peaks were rather broad with coherence lengths as low as 20 nm and this was attributed to rapid quenching. It was proposed that the carbon atoms are arranged in polyyne chains ($n = 4$) along the c-axis. The density of Carbolite (1.46 g·cm⁻³) is lower than values for other carbynes and for diamond and graphite - hence the name - and this was attributed to a rapid quenching process.

Molecular orbital calculations indicate that cyclo C-18 carbyne should be relatively stable and experimental evidence for cyclocarbynes has been found [25], Fig. 3B. Diederich *et al* [25] synthesised a precursor of cyclo C-18 and showed by laser flash heating and time-of flight mass spectrometry that a series of retro Diels-Alder reactions occurred leading to cyclo C-18 as the predominant fragmentation pattern. Diederich has also presented a fascinating review of possible cyclic all-carbon molecules and other carbon-rich nanometre-sized carbon networks that may be susceptible to synthesis using organic chemical techniques [26].

Despite many publications on carbynes, their existence has not been universally accepted and the literature has been characterised by conflicting claims and counter claims [e.g., 27-29]. This is particularly true of meteoritic carbynes. An interesting account of the nature of elemental carbon in interstellar dust (including diamond, graphite and carbynes) was given by Pillinger [30]. Reitmeyer [31] has re-interpreted carbyne diffraction data and has concluded that carbynes could be stratified or mixed layer carbons with variable heteroelement content (H,O,N) rather than a pure carbon allotrope.

In addition to questions over interpretation of diffraction data, there are reservations about the stability of carbynes. Lagow *et al* [32] note that the condensation of the compound Li-C≡C-Br to form carbon chains is potentially explosive. There is also the possibility of cross-linking between carbyne chains and the nature of the termination of the carbyne chains is unclear. Eastmond *et al* [33] showed that polyyne compounds of the type:



are stabilised by the bulky silyl end-groups. Lagow *et al* [32] also synthesised and determined the crystal structure of a polyyne with tertiary butyl end groups:



that was stable to $\sim 130^\circ\text{C}$. They also found mass spectrometric evidence both for polyynes of the type



where R = phenyl and $n = 16\text{-}28$, and of carbyne chains with lengths up to C_{300} after laser ablation of graphite in the presence of C_2N_2 and C_2F_6 . The presumption was that these carbynes were stabilised by nitrile and trifluoromethyl end caps. For composites of carbynes and alkali metal fluorides produced by reduction of fluoropolymers with alkali metal amalgams, it is argued that the alkali metal matrix suppresses cross-linking of the carbyne chains [34].

Despite the scepticism in some quarters, a large number of chemical and physical methods have been developed for producing carbynoid materials. These include: dehydropolymerisation of acetylene, dehydrohalogenation of polyvinylidene halides and reductive dehalogenation of poly(tetrafluoroethylene) and related compounds, condensation of carbon vapour produced by various means, e.g., laser ablation and arc discharge, shock compression of graphite and other solid forms of carbon [35]. At present, no all-carbon carbynoid material has been isolated in large single crystal form and, consequently, full X-ray structural analyses and bulk property measurements have not been performed. (Note. An extensive review of carbynes by Russian workers [36] was published after this Section of the Chapter was completed.)

2.4 Fullerenes

Fullerenes are described in detail in Chapter 2 and therefore only a brief outline of their structure is presented here to provide a comparison with the other forms of carbon. The C_{60} molecule, Buckminsterfullerene, was discovered in the mass spectrum of laser-ablated graphite in 1985 [37] and crystals of C_{60} were first isolated from soot formed from graphite arc electrodes in 1990 [38]. Although these events are relatively recent, the C_{60} molecule has become one of the most widely-recognised molecular structures in science and in 1996 the co-discoverers Curl, Kroto and Smalley were awarded the Nobel prize for chemistry. Part of the appeal of this molecule lies in its beautiful icosahedral symmetry - a truncated icosahedron, or a molecular soccer ball, Fig. 4A.

The C_{60} molecule contains 12 pentagons and 20 hexagons. This type of hexagonal-pentagonal structure closely resembles the geodesic domes developed by the architect and engineer R. Buckminster Fuller, after whom the molecule is named. In the C_{60} molecule each carbon atom is bonded to three

molecule is named. In the C_{60} molecule each carbon atom is bonded to three others by two longer bonds (length ~ 145 pm) and one shorter bond (bond length ~ 140 pm). These are conventionally referred to in the Fullerene literature as two C-C single bonds and one C=C double bond, although their bond orders are intermediate between a pure Csp^3-Csp^3 bond and a purely aromatic $Car\sim Car$ bond, being close to the value for the C-C bond in the graphite basal plane, cf. Tables 1 and 2. The double bonds lie between two hexagons and are therefore known as 6:6 bonds whereas the single bonds link a hexagon to a pentagon and are known as 6:5 bonds. It follows that there is bonding anisotropy in the C_{60} molecule since bonds around a pentagon are all single bonds and bonds around a hexagon are alternately single bonds and double bonds. It appears therefore that the bonding in C_{60} is mainly sp^2 with delocalised π electrons, but with some sp^3 character resulting from curvature of the C-C bonds.

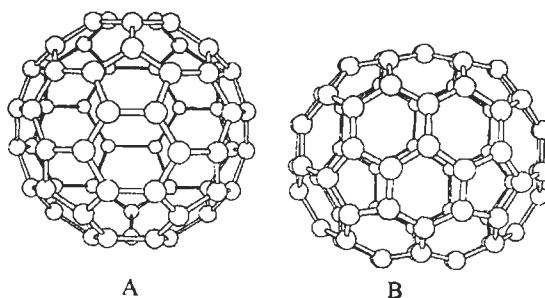


Fig. 4. Fullerene molecules: A, C_{60} ; B, C_{70} .

Crystals of C_{60} formed by vacuum sublimation have a face-centred cubic (fcc) crystal structure at room temperature, $a_0 = 1417$ pm [38,39]. Those grown from solution have a variety of crystal structures depending upon the solvent used, e.g., fcc, hexagonal close packed, hcp, or orthorhombic structures [40, 41]; some of these structures may be stabilised by solvent molecules. Solid state ^{13}C nuclear magnetic resonance, nmr, and other spectroscopic studies show that, despite the bonding anisotropy, all carbon atoms in the C_{60} molecule are equivalent [42-44]. This is because at room temperature the C_{60} molecules are re-orienting rapidly on their lattice sites. As the temperature is reduced, there is a phase transition at $\sim 260K$ to a primitive cubic structure [45] as a result of orientational ordering of some of the C_{60} molecules. At 86K there is a glass transition in which the orientational ordering is frozen [46, 47].

Fullerenes are a range of stable closed-shell carbon molecules and their derivatives, of which C_{60} is the archetype. The next highest stable member of the series is C_{70} which is found in small quantities with C_{60} in arc electrode soot. C_{70} may be regarded as a C_{60} molecule with an extra belt of hexagons inserted at the

the stability of Fullerenes and the occurrence of 'magic numbers' in the Fullerene series. The rule states that closed carbon cages in which the pentagons are isolated from each other are likely to be more stable than those in which pentagons are in contact. C_{60} is the smallest closed shell carbon cluster that avoids abutting pentagons and C_{70} is the next smallest. Other Fullerenes such as C_{76} , C_{78} , C_{82} , C_{84} , have been isolated [50,51]. Mass fragments in the range C_{240} - C_{960} detected in mass spectra [52,53] have been attributed to giant Fullerenes but none has been isolated.

As expected from its oblate spheroidal shape (a molecular rugby ball), the C_{70} molecule has lower symmetry than the C_{60} molecule. There are also five different types of C atom sites and eight different types of C-C bond in the C_{70} molecule. The structural chemistry of C_{70} crystals is also much more complex than for C_{60} crystals. At high temperatures an fcc structure is found ($a_0 = 1501$ pm). As the temperature is progressively lowered there is a complex series of transitions to rhombohedral, hexagonal, and monoclinic phases [54]. Limited crystal structure studies on the higher Fullerenes, C_{72} - C_{84} , using scanning tunnelling microscopy [55,56] and micro-diffraction [57] show fcc structures in each case. An excellent monograph on Fullerenes and carbon nanotubes has been published recently [58].

2.5 Some properties of the crystalline forms of carbon

It is outside the scope of this Chapter to undertake a comprehensive review of structure-property relationships for the different forms of carbon. However, a limited comparison of properties is useful for illustrating the influence of chemical bonding upon the properties of diamond, graphite and Buckminsterfullerene, C_{60} , Table 4. Carbynes are omitted from the comparison since insufficient is known of their properties.

Table 4. Some properties of crystalline forms of carbon

Property	diamond ^a (cubic)	graphite ^b (hexagonal)	C_{60} ^c (fcc)
Bond length/pm	154	142, 335	146,144
Density/(g·cm ⁻³)	3.52	2.26	1.72
Bulk modulus/GPa	442	286	6.8
Young's modulus/GPa	1054	1020, 36.3	16
Melting point/K	4500	4450	1180
Thermal conductivity ^d	15000 ^e	2800, 5 ^f	0.4 ^g

a. data from [5]; b, data from [8], anisotropic properties: a-axis value, c-axis value.

c. data from [58]; d. W·m⁻¹K⁻¹; e, type IIa diamond at 80 K; f, maximum values at ~80K; g, value at 300 K.

Diamond and graphite have extended network structures, whereas C_{60} crystals are molecular solids in which the molecules are bound together by Van der Waals forces. This is reflected in the low melting temperature of C_{60} compared with diamond and graphite. The high volumetric density of strong sp^3 bonds in diamond leads to a very high value of Young's modulus. For similar reasons, the value of Young's modulus for graphite in the basal plane is comparable to that of diamond. This is exploited in the development of high modulus carbon fibers that have basal planes preferentially oriented along the fiber axis, see Chapters 4 and 5. However the weak Van der Waals bonding between basal planes in graphite results in a low value of Young's modulus perpendicular to the basal plane that is comparable to that found for C_{60} , Table 4. Similar arguments can be used to explain the range of bulk modulus values found for the three crystalline forms of carbon. Diamond has the highest known thermal conductivity of any material. The thermal conductivity of graphite is much higher than that of copper in the basal plane, but the value perpendicular to the basal plane is low. The thermal conductivity of C_{60} is very low.

3 The Phase and Transition Diagram for Carbon

Elucidation of the phase relationships between the different forms of carbon is a difficult field of study because of the very high temperatures and pressures that must be applied. However, the subject is one of great technical importance because of the need to understand methods for transforming graphite and disordered forms of carbon into diamond. The diagram has been revised and reviewed at regular intervals [59-61] and a simplified form of the most recent diagram for carbon [62] is in Fig. 5.

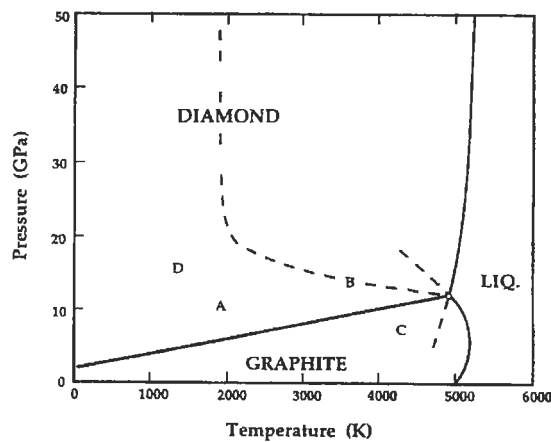


Fig. 5. The phase and transition diagram for carbon (simplified from [62]).

Graphite is thermodynamically more stable than diamond at low pressures and the reverse is true at high pressures; the standard free energy for the solid state transition from graphite to diamond is $+2.90 \text{ kJ}\cdot\text{mol}^{-1}$ at 25°C . The equilibrium phase boundary between graphite and diamond increases linearly with temperature and pressure from $\sim 1.7 \text{ GPa}$, 0 K to the diamond-graphite-liquid (d-g-l) triple point at $\sim 12 \text{ GPa}$, 5000 K . The melting line for diamond increases steeply with temperature above the d-g-l triple point. The melting line for graphite lies between the d-g-l triple point and the graphite-liquid-vapour triple point at $\sim 0.011 \text{ GPa}$, 5000 K and it passes through a temperature maximum at $\sim 5 \text{ GPa}$, 5200 K .

Transitions between the different forms of carbon are characterised by high activation energies so that metastable forms of carbon can persist for long periods under conditions where another form of carbon is thermodynamically stable. The stability of diamonds under ambient conditions is the most obvious example. The region marked 'A' on the diagram defines the pressure, temperature, (P,T) region for the catalysed transformation of graphite to diamond. This is not a solid-solid transformation since the graphite is dissolved in the catalyst and the solute carbon atoms re-precipitate as diamond [6]. The point 'B' defines the much higher threshold P,T values for rapid uncatalysed solid-solid transformation of graphite to diamond, while in the P,T region denoted as 'C', diamond is rapidly converted to graphite by a solid-solid transformation. Various other solid-solid transformations can be produced by appropriate P,T cycles, e.g., rapid shock compression/quench and flash heating. These are described by Bundy *et al*, [62] but are omitted from Fig. 6 for the sake of clarity. As an example, 'D' denotes the P,T, region where single crystal graphite is slowly converted to hexagonal diamond by application of a multiaxial stress of at least 12 GPa with the principal stress parallel to the graphite c axis.

Liquid carbon is formed at high temperatures and pressures. The balance of evidence, reviewed by Bundy *et al* [62], indicates that liquid carbon is a semi-metal and recent work does not support the earlier suggestion that there is an insulating liquid carbon phase. Carbynes have been proposed [63,64] as a thermodynamically stable phase at low pressures and high temperatures ($\sim 0.2 \text{ GPa}$, 5000 K) but this remains controversial (see Section 2.3). Some theoretical studies [65] indicate that a metallic form of carbon, BC8, is stable at very high pressures (above $\sim 1 \text{ TPa}$). However, other theoretical [66-68] studies suggest that cubic diamond is more stable than possible metallic forms up to $1.3\text{-}2.3 \text{ TPa}$. The high pressure-high temperature (up to $\sim 2 \text{ TPa}$, 14000 K) phase and transformation diagram for carbon has been reviewed by Sekine [69].

4 Carbon Films

The transformations between one form of carbon and another can be classified as follows:

- a) solid-solid transformations, as between diamond and graphite at points 'B' and 'C' in Fig. 5;
- b) solid-solute-solid transformations as in the catalysed transformation of graphite to diamond at 'A' in Fig. 5;
- c) solid-liquid-solid transformations; these occur when solid carbon phases are flash heated to temperatures above the melting line for the solid phase; some examples are described by Bundy *et al* [62];
- d) solid-gas-solid transformations in which the product form of carbon is produced by condensation of gaseous carbon species produced by evaporation from the reactant form.

The last process is important in the production of carbon films. Gaseous carbon species can be produced from solid carbon phases by electric arc-induced evaporation, by other forms of plasma-assisted and laser-induced evaporation, and also by electron and ion beam sputtering. Metastable carbon films can be produced from the gaseous phase, particularly under conditions of rapid cooling or quenching. Transformation of the metastable forms to the thermodynamically stable form (i.e., graphite under ambient conditions) is kinetically limited by the high activation energy for the transformation. Some carbynoid forms of carbon, e.g., Carbolite [24], may fall into this category, as do amorphous carbon films (see below).

4.1 Amorphous carbon films

As noted above, amorphous carbon films can be produced from carbon-containing gas phases (physical vapour deposition, PVD). They can also be produced from hydrocarbon-containing gases (chemical vapour deposition, CVD). Both PVD and CVD processes can be thermally-activated or can be plasma- and/or electric field-assisted processes (e.g., microwave assisted CVD and ion beam deposition). As a consequence a wide range of processes have been developed to form amorphous carbon films and a correspondingly complex nomenclature has evolved [70, 71].

Amorphous carbon films may be broadly classified as: (i) amorphous carbon films, a-C films, deposited from carbon-containing gases with low or zero hydrogen content [72] and (ii) hydrogenated carbon films, a-C:H films, formed from hydrocarbon-containing gases [73,74]. Both types of film contain different amounts of sp^2 and sp^3 bonded carbon. The amount of sp^2 bonded carbon can be estimated from X-ray absorption near edge spectroscopy,

XANES, and in a-C:H films the $sp^2:sp^3$ ratio can be measured directly using nmr spectroscopy [71].

The classification of amorphous carbon films according to carbon bond type and hydrogen content can be represented in a triangular diagram, Fig. 6 [e.g., 70]. The corners at the base of the triangle correspond to graphite (100% sp^2 carbon) and diamond (100% sp^3 carbon). The apex represents 100% H, but the upper limit for formation of solid films is defined by the tie line between the compositions of polyethene, $-(CH_2)_n-$, and polyethyne, $-(CH)_n-$.

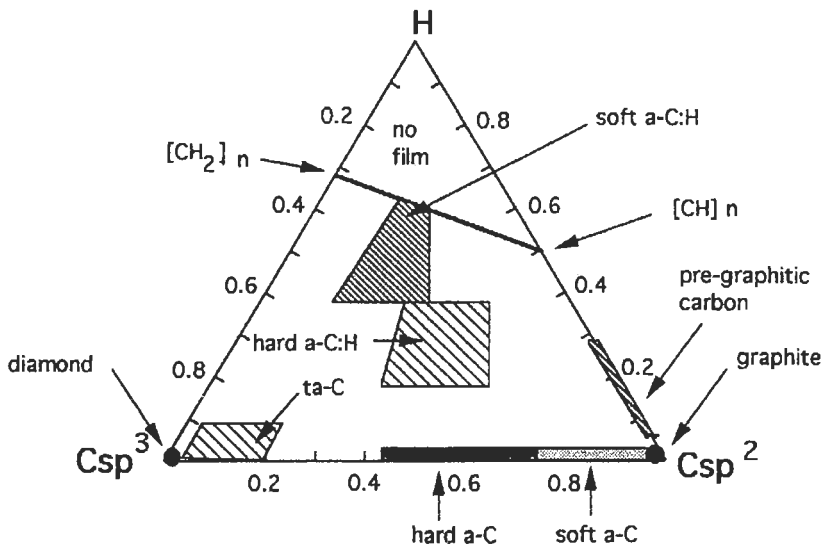


Fig. 6. Classification diagram for amorphous carbon films (e.g., [70]).

The majority of a-C films contain mainly sp^2 carbon, but the sp^3 carbon content can be varied over the range 5-55%; the hardness of the films increase with sp^3 content. The H content of a-C:H films can be varied over a wide range and the hardness of a-C:H films is inversely related to the hydrogen content. For both types of films a high sp^3 content is produced by ion beam deposition. Films with a very high sp^3 content (~80-90%) and a correspondingly high hardness have been called tetrahedrally-bonded amorphous carbon films, ta-C films [70]. Hard a-C:H films were called 'diamond-like carbon', DLC, and this term has been used as a generic name for all amorphous carbon films. Thus, as a general rule, hardness increases with sp^3 carbon content, as the proportion of 'diamond-like' carbon increases. Conversely, the films become softer as the sp^2 carbon content and/or the hydrogen content increases, reflecting the increasing content

of 'graphite-like' carbon or 'polymer-like' carbon respectively. Clearly, there is considerable scope for varying properties of the carbon films by careful control of processing parameters.

There is evidence for segregation of sp^2 and sp^3 bonded carbon in a-C and a-C:H films. The structure of a-C films with a high sp^2 carbon content is envisaged as clusters of warped graphitic domains bounded by sp^3 carbon [71]. In a-C:H films the extent of segregation of sp^2 and sp^3 carbon decreases with increasing carbon content. The sp^2 carbon content of both a-C and a-C:H films increases on heat-treatment in the range 300-600 °C, i.e., there is thermal transformation to graphitic structures; ta-C films are thermally stable to ~1000 °C.

4.2 CVD Diamond Films

The standard free energy changes for the process $C_{\text{gas}} \rightarrow \text{graphite}$ and $C_{\text{gas}} \rightarrow \text{diamond}$ are -671.26 and -668.36 kJ·mol⁻¹ at 298 K respectively. This comparison shows that the thermodynamic driving forces for forming graphite and diamond from the vapour phase are similar. Also, the work on amorphous carbon films shows that the proportions of sp^2 and sp^3 bonded carbon in films formed from the vapour phase can be varied by careful control of processing conditions, Fig. 6. Taken together these considerations suggest that it may be possible to produce films consisting entirely of sp^3 carbon, i.e., diamond films, by low pressure CVD processes. This objective was first realised in the early 1980s by Russian and Japanese workers [75-78] and since that time there have been considerable international efforts made to develop and improve the quality of CVD diamond films.

A large number of CVD diamond deposition technologies have emerged; these can be broadly classified as: thermal methods (e.g., hot filament methods) and plasma methods (direct current, radio frequency, and microwave) [79]. Film deposition rates range from less than 0.1 $\mu\text{m}\cdot\text{h}^{-1}$ to ~1 $\text{mm}\cdot\text{h}^{-1}$ depending upon the method used. The following are essential features of all methods.

- a) A carbon source gas that is rich in hydrogen but dilute (typically ~1.0 vol%) in the carbon-containing gas. The gas mixture may also contain molecular oxygen or oxygen-containing molecules, e.g., CO. Some experiments have also included halogen-containing gases.
- b) A means of activating the gas to produce free radicals, excited molecular species, or a plasma (see above).
- c) A temperature-controlled substrate (typically at 500-900 °C).

CVD diamond films can be deposited on a wide range of substrates (metals, semi-conductors, insulators; single crystals and polycrystalline solids, glassy and amorphous solids). Substrates can be abraded to facilitate nucleation of the diamond film.

The majority of CVD diamond films are polycrystalline, although single crystals can be grown. The chief impurities are non-diamond carbon at grain boundaries in polycrystalline films and hydrogen (from 300 to 2000 ppm). Other impurities can be avoided by using clean conditions and CVD diamond films with purities similar to natural type IIa diamonds can be grown. CVD diamond films contain a high concentration of dislocations and stresses associated with crystal defects and impurities that can adversely affect the adhesion of the film to the substrate. Emerging applications for CVD diamond films include heat sinks for electronic devices, optical windows and coatings, and wire drawing dies .

The mechanism of growth of diamond films is not understood in detail. A useful perspective is provided by the triangular CHO diagram of Bachmann *et al* [80], Fig. 7. This diagram shows that gas compositions for diamond growth for a very wide range of thermal and plasma CVD experiments are defined by a narrow triangular field denoted as the 'diamond domain'. Gas compositions richer in carbon than those in the diamond domain resulted in non-diamond carbon growth, e.g., pyrocarbon. No carbon films form if gas compositions are richer in hydrogen and oxygen than those in the diamond domain. Bachmann *et al* [80] were also able to link gas compositions in the diamond domain to the quality of the diamond films obtained. Subsequently, Prijaya *et al* [81] used thermochemical considerations to rationalise the Bachmann diagram. They showed that the diamond domain includes gas compositions that are close to the carbon solubility limit for the excitation temperatures used to activate the gas. Supersaturation occurs on cooling towards the substrate temperature, so creating conditions for carbon deposition.

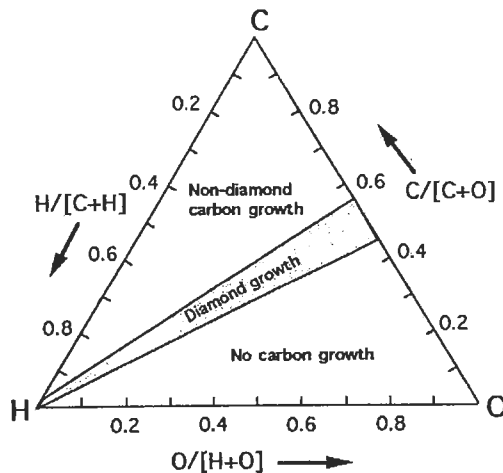


Fig. 7. Bachmann diagram for CVD diamond film growth (adapted from [80].)

An understanding of the mechanism of CVD diamond growth requires a knowledge of the thermodynamics and kinetics of a complex sequence of homogeneous gas phase reactions and surface reactions. A detailed kinetic treatment of diamond deposition has been developed by Frenklach and Wang [82]. Clearly, the processing window in which CVD diamond grows favours formation of sp^3 carbon rather than the more stable sp^2 carbon. The role of hydrogen is crucial and it appears that it both promotes growth and stabilises sp^3 carbon at the reaction interface and gasifies or selectively etches sp^2 carbon.

A new, low-pressure, plasma-assisted process for synthesising diamonds has been found by Roy *et al* [83,84]. An intimate mixture of various forms of carbon with one of many metals (e.g., Au, Ag, Fe, Cu, Ni) is exposed to a microwave plasma derived from pure hydrogen at temperatures ranging from 600-1000 °C. Roy *et al* postulate a mechanism in which a solid solution of atomic hydrogen and the metal, Me, facilitates dissolution of carbon to form molten droplets of $Me_x-C_y-H_z$. Diamonds nucleate at the surface of the droplets as the temperature is reduced.

5 Carbon Nanoparticles

In addition to diamond and amorphous films, nanostructural forms of carbon may also be formed from the vapour phase. Here, stabilisation is achieved by the formation of closed shell structures that obviate the need for surface heteroatoms to stabilise dangling bonds, as is the case for bulk crystals of diamond and graphite. The now-classical example of closed-shell stabilisation of carbon nanostructures is the formation of C_{60} molecules and other Fullerenes by electric arc evaporation of graphite [38] (Section 2.4).

5.1 Carbon nanotubes

Carbon nanotubes are discussed in more detail in Chapter 2 and so only a brief account of them is given here. In early studies of Fullerenes [85] it was observed that carbon nanotubes, also called carbon tubules, were formed at the cathode in the electric arc apparatus. Carbon nanotubes may be viewed as a cylindrical structure formed from graphene sheets and closed by Fullerenoid end-caps, Fig. 8A. There are single wall carbon nanotubes and multiwall carbon nanotubes, consisting of several nested co-axial single wall tubules. Typical dimensions of multiwall nanotubes are: outer diameter, 2-20 nm, inner diameter, 1-3 nm, lengths $\sim 1 \mu m$. The intertubular distance is 340 pm, which is slightly larger than the interplanar distance in graphite. Carbon nanotubes can also be grown from the vapour phase [86]. Whether produced from the arc method or from the vapour phase, carbon nanotubes are usually mixed with other forms of

carbon; however, methods for producing substantial quantities of carbon nanotubes in bundle form have been published [87, 88].

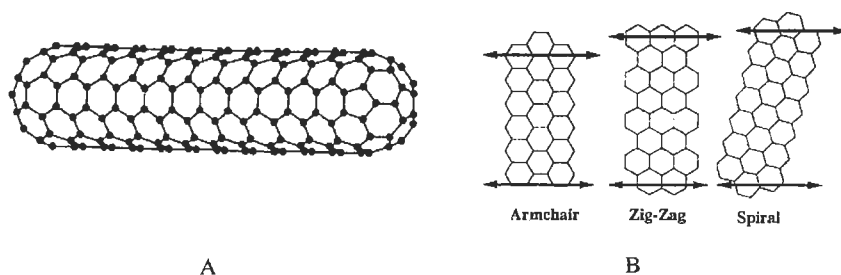


Fig. 8. A, Structure of a single wall nanotube; B, schematic illustration of arm-chair, zig-zag and spiral forms of single wall nanotubes; the arrows denote the tubule axis.

The structure of carbon nanotubes depends upon the orientation of the hexagons in the cylinder with respect to the tubule axis. The limiting orientations are zig-zag and arm chair forms, Fig. 8B. In between there are a number of chiral forms in which the carbon hexagons are oriented along a screw axis, Fig. 8B. The formal topology of these nanotube structures has been described [89]. Carbon nanotubes have attracted a lot of interest because they are essentially one-dimensional periodic structures with electronic properties (metallic or semi-conducting) that depend upon their diameter and chirality [90,91]. (Note. After this section was written a book devoted to carbon nanotubes has been published [92], see also [58].)

5.2 Carbon nanocones and multiwall carbon spheres

Carbon nanocones have been observed as free-standing structures among the products of the carbon arc method for producing Fullerenes and carbon nanotubes [93, 94]. The hemispherical end-caps on carbon nanotubes contain six pentagons, i.e., half of the number of pentagons in C_{60} . A conical nanostructure occurs when there are less than six pentagons in the end cap. For example, an end-cap containing one pentagon has a cone angle of 19.2° and for an end cap with three pentagons the cone angle is 60° . [94]. Carbon nanocones with geometries conforming to these rules have been observed using STM [94] and carbon nanotubes with conical end caps (cone angle $\sim 20^\circ$) have been observed using transmission electron microscopy, TEM [95]. Fig. 9A shows a molecular model for the apex of a carbon nanocone incorporating one pentagon and with a cone angle of 19.2° [94].

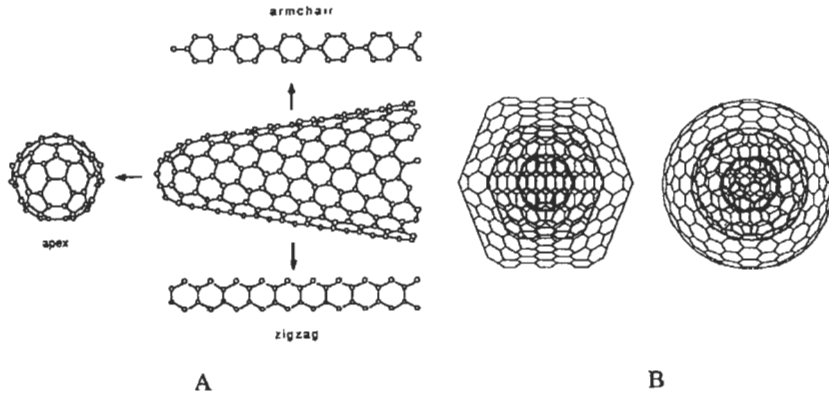


Fig. 9. A, Model for the apex of a carbon nanocone with a cone angle of 19.2° [94]; B, polyhedral and spherical forms of a multiwall carbon particle formed from C_{60} , C_{240} and C_{540} [98].

Ugarte has shown that faceted carbon particles with structures similar to graphitised carbon black are converted to spherical carbon shell structures under intense electron beam irradiation [96-98]. These have been called carbon onions or 'Buckyonions'. The shells have external diameters up to ~ 30 nm and hollow centres with diameters similar to that of the C_{60} molecule. Ugarte has suggested that the concentric carbon shells are formed about a central C_{60} molecule. Theoretical calculations of the stability of a concentric duplet formed by C_{240} about C_{60} yield a stabilisation energy of 14 MeV per C atom and an optimal interlayer spacing of 352 pm, close to the value for graphite [99]. Other calculations on the concentric structure formed by C_{540} about C_{240} show that a spherical conformation of the two layers is more stable than the analogous polyhedral duplet [98]. Fig. 9B shows a model for a triple wall carbon particle in spherical and polyhedral forms constructed from C_{60} , C_{240} , and C_{540} [98].

6 Engineering Carbons

6.1 Introduction

There are many applications for diamonds and related materials, e.g., diamond-like carbon films, and there are potential applications for Fullerenes and carbon nanotubes that have not yet been realised. However, the great majority of engineering carbons, including most of those described in this book, have graphitic microstructures or disordered graphitic microstructures. Also, most engineering carbon materials are derived from organic precursors by heat-treatment in inert atmospheres (carbonisation). A selection of technically-

important carbons obtained from solid, liquid and gaseous organic precursors is presented in Table 5.

Table 5. Precursors for engineering carbons

<i>Primary precursor</i>	<i>Secondary precursor</i>	<i>Example products</i>
Hydrocarbon gases		pyrocarbons, carbon blacks, vapour grown carbon fibres, matrix carbon ^a
Petroleum	petroleum pitch	delayed coke, calcined coke needle coke, carbon fibers, binder and matrix carbon ^a
	mesophase pitch	mesocarbon microbeads, carbon fibers
Coals	coal chars	semi-coke, calcined coke activated carbons
	coal tar pitch	premium cokes, carbon fibers, binder and matrix carbons ^a
	mesophase pitch	mesocarbon microbeads, carbon fibers
Polymers	polyacrylonitrile	PAN-based carbon fibers
	phenolic and furan resins	glassy carbons, binder and matrix carbons ^a
	polyimides	graphite films and monoliths
Biomass ^b		activated carbons

a. precursor for binder in polygranular carbons and graphites, precursor for matrix in carbon-carbon composites; b, especially wood and nutshells

During carbonisation the organic precursor is thermally degraded by heat-treatment at temperatures in the range ~450-1000 °C to form products that undergo either condensation or volatilisation reactions, the competition between these processes determining the carbon yield. Fig. 10 provides examples of the chemical processes that occur during carbonisation of the model precursor acenaphthylene [100]. Some of the volatilised products produced during carbonisation may be recovered to produce useful secondary precursors for carbons. For example, petroleum pitch and coal tar pitch are secondary precursors that are produced during carbonisation of petroleum and coal, Table 5. Carbons formed after heating up to ~1000 °C (primary carbonisation) are low-temperature carbons. They are usually disordered without any evidence for three-dimensional graphitic order and they may also retain significant concentrations of heteroelements, especially O, H, and S, and mineral matter.

It is beyond the scope of this chapter to review structure and bonding in each class of engineering carbons listed in Table 5. Instead, a generic description of microstructure and bonding in these materials will be attempted. The evolution in understanding of the structure of engineering carbons and graphites has followed the initial application of X-ray diffraction and subsequent application

of electron and neutron diffraction, and high resolution electron microscopy, supplemented by a wide range of other analytical techniques.

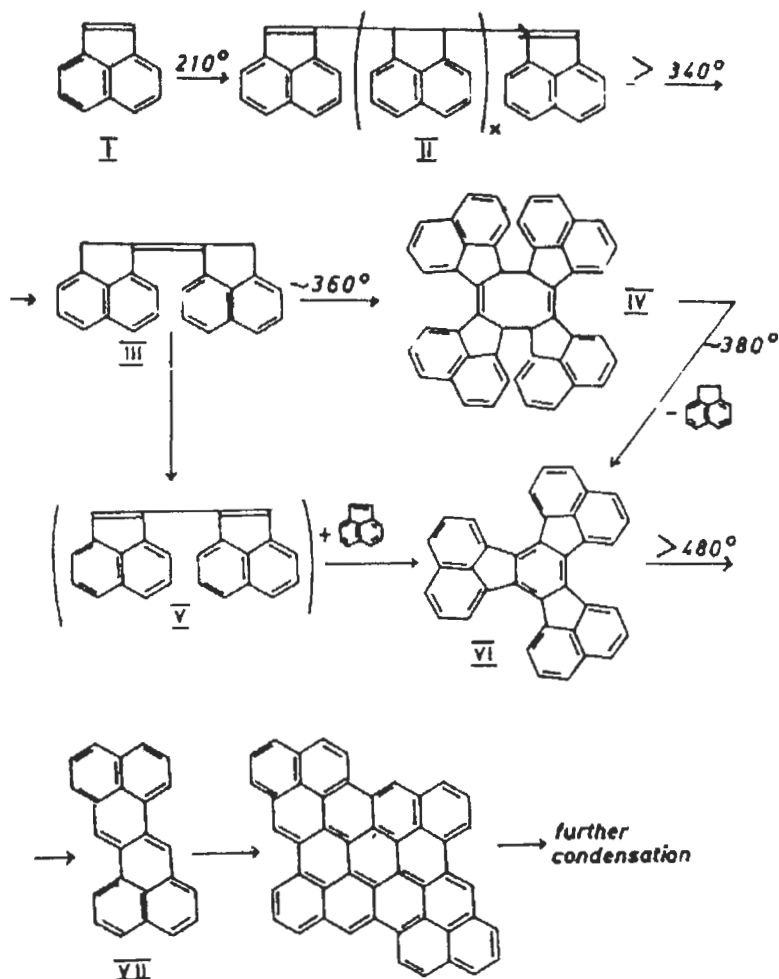


Fig. 10. Mechanism of carbonisation of acenaphthylene [100]. I, acenaphthylene; II, polyacenaphthylene; III, biacenaphthylidene; IV, fluorocyclene; V, dinaphthylenebutadiene; VI, decacyclene; VII, zethrene. Reprinted from [100] courtesy of Marcel Dekker Inc.

6.2 X-ray studies of engineering carbons

In the 1930s Hoffman and Wilm [101] found only (hk0) graphite reflections in an x-ray diffraction study of a carbon black. The absence of graphitic (hkl) reflections led them to propose a structure consisting of graphitic carbon layer

planes in parallel array but without any three-dimensional order. They also noted from the position of the [002] line that the interlayer spacing, d , was greater than that for the graphite crystal ($d = 0.3354$ nm). This early concept of the microstructure of an engineering carbon forms the basis of the more refined models that have been developed in subsequent years. Biscoe and Warren [102] coined the term 'turbostratic' to describe a parallel stack of carbon layer planes with random translation about the a -axis and rotation about the c -axis. Turbostratic carbon is therefore without three-dimensional order and the turbostratic value of the interlayer spacing d , 0.344 nm, is greater than that for graphite. The dimensions of the turbostratic stack in the a and c crystallographic directions are characterised from the pronounced X-ray line broadening by the width and height, L_a and L_c respectively, as well as the interlayer spacing, d . Values found by Hoffmann and Wilm [101] for a range of technical carbons ranged from $L_a = 2.1$ -12 nm and $L_c = 0.9$ -18 nm; the latter values imply stacks containing from 3 to about 50 layer planes. The broadening of X-ray lines is also influenced by imperfections in the carbon layer planes so that the dimensions of stacks, particularly the width, may be larger than is indicated by L_a and L_c values. High resolution electron microscopic studies lend some support to this view (see Section 6.4).

A notable advance was made by Franklin [103] in an X-ray diffraction study of polymer chars. She found that for a low-temperature PVDC char that 65% was in the form of turbostratic carbon and the remainder was an unspecified form of disordered carbon. Subsequently, [104] Franklin classified low temperature carbons into graphitising carbons which develop three-dimensional graphitic order on heat-treatment above 2000 °C and non-graphitising carbons which do not. The structure of graphitising carbons was envisaged an array of turbostratic carbon units that were oriented in near-parallel (pre-graphitic) array; non-graphitising carbons contained turbostratic units in random array that were cross-linked by disorganised carbon, Fig. 11. Franklin's classification is now recognised as oversimplified, since there is a near-continuum from graphitising to non-graphitising microstructures. Nevertheless, the concepts of graphitising and non-graphitising carbons are useful and they have been retained.

Amorphous carbon films of the type a-C and a-C:H produced by physical or chemical vapour deposition from the gas phase contain varying amounts of sp^2 and sp^3 bonded carbon atoms, see section 4.1. The possibility of both sp^2 and sp^3 bonded atoms in carbons produced by carbonisation of organic precursors has been considered by a number of workers. The presence of sp^3 bonded carbon, particularly in the disorganised carbon that links the carbon layer planes in non-graphitising carbons, seems reasonable in principle. In an X-ray study Noda and co-workers [105] obtained radial distribution functions for a glassy carbon and proposed that some sp^3 carbon atoms were present. However, a later high resolution X-ray study of a high temperature glassy carbon by Wignall and

Pings [106], and a neutron diffraction study by Mildner and Carpenter [107], both concluded that there is no clear evidence for sp^3 carbon and that the radial distribution functions can be satisfactorily indexed to a hexagonal arrays of carbon atoms. A similar conclusion was reached in a recent neutron diffraction study of activated carbons by Gardner *et al* [108].

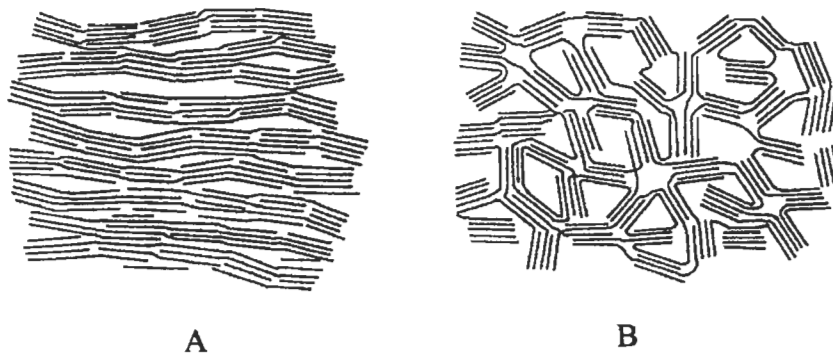


Fig. 11. Schematic models for the structure of: A, graphitising carbons, and B, non-graphitising carbons [104].

6.3 *The carbonaceous mesophase*

It is now known that the development of graphitising carbons depends upon the formation of a liquid crystal phase called the carbonaceous mesophase during a fluid stage in carbonisation. The mesophase appears initially as small, optically anisotropic spheres growing out of an optically isotropic fluid pitch. The mesophase spheres contain polynuclear aromatic hydrocarbons (molecular weight ~ 2000) in parallel arrays [109], Figs. 12A, 12Ba). As carbonisation proceeds, higher molecular weight hydrocarbons are formed by condensation and these are incorporated into the mesophase. With growth and coalescence of the mesophase, there is eventually a phase inversion when the coalesced mesophase becomes the dominant phase, Fig. 12Bb). Condensation and polymerisation proceed as the carbonisation temperature is raised until eventually the material solidifies into a semi-coke, Fig. 12Bc). The relics of the coalesced mesophase in the semi-coke have complex anisotropic structures that contains disclinations that can be used to deduce their molecular orientation [110]. The essential point is that the coalesced mesophase generates a pre-graphitic structure that can be developed into graphite on high temperature heat-treatment. The carbonisation of polyacenaphthylene, Fig. 10, is an example of a process that involves the formation of mesophase. By contrast, the carbonisation of precursors of non-graphitising carbons does not involve the formation of mesophase. Either, the non-graphitising precursor is extensively cross-linked, as in the case of phenolic resins, or cross-linking reactions occur in the early stages of carbonisation.

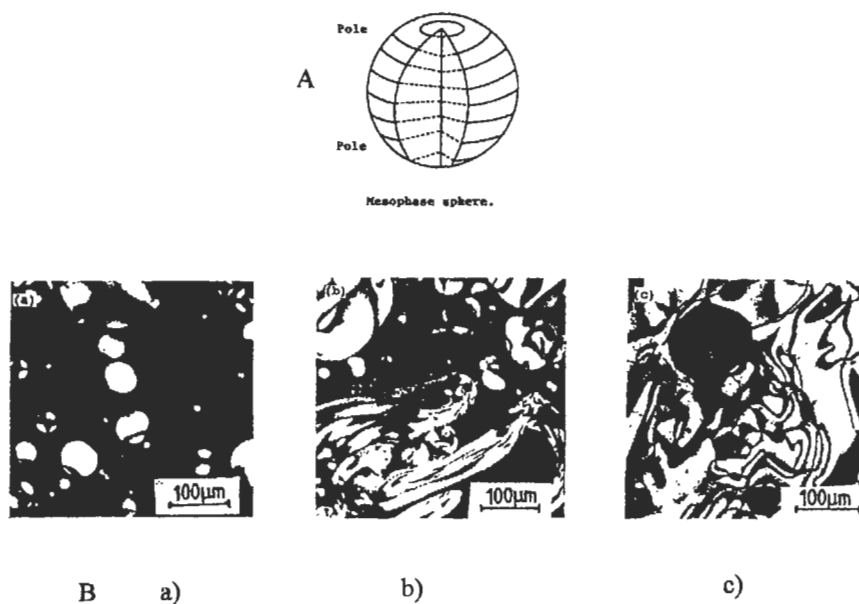


Fig. 12. A, Schematic representation of parallel arrays of polynuclear aromatic hydrocarbon molecules in a mesophase sphere. B, a) isolated mesophase spheres in an isotropic fluid pitch matrix; b) coalescence of mesophase; c) structure of semi-coke after phase inversion and solidification.

Carbon layer planes in low temperature carbons are highly defective and they have heteroelements bound to their edges. Heat treatment of graphitising carbons brings about an improvement in microstructural order, elimination of heteroelements and eventually the development of a three-dimensional graphite crystal structure. Abundant X-ray studies of a wide range of graphitising carbons, Fig. 13, show that the stack width, L_a , for graphitising carbons increases almost exponentially with heat-treatment temperature, HTT, from ~ 5 nm at HTT ~ 1500 °C to $\sim 35-65$ nm at HTT = 2800 °C; the stack thickness, L_c , increases in a similar fashion from $\sim 2-6$ nm at HTT ~ 1400 °C to $\sim 15-60$ nm at HTT = 3000 °C [112]. At the same time the interlayer spacing d decreases from the turbostratic value, 0.344 nm, towards the value for graphite, 0.335 nm. By contrast, the stack dimensions of non-graphitising carbons increase only slightly with HTT accompanied by small decreases in interlayer spacings [104, 113].

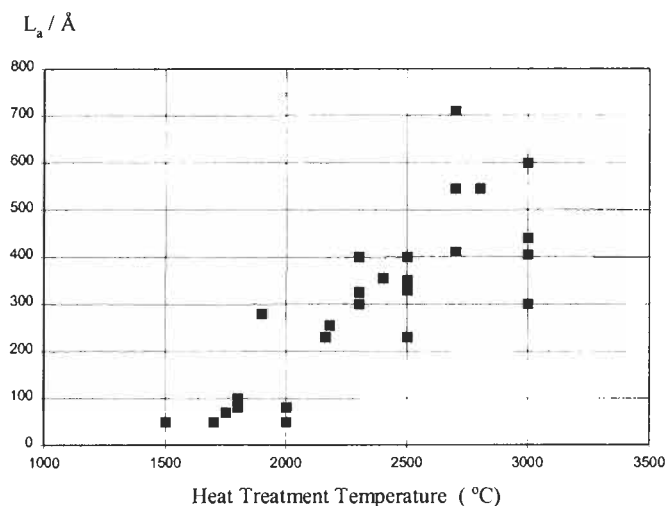


Fig. 13. Increase in stack width parameter, L_a , with heat treatment temperature, HTT, for some graphitising cokes, [Adapted from 112].

6.4. Electron microscopical studies of engineering carbons

The microstructural model for disordered carbons has been greatly elaborated following the application of high resolution transmission electron microscopy. The early work by Ban [114] and Jenkins *et al* [115] lead to the development of the ribbon model for glassy carbon, Fig. 14, which envisages the non-graphitic structure as a network of twisted and folded carbon layer planes. Interestingly, this microstructural model for carbons was perhaps the first to depart from the flat graphite layer model and introduce concepts of curvature that can now be rationalised using microstructural elements borrowed from Fullerenes and nanotubes. However, the Jenkins model is essentially intuitive and later workers [116] have cautioned against the use of such simplistic readings of electron microscopical images.

Perhaps the most elaborate and extensive electron microscopical studies of carbonaceous materials were carried out by Agnes Oberlin and her group [116] who showed that a great deal of microstructural information on carbons can be obtained using a combination of selected area diffraction and dark field and light field imaging. For all carbons, Oberlin defines a basic structural unit, BSU, as a parallel stack of two to four layer planes each containing less than 10-20 aromatic rings. A related concept is local molecular ordering, LMO, which consists of an array of BSU with a near-common orientation, Fig. 15. In non-

graphitising carbons there is a high degree of misorientation of BSU so that LMO is small or non-existent, whereas in graphitising carbons the misorientation between adjacent BSU is small and consequently there is extensive LMO extending to the order of microns.

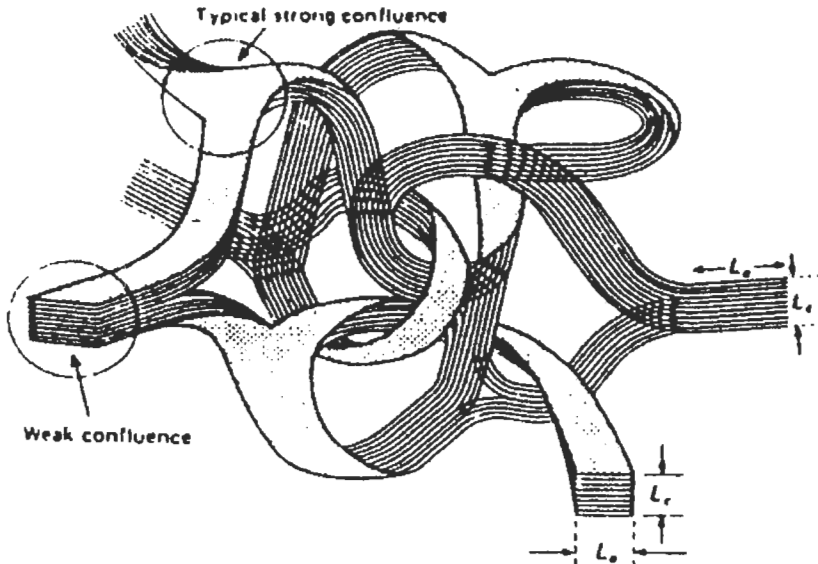


Fig. 14. The ribbon model for the microstructure of a glassy carbon [115].

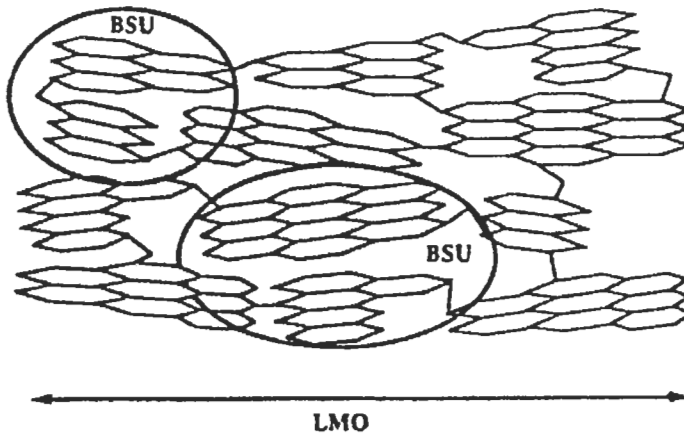


Fig. 15. A schematic model illustrating the concepts of basic structural unit, BSU, and local molecular ordering, LMO [c.g., 116].

The Oberlin group have elaborated the mechanism of graphitisation as shown in Fig. 16. Earlier work on graphitisation mechanisms has been reviewed on several occasions [117-119]. In stage 1, up to $\text{HTT} = 1000\text{ }^\circ\text{C}$, the carbons contains flat BSU with a high degree of misorientation. Between 1000 and $1500\text{ }^\circ\text{C}$ (stage 2) the BSU grow thicker and columnar arrays of BSU (like stacks of coins) develop with misoriented BSU trapped between them. In stage 3, between $\text{HTT} = 1500$ to $2000\text{ }^\circ\text{C}$ the misorientation between the columns of BSU decreases, so that extensive, but distorted, carbon layer planes can form by coalescence of adjacent BSU. The final stage, above $\text{HTT} = 2000\text{ }^\circ\text{C}$, involves the annealing out of defects within the distorted carbon layer planes, so that perfect flat carbon layer planes are produced that allow the formation and growth of graphite crystallites.

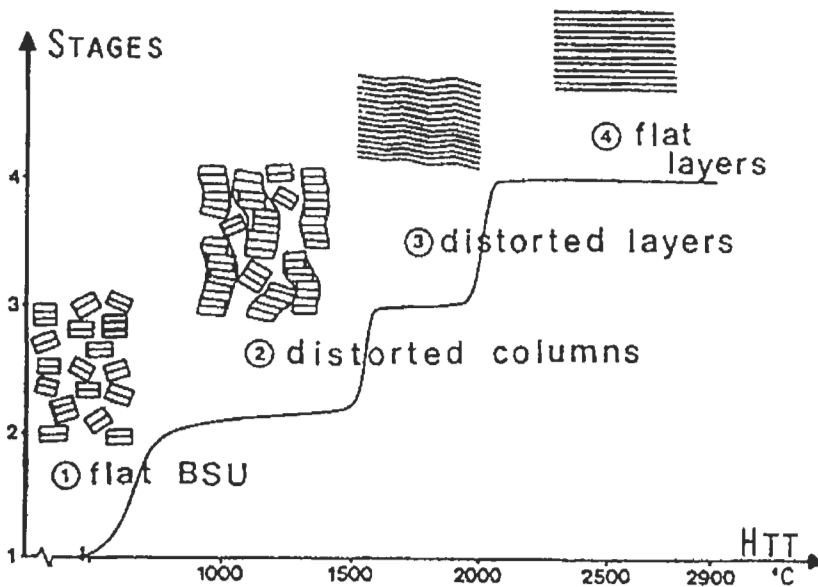


Fig. 16. The mechanism of graphitisation (Reprinted from [116] by courtesy of Marcel Dekker Inc.

7 Concluding Remarks

The majority of engineering carbon materials have more-or-less disordered microstructures that are based on that of graphite and in which, therefore, sp^2 carbon bonding is dominant. The degree of graphitic order varies widely from very low values for glassy carbons derived from polymer resins [113] to highly graphitic microstructures, e.g., in HOPG [14]. Engineering carbons are also

manufactured in an astounding range of physical forms: powders, granules, beads, films, foams, fibers, textiles, composites, and monoliths, and in sizes that range from sub-micron carbon aerogels to arc furnace electrodes with dimensions of several metres. The steady development of graphitic carbon materials over many years has been complemented by recent developments in amorphous carbon films with mixed sp^2 and sp^3 bonding and, especially rapid developments in CVD diamond films with sp^3 carbon bonds. However, the discoveries of Fullerenes and related materials represent the most exciting new developments in carbon science. Indeed, these discoveries have resulted in a paradigm shift in our perception of chemical bonding and microstructure in carbon materials and have helped to stimulate further advances in various areas of carbon science and technology that are discussed elsewhere in this book.

8 Acknowledgements

I thank Marcel Dekker Inc. for permission to reprint Figures 10 and 16.

9 References

1. Atkins, P.W., *Physical Chemistry*, 5th Edition, Oxford University Press, Oxford, 1994, Chapter 14.
2. *Handbook of Chemistry and Physics*, 74th edition, ed., D.R. Lide, CRC Press, London, 1994, pp 9-2 to 9-5.
3. Davies, G., *Diamond*, Hilger, Bristol, 1984.
4. Wilks, J. and Wilks, E., *Properties and Applications of Diamonds*, Butterworth-Heinemann, Oxford, 1991.
5. *The Properties of Natural and Synthetic Diamond*, ed. J.E. Field, Academic Press, London, 1992.
6. Bundy, F.P., Hall, H.T., Strong, H.M. and Wenthof, R.H., *Nature (London)*, 1956, **176**, 51.
7. Spytin, B.V., Boulov, L.L. and Deraguin, B.V., *J. Cryst. Growth*, 1981, **52**, 219.
8. Kelly, B.T. *Physics of Graphite*, Applied Science Publishers, London, 1981.
9. Hull, A.W., *Phys. Rev.*, 1917, **10**, 661.
10. Bernal, J.D., *Proc. Roy. Soc.*, 1924, **A106**, 749.
11. Hassel, O. and Mark, H., *Z. Phys.*, 1924, **25**, 317.
12. Bacon, G., *Acta Cryst.*, 1958, **3**, 320.
13. Tománek, D., Louie, S.G., Mamin, H.J., Abraham, D.W., Thomson, R.E., Ganz, E. and Clarke, J., *Phys. Rev. B*, 1987, **35**, 7790.
14. Moore, A.W., In *Chemistry and Physics of Carbon*, Vol. 17, ed., P.L. Walker Jr. and P.A. Thrower, M. Dekker, New York, 1981, pp 233-286.
15. Hishiyama, Y., Yasuda, S., Yoshida, A. and Inagaki, M., *J. Mater. Sci.*, 1988, **23**, 3272.

16. Colcs, B.F., Hitchcock, P.B. and Walton, D.R.M., *J. Chem. Soc. Dalton*, 1975, **5**, 442.
17. El Goreisy, A. and Donnay, G. , *Science*, 1968, **161**, 363.
18. Kasatochkin, V.I., Sladkov, A.M., Kudryatsev, Yu.P., Popov, N.M. and Korshak, V.V., *Dokl. Chem.*, 1967, **177**, 1031.
19. Kasatochkin, V.I., Korshak, V.V., Kudryatsev, Yu. P., Sladkov, A.M. and Sterenberg, L.E., *Carbon*, 1973, **11**, 70.
20. Whittaker, A.G. and Wolten, G.M. , *Science*, 1972, **178**, 54.
21. Whittaker, A.G., *Carbon*, 1979, **17**, 21.
22. Whittaker, A.G., Neudorffer, M.E. and Watts, E.J., *Carbon*, 1983, **21**, 597.
23. Heimann, R.B., Kleiman, J. and Salansky, N.M. , *Carbon*, 1984, **22**, 147.
24. Tanuma, S.I. and Palnichenko, A., *J. Mater. Res.*, 1995, **10**, 1120.
25. Diederich, F., Rubin, Y., Knobler, C.B., Whetten, R.L., Schriver, K.F., Houk, K.N. and Li, Y., *Science*, 1989, **245**, 1088.
26. Diederich, F., *Science*, 1994, **369**, 199.
27. Smith, P.P.K. and Busek, P.R., *Science*, 1982, **216**, 984.
28. Whittaker, A.G., *Science*, 1985, **229**, 485.
29. Smith, P.P.K. and Busek, P.R., *Science*, 1985, **229**, 486.
30. Pillinger, C.T., *Phil. Trans. Roy. Soc. London A*, 1993, **343**, 73.
31. Reitseijer, F.J.M., *Meteoritics*, 1993, **28**, 242.
32. Lagow, R.J., Kampa, J.L., Wei, H-C., Battle, S.L., Genge, J.W., Laude, D.A., Harper, C.J., Bau, R., Stevens, R.C., Haw, J.F., and Munson, E., *Science*, 1995, **267**, 362.
33. Eastmond, R., Johnston, T.R. and Walton, D.R.M., *Tetrahedron*, 1972, **28**, 4601.
34. Jansta. J. and Dousek, F.P., *Carbon*, 1980, **18**, 433.
35. Kavan, L. and Kastner, J., *Carbon*, 1994, **32**, 1533.
36. Kudryatsev, Yu.P., Evsyukov, S., Guseva, M., Babaev, V. and Khvostov, V., In *Chemistry and Physics of Carbon*, ed. P.A. Thrower, Vol. 25, M. Dekker, New York, 1997, pp 1-69.
37. Kroto, H.W., Heath, J.R., O'Brien, S.C., Curl, R.F. and Smalley, R.E., *Nature (London)* 1985, **318**, 162.
38. Kratschmer, W., Lamb, L.D., Fostiropoulos, K., and Huffman, D.R., *Nature (London)* 1990, **347**, 354.
39. Hawkins, J.M., Mayer, A., Lewis, T.A., Loren, S. and Hollander, F.J., *Science*, 1991, **252**, 312.
40. Kikuchi, K., Susuki, S., Saito, K., Shiramura, H., Ikemoto, I., Ichiba, Y., Zhakidov, A., Ugawa, A., Imaeda, K., Inokuchi, H. and Yashuki, K., *Physica C*, 1991, **185**, 415.
41. Saito, Y., Susuki, N., Shinohara, H., Hayashi, T. and Tomita, M., *Ultramicroscopy*, 1992, **41**, 1.
42. Taylor, R., Hare, J.P., Abdul-Sada, A.K. and Kroto, H.W., *J. Chem. Soc. Commun.*, 1990, 1423.
43. Yannoni, C.S., Johnson, R.D., Meijer, G., Bethune, D.S. and Salem, J.R., *J. Phys. Chem.*, 1991, **95**, 9.

44. Tycko, R., Haddon, R.C., Dabbagh, G., Glarum, S.H., Douglas, D.C. and Mujcsce, A.M., *J. Phys. Chem.*, 1991, **95**, 518.
45. David, W.I.F., Ibberson, R.M., Matthewman, J.C., Prassides, K., Dennis, T.J.S., Hare, J.P., Kroto, H.W., Taylor, R. and Walton, D.R.M., *Nature (London)*, 1991, **353**, 147.
46. David, W.I.F., Ibberson, R.M. and Matsuo, T., *Proc. Roy. Soc. (London) A* **442**, 1993, 129.
47. Prassides, K., Kroto, H.W., Taylor, R., Walton, D.R.M., David, W.I.F., Tomkinson, J., Haddon, R.C., Rosseinsky, M.J. and Muphy, D.W., *Carbon*, 1992, **30**, 1277.
48. Kroto, H.W., *Nature (London)* 1987, **329**, 529.
49. Schmalz, T.G., Seitz, W.A., Klein, D.J. and Ilite, G.E. *J. Amer. Chem. Soc.*, 1988, **110**, 113.
50. Diederich F. and Whetten R.L. *Acc. Chem. Res.*, 1992, **25**, 119.
51. Saito, S., Sawada, S.I., Hamada, N. and Oshiyama, A., *Mater. Sci. Eng.*, 1993, **B19**, 105.
52. Smalley, R.E., *Acc. Chem. Res.* 1992, **25**, 98.
53. Holmes-Parker, D., Chatterjee, K., Wurcz, P., Lykke, K.R., Pellin, M.J., Stock, L.M. and Hemminger, J.C., *Carbon*, 1992, **30**, 1167.
54. Verheijen, M.A., Meckes, H., Meijer, G., Bennema, P., de Boer, J.L., van Smaalen, S., Tendeloo, G.V., Amelinckx, S., Muto, S. and van Landuyt, J. *Chem. Phys.*, 1992, **166**, 287.
55. Li, Y.Z., Patrin, J.C., Chandler, M., Weaver, J.H., Kikuchi, K. and Achiba, Y., *Phys. Rev. B*, 1993, **47**, 10867.
56. Wang, X.D., Ihashizume, T., Shinohara, H., Saito, Y., Nishina, Y. and Sakurai, T., *Phys. Rev. B*, 1993, **47**, 15923.
57. Armbruster, J.F., Romberg, H.A., Schweiss, P., Adelman, P., Knupfer, M., Fink, J., Michel, R.H., Rockenberger, J., Hennrich, F., Schreiber, H. and Kappes, M.M., *Z. Phys. B*, 1994, **95**, 469.
58. Dresselhaus, M.S., Dresselhaus, G. and Eklund, P.C., *Science of Fullerenes and Carbon Nanotubes*, 1996, Academic Press, San Diego.
59. Bundy, F.P., *J. Geophys. Res.*, 1980, **85**, 6930.
60. Gustafson, P., *Carbon*, 1986, **24**, 169.
61. Bundy, F.P., *Physica*, 1989, **A156**, 169.
62. Bundy, F.P., Bassett, W.A., Weather, M.S., Hemley, R.J., Mao, H.K. and Goncharov, A.F., *Carbon*, 1996, **34**, 141.
63. Deraguin, B.V., Fedoseev, D.V., Varnin, V.P. and Vnukov, S.P., *Nature (London)* 1977, **269**, 398.
64. Whittaker, A.G., *Science*, 1978, **200**, 763.
65. Young, D.A. and Grover, R., In *Shock Waves in Condensed Matter*, ed. S.C. Schmidt and N.C. Holmes, North Holland, Amsterdam, 1988, p. 131.
66. Yin, M.T. and Cohen, M.L., *Phys. Rev. Lett.*, 1983, **50**, 2006.
67. Biswas, R., Martin, R.M., Needs, R.J. and Nielsen, O.H., *Phys. Rev. B.*, 1984, **30**, 3210.

68. Biswas, R., Martin, R.M., Needs, R.J. and Nielson, O.H., *Phys. Rev. B.*, 1987, **35**, 9559.
69. Sekine, T., *Carbon*, 1993, **31**, 227.
70. Bachmann, P.K., In *Ullman's Encyclopaedia of Industrial Chemistry*, 1996, Vol. A26, pp 720-725.
71. Robertson, J., *Adv. Phys.*, 1986, **35**, 317.
72. McLintock, I.S. and Orr, J.C., In *Chemistry and Physics of Carbon*, Vol. 11, ed. P.L. Walker Jr., M. Dekker, New York, 1973.
73. Anderson, D.A., *Phil. Mag.*, 1977, **35**, 17.
74. Weissmantel, C., Bewilogua, K., Breuer, K., Dietrich, D., Ebersach, U., Erler, H.J., Rau, B. and Reissen, G., *Thin Solid Films*, 1982, **96**, 31.
75. Spytysin, B.V., Bouilov, L.L. and Derjaguin, B.V., *J. Cryst. Growth*, 1981, **52**, 219.
76. Matsumoto, S., Sato, Y., Kamo, M. and Setaka, N., *Jap. J. Appl. Phys.*, 1982, **21**, L183-185.
77. Kamo, M., Sato, Y., Matsumoto, S., Setaka, N., *J. Cryst. Growth*, 1983, **62**, 642.
78. Y. Sato and M. Kamo, In *The Properties of Natural and Synthetic Diamond*, ed. J.E. Field, Academic Press, London, 1992, pp. 423-469.
79. Bachmann, P.K. and van Enkevort, W., *Diamond Relat. Mater.*, 1992, **1**, 1021.
80. Bachmann, P.K., Leers, D and Lydtin, II., *Diamond Relat Mater*, 1991, **1**, 1.
81. Prijaya, N.A., Angus, J.C. and Bachmann, P.K., *Diamond Relat Mater.*, 1993, **3**, 129.
82. Frenklach, M. and Wang, H., *Phys. Rev. B.*, 1991, **43**, 1520.
83. Roy, R., Dewan, H.S. and Ravindranathan, P., *J. Mater. Chem.*, 1993, **3**, 685.
84. Roy, R., Cherian, K.A., Cheng, J.P., Badzian, A., Langlade, C., Dewan, II. and Drawl, W., *Innov. Mater. Res.*, 1996, **1**, 65.
85. Ijima, S., *Nature (London)*, 1991, **354**, 56.
86. Endo, N., Takeuchi, K., Igarashi, S., Kobori, K., Shiraishi, M. and Kroto, II.W., *J. Phys. Chem. Solid*, 1993, **54**, 1841.
87. Ajayan, P.M. and Ijima, S., *Nature (London)*, 1992, **358**, 23.
88. Dresselhaus, M.S., *Nature (London)*, 1992, **358**, 195.
89. Dresselhaus, M.S., Dresselhaus, G. and Saito, R., *Phys. Rev. B.*, 1992, **45**, 6234.
90. Hamada, N., Sawada, S.I. and Oshiyama, A., *Phys. Rev. Lett.*, 1992, **68**, 1579.
91. White, C.T., Robertson, D.H. and Mintmire, J.W., *Phys. Rev. B.*, 1993, **47**, 5485.
92. *Carbon Nanotubes: Preparation and Properties*, ed. T.W. Ebbesen, 1997, CRC Press, Boca Raton.
93. Balaban, A.T., Klein, D.J. and Liu, X., *Carbon*, 1994, **32**, 357.
94. Sattler, K., *Carbon*, 1995, **33**, 915.
95. Ijima, S., Ichihashi, T. and Ando, Y., *Nature (London)*, 1992, **356**, 776.
96. Ugarte, D., *Nature (London)*, 1992, **359**, 707.
97. Ugarte, D., *Chem. Phys. Lett.*, 1993, **207**, 473.
98. Ugarte, D., *Carbon*, 1995, **33**, 989.
99. Yosida, Y., *Fullerene Sci. Tech.*, 1993, **1**, 55.

100. Fitzer, E., Mueller, K. and Schacffer, W., In *Chemistry and Physics of Carbon*, Vol. 7, ed., P.L. Walker Jr., M. Dekker, New York, 1971, p. 237.
101. Hoffman, U. and Wilm, D., *Z. Elektrochem.*, 1936, **42**, 504.
102. Biscoe, J. and Warren, B.E., *J. Appl. Phys.*, 1942, **13**, 364.
103. Franklin, R.E., *Acta. Cryst.*, 1950, **3**, 107.
104. Franklin, R.E., *Proc. Roy. Soc.*, 1951, **A209**, 196.
105. Noda, T., Inagaki, M. and Yamada, Y.J., *J. Noncryst. Solid*, 1969, **1**, 285.
106. Wignall, G.D. and Pings, C.J., *Carbon*, 1974, **12**, 51.
107. Mildner, D.F.R. and Carpenter, J.M., *J. Noncryst. Solid*, 1982, **47**, 391.
108. Gardner, M.A., Dore, J.C., North, A.N., Cazorla-Amoros, D., Salinas-Martinez de Lecea, C. and Bellissent Funcl, M-C., *Carbon*, 1996, **34**, 857.
109. Brooks, J.D. and Taylor, G.H., in *Chemistry and Physics of Carbon*, ed. P.L. Walker, Jr., Vol. 4, 1968, M. Dekker, New York, p. 243.
110. White, J.I. and Zimmer, J.E. in *Surface and Defect Properties of Solids*, ed. M.W. Roberts and J.M. Thomas, Vol. 5, 1976, Chemical Society, London, p 16.
111. Jackson, W.M. and Conley, W.T., *J. Appl. Polym. Sci.*, 1964, **8**, 2163.
112. Hutcheon, J.M., In *Modern Aspects of Graphite Technology*, ed. L.C.F. Blackman, 1970, Academic Press, London, pp 2-48.
113. Jenkins, G.M. and Kawamura, K., *Polymeric Carbons: Carbon Fibre, Glass, and Char*, Cambridge University Press, Cambridge, 1976.
114. Ban, L.L., In *Surface and Defect Properties of Solids*, ed. M.W. Roberts and J.M. Thomas, Vol. 1, 1972, Chemical Society, London, p. 54.
115. Jenkins, G.M., Kawamura, K. and Ban, L.L., *Proc. Roy. Soc. (London)*, 1972, **A327**, 501.
116. Oberlin, A., In *Chemistry and Physics of Carbon*, Vol. 22, 1989, ed. P.A. Thrower, M. Dekker, New York, pp 1-144.
117. Maire, J. and Mering, J., In *Chemistry and Physics of Carbon*, Vol. 6, 1970, ed. P.L. Walker Jr., M. Dekker, New York, p. 125.
118. Fischbach, D., In *Chemistry and Physics of Carbon*, Vol. 7, 1971, ed. P.L. Walker Jr., M. Dekker, New York, p. 1.
119. Pacault, A., In *Chemistry and Physics of Carbon*, Vol. 7, 1971, ed. P.L. Walker Jr., M. Dekker, New York, p. 107.

CHAPTER 2

Fullerenes and Nanotubes

M.S. DRESSELHAUS

*Department of Electrical Engineering and Computer Science
and Department of Physics
Massachusetts Institute of Technology,
Cambridge, Massachusetts 02139, USA*

P.C. EKLUND

*Department of Physics and Astronomy and
Center for Applied Energy Research
University of Kentucky, Lexington, KY. 40506, USA*

G. DRESSELHAUS

*Francis Bitter Magnet Laboratory
Massachusetts Institute of Technology,
Cambridge, Massachusetts, 02139, USA*

The structure-property relations of fullerenes, fullerene-derived solids, and carbon nanotubes are reviewed in the context of advanced technologies for carbon-based materials. The synthesis, structure and electronic properties of fullerene solids are then considered, and modifications to their structure and properties through doping with various charge transfer agents are reviewed. Brief comments are included on potential applications of this unique family of new materials.

1 Introduction

Fullerenes and carbon nanotubes are unique, respectively, in the larger family of carbon-based materials as interrelated prototypes for zero-dimensional quantum dots and one-dimensional quantum wires. The fullerene molecule is the fundamental building block of the crystalline phase, and through doping and chemical reactions, forms the basis of a large family of materials, many having especially interesting properties. Likewise, carbon nanotubes, which are capped at each end by half of a fullerene, have aroused great interest in the

research community because of their exotic electrical and mechanical properties. The unique properties of fullerenes and carbon nanotubes described in this chapter are also expected to be of interest for practical applications.

In 1985, the existence of a stable molecule or cluster with 60 carbon atoms (designated as C_{60}) was established experimentally by mass spectrographic analysis [1], and it was conjectured that the C_{60} cluster was a molecule with icosahedral symmetry. The name of “fullerene” was given to the family of closed cage carbon molecules by Kroto and Smalley [1] because of their resemblance to the geodesic domes designed and built by R. Buckminster Fuller [2]. The name “buckminsterfullerene” or simply “buckyball” was given specifically to the C_{60} molecule. In the early gas phase work, the fullerene molecules were produced by the laser vaporization of carbon from a graphite target in a pulsed jet of helium [1, 3].

In the fall of 1990, a new crystalline form of carbon, based on C_{60} , was synthesized for the first time by Krätschmer, Huffman and co-workers [4]. Their discovery of a simple method using a carbon arc for preparing gram quantities of C_{60} and C_{70} represented a major advance to the field because previous synthesis techniques could only supply trace quantities [1, 5]. The availability of large quantities of C_{60} and C_{70} fullerenes provided a great stimulus to this research field. It was soon found [6, 7] that the intercalation of alkali metals into solid C_{60} to a stoichiometry M_3C_{60} (where $M = K, Rb$) could greatly modify the electronic properties of the host fullerene lattice, yielding not only metallic conduction, but also relatively high transition temperature ($18 \leq T_c \leq 40K$) superconductors [8]. The discovery of relatively high temperature superconductivity [9, 10] in these compounds (see §2.6.2) further spurred research activity in this field of C_{60} -related materials.

Regarding a historical perspective on carbon nanotubes, very small diameter (less than 10 nm) carbon filaments were observed in the 1970's through synthesis of vapor grown carbon fibers prepared by the decomposition of benzene at $1100^\circ C$ in the presence of Fe catalyst particles of ~ 10 nm diameter [11, 12]. However, no detailed systematic studies of such very thin filaments were reported in these early years, and it was not until Iijima's observation of carbon nanotubes by high resolution transmission electron microscopy (HRTEM) that the carbon nanotube field was seriously launched. A direct stimulus to the systematic study of carbon filaments of very small diameters came from the discovery of fullerenes by Kroto, Smalley, and coworkers [1]. The realization that the terminations of the carbon nanotubes were fullerene-like caps or hemispheres explained why the smallest diameter carbon nanotube observed would be the same as the diameter of the C_{60} molecule, though theoretical predictions suggest that nanotubes are more stable than fullerenes of the same radius [13]. The Iijima observation heralded the entry of many scientists into the field of carbon nanotubes, stimulated especially by the un-

usual quantum effects predicted for their electronic properties. Independently, Russian workers also reported discovery of carbon nanotubes and nanotube bundles, but generally having much smaller aspect (length to diameter) ratios [14, 15].

This article reviews the structure and properties of fullerenes, fullerene-based materials and carbon nanotubes in the context of carbon materials for advanced technologies.

2 Fullerenes and Fullerene-based Solids

2.1 Synthesis

Fullerene molecules are usually synthesized using an ac discharge between graphite electrodes in approximately 200 torr of He gas. The heat generated between the electrodes evaporates carbon to form soot and fullerenes. Typically the fullerene-containing soot, has up to $\sim 15\%$ fullerenes: C_{60} ($\sim 13\%$) and C_{70} ($\sim 2\%$). The fullerenes are extracted from the soot and separated according to their mass, size or shape, using techniques such as liquid chromatography, and a solvent such as toluene. A variety of techniques and experimental conditions have been employed in the synthesis and separation (purification) of fullerenes, depending on the desired mass distribution, mass purity, and cost.

Property measurements of fullerenes are made either on powder samples, films or single crystals. Microcrystalline C_{60} powder containing small amounts of residual solvent is obtained by vacuum evaporation of the solvent from the solution used in the extraction and separation steps. Pristine C_{60} films used for property measurements are typically deposited onto a variety of substrates (*e.g.*, a clean silicon (100) surface to achieve lattice matching between the crystalline C_{60} and the substrate) by sublimation of the C_{60} powder in an inert atmosphere (*e.g.*, Ar) or in vacuum. Single crystals can be grown either from solution using solvents such as CS_2 and toluene, or by vacuum sublimation [16, 17, 18]. The sublimation method yields solvent-free crystals, and is the method of choice.

Doping is used to modify the properties of fullerenes, particularly their electronic properties. Although fullerene solids (called fullerites) can be doped in three ways (endohedrally, substitutionally, and exohedrally), the exohedral doping has been of primary interest. Endohedral doping denotes the addition of a rare earth, an alkaline earth or an alkali metal ion into the interior of the C_{60} molecule. This step in the synthesis must occur while the molecule is being formed since dopant atoms cannot penetrate the fully formed fullerene cage. As an example of the notation used to denote an endohedral fullerene, $La@C_{60}$ denotes one endohedral lanthanum in C_{60} , or

$Y_2@C_{82}$ denotes two Y atoms inside a C_{82} fullerene [19]. Thus far, only small quantities of endohedrally-doped fullerenes have been prepared and only limited investigations of endohedrally-doped crystalline materials have been reported but steady progress is being made both in synthesis and in properties measurements [20].

A second doping method is the substitution of an impurity atom with a different valence state for a carbon atom on the surface of a fullerene molecule. Because of the small carbon-carbon distance in fullerenes (1.44Å), the only species that can be expected to substitute for a carbon atom in the cage is boron. There has also been some discussion of the possibility of nitrogen doping, which might be facilitated by the curvature of the fullerene shell. However, substitutional doping has not been widely used in practice [21].

The most common method of doping fullerene solids is exohedral doping (also called intercalation if the solid C_{60} host is formed first). In this case, the dopant (*e.g.*, an alkali metal or an alkaline earth, M) is diffused into the interstitial positions between adjacent molecules (exohedral locations). Charge transfer takes place between the M atoms and the fullerene molecules, so that the M atoms become positively charged ions and the fullerene molecules become negatively charged with the additional electrons delocalized in π orbitals over the surface of the molecule. With exohedral doping, the conductivity of fullerene solids can be increased by many orders of magnitude [22]. Doping fullerenes with acceptors has been considerably more difficult than with donors because of the high electron affinity of C_{60} [23, 24], though examples of stable compounds with acceptor-type dopants have been synthesized [7].

Among the alkali metals, Li, Na, K, Rb, and Cs and their alloys have been used as exohedral dopants for C_{60} [25, 26], with one electron typically transferred per alkali metal dopant. Although the metal atom diffusion rates appear to be considerably lower, some success has also been achieved with the intercalation of alkaline earth dopants, such as Ca, Sr, and Ba [27, 28, 29], where two electrons per metal atom M are transferred to the C_{60} molecules for low concentrations of metal atoms, and less than two electrons per alkaline earth ion for high metal atom concentrations. Since the alkaline earth ions are smaller than the corresponding alkali metals in the same row of the periodic table, the crystal structures formed with alkaline earth doping are often different from those for the alkali metal dopants. Except for the alkali metal and alkaline earth intercalation compounds, few intercalation compounds have been investigated for their physical properties.

Fullerene chemistry leading to novel fullerene-like molecules with new chemical groups that are radially attached has become a very active research field, largely because of the uniqueness of the C_{60} molecule and the variety of chemical reactions that appear to be possible [30, 31]. Many new fullerene-based molecules have already been synthesized and characterized chemically,

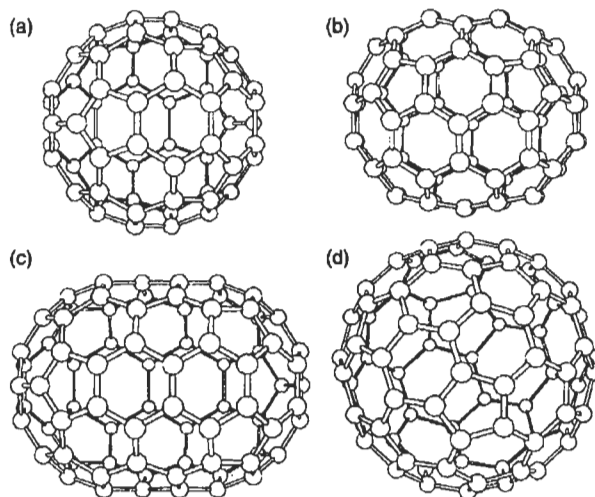


Fig. 1. (a) The icosahedral C_{60} molecule (soccer ball). (b) The C_{70} molecule as a rugby-ball-shaped molecule. Two C_{80} isomers: (c) the C_{80} molecule as an extended rugby-ball-shaped molecule. (d) The C_{80} molecule as an icosahedron.

and a few of these molecules have been incorporated into crystal structures. The chemical additions are made at or across the double ($C=C$) bonds located at the fusion of two hexagons (Fig. 1). Attention has also been given to functional groups which lead to water-soluble products.

2.2 Structural Properties

Since the structure and properties of fullerene solids are strongly dependent on the structure and properties of the constituent fullerene molecules, we first review the structure of the molecules, which is followed by a review of the structure of the molecular solids formed from C_{60} , C_{70} and higher mass fullerenes, and finally the structure of C_{60} crystals.

2.2.1 Structure of molecular C_{60}

The 60 carbon atoms in C_{60} are in potential minima located at the vertices of a regular truncated icosahedron. Every carbon site on the C_{60} molecule is equivalent to every other site [see Fig. 1(a)], consistent with a single sharp line in the NMR spectrum [32, 33]. All the C-atoms reside at a distance of $\sim 3.55\text{\AA}$ from the center of the molecule. The average nearest-neighbor carbon-carbon ($C-C$) distance a_{C-C} in C_{60} (1.44\AA) is almost identical to that in graphite (1.42\AA). Each carbon atom in C_{60} (and also in graphite) is trigonally bonded to three nearest-neighbor carbon atoms, and in some sense, the C_{60} molecule can be considered as a “rolled-up” graphene sheet (a single layer of crystalline graphite). The regular truncated icosahedron has 20

hexagonal faces and 12 additional pentagonal faces to form a closed shell, in keeping with Euler's theorem, which states that a closed surface consisting of hexagons and pentagons has exactly 12 pentagons and an arbitrary number of hexagons [21]. Pentagons or heptagons are required to form curved surfaces; the flat graphene sheet contains only hexagonal rings.

The symmetry operations of the icosahedral C_{60} molecule consist of the identity operation, 12 five-fold axes through the centers of the pentagonal faces, 20 three-fold axes through the centers of the hexagonal faces, and 15 two-fold axes through centers of the edges joining two hexagons. Each of the 60 rotational symmetry operations can be compounded with the inversion operation, resulting in 120 symmetry operations in the icosahedral point group I_h [34]. Molecules with I_h symmetry, C_{60} being the most prominent example, have the highest degree of symmetry or possess the largest number of symmetry operations of any known molecule.

From Euler's theorem on the structure of general polyhedra, it follows that the smallest geometrically possible fullerene is C_{20} which would form a regular dodecahedron with 12 pentagonal faces. It is, however, considered energetically unfavorable for two pentagons to be adjacent to each other (referred to as the isolated pentagon rule) since two adjacent pentagons would lead to a very high local curvature and therefore high strain on the fullerene molecule. Therefore, C_{20} is relatively unstable. Since the addition of a single hexagon adds two carbon atoms, all fullerenes must have an even number of carbon atoms, in agreement with the observed mass spectra for fullerenes [3].

Although each carbon atom in C_{60} is equivalent to every other carbon atom, the three bonds emanating from each atom [see Fig. 1(a)] are not completely equivalent. Each of the four valence electrons of the carbon atoms are engaged in covalent bonds, so that two of the three bonds (along the pentagon edges) are electron-poor single bonds, and one (between two hexagons) is an electron-rich double bond. The structure of C_{60} is stabilized by introducing a small distortion of the bond lengths to form the Kekulé structure of alternating single and double bonds around the hexagonal face, with the single bonds increased from the average bond length of 1.44\AA to 1.46\AA , while the double bond lengths are decreased to 1.40\AA [35, 36]. The Kekulé structure gives rise to a truncated icosahedron with I_h symmetry, with the same point group symmetry as the regular truncated icosahedron where all bond lengths are identical. Since each carbon atom on a C_{60} molecule has its bonding requirements fully satisfied, solid C_{60} is expected to form a van der Waals bonded solid with a semiconducting energy gap in the electronic density of states comparable to the molecular HOMO–LUMO gap ($\sim 1.9\text{ eV}$, *i.e.*, the gap between the highest occupied molecular orbital and the lowest unoccupied molecular orbital).

2.2.2 Structure of C_{70} and higher fullerenes

In the synthesis of C_{60} , larger molecular weight fullerenes C_n ($n > 60$) are also formed, by far the most abundant being C_{70} . However, sufficient quantities of C_{76} , C_{78} , and C_{84} have also been isolated to be studied in some detail.

C_{70} has been found to exhibit a rugby ball shape [37], and its form can be envisioned either by adding a ring of 10 carbon atoms or a belt of 5 hexagons around the equatorial plane of the C_{60} molecule oriented normally to one of the five-fold axes [see Fig. 1(b)]. In contrast to the C_{60} molecule with I_h symmetry, the C_{70} molecule has the lower symmetry D_{5h} which is a subgroup of I (lacking inversion symmetry). Careful chromatographic separations [7, 38] have shown that higher fullerenes can form isomers, *i.e.*, a given number n of carbon atoms C_n can form molecules with different geometrical structures [37, 39]. As an illustration, C_{80} might be formed in the shape of an elongated rugby ball prepared by adding two rows of 5 hexagons normal to a five-fold axis of C_{60} at the equator [see Fig. 1(c)]; an icosahedral form of C_{80} can also be specified as shown in Fig. 1(d). Another example of a family of fullerene isomers is C_{78} which has 5 distinct isomers, none of which are icosahedral [40].

2.2.3 Crystalline C_{60}

In the solid state, the C_{60} molecules crystallize into a cubic structure with a lattice constant of 14.17Å, a nearest neighbor C_{60} - C_{60} distance of 10.02Å [41], and a mass density of 1.72 g/cm³ (corresponding to 1.44×10^{21} C_{60} molecules/cm³). Taking advantage of both the nearly spherical shape and the weak intermolecular bonding, the C_{60} molecules at thermal energies corresponding to room temperature, each rotate rapidly about their equilibrium lattice position with three degrees of rotational freedom. In this rapidly rotating state, the molecules are equivalent and are arranged on a face centered cubic (fcc) lattice (space group O_h^5 or $Fm\bar{3}m$) with one C_{60} molecule per primitive fcc unit cell, or 4 molecules per conventional simple cubic unit cell [see Fig. 2(a)] [43, 44, 45]. Relative to the other allotropic forms of carbon, solid C_{60} is relatively compressible, with an isothermal volume compressibility of 6.9×10^{-12} cm²/dyn [35], which is about two times greater than graphite, which is highly compressible only in the c -axis direction.

Below a temperature of $T_{01} \simeq 260$ K, the C_{60} molecules completely lose two of their three degrees of rotational freedom, and the residual degree of freedom is a ratcheting rotational motion for each of the four molecules within the unit cell about a different (111) axis [43, 45, 46, 47]. The structure of solid C_{60} below T_{01} becomes simple cubic (space group T_h^6 or $Pa\bar{3}$) with a lattice constant $a_0 = 14.17$ Å and four C_{60} molecules per unit cell, as the four oriented molecules within the fcc structure become inequivalent [see Fig. 2(a)] [43, 45]. Supporting evidence for the phase transition at $T_{01} \simeq 260$ K is

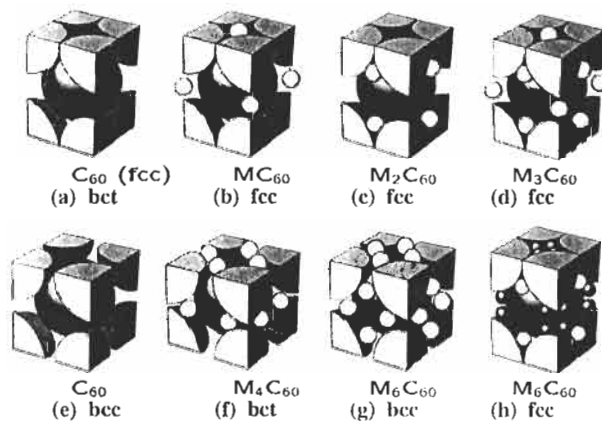


Fig. 2. Structures for the solid (a) fcc C_{60} , (b) fcc MC_{60} , (c) fcc M_2C_{60} (d) fcc M_3C_{60} , (e) hypothetical bcc C_{60} , (f) bct M_4C_{60} , and two structures for M_6C_{60} : (g) bcc M_6C_{60} for ($M = K, Rb, Cs$), and (h) fcc M_6C_{60} which is appropriate for $M = Na$, using the notation of Ref. [42]. The notation fcc, bcc, and bct refer, respectively, to face centered cubic, body centered cubic, and body centered tetragonal structures. The large spheres denote C_{60} molecules and the small spheres denote alkali metal ions. For fcc M_3C_{60} , which has four C_{60} molecules per cubic unit cell, the M atoms can either be on octahedral or tetrahedral symmetry sites. Undoped solid C_{60} also exhibits the fcc crystal structure, but in this case all tetrahedral and octahedral sites are unoccupied. For (g) bcc M_6C_{60} all the M atoms are on distorted tetrahedral sites. For (f) bct M_4C_{60} , the dopant is also found on distorted tetrahedral sites. For (c) pertaining to small alkali metal ions such as Na, only the tetrahedral sites are occupied. For (h) we see that four Na ions can occupy an octahedral site of this fcc lattice.

provided by many property measurements [21]. As the temperature is lowered below 260 K, further ordering of the C_{60} molecules occurs, whereby adjacent C_{60} molecules develop correlated orientations.

In this low temperature structure, the relative orientation of adjacent molecules is stabilized by aligning an electron-rich double bond on one molecule opposite the electron-poor pentagonal face of an adjacent molecule to achieve a minimum in the orientational potential energy. Another structure with only slightly higher energy places the electron-rich double bond of one C_{60} molecule opposite an electron-poor hexagonal face. This orientation can be achieved from the lower energy orientation described above by rotation of the C_{60} molecule by 60° around a $\langle 111 \rangle$ axis [46]. As the temperature T is lowered below 260 K, the probability of occupying the lower energy configuration increases [46]. The mechanism by which partial orientational alignment is achieved is by the ratcheting motion of the C_{60} molecules around the $\langle 111 \rangle$ axes as they execute their hindered rotational motion. The ratcheting motion begins below the 260 K phase transition and continues down to low temperatures. Since the icosahedral C_{60} molecules lack four-fold symmetry axes, it is not possible to achieve full molecular alignment of C_{60} molecules in a cubic crystal structure with 4-fold axes. The residual orientational disorder that results is called merohedral disorder, which gives rise to an important scattering process for the transport properties of fullerene solids.

2.2.4 Crystalline C_{70} and higher fullerenes

The crystal structure of C_{70} is more complex than that of crystalline C_{60} [48, 49, 50, 51, 52], and has been studied in much detail. Less detailed structural information is available for the higher mass fullerenes. At high temperature ($T \gg 340$ K), the fcc phase ($a = 15.01\text{\AA}$) of C_{70} with freely rotating molecules is most stable, but since the ideal hexagonal close packed (hcp) phase with $c/a = 1.63$ is almost equally stable, fcc crystals of C_{70} tend to be severely twinned and show many stacking faults. A transition to another hcp phase with $a = b = 10.11\text{\AA}$ and a larger c/a ratio of 1.82 occurs at ~ 340 K. This larger c/a ratio is associated with the orientation of the C_{70} molecules along their long axis, as the free molecular rotation (about any axis) that is prevalent in the higher temperature phase evolves into a free rotation about the 5-fold axis of the C_{70} molecule [49, 52]. As the temperature is further lowered to ~ 280 K, the free rotation about the c -axis also becomes frozen, resulting in a monoclinic structure with the high symmetry axis along the c -axis of the hcp structure.

The higher mass fullerenes (C_{76} , C_{84}), with multiple isomers of different shapes, also crystallize in the fcc structure at room temperature, with an fcc lattice constant which is approximately proportional to $n^{1/2}$, where n is the number of carbon atoms in the fullerene [53].

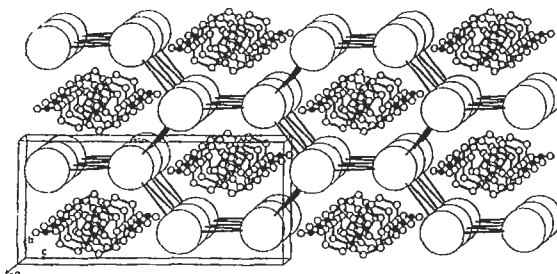


Fig. 3. Crystal structure of the compound $C_{60}(S_8)_2CS_2$ projected normal to the a -axis. Large circles denote C_{60} , small circles denote sulfur, black balls denote carbon. In this structure, the C_{60} – C_{60} distance is nearly 11 Å, and the diameter of the C_{60} molecule has been reduced relative to the other atoms for clarity [54].

2.2.5 Doped C_{60} crystals

Several stable crystalline phases for exohedrally doped (or intercalated) solid C_{60} have been identified. Most widely studied are the crystalline phases formed by intercalation of alkali metals, though some structural reports have been given for fullerene-derived crystals doped with alkaline earths [27]. In this review, we focus attention primarily on doped C_{60} materials where charge transfer occurs. However, clathrate C_{60} compounds involving organic spacer molecules, where there is no significant charge transfer, also show some interesting crystal structures such as that for $C_{60}(S_8)CS_2$ (see Fig. 3) [54]. As more C_{60} -based compounds are synthesized, we can expect further studies of their crystalline structure and properties.

When C_{60} is doped with the alkali metals ($M = Na, K, Rb, Cs$), stable crystalline phases are formed for the compositions M_1C_{60} , M_3C_{60} , M_4C_{60} , and M_6C_{60} [21, 42, 55, 56]. The phase diagram for K_xC_{60} , illustrated in Fig. 4 [57], shows stability regions for the rock salt phase of K_1C_{60} , the fcc phase of K_3C_{60} , the bct phase of K_4C_{60} , and the bcc phase of K_6C_{60} . The phase diagram for K_xC_{60} , stable regions are illustrated in the cross-hatched areas of this binary phase diagram [57], and the location of the guest species relative to the fullerenes is shown in Fig. 2. At lower temperatures (not shown in Fig. 4), the M_1C_{60} phase is transformed into a polymer chain structure with short C_{60} – C_{60} bonds between molecules along the chain direction.

For the alkali metal doped C_{60} compounds, charge transfer of one electron per M atom to the C_{60} molecule occurs, resulting in M^+ ions at the tetrahedral and/or octahedral symmetry interstices of the cubic C_{60} host structure. For the composition M_3C_{60} , the resulting metallic crystal has basically the fcc structure (see Fig. 2). Within this structure the alkali metal ions can sit on either tetrahedral symmetry ($1/4, 1/4, 1/4$) sites, which are twice as numerous as the octahedral ($1/2, 0, 0$) sites (referenced to a simple cubic coordinate system). The electron-poor alkali metal ions tend to lie adjacent to a $C=C$ double

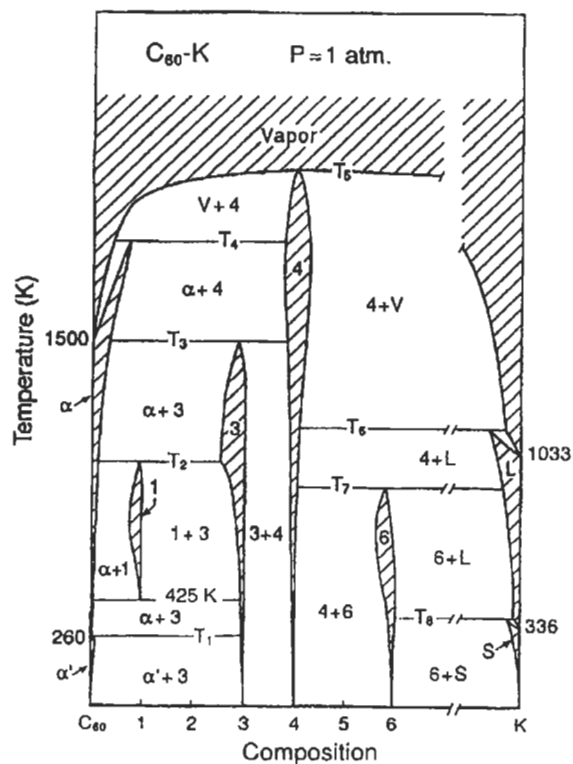


Fig. 4. Provisional binary phase diagram for K_xC_{60} at 1 atm pressure. Experimentally determined temperatures are indicated, while unknown temperatures of predicted transformations are labeled T_1, \dots, T_8 . [57].

bond, thereby orienting the C_{60} molecules somewhat, and restraining their rotational degrees of freedom [58]. From the standpoint of the nearest neighbors, the K^+ ions in K_3C_{60} are surrounded by either four C_{60}^{3-} ions (tetrahedral site) or six C_{60}^{3-} ions (octahedral site). For the tetrahedral sites, the radius of the cavity available to a K^+ ion is 1.12\AA while for an octahedral site it is 2.07\AA [41]. The structure of the doped C_{60} shows different orientational alignments because of differences in the orientational potentials experienced by the fullerenes. The shortest distance between a K^+ ion at a tetrahedral site and a carbon atom on a freely rotating C_{60} molecule is 2.66\AA [41]. It is of interest to note that the Cs^+ ion is too large to form a stable Cs_3C_{60} compound with the $Fm\bar{3}m$ fcc structure [44], unless pressure is applied [10].

The structure of the alkaline-earth metal compound Ca_yC_{60} (for $y \leq 5$) follows the same space group $Fm\bar{3}m$ as for the heavy ($M = K, Rb$ and Cs) alkali metal M_xC_{60} compounds ($x \leq 3$) [27] and the Ca ions occupy both tetrahedral and octahedral sites. Because of the smaller size of the calcium ion, the octahedral sites can accommodate multiple Ca ions, and it is believed that up to three Ca ions can be accommodated in a single octahedral site [27]. Ba_6C_{60} and Sr_6C_{60} , in contrast, exhibit different crystal phases, such as the A15 and other bcc phases [28, 59].

2.3 Electronic Properties

Because of their weak intermolecular forces, the undoped fullerenes form molecular solids. Thus, their electronic structures are expected to be closely related to the electronic levels of the isolated molecules. Referring to Fig. 1a, each carbon atom in C_{60} has two single bonds along adjacent sides of a pentagon and one double bond between two adjoining hexagons, thereby accounting for the bonding for the four valence electrons for carbon, indicating that fullerenes should be semiconductors. If these bonds were coplanar, they would be very similar to the sp^2 trigonal bonding in graphite. The curvature of the C_{60} surface causes the planar-derived trigonal orbitals to hybridize, thereby admixing some sp^3 character to the sp^2 bonding. The shortening of the double bonds and lengthening of the single bonds in the Kekulé arrangement of the C_{60} molecule strongly influence the electronic structure near the Fermi level.

The nature of the electronic states for fullerene molecules depends sensitively on the number of π -electrons in the fullerene. The number of π -electrons on the C_{60} molecule is 60 (*i.e.*, one π electron per carbon atom), which is exactly the correct number to fully occupy the highest occupied molecular orbital (HOMO) level with h_u icosahedral symmetry. In relating the levels of an icosahedral molecule to those of a free electron on a thin spherical shell (full rotational symmetry), 50 electrons fully occupy the angular momentum states of the shell through $\ell = 4$, and the remaining 10 electrons are available

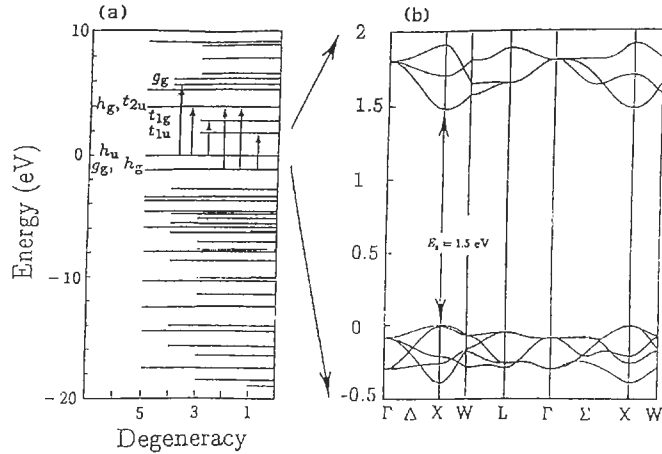


Fig. 5. Calculated electronic structure by the LDA method of (a) an isolated C_{60} molecule and (b) fcc solid C_{60} where the direct band gap at the X-point is 1.5 eV [60]. for filling the $\ell = 5$ angular momentum state for which the lowest energy multiplet in icosahedral symmetry is an h_u state that can accommodate 10 electrons [see Fig. 5(a)].

The most extensive calculations of the electronic structure of fullerenes so far have been done for C_{60} . Representative results for the energy levels of the free C_{60} molecule are shown in Fig. 5(a) [60]. Because of the molecular nature of solid C_{60} , the electronic structure for the solid phase is expected to be closely related to that of the free molecule [61]. An LDA calculation for the crystalline phase is shown in Fig. 5(b) for the energy bands derived from the highest occupied molecular orbital (HOMO) and lowest unoccupied molecular orbital (LUMO) for C_{60} , and the band gap between the LUMO and HOMO-derived energy bands is shown on the figure. The LDA calculations are one-electron treatments which tend to underestimate the actual bandgap. Nevertheless, such calculations are widely used in the fullerene literature to provide physical insights about many of the physical properties.

Calculations for C_{60} in the LDA approximation [62, 60] yield a narrow band (~ 0.4 - 0.6 eV bandwidth) solid, with a HOMO-LUMO-derived direct band gap of ~ 1.5 eV at the X point of the fcc Brillouin zone. The narrow energy bands and the molecular nature of the electronic structure of fullerenes are indicative of a highly correlated electron system. Since the HOMO and LUMO levels both have the same odd parity, electric dipole transitions between these levels are symmetry forbidden in the free C_{60} molecule. In the crystalline solid, transitions between the direct bandgap states at the Γ and X points in the cubic Brillouin zone are also forbidden, but are allowed at the lower symmetry points in the Brillouin zone. The allowed electric dipole

transitions between one-electron states for the free C_{60} molecule are indicated by arrows in Fig. 5(a).

Doping C_{60} with an alkali metal transfers electrons to the LUMO levels, which because of their t_{1u} symmetry (Fig. 5) can accommodate three spin up and three spin down electrons. Assuming one electron to be transferred to the C_{60} molecule per alkali-metal atom dopant, the LUMO levels are expected to be half occupied at the alkali metal stoichiometry M_3C_{60} and totally full at M_6C_{60} , leading to a filled shell configuration. Thus M_6C_{60} would be expected to be semiconducting with a band gap between the t_{1u} - and t_{2g} -derived bands (see Fig. 5), while M_3C_{60} should be metallic. Consistent with these arguments, a large increase in optical absorptivity (due to free carriers) in M_xC_{60} is observed and the electrical resistivity drops precipitously with alkali metal doping as $x \rightarrow 3$; this observation supports the metallic nature of M_3C_{60} . Below ~ 0.5 eV, the free electron contribution to the optical properties is dominant, and above ~ 0.5 eV, interband transitions from the partially occupied t_{1u} level to the higher lying t_{1g} level take place.

Fermi surface calculations for K_3C_{60} indicate a hole Fermi surface around the Γ -point which contributes about 12% to the density of states at the Fermi surface [63, 64]. These calculations also indicate a larger and more complicated Fermi surface consisting of both electron and hole orbits which contribute the remaining 88% to the density of states. All of these states near the Fermi surface are primarily derived from the t_{1u} molecular orbitals. Because of the weak interaction of the molecules with each other and with the alkali metal dopants, solid M_3C_{60} , is close to being an ideal molecular solid having energy levels with little dispersion, thus giving rise to a very high density of states near the Fermi level. This property is important to the occurrence of superconductivity in M_3C_{60} and to the high T_c values that are observed. The total density of states at E_F is estimated to be $\sim 13/eV/C_{60}$ molecule per spin state [64, 65]. Calculated values for the effective mass m^* based on a band model yield $1.3m_e$ (where m_e is the free electron mass) for the t_{1u} -derived conduction band of C_{60} and $1.5m_e$ and $3.4m_e$ for the h_u -derived valence bands [62].

2.4 Optical Properties

Since the optical transitions near the HOMO-LUMO gap are symmetry-forbidden for electric dipole transitions, and their absorption strengths are consequently very low, study of the absorption edge in C_{60} is difficult from both an experimental and theoretical standpoint. To add to this difficulty, C_{60} is strongly photosensitive, so that unless measurements are made under low light intensities, photo-induced chemical reactions take place, in some cases giving rise to irreversible structural changes and polymerization of the

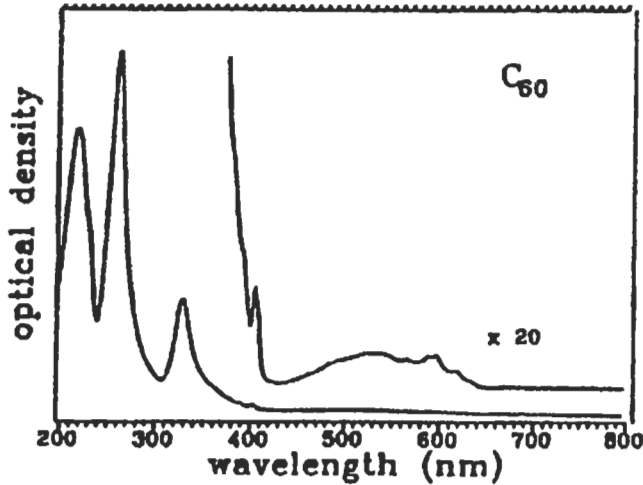


Fig. 6. Optical density vs wavelength for C_{60} in hexane solution. The optical density vs wavelength data for long wavelengths are shown on an expanded scale [67].

C_{60} samples [66]. At higher photon energies, dipole-allowed transitions can occur, and the optical absorption increases dramatically.

Results for the optical absorbance of C_{60} molecules in solution (hexane) are shown in Fig. 6 as the optical density [which is defined as $\log_{10}(1/\text{transmittance})$] vs wavelength in the ultraviolet (UV)-visible range (200 – 700 nm) [67]. The strong absorption bands in the figure (below ~ 400 nm in wavelength or above ~ 2.9 eV in energy) are identified in the one-electron model with electric dipole-allowed transitions between occupied (bonding) and empty (antibonding) molecular orbitals denoted in Fig. 5(a) by either the $h_u \rightarrow t_{1g}$ or $h_g \rightarrow t_{1u}$ transitions. At longer wavelengths $490 < \lambda < 640$ nm (or $1.9 < E < 2.5$ eV), weak absorption takes place, and is associated with electric dipole-forbidden transitions between the one-electron HOMO level with h_u symmetry and the one-electron t_{1u} LUMO level.

In the lowest optically excited state of the molecule, we have one electron (t_{1u}) and one hole (h_u^9), each with spin 1/2 which couple through the Coulomb interaction and can either form a singlet S_i state ($S = 0$), or a triplet T_i state ($S = 1$). Since the electric dipole matrix element for optical transitions $\mathcal{H}'_{em} = (e\vec{p} \cdot \vec{A})/(mc)$ does not depend on spin, there is a strong spin selection rule ($\Delta S = 0$) for optical electric dipole transitions. This strong spin selection rule arises from the very weak spin-orbit interaction for carbon. Thus, to “turn on” electric dipole transitions, appropriate odd-parity vibrational modes must be admixed with the initial and (or) final electronic states, so that the weak absorption below 2.5 eV involves optical transitions between appropriate vibronic levels. These vibronic levels are energetically favored by virtue

of a strong electron-vibration interaction. Optical transitions between the HOMO and LUMO levels can thus occur through the excitation of a vibronic state involving the appropriate odd-parity vibrational mode [68, 69, 70, 71]. Because of the involvement of a vibrational energy in the vibronic state, there is an energy difference between the lowest energy absorption band [67] and the lowest energy luminescence band [71].

Using these molecular states, the weak absorption observed between 490 and 640 nm for C_{60} in solution (Fig. 6) [67] is assigned to transitions between the singlet ground state S_0 and the lowest excited singlet state S_1 (associated with the t_{1u} orbital and activated by vibronic coupling).

For C_{70} , molecular orbital calculations [60] reveal a large number of closely-spaced orbitals both above and below the HOMO-LUMO gap [60]. The large number of orbitals makes it difficult to assign particular groups of transitions to structure observed in the solution spectra of C_{70} . UV-visible solution spectra for higher fullerenes (C_n ; $n = 76, 78, 82, 84, 90, 96$) have also been reported [37, 39, 72].

Further insight into the electronic structure of fullerene molecules is provided by pulsed laser studies of C_{60} and C_{70} . Such time-resolved studies of fullerenes in solution have been used to probe the photo-dynamics of the optical excitation/luminescence spectra. The importance of these dynamic studies is to show that photo-excitation in the long-wavelength portion of the UV-visible spectrum leads to the promotion of C_{60} from the singlet S_0 ground state (1A_g) into a singlet S_1 excited state, which decays quickly with a nearly 100% efficiency [73, 74] via an inter-system (*i.e.*, $S_n \rightarrow T_n$) crossing to the lowest excited triplet state T_1 . This rapid singlet-triplet decay (~ 33 ps [74]) is fostered by the overlap in energy between the vibronic manifold of electronic states associated with the lowest singlet S_1 state and the corresponding vibronic manifold for the triplet T_1 state, and the very weak spin-orbit coupling mentioned above.

For higher energy optical excitations, once in the T_i triplet excitonic manifold, a very rapid transition occurs to the lowest level of the T_1 triplet manifold, about 1.55 eV above the ground state energy. The T_1 state is a metastable state. It lies ~ 0.3 eV lower in energy than the singlet S_1 manifold [74], and has a long lifetime ($> 2.8 \times 10^{-4}$ s) relative to the lowest singlet state (1.2 ns) in the room temperature solution spectra [75]. The efficient populating of the metastable T_1 level in C_{60} by optical pumping leads to interesting non-linear optical properties. One practical application which may follow from this non-linear property may be the development of an optical limiting material, whose absorptivity increases with increasing light intensity [76, 77].

A close correspondence is found in the photoluminescence spectrum in solution and in solid films [71]. Using the inter-system crossing to populate the T_1

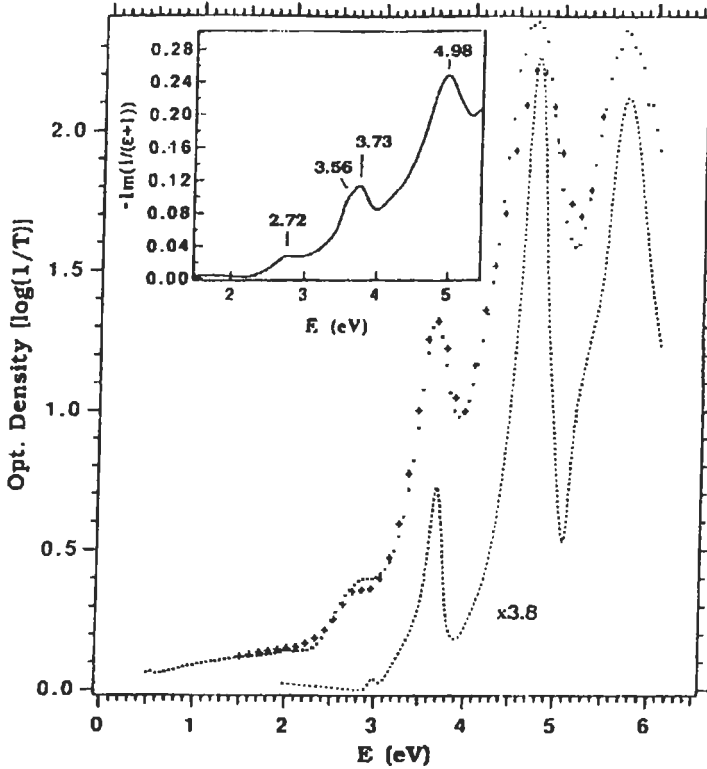


Fig. 7. Optical density of solid C_{60} on Suprasil based on two different optical techniques (+,•). For comparison, the solution spectrum for C_{60} dissolved in decalin (small dots) is shown. The inset is a plot of the electron loss function $-Im[(1 + \epsilon)]^{-1}$ vs E shown for comparison (HREELS) [78].

level, the stronger $T_1 - T_n$ absorption relative to the $S_0 \rightarrow S_n$ absorption, can be exploited to enhance non-linear absorption and optical limiting effects.

As shown in Fig. 7, a large increase in optical absorption occurs at higher photon energies above the HOMO–LUMO gap where electric dipole transitions become allowed. Transmission spectra taken in this range (see Fig. 7) confirm the similarity of the optical spectra for solid C_{60} and C_{60} in solution (decalin) [78], as well as a similarity to electron energy loss spectra shown as the inset to this figure. The optical properties of solid C_{60} and C_{70} have been studied over a wide frequency range [78, 79, 80] and yield the complex refractive index $\tilde{n}(\omega) = n(\omega) + ik(\omega)$ and the optical dielectric function $\epsilon(\omega) = \epsilon_1(\omega) + i\epsilon_2(\omega) = \tilde{n}^2(\omega)$. Results are shown in Fig. 8 for a solid film of C_{60} at $T = 300$ K [82, 83]. The strong, sharp structure at low energy is identified with infrared-active optic phonons and at higher energies the structure is due to electronic transitions.

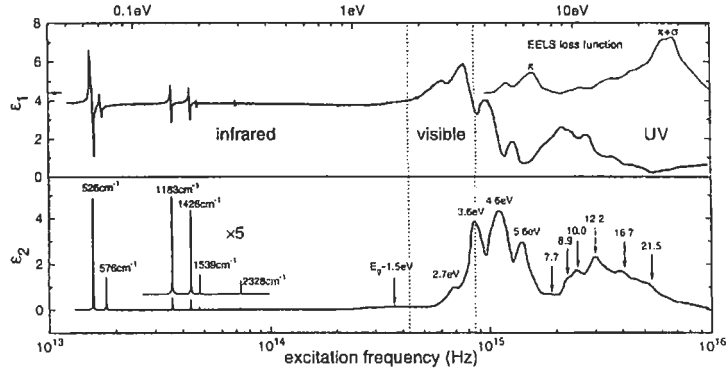


Fig. 8. Summary of real $\epsilon_1(\omega)$ and imaginary $\epsilon_2(\omega)$ parts of the dielectric function for C_{60} vacuum-sublimed solid films at room temperature over a wide frequency range, using a variety of experimental techniques. The arrow at the left axis points to $\epsilon_1 = 4.4$, the observed low frequency value of ϵ_1 obtained from optical data [81].

Near-normal incidence, transmission/reflection studies on C_{60} and M_6C_{60} ($M = K, Rb, Cs$) [84] have been carried out in the range 0.5 – 6 eV to determine the optical dielectric function $\epsilon(\omega)$ [78]. For alkali metal-saturated C_{60} solid films (e.g., M_6C_{60} : $M = K, Rb, Cs$), the transmission and reflection spectra are largely insensitive to the dopant or intercalate species (M) [84], thus giving strong evidence for only weak hybridization between M and C_{60} states. The optical spectra are thus consistent with complete charge transfer of the alkali metal s -electrons to fill a lower lying, six-fold degenerate C_{60} band (t_{1u} symmetry). The energy gap between the t_{1u} -derived and t_{1g} -derived states [64] is ~ 1 eV for the M_6C_{60} compounds.

Using a pulsed Nd:YAG laser, nonlinear optical behavior has been observed in solid C_{60} films at $T = 300$ K [85, 86, 87]. Time-resolved four-wave mixing experiments [85, 86], yield a fast (< 35 ps) nonlinear response (including third- and fifth-order contributions) with a substantial third-order optical susceptibility $\chi_{xxxx}(3) = 7 \times 10^{-12}$ esu. The origin of the optical non-linearity is probably connected to the high efficiency ($\sim 100\%$) in transferring electrons from the excited singlet state S_n manifold to the T_n triplet excited states.

2.5 Vibrational Properties

The normal modes for solid C_{60} can be clearly subdivided into two main categories: “intramolecular” and “intermolecular” modes, because of the weak coupling between molecules. The former vibrations are often simply called “molecular” modes, since their frequencies and eigenvectors closely resemble those of an isolated molecule. The latter are also called lattice modes or phonons, and can be further subdivided into librational, acoustic and optic modes. The frequencies for the intermolecular modes are low, reflecting, the

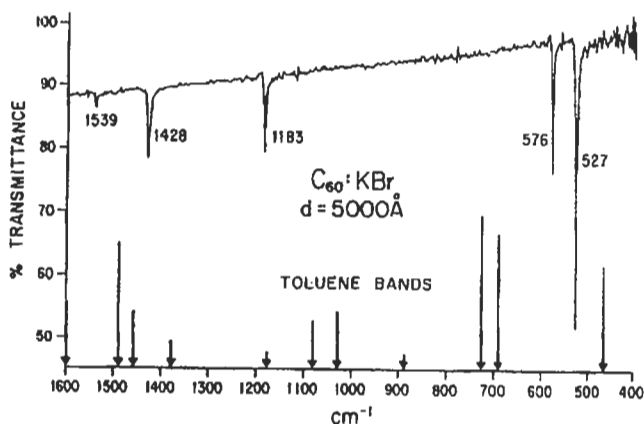


Fig. 9. The infrared spectra of C_{60} on a KBr substrate. Also shown schematically are the IR bands for toluene, a common solvent for fullerenes.

weak van der Waals bonds between heavy fullerene molecules. In the limit that the molecule is treated as a “point”, the molecular moment of inertia I approaches zero, and the librational modes are lost from the spectrum. In addition, there are optic modes associated with metal-doped C_{60} , in which the metal ions vibrate out of phase with the C_{60} counter ion.

At higher frequencies (above $\sim 200\text{ cm}^{-1}$) the vibrational spectra for fullerenes and their crystalline solids are dominated by the intramolecular modes. Because of the high symmetry of the C_{60} molecule (icosahedral point group I_h), there are only 46 distinct molecular mode frequencies corresponding to the $180 - 6 = 174$ degrees of freedom for the isolated C_{60} molecule, and of these only 4 are infrared-active (all with T_{1u} symmetry) and 10 are Raman-active (2 with A_g symmetry and 8 with H_g symmetry). The remaining 32 eigenfrequencies correspond to silent modes, *i.e.*, they are not optically active in first order.

Raman and infrared spectroscopy provide sensitive methods for distinguishing C_{60} from higher molecular weight fullerenes with lower symmetry (*e.g.*, C_{70} has D_{5h} symmetry). Since most of the higher molecular weight fullerenes have lower symmetry as well as more degrees of freedom, they have many more infrared- and Raman-active modes.

2.5.1 Infrared-active modes in C_{60}

The simplicity of the infrared spectrum of solid C_{60} (see Fig. 9), which shows four prominent lines at 527, 576, 1183, 1428 cm^{-1} each with T_{1u} symmetry [4], provides a convenient method for characterizing C_{60} samples [4, 88]. The IR spectrum of solid C_{60} remains almost unchanged relative to the isolated C_{60} molecule, with the most prominent addition being the weak feature at

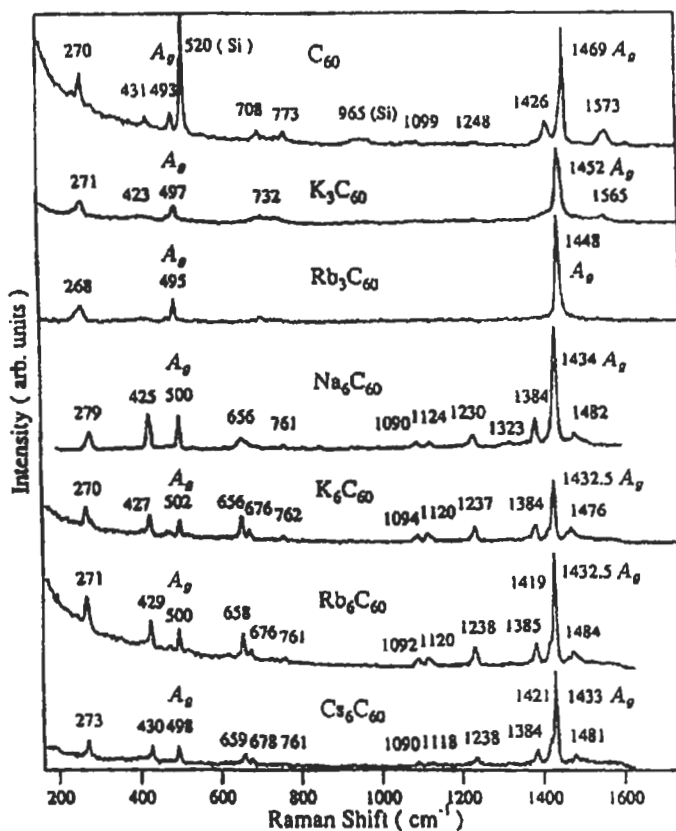


Fig. 10. Unpolarized Raman spectra ($T = 300$ K) for solid C_{60} , K_3C_{60} , Rb_3C_{60} , Na_6C_{60} , K_6C_{60} , Rb_6C_{60} and Cs_6C_{60} [92, 93]. The tangential and radial modes of A_g symmetry are identified, as are the features associated with the Si substrates. From the insensitivity of these spectra to crystal structure and specific alkali metal dopant, it is concluded that the interactions between the C_{60} molecules are weak, as are also the interactions between the C_{60} anions and the alkali metal cations.

1539 cm^{-1} [89, 90, 91], identified with a combination (*i.e.*, $\nu_1 + \nu_2$) mode. The strong correspondence between the solution and/or gas phase IR spectrum and the solid state IR spectrum [71] is indicative of the highly molecular nature of solid C_{60} .

2.5.2 Raman-active modes in C_{60}

The Raman spectrum in Fig. 10 for solid C_{60} shows 10 strong Raman lines, the number of Raman-allowed modes expected for the intramolecular modes of the free molecule [6, 94, 92, 93, 95, 96, 97]. As first calculated by Stanton and Newton [98], the normal modes in molecular C_{60} above about 1000 cm^{-1} involve carbon atom displacements that are predominantly tangential

to the C_{60} surface, while the modes below $\sim 800\text{ cm}^{-1}$ involve predominantly radial motion. The displacements of adjacent atoms in the totally symmetric 493 cm^{-1} A_g breathing mode are in the radial direction and of equal magnitude.

The high frequency A_g mode (1469 cm^{-1}) [99] corresponds to an in-plane tangential displacement of the 5 carbon atoms around each of the 12 pentagons and therefore is called the “pentagonal pinch” mode. Under high laser flux from an Ar ion laser, this mode frequency down-shifts to 1458 cm^{-1} . This down-shift has been interpreted as a signature of a photo-induced structural transformation [99]. In this phototransformation, numerous additional radial and tangential molecular modes are activated by the apparent breaking of the icosahedral symmetry resulting from bonds that cross-link adjacent molecules. A new Raman-active mode is also observed at 116 cm^{-1} [100] which is identified with a stretching of the cross-linking bonds between molecules. This frequency falls in the gap between the lattice and molecular modes of undoped C_{60} .

2.5.3 Silent modes in C_{60}

The thirty-two silent modes of C_{60} have been studied by various techniques [7], the most fruitful being higher-order Raman and infra-red spectroscopy. Because of the molecular nature of solid C_{60} , the higher-order spectra are relatively sharp. Thus overtone and combination modes can be resolved, and with the help of a force constant model for the vibrational modes, various observed molecular frequencies can be identified with specific vibrational modes. Using this strategy, the 32 silent intramolecular modes of C_{60} have been determined [101, 102].

2.5.4 Vibrational spectra for C_{70}

The Raman and infrared spectra for C_{70} are much more complicated than for C_{60} because of the lower symmetry and the large number of Raman-active modes (53) and infrared active modes (31) out of a total of 122 possible vibrational mode frequencies. Nevertheless, well-resolved infrared spectra [88, 103] and Raman spectra have been observed [95, 103, 104]. Using polarization studies and a force constant model calculation [103, 105], an attempt has been made to assign mode symmetries to all the intramolecular modes. Making use of a force constant model based on C_{60} and a small perturbation to account for the weakening of the force constants for the belt atoms around the equator, reasonable consistency between the model calculation and the experimentally determined lattice modes [103, 105] has been achieved.

2.5.5 Vibrational modes in doped fullerene solids

The addition of alkali metal dopants to form the superconducting M_3C_{60} ($M = K, Rb$) compounds and the alkali metal saturated compounds M_6C_{60} ($M = Na, K, Rb, Cs$) perturbs the Raman spectra only slightly relative to the spectra for the undoped solid C_{60} . This is seen in Fig. 10, where the Raman spectra for a C_{60} film are shown in comparison to various M_3C_{60} and M_6C_{60} spectra [92, 93]. One can, in fact, identify each of the lines in the M_xC_{60} spectra with those of pristine C_{60} , and very little change is found from one alkali metal dopant to another [4]. The small magnitude of the perturbation of the Raman spectrum by alkali metal doping and the insensitivity of the M_6C_{60} spectra to the specific alkali metal species indicates a very weak coupling between the C_{60} anions and the M^+ cations. In the case of the superconducting M_3C_{60} phase ($M = K, Rb$), the spectra (see Fig. 10) are again quite similar to that of C_{60} , except for the apparent absence in the M_3C_{60} spectra of several of the Raman lines derived from the H_g modes in C_{60} . This is particularly true in the spectrum of Rb_3C_{60} for which the same sample was shown resistively to exhibit a $T_c \sim 28$ K [99]. For both K_3C_{60} [92] and Rb_3C_{60} [103] (see Fig. 10), the coupling between the phonons and a low energy continuum asymmetrically broadens the $H_g(1)$ mode and broadens several other H_g modes considerably [92, 97]. The observed broadening has been used to quantitatively determine the contribution of the intramolecular modes to the electron pairing in the superconducting state [108, 109].

As a result of alkali metal doping, electrons are transferred to the π -electron orbitals on the surface of the C_{60} molecules, elongating the C–C bonds and down-shifting the intramolecular tangential modes. A similar effect was noted in alkali metal-intercalated graphite where electrons are transferred from the alkali-metal M layers to the graphene layers [110]. The magnitude of the mode softening in alkali metal-doped C_{60} is comparable ($\sim 60\%$) to that for alkali metal-doped GICs, and can be explained semiquantitatively by a charge transfer model [111]. The softening of the 1469 cm^{-1} tangential $A_g(2)$ mode by alkali metal doping (by $\sim 6\text{ cm}^{-1}/\text{K atom}$) has been used as a convenient method to characterize the stoichiometry x of stable K_xC_{60} samples [89].

2.6 Electrical Transport

2.6.1 Normal state electrical transport

The doping of C_{60} with alkali metals creates carriers at the Fermi level in the t_{1u} -derived band and decreases the electrical resistivity ρ of pristine solid C_{60} by several orders of magnitude. As x in M_xC_{60} increases, the resistivity $\rho(x)$ approaches a minimum at $x = 3.0 \pm 0.05$ [9, 112], corresponding to a half-filled t_{1u} -derived conduction band. Then, upon further increase in x from 3 to 6, $\rho(x)$ again increases, as is shown in Fig. 11 for various alkali metal dopants

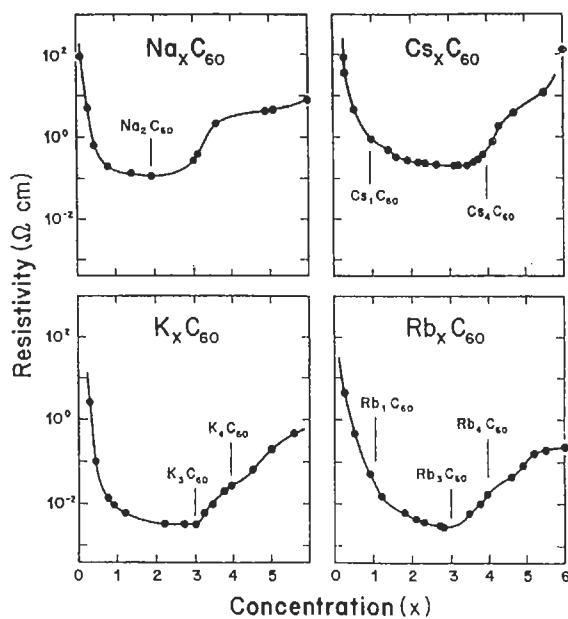


Fig. 11. Composition dependence of the resistivity $\rho(x)$ for thick films of C_{60} doped with Na, K, Rb, and Cs. Points indicate where exposure to the alkali-metal source was stopped and x-ray and ultraviolet photoemission spectra were acquired to determine the concentration x . The labels indicate the known fulleride phases at 300 K. The minima in $\rho(x)$ occur for stoichiometries corresponding to Na_2C_{60} , K_3C_{60} and $Cs_{3.5}C_{60}$ [113].

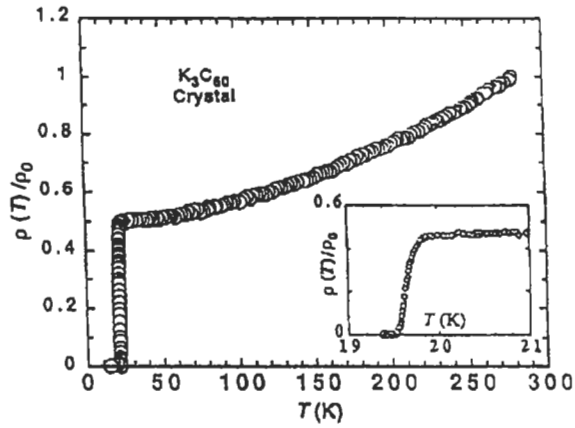


Fig. 12. Normalized dc electrical resistivity $\rho(T)$ of single crystal K_3C_{60} . The inset shows the $\rho(T)$ behavior near the superconducting transition temperature $T_c = 19.8$ K [114]. The curvature in $\rho(T)$ for $T > T_c$ is due to the volume expansion of the sample [7, 43].

[113]. It should be noted that stable M_xC_{60} compounds only occur for $x = 0, 3, 4,$ and 6 at room temperature, though $x = 1$ (the quenched Rb_1C_{60} polymer at 300 K) forms a stable rock salt phase at elevated temperatures (see §2.2.5). The compounds corresponding to filled molecular levels (C_{60} and M_6C_{60}) exhibit maxima in the resistivity. Furthermore, even at the minimum resistivity in M_xC_{60} , the value of ρ found for K_3C_{60} (2.5×10^{-3} Ω -cm) is high, consistent with a high resistivity metal with strong carrier scattering.

Studies of the temperature dependence of the resistivity of polycrystalline M_xC_{60} samples in the normal state show that conduction is by a thermally-activated ($\propto \exp[-E_a/kT]$) hopping process except for a small range of x near 3 where the conduction is metallic [9, 114]. The activation energy E_a for the hopping process increases as x deviates further and further from the resistivity minimum at $x \simeq 3$ [112, 113]. In the metallic regime ($E_a = 0$), results for $\rho(T)$ for a superconducting single crystal K_3C_{60} sample (see Fig. 12) show a quadratic increase in $\rho(T)$ above T_c [114, 115], though more detailed studies [7] show that under conditions of constant volume, the increase in $\rho(T)$ is linear in T . A number of studies have shown that the temperature dependence of the resistivity $\rho(T)$ is strongly dependent on whether the sample is a single crystal or a film [114, 115]. Film samples tend to exhibit a negative temperature coefficient of $\rho(T)$ just above the superconducting transition temperature T_c while single crystal samples exhibit a positive $\partial\rho(T)/\partial T$ just above T_c .

Temperature dependent Hall effect measurements have also been carried out in the temperature range 30 to 260 K on a K_3C_{60} thin film [116]. For three

electrons per C_{60} , the expected Hall coefficient R_H based on a one-carrier model would be about one order of magnitude larger than the experimentally observed value [116]. The small value of the observed Hall coefficient suggests multiple carrier types including both electrons and holes. This interpretation is corroborated by the observed sign change in R_H from negative below 220 K to positive above 220 K. Multiple carrier types are consistent with Fermi surface calculations [64], which also suggest both electron and hole orbits on the Fermi surface.

The high electrical resistivity and the magnitude of the optical bandgap of C_{60} can be reduced by the application of high pressure, with decreases in resistivity of about one order of magnitude observed per 10 GPa pressure [117]. However, at a pressure of ~ 20 GPa, an irreversible phase transition to a more insulating phase has been reported [117].

2.6.2 Superconductivity

The most striking electronic property of the C_{60} -related materials has been the observation of high temperature superconductivity ($T_c \leq 40$ K) [10, 56]. The first observation of superconductivity in an alkali metal-doped carbon material goes back to 1965 when superconductivity was observed in the first stage alkali metal graphite intercalation compound (GIC) C_8K [118]. Except for the novelty of observing superconductivity in a compound having no superconducting constituents, this observation did not attract a great deal of attention, since the T_c was very low (~ 140 mK) [22]. Later, higher T_c 's were observed in GICs using superconducting intercalants (*e.g.*, $KHgC_8$, for which $T_c = 1.9$ K [119]), and in subjecting the alkali metal GICs to pressure (*e.g.*, NaC_2 , for which $T_c \sim 5$ K) [120].

The early observation of superconductivity at 18 K in K_3C_{60} [6] was soon followed by observations of superconductivity at even higher temperatures: in Rb_3C_{60} ($T_c = 29$ K) [9, 121], and $Rb_xCs_yC_{60}$ ($T_c = 33$ K) [26], and finally by applying pressure to stabilize Cs_3C_{60} ($T_c = 40$ K) [10]. A large increase in T_c was achieved in the early research by going to compounds with larger intercalate atoms, resulting in unit cells with larger lattice constants [122]. As the lattice constant increases, the C_{60} - C_{60} coupling decreases, narrowing the electronic bandwidth derived from the LUMO level, and thereby increasing the corresponding density of states consistent with the BCS expression relating the transition temperature to the density of states $N(E_F)$

$$T_c \sim \omega_{ph} \exp[-1/VN(E_F)], \quad (1)$$

where V is the electron-phonon coupling energy. Figure 13 shows an empirical, nearly linear, relation between T_c and the lattice constant a for superconducting alkali-metal doped C_{60} [44]. This correlation includes compounds derived from alkali-metal dopants, alloys of different alkali metals [123] and

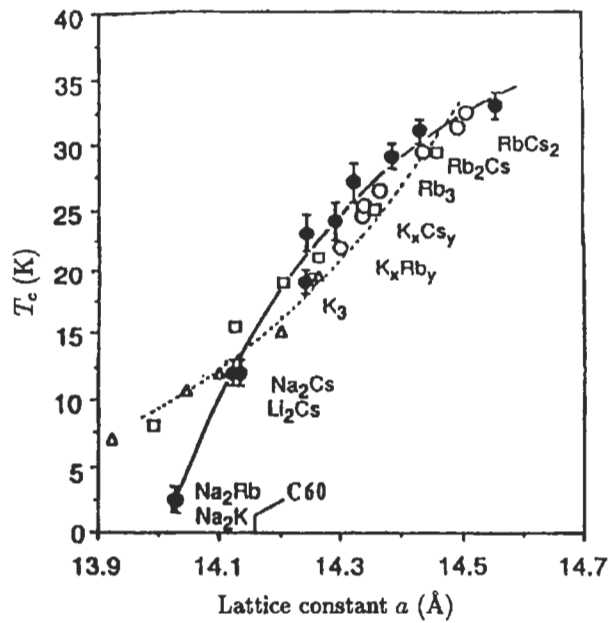


Fig. 13. Dependence of T_c for various M_3C_{60} and $M_{3-x}M'_xC_{60}$ compounds on the lattice constant a . Also included on the figure are data for superconducting samples under pressure [44].

samples under pressure [124, 125, 126]. Because of the close connection between the electronic density of states at the Fermi level $N(E_F)$ and the lattice constant a , plots of T_c vs $N(E_F)$ similar to Fig. 13 have been made [62].

The reason why the T_c is so much higher for M_3C_{60} relative to other carbon-based materials appears to be closely related to the high density of states [c.f., Eq. (1)] that can be achieved at the Fermi level when the t_{1u} LUMO molecular level is half filled with carriers. It is believed [127, 128] that the dominant coupling mechanism for superconductivity is electron-phonon coupling and that the H_g -derived high frequency phonons play a dominant role in the coupling. The observation of broad H_g -derived Raman lines [89, 97] in M_3C_{60} is consistent with a strong electron-phonon coupling.

The magnitude of the superconducting bandgap 2Δ has been studied by a variety of experimental techniques [122, 129] leading to the conclusion that the superconducting bandgap for both K_3C_{60} and Rb_3C_{60} is close to the BCS value of $3.5 kT_c$ [56, 64, 122, 130]. A good fit for the functional form of the temperature dependence of the bandgap to BCS theory was also obtained using the scanning tunneling microscopy technique [131]. Measurements of the isotope effect also suggest that $T_c \propto M^{-\alpha}$. Both small ($\alpha \sim 0.3 - 0.4$) values [132, 133] and large ($\alpha \sim 1.4$) values [134, 135] of α have been reported. Future work is needed to clarify the experimental picture of the isotope effect in the M_3C_{60} compounds. Closely related to the high compressibility of C_{60} [35] and M_3C_{60} ($M = K, Rb$) [125] is the large linear decrease in T_c with pressure.

These superconductors are strongly type II superconductors, with high values for the upper critical field H_{c2} and a short superconducting coherence length ξ_0 , with values of ξ_0 (2–3 nm) only slightly larger than a lattice constant for the fcc unit cell (~ 1.4 nm). A listing of values for the various parameters pertinent to the superconductivity of M_3C_{60} ($M = K, Rb$) is given in Table 1. In this table: a_0 is the lattice constant; T_c is the superconducting transition temperature; 2Δ is the superconducting bandgap; P is the pressure; H_{c1} , H_{c2} , and H_c are, respectively, the lower critical field, upper critical field, and thermodynamic critical field; J_c is the critical current density; ξ_0 is the superconducting coherence length; λ_L is the London penetration depth; and ℓ is the electron mean free path.

3 Carbon Nanotubes

The field of carbon nanotube research was launched in 1991 by the initial experimental observation of carbon nanotubes by transmission electron microscopy (TEM) [151], and the subsequent report of conditions for the synthesis of large quantities of nanotubes [152, 153]. Though early work was done on

Table 1. Experimental values for the macroscopic parameters of the superconducting phases of K_3C_{60} and Rb_3C_{60} .

Parameter	K_3C_{60}	Rb_3C_{60}
fcc a_0 (Å)	14.253 ^a	14.436 ^a
T_c (K)	19.7 ^b	30.0 ^b
$2\Delta(0)/kT_c$	5.2 ^c , 4.0 ^e , 3.6 ^g , 3.6 ^h	5.3 ^d , 3.1 ^e , 3.6 ^f , 3.0 ^g , 2.98 ^h
$(dT_c/dP)_{P=0}$ (K/GPa)	-7.8 ⁱ	-9.7 ⁱ
$H_{c1}(0)$ (mT)	13 ^j	26 ^j , 19 ^k
$H_{c2}(0)$ (T)	26 ^j , 30 ^l , 29 ^m , 17.5 ^b	34 ^j , 55 ^l , 76 ^b
$H_c(0)$ (T)	0.38 ⁱ	0.44 ⁱ
J_c (10^6 A/cm ²)	0.12 ^j	1.5 ^j
ξ_0 (nm)	2.6 ⁱ , 3.1 ^l , 3.4 ⁿ , 4.5 ^b	2.0 ⁱ , 2.0 ^b , 3.0 ⁿ
λ_L (nm)	240 ^j , 480 ^o , 600 ^p , 800 ^q	168 ^j , 370 ^j , 460 ^p , 800 ^q , 210 ^k
$\kappa = \lambda_L/\xi_0$	92 ^j	84 ^j , 90 ^k
dH_{c2}/dT (T/K)	-1.34 ^b , -3.5 ^r	-3.8 ^b
ℓ (nm)	3.1 ^b , 1.0 ^s	0.9 ^b

^aRef. [27]; ^bRef. [136]; ^cSTM measurements in Ref. [137]; ^dSTM measurements in Ref. [131]; ^eNMR measurements in Ref. [138, 139]; ^f μ SR measurements in Ref. [140]; ^gFar-IR measurements in Ref. [141]; ^hFar-IR measurements in Ref. [142]; ⁱRef. [125]; ^jRef. [143]; ^kRef. [144]; ^lRef. [145]; ^mRef. [146]; ⁿRef. [147]; ^oRef. [148]; ^pRef. [138]; ^qRef. [129, 149]; ^rRef. [150]; ^sRef. [132].

coaxial carbon cylinders called multi-wall carbon nanotubes, the discovery of smaller diameter single-wall carbon nanotubes in 1993 [154, 155], one atomic layer in thickness, greatly stimulated theoretical and experimental interest in the field. Other breakthroughs occurred with the discovery of methods to synthesize large quantities of single-wall nanotubes with a small distribution of diameters [156, 157], thereby enabling experimental observation of the remarkable electronic, vibrational and mechanical properties of carbon nanotubes. Various experiments carried out thus far (*e.g.*, high resolution TEM, STM, resistivity, and Raman scattering) are consistent with identifying single-wall carbon nanotubes as rolled up seamless cylinders of graphene sheets of sp^2 bonded carbon atoms organized into a honeycomb structure as a flat graphene sheet. Because of their very small diameters (down to ~ 0.7 nm) and relatively long lengths (up to \sim several μ m), single-wall carbon nanotubes are prototype hollow cylindrical 1D quantum wires.

3.1 Synthesis

The earliest observations of carbon nanotubes with very small (nanometer) diameters [151, 158, 159] are shown in Fig. 14. Here we see results of high resolution transmission electron microscopy (TEM) measurements, providing evidence for μ m-long multi-layer carbon nanotubes, with cross-sections showing several concentric coaxial nanotubes and a hollow core. One nanotube has

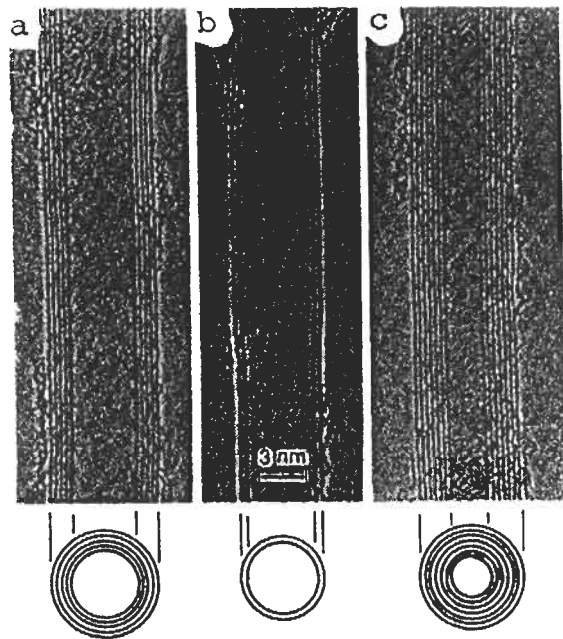


Fig. 14. High resolution TEM observations of three multi-wall carbon nanotubes with N concentric carbon nanotubes with various outer diameters d_o (a) $N = 5$, $d_o = 6.7$ nm, (b) $N = 2$, $d_o = 5.5$ nm, and (c) $N = 7$, $d_o = 6.5$ nm. The inner diameter of (c) is $d_i = 2.3$ nm. Each cylindrical shell is described by its own diameter and chiral angle [151].

only two coaxial carbon cylinders [Fig. 14(b)], and another has an inner diameter of only 2.3 nm [Fig. 14(c)] [151]. These carbon nanotubes were prepared by a carbon arc process (typical dc current of 50–100 A and voltage of 20–25 V), where carbon nanotubes form as bundles of nanotubes on the negative electrode, while the positive electrode is consumed in the arc discharge in a helium atmosphere [160]. The apparatus is similar to that used to synthesize endohedral fullerenes, except that the metal added to the anode is viewed as a catalyst keeping the end of the growing nanotube from closing [156]. Typical lengths of the arc-grown multi-wall nanotubes are $\sim 1 \mu\text{m}$, giving rise to an aspect ratio (length to diameter ratio) of 10^2 to 10^3 . Because of their small diameter, involving only a small number of carbon atoms, and because of their large aspect ratio, carbon nanotubes are classified as 1D carbon systems. Most of the theoretical work on carbon nanotubes has been on single-wall nanotubes and has emphasized their 1D properties. In the multi-wall carbon nanotubes, the measured interlayer distance is 0.34 nm [151], comparable to the interlayer separation of 0.344 nm in turbostratic carbons.

Single-wall nanotubes were first discovered in an arc discharge chamber using a catalyst, such as Fe, Co and other transition metals, during the synthesis process [154, 155]. The catalyst is packed into the hollow core of the electrodes and the nanotubes condense in a cob-web-like soot sticking to the chamber walls. Single-wall nanotubes, just like the multi-wall nanotubes and also conventional vapor grown carbon fibers [161], have hollow cores along the axis of the nanotube.

The diameter distribution of single-wall carbon nanotubes is of great interest for both theoretical and experimental reasons, since theoretical studies indicate that the physical properties of carbon nanotubes are strongly dependent on the nanotube diameter. Early results for the diameter distribution of Fe-catalyzed single-wall nanotubes (Fig. 15) show a diameter range between 0.7 nm and 1.6 nm, with the largest peak in the distribution at 1.05 nm, and with a smaller peak at 0.85 nm [154]. The smallest reported diameter for a single-wall carbon nanotube is 0.7 nm [154], the same as the diameter of the C_{60} molecule (0.71 nm) [162].

Two recent breakthroughs in the synthesis of single-wall carbon nanotubes [156, 157] have provided a great stimulus to the field by making significant amounts of available material for experimental studies. Single-wall carbon nanotubes prepared by the Rice University group by the laser vaporization method utilize a Co–Ni/graphite composite target operating in a furnace at 1200°C. High yields with >70%–90% conversion of graphite to single-wall nanotubes have been reported [156, 163] in the condensing vapor of the heated flow tube when the Co–Ni catalyst/carbon ratio was 1.2 atom % Co–Ni alloy with equal amounts of Co and Ni added to the graphite (98.8 atom %). Two sequenced laser pulses separated by a 50 ns delay were used to

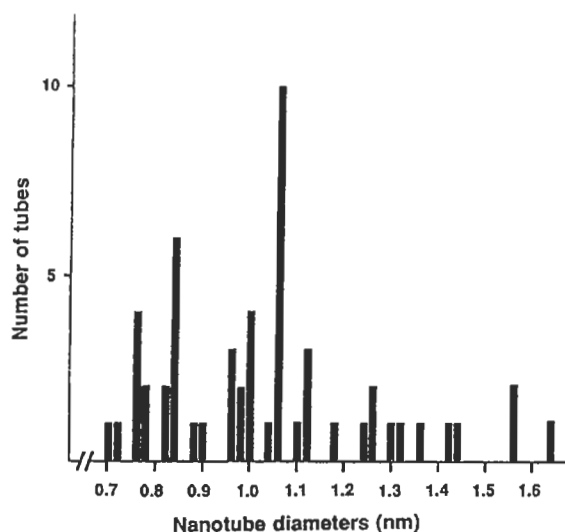


Fig. 15. Histogram of the single-wall nanotube diameter distribution for Fe-catalyzed nanotubes [154]. A relatively small range of diameters are found, the smallest diameter corresponding to that for the fullerene C_{60} .

provide a more uniform vaporization of the target and to gain better control of the growth conditions. Flowing argon gas sweeps the entrained nanotubes from the high temperature zone to a water-cooled Cu collector downstream, just outside the furnace [156]. Subsequently, an efficient (>70% conversion) carbon arc method (using a Ni-Y catalyst) was found by a French group at Montpellier [157] for growing single-wall carbon nanotube arrays with a small distribution of nanotube diameters, very similar to those produced by the Rice group [156, 163]. Other groups worldwide are now also making single-wall carbon nanotube ropes using variants of the laser vaporization or carbon arc methods.

The nanotube material produced by either the laser vaporization method or the carbon arc method appears in a scanning electron microscope (SEM) image as a mat of carbon “ropes” 10–20 nm in diameter and up to 100 μm or more in length. Under transmission electron microscope (TEM) examination, each carbon rope is found to consist primarily of a bundle of single-wall carbon nanotubes aligned along a common axis. X-ray diffraction (which views many ropes at once) and transmission electron microscopy (which views a single rope) show that the diameters of the single-wall nanotubes have a strongly peaked narrow distribution of diameters. For the synthesis conditions used by the Rice and Montpellier groups, the diameter distribution was strongly peaked at 1.38 ± 0.02 nm, very close to the diameter of an ideal (10,10) nanotube. X-ray diffraction measurements [156, 157] showed that these single-wall nanotubes form a two-dimensional triangular lattice with a

lattice constant of 1.7 nm, and an inter-tube separation of 0.315 nm at closest approach within a rope, in good agreement with prior theoretical modeling results [164, 165].

Whereas multi-wall carbon nanotubes require no catalyst for their growth, either by the laser vaporization or carbon arc methods, catalyst species are necessary for the growth of the single-wall nanotubes [156], while two different catalyst species seem to be needed to efficiently synthesize arrays of single wall carbon nanotubes by either the laser vaporization or arc methods. The detailed mechanisms responsible for the growth of carbon nanotubes are not yet well understood. Variations in the most probable diameter and the width of the diameter distribution is sensitively controlled by the composition of the catalyst, the growth temperature and other growth conditions.

3.2 Structure of Carbon Nanotubes

The structure of carbon nanotubes has been explored by high resolution TEM and STM characterization studies, yielding direct confirmation that the nanotubes are cylinders derived from the honeycomb lattice (graphene sheet). Strong evidence that the nanotubes are cylinders and are not scrolls comes from the observation that the same numbers of walls appear on the left and right hand sides of thousands of TEM images of nanotubes, such as shown in Fig. 14. In pioneering work, Bacon in 1960 [166] synthesized graphite whiskers which he described as scrolls, using essentially the same conditions as for the synthesis of carbon nanotubes, except for the use of helium pressures higher by an order of magnitude to synthesize the scrolls. It is believed that the cross-sectional morphology of multi-wall nanotubes and carbon whisker scrolls is different.

A single-wall carbon nanotube is conveniently characterized in terms of its diameter d_t , its chiral angle θ and its 1D (one-dimensional) unit cell, as shown in Fig. 16(a). Measurements of the nanotube diameter d_t and chiral angle θ are conveniently made by using STM (scanning tunneling microscopy) and TEM (transmission electron microscopy) techniques. Measurements of the chiral angle θ have been made using high resolution TEM [154, 167], and θ is normally defined by taking $\theta = 0^\circ$ and $\theta = 30^\circ$, for zigzag and armchair nanotubes, respectively. While the ability to measure the diameter d_t and the chiral angle θ of individual single-wall nanotubes has been demonstrated, it remains a major challenge to determine d_t and θ for specific nanotubes that are used for an actual physical property measurements, such as resistivity, Raman scattering, infrared spectra, etc.

The circumference of any carbon nanotube is expressed in terms of the chiral vector $\vec{C}_h = n\hat{a}_1 + m\hat{a}_2$ which connects two crystallographically equivalent sites on a 2D graphene sheet [see Fig. 16(a)] [162]. The construction in

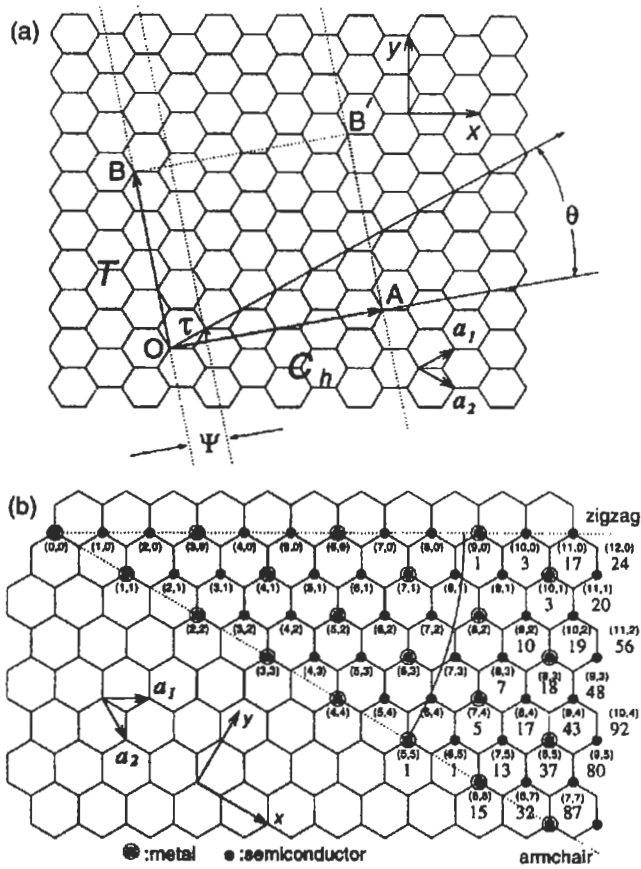


Fig. 16. (a) The chiral vector \vec{OA} or $\vec{C}_h = n\hat{a}_1 + m\hat{a}_2$ is defined on the honeycomb lattice of carbon atoms by unit vectors \hat{a}_1 and \hat{a}_2 of a graphene layer and the chiral angle θ with respect to the zigzag axis ($\theta = 0^\circ$). Also shown are the lattice vector $\vec{OB} = \mathbf{T}$ of the 1D nanotube unit cell, the rotation angle ψ and the translation $\vec{\tau}$. The lattice vector of the 1D nanotube \mathbf{T} is determined by \vec{C}_h . Therefore the integers (n, m) uniquely specify the symmetry of the basis vectors of a nanotube. The basic symmetry operation for the carbon nanotube is $R = (\psi|\vec{\tau})$. The diagram is constructed for $(n, m) = (4, 2)$. (b) Possible chiral vectors \vec{C}_h specified by the pairs of integers (n, m) for general carbon nanotubes, including zigzag, armchair, and chiral nanotubes. According to theoretical calculations, the encircled dots denote metallic nanotubes, while the small dots are for semiconducting nanotubes [162].

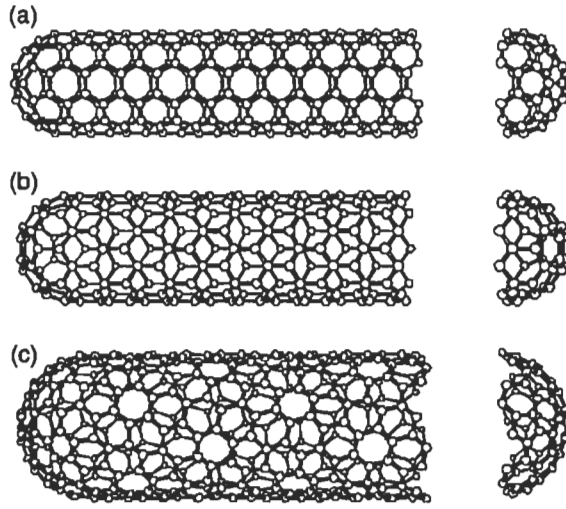


Fig. 17. Schematic models for a single-wall carbon nanotubes with the nanotube axis normal to: (a) the $\theta = 30^\circ$ direction (an “armchair” (n, n) nanotube), (b) the $\theta = 0^\circ$ direction (a “zigzag” $(n, 0)$ nanotube), and (c) a general direction, such as \vec{OB} (see Figure 16), with $0 < \theta < 30^\circ$ (a “chiral” (n, m) nanotube). The actual nanotubes shown here correspond to (n, m) values of: (a) $(5, 5)$, (b) $(9, 0)$, and (c) $(10, 5)$ [168].

Fig. 16(a) shows the chiral angle θ between the vector \vec{C}_h and the “zigzag” direction ($\theta = 0$), and shows the unit vectors \hat{a}_1 and \hat{a}_2 of the hexagonal honeycomb lattice [Figs. 16(a) and 17]. An ensemble of chiral vectors specified by pairs of integers (n, m) denoting the vector $\vec{C}_h = n\hat{a}_1 + m\hat{a}_2$ is given in Fig. 16(b) [169].

The cylinder connecting the two hemispherical caps of the carbon nanotube is formed by superimposing the two ends of the vector \vec{C}_h and the cylinder joint is made along the two lines OB and AB' in Fig. 16(a). The lines OB and AB' are both perpendicular to the vector \vec{C}_h at each end of \vec{C}_h [162]. The intersection of OB with the first lattice point determines the fundamental 1D translation vector \vec{T} and thus defines the length of the unit cell of the 1D lattice [Fig. 16(a)]. The chiral nanotube, thus generated has no distortion of bond angles other than distortions caused by the cylindrical curvature of the nanotube. Differences in the chiral angle θ and in the nanotube diameter d_t give rise to differences in the properties of the various graphene nanotubes. In the (n, m) notation for $\vec{C}_h = n\hat{a}_1 + m\hat{a}_2$, the vectors $(n, 0)$ or $(0, m)$ denote zigzag nanotubes and the vectors (n, n) denote armchair nanotubes. All other vectors (n, m) correspond to chiral nanotubes [169]. In terms of the integers (n, m) , the nanotube diameter d_t is given by

$$d_t = \sqrt{3}a_{C-C}(m^2 + mn + n^2)^{1/2}/\pi \quad (2)$$

and the chiral angle θ is given by

$$\theta = \tan^{-1}(\sqrt{3}n/(2m + n)). \quad (3)$$

The number of hexagons, N , per unit cell of a chiral nanotube is specified by the integers (n, m) and is given by

$$N = \frac{2(m^2 + n^2 + nm)}{d_R} \quad (4)$$

where d_R is the greatest common divisor of $(2n + m, 2m + n)$ and is given by

$$d_R = \begin{cases} d & \text{if } n - m \text{ is not a multiple of } 3d \\ 3d & \text{if } n - m \text{ is a multiple of } 3d, \end{cases} \quad (5)$$

where d is the greatest common divisor of (n, m) . The addition of a hexagon to the structure corresponds to the addition of two carbon atoms. As an example, application of Eq. (4) to the $(5, 5)$ and $(9, 0)$ nanotubes yields values of 10 and 18, respectively, for N . Since the 1D nanotube unit cell in real space is much larger than the 2D graphene unit cell, the 1D Brillouin zone is therefore much smaller than the one corresponding to a single 2-atom graphene unit cell. The application of Brillouin zone-folding techniques has been commonly used to obtain approximate electron and phonon dispersion relations for carbon nanotubes with specific symmetry (n, m) , as discussed in §3.3.

Because of the special atomic arrangement of the carbon atoms in a carbon nanotube, substitutional impurities are inhibited by the small size of the carbon atoms. Furthermore, the screw axis dislocation, the most common defect found in bulk graphite, is inhibited by the monolayer structure of the C_{60} nanotube. For these reasons, we expect relatively few substitutional or structural impurities in single-wall carbon nanotubes. Multi-wall carbon nanotubes frequently show “bamboo-like” defects associated with the termination of inner shells, and pentagon-heptagon ($5 - 7$) defects are also found frequently [7].

3.3 Electronic Structure

Structurally, carbon nanotubes of small diameter are examples of a one-dimensional periodic structure along the nanotube axis. In single wall carbon nanotubes, confinement of the structure in the radial direction is provided by the monolayer thickness of the nanotube in the radial direction. Circumferentially, the periodic boundary condition applies to the enlarged unit cell that is formed in real space. The application of this periodic boundary condition to the graphene electronic states leads to the prediction of a remarkable electronic structure for carbon nanotubes of small diameter. We first present

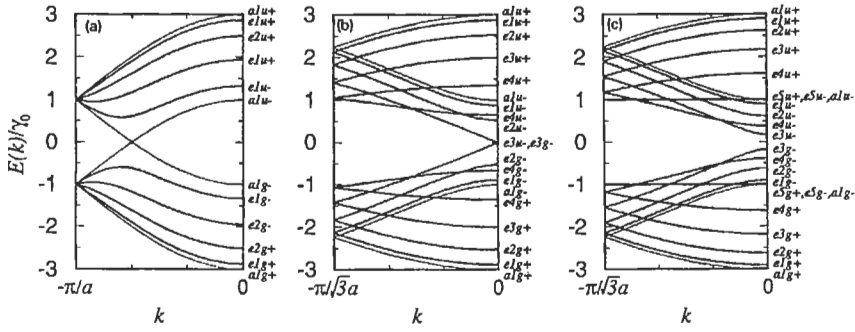


Fig. 18. One-dimensional energy dispersion relations for (a) armchair (5,5) nanotubes, (b) zigzag (9,0) nanotubes, and (c) zigzag (10,0) nanotubes. The energy bands with a symmetry are non-degenerate, while the e -bands are doubly degenerate at a general wave vector k [169, 175, 176].

a summary of theoretical predictions, followed by a summary of experimental observations which lend support to these predictions.

The 1D electronic energy bands for carbon nanotubes [170, 171, 172, 173, 174] are related to bands calculated for the 2D graphene honeycomb sheet used to form the nanotube. These calculations show that about 1/3 of the nanotubes are metallic and 2/3 are semiconducting, depending on the nanotube diameter d_t and chiral angle θ . It can be shown that metallic conduction in a (n, m) carbon nanotube is achieved when

$$2n + m = 3q \quad (6)$$

where q is an integer. All armchair carbon nanotubes ($\theta = 30^\circ$) are metallic and satisfy Eq. (6). The metallic nanotubes, satisfying Eq. (6), are indicated in Fig. 16(b) as encircled dots, and the small dots correspond to semiconducting nanotubes.

Calculated dispersion relations based on these simple considerations are shown for metallic nanotubes $(n, m) = (5, 5)$ and $(9, 0)$ in Figs. 18(a) and (b), respectively, and for a semiconducting nanotube $(n, m) = (10, 0)$ in Fig. 18(c) [175]. Figure 16(b) and Eq. (6) shows that all armchair nanotubes (n, n) are metallic, but only 1/3 of the possible zigzag nanotubes $(n, 0)$ and $(0, m)$ are metallic [169]). The calculated electronic structure can be either metallic or semiconducting depending on the choice of (n, m) , although there is no difference in the local chemical bonding between the carbon atoms in the nanotubes, and no doping impurities are present [169].

These surprising results can be understood on the basis of the electronic structure of a graphene sheet which is found to be a zero gap semiconductor [177] with bonding and antibonding π bands that are degenerate at the K -point (zone corner) of the hexagonal 2D Brillouin zone. The periodic boundary

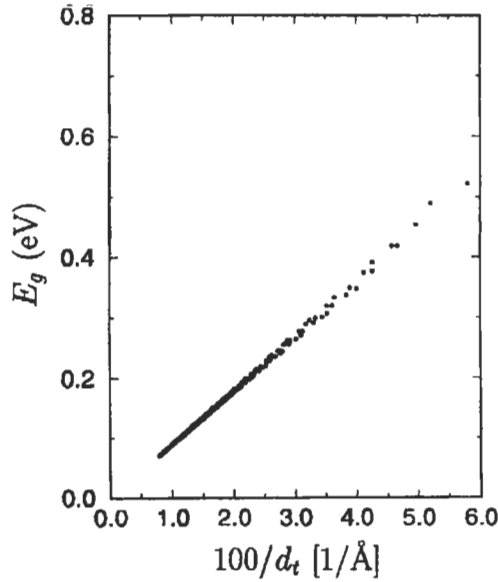


Fig. 19. The energy gap E_g for a general chiral single-wall carbon nanotube as a function of $100 \text{ \AA}/d_t$, where d_t is the nanotube diameter in \AA [179].

conditions for the 1D carbon nanotubes of small diameter permit only a few wave vectors to exist in the circumferential direction and these satisfy the relation $n\lambda = \pi d_t$ where $\lambda = 2\pi/k$. Metallic conduction occurs when one of these wave vectors k passes through the K -point of the 2D Brillouin zone, where the valence and conduction bands are degenerate because of the symmetry of the 2D graphene lattice.

As the nanotube diameter increases, more wave vectors become allowed for the circumferential direction, the nanotubes become more two-dimensional and the semiconducting band gap disappears, as is illustrated in Fig. 19 which shows the semiconducting band gap to be proportional to the reciprocal diameter $1/d_t$. At a nanotube diameter of $d_t \sim 3 \text{ nm}$ (Fig. 19), the bandgap becomes comparable to thermal energies at room temperature, showing that small diameter nanotubes are needed to observe these quantum effects. Calculation of the electronic structure for two concentric nanotubes shows that pairs of concentric metal-semiconductor or semiconductor-metal nanotubes are stable [178].

Closely related to the 1D dispersion relations for the carbon nanotubes is the 1D density of states shown in Fig. 20 for: (a) a semiconducting (10,0) zigzag carbon nanotube, and (b) a metallic (9,0) zigzag carbon nanotube. The results show that the metallic nanotubes have a small, but non-vanishing 1D density of states, whereas for a 2D graphene sheet (dashed curve) the density of states

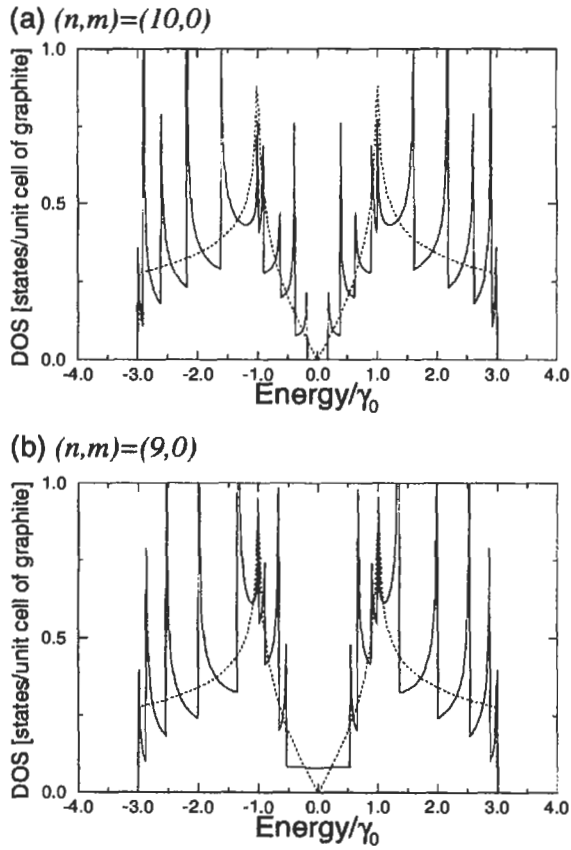


Fig. 20. Electronic 1D density of states per unit cell of a 2D graphene sheet for two $(n, 0)$ zigzag nanotubes: (a) the $(10, 0)$ nanotube which has semiconducting behavior, (b) the $(9, 0)$ nanotube which has metallic behavior. Also shown in the figure is the density of states for the 2D graphene sheet (dotted line) [178].

is zero at the Fermi level, and varies linearly with energy, as we move away from the Fermi level. In contrast, the density of states for the semiconducting 1D nanotubes is zero throughout the bandgap, as shown in Fig. 20(a).

From these results, one could imagine designing an electronic shielded wire device less than 3 nm in diameter, consisting of two concentric graphene nanotubes with a smaller diameter metallic inner nanotube surrounded by a larger diameter semiconducting (or insulating) outer nanotube. Such concepts could in principle be extended to the design of tubular metal-semiconductor all-carbon devices without introducing any doping impurities [169],

Experimental measurements to test the remarkable theoretical predictions of the electronic structure of carbon nanotubes are difficult to carry out because

of the strong dependence of the predicted properties on nanotube diameter and chirality. The experimental difficulties arise from the great experimental challenges in making electronic or optical measurements on individual single-wall nanotubes, and further challenges arise in making such demanding measurements on individual nanotubes that have been characterized with regard to diameter and chiral angle (d_t and θ). Despite these difficulties, pioneering work has already been reported on experimental observations relevant to the electronic structure of individual multi-wall nanotubes, on bundles of multi-wall nanotubes, on a single bundle or rope of single-wall carbon nanotubes, and even on an individual single-wall nanotube.

The most promising present technique for carrying out sensitive measurements of the electronic properties of individual nanotubes is scanning tunneling spectroscopy (STS) because of the ability of the tunneling tip to sensitively probe the electronic density of states of either a single-wall nanotube [180, 181] or the outermost cylinder of a multi-wall nanotube [182], because of the exponential dependence of the tunneling current on the distance between the nanotube and the tunneling tip. With this technique, it is further possible to carry out both STS and scanning tunneling microscopy (STM) measurements on the same nanotube and therefore to measure the nanotube diameter concurrently with the STS spectrum [182]. It has also been demonstrated that the chiral angle θ of a carbon nanotube can be determined using atomic resolution STM techniques [183, 181] or high-resolution TEM [151, 154, 184, 185, 186].

Several groups have thus far attempted STS studies of individual nanotubes [186, 182, 181]. The studies which appear to provide the most detailed test of the theory for the electronic properties of 1D carbon nanotubes, thus far, use the combined STM/STS technique [182, 181]. In this early STM/STS study, more than nine individual multi-wall nanotubes with diameters ranging from 1.7 to 9.5 nm were examined. Topographic STM measurements were also made to obtain the maximum height of the nanotube relative to the gold substrate, thus determining the diameter of an individual nanotube [182]. Then switching to the STS mode of operation, current-voltage (I-V) plots were made on the same region of the same nanotube as was characterized for its diameter by the STM measurement. The I-V plots for three typical nanotubes are shown in Fig. 21. The results on this figure provide evidence for one metallic nanotube with $d_t = 8.7$ nm [trace (1)] showing ohmic behavior, and two semiconducting nanotubes [trace (2) for a nanotube with $d_t = 4.0$ nm and trace (3) for a nanotube with $d_t = 1.7$ nm] showing plateaus at zero current and passing through $V = 0$. The dI/dV plot in the upper inset provides a tunneling density of states measurement for carbon nanotubes, the peaks in the dI/dV plot being attributed to singularities in the 1D density of states, as are shown in Fig. 20. Similar studies on single-wall nanotubes under higher resolution conditions show much more clearly defined density of states

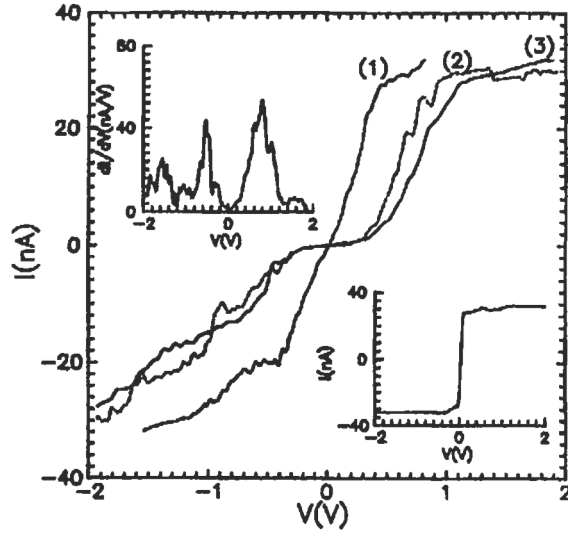


Fig. 21. Current–voltage I vs. V traces taken with scanning tunneling spectroscopy (STS) on individual nanotubes of various outer diameters: (1) $d_t = 8.7$ nm, (2) $d_t = 4.0$ nm, and (3) $d_t = 1.7$ nm. The top inset shows the conductance vs. voltage plot for data taken on the 1.7 nm nanotube. The bottom inset shows an I – V trace taken on a gold surface under the same conditions [182].

singularities [182, 181]. The results for all the semiconducting nanotubes measured so far [182, 181] showed a linear dependence of their energy gaps on $1/d_t$, the reciprocal nanotube diameter, consistent with the predicted functional form shown in Fig. 19.

Density of states measurements by scanning tunneling spectroscopy (STS) provide a powerful tool for probing the electronic structure of carbon nanotubes [182, 181]. Such measurements confirm that some nanotubes (about 1/3) are conducting, and some (about 2/3) are semiconducting [see Fig. 16(b)]. Measurements on semiconducting nanotubes (Fig. 21) confirm that the band gap is proportional to $1/d_t$ (see Fig. 19) [182, 181]. Spikes in the density of states (see Fig. 20) have been observed by STS measurements on metallic and semiconducting nanotubes, whose diameters and chiral angles were determined by operating the instrument in the scanning tunneling microscopy (STM) mode [181]. The STS results confirm the theoretical model that the energy between the lowest-lying resonance in the conduction band and the highest-lying resonance in the valence band is smaller for semiconducting nanotubes and larger for metallic nanotubes, and that the density of states at the Fermi level is non-zero for metallic nanotubes, but zero for semiconducting nanotubes [181]. Thus the main 1D quantum features predicted theoretically for the electronic properties of carbon nanotubes have now been observed experimentally.

3.4 *Transport Properties*

Early transport measurements on individual multi-wall nanotubes [187] were carried out on nanotubes with too large an outer diameter to be sensitive to 1D quantum effects. Furthermore, contributions from the inner constituent shells which may not make electrical contact with the current source complicate the interpretation of the transport results, and in some cases the measurements were not made at low enough temperatures to be sensitive to 1D effects. Early transport measurements on multiple ropes (arrays) of single-wall armchair carbon nanotubes [188], addressed general issues such as the temperature dependence of the resistivity of nanotube bundles, each containing many single-wall nanotubes with a distribution of diameters d_t and chiral angles θ . Their results confirmed the theoretical prediction that many of the individual nanotubes are metallic.

Early reports of transport measurements on an individual single-wall carbon nanotube of about 1 nm diameter have now been reported [189] and related measurements on a single rope of single-wall carbon nanotubes with a small diameter distribution were also reported [190]. Both of these studies, carried out in the milli-kelvin range, focus on the quantum dot aspect of single-wall carbon nanotubes and single-electron phenomena. Though very long in comparison to their diameter, carbon nanotubes are nevertheless finite in

length. Because of their finite length, the nanotubes have a discrete number of allowed wavevectors along the nanotube axis direction, thus giving rise to discrete energy states which can be determined by measurement of the conductance as a function of bias voltage (which controls the energy range of the detector) and gate voltage (which raises or lowers the energy levels of the nanotube relative to the Fermi level) [189, 190]. For a nanotube 3 μm in length [189], energy separations of 0.6 meV between the discrete states near the Fermi level were reported. “Coulomb blockade” phenomena have also been observed in an individual single-wall nanotube, [189] with a charging energy of 2.6 meV. Because of the large length to diameter ratio of carbon nanotubes, it is possible to make electrical contacts to these nanometer size structures by modern lithographic techniques. Single-wall carbon nanotubes thus provide a unique system for studying single molecule transistor effects where a third gate electrode in close proximity to the conducting nanotube is used to modulate the conductance [191].

Measurements of the temperature-dependent resistance and magnetoresistance down to the milli-kelvin range have been reported for an individual (multi-wall) carbon nanotube 20 nm in diameter using four attached electrical contacts [192]. The resistivity measurements confirm that some of the nanotubes have metallic conductivity, though large variations in the magnitude of the resistivity were found between samples measured within a single research group and between different research groups [193]. Because of the geometry of the multi-wall nanotubes it is difficult to make electrical contact to each of the constituent shells, and because of the high anisotropy of the conductivity along the nanotube axis and between two adjacent shells, and this contact problem makes it difficult to obtain reliable quantitative resistivity measurements. The results on multi-wall carbon nanotubes in the milli-kelvin temperature range show several characteristic behaviors, including negative magnetoresistance, evidence for weak carrier localization, and evidence for universal conductance fluctuations. All of these phenomena that are observed in a 20 nm multi-wall nanotube appear to relate to 2D rather than 1D transport behavior, presumably due to the large diameter of the nanotube and to the turbostratic relation between carbon atoms on adjacent shells of the nanotube.

3.5 *Vibrational Properties*

In analogy to the calculations described above for the electronic energy band structure, the phonon modes for carbon nanotubes have been calculated based on the well-established phonon dispersion relations for a two-dimensional (2D) graphene layer [194]. Detailed attention, however, must also be given to the radial breathing mode which is a characteristic mode of the cylindrical geometry of the nanotubes, but is not present on a graphene sheet. Using such

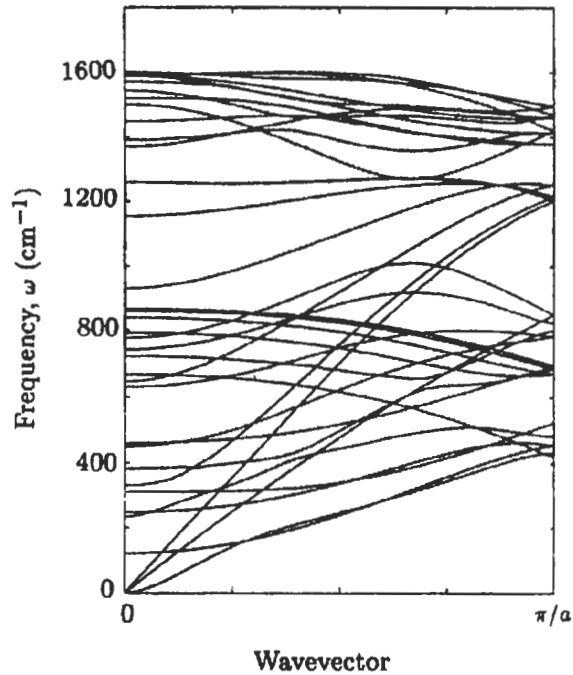


Fig. 22. Phonon dispersion relations for a (5,5) carbon nanotube. This armchair nanotube would be capped with a C₆₀ hemisphere [194].

an approach, the evaluation of the phonon mode frequencies in the nanotube requires the diagonalization of the dynamical matrix for the 1D unit cell of a graphene sheet, which has the area of a single hexagon [see Fig. 16(a)]. As in the case of the calculated electronic structure, the zone folding model for phonons neglects the effect of nanotube curvature, which becomes important for small diameter nanotubes (< 3 nm). Since the length of the nanotubes is much larger than their diameters, the nanotubes can be described in the 1D limit where the nanotubes have infinite length and the contributions from the carbon atoms in the end caps can be neglected.

To illustrate the phonon dispersion relations for carbon nanotubes and the large number of phonon branches that result from zone folding, we show in Fig. 22 calculated results for the 36 phonon branches for a (5,5) carbon nanotube [194]. This (5,5) armchair nanotube has ten hexagons per circumferential 1D unit cell of the nanotube, *i.e.*, going completely around the circumference, ($N = 10$), and 60 degrees of freedom per 1D unit cell, 12 nondegenerate phonon branches, and 24 doubly degenerate phonon branches. The (5,5) nanotube furthermore has 7 nonvanishing IR-active mode frequencies, 15 mode frequencies that are Raman active, 3 that are of zero frequency

and 11 silent mode frequencies, thereby accounting for the 36 distinct phonon branches.

In general, the number of phonon branches for a carbon nanotube is very large, since every nanotube has $6N$ vibrational degrees of freedom. The symmetry types of the phonon branches for a general chiral nanotube are obtained using a standard group theoretical analysis [194]

$$\Gamma_N^{\text{vib}} = 6A + 6B + 6E_1 + 6E_2 + \cdots + 6E_{N/2-1}, \quad (7)$$

where the A and B modes are nondegenerate and all the E modes are doubly-degenerate. Of these modes, the Raman-active modes are those that transform as A , E_1 , and E_2 and the infrared-active modes are those that transform as A or E_1 . Thus, the number of phonon branches increases six times as fast as N , though the number of Raman-active and infrared-active modes remains constant and independent of N , with 15 nonzero Raman-active mode frequencies and 9 nonzero infrared-active mode frequencies, after subtracting the modes associated with acoustic translations ($A + E_1$) and with rotation of the cylinder (A). As an example, consider the $(n, m) = (7, 4)$ nanotube, with $N = 62$, so that the 1D unit cell has 372 degrees of freedom and 192 phonon branches in all. Of these, 15 are Raman active at $k = 0$, while 9 are infrared active, 3 corresponding to zero-frequency modes at $k = 0$, and 162 are silent.

The samples used for Raman experiments on single-wall carbon nanotubes have a narrow distribution of diameters and chiralities, which depend sensitively on the catalysts that are used in the synthesis and the growth conditions, especially the growth temperature. Among the 15 Raman-allowed zone-center modes, the experiments using a laser excitation wavelength of 514.5 nm show a few intense lines and several weaker lines, taken on a sample for which the mean diameter corresponded to that midway between a (9,9) and a (10,10) armchair nanotube [195]. Between 1550 and 1600 cm^{-1} , two strong lines are observed at 1567 cm^{-1} and 1593 cm^{-1} , which are derived from the same optic phonon branch as the graphite E_{2g_2} optic mode ($\omega = 1582 \text{ cm}^{-1}$ at the Brillouin zone center) which has been extensively studied in HOPG (highly oriented pyrolytic graphite) [196]. The strong lines between 1550 and 1600 cm^{-1} may be assigned to the E_{1g} , E_{2g} and A_{1g} modes in carbon nanotubes with different diameters. The Raman frequencies in this frequency region do not vary much with carbon nanotube diameter, as shown in Fig. 24 which presents the calculated diameter dependence of the various Raman-active modes for armchair nanotubes. The very weak lines observed between 300–1500 cm^{-1} correspond to modes for which calculations predict very low intensities [197, 198].

At 186 cm^{-1} , a strong line is seen in Fig. 23. This feature is identified with the A_{1g} radial breathing mode and depends only on the nanotube diameter. The linewidth and lineshape is due to contributions from nanotubes of different

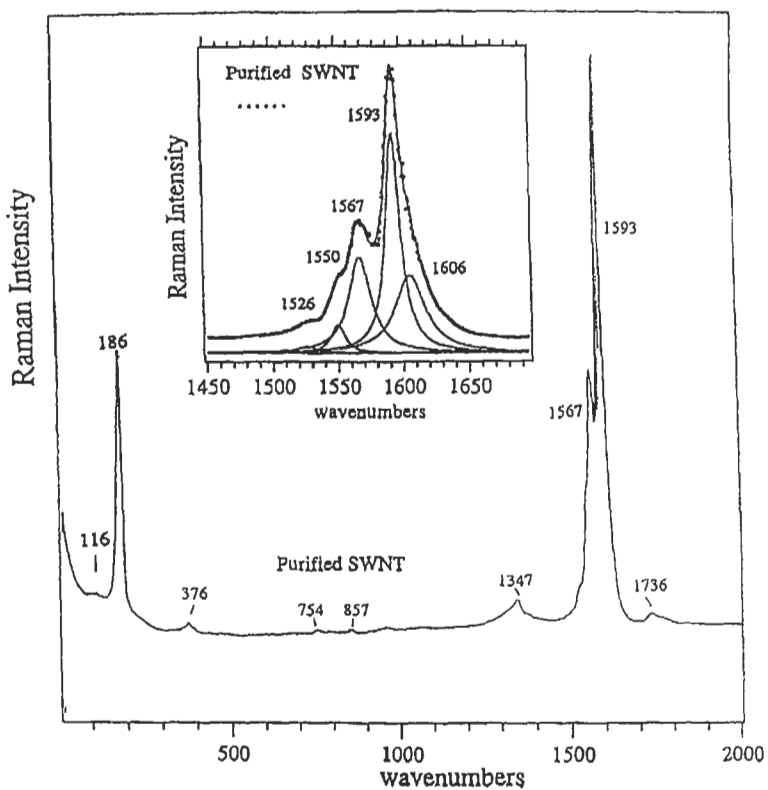


Fig. 23. Experimental room temperature Raman spectrum from a sample consisting primarily of bundles or “ropes” of single-wall nanotubes with diameters near that of the (10,10) nanotube. The excitation laser wavelength is 514.5 nm. The inset shows the lineshape analysis of the vibrational modes near 1580 cm^{-1} . SWNT refers to “single-wall carbon nanotubes” [195].

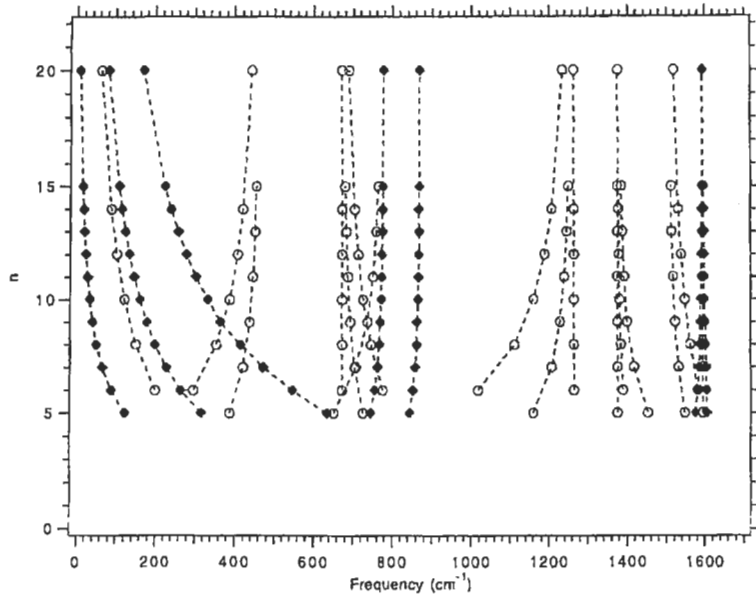


Fig. 24. The armchair index n vs mode frequency for the Raman-active modes of single-wall armchair (n, n) carbon nanotubes [195]. From Eq. (2), the nanotube diameter is given by $d = 3a_{C-C}n/\pi$.

diameters. This feature can be used as a marker for assigning the diameter and chirality of the carbon nanotube under investigation. Since the frequency of the A_{1g} breathing mode depends on the number of carbon atoms in the circumferential direction, the frequency of the A_{1g} mode depends sensitively on the nanotube diameter (Fig. 24). The radial breathing mode does not depend directly on the chiral angle, since all atoms in the unit cell have displacements that are in phase with each other. The apparent dependence on chiral angle arises through the relation between the nanotube diameter d_t and the chiral angle θ because of the finite number of possible nanotubes (n, m) .

In the low frequency region, the calculations predict nanotube-specific E_{1g} and E_{2g} modes around 116 cm^{-1} and 377 cm^{-1} , respectively, for (10,10) armchair nanotubes, but their intensities are expected to be lower than that for the A_{1g} mode. However, these E_{1g} and E_{2g} modes are important, since they also show a diameter dependence of their mode frequencies. In the very low frequency region below 30 cm^{-1} , a strong low frequency Raman-active E_{2g} mode is expected. However, it is difficult to observe Raman lines in the very low frequency region, where the background Rayleigh scattered is very strong.

The Raman spectra are strongly dependent on the frequency of the excitation laser because of the resonant Raman effect associated with the singularities in the density of states shown in Fig. 20. These van Hove singularities arise from the folding the two-dimensional energy bands of the graphene layer into the one-dimensional energy bands of the carbon nanotube. For every one-dimensional band edge, as in a carbon nanotube, a $1/\sqrt{E}$ singularity is expected for the energy dependence of the one-dimensional density of states (see Fig. 20). The energy separation of these singularities in the 1D density of states depends on the diameter of the nanotube. Under resonant conditions, more light can be absorbed, thereby enhancing the production of phonons via the electron-phonon coupling process. In Fig. 25 are shown Raman spectra obtained with different laser excitation wavelengths. The Raman modes that are preferentially enhanced correspond to those nanotubes for which the laser frequency is equal to the separation between resonances in the valence and conduction bands, such as shown in Fig. 25. The Raman scattering resonance condition thus selects the particular carbon nanotube (n, m) which has a singularity in its joint electronic density of states at the laser frequency. The observed phonon frequency of the low frequency A_{1g} mode can provide the value of the nanotube diameter that is in resonance electronically. Thus the resonance effect is a quantum effect that can be understood in terms of both the electronic and phonon dispersion relations of the nanotubes.

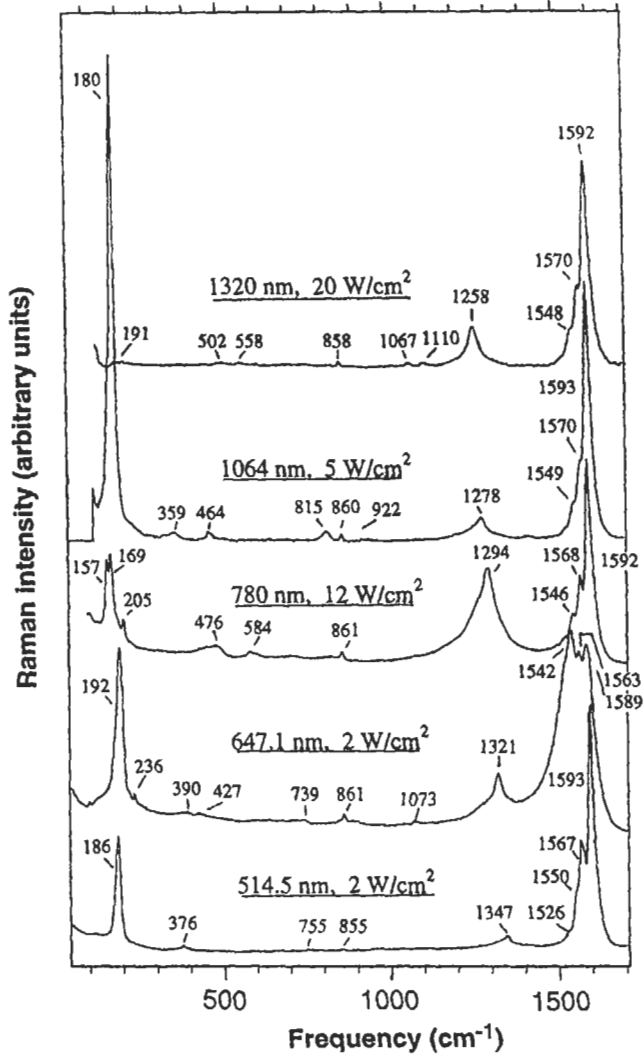


Fig. 25. Room temperature Raman spectra for purified single-wall carbon nanotubes excited at five different laser wavelengths, showing evidence for the resonant enhancement effect. As a consequence of the 1D density of states, specific nanotubes (n, m) are resonant at each laser frequency [195].

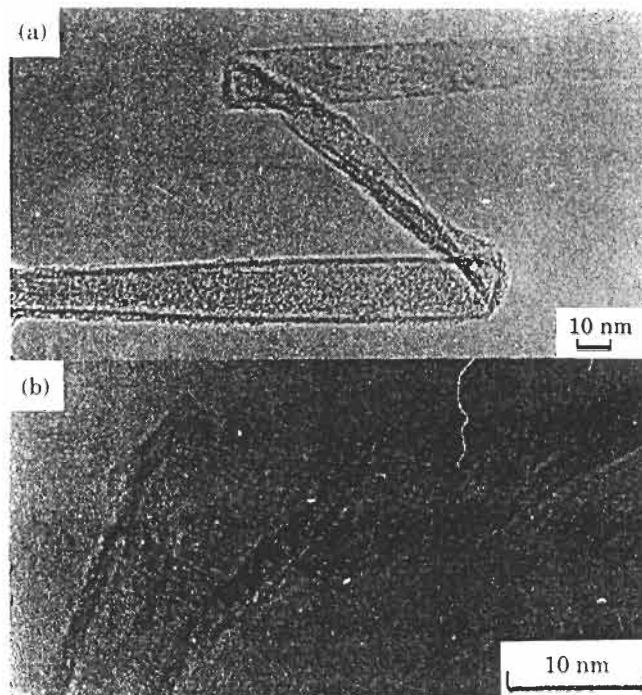


Fig. 26. High-resolution TEM images of bent and twisted carbon nanotubes. The length scales for these images are indicated [199].

3.6 Mechanical Properties

The elastic properties of fullerene-related nanotubes have been discussed both theoretically and experimentally. Direct observations, mostly using high-resolution TEM, have shown that small diameter single-wall carbon nanotubes are remarkably flexible, and bend into curved arcs with radii of curvature as small as 20 nm. This flexibility suggests excellent mechanical properties, consistent with the high tensile strength and bulk modulus of commercial and research-grade vapor grown carbon fibers [196]. As shown in Fig. 26, even relatively large diameter (~ 10 nm) carbon nanotubes grown from the vapor phase can bend, twist, and kink without fracturing [199, 200]. The basic mechanical properties of the nanotubes are very different from those of conventional PAN-based and vapor-grown carbon fibers, which are much more fragile and are easily broken when bent or twisted. It is of interest to note that when bent or twisted, the nanotubes appear to flatten in cross section, especially single wall nanotubes with larger diameters [200, 201].

Theoretical studies indicate that for $d_t < 2$ nm the effect of strain energy exceeds that of the room temperature thermal energy, so that it is only at small nanotube diameters that the strain energy associated with nanotube

curvature is important. The strain energy per carbon atom for fullerenes of similar diameter is much larger than for the comparable nanotube, reflecting the two-dimensional curvature of fullerenes in comparison with nanotubes which have only one-dimensional curvature. Calculations for the energetics of the stretching and compression of multi-wall nanotubes show good agreement with an elastic continuum model based on the elastic constant of C_{11} for graphite [202, 13, 203].

The large value measured for the elastic modulus [~ 1 TPa (terapascal)] [204] accounts for the straightness of small diameter nanotubes in TEM micrographs [201]. As a consequence of the elastic limit model, the thermal conductivity of carbon nanotubes along the nanotube axis is expected to be high, based on observations on carbon fibers, while the thermal conductivity between shells of a multi-wall nanotube or between single-wall nanotubes within a single rope is expected to be very low. Very low expansion coefficients are also expected tangential to the nanotube surface, consistent with the anisotropic and anomalous thermal expansion coefficient for graphite which is small and negative in-plane, and large and positive along the c -axis. The magnitude of the beam rigidity of carbon nanotubes is found to exceed that of presently available materials [205], so that graphene nanotubes are expected to offer outstanding mechanical properties, consistent with observations shown in Fig. 26. Single-wall carbon nanotubes are also remarkable regarding their mechanical properties under compression. Whereas carbon fibers fracture easily under compression, carbon nanotubes form kink-like ridges under compression and these ridges can relax elastically when the stress is released. Extreme hardness was also found for bundles of carbon nanotubes, exceeding that of the toughest alloys used as substrates [14]. Thus single-wall carbon nanotubes are believed to possess many of the desirable mechanical properties of carbon fibers, but, in addition, single-wall carbon nanotubes have a number of other desirable properties with regard to bending into loops, cross-sectional distortions, twisting distortions, elongation and compression without fracture.

4 Applications

Although research on solid C_{60} , carbon nanotubes, and related materials is still at an early stage, these materials are already beginning to show many exceptional properties, some of which may lead to practical applications. Large scale production of C_{60} and C_{70} has already occurred. However, the production of significant quantities of reasonably pure carbon nanotubes has yet to occur.

One promising application for C_{60} is as an optical limiter. Optical limiters are used to protect people and materials from damage by high light intensities usually associated with intense pulsed sources. Optical limiting is accom-

plished through a saturation of the transmitted light intensity with increasing incident intensity. Outstanding performance for C_{60} relative to presently used optical limiting materials has been observed at 5320Å for 8 ns pulses using solutions of C_{60} in toluene and in chloroform (CH_3Cl) [77]. The proposed mechanism for the optical limiting is that C_{60} is more absorptive for molecules in the triplet excited state than for the ground state (see §2.4). In this process, the initial absorption of a photon takes an electron from singlet S_0 state to an excited singlet state. This is followed by a rapid inter-system crossing from the singlet to a metastable triplet state from which dipole-allowed transitions to the higher-lying triplet states can occur. Because of the higher excitation cross section for electrons in the metastable triplet state (relative to those in the ground state), an increase in the population of the metastable triplet state promotes further stronger absorption of photons [77].

Another interesting applications area for fullerenes is based on materials that can be fabricated using fullerene-doped polymers. Polyvinylcarbazole (PVK) and other selected polymers, such as poly(paraphenylene-vinylene) (PPV) and phenylmethylpolysilane (PMPS), doped with a mixture of C_{60} and C_{70} have been reported to exhibit exceptionally good photoconductive properties [206, 207, 208] which may lead to the development of future polymeric photoconductive materials. Small concentrations of fullerenes (*e.g.* ~3% by weight) lead to charge transfer of the photo-excited electrons in the polymer to the fullerenes, thereby promoting the conduction of mobile holes in the polymer [209]. Fullerene-doped polymers also have significant potential for use in applications, such as photo-diodes, photo-voltaic devices and as photo-refractive materials.

Fullerenes have been shown to benefit the synthesis of SiC and diamond. Gruen and coworkers [210] have demonstrated that, by fragmentation of individual C_{60} molecules, diamond films of very small grain size can be synthesized, yielding superior wear resistance, and lubrication properties [210]. Hamza and coworkers [211] have shown that by use of vacuum deposited C_{60} films, SiC thin films can be prepared at lower temperatures, and with several desirable properties. For example, by using a patterned Si/SiO₂ substrate, a patterned SiC surface could be prepared (though no effective etch is known for SiC), exploiting the fact that C_{60} bonds well to Si, but poorly to SiO₂. Thus conventional Si technology could be used to prepare a surface with Si in the regions where the SiC coat is eventually to form, and SiO₂ in the regions where it should not form. Then the C_{60} is introduced, covering the Si regions and avoiding the SiO₂ regions. Finally, heating to 950–1250°C, converts the C_{60} on Si to an adhering SiC patch. Such patterned materials have potential as light-emitting diodes in optoelectronic circuits.

In other materials synthesis applications, the utilization of the strong bonding of fullerenes to clean silicon surfaces, has led to the application of a monolayer

of C_{60} as a bonding agent between thin silicon wafers [208]. This strong bonding property, together with the low chemical reactivity of fullerenes, have been utilized in the passivation of reactive surfaces by the adsorption of monolayers of C_{60} on aluminum and silicon surfaces [208].

Many research opportunities exist for the controlled manipulation of structures of nm dimensions. Advances made in the characterization and manipulation of carbon nanotubes should therefore have a substantial general impact on the science and technology of nanostructures. The exceptionally high modulus and strength of thin multi-wall carbon nanotubes can be used in the manipulation of carbon nanotubes and other nanostructures [212, 213].

Many of the carbon nanotube applications presently under consideration relate to multi-wall carbon nanotubes, partly because of their greater availability, and because the applications do not explicitly depend on the 1D quantum effects associated with the small diameter single-wall carbon nanotubes.

The caps of carbon nanotubes were shown to be more chemically reactive than the cylindrical sections [214], and the caps have been shown to be efficient electron emitters [215, 216, 217]. Therefore, applications of nanotubes for displays and for electron probe tips have thus been discussed in the literature. The ability of carbon nanotubes to retain relatively high gas pressures within their hollow cores suggest another possible area for applications [218]. Carbon nanotubes have also been proposed as a flexible starting point for the synthesis of new nano-scale and nano-structured carbides, whereby the carbon nanotube serves as a template for the subsequent formation of carbides. The sandwiching of layers of carbon cylinders surrounded by insulating BN cylinders on either side offers exciting possibilities for electronic applications [219]. By analogy with carbon fibers which are used commercially in composites for structural strengthening and for enhancement of the electrical conductivity, it should also be possible to combine carbon nanotubes with a host polymer (or metal) to produce composites with physical properties that can be tailored to specific applications. The small size of carbon nanotubes allow them to be used in polymer composite materials that can be extruded through an aperture (die) to form shaped objects with enhanced strength and stiffness. Carbon nanotubes can be added to low viscosity paints that can be sprayed onto a surface, thereby enhancing the electrical conductivity of the coating.

As further research on fullerenes and carbon nanotubes materials is carried out, it is expected, because of the extreme properties exhibited by these carbon-based materials, that other interesting physics and chemistry will be discovered, and that promising applications will be found for fullerenes, carbon nanotubes and related materials.

5 Acknowledgments

The authors acknowledge fruitful discussions with Professors M. Endo, R. Saito, and R. A. Jishi. The MIT authors gratefully acknowledge support from NSF Grant #DMR-95-10093 and from AFOSR grant F49620-93-1-0160. The work at UK was supported by NSF OSR-94-52895 and also the US-Japan exchange program NSF INT 93-15165.

6 References

- 1 H. W. Kroto, J. R. Heath, S. C. O'Brien, R. F. Curl, and R. E. Smalley, *Nature (London)* **318**, 162–163 (1985).
- 2 R. Buckminster Fuller. In *The Artifacts of R. Buckminster Fuller: A Comprehensive Collection of His Designs and Drawings*, edited by W. Marlin, Garland Publishing, New York, 1984.
- 3 E. A. Rohlfing, D. M. Cox, and A. Kaldor, *J. Chem. Phys.* **81**, 3322 (1984).
- 4 W. Krätschmer, L. D. Lamb, K. Fostiropoulos, and D. R. Huffman, *Nature (London)* **347**, 354–358 (1990).
- 5 R. F. Curl and R. E. Smalley, *Science* **242**, 1017 (1988).
- 6 R. C. Haddon, A. F. Hebard, M. J. Rosseinsky, D. W. Murphy, S. J. Duclos, K. B. Lyons, B. Miller, J. M. Rosamilia, R. M. Fleming, A. R. Kortan, S. H. Glarum, A. V. Makhija, A. J. Muller, R. H. Eick, S. M. Zahurak, R. Tycko, G. Dabbagh, and F. A. Thiel, *Nature (London)* **350**, 320 (1991).
- 7 M. S. Dresselhaus, G. Dresselhaus, and P. C. Eklund, *Science of Fullerenes and Carbon Nanotubes* (Academic Press, New York, NY, 1996).
- 8 A. F. Hebard, M. J. Rosseinsky, R. C. Haddon, D. W. Murphy, S. H. Glarum, T. T. M. Palstra, A. P. Ramirez, and A. R. Kortan, *Nature (London)* **350**, 600 (1991).
- 9 A. F. Hebard, *Phys. Today* **45**, 26 (1992). November issue.
- 10 T. T. M. Palstra, O. Zhou, Y. Iwasa, P. Sulewski, R. Fleming, and B. Zegarski, *Solid State Commun.* **93**, 327 (1995).
- 11 M. Endo. *Mecanisme de croissance en phase vapeur de fibres de carbone (The growth mechanism of vapor-grown carbon fibers)*. PhD thesis, University of Orleans, Orleans, France, 1975. (in French).
- 12 M. Endo. PhD thesis, Nagoya University, Japan, 1978. (in Japanese).
- 13 D. H. Robertson, D. W. Brenner, and J. W. Mintmire, *Phys. Rev. B* **45**, 12592 (1992).
- 14 Z. Ya. Kosakovskaya, L. A. Chernozatonskii, and E. A. Fedorov, *JETP Lett. (Pis'ma Zh. Eksp. Teor.)* **56**, 26 (1992).
- 15 E. G. Gal'pern, I. V. Stankevich, A. L. Christyakov, and L. A. Chernozatonskii, *JETP Lett. (Pis'ma Zh. Eksp. Teor.)* **55**, 483 (1992).
- 16 R. L. Meng, D. Ramirez, X. Jiang, P. C. Chow, C. Diaz, K. Matsuishi, S. C. Moss, P. H. Hor, and C. W. Chu, *Appl. Phys. Lett.* **59**, 3402 (1991).
- 17 M. Haluška, H. Kuzmany, M. Vybornov, P. Rogl, and P. Fejdi, *Appl. Phys. A* **56**, 161 (1993).
- 18 M. A. Verheijen, H. Meeke, G. Meijer, E. Raas, and P. Bennema, *Chem. Phys. Lett.* **191**, 339 (1992).
- 19 R. E. Smalley, *Accounts Chem. Res.* **25**, 98 (1992).
- 20 D. S. Bethune, R. D. Johnson, J. R. Salem, M. S. de Vries, and C. S. Yannoni, *Nature (London)* **366**, 123 (1993).
- 21 M. S. Dresselhaus, G. Dresselhaus, and P. C. Eklund, *J. Mater. Res.* **8**, 2054 (1993).

- 22 M. S. Dresselhaus and G. Dresselhaus, *Advances in Phys.* **30**, 139–326 (1981).
- 23 L. S. Wang, J. Conceicao, C. Jin, and R. E. Smalley, *Chem. Phys. Lett.* **182**, 5 (1991).
- 24 W. R. Datars, T. R. Chien, R. K. Nkum, and P. K. Ummat, *Phys. Rev. B* **50**, 4937 (1994).
- 25 M. J. Rosseinsky, D. W. Murphy, R. M. Fleming, R. Tycko, A. P. Ramirez, T. Siegrist, G. Dabbagh, and S. E. Barrett, *Nature (London)* **356**, 416 (1992).
- 26 K. Tanigaki, T. W. Ebbesen, S. Saito, J. Mizuki, J. S. Tsai, Y. Kubo, and S. Kuroshima, *Nature (London)* **352**, 222 (1991).
- 27 A. R. Kortan, N. Kopylov, S. H. Glarum, E. M. Gyorgy, A. P. Ramirez, R. M. Fleming, F. A. Thiel, and R. C. Haddon, *Nature (London)* **355**, 529 (1992).
- 28 A. R. Kortan, N. Kopylov, E. Özdas, A. P. Ramirez, R. M. Fleming, and R. C. Haddon, *Chem. Phys. Lett.* **223**, 501 (1994).
- 29 Y. Chen, F. Stepniak, J. H. Weaver, L. P. F. Chibante, and R. E. Smalley, *Phys. Rev. B* **45**, 8845–8848 (1992).
- 30 R. Taylor and D. R. M. Walton, *Nature (London)* **363**, 685 (1993).
- 31 G. A. Olah, I. Bucsi, R. Anisfeld, and G. K. Surya Prakash, *Carbon* **30**, 1203–1211 (1992).
- 32 R. Taylor, J. P. Hare, A. K. Abdul-Sada, and H. W. Kroto, *J. Chem. Soc. Chem. Commun.* **20**, 1423–1425 (1990).
- 33 R. D. Johnson, G. Meijer, and D. S. Bethune, *J. Amer. Chem. Soc.* **112**, 8983–8984 (1990).
- 34 G. Dresselhaus, M. S. Dresselhaus, and P. C. Eklund, *Phys. Rev. B* **45**, 6923 (1992).
- 35 D. S. Fischer, *Phys. Rev. B* **43**, 130–159 (1991).
- 36 J. E. Fischer, P. A. Heiney, and A. B. Smith III, *Accounts Chem. Res.* **25**, 112 (1992).
- 37 F. Diederich and R. L. Whetten, *Accounts Chem. Res.* **25**, 119 (1992).
- 38 J. M. Hawkins, *Accounts Chem. Res.* **25**, 150 (1992).
- 39 K. Kikuchi, N. Nakahara, T. Wakabayashi, S. Suzuki, H. Shiramaru, Y. Miyake, K. Saito, I. Ikemoto, M. Kainosho, and Y. Achiba, *Nature (London)* **357**, 142 (1992).
- 40 D. E. Manolopoulos and P. W. Fowler, *Chem. Phys. Lett.* **187**, 1 (1991).
- 41 P. W. Stephens, L. Mihaly, P. L. Lee, R. L. Whetten, S. M. Huang, R. Kaner, F. Diederich, and K. Holczer, *Nature (London)* **351**, 632 (1991).
- 42 R. M. Fleming, M. J. Rosseinsky, A. P. Ramirez, D. W. Murphy, J. C. Tully, R. C. Haddon, T. Siegrist, R. Tycko, S. H. Glarum, P. M. Marsh, G. Dabbagh, S. M. Zahurak, A. V. Makhija, and C. Hampton, *Nature (London)* **352**, 701 (1991).
- 43 P. A. Heiney, G. B. M. Vaughan, J. E. Fischer, N. Coustel, D. E. Cox, J. R. D. Copley, D. A. Neumann, W. A. Kamitakahara, K. M. Creegan, D. M. Cox, J. P. McCauley, Jr., and A. B. Smith, III, *Phys. Rev. B* **45**, 4544–4547 (1992).
- 44 R. M. Fleming, A. P. Ramirez, M. J. Rosseinsky, D. W. Murphy, R. C. Haddon, S. M. Zahurak, and A. V. Makhija, *Nature (London)* **352**, 787 (1991).
- 45 P. A. Heiney, J. E. Fischer, A. R. McGhie, W. J. Romanow, A. M. Denenstein, J. P. McCauley, Jr., A. B. Smith, III, and D. E. Cox, *Phys. Rev. Lett.* **67**, 1468 (1991).
- 46 W. I. F. David, R. M. Ibberson, T. J. S. Dennis, J. P. Hare, and K. Prassides, *Europhys. Lett.* **18**, 219 (1992).
- 47 J. D. Axe, S. C. Moss, and D. A. Neumann. In *Solid State Physics: Advances in Research and Applications*, edited by H. Ehrenreich and F. Spaepen, pages 149–224, Academic Press, New York, 1994. Chapter 3.
- 48 G. B. Vaughan, P. A. Heiney, J. E. Fischer, D. E. Luzzi, D. A. Ricketts-Foot, A. R. McGhie, Y. W. Hui, A. L. Smith, D. E. Cox, W. J. Romanow, B. H. Allen, N. Coustel, J. P. McCauley, Jr., and A. B. Smith III, *Science* **254**, 1350 (1991).

- 49 M. A. Verheijen, H. Meekes, G. Meijer, P. Bennema, J. L. de Boer, S. van Smaalen, G. Van Tendeloo, S. Amelinckx, S. Muto, and J. van Landuyt, *Chem. Phys.* **166**, 287 (1992).
- 50 G. Van Tendeloo, S. Amelinckx, M. A. Verheijen, P. H. M. van Loosdrecht, and G. Meijer, *Phys. Rev. Lett.* **69**, 1065 (1992).
- 51 G. B. M. Vaughan, P. A. Heiney, D. E. Cox, J. E. Fischer, and A. R. McGhie, *Chem. Phys.* **178**, 599 (1993).
- 52 A. R. McGhie, J. E. Fischer, P. W. Stephens, R. L. Cappelletti, D. A. Neumann, W. H. Mueller, H. Mohn, and H. U. ter Meer, *Phys. Rev. B* **49**, 12614 (1994).
- 53 J. F. Armbruster, H. A. Romberg, P. Schweiss, P. Adelman, M. Knupfer, J. Fink, R. H. Michel, J. Rockenberger, F. Hennrich, H. Schreiber, and M. M. Kappes, *Z. Phys. B* **95**, 469–474 (1994).
- 54 G. Roth, P. Adelman, and R. Knitter, *Materials Lett.* **16**, 357–363 (1993).
- 55 J. H. Weaver and D. M. Poirier. In *Solid State Physics*, edited by H. Ehrenreich and F. Spaepen, page 1, Academic Press, New York, 1994. Chapter 1.
- 56 C. M. Lieber and C. C. Chen. In *Solid State Physics*, edited by H. Ehrenreich and F. Spaepen, page 109, Academic Press, New York, 1994.
- 57 D. M. Poirier, D. W. Owens, and J. H. Weaver, *Phys. Rev. B* **51**, 1830–1843 (1995).
- 58 R. M. Fleming, T. Siegrist, P. M. Marsh, B. Hessen, A. R. Kortan, D. W. Murphy, R. C. Haddon, R. Tycko, G. Dabbagh, A. M. Mujsce, M. L. Kaplan, and S. M. Zahurak. In *Clusters and Cluster-Assembled Materials, MRS Symposia Proceedings, Boston*, edited by R. S. Averback, J. Bernholc, and D. L. Nelson, pages 691–696, Materials Research Society Press, Pittsburgh, PA, 1991.
- 59 A. R. Kortan, N. Kopylov, and F. A. Thiel, *J. Phys. Chem. Solids* **53**, 1683–1688 (1992).
- 60 S. Saito and A. Oshiyama, *Phys. Rev. Lett.* **66**, 2637 (1991).
- 61 F. Negri, G. Orlandi, and F. Zerbetto, *J. Am. Chem. Soc.* **114**, 2910 (1992).
- 62 A. Oshiyama, S. Saito, N. Hamada, and Y. Miyamoto, *J. Phys. Chem. Solids* **53**, 1457–1471 (1992).
- 63 S. C. Erwin and M. R. Pederson, *Phys. Rev. Lett.* **67**, 1610 (1991).
- 64 W. E. Pickett. In *Solid State Physics*, edited by H. Ehrenreich and F. Spaepen, page 225, Academic Press, Volume 48, New York, 1994.
- 65 M. P. Gelfand, *Superconductivity Review* **1**, 103–150 (1994).
- 66 A. M. Rao, P. Zhou, K.-A. Wang, G. T. Hager, J. M. Holden, Ying Wang, W. T. Lee, Xiang-Xin Bi, P. C. Eklund, D. S. Cornett, M. A. Duncan, and I. J. Amster, *Science* **259**, 955–957 (1993).
- 67 H. Ajie, M. M. Alvarez, S. J. Anz, R. D. Beck, F. Diederich, K. Fostiropoulos, D. R. Huffman, W. Krätschmer, Y. Rubin, K. E. Schriver, D. Sensharma, and R. L. Whetten, *J. Phys. Chem.* **94**, 8630–8633 (1990).
- 68 T. Pichler, M. Matus, J. Kürti, and H. Kuzmany, *Solid State Commun.* **81**, 859 (1992).
- 69 S. P. Sibley, S. M. Argentine, and A. H. Francis, *Chem. Phys. Lett.* **188**, 187–193 (1992).
- 70 M. Matus, H. Kuzmany, and E. Sohmen, *Phys. Rev. Lett.* **68**, 2822 (1992).
- 71 Ying Wang, J. M. Holden, A. M. Rao, P. C. Eklund, U. Venkateswaran, D. Eastwood, R. L. Lidberg, G. Dresselhaus, and M. S. Dresselhaus, *Phys. Rev. B* **51**, 4547–4556 (1995).
- 72 F. Diederich, R. Ettl, Y. Rubin, R. L. Whetten, R. Beck, M. Alvarez, S. Anz, D. Sensharma, F. Wudl, K. C. Khemani, and A. Koch, *Science* **252**, 548 (1991).
- 73 J. B. Birks, in , (Wiley and Sons, London, 1970). A general review of the molecular spectroscopy of aromatic molecules.
- 74 R. R. Hung and J. J. Grabowski, *J. Phys. Chem.* **95**, 6073–6074 (1991).

- 75 T. W. Ebbesen, K. Tanigaki, and S. Kuroshima, *Chem. Phys. Lett.* **181**, 501 (1991).
- 76 L. W. Tutt and T. F. Boggess, *Progress in Quantum Electronics* **17**, 299–338 (1993).
- 77 L. W. Tutt and A. Kost, *Nature (London)* **356**, 225 (1992).
- 78 S. L. Ren, Y. Wang, A. M. Rao, E. McRae, G. T. Hager, K. A. Wang, W. T. Lee, H. F. Ni, J. Selegue, and P. C. Eklund, *Appl. Phys. Lett.* **59**, 2678 (1991).
- 79 S. L. Ren, K. A. Wang, P. Zhou, Y. Wang, A. M. Rao, M. S. Meier, J. Selegue, and P. C. Eklund, *Appl. Phys. Lett.* **61**, 124 (1992).
- 80 E. Sohmen, J. Fink, and W. Krätschmer, *Z. Phys. B* **86**, 87 (1992).
- 81 A. F. Hebard, R. C. Haddon, R. M. Fleming, and A. R. Kortan, *Appl. Phys. Lett.* **59**, 2109–2111 (21 Oct 1991).
- 82 B. Pevzner, A. F. Hebard, R. C. Haddon, S. D. Senturia, and M. S. Dresselhaus. In *Science and Technology of Fullerene Materials: MRS Symposia Proceedings, Volume 359, Boston, Fall 1994*, edited by P. Bernier, T. W. Ebbesen, D. S. Bethune, R. M. Metzger, L. Y. Chiang, and J. W. Mintmire, pages 423–428, Materials Research Society Press, Pittsburgh, PA, 1995.
- 83 H. Romberg, E. Sohmen, M. Merkel, et al., *Synthetic Metals* **56**, 3038–3043 (1993).
- 84 Y. Wang, J. M. Holden, A. M. Rao, W. T. Lee, X. X. Bi, S. L. Ren, G. W. Lehman, G. T. Hager, and P. C. Eklund, *Phys. Rev. B* **45**, 14396–14399 (1992).
- 85 Z. H. Kafafi, J. R. Lindle, R. G. S. Pong, F. J. Bartoli, L. J. Lingg, and J. Milliken, *Chem. Phys. Lett.* **188**, 492 (1992).
- 86 S. R. Flom, R. G. S. Pong, F. J. Bartoli, and Z. H. Kafafi, *Phys. Rev. B* **46**, 15598 (1992).
- 87 H. Hoshi, N. Nakamura, Y. Maruyama, T. Nakagawa, S. Suzuki, H. Shiromaru, and Y. Achiba, *Jpn. J. Appl. Phys.* **30**, L1397 (1991).
- 88 D. S. Bethune, G. Meijer, W. C. Tang, and H. J. Rosen, *Chem. Phys. Lett.* **174**, 219 (1990).
- 89 P. C. Eklund, Ping Zhou, Kai-An Wang, G. Dresselhaus, and M. S. Dresselhaus, *J. Phys. Chem. Solids* **53**, 1391 (1992).
- 90 A. M. Vassallo, L. S. Pang, P. A. Cole-Clark, and M. A. Wilson, *J. Am. Chem. Soc.* **113**, 7820 (1991).
- 91 B. Chase, N. Herron, and E. Holler, *J. Phys. Chem.* **96**, 4262 (1992).
- 92 K. A. Wang, Y. Wang, Ping Zhou, J. M. Holden, S. L. Ren, G. T. Hager, H. F. Ni, P. C. Eklund, G. Dresselhaus, and M. S. Dresselhaus, *Phys. Rev. B* **45**, 1955 (1992).
- 93 Ping Zhou, Kai-An Wang, Ying Wang, P. C. Eklund, M. S. Dresselhaus, G. Dresselhaus, and R. A. Jishi, *Phys. Rev. B* **46**, 2595 (1992).
- 94 P. H. M. van Loosdrecht, P. J. M. van Bentum, and G. Meijer, *Phys. Rev. Lett.* **68**, 1176 (1992).
- 95 D. S. Bethune, G. Meijer, W. C. Tang, H. J. Rosen, W. G. Golden, H. Seki, C. A. Brown, and M. S. de Vries, *Chem. Phys. Lett.* **179**, 181 (1991).
- 96 G. Meijer, D. S. Bethune, W. C. Tang, H. J. Rosen, R. D. Johnson, R. J. Wilson, D. D. Chambliss, W. G. Golden, H. Seki, M. S. de Vries, C. A. Brown, J. R. Salem, H. E. Hunziker, and H. R. Wendt. In *Clusters and Cluster-Assembled Materials, MRS Symposia Proceedings, Boston*, edited by R. S. Averback, J. Bernholc, and D. L. Nelson, page 619. Materials Research Society Press, Pittsburgh, PA, 1991.
- 97 S. J. Duclos, R. C. Haddon, S. H. Glarum, A. F. Hebard, and K. B. Lyons, *Science* **254**, 1625 (1991).
- 98 R. E. Stanton and M. D. Newton, *J. Phys. Chem.* **92**, 2141 (1988).
- 99 P. Zhou, A. M. Rao, K. A. Wang, J. D. Robertson, C. Eloi, M. S. Meier, S. L. Ren, X. X. Bi, P. C. Eklund, and M. S. Dresselhaus, *Appl. Phys. Lett.* **60**, 2871 (1992).

- 100 A. M. Rao, K. A. Wang, P. Zhou, Y. Wang, S. L. Ren, and P. C. Eklund. Springer-Verlag, New York, Berlin, 1992. Springer series in solid-state sciences.
- 101 Z. H. Dong, P. Zhou, J. M. Holden, P. C. Eklund, M. S. Dresselhaus, and G. Dresselhaus, *Phys. Rev. B* **48**, 2862 (1993).
- 102 K. A. Wang, A. M. Rao, P. C. Eklund, M. S. Dresselhaus, and G. Dresselhaus, *Phys. Rev. B* **48**, 11375–11380 (1993).
- 103 R. A. Jishi, M. S. Dresselhaus, G. Dresselhaus, K. A. Wang, Ping Zhou, A. M. Rao, and P. C. Eklund, *Chem. Phys. Lett.* **206**, 187 (1993).
- 104 D. W. Snoke, Y. S. Raptis, and K. Syassen, *Phys. Rev. B* **45**, 14419–14422 (1992).
- 105 R. A. Jishi, R. M. Mirie, M. S. Dresselhaus, G. Dresselhaus, and P. C. Eklund, *Phys. Rev. B* **48**, 5634–5642 (1993).
- 106 T. Pichler, M. Matus, J. Kürti, and H. Kuzmany, *Phys. Rev. B* **45**, 13841 (1992).
- 107 S. H. Glarum, S. J. Duclos, and R. C. Haddon, *J. Am. Chem. Soc.* **114**, 1996–2001 (1992).
- 108 P. Zhou, K. A. Wang, P. C. Eklund, G. Dresselhaus, and M. S. Dresselhaus, *Phys. Rev. B* **48**, 8412 (1993).
- 109 M. G. Mitch and J. S. Lannin, *J. Phys. Chem. Solids* **54**, 1801 (1993).
- 110 M. S. Dresselhaus and G. Dresselhaus, *Light Scattering in Solids III* **51**, 3 (1982). edited by M. Cardona and G. Güntherodt, Springer-Verlag Berlin, Topics in Applied Physics.
- 111 R. A. Jishi and M. S. Dresselhaus, *Phys. Rev. B* **45**, 6914 (1992).
- 112 G. P. Kochanski, A. F. Hebard, R. C. Haddon, and A. T. Fiory, *Science* **255**, 184 (1992).
- 113 F. Stepniak, P. J. Benning, D. M. Poirier, and J. H. Weaver, *Phys. Rev. B* **48**, 1899 (1993).
- 114 X.-D. Xiang, J. G. Hou, G. Briceño, W. A. Vareka, R. Mostovoy, A. Zettl, V. H. Crespi, and M. L. Cohen, *Science* **256**, 1190 (1992).
- 115 Y. Maruyama, T. Inabe, H. Ogata, Y. Achiba, S. Suzuki, K. Kikuchi, and I. Ikemoto, *Chem. Lett.* **10**, 1849 (1991). The Chemical Society of Japan.
- 116 T. T. M. Palstra, R. C. Haddon, A. F. Hebard, and J. Zaanen, *Phys. Rev. Lett.* **68**, 1054 (1992).
- 117 M. Núñez Regueiro, P. Monceau, A. Rassat, P. Bernier, and A. Zahab, *Nature (London)* **354**, 289 (1991).
- 118 N. B. Hannay, T. H. Geballe, B. T. Matthias, K. Andres, P. Schmidt, and D. MacNair, *Phys. Rev. Lett.* **14**, 225–226 (1965).
- 119 A. Chaiken, M. S. Dresselhaus, T. P. Orlando, G. Dresselhaus, P.M. Tedrow, D. A. Neumann, and W. A. Kamitakahara, *Phys. Rev. B* **41**, 71 (1990).
- 120 I. T. Belash, A. D. Bronnikov, O. V. Zharikov, and A. V. Pal'nichenko, *Synth. Metals* **36**, 283 (1990).
- 121 K. Holczer, O. Klein, G. Grüner, S.-M. Huang, R. B. Kaner, K.-J. Fu, R. L. Whetten, and F. Diederich, *Science* **252**, 1154 (1991).
- 122 M. S. Dresselhaus, G. Dresselhaus, and R. Saito. In *Physical Properties of High Temperature Superconductors IV*, edited by D. M. Ginsberg, World Scientific Publishing Co., Singapore, 1994. Vol. IV, Chapter 7.
- 123 K. Tanigaki, I. Hirosawa, T. W. Ebbesen, J. Mizuki, Y. Shimakawa, Y. Kubo, J. S. Tsai, and S. Kuroshima, *Nature (London)* **356**, 419–421 (1992).
- 124 G. Sparn, J. D. Thompson, S.-M. Huang, R. B. Kaner, F. Diederich, R. L. Whetten, G. Grüner, and K. Holczer, *Science* **252**, 1829 (1991).
- 125 G. Sparn, J. D. Thompson, R. L. Whetten, S.-M. Huang, R. B. Kaner, F. Diederich, G. Grüner, and K. Holczer, *Phys. Rev. Lett.* **68**, 1228 (1992).
- 126 J. E. Schirber, D. L. Overmyer, H. H. Wang, J. M. Wang, K. D. Carlson, A. M. Kini, M. J. Pellin, U. Welp, and W.-K. Kwok, *Physica C* **178**, 137 (1991).

- 127 C. M. Varma, J. Zaanen, and K. Raghavachari, *Science* **254**, 989 (1991).
- 128 K. H. Johnson, M. E. McHenry, and D. P. Clougherty, *Physica C* **183**, 319 (1991).
- 129 L. Degiorgi, P. Wachter, G. Grüner, S. M Huang, J. Wiley, and R. B. Kaner, *Phys. Rev. Lett.* **69**, 2987 (1992).
- 130 M. P. Gelfand and J. P. Lu, *Appl. Phys. A* **56**, 215 (1993).
- 131 Z. Zhang, C. C. Chen, and C. M. Lieber, *Science* **254**, 1619 (1991).
- 132 A. P. Ramirez, A. R. Kortan, M. J. Rosseinsky, S. J. Duclos, A. M. Mujsce, R. C. Haddon, D. W. Murphy, A. V. Makhija, S. M. Zahurak, and K. B. Lyons, *Phys. Rev. Lett.* **68**, 1058 (1992).
- 133 C.-C. Chen and C. M. Lieber, *J. Am. Chem. Soc.* **114**, 3141 (1992).
- 134 T. W. Ebbesen, J. S. Tsai, K. Tanigaki, J. Tabuchi, Y. Shimakawa, Y. Kubo, I. Hirotsawa, and J. Mizuki, *Nature (London)* **355**, 620 (1992).
- 135 A. A. Zakhidov, K. Imaeda, D. M. Petty, K. Yakushi, H. Inokuchi, K. Kikuchi, I. Ikemoto, S. Suzuki, and Y. Achiba, *Phys. Lett. A* **164**, 355 (1992).
- 136 M. L. Cohen, *Mater. Sci. Eng.* **B19**, 111–116 (1993).
- 137 Z. Zhang, C.-C. Chen, S. P. Kelty, H. Dai, and C. M. Lieber, *Nature (London)* **353**, 333 (1991).
- 138 R. Tycko, G. Dabbagh, M. J. Rosseinsky, D. W. Murphy, A. P. Ramirez, and R. M. Fleming, *Phys. Rev. Lett.* **68**, 1912 (1992).
- 139 K. Holczer, O. Klein, H. Alloul, Y. Yoshinari, and F. Hippert, *Europhys. Lett.* **23**, 63 (1993).
- 140 R. F. Kiefl, W. A. MacFarlane, K. H. Chow, S. Dunsiger, T. L. Duty, T. M. S. Johnston, J. W. Schneider, J. Sonier, L. Brard, R. M. Strongin, J. E. Fischer, and A. B. Smith III, *Phys. Rev. Lett.* **70**, 3987 (1993).
- 141 L. D. Rotter, Z. Schlesinger, J. P. McCauley, Jr., N. Coustel, J. E. Fischer, and A. B. Smith III, *Nature (London)* **355**, 532 (1992).
- 142 L. Degiorgi, G. Grüner, P. Wachter, S. M Huang, J. Wiley, R. L. Whetten, R. B. Kaner, K. Holczer, and F. Diederich, *Phys. Rev. B* **46**, 11250 (1992).
- 143 K. Holczer and R. L. Whetten, *Carbon* **30**, 1261 (1992).
- 144 A. I. Sokolov, Yu. A. Kufaev, and E. B. Sonin, *Physica C* **212**, 19–22 (1993).
- 145 S. Foner, E. J. McNiff, Jr., D. Heiman, S. M. Huang, and R. B. Kaner, *Phys. Rev. B* **46**, 14936 (1992).
- 146 G. S. Boebinger, T. T. M. Palstra, A. Passner, M. J. Rosseinsky, D. W. Murphy, and I. I. Mazin, *Phys. Rev. B* **46**, 5876 (1992).
- 147 R. D. Johnson, D. S. Bethune, and C. S. Yannoni, *Accounts Chem. Res.* **25**, 169 (1992).
- 148 Y. J. Uemura, A. Keren, L. P. Le, G. M. Luke, B. J. Sternlieb, W. D. Wu, J. H. Brewer, R. L. Whetten, S. M. Huang, S. Lin, R. B. Kaner, F. Diederich, S. Donovan, and G. Grüner, *Nature (London)* **352**, 605–607 (1991).
- 149 L. Degiorgi, E. J. Nicol, O. Klein, G. Grüner, P. Wachter, S. M. Huang, J. Wiley, and R. B. Kaner, *Phys. Rev. B* **49**, 7012 (1994).
- 150 A. P. Ramirez, M. J. Rosseinsky, D. W. Murphy, and R. C. Haddon, *Phys. Rev. Lett.* **69**, 1687–1690 (1992).
- 151 S. Iijima, *Nature (London)* **354**, 56 (1991).
- 152 T. W. Ebbesen and P. M. Ajayan, *Nature (London)* **358**, 220 (1992).
- 153 T. W. Ebbesen, H. Hiura, J. Fujita, Y. Ochiai, S. Matsui, and K. Tanigaki, *Chem. Phys. Lett.* **209**, 83–90 (1993).
- 154 S. Iijima and T. Ichihashi, *Nature (London)* **363**, 603 (1993).
- 155 D. S. Bethune, C. H. Kiang, M. S. de Vries, G. Gorman, R. Savoy, J. Vazquez, and R. Beyers, *Nature (London)* **363**, 605 (1993).
- 156 A. Thess, R. Lee, P. Nikolaev, H. Dai, P. Petit, J. Robert, C. Xu, Y. H. Lee, S. G. Kim, A. G. Rinzler, D. T. Colbert, G. E. Scuseria, D. Tománek, J. E. Fischer, and

- R. E. Smalley, *Science* **273**, 483 (1996).
- 157 C. Journet, W. K. Maser, P. Bernier, A. Loiseau, M. Lamy de la Chapelle, S. Lefrant, P. Deniard, R. Lee, and J. E. Fischer, *Nature (London)* **388**, 756 (1997).
- 158 M. Endo, H. Fujiwara, and E. Fukunaga, Meeting of Japanese Carbon Society pages 34–35 (1991). (unpublished).
- 159 M. Endo, H. Fujiwara, and E. Fukunaga, Second C₆₀ Symposium in Japan pages 101–104 (1992). (unpublished).
- 160 T. W. Ebbesen, *Annu. Rev. Mater. Sci.* **24**, 235–264 (1994).
- 161 M. Endo, *CHEMTECH* **18**, 568 (1988). September issue.
- 162 M. S. Dresselhaus, G. Dresselhaus, and R. Saito, *Phys. Rev. B* **45**, 6234 (1992).
- 163 T. Guo, C.-M. Jin, and R. E. Smalley, *Chem. Phys. Lett.* **243**, 49–54 (1995).
- 164 J. C. Charlier and J. P. Michenaud, *Phys. Rev. Lett.* **70**, 1858–1861 (1993).
- 165 J.-C. Charlier, T. W. Ebbesen, and Ph. Lambin, *Phys. Rev. B* **53**, 11108 (1996).
- 166 R. Bacon, *J. Appl. Phys.* **31**, 283–290 (1960).
- 167 K. Sattler, *Carbon* **33**, 915 (1995).
- 168 M. S. Dresselhaus, G. Dresselhaus, and R. Saito, *Carbon* **33**, 883–891 (1995).
- 169 R. Saito, M. Fujita, G. Dresselhaus, and M. S. Dresselhaus, *Appl. Phys. Lett.* **60**, 2204–2206 (1992).
- 170 R. Saito, G. Dresselhaus, and M. S. Dresselhaus, *Chem. Phys. Lett.* **195**, 537 (1992).
- 171 J. W. Mintmire, B. I. Dunlap, and C. T. White, *Phys. Rev. Lett.* **68**, 631–634 (1992).
- 172 T. Hamada, M. Furuyama, T. Tomioka, and M. Endo, *J. Mater. Res.* **7**, 1178–1188 (1992). *ibid.*, 2612–2620.
- 173 K. Harigaya, *Chem. Phys. Lett.* **189**, 79 (1992).
- 174 K. Tanaka, M. Okada, K. Okahara, and T. Yamabe, *Chem. Phys. Lett.* **191**, 469 (1992).
- 175 R. Saito, M. Fujita, G. Dresselhaus, and M. S. Dresselhaus. In *Electrical, Optical and Magnetic Properties of Organic Solid State Materials, MRS Symposia Proceedings, Boston*, edited by L. Y. Chiang, A. F. Garito, and D. J. Sandman, page 333, Materials Research Society Press, Pittsburgh, PA, 1992.
- 176 Riichiro Saito, Mitsutaka Fujita, G. Dresselhaus, and M. S. Dresselhaus, *Phys. Rev. B* **46**, 1804–6242 (1992).
- 177 G. S. Painter and D. E. Ellis, *Phys. Rev. B* **1**, 4747 (1970).
- 178 R. Saito, G. Dresselhaus, and M. S. Dresselhaus, *J. Appl. Phys.* **73**, 494 (1993).
- 179 M. S. Dresselhaus, R. A. Jishi, G. Dresselhaus, D. Inomata, K. Nakao, and Riichiro Saito, *Molecular Materials* **4**, 27–40 (1994).
- 180 S. Wang and D. Zhou, *Chem. Phys. Lett.* **225**, 165 (1994).
- 181 J. W. G. Wildöer, L. C. Venema, A. G. Rinzler, R. E. Smalley, and C. Dekker, *Nature (London)* **388** (1997).
- 182 C. H. Olk and J. P. Heremans, *J. Mater. Res.* **9**, 259 (1994).
- 183 M. Ge and K. Sattler, *Science* **260**, 515 (1993).
- 184 V. P. Dravid, X. Lin, Y. Wang, X. K. Wang, A. Yee, J. B. Ketterson, and R. P. H. Chang, *Science* **259**, 1601 (1993).
- 185 S. Amelinckx, D. Bernaerts, X. B. Zhang, G. Van Tendeloo, and J. Van Landuyt, *Science* **267**, 1334 (1995).
- 186 Z. Zhang and C. M. Lieber, *Appl. Phys. Lett.* **62**, 2792–2794 (1993).
- 187 T. Ebbesen. In *Fullerenes and Nanotubes*, edited by Pierre Delhaès and P. M. Ajayan, Gordon and Breach, Paris, France, 1998. Series: World of Carbon, volume 2.
- 188 J. E. Fischer, H. Dai, A. Thess, N. M. Hanjani, D. L. Dehaas, and R. E. Smalley, *Phys. Rev. B* **55**, R4921 (1997).
- 189 S. J. Tans, M. H. Devoret, H. Dal, A. Thess, R. E. Smalley, L. J. Geerligs, and

- C. Dekker, *Nature (London)* **386**, 474 (1997).
- 190 M. Bockrath, D. H. Cobden, P. L. McEuen, N. G. Chopra, A. Zettl, A. Thess, and R. E. Smalley, *Science* **275**, 1922 (1997).
- 191 L. Kouwenhoven, *Science* **275**, 1896 (1997).
- 192 L. Langer, V. Bayot, J. P. Issi, L. Stockman, C. Van Haesendonck, Y. Bruynseraede, J. P. Heremans, and C. H. Olk, *Extended Abstracts of the Carbon Conference* page 348 (1995).
- 193 T. W. Ebbesen, *Phys. Today* **49**, 26 (1996). June issue.
- 194 R. A. Jishi, L. Venkataraman, M. S. Dresselhaus, and G. Dresselhaus, *Chem. Phys. Lett.* **209**, 77–82 (1993).
- 195 A. M. Rao, E. Richter, S. Bandow, B. Chase, P. C. Eklund, K. W. Williams, M. Menon, K. R. Subbaswamy, A. Thess, R. E. Smalley, G. Dresselhaus, and M. S. Dresselhaus, *Science* **275**, 187–191 (1997).
- 196 M. S. Dresselhaus, G. Dresselhaus, K. Sugihara, I. L. Spain, and H. A. Goldberg, *Graphite Fibers and Filaments* (Springer-Verlag, Berlin, 1988), Vol. 5 of *Springer Series in Materials Science*.
- 197 E. Richter and K. R. Subbaswamy, *Phys. Rev. Lett.* (1997). in press.
- 198 R. Saito, T. Takeya, T. Kimura, G. Dresselhaus, and M. S. Dresselhaus, *Phys. Rev. B* (1998).
- 199 M. Endo, K. Takeuchi, S. Igarashi, K. Kobori, M. Shiraishi, and H. W. Kroto, *J. Phys. Chem. Solids* **54**, 1841–1848 (1993).
- 200 J. Tersoff and R. S. Ruoff, *Phys. Rev. Lett.* **73**, 676 (1994).
- 201 R. S. Ruoff and D. C. Lorents, *Carbon* **33**, 925 (1995).
- 202 B. T. Kelly, in *Physics of Graphite*, (Applied Science (London), 1981).
- 203 J. Tersoff, *Phys. Rev. B* **46**, 15546 (1992).
- 204 M. M. J. Treacy, T. W. Ebbesen, and J. M. Gibson, *Nature (London)* **381**, 678 (1996).
- 205 G. Overney, W. Zhong, and D. Tománek, *Z. Phys. D* **27**, 93 (1993).
- 206 Y. Wang, *Nature (London)* **356**, 585–587 (1992).
- 207 M. E. Orczyk and P. N. Prasad, *Photonics Science News* **1**, 3–11 (1994).
- 208 Q.-Y. Tong, C. B. Eom, U. Gösele, and A. F. Hebard, *J. Electrochem. Soc.* **141**, L137–L138 (1994).
- 209 N. S. Sariciftci and A. J. Heeger, *Int. J. Mod. Phys. B* **8**, 237–274 (1994).
- 210 D. M. Gruen, Shengzhong Liu, A. R. Krauss, Jianshu Luo, and Xianzheng Pan, *Appl. Phys. Lett.* **64**, 1502 (1994).
- 211 A. V. Hamza, J. Dykes, W. D. Mosley, L. Dinh, and M. Balooch, *Surf. Sci.* **318**, 368–378 (1994).
- 212 B. I. Yakobson and R. E. Smalley, *American Scientist* **85**, 324 (1997).
- 213 M. R. Falvo, G. J. Clary, R. M. Taylor II, V. Chi, F. P. Brooks Jr, S Washburn, and R. Superfine, *Nature (London)* **385** (1997).
- 214 D. L. Carroll, P. Redlich, P. M. Ajayan, J. C. Charlier, X. Blase, A. De Vita, and R. Car, *Phys. Rev. Lett.* **78**, 2811 (1997).
- 215 W. A. de Heer, A. Châtelain, and D. Ugarte, *Science* **270**, 1179 (1995). see also *ibid* page 1119.
- 216 A. G. Rinzler, J. H. Hafner, P. Nikolaev, L. Lou, S. G. Kim, D. Tománek, P. Nordlander, D. T. Colbert, and R. E. Smalley, *Science* **269**, 1550 (1995).
- 217 P. G. Collins and A. Zettl, *Appl. Phys. Lett.* **69**, 1969 (1996).
- 218 A. C. Dillon, K. M. Jones T. A. Bekkedahl, C.-H. Kiang, D. S. Bethune, and M. J. Heben, *Nature (London)* **386**, 377 (1996).
- 219 K. Suenaga, C. Colliex, N. Demoncy, A. Loiseau, H. Pascard, and F. Willaime, *Science* **278** (1997).

CHAPTER 3

Active Carbon Fibers

TIMOTHY J. MAYS

*Department of Materials Science and Engineering
University of Bath
Bath BA2 7AY, United Kingdom*

1 Introduction

It is usually the physical, especially mechanical, properties of carbon fibers that promote their use in advanced technologies. For instance, on account of the high tensile strength and Young's modulus of some carbon fibers, and their low density, a major use of these materials is as reinforcement in aerospace composites. Indeed, modern carbon fibers were originally developed in the late-1950s and early-1960s with this application in mind. A review of high (mechanical) performance carbon fibers is in chapter 4 in this book [1]. However, here such properties and applications are of secondary interest. Rather, attention is focused on the pore and surface structures of carbon fibers, especially those fibers that have been treated, or activated, so that they contain a large number of pores narrower than 50 nm (micropores and mesopores). These active carbon fibers, ACF, are of increasing interest as adsorbents and catalyst supports, in competition with the more traditional, particulate forms of active carbons, as outlined below.

There is a number of advantages of ACF over particulate (powdered or granulated) active carbons, PAC. Compared with PAC, there is improved access of adsorptive or reactive fluids to pores and active surface sites in ACF, together with generally higher pore volumes and surface areas. This is mainly due to the limited dimensions of carbon fibers, which have diameters around 10 μm , compared with particle sizes in PAC which are generally orders of magnitude larger than this. ACF can also be consolidated into a wide range of textiles, felts and composites which allow greater flexibility in the forms of materials based on ACF, and the ease (and hence low cost) with which they may be contained and handled compared with PAC. For example, a new, low-density composite containing ACF, which is of potential use in adsorbent applications, is discussed in chapter 6 in this book [2]. Other advantages are that materials based on ACF do not suffer from channeling, settling or attrition to the same extent as PAC packed in beds or columns. However, at around 10 to 100 US\$/lb [3], ACF are at present 10-100 times more expensive than PAC

(and are even more expensive than high-modulus carbon fibers), due mainly to the cost of activation, so the use of these relatively new materials is confined to low-volume niche applications (ACF comprise less than 2 % of the carbon fiber market in terms of amount of material), mainly as specialist adsorbents and catalysts or catalyst supports in areas such as fluid separations and reactions for environmental control. However, as discussed below, there are also emerging advanced technology markets for ACF in medicine and power storage.

This chapter elaborates on these points as follows. First, a background to ACF is given. This is in the form of a brief history of the development of ACF, which covers the 30 year period from the mid-1960s, when the first patents involving these materials were taken out, to date. It should be noted at this stage that the ACF dealt with in this chapter are based on organic fiber precursors, such as rayon, poly(acrylonitrile), PAN, and pitch; vapor-grown fibers, nanotubes and other carbon fiber forms are not considered. Following the background section the applications of ACF are described, mainly in adsorption and catalysis, though the use of ACF in other advanced technologies such as power storage will also be discussed. In this section, areas such as the preparation, structure and properties of ACF for specific applications will be covered. The chapter will end with some concluding remarks, including comments on the future of ACF, and a list of references.

2 Background

2.1 Carbon fibers

The original drive for the development of 'modern' carbon fibers, in the late-1950s, was the demand for improved strong, stiff and lightweight materials for aerospace (and aeronautical) applications, particularly by the military in the West. The seminal work on carbon fibers in this period, at Union Carbide in the U.S.A., by Shindo, *et al.*, in Japan and Watt, *et al.*, in the U.K., is well-documented [4-7]. It is always worth pointing out, however, that the first carbon fibers, prepared from cotton and bamboo by Thomas Edison and patented in the U.S.A. in 1880, were used as filaments in incandescent lamps.

Carbon fibers were first considered as engineering materials on account of the prospect of transferring the inherent high specific mechanical properties of graphitic to fiber-reinforced composite materials. The combination of low density ($\sim 2.26 \text{ g cm}^{-3}$) and high Young's modulus of ($\sim 1 \text{ TPa}$ in-plane) of perfect graphite was found to be particularly attractive. That carbons could also operate in non-oxidative environments at high temperatures (up to $3,000 \text{ }^\circ\text{C}$), were chemically inert, and had high electrical and thermal conductivities were also thought of as potential advantages.

Today, carbon fibers are still mainly of interest as reinforcement in composite materials [7] where high strength and stiffness, combined with low weight, are required. For example, the world-wide consumption of carbon fibers in 1993 was 7,300 t (compared with a production capacity of 13,000 t) of which 36 % was used in aerospace applications, 43 % in sports materials, with the remaining 21 % being used in other industries. This consumption appears to have increased rapidly (at ~15 % *per* year since the early 1980s), at about the same rate as production, accompanied by a marked decrease in fiber cost (especially for high modulus fibers).

The initial processing steps of most carbon fibers involve stabilization (heating of an organic fiber precursor, *e.g.*, PAN, in air to temperatures up to 300 °C to render the fibers thermoset *via* cross-linking), followed by heating to temperatures < 1,000 °C to convert the stabilized fibers to carbon. Pyrolysis is usually carried out in an inert atmosphere to prevent carbon oxidation. The processing of aerospace or sports carbon fibers may also involve heating to higher (graphitization) temperatures (up to 3,000 °C), also in an inert atmosphere, and stretching. These treatments are to develop and orient graphitic layer planes along the long axis of fibers, and hence to promote the transfer of graphitic properties, such as stiffness, to the final product. However, carbon fibers made in this way are not of primary interest here. Rather, attention is focused on the pore and surface structures of carbon fibers, especially those fibers that have been treated, or activated, so that they contain a large number of micropores and mesopores (micropores are narrower than 2 nm, mesopores have widths in the range 2 to 50 nm, and macropores are wider than 50 nm, as defined by the International Union of Pure and Applied Chemistry, IUPAC [8,9]). Activation typically involves a low temperature treatment (< 1,000 °C) instead of graphitization, where small pores are developed *via* selective oxidation of carbon. This activation process has been covered in detail elsewhere [10], especially for powdered or granular active carbons.

Thus in this chapter on ACF we are dealing with the overlap or intersection of two classes of carbon materials: carbon fibers and active carbons. This is illustrated in the Venn diagram, Fig. 1, which is based on a classification of carbon materials recommended by IUPAC [11].

It is appropriate at this stage to consider active carbons generally, before leading on to introduce active carbon fibers, which are a relatively recent development of these materials.

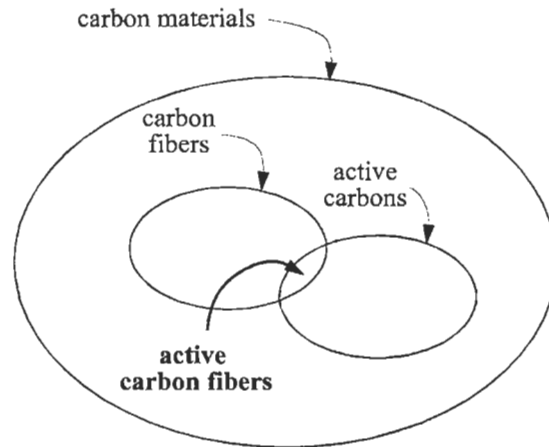


Fig. 1. Venn diagram illustrating where active carbon fibers lie in the classification of carbon materials.

2.2 Active carbons

Active carbons, AC, comprise carbons that have been prepared so that they contain a large number of open or accessible micropores and mesopores [10,13]. The large pore volumes (up to $1 \text{ cm}^3 \text{ g}^{-1}$) and surface areas (up to $2,500 \text{ m}^2 \text{ g}^{-1}$) associated with these pores result in carbons that have high capacities for adsorbing fluids. While active carbons were mentioned by the ancient Egyptians in $\sim 1,550 \text{ B.C.}$ as a purifying agent, modern AC technology extends from the early 1900s when active wood chars were used as a replacement for bone black in sugar refining. Later developments included the use of AC as adsorbents in gas masks during World War I. Modern applications include the use of AC as liquid-phase adsorbents, in water purification for instance, and in the gas-phase as adsorbents for gas storage and separations [10,13], and as catalysts and catalyst supports [14].

Traditionally, active carbons are made in particulate form, either as powders (particle size $< 100 \mu\text{m}$, with an average diameter of $\sim 20 \mu\text{m}$) or granules (particle size in the range $100 \mu\text{m}$ to several mm). The main precursor materials for particulate active carbons, PAC, are wood, coal, lignite, nutshells especially from coconuts, and peat. In 1985, 360 kt of such precursors (including 36 % wood and 28 % coal) were used to make active carbons [10], of which nearly 80 % were used in liquid-phase applications, with the rest being used in gas-phase applications. Important factors in the selection of a precursor material for an active carbon include availability and cost, carbon yield and inorganic (mainly mineral) matter content, and ease of activation.

Activation may be achieved in two ways: physical and chemical. In physical activation a carbon is exposed to an oxidizing gas, usually steam or CO₂ at temperatures in the range 800-1,000 °C, which gasifies the carbon to form a complex array of micropores and mesopores. Non-graphitizable carbons, *i.e.*, carbons made from precursors that do not pass through a liquid stage in pyrolysis (such as the active carbon precursors mentioned above), are especially suited to physical activation as they contain many defective and disordered regions that originate the development of porosity. By contrast, graphitizable carbons, such as those made from mesophase pitch or poly(vinyl chloride), are more ordered structurally and are difficult to activate physically, especially if they have been heated to graphitization temperatures (up to 3,000 °C). Chemical activation involves first mixing the precursor with compounds such as zinc chloride, phosphoric acid or potassium hydroxide, followed by pyrolysis to temperatures in the range 400-850 °C, and final washing to remove the activation agent. The mechanism of chemical activation is complicated, involving a modification of pyrolysis, but the net result is often a fine, high surface-area powder. Chemical activation is generally applicable to a wider range of carbon precursors than physical activation, as it does not depend on disorder in a pyrolysed material, though the finely-divided product may not be suitable for some processes.

2.3 Active carbon fibers

Essentially, the technology of active carbon fibers is a combination of the technologies for carbon fibers and active carbons summarized above. This section is an outline of the historical development of ACF.

As already mentioned, the driving force behind the development of modern carbon fibers was the demand in the late-1950s for high strength and stiffness, low density materials for aerospace applications, especially in the military. However, in the early-1960s it was recognized that carbon fibers might also be used in other, less mechanically-demanding applications. A 1962 U.S. patent [14] refers to the use of carbon fibers made from viscose rayon being of potential use as thermal insulation and in air filters. Critically that work also refers - it seems for the first time - to the potential of active carbon fibers as adsorbents. The idea of general purpose, mainly rayon-based carbon fibers, and especially adsorbent ACF, was taken up by subsequent workers around that time [15-17]. It is interesting to note that a new ACF adsorbent material developed at Oak Ridge National Laboratory [2] by the Editor of this book has a direct predecessor in original work at ORNL on ACF for filtering radioactive iodine [15].

Studies on ACF based on this early work have continued to this day [3,18]. Some important developments in the 1970s include: academic studies of ACF

based on poly(vinylidene chloride) (PVDC or Saran) fibers [19-21]; ACF based on phenolic fibers (Kynol™) [22-27 (U.S. Army); 28-30 (Carborundum)], and ACF based on poly(acrylonitrile), PAN, and rayon fibers [31-33 (U.K. military)]. There has also been extensive work on ACF in Japan. Much of this has been published in Japanese, and is not readily assimilated by those who do not communicate in that language. However, a recent review [18] highlights the most important developments in Japan in ACF. These originated mainly from industry: companies such as Toho Beslon (now part of Toho Rayon) and Toyobo seem to have been particularly active.

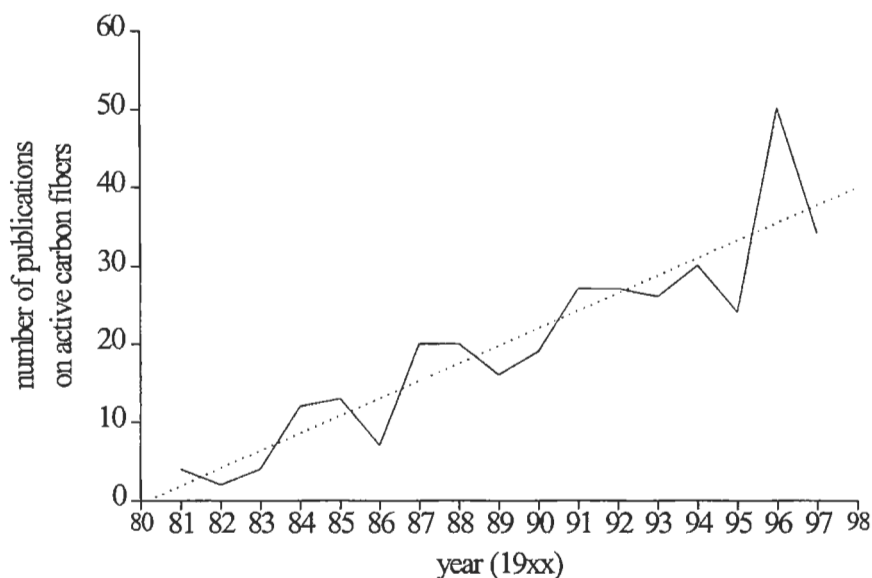


Fig. 2. Number of publications on active carbon fibers between 1981 and 1997 (dotted line is best fit linear trend).

While rayon is still used as precursor for ACF, there has been a good deal of work since the 1970s on developing materials made from PAN, pitch and phenolic-resin, as these appear to be easier and/or more economical to make than those based on rayon or other organic fibers, as well as generally having greater surface areas and other associated properties. Both fundamental and applied aspects of ACF are of continuing interest. As an idea of the degree of effort in this area, over 500 papers, patents, books, *etc.*, have been published in English on ACF. To illustrate this Fig. 2 is a plot of number of publications on ACF over time in the period 1981-1997; the publications all contain the words active (or activated) carbon fiber(s) in their titles. While only a (large) subset of all publications involving ACF (some papers on activated carbon cloths might

not be included, for instance), the data in Fig. 2 suggest that there has been a steady (approximately linear) increase in public output on ACF since 1981, with an extra two or three publications appearing *per* year.

The main themes of this significant output, especially the applications of ACF in advanced technologies, are dealt with below. However it should be emphasized that only information on ACF in the public domain is covered in this review; details on commercial and military ACF are often confidential, and any publicly-available information in these areas is usually, for obvious reasons, limited in depth and scope.

3 Applications of Active Carbon Fibers

3.1 Introduction

Materials based on ACF can be made with a wide range of structures, compositions and properties, depending on the nature of the precursor, and subsequent processing and forming methods. For example, there are, *inter alia*, rayon, PAN, pitch and phenolic resin precursors which may be spun to yield different size and shape fibers, which may then be stabilized and activated in a number of different ways before finally being formed into different types of cloths, fabrics and composites. It is therefore difficult to generalize about ACF and materials based on ACF. However, a number of basic studies, using different experimental methods, have been undertaken on the structures and properties of ACF. Some of these have been with an application in mind, while others have been more fundamental in nature. Examples of the latter include: transmission electron microscopy [34,35], scanning tunneling microscopy [36,37], small-angle scattering [38,39], x-ray diffraction [40-42], surface analysis [43-45], electrical/magnetic properties [46,47], mechanical properties [48,49], adsorption [50-53] plus various other characterization methods [54-58].

Measurements of adsorption, including evidence for high adsorption capacities and (especially) fast adsorption rates relative to traditional carbon adsorbents, are one of the main reasons why ACF have received so much attention in recent years. The background to this is a demand for low volume, high throughput adsorption devices which are difficult to engineer either with slow uptake granular materials, or with finer powders that compact (and hence inhibit transport) in flow conditions. For example it has been shown that adsorption of methylene blue from solution at ambient temperature in a rayon-based ACF is two orders of magnitude faster than in a granular active carbon and one order of magnitude faster than in a powdered active carbon [59,60]. The main reason for this acceleration is that adsorptive molecules do not have so far to travel (by diffusion or permeation) to adsorption sites (micropores and mesopores) in

small ACF (~10 μm diameter) compared to larger powdered or granular active carbons (~100 μm and ~1,000 μm diameter respectively). Adsorption capacities in ACF were also observed to be relatively high [59,60], due to the lack of non-adsorbing macropore spaces in them compared with PAC. This pattern of fast, high-capacity adsorption in ACF compared with PAC has also been observed in other systems [61-67]. Faster fluid transport to and from micropores and mesopores in ACF compared with other carbons is also attractive in regenerating adsorbents (*i.e.*, removing adsorbates) [68-69] and in catalysis [70-75], where extensive dispersion of catalytic sites, and quick reactant supply to, and subsequent product removal from, these sites are clearly a benefit.

Accordingly, the main potential applications of ACF are as adsorbents and catalysts, as described below. Other possible, smaller-scale applications, in emerging areas such as medicine and power storage, are also considered.

3.2 Active carbon fibers in adsorption and catalysis

As alternative materials to traditional particulate active carbons, much research has been carried out on the potential of active carbon fibers as gas and liquid phase adsorbents and catalysts/catalyst supports, as outlined below.

3.2.1 Active carbon fibers in SO_2/NO_x removal from air

Air contamination by SO_2 , NO and NO_2 from the combustion of coal and gasoline fuels can be limited by the presence of active carbons. These materials may remove contaminants by catalysis, *e.g.*, by forming sulfuric acid from SO_2 in moist air, or by the selective catalytic reduction of NO/NO_2 to N_2 and steam in the presence of ammonia. Active carbons may also react with NO/NO_2 to yield N_2 and CO_2 . These decontamination processes are promoted by high surface area carbons (*i.e.*, many sites for adsorption and reaction), together with quick delivery of reactants to, and removal of products from, these surfaces. ACF clearly might have advantages over traditional active carbons in both these areas, as much recent work has sought to prove. For example, many papers on the use of ACF for SO_2/NO_x removal from air were presented at a 1996 American Chemical Society (Division of Fuel Chemistry) symposium on the use of carbon-based materials for environmental cleanup [76]. The potential application of ACF in flue gas cleanup is discussed below.

SO_2 and NO_x in flue gas from coal combustion contribute to smog and acid rain. Methods to remove these pollutants include alkaline wet scrubber systems that fix SO_2 to solid CaSO_4 , and selective catalytic reduction by metal/metal oxide systems of NO/NO_2 to N_2 and steam in the presence of ammonia. Particulate active carbons have also been used in flue gas decontamination, especially as they avoid costly scrubber processes and can operate at lower temperatures. The potential of active carbon fibers in this application has been explored by a

number of authors. For example, ACF based on pitch [72], PAN [74,77,78] and Kynol™ (phenolic resin) [79,80] have been studied for SO₂ removal. It appears that PAN is especially effective in this application. The effectiveness of pitch- and PAN-based ACF for NO_x removal has also been studied [75,81-85]. It has been found that pitch-based ACF calcined at 850 °C are particularly successful in NO_x reduction, though this activity is reduced considerably in humid air. However, there is as yet no compelling evidence that ACF perform better in removing either SO₂ or NO_x than materials such as active coal chars. ACF may only become serious alternative materials in flue gas clean up (and SO₂/NO_x removal in general) when their cost declines.

3.2.2 Active carbon fibers for removing volatile organic compounds from air
Volatile organic compounds, VOCs, comprise generally toxic, low boiling point compounds, including aromatics such as toluene (methylbenzene) and the xylenes (dimethylbenzenes), and aliphatics, such as acetone (propanone) and *n*-hexane. These and other VOCs are produced from various activities including food processing, wastewater treatment, the electronics, oil and petroleum industries, polymer processing and dry cleaning. In 1991 in the U.S.A., for example, of the order of 10⁹ kg of toxic chemicals were released into the atmosphere, of which about half were VOCs [86].

Low concentrations of VOCs in ambient air of 1 to 1,000 ppmv (parts per million based on volume) are often harmful to human health. VOCs also promote the photochemical formation of ozone and other contaminants, and in high concentrations are a fire hazard. These severe environmental implications have resulted in increasingly stringent legislation in the U.S.A. and elsewhere to limit release of VOCs into the atmosphere. Control technologies for VOCs release include combustion and vapor recovery. Vapor recovery is preferred as combustion may result in the production of other air pollutants, and destroy valuable VOCs.

Vapor recovery methods for VOCs include adsorbers and condensers, often in combined systems. Granular active carbons, GAC, are a popular choice as adsorbents for VOCs. However, these materials require expensive containment and need to be replaced periodically to regenerate (with some loss of carbon) and recover adsorbed VOCs. To overcome these drawbacks, ACF based on Kynol™ phenolic resin fibers have been suggested as alternative materials [87-92]. Adsorbents for VOCs in the form of active carbon cloths, ACC, made from these fibers are relatively easily contained, generally adsorb more and faster than GAC and can be regenerated *in situ* using electrothermal methods. For example, an interesting integrated cryogenic recovery system for VOCs using ACC was described recently [91], see Fig. 3.

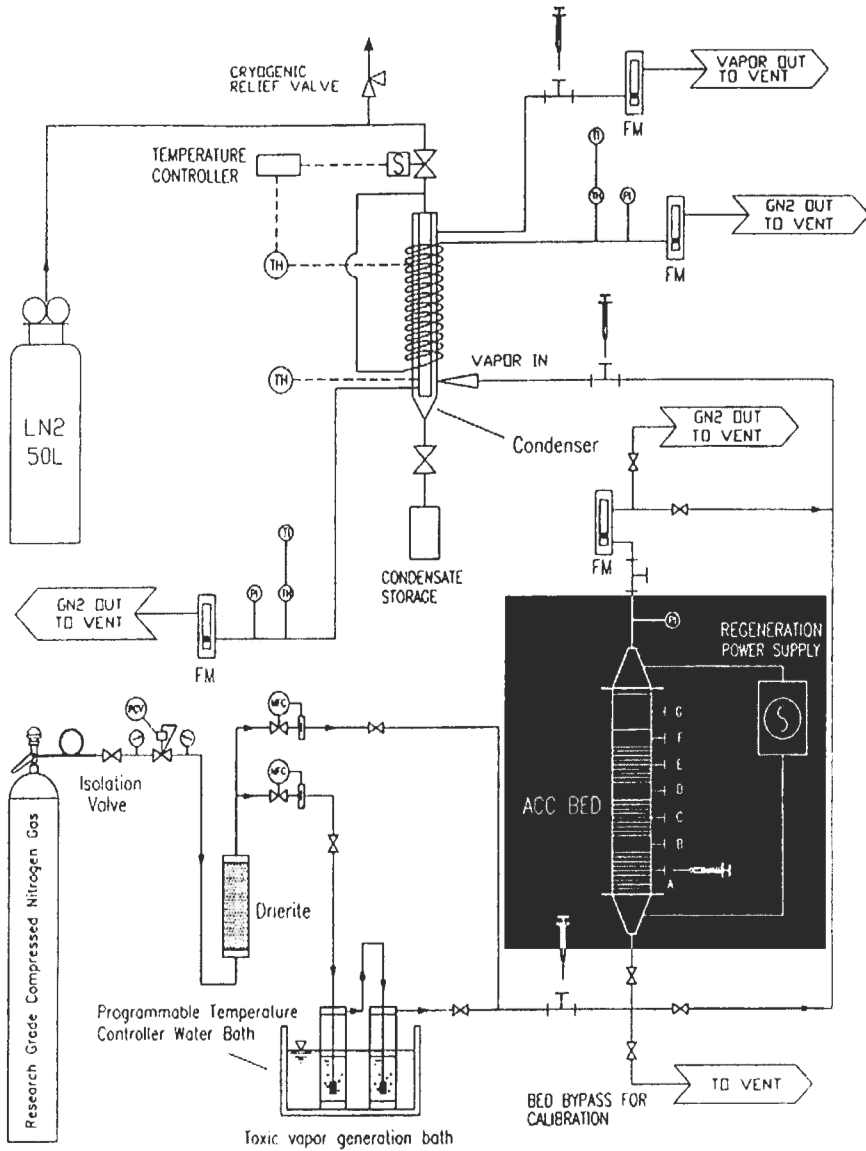


Fig. 3. A model integrated adsorption/electrothermal regeneration/cryogenic vapor recovery system for volatile organic compounds [91]. Reprinted from *Gas Sep. Purif.*, Volume 10, Lordgooei, M., Carmichael, K. R., Kelly, T. W., Rood, M. J. and Larson, S. M., Activated carbon cloth adsorption cryogenic system to recover toxic volatile organic compounds, pp.123-130, Copyright 1996, with permission from Elsevier Science.

In this system, VOCs were introduced into a fixed bed of ACC, highlighted in the figure. After the VOCs broke through the bed, the compounds were desorbed from the ACC electrothermally (by resistive heating), subsequently condensed cryogenically using liquid nitrogen, and hence made available for reuse. The effectiveness for this system was tested by replacing the ACC with Calgon BPL, a well-known commercial GAC. It was shown that breakthrough times for the ACC were considerably longer than for the GAC. This was mainly attributed to greater adsorption capacity of the ACC, though steeper breakthrough curves also suggested less mass transfer resistance (hence less energetically demanding throughput) in the fiber bed compared to the granular bed.

3.2.3 Other gas phase adsorbent applications of active carbon fibers

As well as VOCs, studies of adsorption of specific gases on ACF have been carried out. For example, 1,1-dichloro-1-fluoroethane (a chlorofluorocarbon with reduced ozone depletion potential) was shown to have improved adsorption and recovery performance on active PAN-based carbon fibers compared with commercial, nutshell-based GAC [65]. In another application in environmental protection, a rayon-based ACF cloth impregnated with organo-metallic compounds such as copper(II) tartrate was shown to be a useful adsorbent for hydrogen cyanide gas [93]. The use of impregnated, rayon-based ACF cloths as adsorbents for toxic gases for protection in military applications has also been outlined [94]. That work gives a modern perspective to early publications and patents in military applications [22-27,31-33] referred to earlier in this chapter.

Another interesting potential gas-phase application of ACF is as a medium for adsorbed natural gas, ANG [52,95]. Natural gas (of which methane is the main calorific component) is an environmentally-friendly and abundant fuel, but suffers from low calorific value on a volume basis compared with other fuels such as gasoline. Compressed natural gas, CNG, is one solution, but high pressures are required (~25 MPa) for liquefaction which are energetically demanding. ANG in active carbons is a useful alternative as much lower pressures (~4 MPa) are required to achieve effective liquefaction in small carbon pores. A challenge is to optimize the carbon structure to maximize delivered gas capacity to rival CNG. This topic is covered in detail in chapter 9 in this book [96]. However it is worth pointing out here that steam or CO₂ activated pitch-based carbon fibers appear to have great potential as adsorbents for natural gas on account of the low meso- and macroporosity contained in arrays of fibers compared to packed beds of GAC. Fig. 4 illustrates this point.

The y-axis in Fig. 4 is the delivered capacity of methane at 298 K; the x-axis is the weight-loss after activation in steam or CO₂. Delivered capacity is the volume of methane at STP delivered at 0.1 MPa (1 atmosphere) *per* volume of adsorbent, after storage at, and de-pressurization from, 4 MPa; it is a convenient

measure of how useful a material is for storing and delivering methane as a motor vehicle fuel. Fig. 4 shows that after extensive activation (> 60% weight loss) methane delivery approaches 150 v(STP)/v, which has been identified as a desirable commercial target. However, there is some way to go to achieve the maximum theoretical delivery approaching 200 v(STP)/v [97], which depends critically on pore size. More detailed studies are required in this area, including measurements of adsorption of components of natural gas in ACF [e.g., 98], and optimization of ACF structure (especially pore size), surface chemistry and fiber packing.

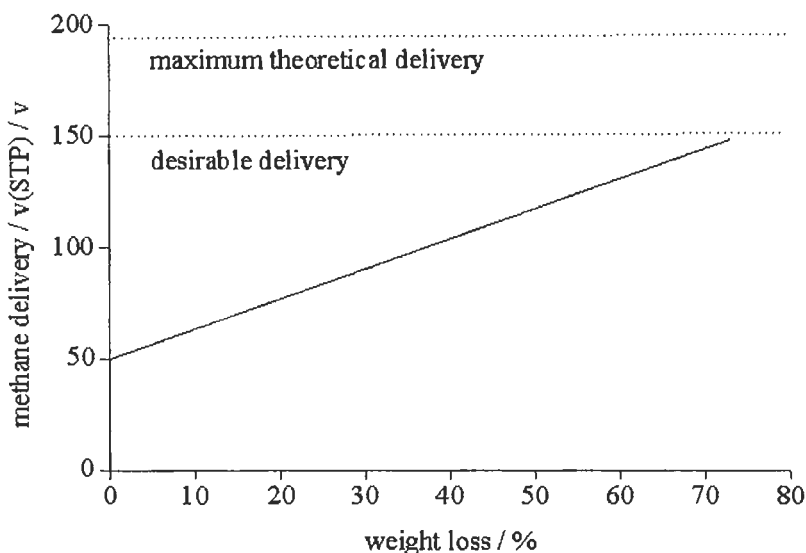


Fig. 4. Methane delivery at 298 K for active pitch-based carbon fibers as a function of weight loss after activation in steam or CO₂ [after 95].

3.2.4 Active carbon fibers in water purification

The purification of domestic and industrial water supplies and the removal of contaminants from wastewaters are required to protect health, industrial plant and the environment. As for air purification, there are increasingly stringent legal requirements for water purity. Granular active carbons are a popular choice of material for water cleanup [10], both for low molecular weight contaminants (of the order of 100 g mol⁻¹) such as trihalomethanes (which occur in chlorinated water), phenolics and some pesticides, and for higher molecular weight contaminants (of the order of 1,000 g mol⁻¹) such as humic substances (e.g., humic acids, fulvo acids, humatmelanic acids) from soil. Active carbon fibers have been studied as possible alternative water purification media to GAC [63,64,67,99-104], with the general conclusion that they offer improved

adsorption capacities and rates for low molecular weight pollutants, and are more easily regenerated. However, bacteria appear to breed easily on ACF, which may itself lead to pollution. This problem has been explored by adding silver to ACF, which makes them antibacterial [105-110].

To illustrate the use of ACF in water purification it is appropriate first to consider the experimental methods used to characterize aqueous adsorption in active carbons generally.

Both kinetic and equilibrium experimental methods are used to characterize and compare adsorption of aqueous pollutants in active carbons. In the simplest kinetic method, the uptake of a pollutant from a static, isothermal solution is measured as a function of time. This approach may also yield equilibrium adsorption data, *i.e.*, amounts adsorbed for different solution concentrations in the limit $t \rightarrow \infty$. A more practical kinetic method is a continuous flow reactor, as illustrated in Fig. 5.

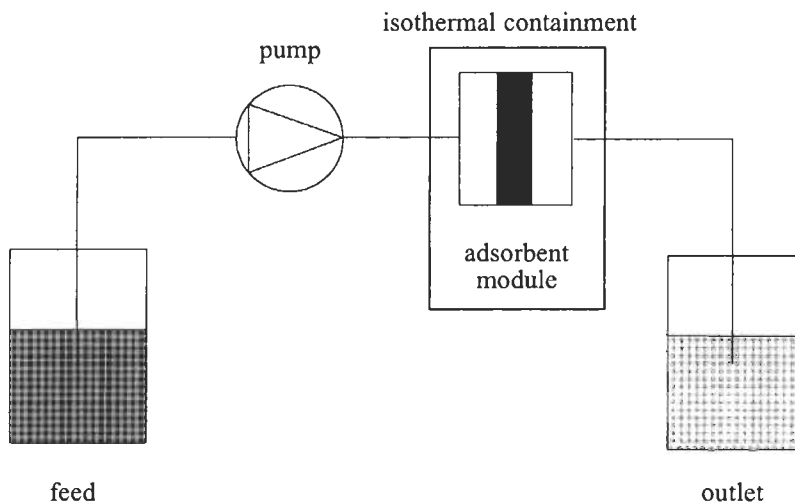


Fig. 5. Schematic continuous flow reactor for characterizing the effectiveness of active carbons for purifying water.

The reactor in Fig. 5 operates as follows. A feed solution containing a given concentration of pollutant is pumped to the adsorbent module at a fixed volumetric flow rate. The module is kept isothermal by a temperature control unit, such as a surrounding water bath. Finally, the concentration of the outlet solution is measured as a function of time from when the feed was introduced to the adsorbent module. These measurements are often plotted as breakthrough curves. Example breakthrough curves for an aqueous acetone solution flowing

through beds of granular active carbon and active carbon fibers are shown in Fig. 6 [64].

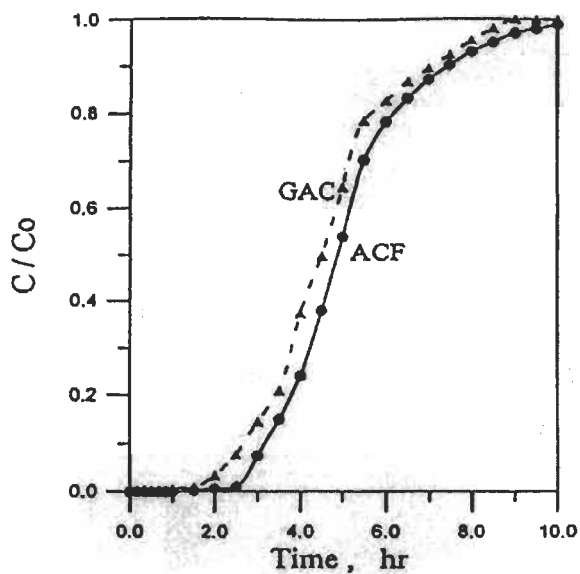


Fig. 6. Breakthrough curves for aqueous acetone (10 mg l^{-1} in feed) flowing through exutshell granular active carbon, GAC, and PAN-based active carbon fibers, ACF, in a continuous flow reactor (see Fig. 5) at 10 ml min^{-1} and 293 K [64]. C/C_0 is the outlet concentration relative to the feed concentration. Reprinted from *Ind. Eng. Chem. Res.*, Volume 34, Lin, S. H. and Hsu, F. M., Liquid phase adsorption of organic compounds by granular activated carbon and activated carbon fibers, pp. 2110-2116, Copyright 1995, with permission from the American Chemical Society.

In this example, acetone breaks through the adsorbent (*i.e.*, is detectable in the outlet) some 1 hr earlier in the GAC than in the ACF, suggesting that ACF might be a better choice as a water purifying agent than GAC for the specified flow system. For example, the commercial, rayon-based ACF material Actitex™ made in France has been observed to be generally more effective than GAC in removing a range of low molecular weight organic water pollutants [100-104]. Interestingly ACF also appear to desorb faster and more completely than GAC when heated, suggesting improved regeneration [64]. This has also been noted for the removal of volatile organic compounds from air, as mentioned in section 3.2.2 above. However, high molecular weight pollutants such as humic substances are not generally removed by ACF, mainly because the pores in these largely microporous materials are smaller than the target molecules [63,100], unlike in GAC which contain mesopores. This suggests that a wide range molecular weight water purification system might require

GAC (or other ultrafiltration medium) and ACF operating in series [101], or the development of ACF with controlled mesoporosity.

3.3 *Emerging applications of active carbon fibers*

The major potential application of active carbon fibers is as an adsorbent in environmental control, as outlined in the previous section. However, there is a number of smaller scale, niche applications that seem to be particularly suited to ACF. These emerging applications include the use of ACF in medicine [111 (see also 59,60),112], as capacitors [113-119] and vapor sensors [120], and in refrigeration [121]. The first two of these applications are summarized below. However, there are not many detailed, publicly-available sources describing any of these applications, partly for commercial reasons and partly because the technology is emerging, so any summary is necessarily limited in scope.

Medical applications of ACF include their use as enteroadsorbents [111] (the commercial rayon-based activated carbon fiber adsorbent Aqualen™ made in Russia [59,60] has been used in this application) and in cloth form as wound dressings and skin substitutes [112]. In both cases, ACF appear to be useful (again) due to their high adsorption capacities and rates for low and medium molecular weight organic compounds in aqueous solution compared to granular active carbons. The ease of containment and formability of dressings based on ACF are also positive attributes. The apparent biocompatibility of ACF is another advantage in these applications, though this can also lead to bacterial growth that in dressings needs to be checked (*e.g.*, by chemical or surface treatment) to avoid infection. Other problems include the drying of wounds due to the high water permeability of ACF.

A second interesting niche application of ACF is in electrical double-layer capacitors. The electric double-layer capacitor is regarded as an attractive rechargeable power device because of its high-rate charge/discharge ability and high energy density compared with common rechargeable batteries [119,122]. This type of capacitor is typically composed of two active carbon electrodes bordering a separator/electrolyte, see Fig. 7.

In a system such as in Fig. 7 electric charges are stored in the electric double layer at the interface between the electrode material and the electrolyte when d.c. voltage is applied across the electrodes. Capacitors using phenolic-based ACF and active fiber cloths, and incorporating both liquid and solid electrolytes, have received considerable attention in Japan for applications such as computer memory back-up devices [113-119]. Perceived advantages of ACF over GAC electrodes include relatively high surface areas and electrical conductivities, and ease of formability and containment. The improved tailorability of ACF compared to GAC electrodes, *e.g.*, by mixing ACF with wood pulp and forming

materials using paper-making technology [115] (which also renders the materials more robust), is also considered to be an advantage.

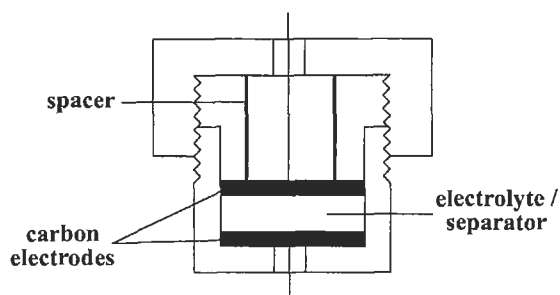


Fig. 7. A schematic diagram of an electric double-layer capacitor using active carbon electrodes.

4 Concluding Remarks

Active carbon fibers are attractive in a number of advanced technologies, such as adsorbents and catalysts/catalyst supports in gas and liquid phase environmental control, medicine and power storage. Special advantages of ACF over more established particulate active carbons include generally higher adsorption capacities (as ACF contain fewer mesopores and macropores than PAC), and faster adsorption/desorption rates (ACF are smaller than active carbon particles). However, in this context there is some scope to develop ACF with increased mesoporosity to enhance adsorption of high molecular weight substances. Other advantages include the relative ease of forming and containing ACF compared to PAC, especially when ACF are consolidated as cloths and textiles. The structure, chemistry and related properties of ACF are also considered to be more controllable than in PAC. An important problem with ACF, however, is their high cost relative to PAC due largely to the combined costs of fiber processing and activation. Lower costs have been suggested by activating ex-phenolic carbon coatings on glass fiber substrates [3], though these materials are still under development. The reduced mechanical properties of ACF, leading to poor abrasion resistance and handling difficulties [48,49,123], is also an unresolved issue. Nevertheless, the future of ACF in advanced technologies in ways discussed above (and in chapter 6 in this book) looks promising indeed.

5 Acknowledgements

The author would like to thank J.-M. Vidal, presently a graduate student in the Department of Materials Science and Engineering, University of Bath, U.K., and H. L. South, Subject Librarian, University of Bath, for their help in compiling references for this chapter.

6 References

1. Edie, D. D. and McHugh, J. J., High performance carbon fibers. In *Carbon Materials for Advanced Technologies*, ed. T. D. Burchell, Elsevier Science, Oxford, 1999, pp. 119 138.
2. Burchell, T. D., Porous carbon fiber-carbon binder composites. In *Carbon Materials for Advanced Technologies*, ed. T. D. Burchell, Elsevier Science, Oxford, 1999, pp. 169 204.
3. Economy, J., Daley, M. and Mangun. C., Activated carbon fibers - past, present and future, *ACS Preprints (Fuel Chemistry Division)*, 1996, 41(1), 321 325.
4. Dresselhaus, M. S., Dresselhaus, G., Sugihara, K., Spain, I. L. and Goldberg, H. A., *Graphite Fibers and Filaments*, Springer-Verlag, Berlin, 1988.
5. Fitzer, E., Carbon fibers - present state and future expectations. In *Carbon Fibers, Filaments and Composites*, ed. J. L. Figueiredo, C. A. Bernardo, R. T. K. Baker and K. J. Hüttinger, Kluwer, Dordrecht, 1989, pp. 3 41.
6. Donnet, J.-B. and Bansal, R. C., *Carbon Fibers*, 2nd edn, Dekker, New York, 1990.
7. Chung, D. D. L., *Carbon Fiber Composites*, Butterworth-Heinemann, Boston, 1994.
8. Sing, K. S. W., Everett, D. H., Haul, R. A. W., Moscou, L., Pierotti, R. A., Rouquérol, J. and Sicmieniwska, T., Reporting physisorption data for gas solid systems with special reference to the determination of surface area and porosity, *Pure Appl. Chem.*, 1985, 57(4), 603 619.
9. Rouquérol, J., Avnir, D., Fairbridge, C. W., Everett, D. H., Haynes, J. H., Pernicone, N., Ramsay, J. D. F., Sing, K. S. W. and Unger, K. K., Recommendations for the characterization of porous solids, *Pure Appl. Chem.*, 1994, 66(8), 1739 1994.
10. Bansal, R. C., Donnet, J.-B. and Stoeckli, H. F., *Active Carbon*, Dekker, New York, 1988.
11. Fitzer, E., Köchling, K.-H., Boehm, H. P. and H. Marsh, Recommended terminology for the description of carbon as a solid, *Pure Appl. Chem.*, 1995, 67(3), 473 506.
12. Rodríguez-Reinoso, F., Activated carbon: structure, characterization, preparation and applications. In *Introduction to Carbon Technologies*, ed. H. Marsh, E. A. Heintz and F. Rodríguez-Reinoso, University of Alicante (Spain) Publications, 1997, pp. 35 101.
13. Radovic, L. R. and Sudhakar, C., Carbon as a catalysis support: production, properties and applications. In *Introduction to Carbon Technologies*, ed. H. Marsh, E. A. Heintz and F. Rodríguez-Reinoso, University of Alicante (Spain) Publications, 1997, pp. 103 165.

14. Abbott, W. F., US Patent No. 3053775, 1962.
15. Rodgers, S. J., Udavcak, R. J. and Mausteller, J. W. In *International Symposium of Fission Product Release and Transport under Accident Conditions*, Oak Ridge National Laboratory, TN, USA, 1965, pp. 1204 1215.
16. Peters, E. M., US Patent No. 323323, 1966.
17. Doying, E. G., US Patent No. 3256206, 1966.
18. Suzuki, M., Activated carbon fiber: fundamentals and applications, *Carbon*, 1994, 32(4), 577 586.
19. Boucher, E. A., Cooper, R. N. and Evcrett, D. H., Preparation and studies of Saran-carbon fibres, *Carbon*, 1970, 8(5), 597 605.
20. Adams, L. B., Boucher, E. A. and Everett, D. H., Adsorption of organic vapours by Saran-carbon fibers and powders, *Carbon*, 1970, 8(6), 761 772.
21. Adams, L. B. and Boucher, E. A., Activation of Saran carbon fibers and powders with carbon dioxide, *Carbon*, 1978, 16(1), 75 76.
22. Arons, G. N. and Macnair, R. N., Activated carbon fiber and fabric achieved by pyrolysis and activation of phenolic precursors, *Text. Res. J.*, 1972, 42(1), 60 63.
23. Arons, G. N., Macnair, R. N. and Erikson, R. L., Sorption characteristics of activated carbon fabric, *Text. Res. J.*, 1973, 43(9), 539 543.
24. Arons, G. N., Macnair, R. N., Coffin, L. G. and Hogan, H. D., Sorptive textile systems containing activated carbon fibers, *Text. Res. J.*, 1974, 44(11), 874 883.
25. Arons, G. N. and Macnair, R. N., Activated carbon fabric prepared by pyrolysis and activation of phenolic fabric, *Text. Res. J.*, 1975, 45(1), 91.
26. Macnair, R. N., Arons, G. N. and Coffin, L. G., Sorptive composite fabrics containing activated carbon yarns, *Text. Res. J.*, 1977, 47(5), 324 327.
27. Macnair, R. N. and Arons, G. N., Sorptive textile systems containing activated carbon fibers. In *Carbon Adsorption Handbook*, ed. P. N. Cheremisinoff and F. Ellerbusch, Ann Arbor Science, Ann Arbor, 1978, pp. 819 859.
28. Economy, J. and Lin, R. Y., German Patent No. 2246572, 1973.
29. Lin, R. Y. and Economy, J., Preparation and properties of activated carbon fibers derived from phenolic resin precursor, *Appl. Polym. Symp.*, 1973, 21, 143 152.
30. Economy, J. and Lin, R. Y., Adsorption characteristics of activated carbon fibers, *Appl. Polym. Symp.*, 1976, 29, 199 211.
31. Bailey, A. and Maggs, F. A. P., GB Patent No. 1301101, 1972.
32. Bailey, A., Maggs, F. A. P. and Williams, J. H., GB Patent No. 1310011, 1973.
33. Bailey, A., Goodyear, D. J., Maggs, F. A. P., Schwabe, P. H. and Williams, J. H., GB Patent No. 1376888, 1974.
34. Endo, M., Takeuchi, K., Sasuda, Y., Matsubayashi, K., Oshida, K. and Dresselhaus, M. S., Fractal analysis on pore structure for activated carbon fibers, *Electron. Commun. Jpn., Part II: Electron.*, 1994, 77(6), 98 107.
35. Oshida, K., Kogiso, K., Matsubayashi, K., Takeuchi, K., Kobayashi, S., Endo, M., Dresselhaus, M. S., Dresselhaus, G., Analysis of pore structure of activated carbon fibers using high resolution transmission electron microscopy and image processing, *J. Mater. Res.*, 1995, 10(10), 2507 2517.
36. Donnet, J. B., Qin, R. Y., Park, S. J., Ryu, S. K. and Rhee, B. S., Scanning tunneling microscopy study of activated carbon fibers, *J. Mater. Sci.*, 1993, 28(11), 2950 2954.

37. Economy, J., Daley, M., Hippo, E. J. and Tandon, D., Elucidating the pore structure of activated carbon fibers through direct imaging using scanning tunneling microscopy (STM), *Carbon*, 1995, 33(3), 344 345
38. Kieffer, J., Investigation of the transitional pore structure of activated carbon fibers by small-angle neutron scattering, *J. Appl. Phys.*, 1992, 72(12), 5649 5656.
39. Cazorla-Amorós, D., de Lecea, C. S. M., Alcañiz-Monge, J., Gardner, M., North, A. and Dore, J., Characterization of activated carbon fibers by small-angle x-ray scattering, *Carbon*, 1998, 36(3), 309 312.
40. Suzuki, T. and Kaneko, K., Structural change of activated carbon fibers with desorption by *in situ* x-ray diffraction, *Carbon*, 1988, 26(5), 744 745.
41. Suzuki, T. and Kaneko, K., The micrographite growth of activated carbon fibers with high temperature treatment studied by computer aided x-ray diffraction, *Carbon*, 1993, 31(8), 1360 1361.
42. Kumar, K., Saxena, R. K., Kothari, R., Suri, D. K., Kaushik, N. K. and Bohra, J. N., Correlation between adsorption and x-ray diffraction studies on viscose rayon-based activated carbon cloth, *Carbon*, 1997, 35(12), 1842 1844.
43. Wang, P. H., Hong, K. L. and Zhu, Q. R., Surface analyses of polyacrylonitrile-based activated carbon fibres by x-ray photoelectron spectroscopy, *J. Appl. Polym. Sci.*, 1966, 62(12), 1987 1991.
44. Polovina, M., Babic, B., Kaluderovic, B. and Dekanski, A., Surface characterization of oxidized activated carbon cloth, *Carbon*, 1997, 35(8), 1047 1052.
45. Shin, S., Jang, J., Yoon, S. H. and Mochida, I., A study on the effect of heat treatment on functional groups of pitch-based activated carbon fiber using FTIR, *Carbon*, 1997, 35(12), 1739 1743.
46. Nakayama, A., Suzuki, K., Enoki, T., Di Vittorio, S. L., Dresselhaus, M. S., Koga, K., Endo, M. and Shindo, N., Magnetic properties of activated carbon fibers, *Synth. Met.*, 1993, 57(1), 3736 3741.
47. Nakayama, A., Suzuki, K., Enoki, T., Koga, K., Endo, M. and Shindo, N., Electronic and magnetic properties of activated carbon fibers, *Bull. Chem. Soc. Jpn.*, 1996, 69(2), 333 339.
48. Ko, T. H., Chiranairadul, P., Lu, C. K. and Lin, C. H., The effects of activation by carbon dioxide on the mechanical properties and structure of PAN-based activated carbon fibers, *Carbon*, 1992, 30(4), 647 655.
49. Alcañiz-Monge, J., Cazorla-Amorós, D., Linares-Solano, A., Yoshida, S. and Oya, A., Effect of the activating gas on tensile strength and pore structure of pitch-based carbon fibers, *Carbon*, 1994, 32(7), 1277 1283.
50. Bohra, J. N. and Saxena, R. K., Microporosity in rayon-based carbonized and activated carbon fibers, *Colloid Surf.*, 1991, 58(4), 375 383.
51. Jaroniec, M., Gilpin, R. K., Kaneko, K. and Choma, J., Evaluation of energetic heterogeneity and microporosity of activated carbon fibers on the basis of gas adsorption isotherms, *Langmuir*, 1991, 7(11), 2719 2722.
52. Jiang, S. Y., Zollweg, J. A. and Gubbins, K. E., High pressure adsorption of methane and ethane in activated carbon and carbon fibers, *J. Phys. Chem.*, 1994, 98(22), 5709 5713.
53. Cazorla-Amorós, D., Alcañiz-Monge, J. and Linares-Solano, A., Characterization of activated carbon fibers by CO₂ adsorption, *Langmuir*, 1996, 12(11), 2820 2824.

54. Di Vittorio, S. L., Dresselhaus, M. S., Endo, M., Issi, J. P., Piraux, L. and Bayot, V., The transport properties of activated carbon fibers, *J. Mater. Res.*, 1991, 6(4), 778 783.
55. Kuriyama, K. and Dresselhaus, M. S., Photoconductivity of activated carbon fibers, *J. Mater. Res.*, 1991, 6(5), 1040 1047.
56. Dresselhaus, M. S., Fung, A. W. P., Rao, A. M., Di Vittorio, S. L., Kuriyama, K., Dresselhaus, G. and Endo, M., New characterization techniques for activated carbon fibers, *Carbon*, 1992, 30(7), 1065 1073.
57. Di Vittorio, S. L., Nakayama, A., Enoki, T., Dresselhaus, M. S., Endo, M. and Shindo, N., ESR study of activated carbon fibers - preliminary results, *J. Mater. Res.*, 1993, 8(9), 2282 2287.
58. Daley, M. A., Tandon, D., Economy, J. and Hippo, E. J., Elucidating the porous structure of activated carbon fibers using direct and indirect methods, *Carbon*, 1996, 34(10), 1191 1200.
59. Pimenov, A. V., Lieberman, A. I., Shmidt, J. L. and Cheh, H. Y., Accelerated adsorption with activated carbon fiber, *Sep. Sci. Technol.*, 1995, 30(16), 3183 3194.
60. Shmidt, J. L., Pimenov, A. V., Lieberman, A. I. and Cheh, H. Y., Kinetics of adsorption with granular, powdered and fibrous activated carbon, *Sep. Sci. Technol.*, 1997, 32(13), 2105 2114.
61. Suzuki, Y., Koizumi, A. and Takeuchi, Y., Adsorption of trihalomethane from the aqueous solution on granular activated carbon and activated carbon fiber, *Kagaku Kogaku Ronbunshu*, 1993, 19(3), 381 388. (In Japanese.)
62. Sigal, V. L., Reasons for the differences in the adsorption effects by granulated and fibrous carbon materials, *J. Appl. Chem. USSR*, 1992, 65(7, Pt.2), 1372 1374.
63. Starek, J., Zukal, A. and Rathousky, J., Comparison of the adsorption of humic acids from aqueous solutions on active carbon and activated charcoal cloths, *Carbon*, 1994, 32(2), 207 211.
64. Lin, S. H. and Hsu, F. M., Liquid phase adsorption of organic compounds by granular activated carbon and activated carbon fibers, *Ind. Eng. Chem. Res.*, 1995, 34(6), 2110 2116.
65. Lin, S. H. and Chen, Y. V., Adsorption and desorption characteristics of 1,1-dichloro-1-fluoroethane by granular activated carbon and activated carbon fiber, *J. Environ. Sci. Health, Part A: Toxic / Hazard Subst. Environ. Eng.*, 1996, 31(6), 1279 1292.
66. Xiu, G. H., Modeling breakthrough curves in a fixed bed of activated carbon fiber - exact solution and parabolic approximation, *Chem. Eng. Sci.*, 1996, 51(16), 4039 4041.
67. Li, J. W., Yu, Z. B., Gao, M. and Cai, X. P., Trihalomethanes adsorption on activated carbon fiber and granular activated carbon, *Water, Air, Soil, Pollut.*, 1997, 97(3-4), 367 378.
68. Ko, T. H. and Chiranairadul, P., Regeneration of PAN-based activated carbon fibers by thermal treatments in air and carbon dioxide, *J. Mater. Res.*, 1995, 10(8), 1969 1976.
69. Lordgoocci, M., Rood, M. J., Carmichael, K. R. and Larson, S. M., Modeling of the adsorption and electrothermal desorption of organic vapors in a fixed bed of activated carbon fiber cloth, *Abs. Pap. ACS*, 1996, 211(Pt.1), 76 FUEL.

70. Jin, H., Park, S. E., Lee, J. M. and Ryu, S. K., The shape selectivity of activated carbon fibers as a palladium catalyst support, *Carbon*, 1996, 34(3), 429-431.
71. Sotowa, C., Kawabuchi, Y. and Mochida, I., Catalytic dehydrochlorination of 1,2-dichloroethane over pyridine deposited pitch-based active carbon fiber, *Chem. Lett.*, 1996, (11), 967-968.
72. Mochida, I., Kuroda, K., Miyamoto, S., Sotowa, C., Korai, Y., Kawano, S., Sakanishi, K., Yasutake, A. and Yoshikawa, M., Remarkable catalytic activity of calcined pitch-based activated carbon fiber for oxidative removal of SO₂ as aqueous H₂SO₄, *Energy Fuels*, 1997, 11(2), 272-276.
73. Perez, M. C. M., de Lecca, C. S. M. and Solano, A. L., Platinum supported on activated carbon cloths as catalyst for nitrobenzene hydrogenation, *Appl. Catal., A*, 1997, 151(2), 461-475.
74. Mochida, I., Kuroda, K., Kawano, S., Matsumura, Y. and Yoshikawa, M., Kinetic study of the continuous removal of SO_x on polyacrylonitrile-based activated carbon fibres. 1. Catalytic activity of PAN ACF heat treated at 800 °C, *Fuel*, 1997, 76(6), 533-536.
75. Mochida, I., Kawabuchi, Y., Kawano, S., Matsumura, Y. and Yoshikawa, M., High catalytic activity of pitch-based activated carbon fibres of moderate surface area for oxidation of NO to NO₂ at room temperature, *Fuel*, 1997, 76(6), 543-548.
76. See papers presented at the ACS Symposium on Production and Use of Carbon-Based Materials for Environmental Cleanup (New Orleans, LA, USA, March 1996), published in *ACS Preprints (Fuel Chemistry Division)*, 1996, 41(1) and *Energy Fuels*, 1997, 11(2).
77. Mochida, I., Kuroda, K., Kawano, S., Matsumura, Y., Yoshikawa, M., Grulke, E. and Andrews, R., Kinetic study of the continuous removal of SO_x using polyacrylonitrile-based activated carbon fibres. 2. Kinetic model, *Fuel*, 1997, 76(6), 537-541.
78. Kisamori, S., Kuroda, K., Kawano, S., Mochida, I., Matsumura, Y. and Yoshikawa, M., Oxidative removal of SO₂ and recovery of H₂SO₄ over poly(acrylonitrile)-based active carbon fiber, *Energy Fuels*, 1994, 8(6), 1337-1340.
79. DeBarr, J. A., Lizzio, A. A. and Daley, M. A., Adsorption of SO₂ on bituminous coal char and activated carbon fiber, *Energy Fuels*, 1997, 11(2), 267-271.
80. Daley, M. A., Mangun, C. L., DeBarr, J. A., Riha, S., Lizzio, A. A., Donnals, G. L. and Economy, J., Adsorption of SO₂ onto oxidized and heat treated activated carbon fibers (ACFS), *Carbon*, 1997, 35(3), 411-417.
81. Mochida, I., Kisamori, S., Hironaka, M., Kawano, S., Matsumura, Y. and Yoshikawa, M., Oxidation of NO into NO₂ over active carbon fibers, *Energy Fuels*, 1994, 8(6), 1341-1344.
82. Mochida, I., Kawano, S., Hironaka, M., Yatsunami, S., Korai, Y., Matsumura, Y. and Yoshikawa, M., Reduction of NO at very low concentration in air with NH₃ at room temperature over a series of calcined pitch-based active carbon fibers, *Chem. Lett.*, 1995, (5), 385-386.
83. Mochida, I., Kawano, S., Hironaka, M., Yatsunami, S., Korai, Y., Matsumura, Y. and Yoshikawa, M., Reduction of NO of very low concentration in air with

- NH₃ at room temperature over calcined active carbon fibers, *Energy Fuels*, 1995, 9(4), 659 664.
84. Mochida, I., Kishino, M., Kawano, S., Iwaizono, H., Yasutake, A. and Yoshikawa, M., Initial period of NO-NH₃ reaction over a heat treated pitch - based active carbon fiber, *Energy Fuels*, 1997, 11(2), 307 310.
 85. Mochida, I., Kawano, S., Hironaka, M., Kawabuchi, Y., Korai, Y., Matsumura, Y. and Yoshikawa, M., Kinetic study on reduction of NO of low concentration in air with NH₃ at room temperature over pitch-based active carbon fibers of moderate surface area, *Langmuir*, 1997, 13(20), 5316 5321.
 86. United States Environmental Protection Agency, *Toxics in the Community: National and Local Perspectives*, USEPA, USA, 1991.
 87. Foster, K. L., Fucrman, R. G., Economy, J., Larson, S. M. and Rood, M. J., Adsorption characteristics of trace volatile organic compounds in gas streams onto activated carbon fibers, *Chem. Mater.*, 1992, 4(5), 1068 1073.
 88. Economy, J., Foster, K., Andreopoulos, A. and Jung, H., Tailoring carbon fibers for adsorbing volatiles, *CHEMTECH*, October 1992, 597 603.
 89. Dimotakis, E. D., Cal, M. P., Economy, J., Rood, M. J. and Larson, S. M., Chemically treated activated carbon cloths for removal of volatile organic carbons from gas streams - evidence for enhanced physical adsorption, *Environ. Sci. Technol.*, 1995, 29(7), 1876 1880.
 90. Cal, M. P., Rood, M. J. and Larson, S. M., Removal of VOCs from humidified gas streams using activated carbon cloth, *Gas Sep. Purif.*, 1996, 10(2), 117 121.
 91. Lordgooci, M., Carmichael, K. R., Kelly, T. W., Rood, M. J. and Larson, S. M., Activated carbon cloth adsorption cryogenic system to recover toxic volatile organic compounds, *Gas Sep. Purif.*, 1996, 10(2), 123 130.
 92. Cal, M. P., Rood, M. J. and Larson, S. M., Gas phase adsorption of volatile organic compounds and water vapor on activated carbon cloth, *Energy Fuels*, 1997, 11(2), 311 315.
 93. Ilic, M. R., Jovanic, P. B., Radosevic, P. B. and Rajakovic, L. V., Sorption of hydrogen cyanide onto activated carbon cloth impregnated with metallo-organic compounds, *Sep. Sci. Technol.*, 1995, 30(13), 2707 2729.
 94. Gurudatt, K., Tripathi, V. S. and Sen, A. K., Adsorbent carbon fabrics: New generation armour for toxic chemicals, *Defence Sci. J.*, 1997, 47(2), 239 250.
 95. Alcañiz-Monge, J., de la Casa-Lillo, M. A., Cazorla-Amorós, D. and Linares-Solano, A., Methane storage in activated carbon fibres, *Carbon*, 1997, 35(2), 291 297.
 96. Cook, T. L., Komodromos, C., Quinn, D. F. and Ragan, S., Adsorbent storage for natural gas vehicles. In *Carbon Materials for Advanced Technologies*, ed. T. D. Burchell, Elsevier Science, Oxford, 1999, pp. 269 302.
 97. Matranga, K. R., Myers, A. L. and Glandt, E. D., Storage of natural-gas by adsorption on activated carbon, *Chem. Eng. Sci.*, 1992, 47(7), 1569 1579.
 98. Mangun, C. L., Daley, M. A., Braatz, R. D. and Economy, J., Effect of pore size on adsorption of hydrocarbons in phenolic-based activated carbon fibers, *Carbon*, 1998, 36(12), 123 129.
 99. Shindo, N., Otani, Y., Inoue, G. and Kawazoe, K., Water treatment by pitch-based activated carbon fiber, *Deslination*, 1994, 98(1-3), 155 160.

100. Brasquet, C., Roussy, J., Subrenat, E. and Le Cloirec, P., Adsorption and selectivity of activated carbon fibers application to organics, *Environ. Technol.*, 1996, 17(11), 1245 1252.
101. Brasquet, C., Roussy, J., Subrenat, E. and Le Cloirec, P., Adsorption of micropollutants onto fibrous activated carbon: Association of ultrafiltration and fibers, *Water Sci. Technol.*, 1996, 34(9), 215 222.
102. Brasquet, C. and Le Cloirec, P., Adsorption onto activated carbon fibers: Application to water and air treatments, *Carbon*, 1997, 35(9), 1307 1313.
103. Brasquet, C., Subrenat, E. and Le Cloirec, P., Selective adsorption on fibrous activated carbon of organics from aqueous solution: Correlation between adsorption and molecular structure, *Water Sci. Technol.*, 1997, 35(7), 251 259.
104. Le Cloirec, P., Brasquet, C. and Subrenat, E., Adsorption onto fibrous activated carbon: Applications to water treatment, *Energy Fuels*, 1997, 11(2), 331 336.
105. Oya, A., Yoshida, S., Abe, Y., Iizuka, T. and Makiyama, N., Antibacterial activated carbon fiber derived from phenolic resin containing silver nitrate, *Carbon*, 1993, 31(1), 71 73.
106. Oya, A., Wakahara, T. and Yoshida, S., Preparation of pitch-based antibacterial activated carbon fiber, *Carbon*, 1993, 31(8), 1243 1247.
107. Oya, A., Kimura, M., Sugo, T., Katakai, A., Abe, Y., Iizuka, T. and Makiyama, N., Antibacterial activated carbon fiber derived from phenolic resin fiber by use of CO-graftpolymerization, *J. Mater. Sci.*, 1993, 28(17), 4731 4734.
108. Oya, A., Kimura, M., Sugo, T., Katakai, A., Abe, Y., Iizuka, T., Makiyama, N., Linares-Solano, A. and de Lecea, C. S. M., Antibacterial activated carbon fiber derived from methyl methacrylate grafted phenolic resin fiber, *Carbon*, 1994, 32(1), 107 110.
109. Oya, A., Yoshida, S., Alcañiz-Monge, J. and Linares-Solano, A., Preparation and properties of an antibacterial activated carbon fiber containing mesopores, *Carbon*, 1996, 34(1), 53 57.
110. Li, C. Y., Wan, Y. Z., Wang, J., Wang, Y. L., Jiang, X. Q. and Han, L. M., Antibacterial pitch-based activated carbon fiber supporting silver, *Carbon*, 1998, 36(12), 61 65.
111. Anisimov, V. N., Zabezhinski, M. A., Popovich, I. G., Lieberman, A. I. and Shmidt, J. L., Prevention of spontaneous and chemically-induced carcinogenesis using activated carbon fiber adsorbent. I. Effect of the activated carbon fiber adsorbent 'Aqualen' on spontaneous carcinogenesis and life span in mice, *Cancer Lett.*, 1998, 126(1), 23 28.
112. Piskin, E. and Atac, A. G., Glow discharge modified activated carbon cloths as skin substitutes, *J. Biomed. Mater. Res.*, 1996, 30(4), 493 499.
113. Nogami, T., Nawa, M. and Mikawa, H., Lightweight, stable and rechargeable battery with an activated carbon fiber electrode, *J. Chem. Soc., Chem. Commun.*, 1982, (20), 1158 1159.
114. Nawa, M., Nogami, T. and Mikawa, H., Application of activated carbon fiber fabrics to electrodes of rechargeable battery and organic electrolyte capacitor, *J. Electrochem. Soc.*, 1984, 131(6), 1457 1459.
115. Tanahashi, I., Yoshida, A. and Nishino, A., Activated carbon fiber sheets as polarizable electrodes of electric double layer capacitors, *Carbon*, 1990, 28(4), 477 482.

116. Tanahashi, I., Yoshida, A. and Nishino, A., Electrochemical characterization of activated carbon fiber cloth polarizable electrodes for electric double layer capacitors. *J. Electrochem. Soc.*, 1990, 137(10), 3052-3056.
117. Tanahashi, I., Yoshida, A. and Nishino, A., Characterization of activated carbon fiber cloths for electric double layer capacitors by adsorption method, *Carbon*, 1991, 29(7), 1033-1037.
118. Ishikawa, M., Morita, M., Ihara, M. and Matsuda, Y., Electric double layer capacitor composed of activated carbon fiber cloth electrodes and solid polymer electrolytes containing alkylammonium salt, *J. Electrochem. Soc.*, 1994, 141(7), 1730-1734.
119. Ishikawa, M., Sakamoto, A., Morita, M., Matsuda, Y. and Ishida, K., Effect of treatment of activated carbon fiber cloth electrodes with cold plasma upon performance of electric double layer capacitors, *J. Power Sources*, 1996, 60(2), 233-238.
120. Byeon, S. H., Oh, S. M., Kim, W. S. and Lee, C. H., Evaluation of an activated carbon felt passive sampler in monitoring organic vapors, *Ind. Health*, 1997, 35(3), 404-414.
121. Wang, R. Z., Jia, J. P., Zhu, Y. H., Teng, Y., Wu, J. Y., Cheng, J. and Wang, Q. B., Study on a new solid absorption refrigeration pair: Active carbon fiber-methanol, *J. Sol. Energy Eng., Trans. ASME*, 1997, 119(3), 214-218.
122. Conway, B. E., Transition from supercapacitor to battery behavior in electrochemical energy-storage, *J. Electrochem. Soc.*, 1991, 138(6), 1539-1548.
123. Capon, A., Maggs, F. A. P. and Robins, G. A., The mechanical properties of activated charcoal cloth, *J. Phys. D: Appl. Phys.*, 1980, 13(4), 897-907.

CHAPTER 4

High Performance Carbon Fibers

DAN D. EDIE AND JOHN J. McHUGH

*Department of Chemical Engineering
and Center for Advanced Engineering Fibers
Clemson University
Clemson, SC 29634-0909, USA*

1 Introduction

Because of their unique blend of properties, composites reinforced with high performance carbon fibers find use in many structural applications. However, it is possible to produce carbon fibers with very different properties, depending on the precursor used and processing conditions employed. Commercially, continuous high performance carbon fibers currently are formed from two precursor fibers, polyacrylonitrile (PAN) and mesophase pitch. The PAN-based carbon fiber dominates the ultra-high strength, high temperature fiber market (and represents about 90% of the total carbon fiber production), while the mesophase pitch fibers can achieve stiffnesses and thermal conductivities unsurpassed by any other continuous fiber. This chapter compares the processes, structures, and properties of these two classes of fibers.

Despite the differences in structure and properties, there are several similarities between the processing methods of PAN- and pitch-based carbon fibers. Both fiber types are subjected to spinning, oxidative stabilization, and high temperature carbonization steps. Also, in both cases, although the ultimate properties are not developed until carbonization, the property limitations and the final structure are due, in large part, to the chemical nature of the precursor and the morphology of the as-spun fiber. The following sections detail the processing method for the PAN-based and pitch-based carbon fibers and reports the structure and properties of both fiber types.

2 Processing Carbon Fibers from Polyacrylonitrile

In addition to their exceptional tensile strengths, PAN-based carbon fibers are far more resistant to compressive failure than are their pitch-based counterparts or polymeric high-performance fibers. However, because the PAN precursor is not

composed of rigid molecules, the as-spun fiber does not achieve a stacking arrangement which is graphitizable over a long range. Thus, the tensile modulus and thermal conductivity of PAN-based carbon fibers do not achieve values comparable to mesophase pitch-based fibers. The repeat unit of polyacrylonitrile is shown in Fig. 1. In reality, PAN is an atactic polymer; that is, the nitrile groups are randomly positioned with respect to the polymer backbone.

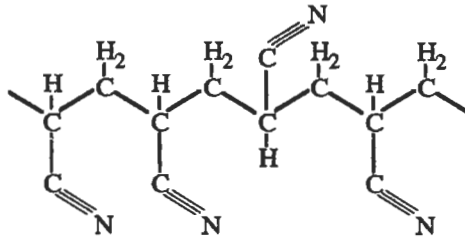


Fig. 1. The chemical repeat unit of polyacrylonitrile.

2.1 Fiber Spinning

Because the polymer degrades before melting, polyacrylonitrile is commonly formed into fibers via a wet spinning process. The precursor is actually a copolymer of acrylonitrile and other monomer(s) which are added to control the oxidation rate and lower the glass transition temperature of the material. Common copolymers include vinyl acetate, methyl acrylate, methyl methacrylate, acrylic acid, itaconic acid, and methacrylic acid [1,2].

2.1.1 Wet-Spinning

In a typical process, a PAN copolymer containing between 93 and 95 percent acrylonitrile is dissolved in a solvent such as dimethylformamide, dimethylacetamide, aqueous sodium thiocyanate, or nitric acid [3] to form a highly concentrated polymer solution (20-30 percent polymer by weight), which is charged to a storage tank and pumped through the wet spinning system shown in Fig. 2. In a fashion similar to melt-spinning, the solution is filtered to minimize the presence of impurities and passed through the spinnerette. The fiber emerges through the small capillary holes of the spinnerette into a coagulation bath containing a fluid, often a diluted composition of the solvent, that begins to extract the solvent from the fiber. In a variation on this process, known as dry-jet wet spinning, the fiber emerges from the spinnerette into a narrow air gap before entering into the coagulation bath.

In wet spinning, the solvent extraction rate can be influenced by changing several processing variables including the type and concentration of coagulation fluid, the

temperature of the bath, or the circulation rate of fluid within the bath.

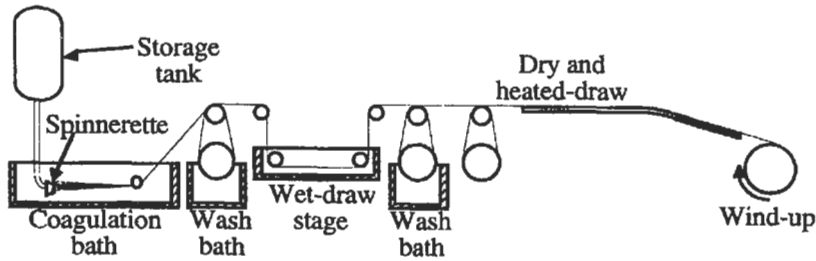


Fig. 2. Wet-spinning of PAN fibers (adapted from [4]).

Controlling the extraction rate is vital because the shape and texture of the resultant fiber is directly influenced by the solvent removal rate. As the solvent is extracted from the surface of the fiber, significant concentration gradients can form. These gradients may result in a warping of the desired circular shape of the fiber. For example, if the solvent is removed too quickly, the fiber tends to collapse into a dog-bone shape. Additionally, the solvent extraction rate influences the development of internal voids or flaws in the fiber. These flaws limit the tensile strength of the fibers.

The gel fiber that emerges from the coagulation bath always undergoes a series of washing, drawing, and drying steps, during which the fiber collapses into its final form. Much of the internal morphology is developed as a result of these processes [3]. Normally, a finish is applied to aid in fiber handling.

2.1.2 Alternative Spinning Technologies

A variation on the wet-spinning technique involves extruding into a heated gas environment. In this dry-spinning process, the temperature and composition of the gas control the extraction process.

Although solution spinning provides high quality PAN fibers, it presents a significant disadvantage. Solution spinning requires the use of a large quantity of an organic or inorganic solvent. This creates the need for efficient solvent recovery, adding additional complexity and cost to the process. Therefore, other spinning strategies have been investigated.

The use of a wet-spinning process with inorganic solvents has also been attempted. Although the details of this process are proprietary, it is clear that these inorganic wet-spun PAN fibers make higher quality carbon fiber precursors than those produced with traditional organic solvents [5].

Another approach to eliminate the need for organic solvents was explored in the late eighties by BASF Structural Materials, Inc. [6]. In their process, the acrylonitrile and other co-monomers are polymerized in an aqueous solution. Next, the resultant slurry is purified, and most of the excess water is removed. The copolymer then is pelletized and fed to an extruder. The remaining water in the pellets serves to plasticize the polymer and enables it to form a homogeneous melt below its degradation temperature. The melt is extruded through a multiple hole spinnerette into a steam-pressurized solidification zone. In addition to eliminating the need for organic solvents, this melt-assisted spinning process provides a more uniform fiber because of the enhanced polymer content of the plasticized PAN [7].

2.2 Stabilization

The as-spun acrylic fibers must be thermally stabilized in order to preserve the molecular structure generated as the fibers are drawn. This is typically performed in air at temperatures between 200 and 400°C [8]. Control of the heating rate is essential, since the stabilization reactions are highly exothermic. Therefore, the time required to adequately stabilize PAN fibers can be several hours, but will depend on the size of the fibers, as well as on the composition of the oxidizing atmosphere. There are numerous reactions that occur during this stabilization process, including oxidation, nitrile cyclization, and saturated carbon bond dehydration [7]. A summary of several functional groups which appear in stabilized PAN fiber can be seen in Fig. 3.

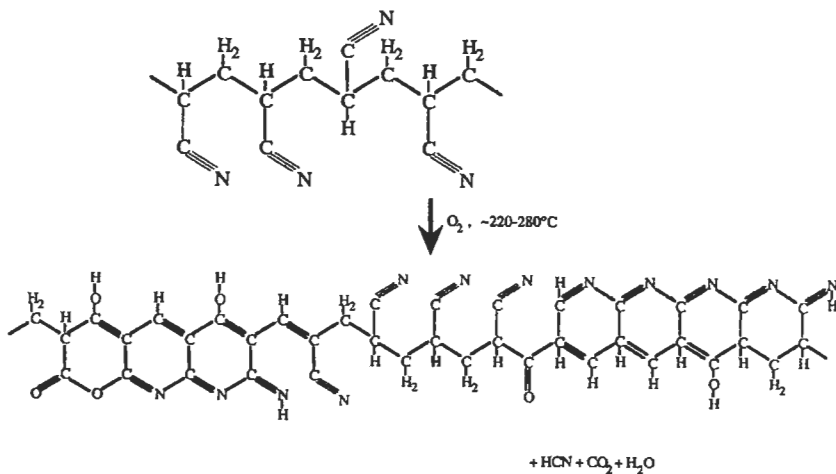


Fig.3 Illustration of functional groups appearing in stabilized PAN fiber [9].

There is recent evidence that stabilization to elevated temperatures (over 350°C) yields a structure with additional intermolecular cross-linking that results in improved mechanical properties in carbonized fibers [10,11]. In addition, it has been noted that the addition of ammonia to the stabilizing environment accelerates stabilization [12].

2.3 Carbonization

The stabilized fiber is carbonized in an inert atmosphere to temperatures ranging from 1000-3000°C, driving off virtually all non-carbon elements. There is a substantial mass loss associated with this pyrolysis. In fact, the yield of carbon fiber upon carbonization of PAN is typically in the range of 40-45% [13]. Controlling the heating rate is essential in preventing the formation of defects as the volatile gases are removed. A decrease in tensile strength with carbonization beyond 1500°C is usually observed [14]. For this reason, the highest strength PAN-based carbon fibers often contain residual nitrogen. Tensile modulus, by contrast, continues to rise with heat treatment temperature. Heat treatment beyond 1700°C is often termed graphitization; however, the term may only be loosely applied to PAN-based fibers, which are not, strictly speaking, graphitizable.

2.4 Fiber Microstructure

Diefendorf and Tokarsky [15] have shown that PAN-based carbon fibers develop a fibrillar microstructure. The microstructure of the PAN-based fibers, shown in a schematic model in Fig. 4, may be viewed as regions of undulating ribbons. This structure is much more resistant to premature tensile failure resulting from microscopic flaws than microstructures exhibiting more extended graphitic regions transverse to the fiber axis, such as those seen in mesophase pitch-based carbon fibers. Thus, PAN-based fibers tend to develop exceptional tensile strengths, but are less suited for developing high tensile moduli.

3 Carbon Fibers from Mesophase Pitch

A relatively new class of high-performance carbon fibers is melt-spun from mesophase pitch, a discotic nematic liquid crystalline material. This variety of carbon fibers is unique in that it can develop extended graphitic crystallinity during carbonization, in contrast to current carbon fibers produced from PAN.

3.1 Mesophase Formation

The mesophase pitches used for high-modulus carbon fiber production can be formed either by the thermal polymerization of petroleum- or coal tar-based

itches, or by the catalytic polymerization of pure compounds such as naphthalene. The mesophase transformation results in an intermediate phase, formed between 400°C and 550°C, during the thermal treatment of aromatic hydrocarbons. During mesophase formation, domains of highly parallel, plate-like molecules form and coalesce until, with time, a 100% anisotropic material may be obtained. It has been well-established that, when mesophase pitch is carbonized, the morphology of the pitch is the primary factor in determining the microstructure of the resulting graphitic material.

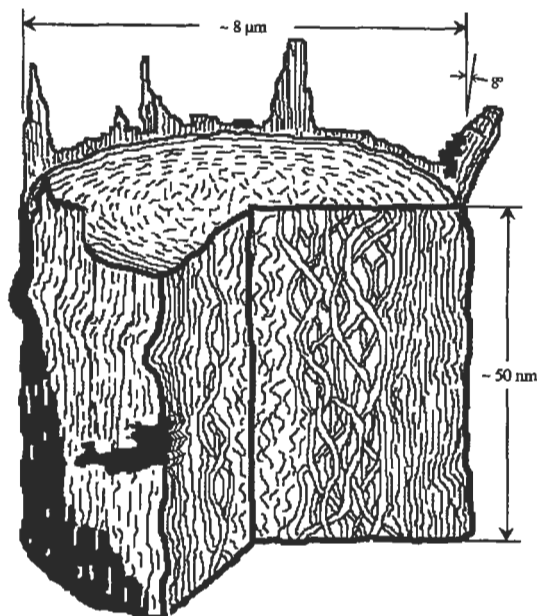


Fig. 4. Illustration of the fibrillar texture of a carbonized PAN fiber [15].

3.1.1 Pyrolysis of Petroleum or Coal Tar Pitch

Raw pitch, a high molecular weight by-product formed during petroleum or coal refining operations, is composed of a rather broad mixture of hundreds of thousands of organic species with an average molecular weight of several hundred. Many of these species are heterocyclic, contain highly aromatic components, and are formed by a variety of thermal decomposition, hydrogen transfer, and oligomerization reactions [16]. In the United States, pitch derived from petroleum has been the only graphitizable carbon fiber precursor employed commercially. Petroleum pitch is commonly formed from the heavy gas oil fraction of crude oil [17]. During gas oil cracking, a heavy by-product called decant oil is formed. This decant oil is often used as fuel oil; however, because of its high aromaticity, it may be pyrolyzed to form pitch.

Often, pitches and oils are classified into four general fractions: saturates, naphthene aromatics, polar aromatics, and asphaltenes [13]. The saturates are the lowest molecular weight fraction and are aliphatic. Naphthene aromatics consist largely of low molecular weight aromatic species. Polar aromatics are larger molecules and may be heterocyclic. Lastly, the asphaltenes are large, plate-like, aromatic molecules which often possess aliphatic side-groups. Oils are composed mostly of saturates and naphthene aromatics, while pitches are often rich in asphaltenes. Since the asphaltenes have a high molecular weight and are highly aromatic, raw petroleum pitches which contain a high percentage of asphaltenes (e.g., Ashland-240, Ashland-260) are often selected as feed stocks for the formation of mesophase. However, the asphaltic residuum fraction of crude oil is not used for pitch production, due to the presence of metallic impurities and structures which are not plate-like in this fraction.

A mesophase can be produced by the heating of a highly aromatic pitch in an inert atmosphere for an extended period of time. The mesophase transformation was first observed by Brooks and Taylor [18] as an intermediate phase of spherules with mosaic structures, formed between 400°C and 550°C during the thermal treatment of aromatic hydrocarbons. It was found that a wide range of materials, such as coals, coke-oven pitch, petroleum tar, bitumen, polyvinyl chloride, naphthacene, or dibenzanthrone, will form similar structures which precipitate from the isotropic phase during prolonged pyrolysis. Selected-area electron diffraction patterns indicated that each mesophase sphere possesses at its center a single direction of preferred orientation. As the pyrolysis continues, the spherules tend to grow and coalesce until a phase inversion takes place, after which the mesophase becomes the continuous phase [19].

It has been established that, when mesophase pitch is carbonized, the morphology of the pitch is the primary factor [20] in determining the microstructure of the resulting graphitic material. This may be attributed to the stacking behavior of mesophase molecules (quite similar to the planar stacking in turbostratic graphite), which may be visualized as shown in Fig. 5.

In the years following the Brooks and Taylor discovery, many researchers attempted to produce a mesophase pitch suitable for carbon fiber production. Otani *et al.* [21] were first to report producing a high-modulus carbon fiber from a "specific pitch-like material." The precursor used was tetrabenzophenazine, and thus, the resulting material might be considered a synthetic pitch.

Singer [22] developed a process for converting 50% of low-cost Ashland 240 isotropic pitch to mesophase by heating the pitch to 400-410°C for approximately 40 hours. During this "heat-soak," mesophase tended to collect at the bottom of the vessel, due to its greater density. The production of highly-oriented, graphitizable

fibers was possible after 55-65 weight % mesophase was formed. Lewis [23] discovered that a more uniform (and thus, more spinnable) product could be obtained by agitating the pitch during the pyrolysis, forming a homogeneous emulsion of the mesophase and isotropic components. Chwastiak and Lewis [24] were able to produce a 100% (bulk) mesophase product by using an inert gas to agitate the reactive mixture and remove the more volatile components. Otani and Oya [25] have reported that a lower softening (more spinnable) product may be obtained if a hydrogenation step is added either before or after mesophase formation. A typical molecule of a heat-soaked mesophase is illustrated in Fig. 6.

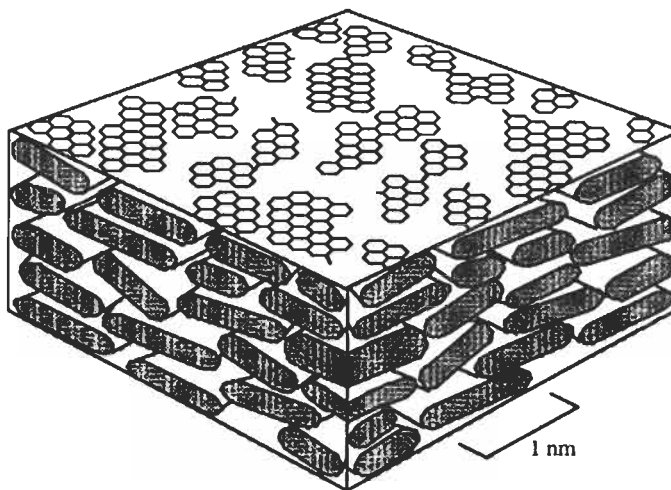


Fig. 5. Schematic illustration of mesophase stacking arrangement (adapted from [20]).

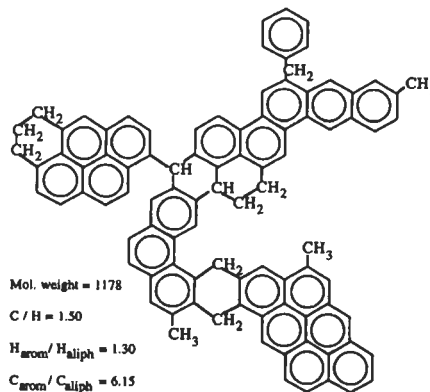


Fig. 6. Typical molecule of a heat-soaked mesophase (adapted from [26]).

3.1.2 Solvent Extraction

Mesophase also can be produced via a solvent extraction technique. Diefendorf and Riggs [27] have shown that an isotropic pitch, such as Ashland 240 or Ashland 260, can be converted to mesophase by first extracting a portion of the pitch with a solvent, such as benzene, toluene, or heptane. The insoluble portion then is pyrolyzed for only ten minutes in the range of 230°C to 400°C, yielding a product which is from 75 to 100% mesophase. While this process greatly reduces the required heat treatment time, the benefit is offset by the potential handling hazards and the high cost of these organic solvents. Furthermore, if the volatile components are not completely removed, spinning can be difficult.

3.1.3 Novel Processes

Both the heat-soaking process (developed at the Union Carbide Corporation and later utilized by Amoco Performance Products) and solvent extraction process (patented by Exxon Research and Engineering Co. and later practiced by E. I. du Pont de Nemours and Co.) convert a natural (petroleum) pitch feed to a mesophase product. Their primary advantage is that the natural pitch feed stock is inexpensive, as it has little other practical value. However, there are three significant disadvantages in using natural pitch as a carbon fiber precursor. First, pitch is a broad mixture, making spinning difficult to control. Also, the composition of the pitch feed stock may vary from day to day, since it is a by-product of a very complex process and is, itself, refined from a variable feed stock (crude oil). A third problem is that in every step of pitch production, refining, and subsequent mesophase formation, a heavy fraction is collected. This means that impurities, which are inevitably present, are sequentially concentrated. The result is a reduction in tensile strength of pitch-based fibers due to inclusions, even after extensive filtration.

These problems have spurred interest in alternate methods of mesophase formation. Hutchenson *et al.* [28] have reported that supercritical fluid (SCF) extraction can be employed to fractionate pitch. By continuously varying pressure or temperature (and, thus, solvent strength), selective pitch fractions of relatively narrow molecular weight distribution can be isolated. Such a process offers the potential of producing a uniform product from a changing feed stock. Furthermore, since the heaviest fraction is not the only one which yields a bulk mesophase, it may be possible to produce a mesophase fraction largely free of impurities. In fact, highly spinnable fractions have already been isolated and used to produce carbon fibers with strengths exceeding 3 GPa and moduli exceeding 800 GPa [29].

Another method which might avoid the problems associated with natural pitch feeds involves producing mesophase from a synthetic precursor. Recently, Mochida *et al.* [30] developed a process in which mesophase is produced by the polymerization of naphthalene or methyl naphthalene, with the aid of a HF/BF₃

catalyst. HF/BF_3 has been studied as a Brönsted acid "super catalyst" in applications such as coal liquefaction and aromatic condensation. Its ability to polymerize aromatic hydrocarbons, however, has only recently been utilized to produce mesophase. The resultant aromatic resin (AR) mesophase (Mitsubishi Gas Chemical Co., Inc.) is reported to be more spinnable and more easily oxidized than the mesophase formed by heat-soaking raw pitch. Furthermore, Mitsubishi Gas Chemical Co. has claimed that the properties of the final carbonized AR fibers are comparable to those of the best commercial mesophase fibers.

3.2 Melt-Spinning

The manufacturing of carbon fibers from mesophase pitch is accomplished in three steps: melt-spinning, oxidative stabilization, and carbonization (see Fig. 7). The peculiar difficulties encountered during spinning and heat treating mesophase pitch fibers result in a high processing cost for this class of fiber. Conversely, improvements in precursor quality and processing technology offer the best opportunity to reduce the price of these high-performance fibers.

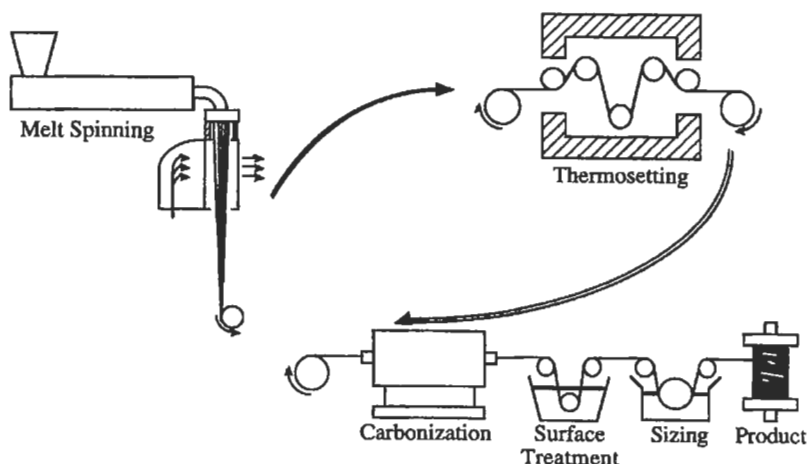


Fig. 7. Processing of carbon fibers from mesophase pitch.

The melt-spinning process used to convert mesophase pitch into fiber form is similar to that employed for many thermoplastic polymers. Normally, an extruder melts the pitch and pumps it into the spin pack. Typically, the molten pitch is filtered before being extruded through a multi-holed spinnerette. The pitch is subjected to high extensional and shear stresses as it approaches and flows through the spinnerette capillaries. The associated torques tend to orient the liquid crystalline pitch in a regular transverse pattern. Upon emerging from the

spinnerette capillaries, the as-spun fibers are drawn to improve axial orientation and collected on a wind-up device.

3.2.1 Mesophase Pitch Rheology

To date, there has been relatively little work reported on the mesophase pitch rheology which takes into account its liquid crystalline nature. However, several researchers have performed classical viscometric studies on pitch samples during and after their transformation to mesophase. While these results provide no information pertaining to the development of texture in mesophase pitch-based carbon fibers, this information is of empirical value in comparing pitches and predicting their spinnability, as well as predicting the approximate temperature at which an untested pitch may be melt-spun.

Nazem [31] has reported that mesophase pitch exhibits shear-thinning behavior at low shear rates and, essentially, Newtonian behavior at higher shear rates. Since isotropic pitch is Newtonian over a wide range of shear rates, one might postulate that the observed pseudoplasticity of mesophase is due to the alignment of liquid crystalline domains with increasing shear rate. Also, it has been reported that mesophase pitch can exhibit thixotropic behavior [32,33]. It is not clear, however, if this could be attributed to chemical changes within the pitch or, perhaps, to experimental factors.

A very unusual characteristic of mesophase pitch is the extreme dependency of its viscosity on temperature [19,34,35]. This factor has a profound influence on the melt-spinning process (described above), as a mesophase pitch fiber will achieve its final diameter within several millimeters of the face of the spinnerette, in sharp contrast to most polymeric fibers.

3.2.2 Liquid Crystal Flow and Orientation

The rigid nature of the mesophase pitch molecules creates a strong relationship between flow and orientation. In this regard, mesophase pitch may be considered to be a discotic nematic liquid crystal. The flow behavior of liquid crystals of the nematic type has been described by a continuum theory proposed by Leslie [36] and Ericksen [37].

The conservation equations developed by Ericksen [37] for nematic liquid crystals (of mass, linear momentum, and angular momentum, respectively) are:

$$(\nabla \cdot \mathbf{v}) = 0, \tag{1}$$

$$\rho \frac{\partial \mathbf{v}}{\partial t} = -\rho(\mathbf{v} \cdot \nabla)\mathbf{v} - \nabla P + [\nabla \cdot \boldsymbol{\tau}], \quad (2)$$

$$[\mathbf{n} \cdot \mathbf{h}] = (\alpha_3 - \alpha_2)[\mathbf{n} \cdot \mathbf{N}] + (\alpha_2 + \alpha_3)[\mathbf{n} \cdot [\mathbf{A} \cdot \mathbf{n}]]. \quad (3)$$

where \mathbf{v} is the velocity, $\boldsymbol{\tau}$ is the viscous stress tensor, P is the pressure, ρ is the fluid density, \mathbf{N} is the director motion vector, \mathbf{A} is the rate of deformation tensor, the α_i values are viscosity coefficients, and \mathbf{h} is the molecular field. Leslie [36] developed a general expression for the viscous stress,

$$\boldsymbol{\tau} = \alpha_1 \mathbf{n}(\mathbf{n} \cdot [\mathbf{A} \cdot \mathbf{n}])\mathbf{n} + \alpha_2 \mathbf{n}\mathbf{N} + \alpha_3 \mathbf{N}\mathbf{n} + \alpha_4 \mathbf{A} + \alpha_5 \mathbf{n}[\mathbf{n} \cdot \mathbf{A}] + \alpha_6 [\mathbf{n} \cdot \mathbf{A}]\mathbf{n}. \quad (4)$$

The rate of deformation and the director motion vector are

$$\mathbf{A} = \frac{1}{2}([\nabla \mathbf{v}] + [\nabla \mathbf{v}]^T), \quad (5)$$

Five of the six coefficients are independent, because of the constraint [38]

$$\alpha_6 - \alpha_5 = \alpha_2 + \alpha_3, \quad (6)$$

The molecular field appearing in equation (3) can be approximated by

$$\mathbf{h} = K \nabla^2 \mathbf{n}. \quad (7)$$

where K is an average elastic constant.

The above equations have been solved to predict the commonly observed radial and line-origin textures seen in circular and non-circular mesophase pitch-based carbon fibers [39].

3.2.3 Spinning Conditions

As the basic fiber microstructure is determined during the spinning and drawing processes, several spinning process variables have a significant impact on fiber properties (*e.g.*, flow rate, winder speed, spinnerette geometry, etc.). Spinning

temperature, in particular, has been shown to greatly affect the degree of preferred orientation within the fiber [40,41] as well as its carbonized properties [42,43]. Unfortunately, the range of temperatures over which a mesophase pitch fiber can be melt-spun is rather narrow, due to the strong viscosity-temperature relationship of the material.

3.3 Stabilization

The as-spun mesophase pitch fiber is extremely weak and must be heat-treated to develop its ultimate mechanical properties. The first step in this process involves fiber oxidation, more descriptively called stabilization. The purpose of oxidation (similar to PAN fibers) is to prevent the fiber from melting during the subsequent carbonization treatment, thus to "lock in" the structure developed during the extrusion process. Typically, stabilization is accomplished by exposing the fibers to flowing air at a temperature of approximately 300°C for a period of time ranging from several minutes to a few hours, depending on the precursor, the fiber size, and the exact temperature employed. The final oxidation temperature can be slightly above the softening point of the pitch, if a slow heating rate is used to ensure some degree of oxidation before the softening point is exceeded. Because of the length of time required, the oxidation process adds significantly to the overall processing cost for mesophase pitch-based carbon fibers.

During the oxidation process, oxygen tends to react first with aliphatic side-groups, cross-linking and adding weight to the fiber. For this reason, a convenient method to characterize the extent of oxidation is thermogravimetric analysis (TGA). Stevens and Diefendorf [44] have reported that a 6% weight gain is required to completely stabilize the fiber. However, Matsumoto and Mochida [45] showed that the uniformity of oxygen pick-up also must be considered if tensile properties are to be maximized. They found that a high degree of uniformity can be achieved if lower heating rates and lower final temperatures are employed. This uniform stabilization, of course, must be balanced by the associated increase in processing costs.

3.4 Carbonization and Graphitization

Once the fibers have been adequately stabilized, carbonization is possible. During this step the fibers are heated in an inert atmosphere to temperatures of up to 3000°C, driving off all non-carbon elements. Typically, carbonization proceeds in two stages. During the first (precarbonization) stage, the fibers are brought to and often held at 1000°C, allowing the majority of the weight loss to occur (mostly as CH₄, H₂, and CO₂). Singer and Lewis [46] claim that the rate limiting step in this low-temperature carbonization is the breakage of carbon-hydrogen bonds by a free-radical process and that the amount of hydrogen evolution (the free

radical concentration) is related to the size of the growing aromatic molecules.

Subsequently, the fibers are carbonized at higher temperature to obtain the high strength, high modulus carbon fiber. By convention, heat treatment at temperatures above 1700°C is termed "graphitization." At these temperatures, the fiber is virtually all carbon, thus, mostly structural changes take place. During graphitization, dislocations in the initially disordered carbon stacks are annealed out, eventually resulting in the formation of a three-dimensional graphite lattice. The graphitization process primarily involves atomic diffusion and crystallite growth [47].

3.5 Observed Fiber Microstructures

The properties of mesophase pitch-based carbon fibers can vary significantly with fiber texture. Inspection of the cross-section of a circular mesophase fiber usually shows that the graphitic structure converges toward the center of the fiber. This radial texture develops when flow is fully developed during extrusion through the spinnerette. Endo [48] has shown that this texture of mesophase pitch-based carbon fibers is a direct reflection of their underlying molecular structure.

Commonly, the texture is not perfectly radial and some degree of folding of the crystallites is observed. This appears to improve the fiber's resistance to crack propagation and, thus, increases its tensile strength. Folding is an artifact of disclinations in the precursor pitch which may, to a lesser extent, remain after spinning (if inadequate time is allowed for reorientation [49,50]). Fibers also can be formed with no clearly defined texture. Creation of a random texture involves complete disruption of the developing flow (for example, by spinning through capillaries containing porous media [51], and such fibers offer the potential of improved compressive strengths.

Production of fibers with a concentric, or "onion-skin," texture has also been reported, but it is difficult to postulate a single mechanism to explain the occurrence of this texture. Matsumoto [14] reports that extrusion through a large diameter capillary can yield fibers with a concentric texture. Hamada *et al.* [52] formed onion-skin fibers by stirring the pitch upstream from the capillary and, thus, inducing a tangential velocity component. Mochida *et al.* [53] have been able to produce fibers with a concentric texture at very high spinning temperatures (low spinning viscosities). Edie *et al.* [54] have found that spinning through non-circular channels yields fibers with a highly linear "line-origin" texture. Each of these textures is illustrated in Fig. 8.

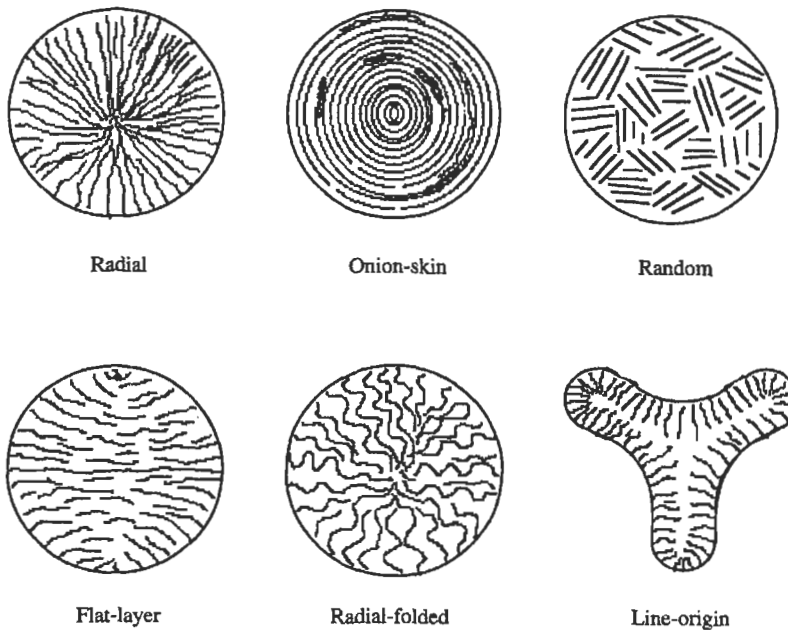


Fig. 8. Observed textures of mesophase pitch-based carbon fibers (adapted from [55]).

4 High Performance Carbon Fibers from Novel Precursors

Recently, the use of high performance polymeric fibers as carbon precursors has been investigated. For example, it has been found that rigid-rod polymers such as poly *p*-phenylene terephthalamide (Kevlar[®]) or poly *p*-phenylene benzobisoxazole (PBO) can be converted to carbon fibers without the need for the expensive stabilization process [56]. This is due to the highly aromatic nature of the polymer backbones which makes these materials impervious to melting. Although research into using high-performance polymers as carbon fiber precursors continues, there are currently no commercial applications for these materials.

5 Carbon Fiber Property Comparison

PAN fibers develop a structure with little point-to-point relationship between atoms in neighboring basal planes. This structure is labeled the turbostratic configuration and is characterized by interplanar spacing values greater than 0.344 nm. The crystallite size in the direction normal to the basal planes, or stack height (L_c), in turbostratic graphite is typically less than 5 nm.

Since PAN-based carbon fibers tend to be fibrillar in texture, they are unable to develop any extended graphitic structure. Hence, the modulus of a PAN-based fiber is considerably less than the theoretical value (a limit which is nearly achieved by mesophase fibers), as shown in Fig. 9. On the other hand, most commercial PAN-based fibers exhibit higher tensile strengths than mesophase-based fibers. This can be attributed to the fact that the tensile strength of a brittle material is controlled by structural flaws [58]. Their extended graphitic structure makes mesophase fibers more prone to this type of flaw. The impure nature of the pitch precursor also contributes to their lower strengths.

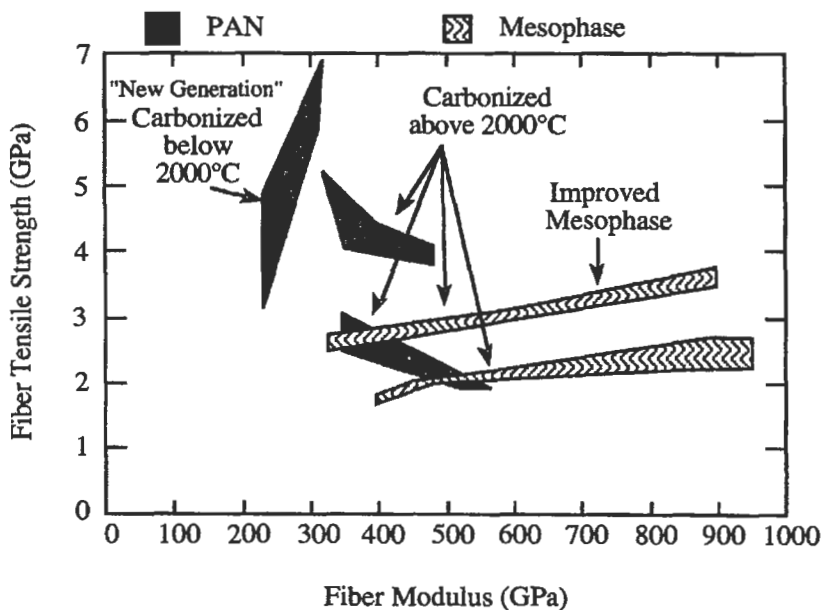


Fig. 9. Tensile strength versus modulus for some commercial carbon fibers (adapted from [57]).

6 Current Areas for High Performance Carbon Fiber Research

Much of the current interest surrounding high performance carbon surrounds their potential for use in thermal management applications. Since some grades of mesophase pitch-based fiber have thermal conductivities three times that of copper, composites fabricated with these fibers are ideal for reducing thermal gradients. The ability to dissipate heat is an important factor in both structural composites and electronic systems. It has been found that spinning pitch fibers of a ribbon-shape is more conducive to developing high thermal conductivity [59]. The potential for this market has contributed to the continued interest in furthering understanding of

structural development during melt-spinning [60,61]. These studies have demonstrated the complex nature of the shear and elongational flow of mesophase.

In contrast, there is also current interest in investigating PAN-based fibers in low thermal conductivity composites [62]. Such fibers are carbonized at low temperature and offer a substitute to rayon-based carbon fibers in composites designed for solid rocket motor nozzles and exit cones.

7 Summary and Conclusions

Although it is clear from the above discussion that there are many similarities in the processing techniques used for all continuous carbon fibers, the structure and properties of the final products are highly variable, depending on the chemical nature of the precursor. Since PAN-based fibers are turbostratic in nature, they are limited in developing ultra-high stiffnesses or thermal conductivities, but the absence of large graphitic crystallites is well-suited for developing extremely high strength. Mesophase pitch fibers, by contrast, are graphitizable and can develop extremely high stiffnesses and thermal conductivities. Unfortunately, the large crystallites necessary to develop these properties carry a cost in tensile strength.

Further improvements in the properties of PAN-based carbon fibers are likely to emerge through improved stabilization, that is, by creating the ideally cross-linked fiber. On the other hand, as purer pitch precursors become available, further improvements in mesophase pitch-based carbon fibers are likely to arise from optimized spinnerette designs and enhanced understanding of the relationship between pitch chemistry and its flow/orientation behavior. Of course, the development of new precursors offers the potential to form carbon fibers with a balance of properties ideal for a given application.

8 References

1. Dunham, M. G., Stabilization of polyacrylonitrile carbon fiber precursors. Ph.D. dissertation, Clemson University, Clemson, SC, 1990.
2. Jain, M. K. and Abhiraman, A. S., Conversion of acrylonitrile-based precursor fibres to carbon fibres, *J Mat Sci*, 1987, 22(1), 278 300.
3. Capone, G. J., Wet-spinning technology. In *Acrylic Fiber Technology and Applications*, ed. J. C. Masson. Marcel-Dekker, New York, 1995, pp. 69 103.
4. Ram, M J. and Riggs, J. P., US Patent No. 3,657,409, 1972.
5. Fitzer, E., PAN-based carbon fibers - present state and trend of the technology from the viewpoint of possibilities and limits to influence and to control the fiber properties by the process parameters, *Carbon*, 1989, 27(5), 621 645.

6. Daumit, G. P. and Ko, Y. S., A unique approach to carbon fiber precursor development. In *High Tech—The Way Into the Nineties*, ed. K. Brunsch *et al.* Elsevier Science, Oxford, 1986, pp. 201 213.
7. Edie, D. D. and Diefendorf, R. J., Carbon fiber manufacturing. In *Carbon—Carbon Materials and Composites*, ed. J. D. Buckley and D. D. Edie. Noyes Publications, Park Ridge, NJ, 1993, pp. 19 39.
8. Peebles, L. H., Carbon fibers from acrylic precursors. In *Carbon Fibers: Formation, Structure, and Properties*. CRC Press, Boca Raton, FL, 1995, pp. 7 26.
9. Clarke, A. J. and Bailey, J. E., Oxidation of acrylic fibres for carbon fibre formation, *Nature*, 1973, **243**(5402), 146 154.
10. Mathur, R. B., Bahl, O. P. and Mittal, J., A new approach to thermal stabilisation of PAN fibres, *Carbon*, 1992, **30**(4), 657 663.
11. Mittal, J., Bahl, O. P., Mathur, R. B. and Sandle, N. K., IR studies of PAN fibres thermally stabilized at elevated temperatures, *Carbon*, 1994, **32**(6), 1133 1136.
12. Bhat, G. S., Cook, F. L., Abhiraman, A. S. and Peebles, L. H., New aspects in the stabilization of acrylic fibers for carbon fibers, *Carbon*, 1990, **28**(2/3), 377 385.
13. Riggs, D. M., Shuford, R. J. and Lewis, R. W., Graphite fibers and composites. In *Handbook of Composites*, ed. G. Lubin. Van Nostrand Reinhold Co., New York, 1982, pp. 196 271.
14. Matsumoto, T., Mesophase pitch and its carbon fibers, *Pure & Appl Chem*, 1985, **57**(11), 1553 1562.
15. Diefendorf, R. J. and Tokarsky, E., High performance carbon fibers, *Polym Eng Sci*, 1975, **15**(3), 150 159.
16. Singer, L. S., The mesophase in carbonaceous pitches, *Faraday Disc Chem Soc*, 1985, **79**, 265 272.
17. Romine, H. E., Petroleum pitch. Presentation at Clemson University, Clemson, SC, 3 December, 1987.
18. Brooks, J. D. and Taylor, G. H., Formation of graphitizing carbons from the liquid phase, *Nature*, 1965, **206**, 697 699. *Carbon*, 1965, **3**(2), 185 193.
19. Rand, B., Carbon fibres from mesophase pitch. In *Handbook of Composites, Vol. 1: Strong Fibres*, ed. W. Watt and B. V. Perov. North-Holland, Amsterdam, 1985, pp. 495 575.
20. Zimmer, J. E. and White, J. L., Disclination structures in the carbonaceous mesophase. In *Advances in Liquid Crystals*, Vol. 5, ed. H. G. Brown. Academic Press, New York, 1982, pp. 157 213.
21. Otani, S., Kokubo, Y. and Koitabashi, T., The preparation of highly-oriented carbon fiber from pitch material, *Bull Chem Soc Japan*, 1970, **43**(10), 3291 3292. Otani, S., Watanabe, S., Ogino, H., Iigima, K. and Koitabashi, T., High modulus carbon fibers from pitch materials," *Bull Chem Soc Japan*, 1972, **45**(12), 3710 3714.
22. Singer, L. S., High modulus high strength fibers produced from mesophase pitch, U. S. Patent 4,005,183, 1977.
23. Lewis, I. C., US Patent No. 4,032,430, 1977.
24. Chwastiak, S. and Lewis, I. C., Solubility of mesophase pitch, *Carbon*, 1978, **16**(2), 156 157.

25. Otani, S. and Oya, A., Progress of pitch-based carbon fibers in Japan, *ACS Symp Ser*, 1986, **303**(22) (*Petroleum-Derived Carbons*), 323 334.
26. Fitzer, E., Kompalik, D. and Mayer, B., Influence of additives on pyrolysis of mesophase pitch. In *Carbon '86: Proceedings of International Carbon Conference*, Baden-Baden, Germany, 1986, pp. 842 845.
27. Diefendorf, R. J. and Riggs, D. M., US Patent No. 4,208,267, 1980.
28. Hutchenson, K. W., Roebers, J. R. and Thies, M. C., Fractionation of petroleum pitch by supercritical fluid extraction, *Carbon*, 1991, **29**(2), 215 223.
29. Liu, G. Z., McHugh, J. J., Edie, D. D. and Thies, M. C., Processing carbon fibers from three sources of mesophase pitch. In *Carbon '92: Proceedings of International Carbon Conference*, Essen, Germany, 1992, pp. 795 797.
30. Mochida, I., Shimizu, K., Korai, Y., Otsuka, H. and Fujiyama, S., Structure and carbonization properties of pitches produced catalytically from aromatic hydrocarbons with HF/BF₃, *Carbon*, 1988, **26**(6), 843 852.
31. Nazem, F. F., Rheology of carbonaceous mesophase pitch, *Fuel*, 1980, **59**, 851 858.
32. Collett, G. W. and Rand, B., Thixotropic changes occurring on reheating a coal tar pitch containing mesophase," *Fuel*, 1978, **57**, 162 170.
33. Balduhn, R. and Fitzer, E., Rheological properties of pitches and bitumina up to temperatures of 500°C, *Carbon*, 1980, **18**(2), 155 161.
34. Nazem, F. F., Flow of molten mesophase pitch, *Carbon*, 1982, **20**(4), 345 354.
35. Edie, D. D. and Dunham, M. G., Melt spinning pitch-based carbon fibers, *Carbon*, 1989, **27**(5), 647 655.
36. Leslie, F. M., Some constitutive equations for anisotropic fluids, *Quart J Mech Appl Math*, 1966, **19**(3), 357 370.
37. Ericksen, J. L., Conservation laws for liquid crystals, *Trans Soc Rheol*, 1961, **5**, 23 34.
38. Parodi, O., Stress tensor for a nematic liquid crystal, *J Physique*, 1970, **31**, 581 84.
39. McHugh, J. J. and Edie, D. D., Orientation of mesophase pitch in capillary and channel flows, *Liq Cryst*, 1995, **18**(2), 327 335.
40. Hamada, T., Furuyama, M., Sajiki, Y., Tomioka, T. and Endo, M., Preferred orientation of pitch precursor fibers, *J Mat Res*, 1990, **5**(6), 1271 1280.
41. Yoon, S.-H., Korai, Y. and Mochida, I., Spinning characteristics of mesophase pitches derived from naphthalene and methylnaphthalene with HF/BF₃, *Carbon*, 1993, **31**(6), 849 856.
42. Mochida, I., Shimizu, K., Korai, Y., Sakai, Y., Fujiyama, S., Toshima, H. and Hono, T., Mesophase pitch catalytically prepared from anthracene with HF/BF₃, *Carbon*, 1992, **30**(1), 55 61.
43. Liu, G. Z. and Edie, D. D., The influence of spinning conditions on the properties of pitch-based carbon fibers. In *Extended Abstracts of the 21st Biennial Conference on Carbon*, Buffalo, NY, 1993, pp. 322 323.
44. Stevens, W. C. and Diefendorf, R. J., Thermosetting of mesophase pitches: experimental. In *Carbon '86: Proceedings of the International Carbon Conference*, Baden-Baden, Germany, 1986, pp. 37 39.

45. Matsumoto, T. and Mochida, I., Oxygen distribution in oxidatively stabilized mesophase pitch fiber, *Carbon*, 1993, **31**(1), 143-147.
46. Singer, L. S. and Lewis, I. C., ESR study of the kinetics of carbonization, *Carbon*, 1978, **16**(6), 417-423.
47. Fischbach, D. B., The kinetics and mechanism of graphitization. In *Chemistry and Physics of Carbon*, Vol. 7, ed. P. L. Walker. Marcel Dekker, New York, 1971, pp. 1-105.
48. Endo, M., Structure of mesophase pitch-based carbon fibres, *J Mat Sci*, 1988, **23**(2), 598-605.
49. Buechler, M., Ng, C. B. and White, J. L. In *Extended Abstracts of the 16th Biennial Conference on Carbon*, San Diego, CA, 1983.
50. Hamada, T., Nishida, T., Sajiki, Y. and Matsumoto, M., Structures and physical properties of carbon fibers from coal tar mesophase pitch, *J Mat Res*, 1987, **2**(6), 850-857.
51. Nazem, F. F., US Patent No. 4,376,747, 1983.
52. Hamada, T., Nishida, T., Furuyama, M. and Tomioka, T., Transverse structure of pitch fiber from coal tar mesophase pitch, *Carbon*, 1988, **26**(6), 837-841.
53. Mochida, I., Yoon, S. H. and Korai, Y., Control of transversal texture in circular mesophase pitch-based carbon fibre using non-circular spinning nozzles, *J Mat Sci*, 1993, **28**, 2331-2336.
54. Edie, D. D., Fox, N. K., Barnett, B. C. and Fain, C. C., Melt-spun non-circular carbon fibers, *Carbon*, 1986, **24**(4), 477-482.
55. Edie, D. D., Pitch and mesophase fibers. In *Carbon Fibers Filaments and Composites*, ed. J. L. Figueiredo *et al.* Kluwer Academic Publ., Dordrecht, The Netherlands, 1990, pp. 43-72.
56. Newell, J. A., Rogers, D. K., Edie, D. D., and Fain, C. C., "Direct Carbonization of PBO Fiber," *Carbon* **32**(4) 651-58 (1994).
57. Bacon, R. Unpublished data, Amoco Performance Products, Inc., Alpharetta, GA, 1989.
58. Johnson, D. J., Structural studies of PAN-based carbon fibers. In *Chemistry and Physics of Carbon*, Vol. 20, ed. P. L. Walker. Marcel Dekker, New York, 1987, pp. 1-58.
59. Edie, D. D., Robinson, K. E., Fleurot, O., Jones, S. P. and Fain, C. C., High thermal conductivity ribbon fibers from naphthalene-based mesophase, *Carbon*, 1994, **32**(6), 1045-1054.
60. Fathollahi, B. and White, J. L., Polarized-light observations of flow-induced microstructures in mesophase pitch, *J Rheol*, 1994, **38**(5), 1591-1607.
61. McHugh, J. J. and Edie, D. D., The orientation of mesophase pitch during fully developed channel flow, *Carbon*, 1996, **34**(11), 1315-1322.
62. Katzman, H. A., Adams, P. M., Le, T. D. and Hemminger, C. S., Characterization of low thermal conductivity PAN-based carbon fibers, *Carbon*, 1994, **32**(3), 379-391.

CHAPTER 5

Vapor Grown Carbon Fiber Composites

MAX L. LAKE AND JYH-MING TING^a*Applied Sciences, Inc.**141 West Xenia Avenue**Cedarville, OH 45314-579, USA***1 Introduction**

Vapor grown carbon fiber (VGCF) is the descriptive name of a class of carbon fiber which is distinctively different from other types of carbon fiber in its method of production, its unique physical characteristics, and the prospect of low cost fabrication. Simply stated, this type of carbon fiber is synthesized from the pyrolysis of hydrocarbons or carbon monoxide in the gaseous state, in the presence of a catalyst; in contrast to a melt-spinning process common to other types of carbon fiber.

Forms of VGCF have long been observed in environments permitting the pyrolysis of hydrocarbons, such as in hydrocarbon cracking operations in the petroleum industry. Frequently the fibers have been discovered and rediscovered by accident, with some of the early work on understanding the origin of the fibers directed towards preventing their formation. Contemporary efforts aimed at understanding the formation and growth of VGCF have been lead by Oberlin, Endo, and Koyama [1], Baker [2], and Tibbetts [3], with notable contributions by many others. The large body of investigation performed over the past thirty years has been primarily devoted to understanding growth mechanisms, and determining the remarkable physical properties of fibers produced from various similar gas phase techniques. Research on VGCF has been fueled by the perceived potential not only for marked improvement in the physical properties of composites, but also for the production of graphitic reinforcements in a wide range of forms at low cost. Excellent reviews by Rodriguez [4], Dresselhaus *et al.* [5], Bartholomew [6], Baker [7], and Trimm [8] of research performed on VGCF, and with comparison to conventional carbon fibers, reflect this activity.

^a Current address: Department of Materials Science and Engineering, National Cheng Kung University, Tainan, Taiwan.

To appreciate the morphology and properties of VGCF, comparisons can be made to both fullerenes and conventional carbon fiber. VGCF is similar to fullerene tubes in the nanoscale domain of initial formation and the highly graphitic structure of the initial fibril. VGCF is dissimilar to fullerenes in that a metal catalyst of mesoscopic domain is used to form the initial filament, and typically, the catalyst particle remains buried in the growth tip of the filament after production, at a relative concentration of a few parts per million, depending on the size to which the fiber is allowed to grow. VGCF is also typically formed in an environment permitting the deposition of pyrolytic carbon, so that the diameter of the fiber may be thicker and the outer layers less graphitic than the core fibril. Figure 1 is a scanning electron micrograph of the broken end of a very thick VGCF which suggests the presence of a highly graphitic core fibril coated with layers of weaker pyrolytic carbon. VGCF can be produced which is quite similar to fullerene tubes, and may be considered for those applications where fullerene tubes are contemplated. Also, VGCF can be grown to lengths which appear to be only limited by the geometry of the reactor, and likewise can be thickened to diameters of tens of microns. Thus with appropriate processing, VGCF can be produced with dimensions similar to conventional melt-spun carbon fiber.

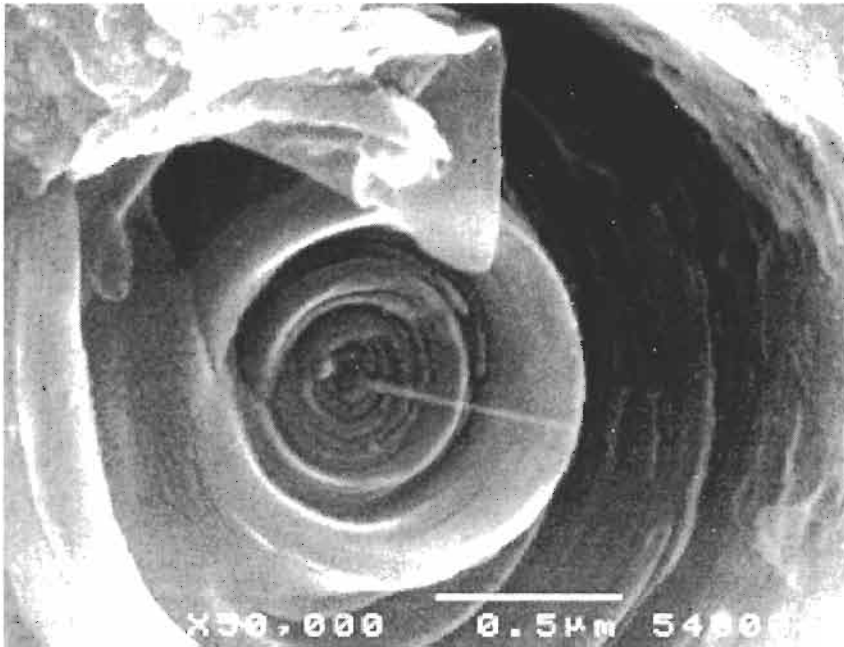


Fig. 1. Micrograph of a broken end of fixed catalyst VGCF.

Compared to PAN and pitch-based carbon fiber, the morphology of VGCF is unique in that the graphene planes are more preferentially oriented around the axis

of the fiber, as illustrated in Fig. 2. As would be expected, the properties of VGCF are strongly influenced by this morphology. Also, because the formation of the core fibril by diffusion through a catalyst particle and subsequent chemical vapor deposition of carbon on the surface of the fibril favors carbon deposition of relatively high purity, VGCF may be highly graphitized with a heat-treatment of about 2800 °C. Consequences of the circumferential orientation of high purity graphene planes are a lack of cross-linking between the graphene layers, and a relative lack of active sites on the fiber surface, making it more resistant to oxidation, and less suitable for bonding to matrix materials. Also in contrast to carbon fiber derived from PAN or pitch precursors, VGCF is produced only in a discontinuous form, where the length of the fiber can be varied from about 100 microns to several centimeters. This fact has significant implications with respect to composite fabrication, since the textile handling methods used for continuous carbon fibers derived from PAN and pitch are not immediately applicable to VGCF.

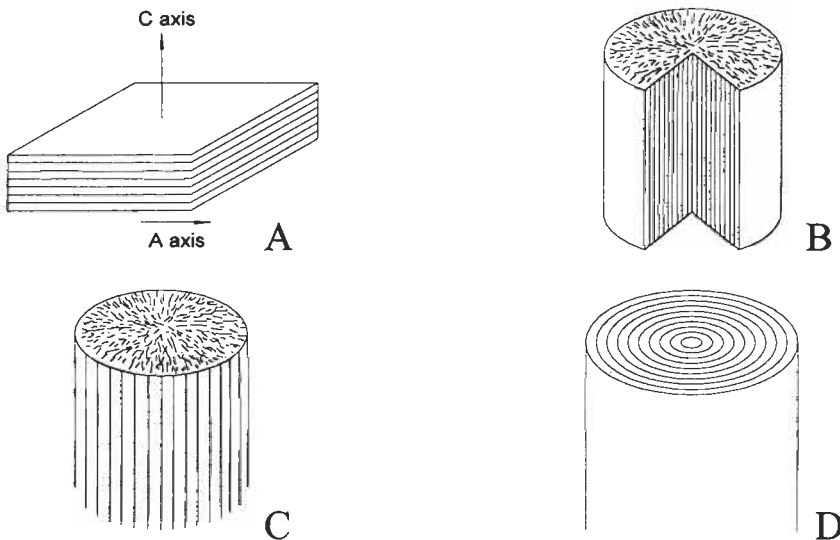


Fig. 2. Schematic representation of basal plane orientation in several types of carbon fibers. (A) Single crystal graphite. (B) ex-pitch carbon fiber. (C) ex-PAN carbon fiber. (D) VGCF.

While a large body of research has been compiled on VGCF growth mechanisms and the properties of the resulting fiber, very little work has been performed on the properties of composites which are reinforced with VGCF. Essentially, the small quantities of the fiber which has been synthesized, typically in laboratory settings, has not been adequate to support such evaluations. Research efforts at Applied Sciences, Inc. have been motivated by the desire to determine the properties of

selected VGCF composites, and have therefore been directed toward developing production processes suitable to support such evaluation, followed by composite fabrication and testing. A synopsis of work in composites of VGCF is presented here, with a summary of the issues which must be overcome before the potential of VGCF can be realized in commercially viable composites.

2 Current Forms

Interestingly, a number of forms of VGCF can be synthesized using a variety of catalysts, and in a fairly wide variety of reactor conditions. At Applied Sciences, Inc. (ASI) the focus has been on the methods developed by Koyama *et al.* [9,10] and Oberlin *et al.* [1], and perfected by Endo *et al.* [11] and Tibbetts [12,13], owing to the relative efficiency of the methods, and the relative uniformity of the fiber product. Current work at ASI with VGCF utilizes two primary production processes developed by these researchers, leading to two distinctive forms of VGCF. The first depends on initially fixing the catalyst on a substrate, so that the resulting fiber is attached to the substrate. The second entails injecting a gas-phase catalyst into a heated gas flow. These two methods, identified hereafter as “fixed catalyst method” and “floating catalyst method”, respectively, are described briefly below:

2.1 Fixed catalyst method

In the fixed catalyst method, the residence time in the reactor may be easily controlled to generate fibers of selected length and diameter, both dimensions which can vary over several orders of magnitude. Most of the physical properties which have been measured for VGCF have been made on this type of fiber.

The fixed catalyst method for production of VGCF is essentially a three stage batch process, consisting of a reduction stage, a fiber growth stage, and a fiber thickening stage. The first stage is reduction of the catalyst, which is supported on a substrate, in a hydrogen atmosphere. Following the reduction stage, the gas flow is changed to a mixture of methane and hydrogen in a linearly increasing temperature sweep to 1100 °C. Fibers are nucleated and elongated as methane decomposes on the catalyst, and the catalytic particle is lifted from the surface of the substrate by the action of graphite deposition into the form of a hollow tube. The catalyst particle remains at the growing tip of the fiber. The direction of fiber growth is influenced by gravity and the direction of gas flow. The fibers lengthen at a rate of a few millimeters per minute. In the third stage, the gas mix is enriched with methane, allowing for more rapid thickening of the fiber through deposition of pyrolytic carbon on the surface of the fiber. The resulting fibers can thus be produced with selected lengths and diameters, depending on the time of growth

and thickening, and on the gas mixtures and flow rates. Typically fiber is allowed to lengthen for about 15 minutes, and is subsequently thickened to a diameter of 5 to 7 microns. This fiber can be grown on any surface which is seeded with catalyst. Typically, several graphite boards are seeded and stacked in a tube furnace. Fiber grown on the top of the board lies close to the board, and is oriented in the direction of gas flow. Such fiber can be harvested with a blade as a semi-woven mat resembling a veil or paper. We identify this fiber as "VGCF mat." Fiber growing from the bottom of the board hangs down due to the pull of gravity and is harvested as sheets resembling fur or hair. We have labeled the latter as "short-staple VGCF."

2.2 Floating catalyst method

Because the fixed catalyst method involves a time-intensive batch process, the duty cycle of the equipment is low, resulting in low production rates and relatively high cost. A second method, the floating catalyst method, was refined to reduce the time (and therefore cost) of production [14]. The floating-catalyst method of VGCF production was developed with the aim of eliminating the need for supporting the catalyst and for cooling the furnace prior to removing the fibers and their supports. Instead of supporting the catalyst on a surface within the furnace, the catalyst is injected into the flowing gas, where it nucleates and grows a fiber. The reactor temperature is maintained at approximately 1100 °C when methane is used as a feedstock. Metal catalysts such as ferrocene are introduced in a gas stream collocated with the hydrocarbon gas feed. The nucleation rate can be markedly enhanced through addition of a small quantity of sulfur, which apparently forms an iron sulfide eutectic, and enables liquid phase diffusion of carbon through the catalyst [15]. Due to the short length of time that the growing fiber remains in the furnace, the diameter and length are not easily controlled independently, and are significantly lower than those of the fixed catalyst method. The typical result is a fiber with sub-micron diameter and length on the order of 100 microns. Since the fiber is entrained in the gas flow, it is easily blown out of the furnace without stopping the process and cooling the furnace. In the fixed catalyst batch process, the majority of the process time is spent in heating and cooling the furnace. The semi-continuous floating catalyst process eliminates these times and greatly increases the efficiency and volume of production.

Both methods result in an easily graphitized, high aspect ratio fiber with a unique lamellar morphology of graphene planes. The novel method by which VGCF is produced thus holds promise for substantially improving the physical properties of composite materials, as well as for designing even higher performance materials through chemical vapor deposition (CVD), addition of dopants, and surface treatments.

3 Fiber Properties

3.1 Fixed catalyst method

As noted, the purity of the carbon source and the mechanics of growth result in a highly graphitic fiber with a unique lamellar morphology. The physical properties of VGCF in some instances can approach those of single-crystal graphite. Single-fiber properties of fibers produced by the fixed catalyst method as measured by Tibbetts and Beetz [16] and Tibbetts [17], are summarized in Table 1 below. These values provide a representative view of the physical properties possible in vapor grown carbon fibers.

It may be noted that while the properties of the heat-treated VGCF consistently improve toward those of single crystal graphite, the values of elastic modulus observed above are somewhat lower than those of high modulus pitch fiber. Jacobsen *et al.* [18], using a vibrating reed method, have observed an average elastic modulus of 680 GPa. It is possible that measurements using static pulling methods are more prone to error due to the morphology of the fiber and susceptibility to damage in handling.

Table 1. Room temperature physical properties of VGCF1 -- Properties of VGCF

Property	As-grown	Heat-treated	Units
Filament Diameter	7	7	μm
Tensile Strength	2.3 to 2.7	3.0 to 7.0	GPa
Tensile Modulus	230 to 400	360 to 600	GPa
Break Elongation	1.5	0.5	%
Density	1.8	2.1	g/cm^3
C.T.E.	-1.0 (Calc.)	ppm/ $^{\circ}\text{C}$	
Electrical Resistivity	1200	55	$\mu\Omega\text{-cm}$
Thermal Conductivity	20	1950	W/mK

Since weight is frequently a factor in the applications of composite structures, values for electrical and thermal conductivity, and tensile strength and modulus are even more impressive when normalized by the mass of the fiber.

Figure 3 shows scanning electron microscope images of heat-treated VGCF filaments produced at ASI. Evident in Fig. 3 is the highly graphitic structure of the heat-treated VGCF produced by the fixed catalyst method. As shown by Brito and Anderson [19], VGCF demonstrates a high degree of graphitization at a temperature of 2800 $^{\circ}\text{C}$, presumably due to its unique morphology, and the purity with which carbon is incorporated into the crystal lattice. Also, the relatively simple CVD process by which VGCF is produced holds promise for radically

decreasing the cost of carbon fiber reinforcements. It is the combination of the unique properties of VGCF and its prospects for low production cost that continue to generate interest in VGCF within the composites industry. The prospect of creating many new types of technically and economically feasible composite applications and products can thus be entertained.

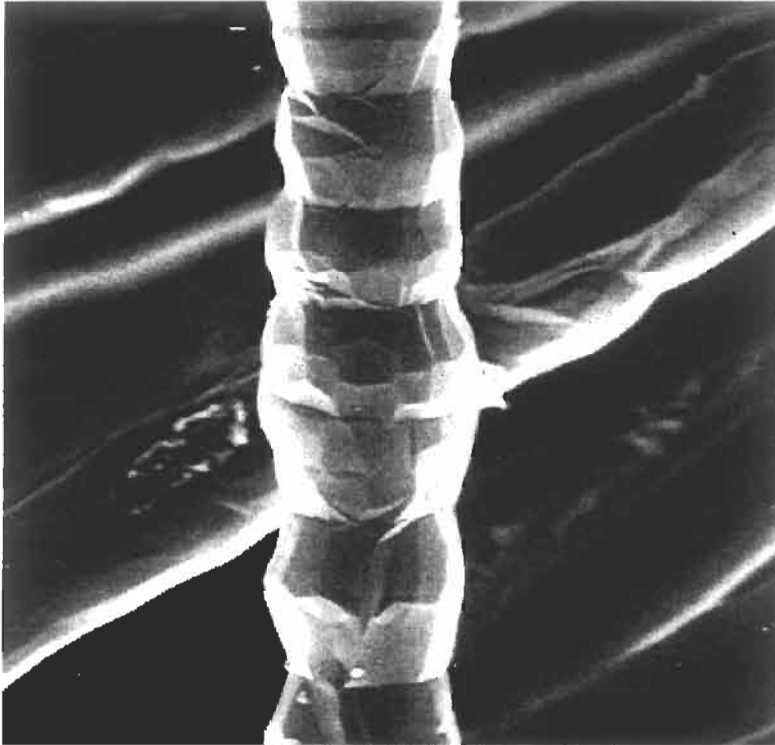


Fig. 3. SEM micrograph of heat treated VGCF. ($2\ \mu\text{m}$)

3.2 *Floating catalyst method*

Properties of VGCF produced by the floating catalyst technique are somewhat more difficult to assess. While this type of fiber is too small to permit measurement of physical properties such as strength, modulus, and thermal conductivity, inferences can be drawn by comparing the graphitic index of the fiber to that of the larger fixed-catalyst fiber, where measurements exist. From these analyses, it is known that the floating catalyst fiber can be quite graphitic even without post production heat treatment. Because of the small diameter, the ratio of CVD carbon to catalytically grown carbon is also small, and a larger percentage of carbon in the fiber has the high degree of ordering of the catalytically grown fibril. This causes the degree of graphitization (and therefore

electrical conductivity) in floating catalyst fibers to be greater than for other carbon fibers, as shown in Table 2 from data compiled by us and by Brito *et al.* [19]. Of course, the graphitization of all carbon fibers can be increased by heat treatment to high temperatures, but with the floating catalyst fiber, it is possible to achieve a high index of graphitization without this costly procedure.

Table 2. X-Ray diffraction results and degree of graphitization of various carbon fibers.

Fiber Type	Heat Treatment, °C	D-Spacing, nm	g_p^* , %
Ex-PAN	1300	.354	-
Ex-PAN	2500	.342	23
P-120 (pitch)	-	.3392	56
Fixed Cat. VGCF	none	.3449	-
Fixed Catalyst VGCF	2200	.342	23
Fixed Catalyst VGCF	2800	.3366	86
Floating Catalyst VGCF	none	.3385	64

$$g_p = (0.3440 - D\text{-spacing}) / (0.3440 - 0.3354)$$

4 Composite Properties

Although extensive data on single fiber properties of VGCF have been determined through fundamental research studies, no manufacturer of large volumes of VGCF exists in the United States, and until recently almost no physical property data has been available for VGCF composites. A focus of work at ASI has been the production of sufficient quantities of the two types of VGCF described above in order to assess their potential as engineering reinforcements, for applications including those requiring superior thermal conductivity, electrical conductivity, strength, and modulus.

To date, composites with carbon matrices have been produced by chemical vapor infiltration and/or pitch infiltration. Polymer matrices have included epoxy and cyanate ester resin. Metal matrix composites, including aluminum, copper, magnesium and lead matrices have been produced. Finally, silicon carbide matrix composites have been fabricated. The objective in these early composite fabrication efforts was to acquire baseline information, since little consideration has been given to optimizing the interface between VGCF and matrix materials. Because of the desire to ascertain the prospects for VGCF composites, most of the composite synthesis has been performed on VGCF from the fixed catalyst method. This form of fiber can be grown to have a diameter in the range of PAN and pitch-derived carbon fiber. Moreover, it can be oriented and compressed into a mold, with fiber volumes comparable to composites reinforced with PAN and pitch-derived fibers. The methods of fabrication and resulting properties are discussed below. Relatively little work on organic matrix composites reinforced with VGCF from the floating catalyst method has

been performed. These efforts and the issues attendant to successful outcomes of such organic composites will also be discussed.

4.1 Composites based on fixed catalyst VGCF

Applied Sciences, Inc. has, in the past few years, used the fixed catalyst fiber to fabricate and analyze VGCF-reinforced composites which could be candidate materials for: thermal management substrates in high density, high power electronic devices and space power system radiator fins; and high performance applications such as plasma facing components in experimental nuclear fusion reactors. These composites include carbon/carbon (CC) composites, polymer matrix composites, and metal matrix composites (MMC). Measurements have been made of thermal conductivity, coefficient of thermal expansion (CTE), tensile strength, and tensile modulus. Representative results are described below.

4.1.1 Carbon/carbon composites

The majority of work done on VGCF reinforced composites has been carbon/carbon (CC) composites [20-26]. These composites were made by densifying VGCF preforms using chemical vapor infiltration techniques and/or pitch infiltration techniques. Preforms were typically prepared using furfuryl alcohol as the binder. Composites thus made have either uni-directional (1D) fiber reinforcement or two-directional, orthogonal (0/90) fiber reinforcement (2D). Composite specimens were heated at a temperature near 3000 °C before characterization. Effects of fiber volume fraction, composite density, and densification method on composite thermal conductivity were addressed. The results of these investigations are summarized below.

Room temperature thermal conductivities of selected 1D composite specimens are given in Table 3 along with the fiber volume fractions and densities. In Table 3, X and Y designate the two orthogonal fiber directions, while Z is perpendicular to the X-Y plane. The specific thermal conductivity shown in Table 3 was determined by dividing thermal conductivity by density. As shown, a CC composite possessing a thermal conductivity (564 W/mK) 40% higher and a density (1.59 g/cm³) more than five times lower than that of copper can be obtained at 36% fiber loading. It is apparent that composites having a higher fiber volume fraction or a higher density exhibit a higher thermal conductivity as shown in Fig. 4.

It has been reported that the room temperature thermal conductivity of single fiber VGCF is 1950 W/mK [27]. However, the room temperature thermal conductivity of VGCF mat may not be comparable to that of single fibers. Since the thermal conductivity of VGCF mat has not been measured or determined, the following

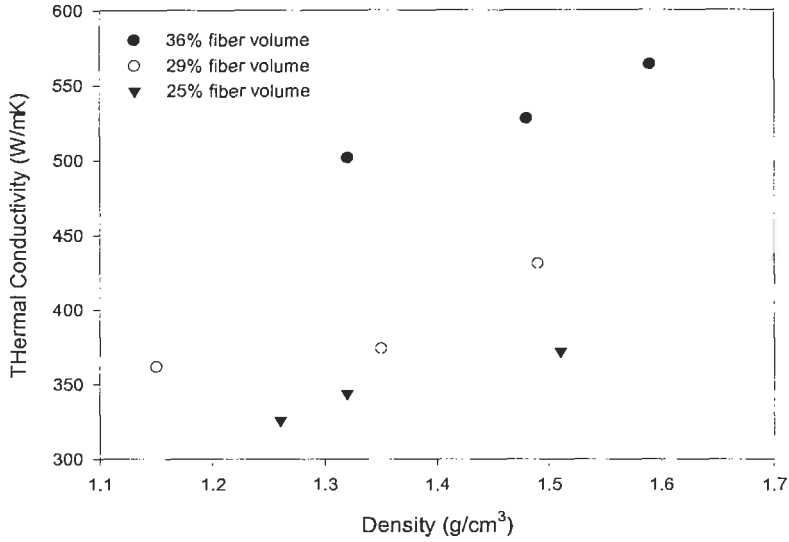


Fig. 4. Composite thermal conductivity as a function of density and fiber loading.

first-order analysis is an attempt to determine the room temperature thermal conductivity of VGCF mat. It is first assumed that the carbon matrix has a density of 2.0 g/cm^3 . The density of VGCF mat, after being heat treated at $2800 \text{ }^\circ\text{C}$, is also taken to be 2.0 g/cm^3 . As a result, a fully densified VGCF reinforced carbon composite would have a density of 2.0 g/cm^3 . The thermal conductivity of such composites with different fiber volume fractions can then be estimated by data extrapolation as listed in Table 3.

Table 3. Room temperature thermal conductivities (κ , W/mK) and specific thermal conductivity (κ/ρ , (W/mK)/(g/cm³)) of CC composites with different fiber volume fractions (V_f) and densities (ρ , g/cm³). The underlined arc data obtained by extrapolation.

ID	ρ	κ	κ/ρ	Preform*
L1	1.26	326(X), 36(Y), 12(Z)	259(X)	A
L2	1.32	344(X)	261(X)	A
L3	1.51	372(X), 38(Y), 16(Z)	246(X)	A
L	<u>2.00</u>	<u>460(X)</u>	-	A
M1	1.15	362(X), 49(Y), 12(Z)	315(X)	B
M2	1.35	374(X), 52(Y), 14(Z)	277(X)	B
M3	1.49	431(X)	289(X)	B
M	<u>2.00</u>	<u>520(X)</u>	-	B
H1	1.32	502(X)	380(X)	C
H2	1.48	528(X)	357(X)	C
H3	1.59	564(X)	355(X)	C
H	<u>2.00</u>	<u>650(X)</u>	-	C

* A: $V_f = 25\%$, $\rho = 0.55 \text{ g/cm}^3$. B: $V_f = 29\%$, $\rho = 0.64 \text{ g/cm}^3$. C: $V_f = 36\%$, $\rho = 0.79 \text{ g/cm}^3$

The extrapolated thermal conductivity, shown in Table 3, was then plotted as a function of fiber volume fraction (Fig. 5). An excellent linear fit was found. As shown in Fig. 5, the linear fit gives thermal conductivities of 20 W/mK and 1760 W/mK for heat treated matrix carbon and heat treated VGCF mat, respectively. It is thought that the matrix carbon exhibits a thermal conductivity similar to the Z direction thermal conductivity of the composite. For VGCF mat, the estimated thermal conductivity is lower than that of single VGCF. This is mainly attributed to the unique structure of VGCF mat. As shown in Fig. 6, fibers in the mat are semi-aligned and some are also semi-continuous, both of which would adversely impact the uni-directional X direction conductivity [28]. Every discontinuity apparently creates a thermal impedance within the mat along the fiber longitudinal direction. In addition, defects are present in the distorted fibers. These defects represent crystalline imperfection, which can strongly reduce the fiber thermal conductivity. Also, the fact that a small fraction of fibers are misoriented makes the actual fiber volume fraction in the longitudinal direction, i.e. X direction in the current case, slightly lower than it would have been, resulting in a lower calculated thermal conductivity for the mat. The misoriented fibers would, on the other hand, enhance the thermal conductivity in the in-plane orthogonal direction, i.e. the Y direction in the current case. This phenomenon explains higher thermal conductivity in the Y direction than in the Z direction, and the thermal conductivity increases with increasing fiber volume fraction in Y direction as shown in Table 3. Normally, the Y (transverse) direction thermal conductivity of a uni-directional composite is dominated by the matrix and independent of the fiber loading [29].

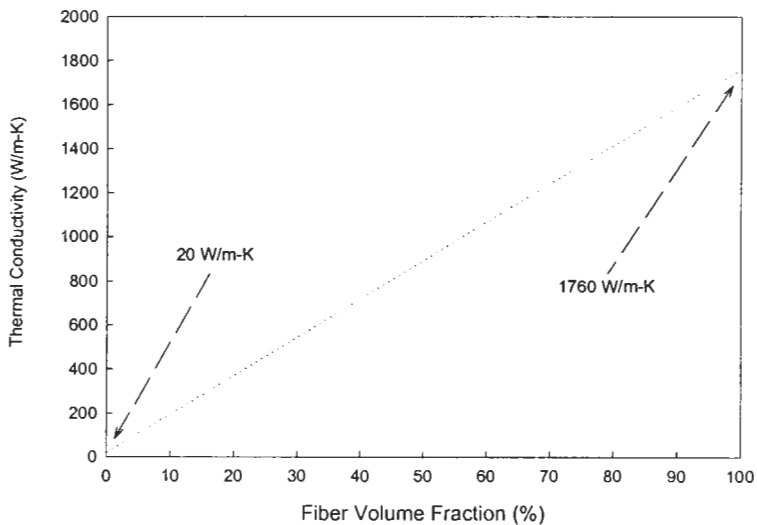


Fig. 5. Estimated thermal conductivity of VGCF reinforced carbon composites.

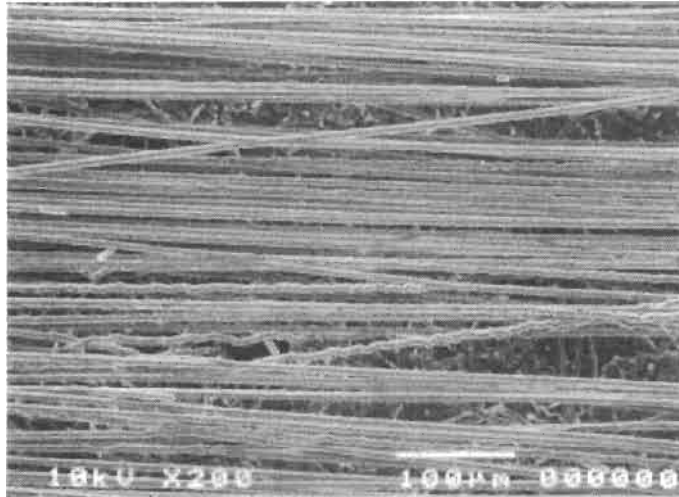


Fig. 6. Micrograph of fixed catalyst VGCF showing the fibers are semi-aligned and semi-continuous.

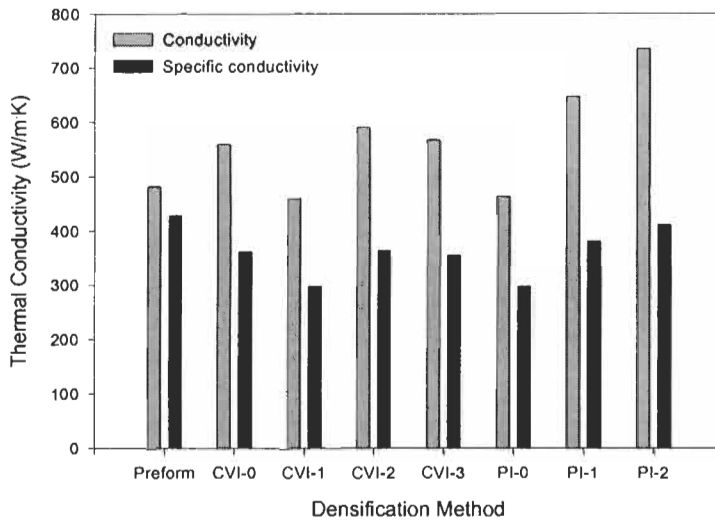
It also appears that increasing fiber loading is much more effective in enhancing composite thermal conductivity than increasing composite density through densification. The specific thermal conductivity decreases with increasing densification which is evidence that the matrix carbon's contribution to the composite thermal conductivity is very limited. This can be further demonstrated by comparing VGCF composites prepared from various densification protocols. Table 4 list the thermal conductivities of several VGCF composites prepared using four CVI techniques and three pitch infiltration (PI) techniques. All of the composites were made from identical master preforms, had a normal fiber volume fraction of 39%, and were heat treated at a temperature near 3000 °C. It is obvious that the composite thermal conductivity mainly comes from the VGCF. This is further illustrated in Fig. 7. The contribution from matrix carbon is minimal. CC composites with higher fiber volume fractions and two directional reinforcement were therefore evaluated for thermal conductivity. The data are given in Table 5 below. As expected, excellent composite thermal conductivities, as high as 910 W/mK, were obtained.

Table 4. Thermal conductivity (κ , W/mK), density (ρ , g/cm³) and specific thermal conductivity (κ/ρ) of various VGCF composites.

Property	Preform	CVI-0	CVI-1	CVI-2	CVI-3	PI-0	PI-1	PI-2
κ	481	559	460	590	568	463	647	736
ρ	1.13	1.55	1.55	1.62	1.60	1.56	1.70	1.79
κ/ρ	428	361	297	364	355	297	381	411

Table 5. Thermal conductivity and density of selected VGCF composites.

ID	V_f , %	Density, g/cm ³	Conductivity, W/mK
14	55 (X), 9 (Y)	1.7	824 (X), 89 (Y), 24 (Z)
01	65 (X), 0 (Y)	1.88	910 (X), 84 (Y), 33 (Z)
03	45 (X), 15 (Y)	1.80	635 (X), 373 (Y), 21 (Z)

**Fig. 7.** Thermal conductivity of composites obtained using various densification processes.

4.1.2. Polymer matrix composites

For comparison, polymer matrix composites were fabricated from four types of fibers and two types of thermosetting matrix resins [29]. The types of fiber were the short staple VGCF, mat VGCF, hybrid VGCF and commercial P-55 pitch derived fiber tow. Hybrid VGCF is a continuous tow of PAN fiber which is coated with pyrolytic carbon under the same condition which VGCF is produced. The types of thermosetting matrix materials were a 121 °C (250 °F) cure cyanate ester resin (Bryte Technologies, Inc. EX-1515) and room temperature curable bisphenol A/polyamide based epoxy resin (Dexter Hysol EA 9396) cured at 121 °C (250 °F). Typical service temperatures exceed the cure temperature.

All VGCF was graphitized prior to composite consolidation. Composites were molded in steel molds lined with fiberglass reinforced, non-porous Teflon release sheets. The finished composite panels were trimmed of resin flash and weighed to determine the fiber fraction. Thermal conductivity and thermal expansion measurements of the various polymer matrix composites are given in Table 6. Table 7 gives results from mechanical property measurements.

The two VGCF forms used, mat and short staple, result in composites with very similar properties. Due to the fluffiness of the short staple VGCF, unidirectional alignment of the fiber is not generally as easy to achieve as with mat VGCF. During compaction of the fiber into the composite, motion of the short staple VGCF sheets results in some degree of off-axis fiber orientation. Thus, "unidirectional" short staple VGCF composites have a lower X but higher Y thermal conductivity than do the mat VGCF unidirectional composites. Some composites were fabricated with two types of reinforcement. These unidirectional composites were fabricated with varying percentages of mat VGCF as the outer surface plies and a low conductivity pitch derived fiber (P-55) with an axial conductivity of 120 W/mK as the remaining core of the panel. The thermal conductivity along the fiber direction is seen to vary linearly with the volume percent of VGCF in the composite (Table 6 and Fig. 8) indicating that the majority of the heat is conducted by the VGCF. The thermal conductivity of the hybrid fiber composites is similar to VGCF reinforced composites, suggesting that the pyrolytic carbon coating of the hybrid fiber is very similar to the graphitic carbon in the VGCF.

Table 6. Thermal properties of VGCF polymer matrix composites.

Material	V_f %	κ , W/mK	CTE, ppm/K	ρ , g/cm ³
M/E	75(X), 0(Y)	661(X), 37 (Y), 9 (Z)	-	1.87
M/E	32(X), 32(Y)	300 (X), 268 (Y), 8 (Z),	-	1.84
S/CER	27(X), 27(Y)	303 (X), 284 (Y), 4 (Z)	2.0 (X), 6.3 (Y)	1.69
S/CER	54(X), 0(Y)	466 (X), 142 (Y), 3 (Z)	-1.5 (X), 18 (Y)	1.68
M+P/CER	6+56(X), 0(Y)	125 (X), 11 (Y), 1 (Z)	0.7 (X), 46.1 (Y)	1.71
M+P/CER	13+47(X), 0(Y)	182 (X), 15 (Y), 2 (Z)	0.7 (X), 38 (Y)	1.75
M+P/CER	25+37(X), 0(Y)	295 (X), 21 (Y), 3 (Z)	-0.7 (X), 34 (Y)	1.75
H/E	44(X), 0(Y)	542 (X), 21 (Y), 6 (Z)	-	1.45
H/E	28(X), 28(Y)	247 (X), 324 (Y), 17 (Z)	-	1.84

Note: X=in-plane 0°, Y=in-plane 90°, Z = through thickness, V_f =fiber volume fraction, M=mat VGCF, H=hybrid VGCF, S=short staple VGCF, P=P-55 fiber, E=epoxy, CER=cyanate ester resin.

Mechanical properties of the all composites given in Table 7 are an average of five coupons in each of the X and Y directions. For VGCF composites, the strengths and moduli are modest compared to other graphite/epoxy composites and to the values expected based on the measured VGCF properties of up to 7 GPa tensile strength and 600 GPa modulus. Factors which may explain this behavior include the discontinuous form of VGCF in the composites, poor alignment of the individual filaments within the composite and a low fiber-matrix interfacial bond strength. The heat treated fibers present a very clean, smooth graphite basal plane to the matrix. Note also that the VGCF has not received any other surface treatment or sizing as is common practice with other commercial carbon fibers. In any case, mechanical properties for thermal management composites are less

demanding than for structural composites. For composites with mixed fiber reinforcement, while the ultimate tensile strength is seen to fall with increasing VGCF content, the modulus remains fairly constant. The transverse tensile strength coupons fractured near the tabs in most cases and both the strength and modulus are very close for all three panels. Tensile strengths of these mixed fiber composites are very close to those of the VGCF reinforced composites in the longitudinal, X, but nearly the same in the transverse, Y, directions. In contrast to the VGCF and mixed fiber reinforced composites, the hybrid fiber reinforced composites exhibit very uniform ultimate tensile strength and tensile modulus from coupon to coupon. The strengths are much higher than those of the short staple VGCF but less than those of the P-55 containing composites. The modulus is also intermediate between the VGCF and mixed fiber reinforced composites.

Table 7. Mechanical properties of VGCF/CER composites.

Fiber	V_f , %	UTS, MPa	Modulus, GPa	Strain, %
M/E	42 (X), 0 (Y)	70(X)	62(X)	
M/E	58 (X), 0 (Y)	74 (X)	52(X)	
S/CER	27 (X), 27 (Y)	52 (X), 43 (Y)	23 (X), 20 (Y)	0.29 (X), 0.29 (Y)
S/CER	54 (X), 0 (Y)	72 (X), 25 (Y)	37 (X), 8 (Y)	0.28 (X), 0.43 (Y)
M+P/CER	6+56 (X), 0 (Y)	692 (X), 17 (Y)	183 (X), 7 (Y)	0.34(X), 0.27 (Y)
M+P/CER	13+47 (X), 0 (Y)	458 (X), 22 (Y)	178 (X), 6 (Y)	0.28 (X), 0.39 (Y)
M-P/CER	25+37 (X), 0 (Y)	345 (X), 20 (Y)	164 (X), 6 (Y)	0.21 (X), 0.37 (Y)
H/CER	27 (X), 27 (Y)	253 (X), 294 (Y)	89(X), 99 (Y)	0.34 (X), 0.37 (Y)

Note: UTS=ultimate tensile strength, X=in-plane 0°, Y=in-plane 90°, Z = through thickness, V_f =fiber volume fraction, M=mat VGCF, H=hybrid VGCF, S=short staple VGCF, P=P-55 fiber, E=epoxy, CER=cyanate ester resin.

An important conclusion drawn from the above results is the apparent linear relationship between the volume fraction of VGCF and/or vapor deposited carbon in the composite and the thermal conductivity. This relationship is evident in Fig. 8 where the conductivity is plotted against fiber volume fraction; or, for 2D composites, as one-half the total fiber volume fraction. In the case of the mixed fiber composites, the VGCF is seen to dominate the thermal conductivity, and the intercept at 0% VGCF is that expected for a nominally 60% P-55 composite. The hybrid fiber composite lies somewhat above the trend, most likely because this is a continuous fiber while the VGCF is not. At lower hybrid fiber volume fractions, the effect of the low conductivity core is more pronounced resulting in a conductivity below the trend. Thus, it is demonstrated that composite thermal conductivity can be optimized by varying the VGCF content. In this manner,

other fibers can be utilized to provide for higher strengths, lower costs, or other properties.

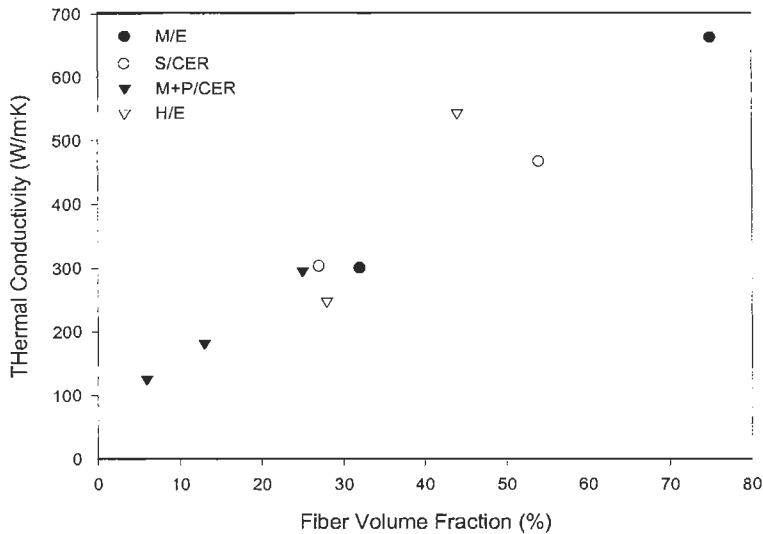


Fig. 8. Composite thermal conductivity as a function of fiber volume fraction.

4.1.3. Aluminum matrix composites

Ting *et al.* [30-32] studied the use of VGCF in aluminum matrix composites. VGCF/Al composites were prepared using a pressure infiltration technique [33-35]. Composite thermal conductivity and electrical resistivity were determined using a modified Kohlrausch method. Table 8 shows the data obtained from six (6) different VGCF/Al composites. As shown in Table 8, the use of VGCF greatly increases the thermal conductivity of aluminum. More than a 50% increase was achieved by using less than 18% of VGCF. An unprecedented high thermal conductivity of 642 W/mK for Al MMC was obtained by using 36.5% of VGCF. When the thermal conductivity in either X or Y direction was plotted as a function of fiber volume fraction, a linear relation was obtained. This indicates that heat was primarily conducted via VGCF in the fiber longitudinal direction. The impedance due to the very low thermal conductivity in the fiber transverse direction did not seem to occur.

VGCF exhibits not only the highest thermal conductivity but also the lowest electrical resistivity among all the carbon fibers. This is of importance since electromagnetic shielding is required in some packaging components. The effect of adding VGCF into aluminum on electrical resistivity is shown in Table 8. Although the electrical resistivity is increased, it remains in the same order of magnitude. It is noted that the increase can be reduced by intercalation. Unlike the thermal conductivity, the electrical resistivity did not increase linearly with

increasing X or Y fiber loading. However, when the electrical resistivity was plotted as a function of the total fiber volume fraction, a linear relationship was found. This demonstrates that impedance exists due to the high electrical resistivity in the fiber transverse direction, and also explains why the electrical resistivity is higher in the Y direction.

Table 8. Room temperature density (ρ , g/cm³) thermal conductivity (κ , W/mK) and electrical resistivity (Ω , microhm-cm) of various VGCF reinforced aluminum matrix composites.

ID	ρ	V_f (total / X / Y), %	κ (X / Y), W/mK	Ω (X / Y)
1	2.58	17.2 / 17.2 / 0	397 / 225	6.21 / 7.70
2	2.55	20.6 / 12.4 / 8.2	339 / 287	7.23 / 8.93
3	2.56	19.3 / 15.4 / 3.9	356 / 265	6.27 / 8.16
T0	2.51	26.6 / 13.3 / 13.3	333 / -	-
T1	2.50	27.9 / 27.9 / 0	534 / -	8.32 / -
T2	2.44	36.5 / 36.5 / 0	642 / -	-
T3	2.53	22.1 / 22.1 / 0	406 / -	-
VGCF	2.0	-	1950 parallel to fiber axis ~20 ^a perpendicular to fiber axis	60 parallel to fiber axis >100 perpendicular to fiber axis
Al	2.7	-	200	~4

a. Estimated value.

Although VGCF/Al composite exhibits excellent thermal conductivity, the mechanical properties are moderate. The average flexural strength and modulus of a 35%, by volume, VGCF/Al composite is about 150 MPa (22 ksi) and 1.50 GPa (0.22 msi), respectively. While the composites indicate relatively modest mechanical property values compared to composites reinforced with, for example, PAN fiber, they are sufficiently robust to allow their use in most applications where aluminum is satisfactory, such as in most electronic packaging applications. In addition, the CTE of aluminum, about 22 to 25 ppm/k, can be dramatically reduced to less than 10 ppm/K by the addition of VGCF. These data demonstrate the prospect of carbon fiber composites having several times the thermal conductivity of aluminum, yet retaining lower mass and coefficient of thermal expansion, promising to substantially improve composite performance while providing important weight savings.

4.1.4. Summary on VGCF composites

The above data represent the first from composites fabricated with fixed catalyst VGCF. A review of the data leads to the conclusion that the thermal and electrical properties of this type of carbon fiber are perhaps the most likely to be exploited in the short term. While mechanical properties of the composites are not as attractive as the thermal and electrical, it may be noted that no effort has

yet been made to develop a fiber-matrix interphase in any of the composites. Also, the mechanical properties may be limited by the frequency of defects manifested in surface crenulations demonstrated on the heat-treated and highly graphitic fixed-catalyst VGCF, as well as a relative lack of cross-linking between graphene planes. Finally, the mechanical strength and modulus, while not high enough to compete with other carbon fiber composites for structural applications, are still sufficiently high to allow components to be fabricated for thermal and electrical applications.

4.2. Composites based on floating catalyst fibers

The premise that discontinuous short fibers such as floating catalyst VGCF can provide structural reinforcements can be supported by theoretical models developed for the structural properties of paper Cox [36]. This work was recently extended by Baxter to include general fiber architecture [37]. This work predicts that modulus of a composite, E_c , can be determined from the fiber and matrix moduli, E_f and E_m respectively, and the fiber volume fraction, V_f , by a variation of the rule of mixtures,

$$E_c = E_m V_m + E_f V_f g\left(\frac{l}{d}\right) f(\theta)$$

where the functions, f and g , take on values between 0 and 1. The function g is small for particles having a low aspect ratio, but increases rapidly as the aspect ratio increases. The function f is dependent upon the orientation of the fibers, θ , and is greatest for uniaxial alignment. Baxter's findings imply that if floating catalyst fibers — which have a very high aspect ratio — can be restricted in orientation to two dimensions, the resulting composite could be several times as stiff as glass-reinforced composites.

It is only recently that limited efforts have been directed towards composite synthesis using the sub-micron floating catalyst form of VGCF. In one experimental effort, Dasch *et al.* [38] reported the fabrication of thermoplastic composites reinforced with randomly oriented VGCF, up to 30% of volume fraction, having diameters of 0.08 mm and lengths of 2.5 mm. All the composites exhibit similar flexural strength near 70 MPa (10.2 ksi), in accord with Baxter's theory for 3D short fiber reinforced composites. Also, flexure modulus increased with fiber volume fraction in accord with calculations based on Cox's theory for random 3D short fiber reinforcements. While these data are relatively inauspicious, the theoretical treatments do indicate that useful reinforcement is obtained through partial 2D reinforcement and controlled fiber/matrix interface. In the above study, no attempt to optimize the fiber/matrix interface was reported.

Due to the success in producing sufficient quantity of floating catalyst VGCF, we recently investigated the tensile properties of polyphenylene sulfide (PPS) matrix composite. The tensile properties were evaluated according to the ASTM D638 (Type D) Standard. The data are given in Table 9. For comparison, the mechanical properties of neat PPS, and 40% (by weight) glass fiber reinforced PPS are also included. It is apparent that the tensile modulus has been greatly enhanced and VGCF is shown to be a better reinforcement than glass fiber in this respect. On the other hand, composite strength is lower than that of neat matrix PPS. This is again attributed to the lack of fiber surface treatment to obtain desired fiber/matrix interface.

Table 9. Tensile properties of PPS composites. All the fiber fractions are in weight percents. Data on Specimens a and b are taken from Modern Plastic Encyclopedia '96, Mid-Nov 1995 Issue.

ID	Fiber	V_f , %	Modulus, GPa	Strength, MPa
P-3	VGCF	< 30	12.5±0.83	28.2±9.7
BM	VGCF	< 30	7.64±0.028	48.2±15.2
a	Glass	40	1.1 to 2.1	
b	none	none	3.3	65.5 to 86.1

VGCF reinforced concrete has also been studied [39]. VGCF in concrete serves to increase the flexural strength, flexural toughness, and freeze-thaw durability, and to decrease the drying shrinkage and electrical resistivity. At a fiber volume fraction of 4.24%, a flexural strength as high as 12.22 MPa, compared to 1.53 MPa for neat concrete, and a flexural toughness as high as 12.305 MPa-mm^{1/2}, compared to 0.038 MPa-mm^{1/2} for neat concrete, were reported. In a similar application, a small amount of the fiber (0.35% by volume) was added to mortar to increase the bonding strength to old mortar. The resultant increase in shear bond strength was up to 89%.

Another application utilizing the excellent electrical conductivity of VGCF is reinforced concrete for smart structures [42,43]. The volume electrical resistivity of such a smart structure increases upon flaw generation or propagation. Thus non-destructive detection of flaws in the concrete may be possible. The change in electrical resistivity can also be correlated to elastic and inelastic deformation, and fracture of the material, offering the potential of non-destructive damage assessment. Other properties, such as thermal and electrical conductivity, of composites based on floating catalyst VGCF have been investigated. Dasch *et al.* [38] studied the thermal conductivity of thermoplastic composites and found that although the thermal conductivity increased with fiber volume fraction, the values were much lower than expected. It is thought that the low thermal conductivity is because threshold values of fiber loading needed for percolation theory were not achieved in these composites [40].

The excellent electrical conductivity of VGCF composites makes them ideal for application in, for example, advanced electroconductive adhesive agents [41]. A number of carbon reinforcement, including VGCF, PAN-based carbon fiber, pitch-based carbon fiber, natural graphite powder, and electroconductive carbon black were evaluated for use in epoxy-based adhesive. The room temperature electrical resistivity of VGCF reinforced epoxy was found to be $0.27 \Omega\text{-cm}$, which could not be achieved using the other carbon fillers investigated. The adhesive strength was found to be higher than that of neat epoxy.

5 Potential Applications

5.1. *Thermal management*

A significant portion of the development work conducted on VGCF composites has been motivated by the potential of these composites for high performance thermal management applications, such as electronic heat sinks, plasma facing materials, and radiator fins. Both the fixed catalyst and the floating catalyst VGCF have the potential to be economically important for thermal management or high temperature composites.

Composites fabricated with fixed catalyst VGCF can be designed with fibers oriented in preferred directions to produce desired combinations of thermal conductivity and coefficient of thermal expansion. While such composites are not likely to be cost-competitive with metals in the near future, the ability to design for thermal conductivity in preferred directions, combined with lower density and lower coefficient of thermal expansion, could warrant the use of such VGCF composites in less price sensitive applications, such as electronics for aerospace vehicles.

Composites fabricated with the smaller floating catalyst fiber are most likely to be used for applications where near-isotropic orientation is favored. Such isotropic properties would be acceptable in carbon/carbon composites for pistons, brake pads, and heat sink applications, and the low cost of fiber synthesis could permit these price-sensitive applications to be developed economically. A random orientation of fibers will give a balance of thermal properties in all axes, which can be important in brake and electronic heat sink applications.

5.2. *Mechanical properties*

A major stimulus for the development of any low-cost carbon fibers is for their potential applications in the automotive industry, which identifies carbon fiber

reinforced composites as being necessary to meet Federal fuel efficiency standards. The projected production costs of floating-catalyst VGCF are within the range needed to be considered as a candidate reinforcement for automotive composite components. The performance of such carbon fiber reinforced composites is at this time still open to conjecture.

A very high degree of graphitic perfection in the fibers, and by inference, a high modulus of elasticity has been determined by x-ray diffraction for selected preparations of floating catalyst VGCF even without subjecting the fiber to any post-growth heat treatment. Though the small diameter of the fibers precludes direct measurement of modulus, this attribute has been substantiated by early investigations of the fiber as a reinforcement in rubber. Based on the presumed high modulus, and as suggested by theory described earlier, VGCF could be used to produce thermoplastic- and thermoset-matrix composites with elastic moduli comparable or exceeding that of aluminum, provided that preferential orientation in two dimensions can be obtained.

Because it is a small discontinuous reinforcement, floating catalyst VGCF may be pelletized and incorporated into commercially available thermoplastics, thermosets and elastomers and perhaps may be used directly in existing high volume molding processes without any significant new manufacturing development. Because of the inferred extraordinary intrinsic properties of the floating-catalyst VGCF, particularly elastic modulus, it is expected to enable a reduction in the amount of material required to produce a given stiffness, thus providing net weight and cost savings. Furthermore, it is produced in a process somewhat analogous to that of carbon black, that is, by direct conversion from a simple hydrocarbon source. Process economics are thus more favorable for VGCF and a cost of less than \$3/lb could be more easily attained than for PAN or pitch-based carbon fibers.

Accordingly, it is perceived that floating-catalyst VGCF may have a significant future as a reinforcement for in automotive components, where they could offer advantages of weight reduction, improved performance, parts consolidation and elimination, and reduction of assembly steps. While discontinuous VGCF is not expected to compete with continuous carbon fiber composites where demanding loads require premium values of mechanical properties, VGCF composites could be used for the manufacture of composite components which are currently reinforced by chopped glass fiber. Such components include sheet molding compounds for automotive body panels, and under-hood components such as fans, radiator parts, air conditioners, air filters, inlet manifolds, brake fluid reservoirs, air control valves, heater housings, windshield wiper reservoirs and gears.

5.3. *Electrical conductivity*

There are applications for engineered plastics where glass fibers are not suitable because they are electrically insulating and/or are too large. These include panels for electromagnetic interference shielding, electrical boxes and connectors, and antistatic composite components. The growth in the electronics industry, and the use of plastic housings within this market, has generated a need for conductive materials to attenuate ambient EMI originating from within and without the housing. While metal coatings, fibers and screens are suitable for this purpose, carbon fiber has been found to provide a lightweight solution for this type of plastic application, and are particularly well-suited for hand-held electronics.

Another application for VGCF is as an electrode material for lithium-ion batteries. These power storage devices require an anode that is conducting, has high effective surface area, and the ability to be easily and reversibly intercalated with the Li ions. VGCF is a candidate material because it can be produced with a small diameter and consequent high surface-to-volume ratio. It additionally possesses a highly graphic structure.

6 Manufacturing Issues

6.1. *Fixed catalyst VGCF*

6.1.1. Cost

As noted previously, cost of carbon fiber is a primary barrier to its more extensive use in commercial markets. The cost of production of the fixed catalyst VGCF will always be high relative to floating catalyst fiber. However, this type of VGCF has shown considerable potential in carbon/carbon composites for high performance applications, and may be applicable in those high performance areas that are less cost sensitive. The current cost of production, approximately \$1,000 per pound, could be reduced by an order of magnitude through higher efficiency and production rates. Such a reduction in production cost could dramatically increase its applicability even for the niche markets where it is most likely to have a future.

6.1.2. Production rate

The production of fixed catalyst VGCF has typically been performed using batch processing. The rate limiting step is the deposition of pyrolytic carbon on the walls of the fiber, thus thickening it. Analogy to semiconductor processing teaches that higher efficiency could be accomplished through conversion to a

semi-continuous process, eliminating the time required to cycle the furnace from room temperature to process temperature.

6.1.3. Understanding/control of defects

As noted, a large variation in the morphology of VGCF is possible, ranging from ribbons, helices (Motojima *et al.* [44]) and fiber which grows in random directions, to relatively long unidirectional cylindrical fibers having uniform diameters and surfaces. Much of the variation in fiber morphology results from the choice of catalyst, coupled with the concentrations of hydrocarbons and hydrogen and the temperature in the fiber growth reactor. See for example recent publications by Herreyre and Gadelle [45], and Nolan *et al.* [46]. One common feature of VGCF which has been thickened to diameters typical of other carbon fibers is the appearance of crenulations along the length of the fiber. The perfect graphite fiber would be one which is devoid of defects and crystallographic imperfections, producing a straight fiber which is free of crenulations would be beneficial. One area of research at ASI has been the lengthening and thickening of the fibers under conditions which can be independently varied in order to illuminate the mechanisms leading to the formation of crenulations [47]. However, the early results of this study have generated more questions than answers, as shown in Fig. 9, which is a scanning electron micrograph showing the fiber produced when thickening at temperatures higher than normal process temperatures. The presence of crenulated fiber, as well as distinctively beaded fiber is observed. The etiology of this phenomenon is as yet unknown, emphasizing the that additional study of fiber growth mechanisms is warranted for further control and improvement of fiber properties.

6.2. Floating catalyst VGCF

6.2.1. Process scale-up

To exploit the numerous applications for floating catalyst VGCF in engineered plastics, production rates are projected to be on the order of several pounds per hour from a single tube reactor. Demonstration experiments on a small scale have shown feasibility of accomplishing the desired rate of production. Economic production of such quantities will involve recapture of energy in the heated unreacted gas which exits the reactor, as well as automated collection, debulking, and preform fabrication systems.

6.2.2. De-bulking

In order for VGCF to be successfully incorporated into engineering composites, it must be available in forms which composite fabricators are equipped to handle. Since VGCF is bulky and discontinuous as produced, it is not amenable to the textile processing used for continuous carbon and glass fiber. Thus fiber

preforms are required which will enable the post-production debulking of the fiber for shipment, and straightforward utilization in conventional composite synthesis operations. Such preforms include pellets, paper, felt, and perhaps woven yarns; the desired preform of the material is expected to be different for different industries. Pelletization and paper fabrication are methods currently under development at ASI.

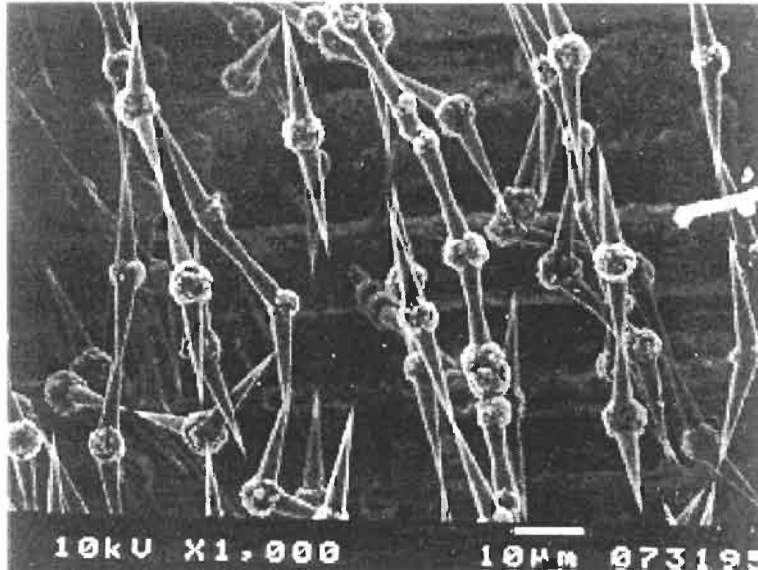


Fig. 9. SEM micrograph showing the presence of crenulated fiber as well as distinctively beaded fiber.

Paper is produced by incorporating fiber into a slurry, and then filtering through a mesh to leave a random, two dimensionally-oriented array of short fibers. Typically a thermoplastic or thermosetting binder which is compatible with the desired matrix is added for papers made of carbon fiber [48]. To achieve appropriate properties of carbon fiber paper, it may be necessary to optimize the length and aspect ratio of the VGCF, or to mix it with other fibers having desired fiber properties. Paper fabricated with VGCF could enable two-dimensional orientation of the fiber, shipment and use of the fiber from rolls, and machine handling to incorporate into desired composite components.

Pelletization can be achieved by using high shear mixing to blend and disperse the VGCF into a slurry which may contain a surfactant and sizing, followed by drying and grinding into chips or pellets [49]. Also ball milling has been used to reduce the aspect ratio, which also serves to reduce the degree of birdnesting and partially de-bulk the fiber.

6.2.3. Sizing/interphase development

A fundamental aspect of any composite system is the establishment of an appropriate interface between fiber and matrix. The mechanical properties of the composite are strongly governed by the degree of adhesion between the fiber and matrix, although the optimum properties are not necessarily achieved with the highest possible degree of adhesion. However, in order to effectively transfer load to and between fibers, a significant degree of coupling must exist. Appropriate interfaces between reinforcement and the desired matrix have been developed for all successful composite systems, including glass fiber and continuous carbon fiber.

Optimization of the interface has not been achieved for any of the VGCF composite systems of choice. In the case of continuous carbon fiber, means of oxidizing the fiber were first developed using batch laboratory processes. These were followed by the development of electrochemical baths to oxidize the continuous fiber for economic application in industrial production volumes. For the discontinuous form in which VGCF currently is produced, such interface optimization to create active sites on the fiber surface and thus promote chemical and physical bonding with selected matrix materials, is expected to include in situ surface treatments as the fiber is produced, and would be followed by application of coupling agents or sizing to add functional groups, and to assist in debulking and handling.

6.2.4. Alignment

A number of composite applications exist where isotropic orientation of the fiber is either preferred for isotropy of composite properties, or is tolerated as long as minimum thresholds for requisite properties are achieved. An example of the former would be carbon/carbon pistons, where a low isotropic coefficient of thermal expansion would be desirable. The latter type application includes polymer matrix composites for EMI shielding or for antistatic applications. As demonstrated by the theoretical modeling discussed earlier, preferred orientation of the fiber will be necessary to optimize mechanical properties in composites. Some degree of alignment may be possible for composites synthesized by injection or other molding processes, and by use of VGCF paper preforms in which the fiber is preferentially oriented into two dimensions. Methods of forming yarns may also be possible, thus enabling VGCF use through conventional textile processing means.

6.2.5. Environmental and safety issues

Airborne particles with diameters less than 1 micron, as in the case of asbestos, are potentially respirable; therefore, the manufacture of all submicron diameter carbon particles includes a responsibility to ensure that no health hazards are

present in the production or use of such VGCF. Additionally, various hydrocarbons can be formed during VGCF production which are of concern for health reasons, analogous to the manufacture of carbon black.

It is envisioned that the first issue, particle size within a respirable range, will be dealt with by continuous containment of the floating catalyst fiber from the point of its formation through to permanent entrainment in the matrix material of choice. As currently produced, this type of fiber is entangled, or birdnested, and resembles cotton (except for the color). The degree of entanglement is so complete that periodic air sampling of the exhaust from the reactor has revealed no evidence of dispersed individual fibers. The fiber tends to be contained into birdnested balls by the current production method. Higher volume production rates may impact this condition; however, higher production rates will also require collection systems such as water spray as the fiber exits the reactor, followed by application of sizing, pelletization, paper formation, or other debulking process, similarly leaving the fiber in a state of agglomeration and containment. The process will be completed by entrainment of the fiber in a polymer or other matrix material when the composite is fabricated. Thus exposure to individual fibers is anticipated to be an extremely rare exception to anticipated normal handling operations.

With respect to the formation of unwanted polyaromatic hydrocarbons in the pyrolytic process, it has been shown that conditions can be maintained where such formation is negligible according to EPA and OSHA standards. As production rates are increased, it will be incumbent on any manufacturer to maintain a set of operating parameters which produce an environmentally-benign product; however, current information regarding the process for fiber formation reveals no barriers to accomplishing this.

7 Conclusions

As observed by Philip Walker, Jr. [50], carbon is an old and yet a new material. Numerous investigations into the mechanisms of vapor grown carbon fiber formation, and the properties of the various types of fibers, have established this material as a unique and intriguing component of the set of forms that may be synthesized from carbon. From these studies, methods of economic production of VGCF have been developed which promise low cost, high modulus graphitic fiber as a new commodity for broad use in commercial applications for engineered plastics. Work on composites of VGCF is essentially still in its infancy, yet composites have been fabricated which have established highest values for properties of thermal and electrical conductivity among similar composites. Future work in the areas of interphase and preform development

are expected to enable the use of VGCF in several automotive and electronics industry applications, stimulating the creation of a manufacturing base for VGCF and VGCF composites synthesis. The versatility of VGCF as an engineering material portends a broad scope of applicability, with prospects of founding a new industry for the 21st century.

8 References

1. Oberlin, Endo, M and Koyama, T., Filamentous growth of carbon through benzene decomposition, *J. of Crystal Growth*, 1976, 32, 335 .
2. Baker, R.T.K., Catalytic growth of carbon filaments, *Carbon* , 1989, 27(3) 315 323.
3. Tibbetts, G.G., Why are carbon filaments tubular?, *J. Crystal Growth*, 1984, 66, 632
4. Rodriguez, N.M., A review of catalytically grown carbon nanofibers *J. Mater. Res.*, 1993, 8(12), 3233.
5. Dresselhaus, M.S., Dresselhaus, G., Sugihara, K., Spain, I.L., Goldberg, H.A., Graphite fibers and filaments, Springer-Verlag, New York, 1988.
6. Bartholomew, C.H., Carbon deposition in steam reforming and methanation, *Catal Rev. Sci. Eng.*, 1982, v24, 67 112.
7. Baker, R.T.K, Chemistry and physics of carbon, Marcel Dekker, New York, 14, 1978,
8. Trimm, D.L., The formation and removal of coke from nickel catalyst, *Catal. Rev. Sci. Eng.*, 1977, 16, 155 189.
9. Koyama, T., Endo M. and Onuma, Y., Carbon fibers obtained by thermal decomposition of vaporized hydrocarbon, *Japan J. Appl. Phys.*, 1972, 11, 445.
10. Koyama, T., Formation of carbon fibers from benzene, *Carbon*, 1972, 10, 757 758.
11. Endo, M. Shikata, M., Momose, T. and Shiraishi, M. ???, in Ext. Abstr. 17th Biennial Conf Carbon, 1985, p, 295
12. Tibbetts, G.G., Vapor-grown carbon fibers: status and prospects, *Carbon*, 1989, 27(5), 745 747.
13. Tibbetts, G.G., Gorkiewicz, D.W., and Alig, R.A. A new reactor for growing carbon fibers from liquid- and vapor-phase hydrocarbons, *Carbon*, 1993, 31(5), 809 814.
14. Tibbetts, G.G., Bernardo, C.A., Gorkiewicz, D.W. and Alig R.L. Role of sulfur in the production of carbon fibers in the vapor phase, *Carbon*, 1994, 32(4), 569 576.
15. Tibbetts, G.G., Beetz, Jr., C.P., Mechanical properties of vapor grown carbon fibers, *J. Appl. Phys.*, 1987, 20, 292
16. Tibbetts, G.G., Endo, M. and Beetz, Jr. C.P., Carbon fibers grown from the vapor phase: A novel material, SAMPE, Sept., Oct., 1986, 22(5).
17. Tibbetts, G.G., Doll, G.L., Gorkiewicz, D.W., Moleski, J.J., Perry, T.A., Dasch, C.J. and Balogh, M.J., Physical properties of vapor grown carbon fibers, *Carbon*, 1993, 31(7), 1039 1047
18. Jacobsen, R.L., Tritt, T.M. Guth, J.R., Ehrlich, A.C. and Gillespie, D.J., Mechanical properties of vapor-grown carbon fiber, *Carbon*, 1995, 33(9), 1217 1221
19. Brito, K.K., Anderson, D.P. and Rice, B.P., Graphitization of vapor grown carbon fibers, Proc. 34th Inter. SAMPE Symp., 1989, 34(1), 190
20. Ting, J.-M. and Lake, M.L., Vapor-grown carbon-fiber reinforced carbon composites, *Carbon*, 1995, 33(5), 663 667
21. Lake, M.L. Ting, J.-M. and Corrigan, M., Carbon/Carbon composites for space

- thermal management, Proc. 1st Ann. Spacecraft Thermal Control Symp., Albuquerque, NM, Nov., 1994
22. Ting J.-M., and Lake, M.L. Processing, fabrication, and applications of advanced composites, Ed., ASM International, Materials Park, OH, 1993, pp 117 127.
 23. Ting J.-M. and Lake, M.L. Khounsary A.M., VGCF/carbon composites for plasma-facing materials, SPIE, Bellingham, WA, 1993, pp 196 205
 24. Ting J.-M., and Lake, M.L., Vapor grown carbon fiber reinforced carbon/carbon composites, Proc. 17th Ann. Conf. Comp., Mat. & Structures, Cocoa Beach, FL, January, 1993, pp. 355.
 25. Ting J.-M., and Lake, M.L. VGCF/carbon as plasma facing materials, Proc. DOE Plasma Facing Materials and Components Task Group Meeting, West Dennis, MA, Sept., 1992.
 26. Ting, J.-M., and Lake, M.L., Carbon/carbon for thermal management, Proc. 16th Ann. Conf. Comp., Mat. & Structures, Cocoa Beach, FL, January, 1992.
 27. Hercmans J. and Beetz, C.P., Thermal conductivity and thermopower of vapor-grown graphite fibers J. Phys. Rev.B 32, 1985, p.1981
 28. Dresselhaus, M.S., Dresselhaus, G.D., Sugihara, K. Spain, I.L. and Goldberg, H.A. Graphite fibers and filaments,, Springer-Verlag,, New York, 1988.
 29. Duffy, D.R., Ting, J.-M., Guth, J.R. and Lake, M.L., Carbon fiber reinforced light-weight composites with ultra high thermal conductivities, Proc. Int. IEPC, Atlanta, GA, Sept., 1994, pp. 442 448.
 30. Ting, J.M. Guth, J.R. and Lake, M.L., Light weight, highly thermal conductive composites for space radiators, Ceram. Eng. & Sci. Proc., July-Aug., 1995, pp. 279. 288.
 31. Ting, J.M. and Lake, M.L., Vapor grown carbon fiber reinforced aluminum composites with very high thermal conductivity J. Mat. Res., 1995, 10(2), 247 250.
 32. Ting, J.M. Lake, M.L. and Duffy D.R., Composites based on thermally hyper-conductive vapor grown carbon fiber, J. Mater. Res., 1995, 10(6), 1478 1484
 33. Mortensen, A., Masur, L.J., Cornie, J.A. and Flemings, M.C., Infiltration of fibrous preforms by a pure metal: Part 1: Theory, Met. Tran., 1989, 20A 2535
 34. Mortensen, A. Masur, L.J., Cornie, J.A. and Flemings, M.C., Infiltration of fibrous preforms by a pure metal, Part 2, Experiment, Met. Tran., 1989, 20A 2549
 35. Klier, E., Mortensen, A, Cornie, J.A., and Flemings, M.C., "Fabrication of Cast Particulate Reinforced Metals Via Pressure Infiltration" J. Mat. Sci., July, 1990.
 36. Cox., H.L., The elasticity and strength of paper and other fibrous materials, *British Journal of Applied Physics*, 1952, 3, 52.
 37. Baxter, W.J., The strength of metal matrix composites reinforced with randomly oriented discontinuous fibers, 1992, Metall Trans. 23A, 3045
 38. Dasch, C.J., Baxter, W.J., and Tibbetts, G.G., Thermoplastic composites using nanometer-size vapor-grown carbon fibers, *Extended Abstracts, 21st Biennial Conference on Carbon*, 1993, pp. 82 83.
 39. Chen P. and Chung, D.D.L, Dispersants for carbon fibers in concrete, *Extended Abstracts, 21st Biennial Conference on Carbon*, 1993, 92 93
 40. Kirkpatrick, S., Percolation and conduction, Rev. Mod. Phys. 1973, 45, p. 574
 41. Katsumata, M. and Endo, M. J., Epoxy composites using vapor-grown carbon fiber fillers for advanced electroconductive adhesive agents, J. Mater. Res., 1994, 9(4), 841 843.
 42. Chen, P. and Chung, D.D.L., Carbon fiber reinforced concrete for smart structures,

- Extended Abstracts, 21st Biennial Conference on Carbon*, 1993, 701 702
43. Chen P. and Chung, D.D.L. , Carbon fiber reinforced concrete as an intrinsically smart concrete for damage assessment during dynamic loading, pp. 168-9, *Extended Abstracts, 22st Biennial Conference on Carbon*, 1995, pp 168 169.
 44. Motojima, S., Asakura, S., Kasemura, T., Takeuchi, S. and Iwanaga, H., Catalytic effects of metal carbides oxides and Ni single crystal on the vapor growth of micro-coiled carbon fibers, *Carbon* , 1996, **34**, (3), 289 296.
 45. Herreyre, S. and Gadelle, P., Effect of hydrogen on the morphology of carbon deposited from the catalytic disproportionation of CO, *Carbon*, 1995, 33(2), 234 237.
 46. Nolan, M.J., Schabel, D.C. Lynch, and Cutler, A.H., Hydrogen control of carbon deposit morphology, *Carbon*, , 1995, 33(1) 79 85.
 47. Jacobsen, R.L., Monthieux, M. and Burton, D., Carbon beads with protruding cones, *Nature*, Jan. 16, 1997, Vol. 385, 211 212
 48. Walker, In *Carbon Fibers: Technology, Uses, and Prospects*, Plastics and Rubber Institute, London, 1986.
 49. Alig, R. L., US Patent No. 5,594,060, 1997
 50. Walker, P.L., Carbon: an old but new material revisited, *Carbon*, 1990, 28(2,3), 261 279

CHAPTER 6

Porous Carbon Fiber-Carbon Binder Composites

TIMOTHY D. BURCHELL

*Metals and Ceramics Division**Oak Ridge National Laboratory**Oak Ridge, Tennessee 37831-6088, USA***1 Introduction**

Low density, carbon fiber-carbon binder composite thermal insulators were developed at the U.S. Department of Energy's Y-12 Plant in Oak Ridge during the 1970s [1,2]. Subsequently, this class of composites was further developed and optimized at the Oak Ridge National Laboratory (ORNL) for an aerospace application. Porous, carbon fiber-carbon binder composite materials are a class of carbon composites that are not widely recognized. Unlike dense, structural carbon-carbon composites, which are used extensively in aerospace and military applications, there are relatively few applications of porous carbon fiber-carbon binder composites. However, their combination of properties makes them uniquely suited to certain applications. Typically, carbon-carbon composites in this class have densities $<1 \text{ g/cm}^3$, and frequently densities $<0.25 \text{ g/cm}^3$. Through judicious selection of the carbon fiber, and modifications to the fabrication process, low density composite materials with a wide range of pore structures and physical properties can be produced. For example, low density carbon composites were recently developed for gas separation and storage applications, and applications that exploit their optical properties. Extensive work has been performed on this class of composites by ORNL. Here, the manufacture, structure, properties, and applications of ORNL's low density, carbon fiber-carbon binder composites are reviewed.

2 Manufacture*2.1 Raw materials*

Low density, carbon fiber-carbon binder composites are fabricated from a variety of carbon fibers, including fibers derived from rayon, polyacrylonitrile (PAN), isotropic pitch, and mesophase pitch. The manufacture, structure, and properties of carbon fibers have been thoroughly reviewed elsewhere [3] and, therefore, are

not discussed here. Details of the precursor fibers utilized for the production of ORNL's porous carbon fiber-carbon binder composites are reported below.

2.1.1 Rayon fibers

Rayon fibers were purchased as apparel rayon from a commercial producer in the form of 1.5 denier per filament, 240,000 total denier, bright, untwisted, low-sulfur, rayon tow. The raw tow was chopped to the desired length ($\sim 250 \mu\text{m}$ for the applications described in Sections 3 and 4). The green fiber was heated in a nitrogen atmosphere to 1400°C over a period of approximately 11 hours. The slow heating rates were found to be necessary to assure acceptable carbon yields. Prior to molding, the fibers were ball milled and screened to attain the required fiber length distribution. The average length of the carbonized rayon fibers was $\sim 150 \mu\text{m}$.

2.1.2 PAN fibers

PAN fibers were purchased from AKZO Fortafil Fibers, Rockwood, Tenn., under the designation F3-O. Fibers with a mean length of $100 \mu\text{m}$ and $200 \mu\text{m}$ have been utilized.

2.1.3 Isotropic pitch-derived fibers

CarboflexTM P200 and P400 milled carbon fibers were used at ORNL, and were obtained from two sources. Initially, the CarboflexTM carbon fibers were obtained from the Ashland Petroleum Company, Ashland, Kentucky, U.S.A. More recently, however, CarboflexTM fibers were purchased from the Anshan East Asia Carbon Company, Anshan, China.

2.1.4 Mesophase pitch-derived fibers

Milled ($200 \mu\text{m}$ length) mesophase pitch-derived carbon fibers were purchased from Amoco Performance Products, Inc., Alpharetta, Ga., under the designation DKDX fibers.

2.2 Manufacturing Process

The synthesis route for ORNL's porous carbon fiber-carbon binder composites is illustrated in Fig. 1. A schematic diagram of the molding arrangement is shown in Figure 2. The selected fibers were mixed in a water slurry with powdered phenolic resin (Durez grade 7716) purchased from the Occidental Chemical Corp., N. Tonawanda, N.Y. 14120, U.S.A. The phenolic resin is a B-stage (insoluble in water or alkaline solutions), two-step, thermosetting resin consisting of a Novalak ($\text{C}_6\text{H}_5\text{OHCH}_2$)_n powder to which $\sim 8 \text{ wt}\%$ of hexamethylenetetramine $(\text{CH}_2)_6\text{N}_4$ is added in powdered form as an activator for polymerization. The average particle size was $\sim 9 \mu\text{m}$, and the carbon yield after pyrolysis is typically 50%.

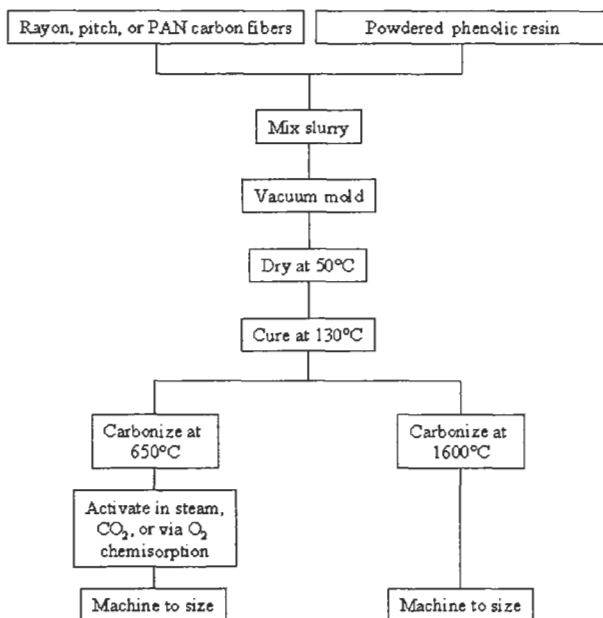


Fig. 1. The synthesis route for ORNL's porous carbon fiber-carbon binder composites.

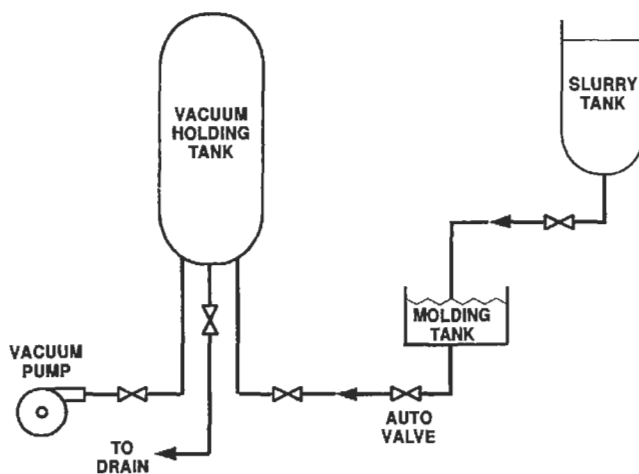


Fig. 2. Schematic diagram of the molding apparatus used for the manufacture of ORNL's porous carbon fiber-carbon binder composites.

For rayon fiber based composites (Sections 3 and 4) the fiber and powdered resins were mixed in a water slurry in approximately equal parts by mass. The isotropic pitch carbon fiber composites (Section 5) were manufactured with less binder, typically a 4:1 mass ratio of fiber to binder being utilized. The slurry was transferred to a molding tank and the water drawn through a porous screen under vacuum. In previous studies [2] it was established that a head of water must be maintained over the mold screen in order to prevent the formation of large voids, and thus to assure uniform properties. The fabrication process allows the manufacture of slab or tubular forms. In the latter case, the cylinders were molded over a perforated tubular mandrel covered with a fine mesh or screen. Moreover, it is possible to mold contoured plates, and tubes, to near net shape via this synthesis route.

The resulting green artifact was dried in air at $\sim 50^{\circ}\text{C}$ and stripped from the mold. The composite was cured at $\sim 130^{\circ}\text{C}$ in air prior to carbonization under an inert gas. Alternately, the dried part may be hot pressed at 300°C to increase the density to as much as 1 g/cm^3 . The carbonization temperature selected depends upon the final application of the porous composite. If the cured or hot pressed composite is to be activated to develop the micropores and mesopores, carbonization generally occurs at $\sim 650^{\circ}\text{C}$. The materials described in Sections 3 and 4 are, however, carbonized at much higher temperatures (1600°C). During carbonization the phenolic resin binder is thermally converted to a glassy carbon. Once carbonized, the porous carbon fiber-carbon binder composite is readily machined to more complex geometries. The carbonized bulk density of the composite material is typically $0.2\text{--}0.4\text{ g/cm}^3$, and depends upon the fiber type and length distribution, and the binder volume fraction.

2.3 Activation

Activation of the porous composite was carried out in moisture saturated He, or CO_2 , in the temperature range $800\text{--}950^{\circ}\text{C}$. Attaining uniform activation in large composite pieces is challenging. The use of a special gas distribution manifold partially alleviated this problem, yet attaining uniform activation in sections > 25 mm thick has proven to be very difficult. Jagtoyen and Derbyshire [4] applied the O_2 chemisorption technique of Nandi and Walker [5] and Quinn and Holland [6] and achieved improved uniformity of activation in monoliths up to $12 \times 7 \times 6$ cm in size. At ORNL, we have also applied this approach and successfully activated porous composite monoliths of 10 cm in diameter and 25 cm in length [7]. The chemisorption/activation procedure adopted was performed in a three zone Lindberg furnace fitted with a 20-cm diameter Inconel retort. The porous composite samples were dried in a vacuum at 300°C , cooled to 200°C for the chemisorption treatment in flowing O_2 , and then heated again to 850°C in He. The chemisorption and activation steps were repeated until the desired burn-off was attained.

3 Carbon Bonded Carbon Fiber

3.1 Application

Carbon bonded carbon fiber (CBCF) is used on a modular heat source known as the general purpose heat source (GPHS) [8,9], which provides thermal power to banks of silicon-germanium thermoelectric couples in a system referred to as a radioisotope thermoelectric generator, or RTG. These electric power devices are used to power deep space exploratory vehicles, such as NASA's Galileo, Ulysses, and Cassini missions. The GPHS utilizes the heat produced by the self-absorption of alpha particles in the $^{238}\text{PuO}_2$ fuel. The GPHS is shown in Fig. 3. Eighteen individual modules are stacked in a column to provide an initial thermal source power of 4500 watts [9]. Each module is comprised of a carbon-carbon composite aeroshell that contains two graphite impact shells (GIS), which are also manufactured from a carbon-carbon composite. The aeroshell serves as the structural element and an ablative material. The $^{238}\text{PuO}_2$ fuel pellet is clad in an iridium alloy and two of these fueled clads are combined in a graphite impact shell, separated by a floating graphite membrane. The impact shells are surrounded by CBCF thermal insulation. The CBCF provides thermal protection for the iridium alloy clad assuring its temperature is maintained within the maximum ductility temperature range, where it offers optimum containment protection to the $^{238}\text{PuO}_2$ fuel.

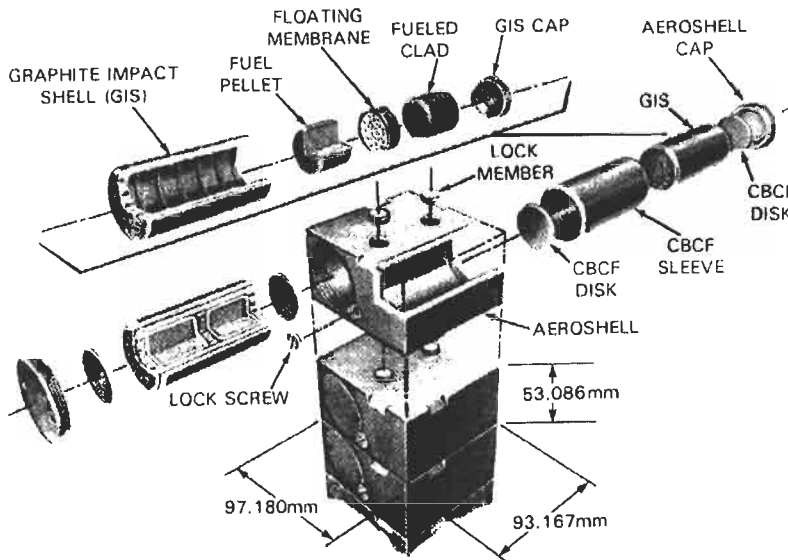


Fig. 3. The general purpose heat source assembly. *Courtesy of the US. Department of Energy.*

The structure of CBCF is shown in the SEM micrograph in Fig. 4. The crenellated surface of the rayon derived carbon fibers is clearly visible, as is the phenolic derived carbon binder. The preferred orientation of the fibers (resulting from the slurry molding operation) is obvious in Fig. 4, and imparts considerable anisotropy to the material. The molding direction is perpendicular to the plane of the carbon fibers in Fig. 4.

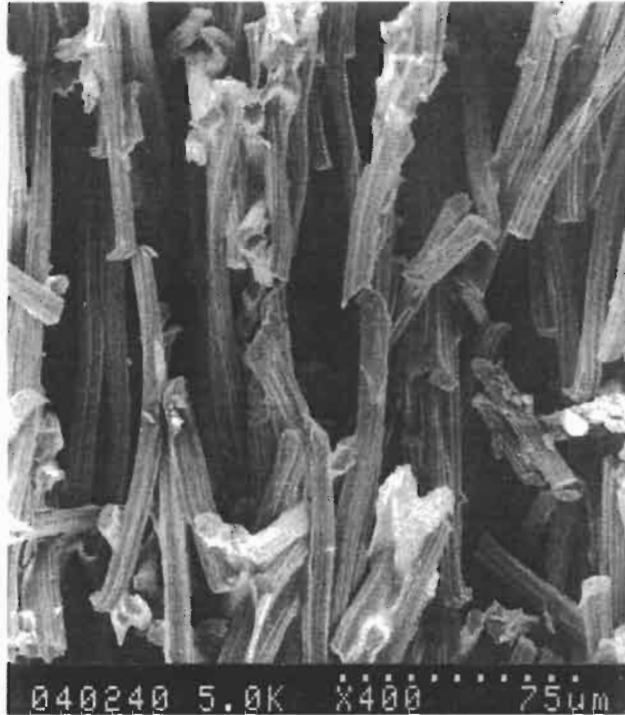


Fig. 4. An SEM micrograph of CBCF revealing its structure and texture.

Several stringent requirements must be met by the thermal insulation of the GPHS [1], chief amongst these are: light-weight; long-term thermal stability and an ability to withstand thermal transients to $\sim 2500^{\circ}\text{C}$; chemical compatibility with other components of the GPHS; low gas evolution, in order not to damage the Si-Ge thermoelectric couples; and sufficient mechanical strength to survive launch induced vibrational stresses. Moreover, the thermal conductivity must be low enough to protect the iridium alloy clad in the manner described above. The use of CBCF thermal insulation in the GPHS reduces the weight of the overall system by 1.4 kg, and increases the specific power by 7% [9] over previous space nuclear power systems or other designs of the GPHS utilizing more conventional insulation materials.

3.2 Physical Properties

Wei and Robbins [10] and Brassell and Wei [2] have reported property data for CBCF. Their data, and more recent unpublished data from ORNL, are summarized below.

3.2.1 Density

In an early study [10] of the density of CBCF forms, a series of 26 tubes (~10 cm in length, and with an outside diameter of ~4 cm and an inside diameter of ~3 cm), and 6 plates (~10 × 10 × 2.5 cm), were examined. The bulk density, determined from the dimensions and the mass of the outgassed forms, varied from 0.19 to 0.27 g/cm³. The density was reported to be a function of packing of the fibers in the composite, which is in turn primarily a function of the fiber length and length distribution. The variation of density within a single CBCF plate was examined by Weaver and Chilcoat [11]. The plate was cut into 80 specimens and the density determined by mensuration. The density varied from 0.2322 - 0.2493 g/cm³, a variation of about 7%. There was a tendency for the density to be slightly lower in the periphery of the plate. Density measurements performed on CBCF tubes by repetitively machining the outside diameter and re-weighing the tube, revealed a higher density in the inner and outer skin of the tube, where the density was ~10% higher than in the center of the tube wall [11].

3.2.2 Mechanical properties

The mechanical properties of CBCF have been determined at ORNL[10]. Compressive strengths were measured at a cross-head speed of 8.5 μm/s using samples core drilled from plates or cylinders. In the direction perpendicular to the fiber (molding direction) the load-deflection curve is linear up to approximately 4% strain. Above 4% strain and up to approximately 40% strain, the load-deflection curve is typically concave downward. As discussed by Wei and Robbins [10], elastic deformation occurs up to about 4% strain, after which structural degradation occurs. The strength of the CBCF was arbitrarily defined as the stress at 5% strain. Over 100 samples taken from multiple fabrication runs were tested. The compressive strength in the molding direction ranged from 0.52 to 1.12 MPa, and sample density varied from 0.19 to 0.25 Mg/m³. The strength data are plotted in Fig. 5. The scatter of the strength data is large, but there is a clear trend for increasing strength with increasing density, which has been attributed to increased bonding between the fibers at greater densities [10]. Compressive strengths measured on specimens cut from three CBCF tubes [11] ranged from 0.774 to 0.958 MPa, similar to the strength reported by Wei and Robbins [10] for CBCF plates. The shear strength of CBCF (measured in the direction perpendicular to the fibers at room temperature), was reported to be 0.59 MPa, which is significantly less than the compressive strength.

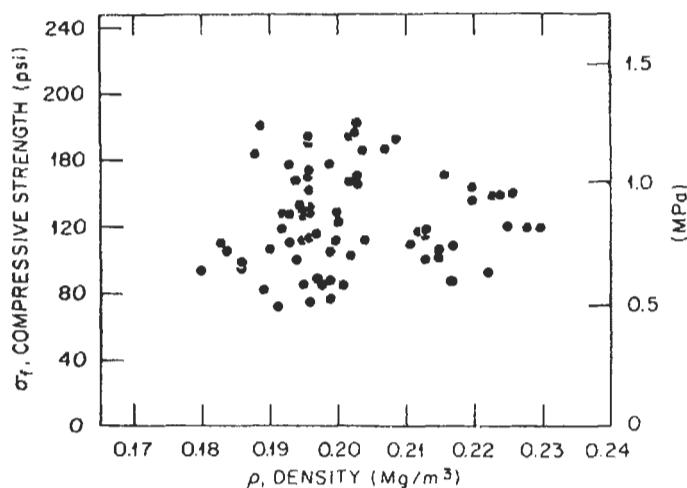


Fig. 5. The variation of CBCF compressive strength with density for samples machined in the molding direction. Reprinted from [10], copyright ©1985 The American Ceramics Society, with permission.

The elastic modulus of CBCF (calculated from the stress-strain curves) ranged from 11-28 MPa in the molding direction [10]. The relatively low elastic modulus bestows excellent thermal shock resistance to the CBCF. The elastic modulus and compressive strength of CBCF in the direction parallel to the fibers (perpendicular to the molding direction) are typically four times greater than those in the molding direction (perpendicular to the fibers). This anisotropy can be attributed to the preferred fiber orientation that develops during the molding operation (Fig. 3). Thermal effects on the strength and modulus are reported to be negligible up to 1200°C (in vacuum or an inert gas)[10]. Indeed, both the strength and modulus were slightly greater at 1200°C than at room temperature. Moreover, prolonged high temperature exposure (1000 hours at 1350°C) had no effect on strength.

3.2.3 Thermal properties

Wci and Robbins [10] have reviewed much of the work performed on the thermal physical properties of CBCF. The emissivity parallel to the fibers was 0.8 over the temperature range from 1000 to 1800°C. This value is higher than the emissivity of *c*-direction pyrolytic graphite (0.5-0.6), but is close to values for graphite and dense carbon-carbon composite (0.8-0.95).

The thermal expansion of CBCF is greater in the direction perpendicular to the fibers than in the parallel direction by a factor of ~1.4. The mean coefficients of thermal expansion (CTE) from room temperature to 1800°C were $3.9 \times 10^{-6}/^\circ\text{C}$ (perpendicular to the fiber direction) and $2.8 \times 10^{-6}/^\circ\text{C}$ (parallel to the direction of

the fibers). These values are lower than those of many fine-grained graphites. Moreover, the perpendicular direction CTE is lower than the corresponding value for a dense carbon-carbon composite, whereas the parallel to fiber direction is significantly greater than those for dense carbon-carbon composites measured in the corresponding direction [12]. The specific heat of CBCF, measured using a scanning calorimeter, varied from 684 J/kg•K at 23°C to 2150 J/kg•K at 2000°C which agrees with specific heat data for POCO graphite [12].

Thermal conductivity is a function of the specimen orientation, due to the preferred alignment of the fibers during molding (Fig. 3), and of the carbonization temperature. For example, increasing the carbonization temperature from 1300 to 1600°C increased the thermal conductivity by ~30%. Moreover, the anisotropy factor for thermal conductivity is ~5 over the temperature range from room temperature to 2000°C. Measured values of thermal conductivity (at room temperature in vacuum) ranged from 0.0422 to 0.0863 W/m•K for samples with densities varying from 0.20 to 0.25 g/cm³. The room temperature conductivity was found to exhibit a linear dependence on density. Weaver and Chilcoat [11] reported the room temperature thermal conductivity within a plate varied from 0.0608 to 0.0757 W/m•K, in good agreement with Robbins and Wei [10].

The temperature dependence of the thermal conductivity of CBCF has been examined by several workers [10,13,14]. Typically, models for the thermal conductivity behavior include a density term and two temperature (T) terms, i.e., a T term representing conduction within the fibers, and a T^3 term to account for the radiation contribution due to conduction. The thermal conductivity of CBCF (measured perpendicular to the fibers) over the temperature range 600 to 2200 K for four samples is shown in Fig. 6 [14]. The specimen to specimen variability in the insulation, and typical experimental scatter observed in the thermal conductivity data is evident in Fig. 6. The thermal conductivity of CBCF increases with temperature due to the contribution from radiation and thermally induced improvements in fiber structure and conductivity above 1873 K.

Recently, Dinwiddie *et al.* [14] reported the effects of short-time, high-temperature exposures on the temperature dependence of the thermal conductivity of CBCF. Samples were exposed to temperatures ranging from 2673 to 3273 K, for periods of 10, 15, and 20 seconds, to examine the time dependent effects of graphitization on thermal conductivity measured over the temperature range from 673 to 2373 K. Typical experimental data are shown in Figs. 7 and 8 for exposure times of 10 and 20 seconds, respectively. The thermal conductivity was observed to increase with both heat treatment temperature and exposure time.

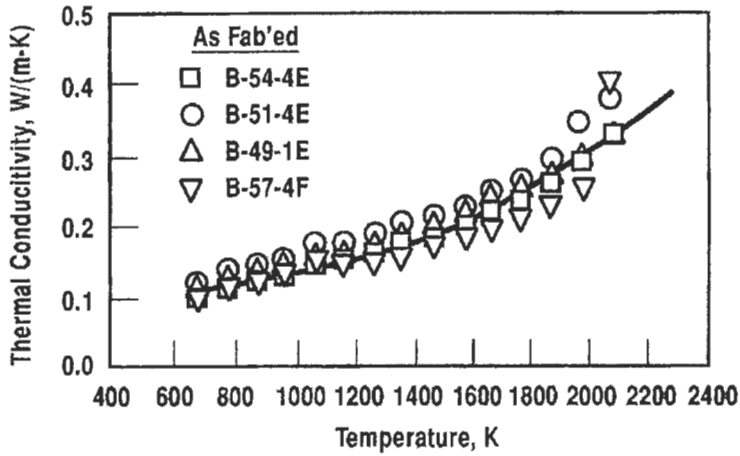


Fig. 6. The temperature dependence of thermal conductivity for CBCF in the "as fabricated" condition. Reprinted from [14], copyright © 1996 Technomic Publishing Company, Inc., with permission.

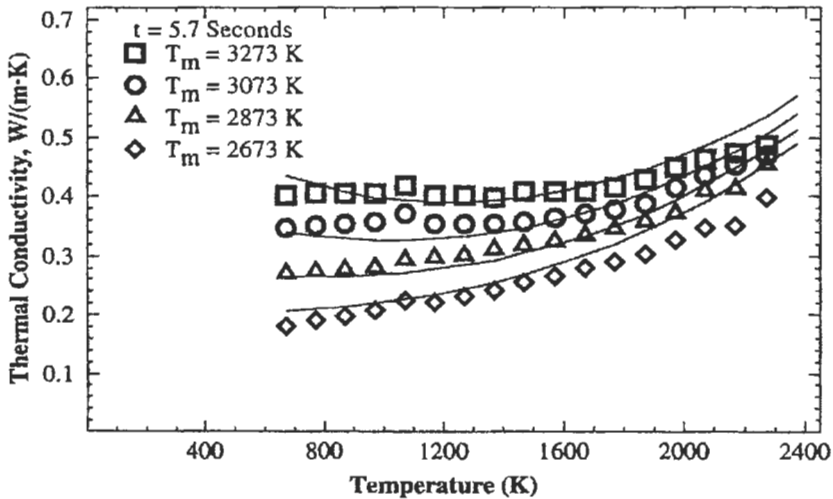


Fig. 7. Thermal conductivity data for CBCF specimens heat treated for 10 seconds (5.7 seconds at temperature) at four different temperatures. Solid lines are predicted curves from Eqs. (5) through (8). Reprinted from [14], copyright © 1996 Technomic Publishing Company, Inc., with permission.

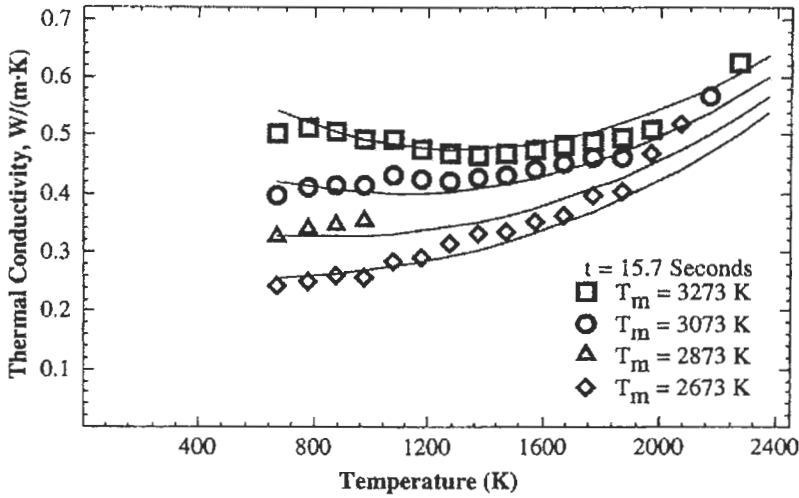


Fig. 8. Thermal conductivity data for CBCF specimens heat treated for 20 seconds (15.7 seconds at temperature) at four different temperatures. Solid lines are predicted curves from Eqs. (5) through (8). Reprinted from [14], copyright © 1996 Technomic Publishing Company, Inc., with permission.

Dinwiddie *et al.* [14] proposed a model for the behavior of the CBCF in which the temperature dependence of thermal conductivity (λ_T) may be expressed as

$$\lambda_T = Af_s\lambda_s + \lambda_R + \lambda_G \quad (1)$$

where A is the fraction of heat transfer in the parallel mode, f_s is the volume fraction of solid (assumed to be approximately 0.1 for production CBCF), λ_s is the thermal conductivity of the solid carbon (fiber and binder), λ_G is the thermal conductivity contribution due to the presence of the gas phase within the specimen (neglected by Dinwiddie *et al.*), and λ_R is the effective thermal conductivity due to radiation, and is given by

$$\lambda_R = [16n^2(\sigma/3)\sigma_e]T^3 \quad (2)$$

where n is the index of refraction (equal to 1), σ is the Stefan-Boltzmann constant [$5.6697 \times 10^{-8} \text{ W}/(\text{m}^2 \cdot \text{K}^4)$], σ_e is the extinction coefficient for CBCF, and T is the absolute temperature. In a previously unpublished work by Eatherly [15], the value of σ_e was taken as 14000 m^{-1} . This value was also adopted by Dinwiddie *et al.* in

their study. The solid carbon thermal conductivity must be scaled to account for density, and the fact that not all of the solid carbon contributes to the solid thermal conductivity. The temperature dependence of the thermal conductivity of graphite is typically modeled as

$$\lambda = A_1 \cdot T^{-\epsilon} \quad (3)$$

where A_1 and ϵ are fitting parameters, with ϵ usually being set to 1 for perfect graphite. For polygranular graphite, which contains a significant numbers of point defects and other phonon scattering sites, ϵ is between 0.5 and 1. Less graphitic carbons, and graphites with lower graphitization temperatures that have a significant population of extended crystal lattice defects, have ϵ values of less than 0.5. For CBCF, Dinwiddie *et al.* decided to modify Eq. (3) for the solid:

$$\lambda_s = XA_1 T^{(\epsilon'+Z)} \quad (4)$$

where X and Z are functions of the heat treatment temperature. A_1 and ϵ' were determined by fitting the thermal conductivity data from “as fabricated” CBCF specimens (Fig. 6) where $X=1$, $Z=0$, and A_1 and ϵ' were found to be 0.02328 and 0.2380, respectively. Combining Eq. (1) and (4) gives the functional form of the equation for the thermal conductivity of CBCF as

$$\lambda = XA_1 T^{(\epsilon'+Z)} + 2.160 \times 10^{-11} T^3 \quad (5)$$

Equation (5) was fitted to experimental data for the thermal conductivity of CBCF heat treated at various temperatures for 10, 15, and 20 seconds, and a linear relationship was determined for Z and the heat temperature, T_m , which is given by Eq. (6).

$$Z = 1.276 - 0.0005659 \times T_m \quad (6)$$

Z varies from ~ -0.23 to ~ -0.64 over the heat treatment temperature range 2673 to 3273 K, and the term $(\epsilon'+Z)$ in Eq. (5) therefore varies from ~ 0 to ~ -0.4 over the same temperature range. Equation (6) was then substituted back into eq. (5) which was used to refit the data to determine the relationship between X and the heat treatment conditions (time and temperature, Eqs. 7 and 8). The empirical parameter X in Eq. (5) was found to be given by

$$X = R \cdot \exp(T_m \times 0.004963) \quad (7)$$

where R is a time dependent variable given by

$$R = 1.261 \times 10^{-5} + 3.617 \times 10^{-7} \times t \quad (8)$$

where t is the time at the heat treatment temperature. By definition X is unity when t is zero (i.e., in the “as fabricated” condition), and from Eq. (8) we see that $R = 1.261 \times 10^{-5}$ when t is zero. To satisfy this condition for R , t must take the value of 4.3 seconds. It was necessary to subtract 4.3 seconds from the time in the furnace hot zone in order to bring the R parameter value in line with the “as fabricated” value. Physically, the 4.3-second correction can be considered to be the time taken for the CBCF to equilibrate at the furnace temperature.

Figures 7 and 8 show thermal conductivity data for CBCF after exposure to temperatures of 2673, 2873, 3073, and 3273 K, for 5.7 and 15.7 seconds, respectively. The symbols in the Figs. 7 and 8 represent measured thermal conductivity values, and the solid lines are the predicted behavior from Eqs. (5) through (8). The model clearly accounts for the effects of measurement temperature, exposure time, and exposure temperature. The fit to the data is good (typically within 10%). However, the fit to the “as fabricated” CBCF data (Fig. 6) was less good (~20%), although the scatter in the data was larger because of the much lower heat treatment temperature (1873 K) in that case.

4 Damage Tolerant Light Absorbing Materials

The optical properties of low density, carbon fiber-carbon binder composites have recently been disclosed by Lauf, *et al* [16,17]. CBCF samples were fabricated according to the method described in Section 2 of this chapter, and were tested to determine their optical properties (light absorption and spectral reflectance). The optical scatter was measured at a wavelength of 10.6 μm for scattering angles from 0.1 to 100 degree from specular. The absorbance, measured as the bidirectional reflected distribution function (BRDF), of abraded CBCF is shown as a function of scattering angle in Fig. 9 for the parallel and perpendicular to molding directions. Significantly, the material is essentially isotropic with respect to its BRDF. Also included in Fig. 9 are data for a commercial light absorbing product, namely Martin Black 54, an aluminum with a black-anodized surface. The CBCF and Martin Black 54 display similar light absorption properties (both appear to be totally Lambertian) showing no specular scattering. The spectral reflectance of

CBCF for infrared wavelength from 2 to 55 μm is compared with that of etched beryllium in Fig. 10. The data show that the CBCF is uniformly light absorbing up to at least 50 μm , in marked contrast to the etched beryllium light absorber which effectively absorbs wavelengths only up to about 20 μm .

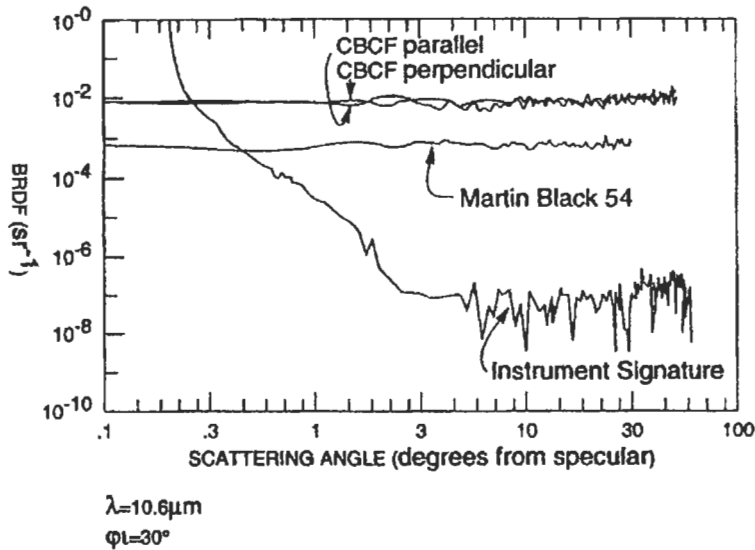


Fig. 9. Light absorption behavior as a function of scattering angle for CBCF in the \parallel and \perp to molding direction, and Martin Black 54 [16].

Light absorbers must be materials that are very absorbent (or “black”) over the widest possible range of wavelengths, ideally including the infrared spectrum, so as to be more effective in sensitive, precision optical systems. Typically, light absorbers are made from light metals, e.g., beryllium or aluminum, and derive their light absorbing properties from a microscopically textured surface coating developed on the metal via a chemical etching or anodizing process. Martin Black 54 is one such material. Martin Black 54 is one of the better light absorbers, exhibiting excellent absorption behavior and very low scatter throughout a broad range of optical and infrared wavelengths. However, the surface of Martin Black 54, and other anodized light absorbers, is very fragile. Once the surface is damaged, the light absorbing properties quickly diminish and the materials loses its effectiveness as a light absorber.

Etched beryllium light absorbers are somewhat more robust than Martin Black 54 but, as shown in Fig. 10, are ineffective above certain wavelengths. Moreover, both beryllium and aluminum are sensitive to environmental degradation and may degrade thermally due to their low melting temperatures.

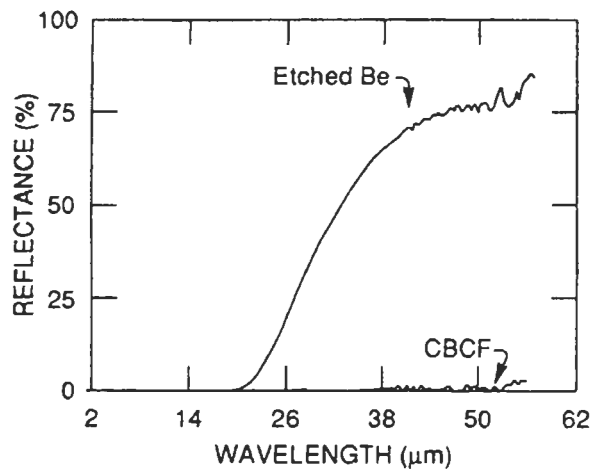


Fig. 10. The spectral reflectance of CBCF and etched beryllium over the wavelength range 2 to 55 μm [16].

In contrast to the above coated metal absorbers, CBCF is rugged and durable. Its optical properties have been shown to be independent of surface condition because they derive from the properties of the bulk material and not the surface condition. CBCF can be readily machined and is easily attached by adhesive bonding or brazing to metallic or graphite substrates. These attributes make CBCF ideally suited for applications such as broadband optical absorbers, baffles, beam stops and other structures to protect detectors from stray light at high power and long wavelengths. Moreover, the combination of the above properties and the uniform emissivity of CBCF (0.62 - 0.63 at ambient temperature), which is independent of surface roughness [17], makes it a suitable measurement or calibration standards for spectrophotometers, scatterometers or other optical instruments [18].

5 Carbon Fiber Composite Molecular Sieves

5.1 Applications

A recently developed adsorbent version of ORNL's porous carbon fiber-carbon binder composite is named carbon fiber composite molecular sieve (CFCMS). The CFCMS monoliths were the product of a collaborative research program between ORNL and the University of Kentucky, Center for Applied Energy Research (UKCAER) [19-21]. The monoliths are manufactured in the manner described in Section 2 from P200 isotropic pitch derived fibers. While development of these materials is in its early stages, a number of potential applications can be identified.

It is anticipated that these materials will only find utility in application that can support the relatively high cost of their manufacture compared to commodity granular activated carbon (GAC). However, the monoliths may also find applications in situations where their novel properties make them uniquely suited. Potential areas of application include gas separation and cleanup, especially in the field of air purity for buildings or vehicles. In this latter area, collective protection systems for military equipment [against nuclear, biological and chemical (NBC) threats] would appear to be a promising application. At UKCAER, researchers have shown the monoliths be extremely effective at removing a common herbicide (sodium pentachlorophenolate, or PCP) from water [22], offering a potential application in ground water cleanup systems. Another possible application of our monoliths is adsorption gas storage, where the potential for high CFCMS bulk density, combined with high micropore volume and high deliverable gas capacity, makes them attractive. The novel electrical desorption capability of the material (Sect. 5.3), combined with the unique pore structure of the monolith, make the material particularly suited to utility as a guard bed for adsorbed natural gas (NG) storage tanks (e.g., on a NG powered vehicle), or for a NG fueled solid oxide fuel cell. The properties, pore structure, and performance of the monoliths are described below and their suitability to specific applications is discussed.

5.2 Pore Structure

5.2.1 The structure of unactivated CFCMS monoliths

The macrostructure of a CFCMS monolith is shown in Fig. 11. The isotropic pitch-derived carbon fibers have a smooth surface and a circular cross-section, which is in marked contrast to the rayon-derived fibers used in the manufacture of CBCF. The fibers are bonded at their contact points by the carbonized phenolic resin, thus forming a continuous three dimensional carbon network. The carbon fibers are 12-14 μm in diameter and, in the monolith shown in Fig. 11, have an approximately normal length distribution with a mean of $\sim 450 \mu\text{m}$. The fiber length distribution mode is $\sim 400 \mu\text{m}$ and the fiber length varies widely from 100 to 1000 μm [23]. The voids between the fibers are typically $>30 \mu\text{m}$ in size and the resultant open structure allows the free flow of fluids through the material. Mercury porosimetry data taken on unactivated CFCMS material are shown in Fig. 12, and indicate the macropore (inter-fiber voids) size range to be approximately 10 to 100 μm , in good agreement with the macropore sizes indicated in the SEM micrograph (Fig. 11). The absence of mesoporosity (2-50 nm) can also be noted in Fig. 12. In the unactivated condition, CFCMS contains a small micropore volume that presumably develops during the carbonization stage. Typical DR micropore volumes and BET surface areas for the unactivated monoliths are 0.01 to 0.04 cm^3/g and 70 to 100 m^2/g , respectively.

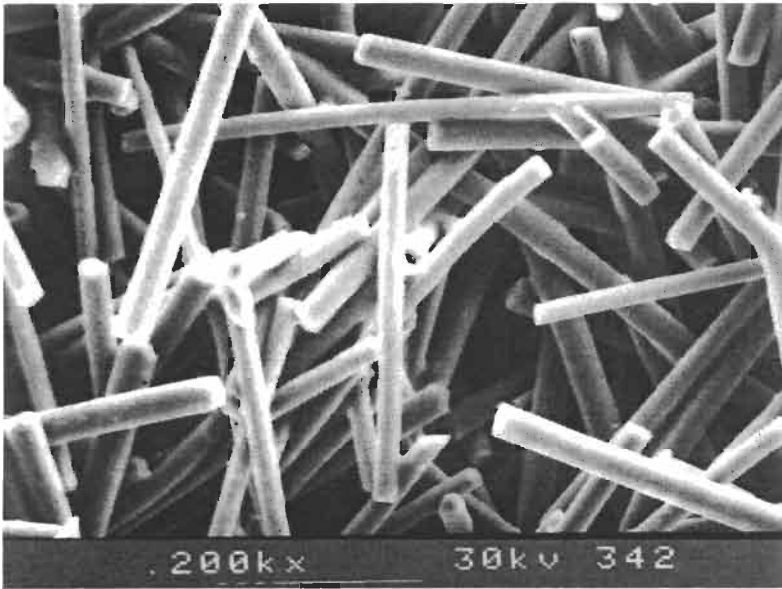


Fig.11. SEM micrograph showing the macrostructure of CFCMS (scale bar represents 100 μm).

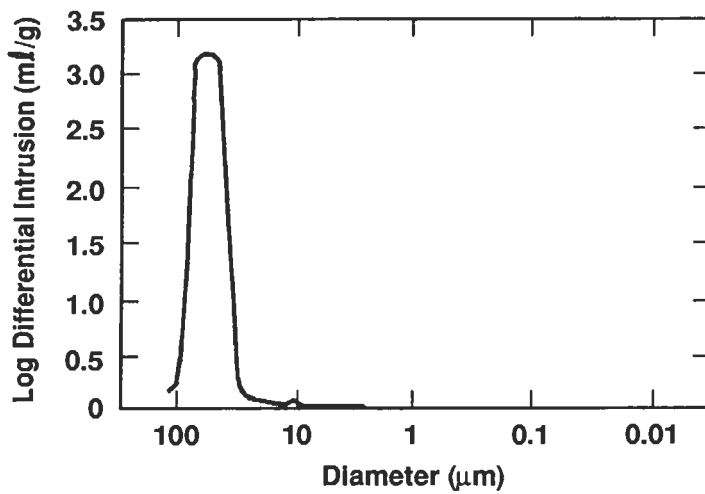


Fig. 12. Mercury intrusion pore size distribution for an unactivated sample of CFCMS monolith.

5.2.2 Microporous CFCMS monoliths

The development of microporosity during steam activation was examined by Burchell *et al.* [23] in their studies of CFCMS monoliths. A series of CFCMS cylinders, 2.5 cm in diameter and 7.5 cm in length, were machined from a 5-cm thick plate of CFCMS manufactured from P200 fibers. The axis of the cylinders was machined perpendicular to the molding direction (\perp to the fibers). The cylinders were activated to burn-offs ranging from 9 to 36 % and the BET surface area and micropore size and volume determined from the N_2 adsorption isotherms measured at 77 K. Samples were taken from the top and bottom of each cylinder for pore structure characterization.

Full accounts of this study can be found elsewhere [23-25]. However, the results are summarized in Table 1, where mean values for the surface area and pore parameters are given for each cylinder. The pore size and volume increased with increasing burn-off, as did the BET surface area, in agreement with previous pore structure development studies conducted on this material [26]. The variation of pore volume and surface area was noted to be particularly large in the data for high burn-off samples (<25%), which was attributed to uneven activation in the monoliths [23]. For example, the BET surface area was noted to vary by almost a factor of three over the 7.5 cm specimen length. In an attempt to achieve uniform activation of larger (10 cm in diameter and 25 cm in length) monoliths, an oxygen chemisorption/activation procedure was adopted (Section 2). The monoliths were subjected to two cycles of O_2 chemisorption/activation and attained total burn-offs of approximately 8.5-13.4 %. One of the monoliths was sectioned and sampled to determine the spatial variation of the BET surface area, and micropore volume and size. Samples were taken at several radial locations across slices cut periodically along the length of the monolith. The spatial variation of the DR micropore volume is shown in Fig. 13.

Table 1. Micropore structure development during steam activation for CFCMS monoliths manufactured from P-200 carbon fibers.

Specimen	Burn-off (%)	BET Area (m^2/g)	Pore volume [t-method] (cm^3/g)	DA Pore radius (nm)
21-11	9	512	0.21	0.68
21-2B	18	1152	0.40	0.71
21-2C	27	1962	0.65	0.75
21-2D	36	1367	0.41	0.79

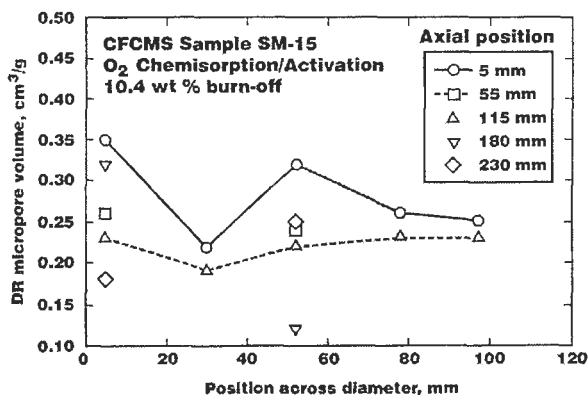


Fig.13. Variation of DR micropore volume in a large CFCMS monolith with 10.4 wt% burn-off [27].

The micropore volume varied from ~ 0.15 to ~ 0.35 cm^3/g . No clear trend was observed with respect to the spatial variation. Data for the BET surface area are shown in Fig. 14. The surface area varied from ~ 300 to ~ 900 m^2/g , again with no clear dependence upon spatial location within the monolith. The surface area and pore volume varied by a factor ~ 3 within the monolith, which had a volume of ~ 1900 cm^3 . In contrast, the steam activated monolith exhibited similar micropore structure variability, but in a sample with less than one fiftieth of the volume. Pore size, pore volume and surface area data are given in Table 2 for four large monoliths activated via O_2 chemisorption. The data in Table 2 are mean values from samples cored from each end of the monolith. A comparison of the data in Table 1 and 2 indicates that at burn-offs $\sim 10\%$ comparable pore volumes and surface areas are developed for both steam activation and O_2 chemisorption/activation, although the process time is substantially longer in the latter case.

Table 2. Micropore structure data for large CFCMS monoliths activated via the O_2 chemisorption/activation route [7,27]

Monolith ID	Burn-off (%)	BET surface area (m^2/g)	DR micropore volume (cm^3/g)	DA micropore diameter (nm)
SMW-1	10	496	0.22	1.59
SMW-3	9.4	528	0.20	1.46
SMW-4	8.5	714	0.27	1.55
SMW-8	13.4	574	0.22	1.51

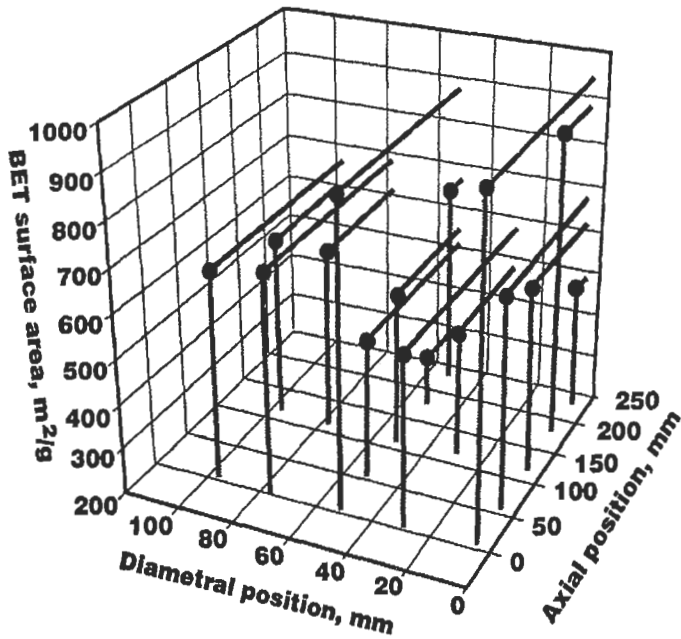


Fig. 14. BET surface area as a function of position in a large CFCMS monolith with 10.4 wt% burn-off [27].

5.2.3 Mesoporous CFCMS monoliths

The pore structure of monoliths made from F3-0 PAN-derived carbon fibers has been examined and found to be highly mesoporous [18,29]. The cumulative mesopore surface area, as a function of pore diameter, is shown in Fig. 15 for the PAN fibers, and monoliths in the dried (50°C) and carbonized (650°C) conditions. The surface area is clearly associated with pores of size <50 nm, i.e., the mesopores. The carbonized monoliths exhibit surface areas >500 m²/g and mesopore volumes >1 cm³/g. In contrast, the “as received” PAN fibers exhibited a mesopore volume of only 0.28 cm³/g and surface area <200 m²/g. The increase in mesopore volume and surface in the monoliths was attributed to the opening of the inner pore structure of the fiber through gasification by reactive species such as O₂, CO₂, H₂O, and CO, which are thought to be adsorbed during monolith production and subsequently desorbed during carbonization [28,29]. The PAN fiber monoliths were subjected to steam activation at 650°C or 850°C to burn-offs up to ~22%. The mesopore volume was observed to reduce significantly with burn-off (Fig.16), reaching a lower limit of ~0.3 cm³/g above ~10% burn-off. A similar trend was observed for the mesopore surface area. Conversely, the mean mesopore diameter increased from ~7 to 8.7 nm over the same burn-off range.

SEM examination of the steam activated PAN fiber monoliths showed the fiber diameter to be significantly reduced during the activation process, suggesting the fibers are consumed radially by a gasification process of the external surface [28].

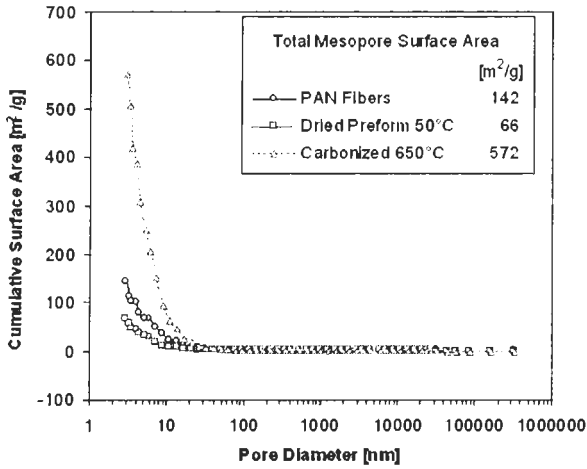


Fig.15. Mesopore surface area as a function of pore diameter obtained from mercury intrusion data for PAN derived carbon fiber porous monoliths [28].

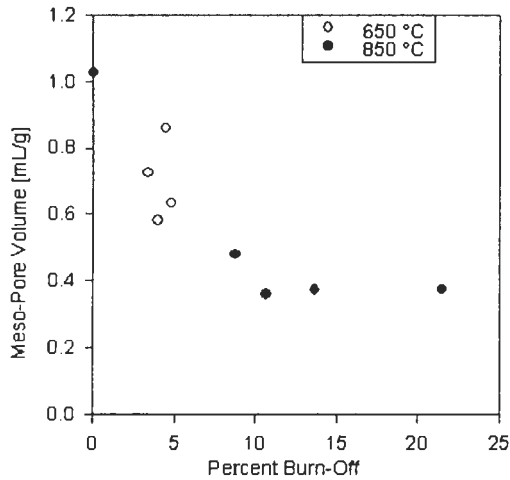


Fig.16. Mesopore volume as a function of burn-off for PAN derived carbon fiber porous monoliths [28].

5.3 Physical Properties

Typical physical properties of our CFCMS monoliths are given in Table 3. The exact value of a particular property is dependent upon the fabrication route, composition, density, etc. Consequently, property ranges are given in Table 3 rather than absolute values.

Table 3. Physical properties of CFCMS monoliths developed by ORNL/UKCAER

Property	Value
Density, g/cm ³	0.2 - 0.4 0.4-1.0*
Compressive strength, MPa	1-3
Electrical resistivity, mΩ•cm	130 @ density of 0.25 g/cm ³
Thermal conductivity, W/m•K	0.14 @ density of 0.25 g/cm ³

* hot-pressed density range

The effect of fiber/binder ratio on the density and strength of the isotropic pitch derived fiber monoliths was examined [23] in a study in which the ratio of P200 fibers was increased by factors of 2, 3, or 4, from the standard fiber/binder ratio. The density was seen to decrease from ~0.38 g/cm³ for the standard formulation to ~0.36 g/cm³ for the 4X formulation. A slight reduction in compressive strength, from ~1.9 to ~1.7 MPa, was observed to accompany the density reduction, although the scatter in the data made it impossible to develop a density-strength correlation. During activation the carbon is selectively gasified, resulting in a mass loss in the monolith. The compressive strength (σ_c) is degraded by this mass loss and follows the relationship [19,23]:

$$\sigma_c = 1.843 \exp(-0.01323x) \quad (9)$$

where x is the fractional weight loss or burn-off.

The electrical behavior of CFCMS is shown in Fig. 17(a). The current-voltage relationship is linear and the electrical resistivity of the monolith in Fig. 17(a) (2.5 cm in diameter and 7.5 cm in length) was 130 mΩ•cm [23,24]. The resistivity of the monolith is considerably greater than that of the carbon fibers, which according to the manufacturer's product literature is 4-6 mΩ•cm. The poorer electrical conductivity of the monolith can be attributed to the large electrical resistance associated with the fiber/binder interface. A consequence of the passage of an electric current through the monolith is resistive (ohmic) heating. Figure 17(b)

shows the temperature of a monolith as a function of the electrical power input (product of the applied voltage and induced current). At relatively low power inputs, the monolith readily heats to 50-100°C, and temperatures >300°C are rapidly attained at a power input of ~45 W.

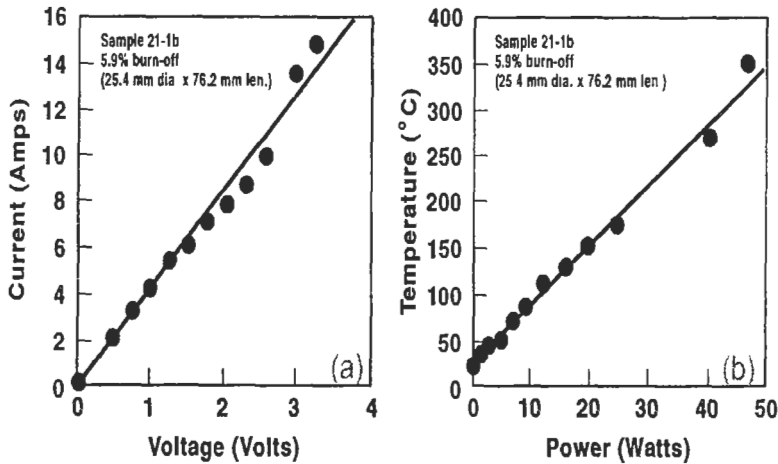


Fig. 17. The voltage-current relationship (a) and resistive heating curve (b) for a CFCMS monolith (sample 21-2B, 18% burn-off, 2.5-cm diameter \times 7.5-cm length) [23]

Data for the thermal conductivity of adsorbent carbons are somewhat limited [23]. Typically, a bed of granular carbon at a packed density of $\sim 0.5 \text{ g/cm}^3$ has a thermal conductivity of 0.14-0.19 W/m·K, while the derived value for the carbon adsorbent is normally between 0.6 and 1.3 W/m·K. CFCMS monoliths typically have comparable thermal conductivities to a packed bed, but at substantially lower density (Table 3). The greater specific thermal conductivity of the monoliths can be attributed to the substantially higher thermal conductivity of the carbon fibers (2-5 W/m·K), which results from the higher density of fiber compared to GAC (1.6 g/cm^3 cf. 0.6 g/cm^3), and the reduced contact resistance between the fibers in the case of the bonded fiber monoliths. For many applications increased thermal conductivity is an extremely desirable attribute for a bed of adsorbent carbon. The flexible process by which CFCMS is manufactured allows the blending of high conductivity mesophase pitch-derived carbon fibers into the material. Moreover, hot pressing the monolith after drying allows the density and thermal conductivity to be increased substantially. To assess the extent to which the thermal conductivity could be enhanced by blending in mesophase pitch-derived carbon fibers, and/or by increasing the bulk density, a series of experimental hybrid monoliths were fabricated. Table 4 reports the composition, density, and room

temperature thermal conductivities of the monoliths.

Table 4. Room temperature thermal conductivity of hybrid monoliths at normal and high density.

Specimen ID	wt % of DKDX fiber	Density (g/cm ³)	Thermal conductivity at 25°C (W/m·K)	
			∥ to fibers	⊥ to fibers
K0-A	0	0.61	0.250	0.07
K2-A	11	0.65	0.485	0.14
K3-A	18	0.63	0.93	0.15
K0-B	0	0.21	0.05	0.02
K0-B	11	0.22	0.12	0.04
K0-B	18	0.26	0.19	0.07

Several significant trends emerge from the data in Table 4. First, the thermal conductivity is greater in the ∥ to fiber direction than in the ⊥ to fiber direction. This is expected from the preferred orientation of the fiber that develops during molding. Second, the thermal conductivity is strongly dependent upon the density. For example, at a density of 0.21 g/cm³ the thermal conductivity (∥) is only 0.05 W/m·K, rising to 0.19 W/m·K at a density of 0.26 g/cm³, and 0.25 W/m·K at a density of 0.61 g/cm³. Finally, the thermal conductivity (both ∥ and ⊥) increases as the fraction of DKDX fiber in the hybrid monolith increases. At a loading of 18% DKDX fibers, the thermal conductivity (∥) is increased to 0.19 W/m·K at a density of 0.26 g/cm³ and 0.93 W/m·K at a density of 0.63 g/cm³. This latter value represents a six-fold increase over the thermal conductivity of the standard CFCMS monoliths and a four- to six-fold increase over the thermal conductivity of a packed bed of GAC. The temperature dependence of the thermal conductivity (∥) of the hybrid monoliths is shown in Fig. 18. The thermal conductivity increases with temperature over the range 30-500°C due to the increasing contribution of radiation conduction in the pores (see the discussion in Section 3 of this chapter). An increased thermal conductivity in a carbon bed will reduce temperature gradients, improve efficiency and, for a storage carbon, will increase the delivered capacity of gas. If, however, the increased thermal conductivity is accompanied by a large reduction in bed adsorption capacity, the potential performance gain may be totally offset by the capacity loss penalty. To assess the extent, if any, of this potential penalty the hybrid monoliths were activated via the O₂ chemisorption/activation process and their micropore structure examined. Table 5 reports micropore characterization data for the hybrid monoliths (standard and

high density). A comparison of the surface area and micropore volumes for the base case (K0A/K0B) and the hybrid monoliths suggests that there is little or no difference (at comparable burn-offs). Moreover, the micropore data for large monoliths (Table 2) compare favorably with the data in Table 5 for the standard density hybrid monoliths. It should also be noted that for storage applications a high volumetric micropore capacity is desirable, i.e., micropore vol./unit volume of storage vessel.

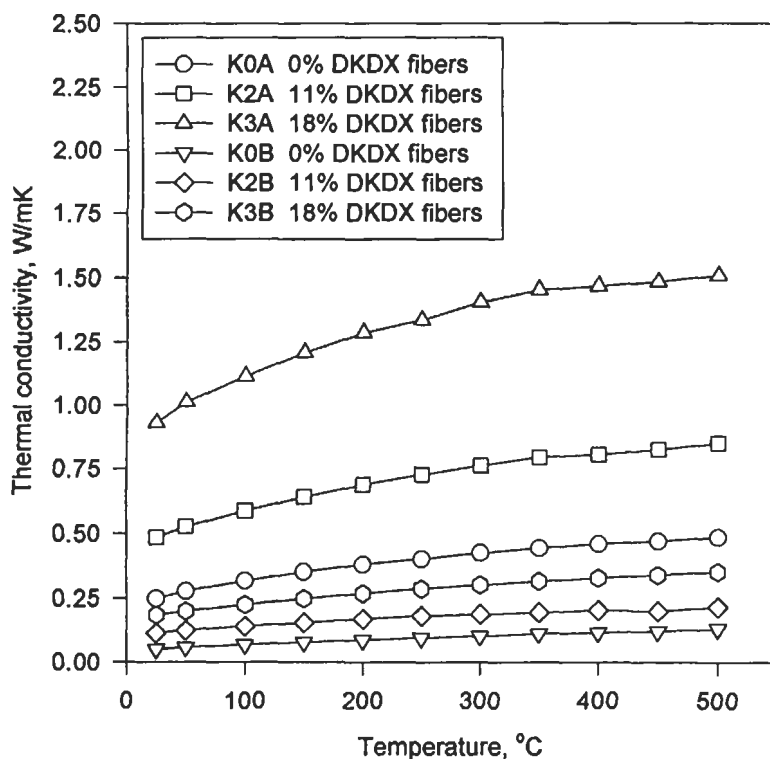


Fig. 18. The temperature dependence of the thermal conductivity of hybrid carbon fiber monoliths measured in the \parallel to fibers direction at two densities.

The high density hybrid monoliths would thus appear to be well suited to storage applications. However, the data presented here are for hybrid monoliths that are far from optimum as storage carbons. A great deal of development work is required to increase the micropore volume and storage capacity of the monoliths. Some of our preliminary work in this context is discussed subsequently.

Table 5. Micropore characterization data for hybrid monoliths at two densities.

Specimen ID	Pre-activation density (g/cm ³)	% DKDX fibers	Burn-off (%)	BET area (m ² /g)	DR pore vol. (cm ³ /g)
K0A	0.67	0	5.5	429	0.16
K1A	0.62	5	7.2	406	0.16
K3A	0.69	18	4.3	307	0.12
K0B	0.21	0	5.6	445	0.16
K1B	0.22	5	9.4	540	0.21
K3B	0.25	18	5.3	429	0.17

5.4 Gas adsorption and separation

The gas adsorption behavior of our monoliths has been studied as part of the U.S. Department of Energy's ongoing Fossil Energy Advanced Research Program. The equilibrium adsorption of CO₂ and CH₄ was found to be strongly temperature dependent, and the uptake of CO₂ was greater than the uptake of CH₄ for a given specimen [23]. For example, volumetric measurements at 30°C and one atmosphere, on CFCMS with moderate burn-off, showed that approximately 50 cm³/g of CO₂ were adsorbed, whereas only approximately 27 cm³/g of CH₄ were adsorbed. High pressure [0.5-59 bar (8-850 psi)] CO₂ and CH₄ isotherms are shown in Fig. 19 for monoliths 21-11 and 21-2B, which had 9 and 18% burn-off, respectively. The measured volumetric and gravimetric (Fig. 19) adsorption capacities at one atmosphere for both CH₄ and CO₂ are in good agreement for the CFCMS specimens. At one atmosphere, approximately 100 mg of CO₂ per g of CFCMS and approximately 19 mg of CH₄ per g of CFCMS were adsorbed. The quantities of gas adsorbed rose to >490 mg/g (CO₂ on specimen 21-2B) and >67 mg/g (CH₄ on specimen 21-2B). Moreover, the CO₂ isotherms are still increasing with pressure whereas the CH₄ isotherms have flattened (i.e., the CFCMS has become saturated with CH₄). The data in Fig. 19 clearly show that CFCMS exhibits selective adsorption of CO₂ over CH₄.

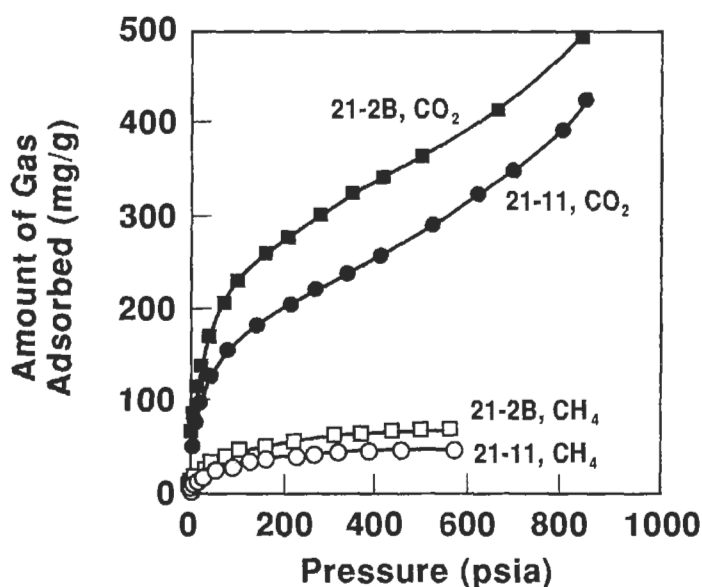


Fig. 19. High pressure isotherms at 25°C of CO₂ and CH₄ for CFCMS monoliths.

The CO₂ adsorption data discussed above suggests that CFCMS might provide an effective media for the separation of CO₂ from CH₄. To determine the efficacy of CFCMS for this purpose, several steam activated samples were tested in a breakthrough apparatus[23-25]. A typical breakthrough plot for a CH₄/CO₂ mixture is shown in Fig. 20. The specimen is heated electrically and any entrained air is initially driven out with a He purge. The input gas is then switched to a 2:1 mixture of CH₄/CO₂ at a flow rate of 0.33 slpm. The outlet stream He concentration decreases and the CH₄ concentration increases rapidly (i.e., CH₄ breaks through). Adsorption of CO₂ occurs and, therefore, the CO₂ concentration remains constant at a low level for approximately six minutes before the CO₂ concentration begins to increase, i.e., CO₂-breakthrough occurs. Table 6 reports data from a preliminary study of CO₂ separation. CO₂ capacities are reported as determined from pure CO₂ and CO₂/CH₄ mixtures on each specimen examined. The reported CO₂ capacities are the means of several repeats of the breakthrough experiments, and the BET surface and other microporosity characterization data are additionally given in Table 1. Two of the CFCMS samples (lowest burn-off) had CO₂ adsorption capacities of almost one liter on 0.037 liters of adsorbent, and only a small capacity reduction was observed in the CO₂/CH₄ gas mixture. The CO₂ adsorption capacity decreases with increasing burn-off, in agreement with the isotherm data.

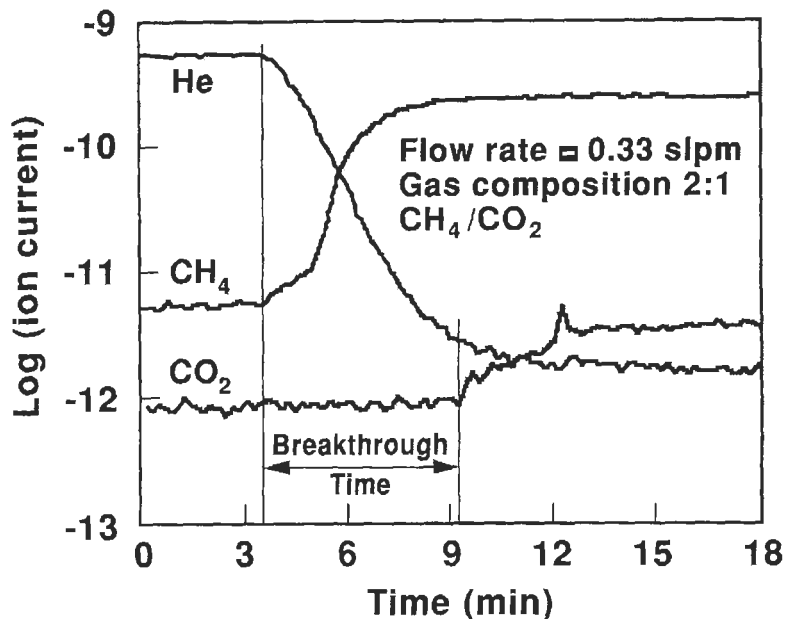


Fig. 20. Typical CO₂/CH₄ breakthrough plot for CFCMS monolith sample 21-11 (9% burn-off) at 25°C

Table 6. CO₂ separation data from our CO₂ and CO₂/CH₄ breakthrough experiments.

Specimen No	Burn-off (%)	BET Surface Area (m ² /g)	CO ₂ Capacity (Liters)	
			CO ₂ /CH ₄	CO ₂ only
21-11	9	512	0.73	0.97
21-2B	18	1152	0.45	0.98
21-2D	27	1962	0.39	0.80
21-2C	36	1367	0.35	0.80

A typical H₂S/H₂ breakthrough plot is shown in Fig. 21 for a gas composition of 5.4% H₂S, 14% Ar, with the balance being H₂. The H₂ (not shown in Fig. 21) is not adsorbed, whereas the H₂S is held on the carbon, producing a H₂S free H₂ stream for approximately 18 minutes. In Fig. 21 the H₂S concentration can be seen to increase sharply after breakthrough is completed. The concentration increase

coincides with the application of a d.c. electrical voltage (4-5 amps at 1 volt) and the He purge gas. H_2S desorption occurs over a relatively short time (18 minutes). The H_2S adsorption capacity (at atmospheric pressure) for sample 21-1B, 18% burn-off, was 0.43 liters (Fig. 21).

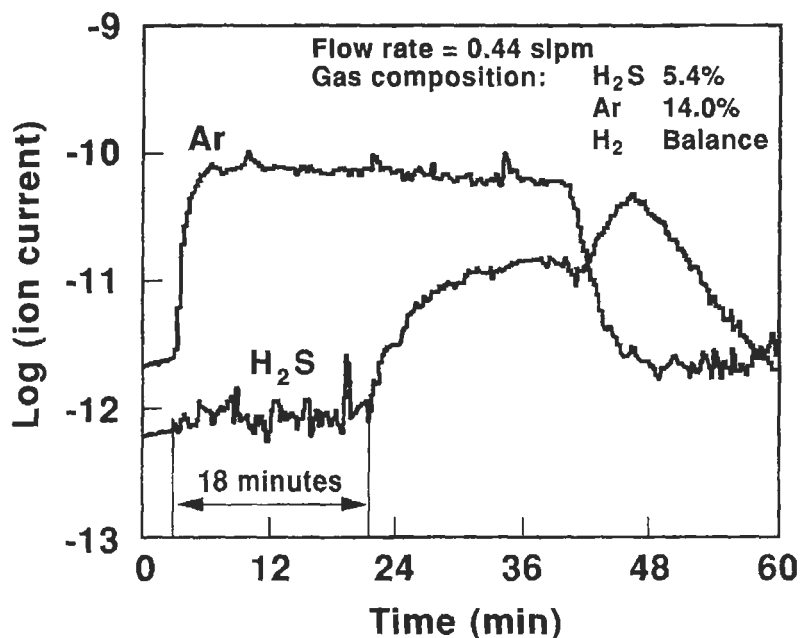


Fig. 21. A typical H_2S breakthrough plot for a CFCMS monolith 21-2B (18% burn-off) at $25^\circ C$

CFCMS has a continuous 3D carbon structure (Fig. 11) which imparts electrical conductivity to the material. We have utilized the electrical properties of CFCMS to affect a rapid desorption of adsorbed gases in our breakthrough apparatus. The benefit of this technique is shown in Fig. 22, which shows the CO_2 and CH_4 gas concentrations in the outlet gas stream of our breakthrough apparatus [23-25]. Three adsorption/desorption cycles are shown in Fig. 22. In the first and second cycles (A and B in Fig. 22) desorption is caused by the combined effect of an applied voltage (1 volt) and a He purge gas. In the third cycle (C in Fig. 22) desorption is caused only by the He purge gas. A comparison of cycles B and C indicates that the applied voltage reduces the desorption time to less than one third of that for the He purge gas alone (cycle C). Clearly, the desorption of adsorbed CO_2 can be rapidly induced by the application of a d.c. electrical potential.

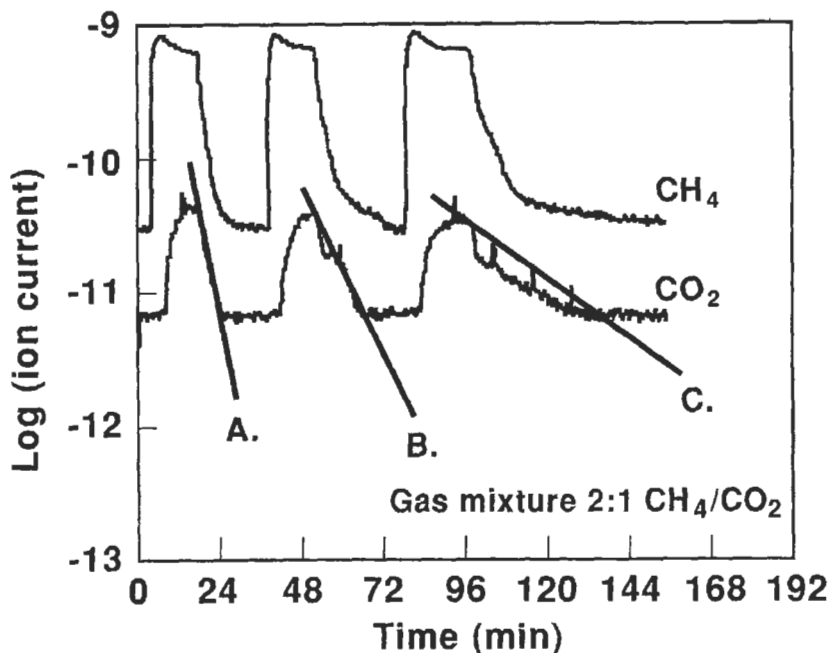


Fig. 22. CO_2/CH_4 breakthrough plots for CFCMS sample 21-1F (10% burn-off) showing the benefit of electrically enhanced desorption: A. 1 volt, He purge @ 0.4 slpm; B. 1 volt, He purge @ 0.06 slpm, and C. 0 volt, He purge 0.06 slpm

Increased adsorbent (CFCMS) temperature results in desorption of the adsorbate. However, desorption occurs immediately when the voltage is applied to the CFCMS, whereas the bulk temperature increase lags the application of the voltage by a finite time, typically several minutes [23]. Evidently, the resistance heating effect is acting directly at the adsorption sites (fiber microporosity) resulting in a rapid desorption of the adsorbate. The heat of adsorption of CO_2 on activated carbon fiber is 30 kJ/mol [30]. A simple calculation for the a typical ESA breakthrough experiment, where approximately 1 litre of CO_2 was adsorbed, indicates that at a power level of 5 Watts, approximately 270 seconds would be required to input the energy (1350 J) required to desorb the CO_2 adsorbed on the CFCMS. Implicit in this calculation is the assumption that all of the electrical energy is converted to thermal energy and transferred to the adsorbed CO_2 . While this analysis is very simplistic, it does explain the observation of a time lag between the initiation of electrical current flow and the CFCMS temperature rise during the electrical desorption of adsorbed gases. Actual measured desorption times are of the order of 6-13 minutes, depending on the purge gas flow rate (Fig. 22). Therefore, other factors must influence heat flow to the adsorption sites in the

carbon fibers. Several explanations have been postulated, the most plausible of which is based on the compensating effect of the heat of adsorption and the temperature dependence of electrical resistivity in carbon [23].

The ability of CFCMS to selectively adsorb a gas from a gas mixture, combined with the electrically enhanced desorption of the adsorbed species, allows for a gas separation system where the separation is effected by electrical swing (ES) rather than the more conventional pressure or temperature swings. Several applications of CFCMS/ES can be considered. For example: (i) the cleanup of sub-quality natural gas; (ii) the separation of hydrogen from coke oven battery reformer waste gas streams; (iii) the separation of landfill gases; and (iv) a guard bed for the removal of higher hydrocarbons, or sulfur bearing odorants, from CH_4 fuels in adsorption storage fuel tanks or solid oxide fuel cells. Moreover, the novel combination of properties make CFCMS attractive for adsorption gas storage systems where the delivery of adsorbed gasses can be hindered by excessive temperature drop in the carbon adsorbent due to the large heat of adsorption. A variant of the CFCMS monolith with appropriately developed microporosity, and a bulk density $\sim 1.0 \text{ g/cm}^3$, would be expected to possess a storage volume equal to or greater than currently available CH_4 storage carbons. Finally, a mesoporous variant of CFCMS might offer advantages as a catalyst support for reforming operations because heating of the support could be effected directly by the passage of an electric current, negating the need to preheat the reactant gasses.

5.5 Near term applications

Two particular applications of CFCMS monoliths can be considered near term. The first, fighting vehicle air clean-up (with respect to NBC contaminants), would appear to be an eminently suitable field for our adsorbent fiber-based monoliths. Several attributes of the monoliths should be considered in this context: (i) the monoliths are rugged and will not suffer attrition under the harsh terrain conditions encountered by fighting vehicles; (ii) the micro/meso pore structure can be controlled by appropriate selection of the fiber type and processing/activation route; (iii) ESA would appear to offer a rapid and low energy desorption/regeneration method, compared to pressure swing or thermal swing regeneration for the adsorbent bed; and (iv) the defense market could stand the higher cost of the monoliths compared to granular carbons. The second near term application of our adsorbent monoliths is in a guard bed for a solid oxide fuel cell (SOFC) [7,27]. Westinghouse solid oxide fuel cells utilize CH_4 and air as fuels [31]. Operating experience with the cells has demonstrated an efficiency degradation associated with the interaction of the sulfur bearing odorants in the natural gas and the ceramic materials used in the construction of the cell. This has necessitated the use of a large GAC guard bed, which must be replaced when saturated. A compact, easily regenerated guard bed has obvious advantages over

the large GAC bed currently employed. In a collaborative venture, a guard bed assembly containing three monoliths (10-cm diameter and 25-cm length) in separate canisters was fabricated and is currently under evaluation at Westinghouse Science and Technology Center, Pittsburgh, USA. The carbon fiber monoliths were prepared from P200 fibers and activated via the oxygen chemisorption/activation route [7,27]. Prior to delivery to Westinghouse, the pressure drop through the monolith/canister was measured, and is shown in Fig. 23.

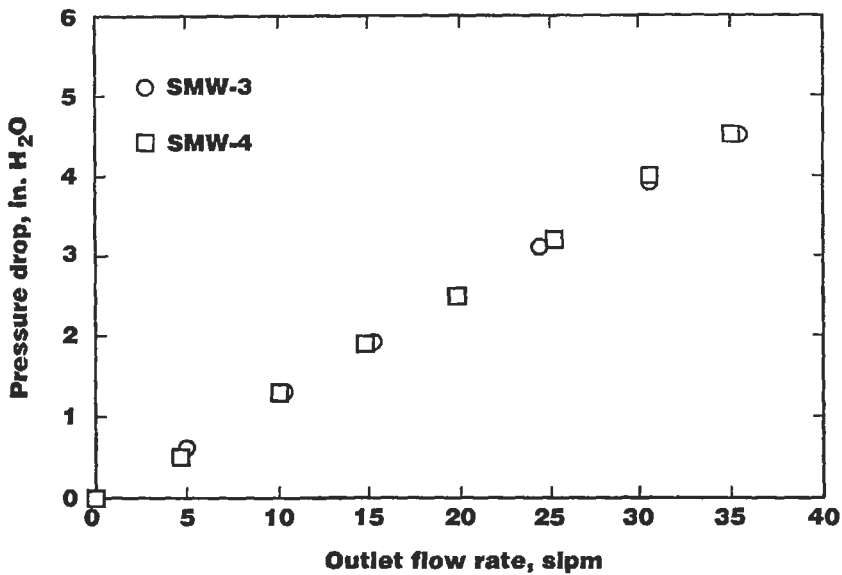


Fig. 23. Pressure drop through a large monolith as a function of He flow rate [27].

The measured pressure drops were slightly greater than literature data would indicate for packed carbon beds. However, they are certainly not prohibitive and a successful outcome of the Westinghouse trial of the SOFC guard bed is anticipated.

6 Summary and Conclusions

Porous carbon fiber-carbon binder composites are a class of materials that are not widely known, yet they fulfill a vital role in the RTG space power systems, and show considerable potential for other uses in light absorption or gas adsorption applications. These applications are enabled through the unique combination of physical properties exhibited by the porous carbon fiber-carbon binder composites. Perhaps the most significant of its physical attributes is the open, yet rugged, form of the material which contributes significantly to its utility in the fields of

application discussed previously. In addition, the ability to tailor other physical properties enhances the potential utility of this class of carbon composite material. The pore structure of the material, which is of paramount importance in fluid separation and gas storage applications, can be controlled through careful selection of the precursor carbon fiber and processing and activation route. It is likely that new applications of porous, adsorbent, carbon fiber based monoliths will be developed in the near term. These applications will be less cost sensitive than many current applications of commodity GAC, but will be applications in which the novel properties of porous carbon fiber-carbon binder composites make them uniquely suited. Current research at ORNL is directed toward improving the uniformity, and key properties of the material, and at containing, or reducing, the cost of our porous carbon fiber-carbon binder composites.

7 Acknowledgments

Research sponsored by the U. S. Department of Energy under contract DE-AC05-96OR22464 with Lockheed Martin Energy Research Corporation at Oak Ridge National Laboratory.

8 References

1. Ardery, Z.L. and Reynolds, C.D., Carbon fiber thermal insulation. Y-12 Report 1803, Oak Ridge Y-12 Plant, Oak Ridge TN, 1972.
2. Brassell, G.W. and Wei, G.C., High temperature thermal insulation, In *Proc. 14th Biennial Conf. on Carbon*, American Carbon Society, 1979, pp. 247 248.
3. Donnett, JB and Bansal, R.C., *Carbon Fibers*, 2nd edition, Marcel Dekker, Inc., New York, 1990.
4. Jagtoyen, M. and Derbyshire, F., Carbon fiber composite molecular sieves for gas separation. In *Proc. Tenth Annual Conf. on Fossil Energy Materials*, CONF-9605167, ORNL/FMP-96/1. Oak Ridge National Laboratory, 1996, pp. 291 300.
5. Nandi, S.P and Walker, P.L. Jr., Carbon molecular sieves from the concentration of oxygen from air, *Fuel*, 1975, 54, 169 178.
6. Quinn, D.F. and Holland, J.A., US Patent No. 5,071,820, 1991.
7. Burchell, T.D., Judkins, R.R. and Rogers, M.R., A carbon fiber based monolithic adsorbent for gas separation. In *Proc. 23rd Biennial Conf. on Carbon*, American Carbon Society, 1997, pp. 158 159.
8. Angelo, J. A. and Buden, D., *Space Nuclear Power*. Orbit Book Company, Inc., Malabar, FL., 1985.
9. A. Schock, Design evolution and verification of the general purpose heat source. In *Proc. of 15th Intersociety Energy Conv. and Eng. Conf.*, vol. 2, ASME, New York, 1980, pp. 1032 1042.
10. Wei, G.C. and Robbins JM., Carbon-bonded carbon fiber insulation for radioisotope space power systems, *Ceramics Bulletin*, 1985, 64(5),691 699.

- 11 Weaver, C.E. and Chilcoat, B.R., Carbon-bonded carbon fiber for space applications. Paper presented at the 1994 American Carbon Society Workshop, Oak Ridge, TN., May 15-18, 1994.
12. Burchell, T.D., and Oku, T., Material properties data for fusion reactor plasma facing carbon-carbon composites, *Nuclear Fusion*, 1994, 5(Suppl.), 77 128.
- 13 Skrabek, E.A., High temperature insulations for radioisotope thermoelectric generators. In *Proc. of 13th Intersociety Energy Conv and Eng Conf.*, vol. 2, ASME, New York, 1978, pp. 1712 1716.
14. Dinwiddie, R.B., Nelson, G.E., and Weaver, C.E., The effect of sub-minute high temperature heat treatments on the thermal conductivity of carbon-bonded carbon fiber (CBCF) insulation. In *Proc. Thermal Conductivity 23*, ed. K.E. Wilkes, R.B. Dinwiddie and R.S. Graves, Technomic Pub. Co., Inc., Lancaster, PA, 1996, pp. 466 477.
15. Eatherly, W P., Some considerations on the thermal conductivity of CBCF, ORNL Internal Report, October 31, 1983.
- 16 Lauf, R.J., Hamby, Jr., C., Akerman, M.A , and Seals, R.D., US Patent No. 5,243,464, 1993.
17. Lauf, R.J., Hamby, Jr., C., Akerman, M.A., and Trivelpiece, A.W., US Patent No. 5,313,325, 1994.
- 18 Broadband optical absorber, *Photonics Spectra*, 1994, 28(5), 85.
- 19 Burchell, T. D., Carbon fiber composite molecular sieves. In *Proc. Eighth Annual Conference on Fossil Energy Materials*, ORNL/FMP-94/1, CONF-9405143, Oak Ridge National Lab, U.S.A., 1994, pp 63 70.
20. Burchell, T.D., Weaver, C.E., Derbyshire, F., Fei, Y.Q. and Jagtoyen M., Carbon fiber composite molecular sieves:synthesis and characterization. In *Proc. Carbon '94*, Granada, Spain, Spanish Carbon Group, 1994, pp. 650 651.
- 21 Derbyshire, F., Fei, Y.Q., Jagtoyen, M., Kimber, G., Matheny, M. and Burchell, T., Carbon fiber composite molecular sieves for gas separation. In "*New Horizons for Materials*" *Advances in Science and Technology* (edited by P. Vincenzini), Techna Srl, Faenza, Italy 1995, Vol. 4, pp. 411 417.
22. Jagtoyen, M., Lafferty, C., Kimber, G, and Derbyshire, F., Novel activated carbon materials for water treatment. In *Proc The CARBON '96 Conf*, 1996, pp. 328 329.
23. Burchell, T.D., Judkins, R.R., Rogers, M.R. and Williams, A.M A novel process and material for the separation of carbon dioxide and hydrogen sulfide gas mixtures. *Carbon* 1997, 35(9), 1279 1294.
24. Burchell, T.D., Judkins, R.R , Rogers, M.R. and Williams, A.M. A novel approach to the removal of CO₂. In *Proc Tenth Annual Conf. On Fossil Energy Materials*, ORNL/FMP-96/1, CONF-9605167, Oak Ridge National Lab, U.S.A , 1996, pp. 135 148.
- 25 Burchell, T.D and Judkins, R.R. A novel carbon fiber based material and separation technology. *Energy Convers Mgmt*, 1997, 38, Suppl., pp S99 S104.
26. Burchell, T.D. and Judkins, R.R. Passive CO₂ removal using a carbon fiber composite molecular sieve, *Energy Convers. Mgmt*, 1996, 37(6-8), 947 954
27. Burchell, T.D. and Rogers, M.R., Carbon fiber composite molecular sieves, In *Proc Eleventh Annual Conf. On Fossil Energy Materials*, ORNL/FMP-97/1, CONF-9705115, Oak Ridge National Lab, U.S.A., 1997, pp. 109 116.
28. Burchell, T.D, Klett J.W , and Weaver, C.E. A novel carbon fiber based porous

- carbon monolith, In *Proc Ninth Annual Conf On Fossil Energy Materials*, ORNL/FMP-95/1, CONF-9505204, Oak Ridge National Lab, U.S.A., 1995, pp 447-456.
29. Klett, J.W. and Burchell T.D., Carbon fiber carbon composites for catalyst supports. In *Proc 22nd Biennial Conf On carbon*, Pub. American Carbon Society, 1995, pp. 124-125
30. M. Kuro-Oka, T. Suzuki, T. Nitta and T. Katayama *J Chem Eng of Japan*, 1984, 17(6), 588.
31. Singh, P., Ruka, R.J., and George, R.A. Direct utilization of hydrocarbon fuels in high temperature solid oxide fuel cells, In *Proc 24th intersociety energy conversion engineering conference*, Pub. Institute of Electrical and Electronics Engineers, New York, 1989, pp 1553-1563.

CHAPTER 7

Coal-Derived Carbons

PETER G. STANSBERRY, JOHN W. ZONDLO,
ALFRED H. STILLER

*Department of Chemical Engineering
West Virginia University
Morgantown, WV 26506-6102*

1 Review of Coal-Derived Carbons*1.1 Introduction*

Complex aromatic raw materials such as petroleum resids, decant oils, coal, and coal tars have been employed for many years by the carbon industry and continue to be used extensively in the fabrication of coke, carbon, and artificial graphite [1]. These same feedstocks also have the potential for use in producing "advanced" carbon products such as carbonaceous mesophase, fibers, and beads [2-4].

Currently, nearly all domestic pitches are obtained from either coal tar or petroleum precursors [5]. The pitch products, whether petroleum-based or coal-tar based, are prized by the ancillary industries that are dependent upon them but such pitches are, nevertheless, considered to be derived from byproduct materials. In addition, besides being derived from byproducts, the yield of pitch typically amounts to no more than 5 wt% based on the initial quantity of coal or crude feedstock [6].

The key feature that makes commercial pitches attractive and practical to the carbon industry is their highly aromatic nature. It is well known that aromaticity is necessary for the development of planar molecular alignment during liquid-phase carbonization which, in turn, is a requirement for graphitizability [7,8]. Because coal itself is predominantly aromatic [9], there has been a resurgence in research focused on producing extracts and other types of pitch-like substances from coal for other than fuel purposes [10]. Depending on how the coal-based material is processed, highly isotropic or anisotropic carbons can be obtained [11].

It is expected that production of coal-derived pitches, liquids, and chemicals will take on a more important role in the future. This is of some strategic concern to the United States, where the demand for domestic petroleum is greater than the supply. Moreover, the quality of imported petroleum crudes is declining in that they contain increasing amounts of contaminant metals and sulfur

In addition to supplying transportation fuels and chemicals, products from coal liquefaction and extraction have been used in the past as pitches for binders and feedstocks for cokes [12]. Indeed, the majority of organic chemicals and carbonaceous materials prior to World War II were based on coal technologies. Unfortunately, this technology was supplanted when inexpensive petroleum became available during the 1940s. Nevertheless, despite a steady decline of coal use for non-combustion purposes over the past several decades, coal tars still remain an important commodity in North America.

In recent years researchers at West Virginia University have developed coal-derived pitches on a laboratory scale in quantities sufficient to make 1 kg samples of calcined coke for fashioning graphite test specimens. The pitches were derived by utilizing solvent extraction with N-methyl pyrrolidone (NMP). This solvent is able to isolate coal-based pitches in high yield and with low mineral matter content [13]. It is this work that will form the basis of the discussion for the later part of this chapter.

1.2 Coke production

Most of the coke produced in the United States today comes from the high-temperature carbonization of coal. The coke is used primarily by the metallurgical industries as a fuel and in the rendering of iron from iron ore in the blast furnace

Essentially, carbonization entails the heating of organic precursors in the absence of air. In so doing, a solid carbon residue along with gaseous and volatile hydrocarbons is created. Bituminous coals are used to make metallurgical-grade coke while wood and other similar substances make charcoal. The condensed volatile material can be further refined to yield chemicals, pitches, or other useful commodities.

Historically, the production of coke from coal resulted from the pressures exerted by environmental and economic forces. In the late 1500s, demand for wood in England began to surpass supply. At that time, wood was converted into charcoal for use as a reductant of iron ore by the burgeoning metallurgical industries. By 1710, Abraham Darby of Coalbrookdale in Shropshire, England, commercialized the production of pig iron by utilizing the coke from coal

carbonization. Soon afterward, in only eight decades, over 80 blast furnaces for iron production were operating in Britain. Coal-derived coke was recognized as a very practical material and was also employed widely for glass making, blacksmithing, beer making, and fuel

The practices of charcoal making influenced early approaches to coal carbonization. The original method, though straightforward and somewhat crude, consisted of simply heating mounds of coal on a hearth. A better method of coke production developed with the appearance of the beehive oven in about 1760. These domed-shaped structures were numerous in the United States with 45 beehive oven plants and over 5,100 beehive ovens ready for operation in 1959 [14]. However, coke production with these ovens peaked earlier in the 20th century. A disadvantage with the beehive oven was the disregard for collecting the evolving volatile matter while the coal was being heated. The problem was ameliorated in the nineteenth century when coal was carbonized in indirectly heated slot ovens. The introduction of the slot oven led to byproduct recovery systems and by 1915 their use was well established in the United States.

Out of the 900 million tons of coal produced in the United States for domestic purposes in 1992, about 34 million tons were used for coking [10]. The overwhelming majority of coal is consumed by the electric utilities. Nevertheless, in 1990, the United States steel industry required about 23 million tons of coke which was produced by the byproduct recovery slot oven [15]. For a typical blast furnace, this translates to 0.5 tons of coke per ton of iron metal.

Coal carbonization is an extremely complicated art. The methods have been developed through centuries of trial and experience. More detailed descriptions on the processes involved can be found in the literature [16]. Modern foundry or blast furnace coke is made in a battery of up to 100 slot ovens placed side by side. Individual ovens are typically 16 meters long, 6.5 meters high, and about 0.5 meters in width. Each oven holds over 20 tons of coal which is charged through the top. The oven is sealed and heated indirectly through refractory-lined walls by the hot gases evolved during carbonization. After about 18 hours, coking is complete with the final temperature reaching over 1000°C. At the end of the coking cycle, side doors to the oven are opened and a large pushing ram forces the incandescent coke out for quenching. The side doors are installed again and the process repeated. Coke batteries are operated nearly continuously to remain productive over their life span of 20 to 30 years.

Petroleum cokes, on the other hand, represent the second largest source of consumable industrial carbon in the United States. In 1992, about 2 million tons of anode coke and 250,000 tons of needle coke were used in the United States.

Unlike coke produced from coal, petroleum cokes are derived from the residua of petroleum refining. Suitable feedstocks for good quality coke are thermal tars, catalytic cracker bottoms, and decant oils [17].

Several petroleum coking methods have been developed and include fluid, contact, and atmospheric-still coking [6]. The preferred coking method used today is conducted in delayed coking units. Delayed coking is attractive because of its ability to produce cokes with controlled microstructures. One highly desirable form is known as needle coke. No coal-based material is presently processed by delayed coking in the United States. Nevertheless, delayed coking of coal-tar feedstocks is practiced in Japan by the Nippon Steel Chemical Corporation, and the Mitsubishi Kasei Corporation.

In delayed coking, an aromatic feed is heated above 400°C and piped into the bottom of one of two tall drums. As the feedstock fills the coker, thermal cracking occurs to produce gas, gasoline, oils, and coke. Generally 24 hours are needed to fill the drum with coke. After the first drum is filled, the feed is introduced into the second drum and the next coking cycle begins. Meanwhile the first drum is quenched with steam and then water. After sufficient cooling, high-pressure water jets drill, cut, and loosen the coke for removal from the drum. The emptied coker drum is inspected and prepared for another run.

The coke at this stage is called "green" because it still contains 5 to 15 wt% volatile matter. If the coke is to be used as a filler in anode and electrode manufacturing, this high level of volatile matter is considered unacceptable because it contributes to shrinkage during subsequent heat treatment and fabrication.

Removal of volatile matter to about 0.5 wt% can be accomplished by calcining in a rotary kiln, rotary hearth, or vertical shaft calciner. All of these processes heat green coke to temperatures in excess of 1000°C where shrinkage and subsequent densification take place. The volatile components are comprised primarily of methane, ethane, hydrogen, and hydrogen sulfide gases which can be employed as fuel for process heat.

1.3 Pitch production

Coal-based pitches are predominantly byproducts of metallurgical coke operations in recovery-type coke ovens. The volatile products from the coke oven are recovered and processed, in simplest terms, into gas, light oils, and tar. The quantity and character of the materials are influenced by the type of coal charge, the design of the coking equipment, and the temperature and time profile of carbonization. Table 1 shows a typical yield of products from the

carbonization of a bituminous coal. Note that the yield of coal tar is very low. Despite the low yield, the large volume of coal carbonized produces a considerable quantity of secondary products.

Table 1. Production yields from coal carbonization

Yield from 1 ton of coal	Weight %
1520 lb coke	76
78 lb coal tar	4
20 lb light oil	1
20 lb ammonium sulfate	1
280 lb gas	14
80 lb miscellaneous	4

Crude coal-tar processing is traditionally accomplished by distillation into pitch and a series of distillate oils. Coal-tar pitch is the material remaining after all the available distillates are removed. The final softening point of the coal-tar pitch can be controlled via the distillation conditions.

Coal-tar pitch is particularly valuable to anode and electrode manufacturers. The main function is to plasticize coke grist so that formed bodies can be extruded or molded without distortion during the later stages of processing. Additionally, the pitch should give a high-carbon yield and not adversely affect the overall properties of the finished article. Although coal-tar pitch remains the binder of choice, petroleum-based binders can perform satisfactorily for the aluminum industry [18].

Coal-tar pitches generally soften around 110°C, are about 70 wt% soluble in toluene and 12 wt% insoluble in quinoline. Excessive amounts of primary quinoline insolubles (QI) would contribute to increased carbon yield, but such a pitch may not wet coke well and could hinder the penetration of pitch into the coke voids.

In many applications where high density and strength are required in the finished carbon product, another type of pitch is incorporated after a baking step. In this instance, impregnation with impregnating pitch reduces the porosity before the final heat treatment. The impregnation process can be repeated several times until the desired properties are achieved. Both coal and petroleum feedstocks are used as impregnants. The most significant features which distinguish impregnating pitches from binder pitches are their high solubility in toluene, low insolubility in quinoline, low viscosity, and low ash content.

1.4 Graphite and anode manufacture

Industrial carbon anodes and artificial graphites are not a single material but are rather members of a broad family of essentially pure carbon. Fortunately, artificial graphites can be tailored to vary widely in their strength, density, conductivity, pore structure, and crystalline development. These attributes contribute to their widespread applicability. Specific characteristics are imparted to the finished product by controlling the selection of precursor materials and the method of processing [19]

The processes for the manufacture of carbon anodes and graphite electrodes are very similar and in some instances overlap. The basic raw materials are calcined coke (filler coke) and coal-tar pitch. Conventionally, the process begins by grinding and sizing calcined petroleum coke to various sizes for recombination in proportions dictated by the end use; fine grain, high-density graphites require coke particles of micron dimensions while coke particles for anodes can be centimeters in size. Metallurgical coke and anthracite coal can be used as fillers but their introduction increases the level of contamination by metals, as well as reduces conductivity. Coal-tar pitch coke is also acceptable and is used in countries with limited petroleum but accessible coal resources. The coke blend is then added to a molten binder pitch and mixed to allow the pitch to wet the coke surface. Depending on the porosity of the coke and other variables, about one part of binder pitch is combined with three parts of coke in each mixing batch. A sufficient temperature is maintained such that the mix is plastic for shaping by either molding or extrusion. The shaped objects are cooled to harden the binder for handling, storage, and eventual further processing.

Baking is the next step. In the selection of the appropriate baking furnace, flexibility of operation and control of temperature are key considerations. A common baking furnace is the pit furnace, into which the formed articles are carefully stacked. Packing material consisting of fine coke particles (breeze) or sand is placed around the green stock to prevent sagging and distortion and to provide a porous medium for the release of volatiles. The firing cycle is carefully monitored to heat from 2 to 10°C per hour up to about 1000°C, often taking several weeks to complete. As the temperature is increased, the binder undergoes pyrolysis and fuses the coke into a solid mass. After cooling, the packing material is removed and the baked articles examined for defects, finished, and used as carbon anodes

In some applications the baked article would be further heat treated (graphitizing). During graphitization, the stock is positioned in the graphitization furnace and covered with packing material. Two stacking

patterns are used. In the Acheson furnace the stock is arranged in vertical columns which are transverse to the furnace axis, with coke packing in between each column. The packing functions as a resistor. In the Castner process, the stock is placed in rows parallel to the furnace axis, with the stock touching one another end to end. In this case, the stock is the resistor.

Graphitization is accomplished by passing an electrical current through either bed. Considerable resistive heating occurs where temperatures exceeding 3000 °C are possible. Normal process parameters utilize heating rates between 30 to 70°C per hour to 2500°C. Total time at temperature depends on the size of the artifact. Several more days are needed to cool the furnace before unpacking.

During the high-temperature treatment, the carbon undergoes dramatic changes in properties. The most important effects are the molecular rearrangement of amorphous carbon into a more ordered, graphitic structure. As a consequence, those characteristics associated with graphite including high crystallinity, low coefficient of thermal expansion, low electrical resistivity, high thermal conductivity, and thermal shock resistance are imparted.

2 Solvent Extraction of Coal

Several methods can be employed to convert coal into liquids, with or without the addition of a solvent or vehicle. Those methods which rely on simple pyrolysis or carbonization produce some liquids, but the main product is coke or char. Extraction yields can be dramatically increased by heating the coal over 350°C in heavy solvents such as anthracene or coal-tar oils, sometimes with applied hydrogen pressure, or the addition of a catalyst. Solvent components which are especially beneficial to the dissolution and stability of the products contain saturated aromatic structures, for example, as found in 1,2,3,4 tetrahydronaphthalene. Hydroaromatic compounds are known to transfer hydrogen atoms to the coal molecules and, thus, prevent polymerization.

Further details and specialized information on the mechanisms, product qualities, and processes applied to the heating of coal in solvents can be found in the abundant literature [20]. What follows are some of the results of research conducted at West Virginia University, where investigations of the conversion of coal into pitches suitable for graphite production have been carried out.

2.1 Solvent extraction procedure

This section summarizes the coals used for the project, some of their characteristics, the preparation of extract and pitch materials, as well as the

results of physical and chemical analyses of the products. Ultimately, these coal-derived pitches were coked and the resultant material used to manufacture graphite test bars for evaluation of their physical and chemical properties. In subsequent sections, these graphite bars will be designated as WVU graphites ranging from WVU-1 to WVU-13. Details of their preparation will be given in later sections.

2.2.1 Preparation of coal-derived extracts

Three West Virginia coals were supplied by the West Virginia Geological Survey (WVGS). The particular coals were chosen on the basis of rank, petrographic composition, and mineral matter content. The coals were limited to the bituminous rank since these coals are the most amenable to the NMP solvent extraction process and are indigenous to the Appalachian region. Some of the coal characteristics are listed in Table 2.

The lump coals, obtained fresh from the mine face, were ground without drying into two size fractions of 100 and 20 mesh (Tyler mesh) top size respectively before being placed into a nitrogen filled glove box. Between 2 to 3 kg samples of each coal were then sealed in plastic bags while still in the glove box to prevent oxidation, and stored in a cold room at about 4°C until ready for use. Just prior to extraction or treatment, coal samples were removed from the plastic bags and dried in a vacuum oven at about 110°C for 24 hours while under a nitrogen purge to ensure the removal of water and to minimize oxidation.

To assess the extraction efficiency of the coals, small-scale extractions were conducted. Approximately 10 g of dried, powdered coal were placed in a round-bottom flask equipped with a reflux condenser, stirrer, and nitrogen purge. Into this flask were poured 100 mL of freshly distilled NMP and stirring commenced. The mixture was heated to the normal boiling point of NMP, 202°C, and, while under a nitrogen atmosphere, allowed to reflux for one hour. Following this period, the dissolved portion of the coal in solution was separated from the undissolved coal and mineral matter using a traditional Buchner filtration apparatus. The filtrate contained the soluble coal fraction while the material that remained on the filter paper contained the insolubles. The filtrate was then placed in a rotary evaporator device where the solvent was removed under reduced pressure. The collected extract was finally dried in a vacuum oven at 150°C under flowing nitrogen overnight. After cooling the oven to room temperature, the extract was recovered as a solid and weighed. All NMP was condensed and recycled.

Table 2. Characteristics of bituminous coals subjected to solvent extraction with NMP

WV geological designation	WVGS 13407	WVGS 13421	WVGS 13423
Coal bed	Bakerstown	Powellton	Lower Powellton
County	Barbour	Raleigh	Mingo
ASTM rank	hVAb	mvb	hVAb
Mean-maximum reflection of Vitrinite	1 059	1 111	1 002
	proximate analysis (as received)		
Moisture	0 68	0 98	0 82
Fixed carbon	55 15	67 87	60 49
Volatile matter	28.23	27 96	34 41
Ash	15 94	3 19	4 27
	pctrographic composition (% volume)		
Vitrinite	59 6	63.3	71 4
Exinite	3 9	5 7	5 5
Inertinite	27.0	30 0	21 7

The extraction results are summarized in Table 3. The percent yield is calculated based on the weight of the recovered residue and is presented on a dry and ash-free basis (daf). The mass balances closed to approximately 100 percent and reproducibility was better than $\pm 2\%$ within the reported value. For most of the coals, the yield of soluble extract is typical for the range of rank studied, generally 20 to 35 percent by weight. However, one of the coals, WVGS 13407, demonstrated exceptionally good behavior, i.e., an extraction yield over 60 wt% was obtained. The other coals, WVGS 13421 and WVGS 13423, gave reasonably good extraction yields near 35 wt%.

Table 3. Results of solvent extraction of selected coals with NMP

Coal	WVGS 13407	WVGS 13421	WVGS 13423
Yield wt% (daf)	66 3	35 7	34 2

In order to process larger quantities of coal, an extraction reactor was constructed. The extractor was essentially a standing metal cylinder sealed on the bottom, approximately 30 cm in diameter and 84 cm in length. An electrical belt-driven stirring mechanism was fitted through the top of the reactor to provide mixing, and three electrical band heaters were wrapped around the outside to supply process heat. A water-cooled condenser was also installed to condense NMP during reflux. The system could routinely extract 1 to 2 kg of coal with 20 to 25 L of NMP.

The products of the extractor were removed from the bottom through a gate valve into one-liter centrifuge bottles. The bottle contents were centrifuged at 4000 rpm for one hour to expedite the separation of insoluble organic and mineral matter. After centrifuging, the dissolved coal extract was decanted and passed through a 1-2 micron filter paper. Excess NMP was removed from the filtered extract solution by rotary evaporation before being finally dried at 150 °C under vacuum. For reference, the extract material produced from the solvent extraction of raw coal will be symbolized as EXT in the subsequent discussion.

To increase the yield of extract and alter the properties of the pitch, the coals were subjected to thermal hydrogenation in tetralin, which was used because it is readily available and functions as a reasonably good hydrogen-donor solvent. Initial hydrogenation studies were conducted on WVGS 13407. The hydrogenation reactor was a 1000-mL Parr stirred autoclave which limited the production of product to about 150 grams. Hence, several runs had to be performed before enough material could be made for coking and calcining. The procedure to carry out the hydrogenation tests was as follows. About 200 g of dried, ground WVGS 13407 were placed along with about 600 mL of tetralin into the 1000-mL autoclave and sealed under 69 bar of hydrogen gas. The reactor temperature was then raised to 350°C and maintained at this temperature for 1 hour. Following reaction, the reactor vessel was cooled slowly to room temperature, vented, and the contents washed out with NMP into a large container. Additional NMP was added until a low-viscosity slurry was formed. The NMP mixture was heated to boiling and filtered through 1-2 micron filter paper as above. The filtrate was then rotary evaporated to remove the solvents (NMP and tetralin) and finally the extract was dried in a vacuum oven at 150°C overnight.

After the initial hydrogenation studies were completed with WVGS 13407, all other liquefaction experiments were conducted in a larger, 3.8-liter bolted-closure autoclave fitted with an electrically driven magnetic stirrer arbitrarily set to provide mixing at 1000 rpm. A temperature controller and power supply were connected to a three-zone furnace to control reaction temperature

Typically, about 500 g of dried coal and 2 L of tetralin were sealed in the autoclave. The overhead space in the reactor was purged with hydrogen through stainless steel tubing. The tube was immersed near the bottom of the system such that the gas passed through the mixture of coal and tetralin. Initially, cold hydrogen pressure was 69 bar for all hydrogenations except for those planned to operate at 450°C. For this temperature the initial hydrogen was reduced to 55 bar. After pressurizing with hydrogen, the stirrer and furnaces were activated. Depending on the set point, between about 2 and 4 hours were required to reach temperature

Each reaction was held at the desired temperature for 1 hour after which the furnaces were turned off. Several hours were required before the reactors cooled to ambient temperature. When cooled, the reactor was vented slowly of excess pressure and opened.

The reactor contents were transferred to a large rotary evaporator, capable of handling 20 L of material at one time, to remove tetralin. A sample of the recovered liquefaction solvent was analyzed by gas chromatography to determine the relative amount of tetralin and naphthalene. By comparing tetralin to naphthalene before and after hydrogenation, an estimate of the degree of hydrogenation can be determined. This aspect is addressed in more detail later. After removal of tetralin, about 7 L of NMP were added to the liquefied coal to dissolve the soluble products. These soluble materials were separated from the mineral matter and unconverted coal by centrifugation at 4000 rpm for 1 hour. The resultant coal pitch was rotary evaporated and then dried further in a vacuum oven at 150°C overnight. The hydrogenation process was repeated several times until the desired quantity of feedstock was obtained.

The recovered, hydrogenated coal products, prepared under identical conditions, were combined and ground to pass through a course-mesh screen (Tyler 8 mesh) in a glove box to reduce oxidation. The ground product was evenly distributed in a rectangular stainless steel pan and the contents of the pan divided into six equal quadrants. Material from each quadrant was sampled representatively and then sealed under nitrogen in plastic bags. Finally, the coal-derived pitch was stored at reduced temperature until ready for use. It was thought that the sampling and storage procedure described above would ensure coke and graphite production feedstock of a relatively uniform and homogeneous nature. The solvent extracted material from the hydrogenated coal will be subsequently referred to as HEXT with the hydrogenation temperature as a suffix.

Table 4 summarizes the yield of soluble pitch for the hydrogenation experiments. Hydrogenation of WVGS 13407 at 350°C increased the pitch yield from about 66 to 84 wt%. Although the incremental yield between untreated and hydrogenated coal is only 18 wt%, there were significant differences in the properties of the pitches in terms of their carbonization behavior.

Hydrogenation of WVGS 13421 at 350°C, on the other hand, increased the pitch yield from about 35 wt% for the untreated coal to 62 wt%. Hydrogenations at 400 and 450°C produced more than double the quantity of soluble material over that of the unhydrogenated coal. Although the yield of products obtained at 400

and 450°C is essentially identical, their behavior upon pyrolysis was dramatically different.

Table 4. Soluble product yields from hydrogenation of bituminous coals

	WVGS		WVGS		WVGS		
	13407		13421		13423		
Hydrogenation Temperature, °C	<u>350</u>	<u>350</u>	<u>400</u>	<u>450</u>	<u>350</u>	<u>400</u>	<u>450</u>
Yield, wt% (daf)	84	62	83	82	74	83	67
Yield from raw coal, wt% (daf)	66.3		35.7		34.2		

Likewise, hydrogenation of WVGS 13423 at 350°C increased the yield of product from about 34 to 74 wt%. Not unexpectedly, hydrogenation at 400°C increased conversion even more to 83 wt%, while hydrogenation at 450°C produced a recoverable product yield of 67 wt%. The apparent reduction in yield upon reaction at 450°C is discussed below.

Mass recoverables for all experiments, except the 450°C run with WVGS 13423, were generally about between 89 and 95 wt%. The loss in mass balance is attributed to product gas, light distillate, and solids unrecoverable during processing and handling. However, mass recoverables for hydrogenation of WVGS 13423 at 450°C barely amounted to 70 wt%. Gas chromatographic analysis of the spent hydrogenation solvent and visual inspection of the amount of coal products collected in the cold traps used during rotary evaporation, indicated that the highly hydrogenated materials from this coal were relatively volatile and, hence, not recoverable. The conclusion that these products were distillable is supported by thermogravimetric analysis (TGA) and coke yield determinations reported in section 3.1

In addition to hydrogenation as a means to vary pitch characteristics, blending of raw coal extract with hydrogenated material was also investigated. About 0.68 kg of pitch blend were prepared at one time by combining the desired amount of raw coal extract and hydrogenated product in the appropriate proportion. For example, a pitch blend precursor which was used to make the WVU-6 graphite, was comprised of 0.51 kg of the NMP-soluble extract (EXT) from raw WVGS 13421 coal and 0.17 kg of NMP-soluble pitch from 400°C hydrogenated (HEXT400) WVGS 13421. The blend composition is thus 75:25 wt% EXT:HEXT400. After weighing, the solid material was transferred to a 10-L container to which was added about 7 L of NMP. The mixture was heated to about 140°C while being agitated for 1 hour or until complete dissolution occurred. The excess NMP was removed by rotary evaporation, the product recovered, and dried in a vacuum oven at 150°C overnight. The blending

procedure was repeated as needed, depending on the quantity of the pitch blend that was required. After drying, the blend was transferred to a nitrogen-purged glove box, sampled representatively as described earlier, sealed in plastic bags, and refrigerated until ready for use.

The dissolution procedure used to prepare the blends is unlike other procedures where pitch components are physically blended. It was observed that dissolving the individual coal-derived materials together in NMP resulted in intimate mixing on the near molecular scale, thus producing a completely homogeneous pitch blend.

A summary of the various pitches, coal source, treatment, and blend composition, and their corresponding test graphites (as referenced with a "WVU" number) is presented in Table 5. Here EXT refers to the NMP-soluble extract from the raw coal and HEXT refers to the NMP extract from the hydrogenated coal

Table 5. Pitch identification and corresponding graphite produced from that pitch

Graphite	WVU-1	WVU-2	WVU-3
Pitch source	WVGS 13407 NMP-soluble extract EXT	WVGS 13407 hydrogenated 350°C HEXT350	WVGS 13421 NMP-soluble extract EXT
Graphite	WVU-4	WVU-5	WVU-6
Pitch source	WVGS 13421 Hydrogenated 400°C HEXT400	WVGS 13421 hydrogenated 450°C HEXT450	WVGS 13421 blend 75:25 wt% EXT HEXT400
Graphite	WVU-7	WVU-8	WVU-9
Pitch source	WVGS 13421 blend 60:40 wt% EXT HEXT350	WVGS 13421 blend 25:75 wt% EXT HEXT450	WVGS 13421 blend 75:25 wt% EXT HEXT450
Graphite	WVU-10	WVU-11	WVU-12
Pitch source	WVGS 13423 NMP-soluble extract EXT	WVGS 13423 blend 75:25 wt% EXT HEXT450	WVGS 13423 blend 25:75 wt% EXT HEXT450
Graphite	WVU-13		
Pitch source	WVGS 13423 hydrogenated 450°C HEXT450		

2.2 Characterization of coal-derived pitches

The hydrogen consumption for the hydrogenation of WVGS 13421 and WVGS 13423, Table 6, qualitatively indicates the relative reactivity of the coals and their products. As discussed previously, prior to and after each experiment, the tetralin was analyzed chromatographically to determine the relative tetralin and

naphthalene content. The assumption was made that during the course of liquefaction each molecule of tetralin converts to naphthalene after donating four hydrogen atoms to the coal. The assumption is also made that the amount of hydrogen from other sources (gas phase hydrogen and coal) is not significant when compared to the amount of hydrogen donated by the tetralin. Thus, the hydrogen consumption figures reported in Table 6 should be considered minimum values. Knowing the relative amount of tetralin conversion and the initial volume of tetralin used in the experiment, the amount of hydrogen transferred to coal can be deduced.

Table 6. Estimated degree of hydrogenation of coals as a function of hydrogenation temperature

	WVGS 13421			WVGS 13423		
	350	400	450	350	400	450
Hydrogenation temperature, °C						
Hydrogenation, wt%	<0.01	----	2.77	0.10	0.64	2.91

% hydrogenation = [(wt hydrogen added)/(wt daf coal)] X 100

Much work has been described in the literature on determining which chemical and physical features distinguish coals in terms of reactivity or hydrogenation potential [21]. Coal rank is certainly one of the features as shown by the difference between WVGS 13421, which is a medium-volatile bituminous coal, and the lower rank WVGS 13423, which is a high-volatile A bituminous coal.

In very broad terms, hydrogenation activity in terms of hydrogen utilization increases as coal rank decreases. Thus, in the absence of any other information, one can expect WVGS 13423 to be the more reactive of the two. Obviously, generalities about hydrogenation behavior should not be extended to other coals based solely on a limited data set. Nevertheless, important differences between the pitches derived from WVGS 13421 and WVGS 13423 are apparent.

The amount of hydrogen added to WVGS 13421 at 350°C was barely measurable, but WVGS 13423 consumed about 0.1 wt%. It is unfortunate that values for hydrogen consumption at 400°C are not available for WVGS 13421. Yet one can conclude that hydrogenation did increase upon going from 400 to 450°C, despite similar product yields. In other words, at these two temperatures and for this coal, hydrogenation did not produce an increase in pitch yield, but rather went into altering the properties of the pitch. Where direct comparison can be made between WVGS 13421 and WVGS 13423 for the 350 and 450°C runs, WVGS 13423 required more hydrogen.

Elemental analysis was performed on various coals, pitches, and blends. Table 7 reports the elemental composition of products from WVGS 13407. Compared to the raw coal, the NMP-soluble extract (EXT) contains essentially the same amount of carbon, though there is slightly more hydrogen as indicated by a

decrease in the atomic C/H ratio. Hydrogenation at 350°C is evident as the hydrogen content was increased to over 6 percent from 5.7 percent for the untreated extract. The nitrogen content is rather high, being over 2 percent for all three samples. There also appears to be a measure of desulfurization during hydrogenation but the oxygen content (calculated by difference) remains high.

Table 7. Elemental composition of soluble products from WVGS 13407 (daf)

	Raw coal	NMP-soluble extract EXT	350°C hydrogenation HEXT350
C	85.9	85.2	85.5
H	5.4	5.7	6.2
N	2.3	2.3	2.8
S	0.8	1.3	0.5
O ^a	5.6	5.5	5.0
C/H atomic ratio	1.32	1.25	1.16

^aoxygen by difference

In Table 8 the effects of hydrogenation are shown on the elemental composition of products from WVGS 13421. Similar to WVGS 13407, the NMP-soluble extract of WVGS 13421 has a lower atomic C/H ratio than the raw coal, indicating a higher hydrogen content. The effect of hydrogenation decreases the atomic C/H ratio as the severity of hydrogenation increases. Nitrogen content of all the soluble materials is still rather high and sulfur content is variable. There is a steady decrease in oxygen upon going from the NMP-soluble extract to the 450°C product.

Table 8. Elemental composition of soluble products from WVGS 13421 (daf)

	Raw coal	NMP-soluble extract EXT	400°C hydrogenation HEXT400	450°C hydrogenation HEXT450
C	86.1	84.2	87.0	88.1
H	5.3	5.5	5.5	5.8
N	1.5	2.1	2.4	2.2
S	0.9	0.8	0.7	0.8
O ^a	6.3	7.4	4.4	3.1
C/H atomic ratio	1.37	1.28	1.32	1.26

^aoxygen by difference

The results of blending the NMP-soluble extract from untreated WVGS 13421 (EXT) with soluble material from 450°C hydrogenated WVGS 13421 (HEXT450) are reported in Table 9.

Table 9. Effect of blending coal-derived pitches from WVGS 13421 on elemental composition (daf)

	NMP-soluble extract EXT	75:25 wt% EXT:HEXT 450	25:75 wt% EXT:HEXT 450	450°C hydrogenation HEXT450
C	84.2	85.9	88.6	88.1
H	5.5	5.3	5.6	5.8
N	2.1	2.4	2.2	2.2
S	0.8	---	0.6	0.8
O ^a	7.4	---	3.0	3.1
C/H atomic ratio	1.28	1.34	1.34	1.26

^aoxygen by difference

For the most part, the elemental analysis data for the blends are consistent with a weighted average of the individual components. Also shown is the elemental analysis for some of the soluble products from WVGS 13423 in Table 10. As was observed for the WVGS 13421 products, hydrogenation increased the total hydrogen content and decreased the atomic C/H ratio.

Table 10. Elemental composition of products from WVGS 13423

	NMP-soluble extract EXT	75:25 wt% EXT:HEXT450	450°C hydrogenation HEXT450
C	84.9	86.3	85.5
H	5.3	5.6	5.9
N	2.0	2.4	1.9
S	0.7	---	0.4
O ^a	7.0	---	3.4
C/H atomic ratio	1.33	1.29	1.26

^aoxygen by difference

One effect of the degree of hydrogenation is to lower the softening point and glass transition temperature, T_g , of the pitch as shown in Table 11. The occurrence of a softening point and glass transition demonstrates the pitch-like character of the hydrogenated products, although these values are still considerably higher than most commercial pitches.

Only a limited number of coal-derived pitches were examined by ¹H NMR because of their low solubility in solvents commonly used in conventional proton magnetic resonance. Table 12 reports the distribution of hydrogen for three of the pitches. Unlike coal-tar pitches, which typically have over 85% of the hydrogen bonded to aromatic carbon, the materials listed in Table 12 are characterized by a high content of aliphatic hydrogen.

Table 11. Characteristics of NMP-soluble pitches from WVGS 13421

	NMP-soluble extract EXT	400°C hydrogenation HEXT400	450°C hydrogenation HEXT450	75.25 wt% EXT:HEXT 450
Glass transition T_g , °C	----	*168	*76	*76
Mettler softening point, °C	>300	173	158	165

† by thermal mechanical analysis, * by differential scanning calorimetry

Table 12. ^1H NMR characterization of coal-derived pitches

	WVGS 13407 NMP-soluble extract	WVGS 13421 450°C hydrogenation	WVGS 13421 75.25 wt% EXT HEXT450
^1H distribution			
Aromatic H, % H_{ar}	29	39	41
Aliphatic H, % H_{al}	71	61	59

Size exclusion chromatography (SEC) using trichlorobenzene as a solvent was used to determine the number average molecular weight (MW_n) distribution of several of the coal-derived pitches. The molecular weight distribution for all the materials is quite broad, with a considerable amount exceeding a MW_n of several hundreds. Typically, the molecular weight averages were between MW_n of 400 and 500. These values are only slightly higher than those for commercial pitches. Moreover, the width and shape of the molecular weight distribution curves for the coal extracts are generally similar to those for commercial pitches.

2.3 Ash reduction in coal-derived pitches

One of the more important considerations in determining the end use of synthetic graphite is its contamination with metallic components. Metals such as iron, vanadium, and especially in nuclear applications, boron are deleterious to the performance of graphite. Table 3 presented the extraction yields of NMP-soluble material for three bituminous coals. For these coals, mineral matter and insoluble coal residue were separated from the extract by simple filtration through 1-2 μm filter paper. Table 13 lists the high-temperature ash content in the dry coal, and in their corresponding NMP-insoluble and NMP-soluble products. The reduced ash content of the extract is typically between 0.1 to 0.3 wt% using traditional filtration techniques for the small-scaled extraction experiments.

To reduce the quantity of ash in the extracts even further, steps were implemented using a sequential solids removal scheme that entailed a combination of centrifugation and filtration. Following extraction of the coal

Table 13. Ash content in WVGS coals and coal products

WVGS ID	Weight % ash		
	13407	13421	13423
Coal, dry	14.0	3.2	3.8
Residue	29.3	4.6	4.7
Extract	0.2	0.1	0.3
Yield of extract (daf)	66.3	35.7	34.2

with NMP, the mixture was placed in a centrifuge during which time the particulates were subjected to 2000 G for two hours. The supernatant liquid was removed from the solids by simply decanting and then filtering through 1-2 μm filter paper. The resulting filtrate was centrifuged again for an extended period of time (overnight) at 2000 G. Again the supernatant liquid was separated by decanting and then filtered through 0.2 μm filter paper. Table 14 shows the results using the above process for WVGS 13421 coal where it can be seen that significant ash reduction is possible.

Table 14. Results of de-ashing experiments using centrifugation and filtration of WVGS 13421

Material	Weight % ash
Dry coal	3.2
Raw extract	0.1
Second centrifugation	0.05

While the quantity of ash in the extracts is rather low, after coking and calcining the ash constituents are slightly concentrated in the carbons because of the small volatile matter loss from the extracts. For example, Table 15 shows the ash content of products from WVGS 13421. The extract was obtained using the large-batch extractor as described earlier. The product was de-ashed by first centrifuging at 2000 G for 90 minutes followed by filtration through 1-2 μm filter paper. The product was recovered, dried, and converted to green and calcined coke.

Table 15. Ash content of WVGS 13421 and its products

	Raw coal	NMP-extract	Residue	Green coke	Calcined coke
Ash, wt%	3.03	0.04	3.34	0.15	0.24

To determine if the ash removal steps could be simplified, experiments were performed on hydrogenated coals. Hydrogenation experiments were conducted at 400°C in tetralin and the pitch isolated from the insoluble mineral matter and

coal by centrifugation alone at 2000 G for 60 minutes without the use of NMP. The supernatant liquid was decanted and dried under vacuum at 150°C. Table 16 lists the yield of products and their ash contents.

Table 16. Ash content of raw coal and their hydrogenated coal products, wt%

Coal sample	Raw coal	Supernatant liquid		Insoluble solids	
		Yield product	Ash content	Yield product	Ash content
WVGS 13407	13.6	43	<0.1	52	19.3
WVGS 13421	3.0	38	<0.1	55	5.4

Note that the yield of extract product presented here is lower than that reported earlier in Table 4 because the hydrogenated products were not extracted with NMP but were centrifuged directly. The data show that centrifugation by itself, and without any accompanying filtration, appears to provide pitches of acceptable purity, albeit with an associated lower yield.

The coal-derived pitch precursors for WVU-1, WVU-2, and WVU-3 test graphites were de-ashed by the combined centrifugation and filtration method while all of the other pitches were de-ashed by centrifugation alone (2000 G, 90 minutes).

3 Preparation and Characteristics of Cokes Produced from Solvent Extraction

3.1 Preparation of green and calcined cokes

Two reactor types were used to convert coal-derived pitches into green coke. A heavy, carbon-steel pipe (about 0.75 m long by 5 cm inside diameter) was machined at both ends such that plugs could be inserted to seal the system. The coking reactor was filled approximately 2/3 full with pitch, flushed with nitrogen, and then sealed. The coking reactor was inserted into a ceramic tube furnace and heated in two stages. In the first stage the coal pitch was heated to 400°C. In this stage the material becomes a molten mass. The tube was kept at this condition for 12 hours. In the second stage, the tube reactor contents were then raised to 600°C and held at this temperature for one hour, whereupon the tube was permitted to cool to room temperature. The product was then recovered and weighed. The green coke precursors for WVU-1, WVU-2, and WVU-3 test graphites, WVGS 13407 NMP-soluble extract, NMP-soluble extract from 350°C hydrogenated WVGS 13407, and WVGS 13421 NMP-soluble extract, respectively, were made with this system.

All subsequent green coke operations were made in a second coker, which was fashioned from steel pipe approximately 18 cm in diameter and 25 cm in length. A metal plate was welded to one end and a metal collar was welded to the other end such that a steel lid could be bolted to the system. Typically, about 250 to 500 g of pitch were sealed under nitrogen in the coker reactor and the system placed in a large temperature-programmable furnace. The heat treatment process was as follows. The temperature was raised 5°C/min to 350 °C and then 1°C/min to 425°C and the temperature held at 425°C for 90 minutes. Finally the temperature was raised further at 3°C/min to between 500 and 600°C, and held there for 3 hours. The coker was cooled to room temperature and the material recovered to determine green coke yield.

The green cokes were calcined by placing a weighed amount of green coke into an alumina tube. The tube was fitted with end caps to allow for a constant purge of nitrogen. The alumina tube was then inserted into a high-temperature furnace and the temperature raised to about 1000°C for a period between 30 and 60 minutes. The furnace was turned off, cooled to room temperature, and the product recovered to determine the calcined coke yield.

The effect of hydrogenation on the yield of green coke is shown in Table 17. Thermogravimetric analysis (TGA) was also conducted for comparison. It can be seen that the pitch from unhydrogenated coal results in a fairly high yield of green coke. As the severity of hydrogenation increased the green coke yield decreased, probably because of molecular weight reduction and loss of low-molecular weight species during coking. Also, in general, TGA yields are lower than the yields obtained from the green coking operation. Undoubtedly, during the green-coke process in the sealed reactor, some reflux occurred, promoting additional condensation and enhanced carbon yield. The TGA experiment, which involves rapid heating under a flowing inert gas atmosphere, tends to promote enhanced distillation of volatile species.

Tables 18 and 19 show the effects of blending extracts of hydrogenated coal with those from untreated coal for WVGS 13421 and WVGS 13423, respectively. For both coals, the amount of hydrogenated material in the blend causes a reduction in coke yield. Again, the TGA yields are generally lower than the yields obtained using the coking reactor. This is particularly pronounced for the WVGS 13423 coal following hydrogenation at 450°C, where the TGA yield is only 34 wt%. As noted previously, the hydrogenated products from WVGS 13423 are relatively volatile.

Table 17. Effect of hydrogenation on green coke yields

Coal	Green coke yield, wt%	TGA yield, wt%
WVGS 13407	71.4	71.0
EXT		
HEXT350	----	60.3
WVGS 13421		
EXT	71.2	80.0
HEXT400	62.8	----
HEXT450	57.1	51.0
WVGS 13423		
EXT	70.3	61.5
HEXT450	52.3	34.0

Table 18. Effect of blending hydrogenated coal-derived pitch and coal extract on green coke yields, WVGS 13421

Blending ratio	Green coke yield, wt%	TGA yield, wt%
100:0 EXT:HEXT450	71.2	80.0
75:25 EXT:HEXT450	69.6	63.5
25:75 EXT:HEXT450	62.9	52.9
0:100 EXT:HEXT450	57.1	51.0

Table 19. Effect of blending hydrogenated coal-derived pitch and coal extract on green coke yields, WVGS 13423

Blending ratio	Green coke yield, wt%	TGA yield, wt%
100:0 EXT:HEXT450	70.3	61.5
75:25 EXT:HEXT450	61.7	57.7
25:75 EXT:HEXT450	47.2	40.4
0:100 EXT:HEXT450	52.3	34.0

Table 20 reports the yield of calcined cokes for several of the graphite precursors. The high-coke yields indicate that most of the volatiles were lost during the green coking operation. Since no visible tar or smoke occurred during calcination, most of the weight loss is attributed to evolution of hydrogen, non-condensable hydrocarbons, and other light gases.

3.2 Analysis of cokes by optical microscopy

Polarized light photomicrographs were taken of the green and calcined cokes, as well as their corresponding test graphites. The untreated extract cokes are characterized by very small anisotropic domains on the order of 3 microns or less. This type of optical structure is believed to be highly desirable for nuclear graphite applications.

Table 20. Yield of calcined coke for WVU test graphites

	Calcined coke yield, wt%
<u>WVGS 13421</u>	
HEXT400	93.8
75:25 EXT:HEXT400	96.1
60:40 EXT:HEXT350	95.5
EXT	92.8
75:25 EXT:HEXT450	91.6
25:75 EXT:HEXT450	92.7
HEXT450	94.2
<u>WVGS 13423</u>	
EXT	87.0
75:27 EXT:HEXT450	91.1
25:75 EXT:HEXT450	93.1
HEXT450	92.0

In contrast, the hydrogenated extracts show much larger anisotropic domain structures, increasing in size with increasing hydrogenation severity, which is consistent with the reduced coefficient of thermal expansion (CTE) exhibited by the test graphites as discussed later. Further, blending hydrogenated material with untreated extract results in anisotropic domains of an intermediate size. Thus by varying the process parameters, a variety of cokes can be prepared to produce tailored graphites with a range of anisotropy. Figure 1 shows the effects of blending on the development of optical texture. Indeed, the manufacture of graphites ranging from very isotropic to highly anisotropic is possible from a single coal source by controlling blending composition and hydrogenation. This finding was also substantiated by Seehra *et al.* [22] in a recent publication.

3.3 Ash analysis of cokes

Table 21 reports the ash content and ash composition (determined by inductively coupled plasma-atomic emission spectroscopy, ICP-AES) for all of the calcined cokes used to fabricate the test graphites. It can be seen that the amount of ash and its make-up are variable, but are within the range observed for petroleum-based calcined cokes. Although the ash contents in all of the calcined cokes appear rather high, these materials may still be acceptable because many of the metallic species are driven off during graphitization. This aspect is addressed in the next section.

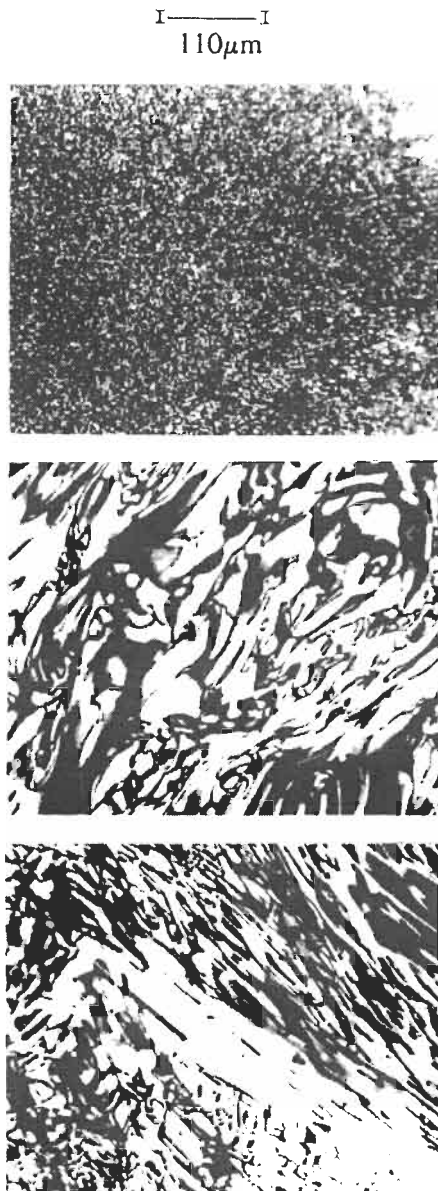


Figure 1. Optical photomicrographs of green cokes derived from WVGS 13421 pitches: top, EXT; middle, 75:25 EXT:HEXT450; bottom, HEXT450

Table 21. Ash content and composition of calcined cokes used to make the WVU graphites

	WVU- 1	WVU- 2	WVU- 3	WVU- 4	WVU- 5	WVU- 6	WVU- 7	WVU- 8	WVU- 9	WVU- 10	WVU- 11	WVU- 12	WVU- 13
						13421 75:25	13421 60:40	13421 25:75	13421 75:25		13423 75:25	13423 25:75	
Precursor	13407 EXT	13407 HEXT	13421 EXT	13421 HEXT	13421 HEXT	EXT: HEXT	EXT: HEXT	EXT: HEXT	EXT: HEXT	13423 EXT	HEXT 450	HEXT 450	13423 HEXT 450
Sulfur wt%	0.53	0.45	0.56	0.54	0.40	0.60	0.65	0.46	0.64	0.62	0.56	0.36	0.32
Ash wt%	0.76	0.76	0.29	0.29	0.24	0.34	0.29	0.16	0.47	0.61	0.91	0.25	0.43
Metals ppm													
B	6.8	5.3	2.1	3.8	3.1	3.1	3.0	2.6	3.6	3.0	2.4	3.4	3.3
Na	346.0	36.0	37.0	56.0	16.0	81.0	79.0	20.0	51.0	27.0	37.0	17.0	126.0
Mg	147.0	38.0	12.0	8.8	5.8	8.0	2.3	8.6	9.5	11.0	15.0	60.0	17.0
Al	274.0	239.0	41.0	94.0	35.0	57.0	19.0	80.0	115.0	93.0	188.0	57.0	297.0
Si	474.0	281.0	60.0	279.0	173.0	88.0	12.0	70.0	341.0	4.0	298.0	80.0	594.0
K	32.0	29.0	8.8	5.7	4.3	0.6	3.9	5.9	11.8	9.0	26.0	----	39.0
Ca	759.0	365.0	87.0	65.0	128.0	20.0	16.0	15.0	16.8	38.0	121.0	132.0	128.0
Ti	429.0	509.0	77.0	125.0	6.6	87.0	94.0	----	59.8	206.0	139.0	60.0	40.0
V	20.0	17.0	4.9	7.9	1.9	7.7	1.8	2.8	5.6	11.0	12.0	6.0	2.0
Cr	28.0	61.0	9.4	23.0	17.0	84.0	63.0	5.0	55.2	300.0	294.0	72.0	170.0
Fe	778.0	1879.0	999.0	643.0	537.0	1209.0	286.0	504.0	1795.0	1779.0	3704.0	597.0	645.0
Mn	11.0	29.0	22.0	10.0	30.0	15.0	12.0	----	18.1	44.0	57.0	40.0	50.0
Ni	13.0	25.0	13.0	20.0	15.0	43.0	33.0	38.0	32.7	162.0	152.0	38.0	38.0
Cu	252.0	25.0	111.0	74.0	444.0	92.1	294.0	----	412.9	1036.0	653.0	449.0	227.0
Zn	24.0	12.0	207.0	77.0	22.0	106.0	10.0	----	8.4	61.0	98.0	27.0	15.0
P	----	45.0	0.4	1.1	----	0.4	0.2	52.0	0.4	----	----	----	----

4 Preparation and Evaluation of Graphite From Coal-Derived Feedstocks

Test graphites were made from calcined coke which was initially milled into a fine flour so that about 50% passed through a 200 mesh Tyler screen. The coke flour was then mixed with a standard coal-tar binder pitch (110°C softening point) at about 155°C. The ratio of pitch to coke is about 34:100 parts by weight. After mixing with the liquid pitch, the blend was transferred to the mud cylinder of an extrusion press heated to about 120°C. The mix was then extruded into 3-cm diameter by 15-cm long cylinders and cooled. These green rods were then packed in coke breeze and baked in saggars to 800°C at a heating rate of 60°C/hour. The baked rods were graphitized to about 3000°C in a graphite tube furnace. In most cases, the graphite rods were machined into rectangular specimens 2-cm wide by 15-cm long for measurement of the CTE.

4.1 Analytical characterization *cf* graphites

In order to assess the loss of inorganic contaminants during graphitization, the ash composition of most of the graphites was analyzed by ICP-AES. The total ash contents of the WVU graphites are compared to those for the precursor calcined cokes in Table 22. Also included are data for H-451 and VNEA, which are the current qualified nuclear-grade graphites.

The elemental ash composition for most of the graphites, as measured by ICP-AES, are compiled in Table 23. The results show that most of the inorganic matter is removed during the graphitization process. The elemental compositions of the WVU graphites are in the same range as the commercial nuclear graphites which have presumably undergone extensive additional halogen purification.

Table 22. Ash contents of calcined cokes and their processed graphites (ppm)

	Calcined coke	Graphite
WVU-1	7600	290
WVU-2	7600	370
WVU-3	2900	680
WVU-4	2900	380
WVU-5	2400	70
WVU-6	3400	130
WVU-7	2900	1020
WVU-8	1600	100
WVU-9	4700	100
VNEA	----	220
II-451	----	60

The results in Table 22 are of crucial importance. Indications are that the ash percentage in the calcined cokes produced from coal may already be low enough to yield acceptable graphite. The WVU graphites have not been halogen purified treated and yet yield metal composition comparable to, or better than H-451 or VNEA graphite. Since the chlorine treatment is quite costly, significant economic advantages may accrue from the production of graphite from coal.

4.2 Correlation of graphite properties with processing methodology

A key factor in the suitability of cokes for graphite production is their isotropy as determined by the coefficient of thermal expansion. After the calcined coke was manufactured into graphite, the axial CTE values of the graphite test bars were determined using a capacitance bridge method over a temperature range of 25 to 100°C. The results are summarized in Table 24. Also included in the table are bulk density measurement of calcined cokes and the resistivity values of their graphites.

The degree of isotropy of the graphites varied, as indicated by the CTE, depending upon the characteristics of the starting coal-derived pitches. Such control can be exercised in two distinct ways. In the first method, the severity of the hydrogenation conditions to which the raw coal was subjected, was varied by changing the hydrogenation temperature. The higher the reaction temperature the more hydrogen was transferred to the coal-derived pitch. The most severe hydrogenation conditions produced the most anisotropic graphites while the least severe, or no hydrogenation at all, produced materials which were more isotropic. For example in Figure 2 the effect of hydrogen addition on the resultant graphite CTE is shown. It is apparent that little hydrogen is required to reduce the CTE value dramatically. Furthermore, the addition of more than about 0.5 wt% hydrogen to the coal pitch only reduces the CTE slightly. Qualitatively, the degree of isotropy could be easily seen by examination of the photomicrographs of the cokes and graphites.

A second method for varying the degree of anisotropy in coal-based graphites was achieved by blending the hydrogenated coal-derived extract with that from the non-hydrogenated raw coal. Hence, by varying the proportions of the unhydrogenated and hydrogenated pitch, graphites with controlled CTE can be obtained. These CTE values range between the most anisotropic graphites in the case of the pure hydrogenated pitch to the most isotropic graphites in the case of the raw coal extract. The effect of blending composition on CTE for pitches derived from WVGS 13421 is shown in Figure 3. When the same types of pitches and graphites were obtained from WVGS 13423 the effect was the same, though the exact functional relationship was different.

Table 23. Metals analysis of WVU graphites by ICP-AES (ppm)

Metal	WVU-1	WVU-2	WVU-3	WVU-4	WVU-5	WVU-6	WVU-7	WVU-8	WVU-9	VNEA	11-451
Na	11	8.6	5.5	4.6	2.2	4.0	6.4	0.9	3.0	10	5.7
Mg	2.2	2.5	1.1	1.6	1.3	0.87	1.9	0.2	0.1	1.1	1.1
Al	9.8	10	7.9	9.1	2.5	6.8	7.8	---	1.0	14	12
Si	24	9.9	51	14	4.0	5.9	432	1.6	1.1	11	23
K	11	11	7.3	11	---	9.0	12	1.8	0.8	13	12
Ca	13	19	96	91	8.2	17	11	2.4	2.1	45	1.6
V	6.5	71	66	55	23	49	33	14	17	5.1	0.84
Fe	16	11	47	5.0	5.6	7.6	6.1	2.8	5.6	43	2.4
P	0.27	---	---	---	0.1	---	0.21	33	---	---	0.10
Ti	55	58	37	15	12	25	36	1.5	22	4.3	7.1
Cr	0.10	0.21	0.42	0.49	0.52	---	0.17	13	0.1	1.7	---
Ni	0.64	1.8	1.8	0.82	0.38	0.58	0.32	34	0.7	4.0	0.42
Zn	0.22	0.14	0.11	0.18	0.21	0.12	0.15	6.7	0.1	0.79	0.13
Mn	0.23	0.10	0.11	---	0.10	0.10	0.16	6.6	---	0.10	---
Cu	1.8	0.94	0.95	0.50	0.51	0.78	0.60	6.5	1.1	4.7	1.0

Table 24. Some properties of WVU coal-derived calcined cokes and their graphites

graphite	WVU-1	WVU-2	WVU-3	WVU-4	WVU-5	WVU-6	WVU-7	WVU-8	WVU-9	WVU-10	WVU-11	WVU-12	WVU-13
CTE	4.42	2.89	5.28	1.59	0.71	4.52	3.77	1.19	3.12	5.28	5.07	1.09	0.96
R	13.16	10.01	13.16	9.98	11.85	14.71	15.10	10.18	11.56	8.96	13.77	10.10	11.76
density	1.51	1.57	1.57	1.48	1.38	1.57	1.50	1.48	1.59	1.51	1.61	1.47	1.42

CTE X 10⁻⁶/°C, R in μohm-m; density in g/cm³

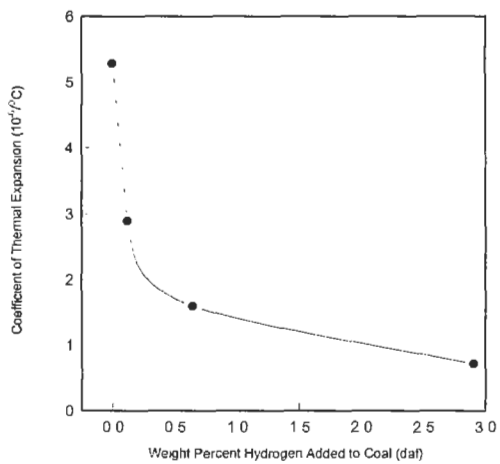


Figure 2. Effects of hydrogenation on CTE of coal-based graphites

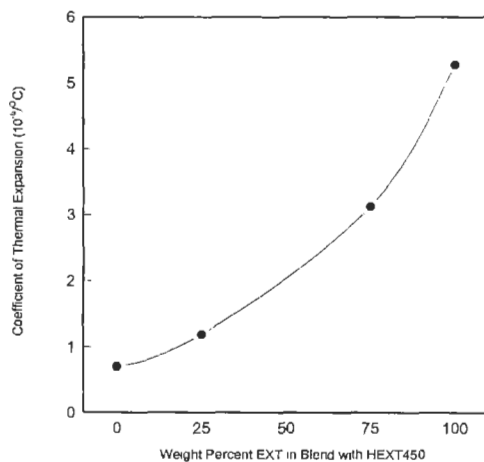


Figure 3. Effects of blend composition on CTE of graphites manufactured from WVGs 13421 derived products

These results are significant since they show that the ultimate characteristics of the graphite product can be unequivocally controlled by the blending of pitches. Further, the results indicate that a single coal source could be utilized, by appropriate treatment, to provide a slate of different pitches and cokes.

5 Summary

It has been demonstrated that a solvent-extraction procedure with N-methyl pyrrolidone is capable of producing coal-derived extract pitches with low-ash contents. Moreover, the properties of the pitches can be varied by partial hydrogenation of the coal prior to extraction. The yield of the pitches along with the physical and chemical properties of the cokes and graphites vary in an understandable fashion.

By a combination of pitch blending and/or hydrogenation, the properties of calcined cokes and their subsequent graphites can be controlled in a predictable manner. Thus by altering processing conditions, graphites ranging from very isotropic to very anisotropic can be produced from a single coal source. As acceptable petroleum supplies dwindle, this technology offers an alternate route for graphite manufacture from the abundant, world-wide reserves of coal.

6 Acknowledgments

The authors wish to thank I. C. Lewis and the UCAR Carbon Company for their assistance in the preparation and characterization of the coal-derived graphites. This work was partially funded by a grant from the U. S. Department of Energy DE-FG02-91NP00159. This support is gratefully acknowledged.

7 References

1. Reis, T., To coke, desulfurize, and calcine, *Hydrocarbon Processing*, 1975, **54**, 145-156.
2. Yamada, Y., Imamura, T., Kakiyama, H., Honda, H., Oi, S., and Fukuda, K., Characteristics of meso-carbon microbeads separated from pitch, *Carbon*, 1974, **12**, 307-319.
3. Edie, D. D., and Dunham, M. G., Melt spinning pitch-based carbon fibers, *Carbon*, 1989, **27**, 647-655.
4. Stansberry, P. G., Zondlo, J. W., Stiller, A. H., and Khandare, P. M., The production of coal-derived mesophase pitch. In *Proceedings of 22nd Biennial Conference on Carbon*, American Carbon Society, San Diego, CA, 1995, pp. 244-245.
5. Irwin, C., and Stiller, A., Carbon products and the potential for coal-derived

- feedstocks. Paper presented at Carbon Materials for Advanced Technologies, American Carbon Society Workshop, Oak Ridge, TN, 18 May 1994.
6. Mantell, C. L., *Carbon and Graphite Handbook*, Robert E. Krieger Publishing Company, Huntington, NY, 1968.
 7. Eser, S., and Jenkins, R. G., Carbonization of petroleum feedstocks I. relationships between chemical constitution of the feedstocks and mesophase development, *Carbon*, 1989, **27**, 877-887.
 8. Lewis, I. C., Chemistry of pitch carbonization, *Fuel*, 1987, **66**, 1527-1531.
 9. Derbyshire, F. J., Vitrinite structure: alterations with rank and processing, *Fuel*, 1991, **70**, 276-284.
 10. Song, C., and Schobert, H. H., Non-fuel uses of coals and synthesis of chemicals and materials. In *Preprint of Papers presented at the 209th American Chemical Society meeting*, Vol 40(2), Anaheim, CA, 1995, pp. 249-259.
 11. Seehra, M. S., and Pavlovic, A. S., X-ray diffraction, thermal expansion, electrical conductivity, and optical microscopy studies of coal-derived graphites, *Carbon*, 1993, **31**, 557-564.
 12. Owen, J., Liquefaction of coal. In *Coal and Modern Coal Processing: An Introduction*, ed. G. J. Pitt and G. R. Millward. Academic Press, New York, 1979, pp. 163-181.
 13. Renegathan, K., Zondlo, J. W., Mintz, E. A., Kneisl, P., and Stiller, A. H., Preparation of an ultra-low ash coal extract under mild conditions, *Fuel Processing Technology*, 1988, **18**, 273-278.
 14. Glenn, R. A., Nonfuel uses of coal. In *Chemistry of Coal Utilization, Supplementary Volume*, ed. H. H. Lowry. John Wiley and Sons, Inc., New York, 1963, pp. 1081-1099.
 15. Surjit, S., Coke for the steel industry. In *Proceedings of the Conference on Coal-Derived Materials and Chemicals*, ed. T. F. Torries and C. L. Irwin. West Virginia University, Morgantown, WV, 1991, pp. 1-14.
 16. Habermehl, D., Orywal, F., and Beycr, H. D., Plastic properties of coal. In *Chemistry of Coal Utilization, Second Supplementary Volume*, ed. M. A. Elliot. John Wiley and Sons, Inc., New York, 1981, pp. 317-368.
 17. Ragan, S., and Marsh, H., Review science and technology of graphite manufacture, *Journal of Materials Science*, 1983, **18**, 3161-3176.
 18. King, L. F., and Robertson, W. D., A comparison of coal tar and petroleum pitches as electrode binders, *Fuel*, 1968, **47**, 197-212.
 19. Hutcheon, J. M., Manufacture technology of baked and graphitized carbon bodies. In *Modern Aspects of Graphite Technology*, ed. L. C. F. Blackman. Academic Press, New York, 1970, pp. 49-78.
 20. Shah, Y. T., *Reaction Engineering in Direct Coal Liquefaction*. Addison-Wesley publishing Company, London, 1981.
 21. Given, P. H., Cronauer, D. C., Spackman, W., Lovell, H. L., Davis, A., and Biswas, B., Dependence of coal liquefaction behavior on coal characteristics I. vitrinite-rich samples, *Fuel*, 1975, **54**, 34-39.
 22. Seehra, M. S., Pavlovic, A. S., Babu, V. S., Zondlo, J. W., Stiller, A. H., and Stansberry, P. G., Measurement and control of anisotropy in ten coal-based graphites, *Carbon*, 1994, **32**, 431-435.

CHAPTER 8

Activated Carbon for Automotive Applications

PHILIP J. JOHNSON AND DAVID J. SETSUDA

*Ford Motor Company
Automotive Components Division
Dearborn, Michigan*

ROGER S. WILLIAMS

*Westvaco
Chemical Division
Covington, Virginia*

1 Background

Research dating back to the mid 1950's has shown that volatile organic compounds (VOC's) photochemically react in the atmosphere and contribute to the formation of ground level ozone, a precursor to smog [1]. Medical studies have shown that human exposure to ozone can result in eye and sinus tract irritation, and can lead to respiratory related illnesses [2]. Due to the unique and severe smog problems that affected many cities in the state of California, studies of the causes of air pollution were initiated in the 1950's [3]. Based on its findings, California formed the Motor Vehicle Pollution Control Board in 1960 to regulate pollution from automobiles.

The generation of air pollutants, including VOC's, from automotive vehicles was identified to come from two principal sources: vehicle exhaust emissions, and fuel system evaporative emissions [4]. Evaporative emissions are defined as the automotive fuel vapors generated and released from the vehicle's fuel system due to the interactions of the specific fuel in use, the fuel system characteristics, and environmental factors. The sources of the evaporative emissions are discussed below and, as presented in the remainder of this chapter, control of these evaporative emissions are the focus of the application of activated carbon technology in automotive systems.

1.1 Evaporative emission sources

Prior to the implementation of any evaporative emission controls, fuel vapors were freely vented from the fuel tank to the atmosphere. Diurnal, hot soak, running losses, resting losses, and refueling emissions are the typical evaporative contributions from a motor vehicle. Diurnal emissions occur while a vehicle is parked and the fuel tank is heated due to daily temperature changes. Hot soak emissions are the losses that occur due to the heat stored in the fuel tank and engine compartment immediately after a fully warmed up vehicle has been shut down. Running loss emissions are the evaporative emissions that are generated as a result of fuel heating during driving conditions. Resting losses are due to hydrocarbon migration through materials used in fuel system components. Refueling emissions occur due to the fuel vapor that is displaced from the fuel tank as liquid fuel is pumped in.

1.2 Development of evaporative emission controls

In 1968 California committed additional resources to fight its unique air pollution problems with the establishment of the California Air Resource Board (CARB). Although the federal government has jurisdiction over the states in the area of automotive emission control regulation, California has been given a waiver to implement its own regulations provided that they are more stringent than the federal requirements [5]. California has since been a leader in the development and implementation of increasingly stringent automotive emission control regulations.

The Environmental Protection Agency (EPA) was established in 1970 by an act of Congress, the primary purpose of the agency being to promulgate and implement environmental regulations that are mandated by law. Congress first mandated automotive pollution control regulations in the Clean Air Act (CAA) Amendments of 1970. The CAA was amended in 1977 and 1990 to further improve air quality. The primary purpose of the amendments was to push industry into developing and implementing control technologies. The 1990 CAA Amendment also gave other states the option of adopting the California regulations.

Industry has not always worked in full cooperation with government to meet the technology forcing standards. In the early 1970's, the U.S. auto industry was characterized by slow development of the required technologies to meet the regulations. The slow response and seemingly insurmountable technical issues forced congressional and administrative delays to the original regulatory implementation [1]. However, since the late 1970's, the auto industry has responded favorably, allocating enormous resources to meet the increasingly stringent regulations.

The buyers of motor vehicles have been substantially positive concerning the need to have cleaner running vehicles. Although the required emission control devices and other mandated safety equipment have increased the cost of new motor vehicles, sales have not been significantly effected. The current environmental awareness and concern are evidence of the general population's new found knowledge and acceptance of both mobile and stationary source emission controls.

1.3 Evaporative emission control measures

The earliest implementation of evaporative emission control occurred in 1963 when the State of California mandated that crankcase emissions be eliminated. This early regulation was easily met by venting crankcase emissions at a metered rate into the air induction system. The next areas to be regulated were the hot soak and diurnal losses, which California required starting in the 1970 model year. Prior to 1970, the uncontrolled hydrocarbon (HC) emission rate was reported to be 46.6 grams per vehicle for a one hour hot soak plus one hour heat build [6]. Canisters containing activated carbon were installed on vehicles to collect the hydrocarbons that were previously freely vented from the vehicles. These vapors are later purged (desorbed) from the canister by pulling air through the carbon bed and into the air induction stream.

The early test methodology [6] employed activated carbon traps sealed to possible HC sources, such as the air cleaner and fuel cap, during the test procedure. The carbon trap's weight was measured before and after the test procedure to establish the total emissions. General Motors [7] developed the Sealed Housing for Evaporative Determination (SHED) as a more precise and repeatable method to measure evaporative losses. The SHED method proved to be more accurate at measuring evaporative emissions that had previously escaped through openings other than where the carbon traps were attached. The EPA and CARB subsequently changed their test procedures from the carbon trap to the SHED method.

The early carbon trap and SHED methods measured two components of evaporative emissions. Hot soak emissions were measured for a one hour period immediately after a vehicle had been driven on a prescribed cycle and the engine turned off. Diurnal emissions were also measured during a one hour event where the fuel tank was artificially heated. The one hour fuel temperature heat build was an accelerated test that was developed to represent a full day temperature heat build.

The latest CARB/EPA procedures require diurnal emissions to be measured during a real time, three day test that exposes the complete vehicle to daily temperature fluctuations. This test method has been employed to more accurately reflect the real world diurnal emissions that occur. Running loss emission measurements were also initiated in the latest test procedures. Evaporative emissions are measured

while the vehicle is driven on a chassis dynamometer with heat applied to the fuel tank simulating a hot reflective road surface.

Onboard Refueling Vapor Recovery (ORVR) regulations were first proposed in 1987 but were met with a litany of technical and safety issues that delayed the requirement. The 1990 CAA amendments required the implementation of ORVR and the EPA regulation requires passenger cars to first have the systems starting in 1998. The ORVR test will be performed in a SHED and will require that not more than 0.2 grams of hydrocarbon vapor per gallon of dispensed fuel be released from the vehicle.

Fig.1 shows the typical events in the EPA's evaporative emission control test sequence. These test procedures cover the entire range of evaporative emissions, including the refueling emissions which are now being addressed through the ORVR system development. Typically, emission regulations are phased in over a number of years. Manufacturers are required to sell a defined percentage of their fleet each year that meet the requirements. Globally, the United States has led the way in terms of technology forcing evaporative emission regulations.

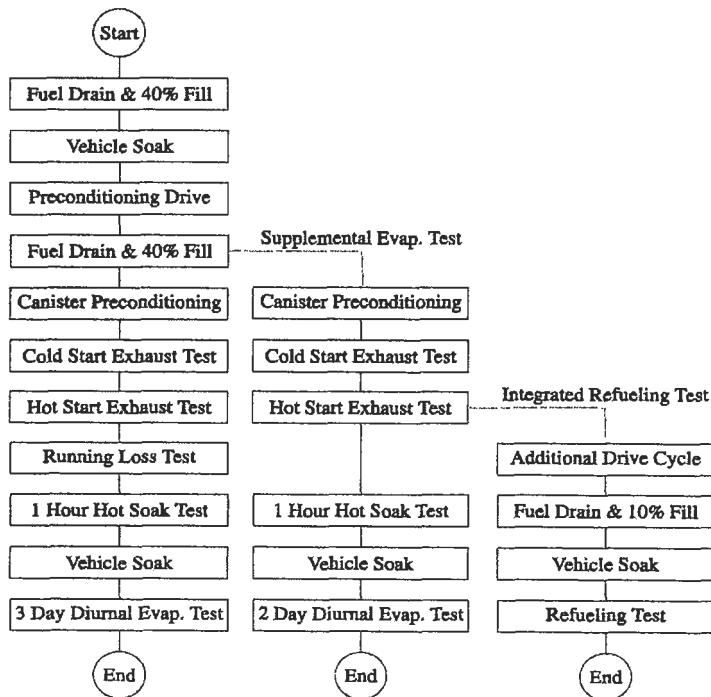


Fig. 1. U. S. EPA federal test procedure

The following countries also have evaporative emission regulations; Canada, European Economic Community (EEC), Japan, Brazil, Mexico, Australia, South Korea. Regulations in these countries have requirements that are typically less stringent than the U.S. imperatives. Table 1 depicts the chronology of evaporative emission regulation developments in the United States.

Table 1. Chronology of U. S. evaporative emission development [1]

Model Year	Mandated Sales Area	Test Method	Certification Standard	Note
1970	California	Carbon Trap	6 grams HC	One hour test
1971	49 States	Carbon Trap	6 grams HC	One hour test
1972	50 States	Carbon Trap	2 grams HC	One hour test
1978	50 States	SHED	6 grams HC	One hour test
1980	California	SHED	2 grams HC	One hour test
1981	50 States	SHED [8]	2 grams HC	One hour test
1995	California	VT SHED [9]	2 grams HC	Three day test
1995	California	Run Loss	0.05 g/mile	
1996	50 States	VT SHED	2 grams HC	Three day test
1996	50 States	Run Loss	0.05 g/mile	
1998	50 States	ORVR [10]	0.2 g/gal	Passenger cars
2001	50 States	ORVR	0.2 g/gal	Lt Duty Trucks

2 Activated Carbon

Activated carbon is an amorphous solid with a large internal surface area/pore structure that adsorbs molecules from both the liquid and gas phase [11]. It has been manufactured from a number of raw materials including wood, coconut shell, and coal [11,12]. Specific processes have been developed to produce activated carbon in powdered, granular, and specially shaped (pellet) forms. The key to development of activated carbon products has been the selection of the manufacturing process, raw material, and an understanding of the basic adsorption process to tailor the product to a specific adsorption application.

2.1 Production methods

Based upon raw material and intended application, the manufacturing of activated carbon falls into two main categories: thermal activation and chemical activation. In general, thermal activation involves the heating/gasification of carbon at high temperatures [13], while chemical activation is characterized by the chemical dehydration of the raw material at significantly lower temperatures [11,14].

2.1.1 Thermal activation processes

Thermal activation is characterized by two processing stages: thermal

decomposition or carbonization of the precursor, and gasification or activation of the carbonized char material. In the carbonization step, hydrogen and oxygen are removed from the precursor (raw material) to generate a basic carbon pore structure. During activation, an oxidizing atmosphere such as steam is used to increase the pore volume and particle surface area through elimination of volatile products and carbon burn-off [14]. Thermal activation precursors include coal and coconut shells. Thermal activation is usually carried out in directly fired rotary kilns or multi-hearth furnaces, with temperatures of greater than 1000 °C achieved in process. A thermal activation process for the production of activated carbon from coal is shown in Fig. 2 [11].

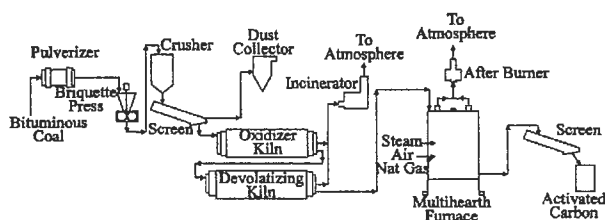


Fig. 2. Thermal activation process for production of activated carbon. Reprinted from [11], copyright © 1992 John Wiley & Sons, Inc., with permission.

2.1.2 Chemical activation processes

In chemical activation processes, the precursor is first treated with a chemical activation agent, often phosphoric acid, and then heated to a temperature of 450 - 700 °C in an activation kiln. The char is then washed with water to remove the acid from the carbon. The filtrate is passed to a chemical recovery unit for recycling. The carbon is dried, and the product is often screened to obtain a specific particle size range. A diagram of a process for the chemical activation of a wood precursor is shown in Fig. 3.

2.2 Applications/characteristics of activated carbon

The activated carbon materials are produced by either thermal or chemical activation as granular, powdered, or shaped products. In addition to the form of the activated carbon, the final product can differ in both particle size and pore structure. The properties of the activated carbon will determine the type of application for which the carbon will be used.

2.2.1 Liquid phase applications

Liquid phase applications account for nearly 80% of the total use of activated carbon. Activated carbon used in liquid phase applications typically have a high fraction of pores in the macropore (>50nm) range. This is to permit the liquid phase molecules to diffuse more rapidly into the rest of the pore structure [15].

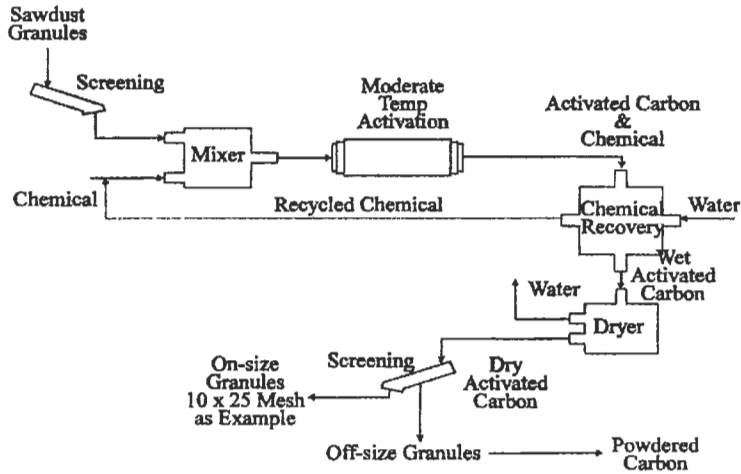


Fig. 3. Chemical activation process for production of activated carbon

The principal liquid phase applications, the type of carbon used, and 1987 consumption levels are presented in Table 2.

Table 2. Liquid phase activated carbon consumption [11,16]. Reprinted from [11], copyright © 1992 John Willey & Sons, Inc., with permission.

U.S. 1987 consumption, metric ton (1000's)

	Granular/Shaped	Powdered	Total
Potable water	4.5	13.6	18.1
Wastewater, industrial	6.4	6.6	13.0
Wastewater, municipal	0.9	2.0	2.9
Sweetener decolorization	6.8	9.1	15.9
Chemical processing and misc.	4.1	2.3	6.4
Food, beverage, and oils	0.9	3.9	4.8
Pharmaceuticals	2.0	.3	4.3
Mining	1.6	2.5	4.1
Groundwater	0.9	2.3	3.2
Household uses	1.4	0.9	2.3
Dry cleaning	0.7	0.4	1.1
Electroplating	<u>0.2</u>	<u>0.4</u>	<u>0.6</u>
Total	30.4	46.3	76.7

2.2.2 Gas phase applications

Gas phase applications of activated carbon fall into the main categories of separation, gas storage, and catalysis. These applications account for about 20% of the total use of activated carbon, with the majority using either granular or pellet type. Table 3 shows the major gas phase applications, again along with 1987 consumption levels.

Table 3. Gas phase activated carbon consumption. Reprinted from [11], copyright © 1992 John Willey & Sons, Inc., with permission.

U.S. 1987 consumption, metric ton (1000's)	
Solvent Recovery	4.5
Automotive/Gasoline Recovery	4.1
Industrial off-gas Control	3.2
Catalysis	2.7
Pressure Swing Separation	1.1
Air Conditioning	0.5
Gas Mask	0.5
Cigarette Filters	0.5
Nuclear Industry	<u>0.3</u>
Total	17.4

2.2.3 Physical properties

Properties for typical activated carbons used in both liquid and gas phase applications are shown in Table 4.

2.3 Automotive applications

The major automotive application for activated carbon is the capture of gasoline vapors from vehicle fuel vapor systems. With the creation of emission control standards in the early 1970's, vehicles began to be equipped with evaporative emission control systems [17,18]. The activated carbons to be used in these emission control systems were required to adsorb gasoline vapors at high efficiency and to release them during the purge regeneration cycle. The durability of the activated carbon became an important characteristic, as the adsorption/purge regeneration cycle would be repeated many times over the life of a vehicle [12]. The operation of the evaporative emission control system is detailed in Section 3.

Initial evaporative emission control systems utilized coal-base granular carbons, which were followed by chemically activated, wood-base carbons [19]. Increasingly stringent emission control standards [20-22] led to further activated carbon development, including the production of a pellet shaped product specifically designed for automotive applications [19]. The most recent emission control requirements have addressed capturing vapors emitted during refueling [23,24], which will require a better understanding of the performance of activated carbon in hydrocarbon adsorption over a larger range of operation.

Properties of activated carbons produced by Westvaco for automotive applications are presented in Table 5.

Table 4. Properties of selected activated carbon products. Reprinted from [11], copyright © 1992 John Wiley & Sons, Inc., with permission.

Manufacturer	Gas-Phase Carbons			Liquid-Phase Carbons			
	Calgon	Norit	Westvaco	Calgon	Norit	Westvaco	
Precursor	Coal	Peat	Wood	Coal	Peat	Wood	
Product Grade	BPL	B4	WV-A 1100	SGL	SA 3	SA-20	
Product Form	Granular	Extruded	Granular	Granular	Powdered	Powdered	
Product Property	Typical Range						
Particle Size (U.S. mesh)	<4	12x30	3.8 mm dia.	10x25	8X30	64% <325	65-85% <325
Apparent Density (g/cm ³)	0.2-0.6	>0.48	0.43	0.27	0.52	0.46	0.34-0.37
Particle Density (g/cm ³)	0.4-0.9	0.8	-	0.5	0.8	-	-
Hardness or Abrasion Number	50-100	>90	99	-	>75	-	-
Ash (wt. %)	1-20	<8	6	-	<10	6	3-5
BET Surface Area (N ₂ , m ² /g)	500-2500	1050-1150	1100-1200	1750	900-1000	750	1400-1800
Total Pore Volume (cm ³ /g)	0.5-2.5	0.8	0.9	1.2	0.85	-	2.2-2.5
CCl ₄ Activity (wt. %)	35-125	>60	-	-	-	-	-
Butane Working Capacity (g/100cm ³)	4-14	-	-	>11	-	-	-
Iodine Number	500-1200	>1050	-	-	>900	800	>1000
Decolorizing Index (Westvaco)	15-25	-	-	-	-	-	>20
Molasses Number (Calgon)	50-250	-	-	-	>200	-	-
(Norit)	300-1500	-	-	-	-	440	-
Heat Capacity (100°C, cal/g/K)	0.2-0.3	0.25	-	-	0.25	-	-
Thermal Conductivity (W/m/K)	0.05-0.1	-	-	-	-	-	-

Table 5. Properties of Westvaco automotive grade activated carbons [19]

Grade	WV-A 900	BAX 950	WV-A 1100	BAX 1100	BAX 1500
Shape	Granular	Pelleted	Granular	Pelleted	Pelleted
Mesh Size	10x25	2mm	10x25	2mm	2mm
BET Surface Area (m ² /g)	1400-1600	1300-1500	1600-1900	1400-1600	1800-2000
Butane Working Capacity (g/100ml)	9.0 min	9.5 min	11.0 min	11.0 min	15.0 min
Apparent Density (g/cm ³)	0.2-0.32	0.3-0.4	0.2-0.32	0.3-0.4	0.27-0.35
Moisture, as Packed (%)	10 max	5 max	10 max	5 max	5 max
Particle Size (U.S.Sieve Series)					
Oversize (%)	8 max	2 max	8 max	2 max	2 max
Undersize (%)	5 max				

3 Vehicle Fuel Vapor System

A current vehicle fuel system designed for evaporative emission control should address enhanced SHED, running loss, and ORVR emission level requirements (see Table 1). A typical vehicle fuel system is shown in Fig. 4. The primary functions of the system are to store the liquid and vapor phases of the fuel with acceptable loss levels, and to pump liquid fuel to the engine for vehicle operation. The operation of the various components in the fuel system, and how they work to minimize evaporative losses during both driving and refueling events, is described below.

3.1 Fuel system operation during driving events

The liquid fuel handling components of the fuel system include the fuel filler pipe, fuel tank, fuel pump, and the fuel supply and return lines. The fuel tank is a low pressure, low hydrocarbon emission vessel designed to contain both the liquid and vapor phases of the fuel. An electric pump located inside the fuel tank is used to transfer liquid fuel from the tank to the engine. The fuel in the tank is suctioned from a small reservoir in the tank which minimizes liquid level transients caused by vehicle motion.

The fuel is delivered to the engine by one of two methods: recirculating or return-less. In a recirculation system, as is shown with dashed lines in Fig. 4, the engine fuel injectors draw a portion of the fuel being delivered in the fuel rail, and the

remainder of the fuel is returned to the fuel tank. In a return-less design, the fuel sent to the fuel injectors is not recirculated back to the fuel tank. Instead, either a mechanical control or a variable speed electronic pump controller maintains the required pressure and flow rate to the injectors.

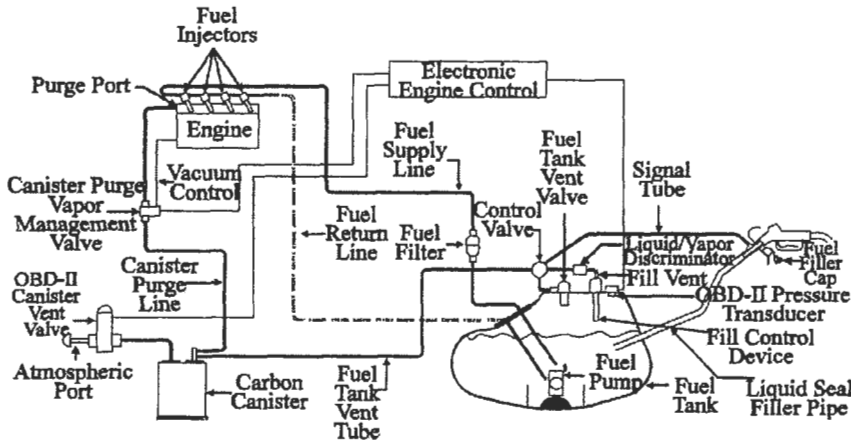


Fig. 4. Representative vehicle fuel system with evaporative emission control

The key components in the fuel vapor control system include the fuel tank, vapor vent valves, vapor control valve, vapor tubing, the activated carbon canister, and the engine vapor management valve (VMV) [25,26]. During normal vehicle operation, fuel tank vapor pressure is relieved through the use of vapor vent valves installed in the vapor dome of the fuel tank. The vent valves are designed to allow for the flow of fuel vapor from the tank, and to assure that liquid fuel does not pass through the valve.

The vapor vent valves are connected to the tank vapor control valve, and ultimately to the carbon canister by tubing that is resistant to swelling in the presence of fuel vapors. The tubing material must also have a low HC permeation rate, so that the evaporative emissions are not increased due to release of HC molecules. The tank vapor control valve connects the carbon canister to two fuel tank vapor sources: the vapor vent valve lines and a refueling vent tube.

During vehicle operations similar to those experienced during the three day diurnal evaporative test outlined in Fig. 1, the following operations occur in the evaporative emission control system:

- a) Fuel vapors generated in the tank are released through the vapor vent valves and the vapor control valve to the carbon canister for storage.
- b) The purge control module (PCM) control strategy senses when the canister

- contains sufficient HC vapor which can be purged from the canister and then injected into the engine inlet manifold for combustion.
- c) Purging is accomplished by using the engine inlet manifold vacuum to draw fresh air into the carbon canister through the atmospheric port. The fresh air causes the HC vapors to desorb from the carbon, and the vapor stream is routed to the engine through the canister purge vapor management valve.
 - d) The PCM strategy accounts for the injection of the purged vapors, and adjusts the engine operating conditions to maintain the stoichiometric air/fuel ratio required in the combustion chambers.

3.2 Fuel system operation during refueling events

Fuel system components involved in the refueling process include the fuel tank, filler pipe, filler cap, vapor control valve, liquid-vapor discriminator (LVD) valve, and the carbon canister [27,28]. During vehicle refueling, which is monitored during the integrated refueling test as outlined in Fig. 1, the following operations occur in the evaporative emission control system:

- a) Removal of the filler cap exposes the filler tube to atmospheric pressure, which causes the vapor control valve to close the path between the vapor vent valves and the canister, and open the path between the tank refueling vent tube and the canister.
- b) When the fuel is dispensed into the tank, the flow of the liquid fuel is used to carry vapors away from the filler inlet. As the liquid fuel enters the tank, the vapors in the tank displaced by the incoming liquid are directed into the canister using the natural pressure in the tank.
- c) After refueling, securing the filler cap causes the vapor control valve to close the vapor path from the refueling vent tube and reopen the path from the vapor vent valves to the canister.
- d) The canister is protected from liquid fuel in the refueling vent line by an LVD valve installed between the fuel tank vent and the vapor control valve.

4 Adsorption

4.1 Adsorption fundamentals

Adsorption on solids is a process in which molecules in a fluid phase are concentrated by molecular attraction at the interface with a solid. The attraction arises from van der Waals forces, which are physical interactions between the electronic fields of molecules, and which also lead to such behavior as condensation. Attraction to the surface is enhanced because the foreign molecules tend to satisfy an imbalance of forces on the atoms in the surface of a solid compared to atoms within the solid where they are surrounded by atoms of the

same kind. The material adsorbing onto the solid phase is referred to as the adsorbate or adsorptive, and the solid is called the adsorbent.

Adsorbents, and activated carbon in particular, are typically characterized by a highly porous structure. Adsorbents with the highest adsorption capacity for gasoline or fuel vapors have a large pore volume associated with pore diameters on the order of 50 Angstroms or less. When adsorption occurs in these pores, the process is comparable to condensation in which the pores become filled with liquid adsorbate. Fig. 5 depicts the adsorption process, including transfer of adsorbate molecules through the bulk gas phase to the surface of the solid, and diffusion onto internal surfaces of the adsorbent and into the pores.

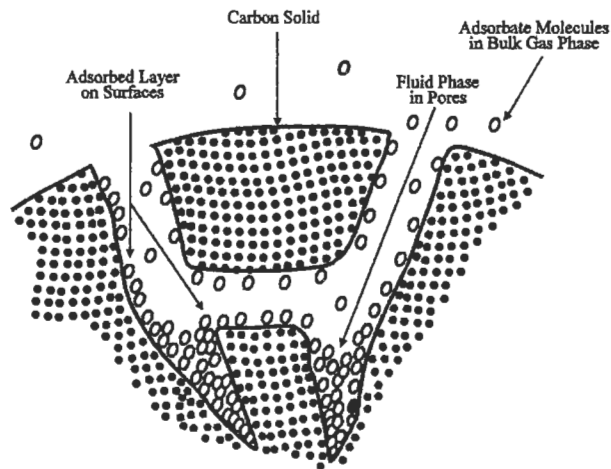


Fig. 5. Transfer of adsorbate molecules to adsorbent. Reprinted from [29] with permission, copyright © 1984 The McGraw Hill Companies.

4.1.1 Adsorption equilibrium

Adsorption is a dynamic process in which some adsorbate molecules are transferring from the fluid phase onto the solid surface, while others are releasing from the surface back into the fluid. When the rate of these two processes becomes equal, adsorption equilibrium has been established. The equilibrium relationship between a specific adsorbate and adsorbent is usually defined in terms of an adsorption isotherm, which expresses the amount of adsorbate adsorbed as a function of the gas phase concentration, at a constant temperature.

Five general types of isotherms have been observed, and the shapes of these characteristic isotherms are shown in Fig. 6 [29]. The Type I isotherm represents systems where only monolayer adsorption occurs, while Type II indicates the

formation of adsorbed multi-layers. A Type III isotherm develops in systems where the amount of material adsorbed increases without limit as its relative saturation approaches unity. The Type IV isotherm describes a multi-layer adsorption process where complete filling of the smallest capillaries has occurred, while the Type V isotherm is typical of systems in which condensation of the adsorbate has occurred. Adsorption of the hydrocarbons found in fuel vapor demonstrates a Type II equilibrium behavior.

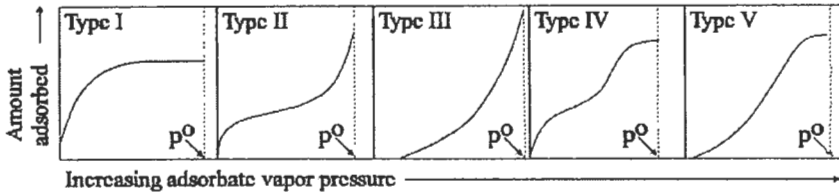


Fig.6. Characteristic isotherm types. Reprinted from [29] with permission, copyright © 1984 The McGraw Hill Companies

4.1.2 Mass and energy balances

Adsorption onto a solid is always accompanied by a liberation of heat. For physical adsorption, this exothermic heat of adsorption is always greater than the heat of condensation of the adsorbate.

Because of this heat generation, when adsorption takes place in a fixed bed with a gas phase flowing through the bed, the adsorption becomes a non-isothermal, non-adiabatic, non-equilibrium time and position dependent process. The following set of equations defines the mass and energy balances for this dynamic adsorption system [30,31]:

Component mass balance

$$\frac{\partial C_i}{\partial t} + V \frac{\partial C_i}{\partial x} + \frac{\rho_s(1-\epsilon)}{\rho_g \epsilon} \frac{\partial q_i}{\partial t} = 0 \quad i=1,2,\dots,n \quad (1)$$

where

- C_i = Gas phase concentration of adsorbate i , mols i /mols gas
- V = Fluid phase velocity, m/s
- t = Time, s
- x = Axial coordinate, m
- ρ_s = Solid phase density, g/m³
- ϵ = Void fraction of adsorbent bed
- q_i = Solid phase concentration of adsorbate i , mols i / g solid
- ρ_g = Gas phase density, mols/m³

n = Number of adsorbates in the system

Total energy balance

$$\frac{\partial T_g}{\partial t} + V \frac{\partial T_g}{\partial x} + \frac{\rho_s C_{p_s} (1-\epsilon)}{\rho_g C_{p_g} \epsilon} \frac{\partial T_s}{\partial t} + \frac{\rho_s (1-\epsilon)}{\rho_g C_{p_g} \epsilon} \sum \Delta H_i \frac{\partial q_i}{\partial t} = 0 \quad (2)$$

where T_g = Temperature of gas phase, K
 C_{p_s} = Heat capacity of solid phase, J/mol K
 C_{p_g} = Heat capacity of gas phase, J/mol K
 T_s = Temperature of solid, K
 ΔH_i = Heat of adsorption of component i, J/mol

Solid phase mass balance

$$\frac{\partial q_i}{\partial t} = \frac{K p_i a}{\rho_s} (q_i^* - q_i) \quad (3)$$

where $K p_i$ = Overall mass transfer coefficient, g/m² s
 a = Surface area per unit volume of adsorbent particle, m²/m³
 q_i^* = Solid phase concentration of adsorbate at equilibrium with gas phase, mol i / g solid

Solid phase energy balance

$$\frac{\partial T_s}{\partial t} = \frac{h a}{\rho_s C_{p_s}} (T_g - T_s) - \frac{1}{C_{p_s}} \sum \Delta H_i \frac{\partial q_i}{\partial t} \quad (4)$$

where h = Overall heat transfer coefficient, J/m² sK

Velocity equation

$$\rho_g \frac{\partial V}{\partial x} = -\sum K p_i a (q_i^* - q_i) \quad (5)$$

The resulting adsorption behavior in an unsteady-state fixed bed adsorber is illustrated in Fig. 7 [32]. As the gas stream enters the carbon bed, which is initially free of adsorbate, the adsorbate is rapidly adsorbed, and the gas is essentially free of adsorbate as it continues through the carbon bed. As the adsorbent at the inlet

of the bed becomes saturated, the adsorption process takes place further along the bed, and thus the adsorption zone moves through the bed until the zone reaches the end of the bed. At this point, breakthrough occurs, and the exit concentration of adsorbate begins to rise.

4.2 Application to evaporative emission vapors

Evaporative emissions from vehicle fuel systems have been found to be a complex mixture of aliphatic, olefinic, and aromatic hydrocarbons [20,24,33]. However, the fuel vapor has been shown to consist primarily of five light paraffins with normal boiling points below 50 °C: propane, isobutane, n-butane, isopentane, and n-pentane [33]. These five hydrocarbons represent the more volatile components of gasoline, and they constitute from 70 to 80 per cent mass of the total fuel vapor [24,33].

4.2.1 Adsorption of fuel vapors

During the process of adsorbing fuel vapors onto a bed of activated carbon, the higher molecular weight components of the vapor mixture tend to build up within the smaller pores in the carbon. While purging (desorption) of the carbon bed is capable of removing a large portion of the adsorbed fuel vapor, these heavier components are not completely removed, and this residual vapor is left in the activated carbon, and is commonly referred to as the "heel" of the carbon bed.

Once the heel has been established in the carbon bed, the adsorption of the fuel vapor is characterized by the adsorption of the dominant light hydrocarbons composing the majority of the hydrocarbon stream. Thus it is common in the study of evaporative emission adsorption to assume that the fuel vapor behaves as if it were a single light aliphatic hydrocarbon component. The predominant light hydrocarbon found in evaporative emission streams is n-butane [20,33]. Representative isotherms for the adsorption of n-butane on activated carbon pellets, at two different temperatures, are shown in Fig. 8. The pressure range covered in the Fig. 8, zero to 101 kPa, is representative of the partial pressures encountered in vehicle fuel vapor systems, which operate in the ambient pressure range.

The n-butane isotherms shown in Fig. 8, in the concentration range up to about 2 per cent n-butane, can be expressed by the Dubinin-Astakov equation [34]:

$$\frac{M}{\rho} = W_0 \exp[-(B_0 RT \ln(\frac{P_0}{P}))^n] \quad (6)$$

where

$$M = \text{Mass of n-butane adsorbed, g/g carbon}$$

ρ	=	Adsorbate liquid density, g/ml
R	=	Universal gas constant, J/mol K
T	=	Temperature, K
P_0	=	Vapor pressure of n-butane at temperature T, kPa
P	=	Pressure of n-butane, kPa
W_0, B_0, n	=	Equation constants determined from isotherm curve fitting

Above a concentration of 2 percent, additional terms must be added to the Dubinin expression, or an empirical expression can be used.

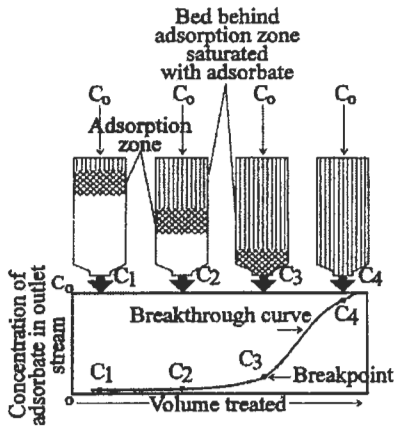


Fig. 7. Movement of adsorption zone through fixed bed adsorber. Reprinted from [32], copyright © 1986 Gulf Publishing Company, with permission

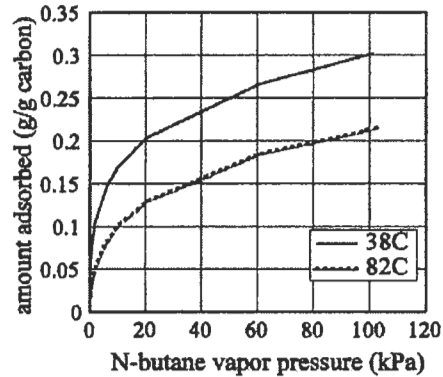


Fig. 8. N-butane adsorption isotherm

4.2.2 Loading and purging of fuel vapors

The n-butane isotherms and the mass and energy balance equations can be used to demonstrate the loading and purging of a carbon canister (a bed of activated carbon pellets usually housed in a plastic shell) in the range of conditions typically found during vehicle evaporative emission control. The loading and break through curves for an activated carbon canister containing one liter of carbon are shown in Fig. 9.

In this example, the one liter canister is designed as a cylinder with a length-to-diameter (L/D) ratio of five. The vapor feed stream to the canister is a 50/50 mixture of n-butane and air, and the inlet flow rate is set at 40 grams per hour of n-butane. The curves in the Fig.9 show that break through occurs shortly after the 100 minute point in the load. Up to break-through, the activated carbon bed has adsorbed about 65 grams of HC.

Fig. 10 shows the curves for the canister weight and the amount of vapor removed for the example canister during a purge event. In this case, the canister is being purged with an air stream flowing at a rate of about 22.6 liters per minute for a total of 15 minutes. The curves show that the n-butane desorption rate is initially quite rapid, and then it levels out at a lower rate.

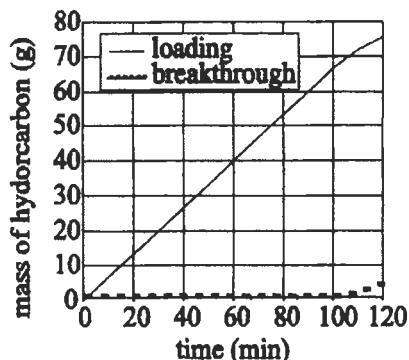


Fig. 9. Loading and breakthrough curves in a one liter canister, 40 g/hr N-butane feed rate

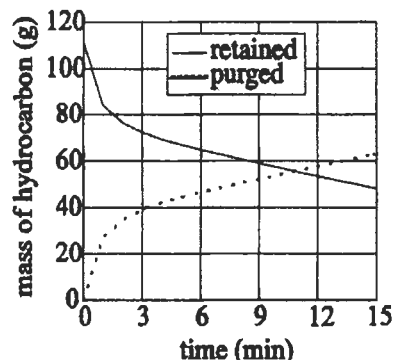


Fig. 10. Purging (desorption) curves for the N-butane in a one liter canister

5 Carbon Canister Design

As initially discussed in Section 3, carbon canisters are used in the automotive emission control system to temporarily store hydrocarbon vapors. The vapors are later purged into the air charge stream of the air induction system, thus regenerating the carbon canister. Carbon canister design is dependent on the characteristics of the vapors sent to the canister and the amount of purge air available. In the following section, factors that affect the performance of the evaporative emission control system will be discussed.

5.1 Effect of carbon characteristics on design

5.1.1 Pore volume distribution

The primary carbon characteristic that has influence on the carbon canister design is the pore volume distribution [35]. The plot in Fig. 11 shows the relationship between the relative, or normalized, pore volume in the mesopores (2-50 nm) and the butane working capacity (BWC). The BWC is defined as the amount of butane purged from a saturated activated carbon bed using dry air at 25 °C. It is most often expressed as grams butane purged per 100 ml carbon bed. The relationship was examined by determining the correlation coefficients for the best fit straight line when BWC was plotted against pore volume in defined size ranges for a

variety of activated carbons. The highest correlation coefficient was obtained when the BWC was plotted against the pore volume in the mesopores. The data indicate that there is a strong relationship between the pore volume in the mesopores and the BWC.

Gasoline working capacity (GWC) also shows a strong relationship with the pore volume in the mesopores. Similar to BWC, GWC is a measure of adsorption capacity in which actual gasoline vapors are used as the adsorbate. The relationship between the BWC and GWC is shown in Fig. 12. The data shows a strong relationship between the BWC and GWC. The relationship would be expected since both the BWC and GWC have excellent linear correlations with the pore volume in the small mesopores.

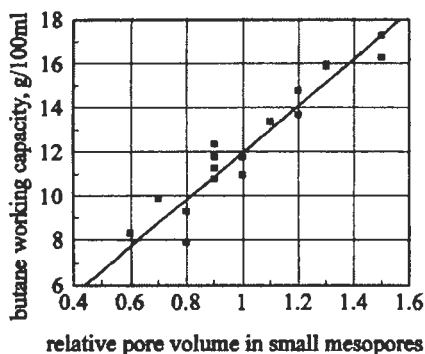


Fig. 11. Relationship between pore volume and butane working capacity

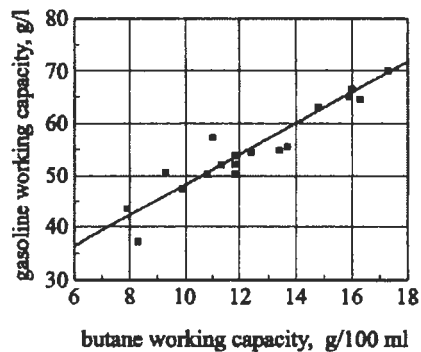


Fig. 12. Relationship between butane and gasoline working capacities

Commercially available carbons for automotive applications have a range of BWC from 9.0 to 15.0 g/100ml. Higher working capacities are simply a function of increasing the relative pore volume distribution in the small mesopores. Increasing the working capacity allows a smaller volume and lighter weight carbon canister to be packaged on the vehicle.

5.1.2 Carbon particle size

The second carbon characteristic affecting performance of carbon canisters is the carbon particle size. Increasing particle size has the primary effect of lowering restriction through the carbon bed. During refueling on vehicles equipped with ORVR systems the nominal gasoline vapor loading rate to the canister will be 50 grams/minute. At these high loading rates, high pressure drops through the canister can cause premature liquid shutoff of the dispensed fuel and unacceptable hydrocarbon emissions.

The pressure drop of a one liter canister during an ORVR event was studied. Canisters were filled with a pelletized carbon with a mean particle diameter of 2.1 mm and a coal granular carbon with a mean diameter of 1.3 mm. During the canister loading of 50 grams/min the canister with the 2.1 mm pellet had a pressure drop that increased from 0.35 to 0.55 kPa (1.4 to 2.2 inches of water). The granular carbon experienced a pressure drop of 0.98 to 1.5 kPa (3.9 to 6.0 inches of water) under the same conditions.

Canister working capacity was studied for a 1.27 mm mean diameter granular versus 2.1 mm mean diameter pellet carbons of equal BWC. Under the ORVR loading conditions the granular carbon had a 6-12% higher GWC. However, the high pressure drop of the granular carbon would make it very difficult to use in an ORVR system.

Another way to examine the effect of carbon particle size on kinetics is to look at the bleed emissions from a carbon canister [20,35]. Bleed emissions are those emissions that occur prior to break through. They are the result of the diffusion of gasoline vapor components that can develop during extended soak times between purge and adsorption events.

The plot in Fig. 13 shows the bleed emissions that were measured after a 24 hour soak. Two canisters were tested, one loaded with a wood granular carbon with a mean particle diameter of 1.27 mm, the second with a wood pellet carbon with a mean particle diameter of 2.10 mm. Both carbon samples had equal BWC of 11.4 g/100ml. Although both carbons had the same BWC, the larger pellet carbon had lower bleed emissions. These diffusion results are expected in light of Fick's Law.

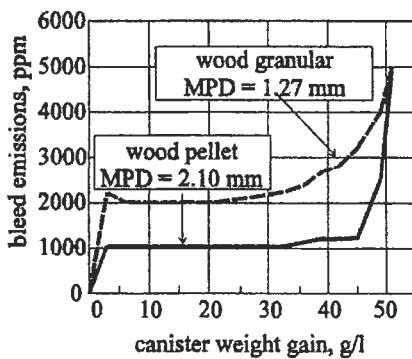


Fig. 13. Bleed emissions after 24 hour soak

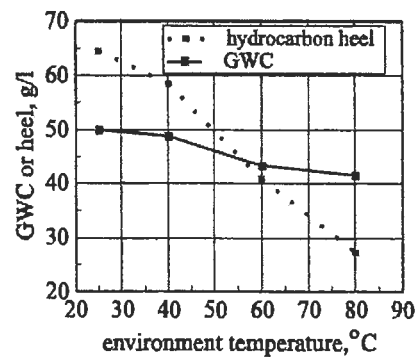


Fig. 14. Effect of environmental temperature

5.2 Canister design characteristics (capacity vs.flow)

5.2.1 Environmental temperature

The operating environmental temperature has an effect on the carbon canister performance [20]. Fig. 14 shows a 10% degradation in GWC as the environmental temperature increases from 25 to 80 °C. The hydrocarbon heel decreases by 55% during the same test. The hot environment helps to purge out the canister, but adsorption is reduced under the same conditions. Ideally the canister would be packaged in an area where it would not pick up heat from vehicle operation.

5.2.2 Heat of adsorption

Heat of adsorption within the activated carbon bed has a negative effect on the GWC. The heat build within the carbon bed increases as the mass of fuel vapors sent to the canister in a given time increase. This has a significant impact on canisters designed to meet the ORVR regulation. Fig. 15 shows the GWC as a function of loading rate. The data shows a 35% reduction in GWC when going from a loading rate of 1 g/min to the ORVR rate of 50 g/min. This reduction in working capacity will tend to cause the volume of activated carbon in ORVR canisters to increase compared with enhanced evaporative emission canisters.

5.2.3 Purge volume

During the cold start, hot start, and running loss driving portions of the Federal Test Procedure(FTP) shown in Fig. 1, approximately 200 bed volumes (200 liters or 7 cubic feet per liter of activated carbon) of purge air can be expected prior to the start of the three day diurnal test. During the two day "Short" diurnal test cycle, the purge volume is reduced by approximately 30% due to exclusion of the running loss emission test. Vehicles that have higher purge air rates during the prescribed driving cycles will have higher canister working capacities. The working capacity of a carbon canister can be increased if the purge air volume is increased [20,36]. Fig. 16 shows the effect of purge volume on GWC for a 11.4 g/ml granular activated carbon.

5.2.4 Canister geometry

The three day diurnal and ORVR test procedures will require significant refinements in canister designs to meet the new test standards. New canister designs will incorporate long diffusion paths and multiple carbon beds to adsorb fuel vapors during the diurnal events without break through. Observation of the GWC indicate that the working capacity of activated carbon increases with increasing L/D ratios [36]. In general, the working capacity of activated carbon reaches its maximum with canister L/D ratios between 3.0 and 6.0.

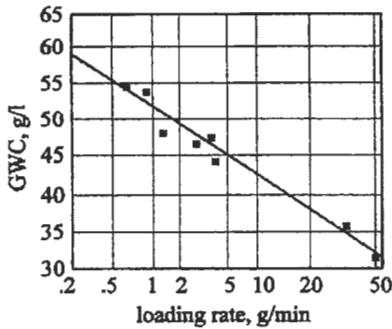


Fig. 15. Effect of vapor loading rate on gasoline working capacity

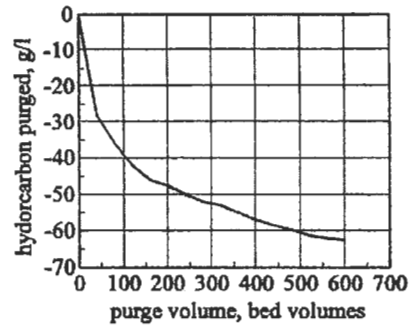


Fig. 16. Effect of purge volume on gasoline working capacity

Hydrocarbon vapor migration within the carbon canister is a significant factor during the real time diurnal test procedure. The phenomenon occurs after the canister has been partially charged with fuel vapors. Initially the hydrocarbons will reside primarily in the activated carbon that is closest to the fuel vapor source. Over time, the hydrocarbons will diffuse to areas in the carbon bed with lower HC concentration. Premature break through caused by vapor migration for two different canisters is shown in Fig. 17. The canister with the L/D ratio of 5.0 shows substantially lower bleed emissions than the canister with an L/D ratio of 3.0.

5.2.5 Canister orientation

During low fuel vapor flow rates gravity can have some measurable effect on loading and distribution. The fuel vapors will tend to be pulled toward the ground, and this may affect canister performance. At higher flow rates the effects of gravity are difficult to measure due to overwhelming flow effects. Orientation effects on canister bleed emissions are shown in Fig. 18. The data indicates that canisters with the atmospheric vent located on the bottom tend to lose vapors at a higher rate than if the vent is located at the top of the canister.

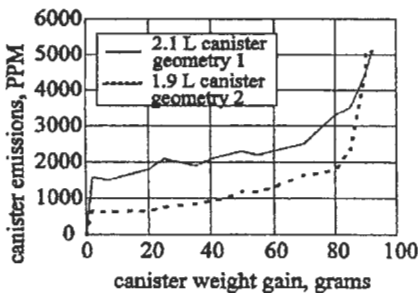


Fig. 17. Vapor migration: effect of canister geometry

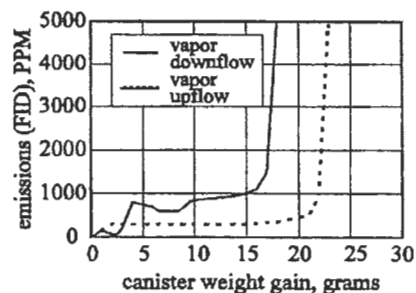


Fig. 18. Vapor migration: effect of canister orientation

5.3 Effect of other parameters

There are many other factors that can affect the performance and on-vehicle reliability of activated carbon canisters. The following items shown in Table 6 represent some of the more important factors that must be taken into consideration when designing an evaporative emission canister.

Table 6. Other parameters/operating conditions affecting canister performance and design

Recirculating Fuel System
Non-Recirculating Fuel System
Single vs. Multiple Carbon Beds
Gasoline vs. Alcohol-based Fuels
Liquid Fuel Ingestion into Carbon Bed
Water Ingestion into Carbon Bed
Dispensed Fuel Temperature
Dispensed Fuel Rate

6 Application of Canisters in Running Loss Emission Control

The use of activated carbon canisters in the control of running loss evaporative emissions will be presented through the use of an example vehicle application. In this example, the vehicle to be studied is a representative standard size sedan equipped with a 3.0 liter, V6 engine and a 72 liter (18 gallon) fuel tank. The vehicle is assumed to have an evaporative emission control system similar to the one presented in Section 3.

The performance of the evaporative emission control system on this example vehicle will be studied as the vehicle goes through a cycle similar to the three-day diurnal evaporative test procedure presented in Fig. 1. The three-day diurnal test is characterized by a fuel tank initially filled to 40% of liquid capacity, an activated carbon canister loaded to the saturation point with butane, an initial drive sequence involving both cold and hot engine starting, an urban and highway running loss drive cycle, a one hour hot soak, a vehicle soak to ambient temperatures, and three consecutive thermal cycles each simulating a 24 hour time period.

The fuel vapor temperature and flow rate generated during the test sequence as a function of time during the drive cycle are shown in Fig. 19. Also presented is the mass fraction of the vapor stream leaving the tank that consists of fuel vapors, with the remaining fraction consisting of air also exiting the fuel tank through the vapor valves. The curves thus describe the feed stream which the carbon canister system must process within the required emission levels. Fig. 19(a) defines the fuel vapor stream from the start of the sequence, through the cold and hot engine starts, a

vehicle soak time, and the run loss portion of the test. The generation of fuel vapors during the drive cycle is demonstrated by the rising temperatures and increasing flow rate during these parts of the test. Fig. 19(b) defines the fuel vapor stream through the vehicle soak following the run loss portion, and continuing into the three diurnal cycles. The continuing generation of fuel vapor is clearly shown during the diurnal temperature swings, even though this is an engine-off test sequence.

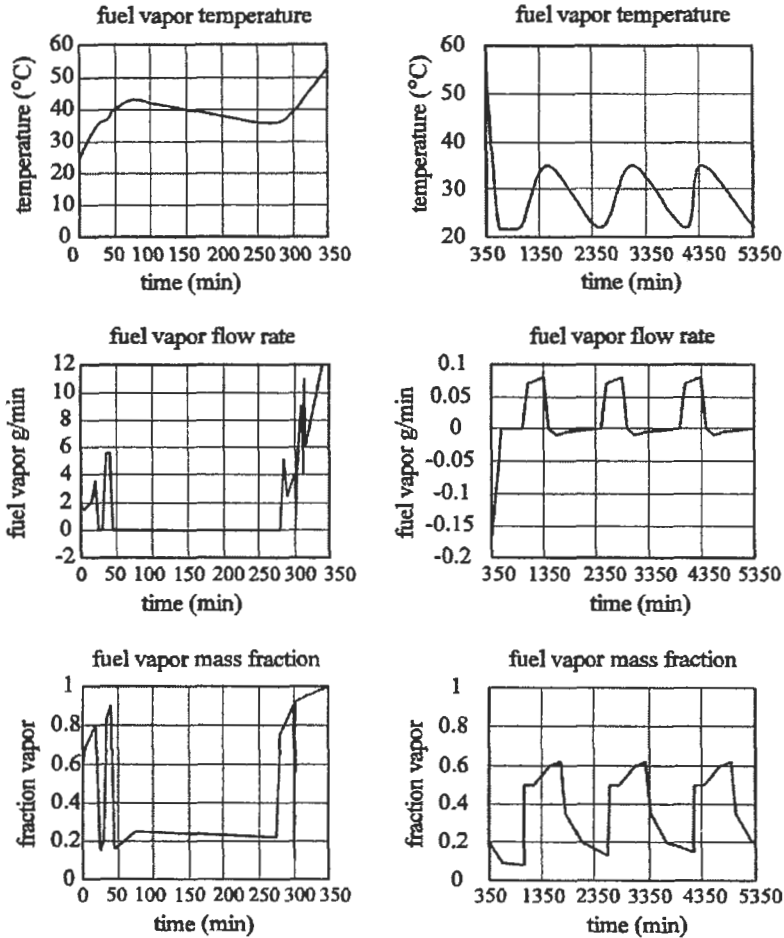


Fig. 19. Example temperatures, fuel vapor flow rates, and mass fractions during a three-day diurnal test sequence

The complete set of curves in Fig. 19 show that the adsorption performance of the activated carbon canister is a continuous requirement, and not an occasional need

of the fuel vapor system. The following sections describe the interaction of several vehicle operation parameters with the design requirements of the carbon canister system.

6.1 Canister volume requirements

A key parameter in the design of the fuel vapor control system is the volume of activated carbon required to meet the emission standards for the various regulatory tests. In the case of the three-day diurnal test sequence, the emission limits are 0.05 grams of HC per mile during the run loss portion of the test (maximum emission - 0.85 grams), and a maximum release of 2.0 grams for the sum of the hot soak period and any one of the three 24-hour periods making up the diurnal test sequence.

The performance of the fuel vapor system for the example vehicle three-day test is shown in Fig. 20. This example compares the use of a one liter and a two liter carbon canister volume. In this comparison the amount of purge air used by the vehicle was kept at the same level of 320 liters (11.3 cubic feet) for both carbon canister volumes studied. The mass of adsorbed hydrocarbons on the one liter and two liter carbon beds show that each canister volume undergoes purge cycles during the early portions of the test. It also shows that the increase in adsorbed mass on the carbon bed during the run loss was greater for the one liter canister. In fact, this increase in HC adsorption was high enough to force a release of HC from the one liter canister during the run loss portion of the test, as shown in the plot of HC released from the carbon bed. The amount of this release, 2.0 grams, is well above the allowed 0.85 gram level. Also, the additional HC adsorbed during the run loss on the one liter canister loaded the carbon bed to the point where the HC loading at the end of the one liter canister nearest to the atmospheric vent is sufficient enough to allow additional release of HC during the three diurnal cycles of the test sequence. On the third diurnal day, the emission level was very close to the allowed level (1.95 grams vs. 2.0 grams).

The two liter carbon canister does not exhibit the HC release during the run loss portion of the test, nor does it release more than the allowable level of HC during the three day diurnals. Thus, for the given vehicle configuration and the level of purge volume obtained by the vehicle, it is clear that a two liter carbon canister is required for this vehicle to pass the EPA certification requirement. This conclusion has an effect on the cost of the evaporative control system, in that the additional activated carbon volume and canister size will have an added cost, as will any additional hardware required to mount the larger canister on the vehicle.

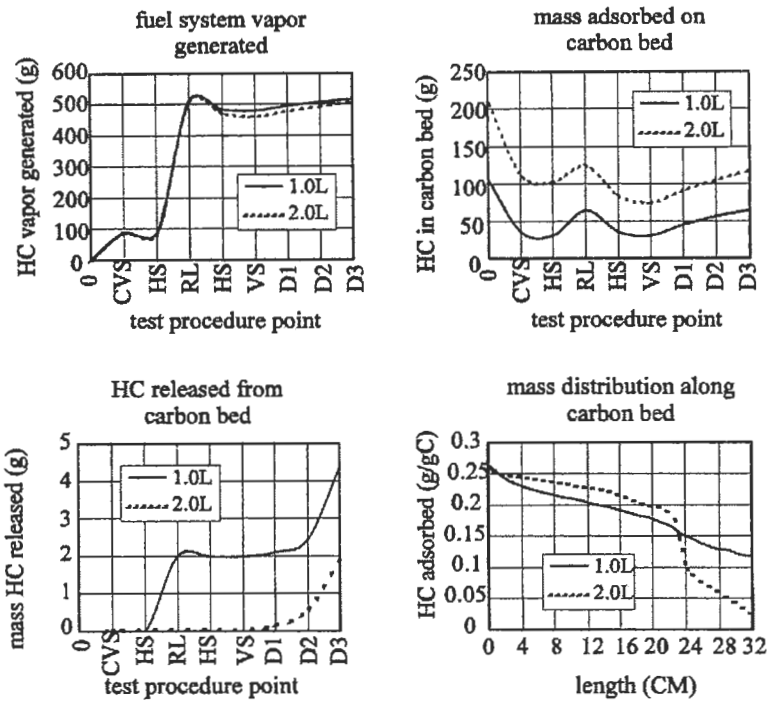


Fig. 20. Effect of canister volume on three-day test sequence

6.2 Purge volume effects

The comparison made in Section 6.1 demonstrates the important effect the amount of purge has on the performance of the carbon canister in terms of limiting the amount of HC release. This effect is also shown in the data presented in Fig. 21. In this example, the vehicle has been subjected to the same test cycle sequence as before, but in this case two different levels of purging are examined. Also, a two liter canister is used on the vehicle for the testing at both purge levels, in order to see the effect of purge level on a single canister volume.

The two purge levels used in this example are 150 BV (300 liters), and a higher level of 200 BV (400 liters). As shown in Fig. 21, the higher purge volume eliminates the increase in the amount of HC adsorbed during the run loss portion of the test, and, as a result, allows the overall loading of the carbon bed to be significantly lowered before the start of the diurnal sequence. This effect is critical, as is shown in the amount of HC released during the test cycle. At the 150 BV purge level, the HC release on Day 3, 2.12 grams, is above the allowable 2.0 gram level, while there are no HC emissions from the 200 BV purge run that are above

the allowable levels. Thus, the higher purge volume allows the vehicle to perform as required with the two liter canister, and no additional carbon canister volume is needed to meet acceptable HC emission levels.

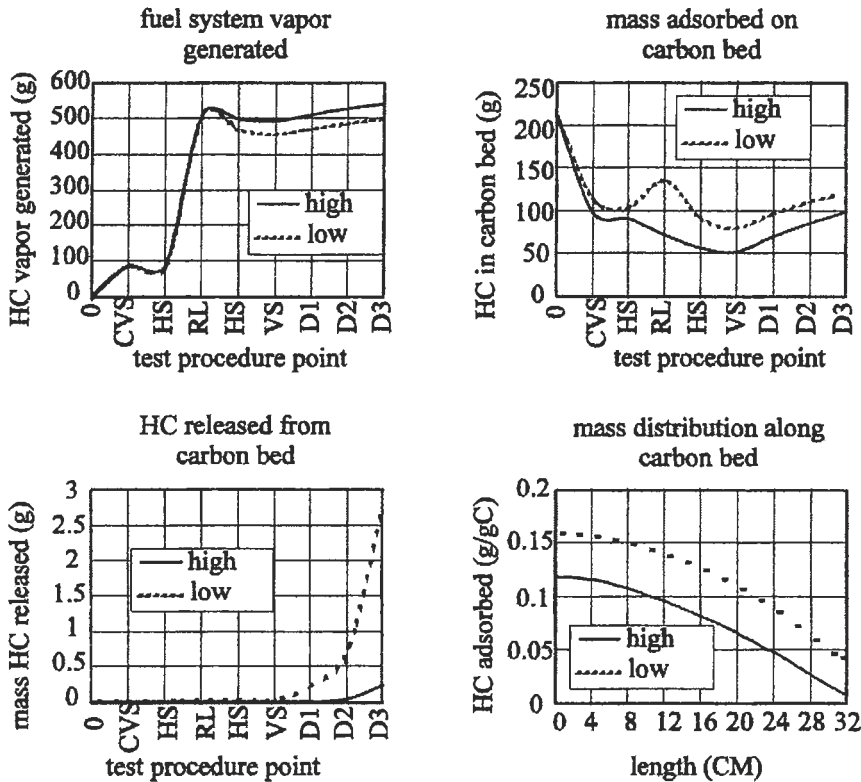


Fig. 21. Effect of purge volume on three-day test sequence

6.3 Return vs. return-less fuel systems

A key parameter in the generation of fuel vapor is the temperature level reached in the fuel tank during vehicle operation. As the temperature approaches the top of the fuel distillation curve, a sizable increase in vapor generation will occur, which severely impacts the amount of HC vapor that the carbon canister system must handle. Limiting the temperature increase in the fuel tank is an important parameter affecting the ability of the evaporative emission system to maintain allowable emission levels.

One method being studied to help in the limiting of fuel tank temperatures is the use of a returnless fuel system. As presented in Section 3.1, the return-less fuel

system eliminates the return of the high temperature fuel from the engine to the fuel tank, which reduces the overall fuel temperature in the tank. The effect of this temperature reduction will be examined, again with the example vehicle and test sequence.

The example vehicle has been run through the test sequence using a two liter carbon canister and a 150 BV purge level. Fig. 22 presents the results for both a return and return-less fuel system used in the vehicle. As shown, the fuel vapor temperature and the amount of fuel vapor generated are both lower for the return-less system. This reduces the amount of HC adsorption required in the carbon canister, and it also reduces the amount of HC emissions in the test sequence. The return fuel system used with the stated purge volume and canister size emits an unacceptable level of HC during one of the diurnal sequences (2.12 grams), while the return-less system emission values are well below the acceptable level.

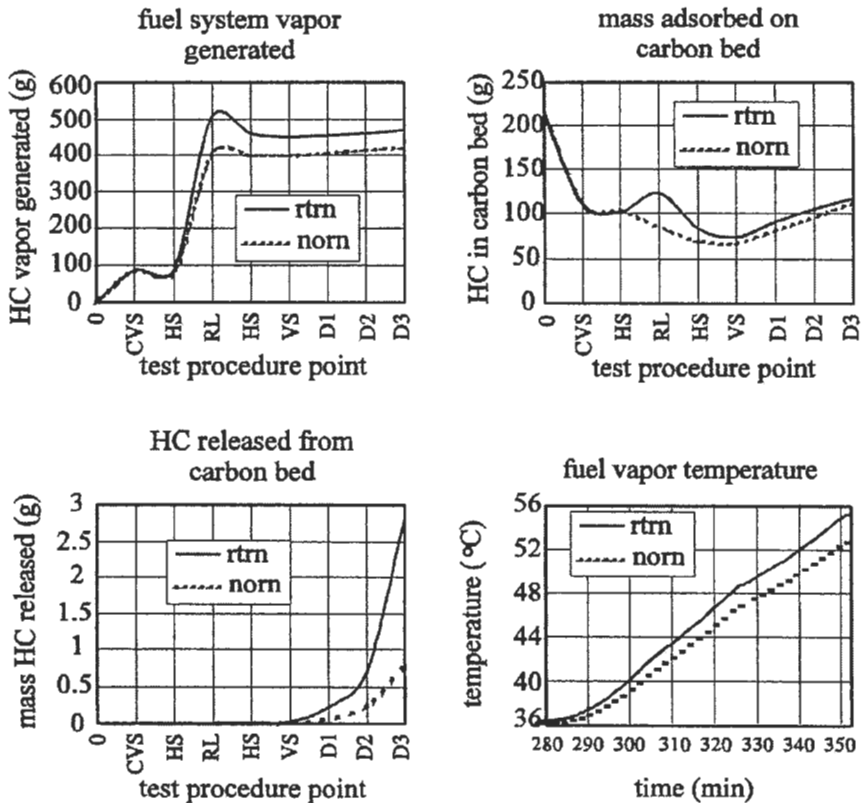


Fig. 22. Effect of fuel return vs. Returnless on three-day test sequence

7 Application of Canisters in ORVR Control

Tests of numerous fuel tanks under EPA refueling test conditions, as outlined in Fig. 1, indicate that most of the fuel vapor generation rates during the refueling event are in a range of 1.25 to 2.0 grams per liter (5 to 8 grams per gallon) of fuel dispensed [28,37,38]. Fig. 23 shows the rate of fuel vapor generation during refueling as a function of fuel dispensing rate and temperature for the fuel tank from the example vehicle presented in Section 6. It should be noted that systems with different fuel filler pipe and fuel tank geometries may show different effects over the dispensing rate range.

7.1 Loading of ORVR fuel vapors

The values shown in Fig. 23 indicate that the ORVR fuel vapor flow rate, based on vapor generation rate and fuel dispensing rate, can vary from 20 g/min to above 50 g/min at high temperature and flow conditions. To compare the HC adsorption at these rates to the low 40 g/hr flow rate shown in Fig. 9, the 50 g/min n-butane load of the one liter canister is presented in Fig. 24. Comparison of the curves in the two Figs. shows the large difference in time till break through for the two inlet flow rates (100 minutes vs. 1.0 minutes). It is also interesting to note the difference in the amount of HC adsorbed by the one liter of activated carbon at the point of break through (71 grams vs. 48 grams). This result, a 32% adsorption capacity reduction, agrees with the effect of HC loading rate that was discussed in Section 5.2.2.

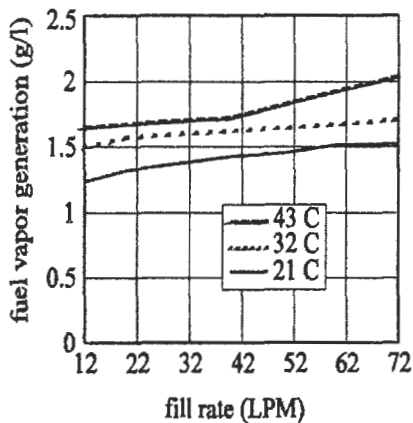


Fig. 23. Fuel tank HC vapor generation rates as a function of fill rate and temperature

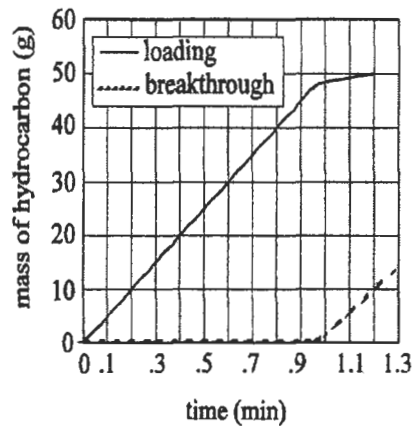


Fig. 24. Loading and breakthrough curves in a one-liter canister, 50 g/min N-butane feed rate

7.2 ORVR applications

As shown in previously in Fig. 1, the EPA refueling test has the same initial steps as the three day diurnal test, including a 40% initial fuel tank fill, a saturated carbon canister, an initial cold and hot engine drive sequence, and a running loss drive cycle. At this point in the refueling test, the fuel tank is drained and refilled to 10% of its capacity. Following a vehicle soak to stabilize the fuel system temperature, the actual refueling of the vehicle is performed. The test requires that at least 85% of the tank capacity be dispensed during the test, within a flow rate range of 16 l/min to 40 l/min (4 gallons per minute to 10 gallons per minute). As stated in Section 1.3, it is required that not more than 0.05 grams of hydrocarbons per liter of dispensed fuel (0.2 grams per gallon) be released from the vehicle during the refueling.

Using a fuel vapor generation rate of 1.25 grams per liter of dispensed fuel (5.0 grams per gallon), an ORVR test of the example vehicle presented in Section 6 can be performed. The amount of fuel dispensed for this vehicle will be 60 liters (15 gallons), and the limit for HC release becomes 3.0 grams. In this test, the vehicle has been subjected to the steps in the test procedure preceding the refueling event using a 200 BV purge. Thus, at the end of the vehicle soak, the canister has an HC loading of 53 grams, which then becomes the condition of the canister at the start of the refueling. The resulting canister loading and breakthrough curves for the ORVR test performed at 16 l/min and 40 l/min is shown in Fig. 25. Both refueling tests show that the two liter carbon canister gained about 73 grams, and released about 1.4 grams of HC, which is well below the allowable level of 3.0 grams.

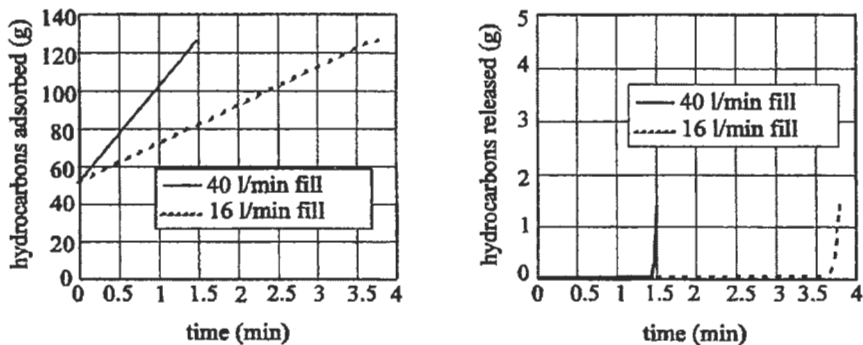


Fig. 25. Hydrocarbon adsorption and release as a function of ORVR fill rate

The effect of the vapor generation rate during ORVR testing is demonstrated in Fig. 26, where the effect of an increase in vapor generation rate from 1.25 g/l to 1.375 g/l (5.0 to 5.5 grams per gallon) is presented. The amount of HC adsorbed in the

canister is about the same for the two cases, but the additional vapor generated at the higher rate caused an HC release of almost 8 grams which is well above the allowed 3.0 gram value. This result shows the importance of fuel vapor generation rate on the design of an emission control system.

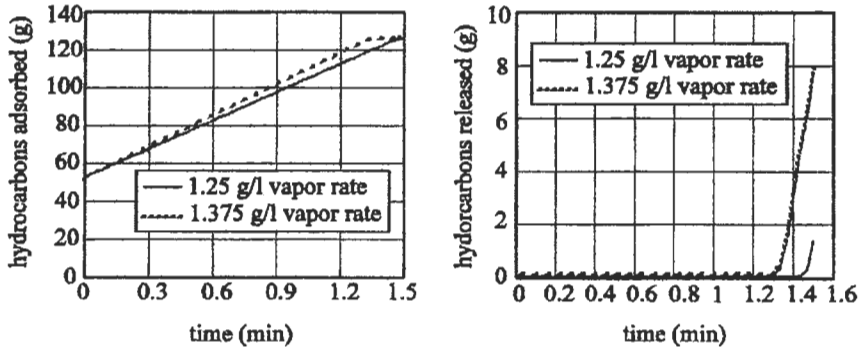


Fig. 26. Hydrocarbon adsorption and release as a function of ORVR vapor generation rate

8 Summary and Conclusions

The role of activated carbon in the control of automotive evaporative emissions is summarized below:

- Automotive evaporative emissions have been identified as a source of HC compounds that can contribute to smog pollution.
- Both the EPA and CARB have established regulations which define the levels of evaporative emissions that can be tolerated.
- These agencies have developed specific test procedures which must be used to verify compliance with the established limits.
- The current requirements have led to the development of pellet shaped activated carbon products specifically for automotive applications. These pellets are typically generated as chemically activated, wood-based carbons.
- The adsorption of hydrocarbons by activated carbon is characterized by the development of adsorption isotherms, adsorption mass and energy balances, and dynamic adsorption zone flow through a fixed bed.
- The design of activated carbon canisters for evaporative emission control is

affected by characteristics of the carbon itself, by physical/geometrical design options, and by the final working environment of the canister.

- A vehicle fuel vapor control system must be designed to meet both driving and refueling emission level requirements. Due to the nature of hydrocarbon adsorption, this emission control is a continuous operation.
- The key sources of evaporative emissions during drive cycles are running loss emissions, hot soak emissions, and diurnal emissions.
- Design concerns for drive cycle emission control include canister volume requirements, purge volume effects, and the use of return vs. returnless fuel systems.
- The rate of vapor generation during refueling is a major parameter affecting the design of carbon canisters to meet ORVR requirements.
- The reduced adsorption capacity at ORVR vapor generation rates requires increased efficiency in the canister design, in order to limit the effect on cost and performance of the evaporative control system.

9 References

1. U.S. Environmental Protection Agency, *Fact Sheet OMS-12*, January, 1993.
2. P. J. Liroy, *Human Exposure Assessment for Airborne Pollutants*, National Academy Press, Washington, D.C.(1991).
3. State of California Air Resource Board, *California Fuel Evaporative Emissions Standard and Test Procedure for 1970 Model Light Duty Vehicles*, April 16, 1968.
4. P. Degobert, *Automobiles and Pollution*, Society of Automotive Engineers, USA(1995).
5. U.S. House of Representatives, *Clean Air Act of 1990, Conference Report*, Section 232, pp. 137.
6. General Motors, Environmental Activities Staff, *Mobile Emission Standards Pocket Reference*, March, 1990.
7. S.W. Martens and K.W. Thurston, *Society of Automotive Engineers Paper Number 680125*, 1968.
8. U.S. Code of Federal Regulations, *Control of Air Pollution From New Motor Vehicles and New Motor Vehicle Engines; Certification and Test Procedures*, Title 40, Part 86.
9. U.S. Environmental Protection Agency, Final Rule, *Control of Air Pollution From New Motor Vehicles and New Motor Vehicle Engines; Evaporative Emission Regulation for Gasoline and Methanol - Fueled Light-Duty Vehicles, Light-Duty Trucks and Heavy-Duty Vehicles*, Federal Register, Vol. 58, No. 55, March 24, 1993.
10. U.S. Environmental Protection Agency, Final Rule, *Control of Air Pollution From New Motor Vehicles and New Motor Vehicle Engines; Refueling Emission Regulations for*

- Light-Duty Vehicles and Light -Duty Trucks*, Federal Register, Vol. 59, No. 66, April 6, 1994.
11. *Kirk-Othmer Encyclopedia of Chemical Technology*, 4th Edition, Volume 4, John Wiley & Sons, New York(1992).
 12. Carrubba, R.V., et.al., *Perspectives of Activated Carbon - Past, Present and Future*, AICHE Symposium Series No. 233, Vol. 80, pp. 76-83.
 13. T.Wigmans, *Carbon*, **27**, 13(1989).
 14. H. Juntgen, *Carbon*, **15**, 273(1977).
 15. R.A. Hutchins, *Chem Eng.*, **87:2**, 101(1980).
 16. P.N. Cheremisinoff and F. Ellerbusch (Eds), *Carbon Adsorption Handbook*, Ann Arbor Science Publications, Inc.(1978).
 17. M.W. Leiferman and S.W. Martens, *Society of Automotive Engineers Paper Number 830630*, 1983.
 18. T.L. Darlington L. Platte, and C. Shih, *Society of Automotive Engineers Paper Number 860529*, 1986.
 19. Westvaco Special Report, *Nuchar Activated Carbons for Automotive Hydrocarbon Emission Control*, Westvaco Corporation, 1986.
 20. J.E. Urbanic, E.S. Oswald, N.J. Wagner, and H.E. Moore, *Society of Automotive Engineers Paper Number 890621*, 1989.
 21. H.M. Haskew and W.R. Cadman, *Society of Automotive Engineers Paper Number 891121*, 1989.
 22. H M. Haskew, W.R. Cadman, and T.F. Liberty, *Society of Automotive Engineers Paper Number 901110*, 1990.
 23. C.H. Schleyer and W.J. Koehl, *Society of Automotive Engineers Paper Number 861552*, 1986.
 24. R.L. Furey and B.E. Nagel, *Society of Automotive Engineers Paper Number 860086*, 1986.
 25. P. Girling, *Automotive Handbook*, Robert Bently, Publishers, Cambridge, MA(1993).
 26. J. Heinemann and B. Gcsenhues, *Society of Automotive Engineers Paper Number 930858*, 1993.
 27. W.J. Koehl, D.W. Lloyd, and L.J. McCabe, *Society of Automotive Engineers Paper Number 861551*, 1986.
 28. G.S. Musser and H.F. Shannon, *Society of Automotive Engineers Paper Number 861560*, 1986.
 29. R.H. Perry, D.W. Green, and J.O. Maloney (Eds), *Chemical Engineer's Handbook*, Sixth Edition, McGraw-Hill, New York(1984).
 30. J.H. Harwell, A.I. Liapis, R. Litchfield, and D.T. Hanson, *Chem Engng. Sci.* **35**, 2287(1980).
 31. K.S. Hwang, J.H. Jun, and W.K. Lee, *Chem. Engng. Sci.* **50**,813(1995).
 32. P.N. Cheremisinoff (Ed), *Handbook of Heat and Mass Transfer, Volume 2: Mass Transfer and Reactor Design*, Gulf Publishing, Houston(1986).
 33. G. Tironi, G.J. Nebel, and R.L. Williams, *Society of Automotive Engineers Paper Number 860087*, 1986.
 34. M.M. Dubinin and Radashkevich, *Compt. Rend. Acad. Sci. USSR* **55(4)**, 327(1959).
 35. H.R. Johnson and R.S. Williams, *Society of Automotive Engineers Paper Number 902119*, 1990.
 36. M.J.Manos, W.C. Kelly, and M. Samfield, *Society of Automotive Engineers Paper Number 770621*, 1977.

37. J.N. Braddock, P.A. Gabele, and T.J. Lemmons, *Society of Automotive Engineers Paper Number 861558*, 1986.
38. G.S. Musser, H.F. Shannon, and A.M. Hochhauser, *Society of Automotive Engineers Paper Number 900155*, 1990.

CHAPTER 9

Adsorbent Storage for Natural Gas Vehicles

T.L. COOK ¹, C. KOMODROMOS ², D.F. QUINN ³
AND S. RAGAN ⁴

¹ *Atlanta Gas Light Co., Atlanta, GA*

² *British Gas plc, Loughborough, England*

³ *Royal Military College of Canada, Kingston, Ontario*

⁴ *Sutcliffe Speakman Carbons Ltd, Ashton-in-Makersfield, England*

1 Introduction.

1.1 Natural Gas Vehicles.

With air quality issues gaining prominence around the world, the use of natural gas as a vehicular fuel has become a more attractive alternative to gasoline and diesel fuels because of its inherent clean burning characteristics. Natural gas vehicles (NGVs) have the potential to lower polluting emissions, especially in urban areas, where air quality has become a major public health concern. The most important environmental benefit of using natural gas is lower ozone levels in urban areas because of lower reactive hydrocarbon emissions. NGVs also have lower emission levels of oxides of nitrogen and sulfur, known to cause "acid rain". Estimates of the greenhouse impact by NGVs vary widely, but it is generally agreed that the global warming potential of an NGV will be less than that of a liquid hydrocarbon-fuelled vehicle [1].

In the United States, in particular, recent legislation has mandated sweeping improvements to urban air quality by limiting mobile source emissions and by promoting cleaner fuels. The new laws require commercial and government fleets to purchase a substantial number of vehicles powered by an alternative fuel, such as natural gas, propane, electricity, methanol or ethanol. However, natural gas is usually preferred because of its lower cost and lower emissions compared with the other available alternative gas or liquid fuels. Even when compared with electricity, it has been shown that the full fuel cycle emissions, including those from production, conversion, and transportation of the fuel, are lower for an NGV [2]. Natural gas vehicles offer other advantages as well. Where natural gas is abundantly available as a domestic resource, increased use

of NGVs would limit dependence on foreign produced oil and petroleum products.

The environmental and energy security advantages offered by natural gas vehicles are important, but NGVs must be competitive on an economic basis in order to be successful in the market. Currently, the commodity and distribution costs for natural gas are lower than those of gasoline and diesel. The natural gas industry is able to take advantage of its substantial investment in a gas pipeline and distribution network put in service for other markets. As a result, an NGV refueling station can be installed at almost any location where natural gas service is available, with the incremental investment for the NGV fuel distribution network being only the station equipment. However, compared with gasoline and diesel vehicles, NGVs are currently at a disadvantage because of high vehicle costs. Gasoline and diesel vehicles benefit from decades of optimization and high volume manufacturing. At the moment NGVs are simply gasoline vehicles converted to operate on natural gas. As a result, the fuel storage system geometry and placement are not optimized for natural gas.

A significant problem arises because natural gas at normal temperature and pressures has a low energy density relative to solids or liquids, making it difficult to store adequate amounts on a vehicle. Despite this, NGVs can compete with conventional vehicle types because of the lower fuel cost, especially in high fuel use markets. Because of the perceived advantages of NGVs the development of improved, lower cost, natural gas fueling and storage systems has been ongoing for several years.

The history of natural gas vehicles dates back to the 1930s when Italy launched an NGV program. Today, Italy has over 290,000 operating NGVs. The continued popularity of NGVs in Italy is mainly due to the price of natural gas, which is less than one third that of gasoline. More than 340,000 vehicles operate on natural gas in Argentina, the largest number of any country, even though NGVs were introduced as recently as 1984. Countries of the former Soviet Union operate more than 200,000 NGVs and other notable programs exist in New Zealand, Canada and the United States, each of which has tens of thousands of NGVs operating on their roads [3].

When NGV programs are initially launched, a refueling infrastructure usually does not exist to support these vehicles. To accommodate this limitation, most NGVs have been bifuel vehicles. The vehicle is operated primarily on natural gas and then switched over to gasoline after the natural gas is depleted. With this scenario, the vehicle operator does not have to be concerned with locating a natural gas refueling station immediately when the level of natural gas stored on board gets low. The drawbacks of the bifuel NGV include reduced cargo volume on the vehicle, since two fuel storage systems are onboard, and lower performance of the vehicle, since its engine is optimized for gasoline. A new

bifuel concept that has emerged is to optimize the vehicle to run on natural gas, but provide a "limp home" capability on gasoline with a small pony tank. This approach is in response to market fears of running out of fuel if the vehicle is a dedicated, or single fuel, natural gas vehicle.

The factory-produced, dedicated NGV is the ultimate goal of the NGV industry because it will reduce the incremental cost of the vehicle, the fuel system will be better integrated into the vehicle, and the vehicle performance can be optimized for natural gas. A dedicated NGV's emissions, power, and driveability can be superior to a comparable gasoline vehicle. There is however, a reluctance by some automobile manufacturers to produce dedicated NGVs until the refueling infrastructure is more fully developed.

1.2 Energy Aspects of NGVs.

Although natural gas, which is mostly methane, has a higher hydrogen to carbon ratio than other fuels and consequently a greater energy per unit mass, it cannot be stored to the same density as these fuels. Even when liquefied at its normal boiling point of -161°C , the energy density (defined as the heat of combustion per unit volume) is only 23 MJ per liter, considerably lower than that of diesel or gasoline with approximately 37 and 32 MJ per liter respectively. Compressed natural gas (CNG) at 20 MPa (200 bar) and ambient temperature (25°C) has an energy density of < 10 MJ per liter. In these conditions, about 230 unit volumes of natural gas at 0.1 MPa (1 bar) are compressed to one unit volume of storage container, often designated as 230 V/V (an ideal gas would be 200 V/V). For the same driving range a CNG vehicle using these pressures, requires a storage vessel at least three times the volume of a gasoline tank. With limited space on board a vehicle, this can present some challenges. The use of even higher pressures for greater energy density has been suggested. It should also be noted that at these pressures, a cylindrical conformation for the vessel is required.

The use of adsorbent materials, such as active carbons, porous silicas and porous polymers, in a storage vessel for storing natural gas at lower pressures, known as adsorbed natural gas, ANG, is another alternative attempting to make NGVs more cost effective when competing with other vehicle types. In ANG technology, natural gas is stored at relatively low pressures, 3.5 to 4.0 MPa (35 to 40 bar) through the use of an adsorbent. Much work has been directed towards the adsorbent, however, for ANG to be successful for vehicular use in contrast to high pressure (20+ MPa) CNG, a complete storage system must be considered. This storage system must address every aspect, both the advantages and disadvantages, of adsorption. This chapter attempts to review the characteristic properties of the adsorbent which are best suited to methane storage at temperatures substantially above its critical temperature (191 K) as well as the fuel, natural gas, with its other non-methane constituents which

affect adsorption storage. Additionally consideration is given to the storage vessel design so that the heat effects which occur during filling and discharge can be minimized and also to the shape of the vessel so that it best utilizes the space available on board the vehicle. Collectively these factors contribute to the overall performance of an ANG storage system.

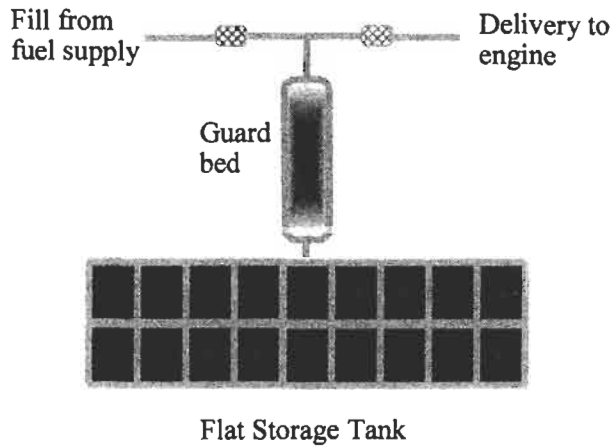


Fig. 1. A basic layout for a vehicular ANG storage system.

A simplified diagram of an ANG storage system is shown in Fig. 1. On filling the natural gas is passed through a small carbon bed which is necessary to remove by adsorption the small amounts of the $C_5 +$ hydrocarbons present in the natural gas before it enters the main storage vessel. If this is not done then a reduction in overall capacity results on repeated fill-empty usage. While discharging the gas from the storage vessel it is passed back through the protective guard bed. The bed is heated to aid desorption of these higher hydrocarbons back into the gas stream which is fuelling the engine.

The generalized statement can be made that the energy density in a vessel filled with adsorbent will be greater than that of the same vessel without adsorbent when filled to the same pressure. The extent to which the above is true depends on many factors and considerations which are discussed more fully later.

Compression of CNG to 20 MPa requires four stage compression. Provision of such facilities is costly, and it is an energy consuming process. There is also a substantial heat of compression which results in a temperature rise of the compressed gas. This means that in practice less than 230 V/V are stored when a CNG vessel is filled to 20 MPa unless the filling process is carried out isothermally.

For simplicity and reduced cost, an adsorption storage system using single stage compression is attractive, which puts a practical upper limit to the adsorption

pressure of about 5 MPa. This is not a serious constraint from consideration of the adsorption process, since at 5 MPa many adsorbents have reached their isotherm plateau, although a few still exhibit some increase in uptake beyond this pressure. Therefore, to be equivalent to a CNG system at 20 MPa, it is necessary to store as ANG the same amount of natural gas but at one quarter or less of this pressure. For some years now a benchmark pressure of 3.5 MPa has been somewhat arbitrarily adopted for the comparison of different adsorbents. This pressure is only one sixth that in use for CNG vehicles in many countries.

Although the requirements for a NGV storage system are demanding, more than a million CNG vehicles and about one thousand LNG trucks or buses are in use worldwide, only a handful are known to operate on ANG. The Atlanta Gas Light Adsorbent Research Group, (AGLARG), a consortium of oil and gas utility companies and Sutcliffe Speakman, a carbon manufacturer, has been at the forefront of advancing ANG technology for vehicles, by developing adsorbents of high storage performance for natural gas, coupled with the design of novel tank containers for better integration into the vehicle. Additionally, as discussed in section 5 of this chapter, they have developed guard beds for the protection of the storage carbon. Also, there are some opportunities for ANG which are less stringent. Examples of possible use may be in small limited range vehicles such as delivery trucks, golf carts, fork lift trucks and garden tractors or lawnmowers. No natural gas storage system will come close in energy density to diesel or gasoline, but, with the emission concerns raised earlier, it can contribute to improved air quality. Moreover, for some parts of the world it can provide a useful domestic vehicular fuel.

1.3 Natural Gas as a Fuel.

The characteristics of natural gas make it an ideal fuel for spark-ignition engines. Methane, the principal component of natural gas, is a clean burning fuel because of its higher hydrogen to carbon ratio than other hydrocarbon fuels. Natural gas also has a higher research octane number, (RON), around 130, compared to 87 for regular unleaded gasoline, which allows the use of higher compression ratio engines, with better performance and fuel efficiency. The combustion of natural gas results in less ash and particulate matter in the engine cylinders, compared with petroleum based liquid fuels. Over time, the ash and particulate contaminate the lubricating oil causing abrasion and wear and also foul the spark plugs. Therefore, from a maintenance perspective, natural gas engines require fewer oil and spark plug changes.

With dedicated vehicles, the engine can be optimized for the attributes of natural gas. In bifuel, or converted NGVs, the engine is usually not modified significantly from its original gasoline configuration. For a bifuel NGV, a fuel pressure regulator, an air/fuel mixer, and an electronic engine controller must be

added to the vehicle in conjunction with the CNG or ANG storage cylinders. The state-of-the-art NGV conversion kit now contains a fully electronic, closed-loop engine controller that provides much improved performance over the open loop mechanical systems of the past. The air/fuel mixer is mounted on the intake manifold to deliver a mixture of air and natural gas to the engine's cylinders, much like the gasoline carburetor. However, most factory produced, dedicated NGVs will use fuel injection, either single point (throttle body) or multiple point (at each engine cylinder), for more precise fuel control and to obtain better economy, performance and lower emissions.

2 Storage of Natural Gas.

2.1 Methods of Natural Gas Storage

Historically, there have been two options for storing natural gas on a vehicle: as compressed gas or in a liquefied state. As stated in the previous section, the energy density of CNG as a fuel is less than that of gasoline. Hence vehicles fuelled by CNG exhibit a reduced driving range, unless a higher percentage of the volume within a vehicle is used for fuel storage.

Liquefied natural gas (LNG) vehicles have a higher energy density, but handling of this cryogenic liquid (-162°C) poses some safety concerns. LNG can also present an operational problem if the vehicle is not operated frequently. The liquid slowly vaporizes, pressurizing the storage vessel which must then be vented to the atmosphere if the vehicle does not use enough fuel to keep this "boil-off" in check. The storage cylinders for CNG and the super-insulated LNG tank add significantly to the incremental cost of a NGV, and therefore current NGVs have a cost premium of several thousand dollars over their gasoline or diesel counterparts.

Several alternative methods have been considered in order to increase the energy density of natural gas and facilitate its use as a road vehicle fuel. It can be dissolved in organic solvents, contained in a molecular cage (clathrate), and it may be adsorbed in a porous medium. The use of solvents has been tested experimentally but there has been little improvement so far over the methane density obtained by simple compression. Clathrates of methane and water, (methane hydrates) have been widely investigated but seem to offer little advantage over ANG [4]. Theoretical comparison of these storage techniques has been made by Dignam [5]. In practical terms, ANG has shown the most promise so far of these three alternatives to CNG and LNG.

For many classes of vehicles, the use of CNG storage is a compromise between volume of gas required to provide an acceptable range dictated by the internal

volume of the storage cylinder, the amount of space available within the vehicle for the cylinder installation, (the external cylinder envelope), and the weight of the storage system. Thus for large vehicles such as transit buses and heavy duty trucks, the emphasis is on reducing the weight of the storage system, while on passenger vehicles, although weight is still important, another concern is the intrusion of the cylindrical storage system on the passenger and load space of the vehicle.

On-board storage at much lower pressures through the use of adsorbents would bring about important benefits by allowing the use of lighter tanks that could be made to conform to otherwise unused spaces within a road-going vehicle. The realization of this advantage, and those discussed above, depends on a detailed understanding of the ANG adsorbent properties and behavior.

2.2 On-board Storage Comparisons

The relative volume and mass for the different fuel systems, normalized to that of diesel, is shown in Fig. 2 and illustrates the disadvantages of most of the alternative fuels compared to gasoline and diesel, in terms of storage density.

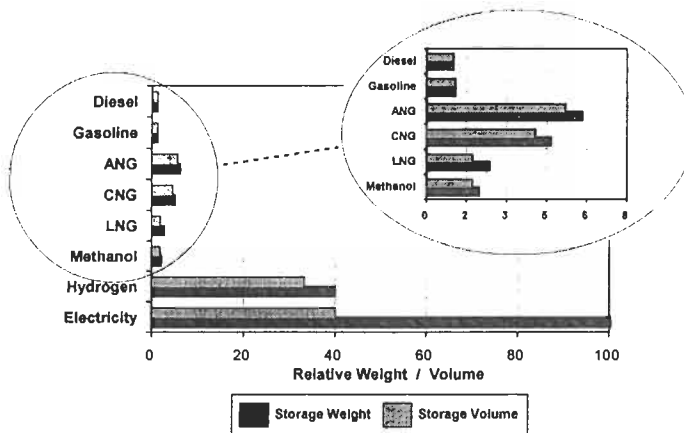


Fig. 2. Relative volume and mass of different fuel systems normalized to diesel fuel in terms of storage density.

For natural gas, LNG begins to approach the energy density of the conventional liquid fuels and provides a goal for other natural gas storage methods. In contrast, CNG and ANG require substantially greater storage volume compared to diesel and gasoline. Additionally, there is a weight penalty due to the containers. For CNG the weight/liter capacity of current steel tanks is 0.9-1.2 kg/liter but 0.4 kg/liter can be achieved using composite tanks. Although ANG tanks may be lighter than steel CNG cylinders, this advantage is offset by the

weight of the adsorbent. The relative volumes used in Fig. 2 for both LNG and CNG are based on internal vessel volume and not the effective external volume, the use of which would lower the energy density.

2.3 ANG Storage for Vehicles

Early trials of vehicle applications of ANG showed that useful on-board storage volumes could be achieved at 3.5 MPa, but the carbons used tended to be highly activated ones in a granular form, having large surface area but with a consequent low packing density, leading to high void volume in the tank [6]. It was recognized that the use of monolithic carbons would lead to improvements in the performance of ANG storage systems. Developments by AGLARG, discussed later in this chapter, using carbon monoliths that can be shaped to completely fill a vessel, coupled with the use of space saving flat tanks, means that ANG storage can be used on vehicles much more effectively than before [7].

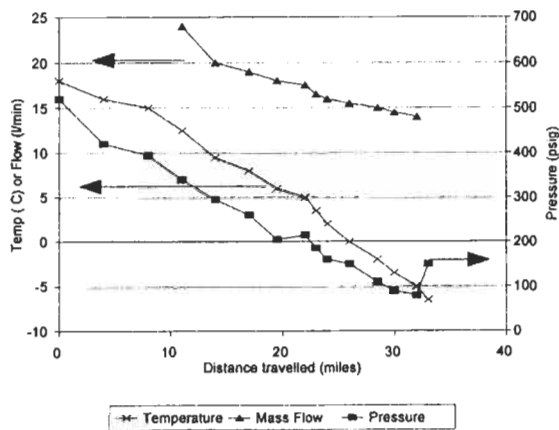


Fig. 3. Tank pressure, gas flow and adsorbent bed temperature of the ANG storage system on the Vauxhall Cavalier at 100 km/h.

AGLARG members have operated several ANG vehicles. For example, a Chevrolet pick-up truck, operated by Atlanta Gas Light Co. used a pelletized form of the Anderson AX-21 carbon. Another vehicle, a Vauxhall Cavalier estate car (station wagon), operated by British Gas, used a high performance coconut shell granular carbon developed by Sutcliffe Speakman. In this vehicle, the carbon was stored as granules in a composite tank supplied by HM International. These vehicles were fully instrumented, allowing gas flow and temperature measurement during on the road performance. Fig. 3 shows how the tank pressure, gas flow and carbon bed temperature of the fuel system varied during a particular run at 60 m.p.h. (100 km/h). Since desorption is an

endothermic process, heat must be supplied from some external source if the adsorbent is to remain at ambient temperature. A reduction in temperature would result in more gas being retained by the adsorbent and so less is available as fuel for the vehicle. In this relatively large and well insulated container, the temperature decreased steadily as the trial proceeded, until after 35 miles (56 km), the temperature had fallen to -5°C and the tank pressure to 0.64 MPa, (6.4 bar). The gas flow rate under these conditions was insufficient to maintain the road speed and the test was stopped. When the tank returned to ambient temperature the pressure rose to 1.45 MPa, (14.5 bar). Comparisons with the isotherm for the carbon used, suggests that only about half the gas stored on the carbon had been consumed and that the potential range had not been approached because of the fall in adsorbent temperature.

The vehicle was subsequently modified to test a developmental batch of active carbon in the form of briquettes. The complete storage system was removed and replaced by an array of 18 cm diameter stainless steel cylinders, in which the briquettes in the form of 16 cm diameter disks were loaded. The briquettes were not a matched fit within the cylinders because stainless steel tube of the correct diameter was unavailable. This resulted in an annular space between the briquettes and the cylinder wall. Three of the filled cylinders were positioned in a cradle on the vehicle floor, and two other cylinders were mounted directly beneath the cradle under the vehicle floor. In this configuration the performance of the vehicle improved, although there was still a marked decrease in temperature during operation. The annular gap around the carbon briquettes was not ideal for promoting heat transfer. Nevertheless, the tests showed that improvements were possible by using immobilized, rather than granular carbon, [8]. These results reinforce the fact that the behavior of an ANG storage tank is governed by heat and mass transfer effects in the adsorbent. The heat of adsorption of methane on carbon, ca. 16 kJ/mole, is also sufficient to cause considerable temperature variations during filling. The effect on ANG is a reduction in potential storage as the temperature increases during filling. The extent of temperature rise is dependent on the adsorption capacity of the carbon, the heat transfer of the system to the surroundings, and on the filling time. There is also a temperature increase during filling of CNG storage systems that reduces the amount of gas dispensed to the storage cylinder, but this is less significant than for ANG.

2.4 ANG Storage Vessels

The characteristics of ANG storage described above suggest a new approach to the design of adsorbent and tanks, including:

- monolithic adsorbents occupying all the available volume of the tank with minimum void volume and with improved thermal conductivity to maximize adsorption capacity
- careful packing of the carbon within the tank to encourage heat transfer
- tanks with a high surface to volume ratio for better heat exchange with the surroundings
- development of shaped vessels which can be "conformable" with the vehicle shape and designed to maximize storage volume and reduce the spatial intrusion within a vehicle.

To meet these requirements, radically new types of fuel containers are needed to exploit fully the unique features of ANG storage, and maximize the on-board storage capability. Thus the use of immobilized carbons, in the form of briquettes which are shaped to match the geometry of the tank, is an important element, since this minimizes void volume within the container. In addition, this can help to reduce thermal gradients throughout the tank, since the thermal conductivity of immobilized carbons has been measured to be around 65% greater than that of corresponding loose particles, thus increasing the heat transfer. The much lower operating pressure of ANG compared to CNG permits non-cylindrical tank designs that can meet the above requirements and are able to be better integrated within vehicle structures, minimizing the impact on the vehicle and improving weight distribution. With CNG storage, cylindrical or spherical geometry vessels are almost mandatory, due to the very high pressures and the resulting hoop stresses generated within the vessel. However, spheres and cylinders are not amenable to efficient packaging within a modern vehicle and there is wasted space around the spherical or cylindrical vessel, (the parasitic volume), when it is fitted to a vehicle. Thus a nearly thirty percent increase in storage volume could be realized by having a rectangular rather than a circular cross section.

In principle, the lower pressures used in ANG can lead to lighter, thinner walled tanks. However, in ANG the weight of the adsorbent increases the weight of the storage system. A number of conceptual containers have been investigated, including completely flat section tanks. However to date, most effort has been directed at obtaining multi-cellular aluminium alloy tanks which are essentially rectangular but have cells with curved external walls to minimize stresses at these points. This is illustrated in Fig. 4 [9]. These tanks are manufactured by a single step extrusion process to form a multi-cell body, followed by careful welding of individual end caps to seal the tank.

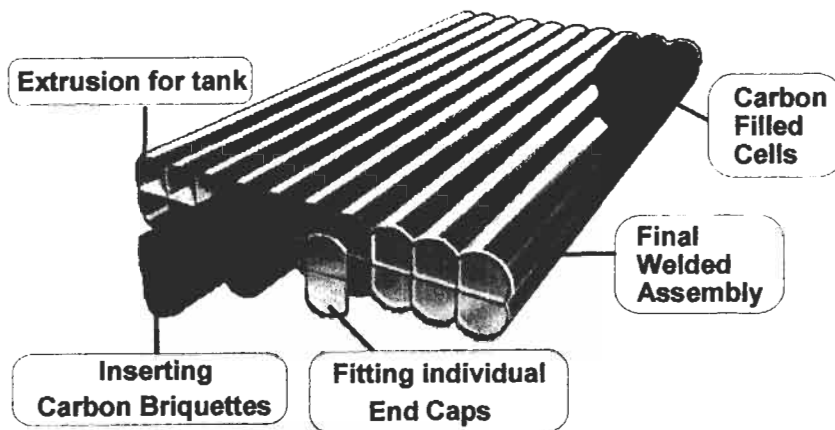


Fig. 4. Schematic of aluminum alloy extruded storage vessel developed by AGLARG specifically for ANG applications.

2.5 Safety

Safety is essential for all pressure vessels, but ideally NGV containers should also be lightweight and inexpensive, with the highest possible capacity for a specified external envelope. In a given application, some degree of compromise is unavoidable between these conflicting requirements.

The prevalence of CNG storage can be attributed to the established use of high pressure steel cylinders for transporting industrial gases, for which there are long established safety standards for construction and use. However, when using pressure vessels as fuel tanks for vehicles, new safety issues arise that have to be carefully considered. Although steel cylinders are the most widely used for CNG vehicle applications, today there is a broad range of cylinder types available, with increasing interest in lightweight composite cylinders. NGV cylinders are characterized by three ratios, weight/capacity, capacity/external volume and cost/capacity [10]. At one extreme, steel cylinders are relatively inexpensive and reasonably space efficient but heavy, whilst at the other extreme, carbon fiber composite cylinders are relatively light but very expensive and bulky. The cost of fully wrapped carbon fiber cylinders is three to four times the cost of a steel cylinder having the same capacity.

A major issue with NGV cylinders has been the lack of a world-wide standard for their manufacture, inspection and testing. Some national standards, such as the New Zealand standard NZS 5454 and the US ANSI/AGA/NGV2 standards have been adopted by other countries. Currently, ISO are working to produce an internationally accepted standard for NGV cylinders.

There are currently no standards or regulations governing ANG containers. The existing regulations for CNG cylinders are not appropriate, particularly if non-cylindrical designs are being considered. Thus the use of ANG tanks requires a comprehensive design and evaluation program to ensure safety. Applying standard pressure vessel codes, such as ASME VIII, invariably leads to a heavy and unnecessarily bulky container. However, in the absence of specific codes, ANG tanks that are to be used on public roads must be designed as closely as possible to an existing pressure vessel standard. The design must be checked by finite element analysis, and the design validated by carrying out a program of pressure testing on sample tanks to establish burst safety factors and the fatigue life. This approach allows the design engineer to assess the fitness-for-purpose of the tank. However, it may not be possible to obtain full certification since some aspect of the tank design may fall outside the ASME VIII Code.

The aluminum multi-cell tank shown in Fig. 4 was designed to a British Standards Institute (BSI) Code for stationary pressure vessels, BS 5500 to ensure the materials specifications, design calculations, stress levels, welding and inspection requirements embodied in the code were incorporated into the design. Moreover, finite element analysis was used extensively. The single stage continuous extrusion method used to manufacture the tank body is not explicitly covered in BS5500 because the extrusion die requires the aluminium to separate and recombine as it flows through the die, forming invisible "seam welds" along the tank body. Nevertheless, careful manufacturing and quality control testing yielded extrusions with very high material strength. Following the development of this type of tank, an addendum to the BSI Code, which allowed this type of extrusion only if the contracting parties agreed on the quality and integrity of the extrusion, was issued.

3 Adsorbents.

3.1 Performance Requirements

One study suggested that a viable ANG system would have to store "12 lb. of natural gas per cubic foot of storage" (192 kg/m^3), equivalent to about 270 V/V [11]. However, this capacity could not be reached with any adsorbent available at that time. The concept of ANG has continued to be attractive and several studies of adsorbents were carried out in the 1980s, see for example [12-16]. In the early 1990s, the US Department of Energy (USDOE) set a target figure of 150 V/V deliverable for an operational ANG vehicle system working at a pressure of 3.5 MPa (35 Bar) and 25°C [17]. This value was considered demanding, but realistic and achievable. Values in excess of 200 V/V have been claimed for laboratory scale samples, but these have not been independently validated. Sometimes storage or delivered quantities have been

estimated by extrapolation of experimental values. It is important to distinguish clearly between an experimentally obtained value and a calculated one which assumes a parameter, such as a packed density, to obtain a stored or delivered value. These calculated quantities may not be practically achievable but have some merit in guiding researchers towards a possible goal.

3.2 Principles of ANG Development

Enhancement of gas storage capacity through adsorption occurs when the overall storage density is increased above that of the normal gas density at a given pressure. The adsorbed phase has a greater density than the gas phase in equilibrium with it. However, enhancement in a storage system of fixed volume can only happen if a greater amount of gas is adsorbed compared to the volume of gas displaced by the adsorbent volume.

Adsorption of supercritical gases takes place predominantly in pores which are less than four or five molecular diameters in width. As the pore width increases, the forces responsible for the adsorption process decrease rapidly such that the equilibrium adsorption diminishes to that of a plane surface. Thus, any pores with widths greater than 2 nm (meso- and macropores) are not useful for enhancement of methane storage, but may be necessary for transport into and out of the adsorbent micropores. To maximize adsorption storage of methane, it is necessary to maximize the fractional volume of the micropores (<2 nm pore wall separation) per unit volume of adsorbent. Macropore volume and void volume in a storage system (adsorbent packed storage vessel) should be minimized [18, 19].

Presently, the most successful adsorbents are microporous carbons, but there is considerable interest in other possible adsorbents, mainly porous polymers, silica based xerogels or zeolite type materials. Regardless of the type of material, the above principles still apply to achieving a satisfactory storage capacity. The limiting storage uptake will be directly proportional to the accessible micropore volume per volume of storage capacity.

The issue of the theoretical maximum storage capacity has been the subject of much debate. Parkyns and Quinn [20] concluded that for active carbons the maximum uptake at 3.5 MPa and 298 K would be 237 V/V. This was estimated from a large number of experimental methane isotherms measured on different carbons, and the relationship of these isotherms to the micropore volume of the corresponding adsorbent. Based on Lennard-Jones parameters [21], Dignum [5] calculated the maximum methane density in a pore at 298 K to be 270 mg/ml. Thus an adsorbent with 0.50 ml of micropore per ml could potentially adsorb 135 mg methane per ml, equivalent to about 205 V/V, while a micropore volume of 0.60 ml/ml might store 243 V/V. Using sophisticated parallel slit

models and Monte Carlo simulations or density functional theory, Matranga, Myers and Glandt [22] and Tan and Gubbins [23], have concluded that the maximum methane density is 223 mg/ml of pore volume. Hence the maximum storage volume at 298 K is 220 V/V, based on a pore width of 1.14 nm [22] or 1.12 nm [23], which is the pore width where maximum density occurs, and assuming that a monolithic carbon of picce density 0.67 g/ml having these properties could be made.

3.3 Pore Size Distribution

Although a correlation between BET surface areas from 77 K nitrogen isotherms and methane uptake at 298 K and 3.5 MPa has been shown for many carbon adsorbents, [11, 20], deviations from this relationship have been observed [20]. However, as a primary screening process for possible carbonaceous adsorbents for natural gas, this remains a useful relationship. It should be noted that this correlation only seems to be applicable for active carbons.

The models of Matranga, Myers and Glandt [22] and Tan and Gubbins [23] for supercritical methane adsorption on carbon using a slit shaped pore have shown the importance of pore width on adsorbate density. An estimate of the pore width distribution has been recognized as a valuable tool in evaluating adsorbents. Several methods have been reported for obtaining pore size distributions, (PSDs), some of which are discussed below.

Many years ago, Dacey and Thomas [24] used the direct approach of adsorbing molecules of different size on the same adsorbent. This method has also been used more recently by Jagiello et al. [25] who adsorbed alkanes of increasing size supercritically on different carbons. Because of the limited range of suitable adsorbate molecules, larger pore dimensions are difficult to determine. It is also a very time consuming technique. Horvath and Kawazoe [26] used the subcritical, 77 K, nitrogen isotherm at very low relative pressures to determine the pore size distributions. Stoeckli [27] has also used subcritical isotherm analyses based on the Dubinin-Radushkevich (D-R) equation for the determination of PSDs. Stoeckli's method [27], however, imposes a Gaussian distribution to the solution of the pore size distribution. Kakei et al. [28] used the D-R plot of subcritical isotherms to observe stepwise pore filling, and from this obtained a PSD. While all of the above methods are useful, the conditions for adsorbate measurement are quite different to supercritical methane storage where no condensed or quasi condensed phase exists. For this reason, and because their interest was in supercritical methane adsorption, Sosin and Quinn [29] have proposed a method of obtaining the PSD for a carbon adsorbent directly by analysis of the supercritical methane isotherm. They calculated methane density data for the various pore widths considered in the model of Tan

and Gubbins [23]. In using this supercritical model, any problems in the isotherm analysis due to possible condensation and uncertain adsorbed phase density are avoided. No restrictions are imposed on the solution of the PSD. Sosin and Quinn's approach makes it possible to compare different carbon adsorbents and gives some indication of how close they come to having the ideal pore width, 1.12 nm, suggested by the Tan and Gubbins model [23]. Since this model defines the pore width as being from the center of each carbon atom forming the pore, the "effective pore width" of this ideal pore, as defined by Everett and Powl [30], becomes 1.12 minus the width of one carbon atom (0.34 nm) to give 0.78 nm. This latter convention is used by Sosin and Quinn. Perhaps more importantly, this analysis of supercritical methane isotherms, gives greater insight into any changes in pore structure which may have occurred because of modification in the preparation conditions of a carbon adsorbent. Fig. 5 shows the methane isotherms at 298 K for two carbons prepared from the same precursor using potassium hydroxide as the activating agent.

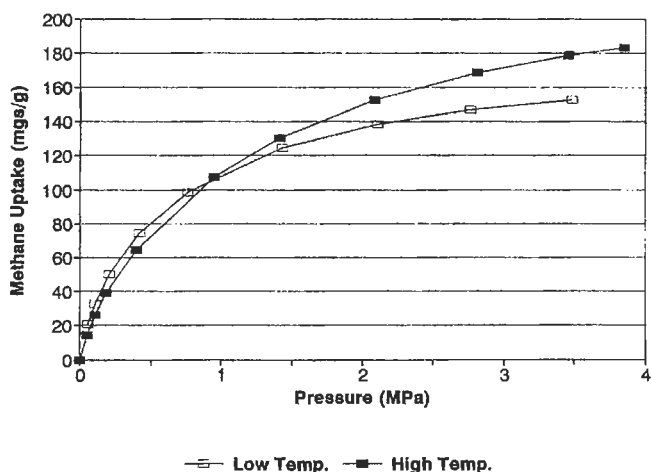


Fig. 5. Methane isotherms at 298 K on two potassium hydroxide activated carbons.

The preparation conditions were the same for both carbons with the exception of temperature, one being made at 200 K higher than the other. These methane isotherms show that at methane pressures up to 1 MPa, the lower temperature carbon adsorbs marginally more methane than the higher temperature carbon, but at pressures greater than 1 MPa, the latter carbon shows greater methane uptake. Clearly these carbons behave differently with respect to methane adsorption. From their isotherms, it might be supposed that the lower temperature carbon has a narrower pore size and a lower pore volume than the higher temperature carbon. Applying the PSD analysis of Sosin and Quinn to each isotherm shows that indeed the lower temperature carbon has a greater

volume of pores in the less than 1.0 nm pore size range, but has a smaller overall pore volume. This result is illustrated in Fig. 6, where the volume in each pore size range is plotted as a bar graph for various pore widths.

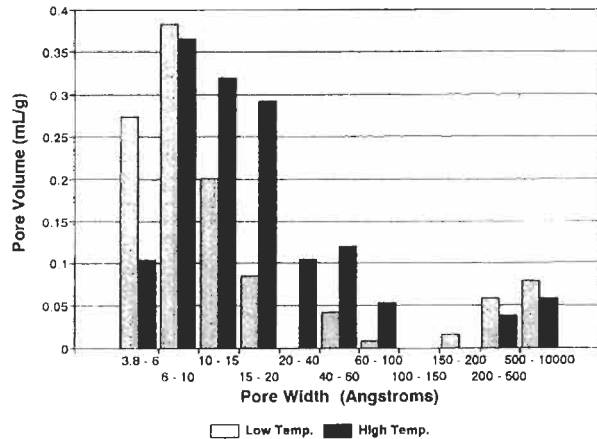


Fig. 6. Pore size distributions obtained by analysis of the methane isotherm for the two potassium hydroxide activated carbons.

Thus, while models may suggest optimal pore structures to maximize methane storage, they give no indication or suggestion as to how such a material might be produced. On the other hand, simple measurement of methane uptake from variously prepared adsorbents is not sufficient to elucidate the difference in the pore structure of adsorbents. Sosin and Quinn's method of determining a PSD directly from the supercritical methane isotherm provides an important and valuable link between theoretical models and the practical production of carbon adsorbents

3.4 Storage Capacity

The most important evaluation of an ANG storage systems performance is the measurement of the amount of usable gas which can be delivered from the system. This is frequently defined as the volume of gas obtained from the storage vessel when the pressure is reduced from the storage pressure of 3.5 MPa (35 bar) to one bar, usually at 298 K. This parameter is referred to as the delivered V/V and is easy to determine directly and free from ambiguity. Moreover, it is independent of the ratio of gas adsorbed to that which remains in the gaseous state. To determine the delivered V/V an adsorbent filled vessel of at least several hundred cubic centimeters is pressurized at 3.5 MPa and allowed to cool under that pressure to 298 K. The gas is then released over a time period sufficient to allow the bed temperature to return to 298 K. A blank, where the vessel is filled with a volume of non-porous material, such as copper shot,

equivalent to the external volume of adsorbent as measured by mercury porosimetry at one bar, is tested in the same manner. The volume of gas delivered from this blank should then be subtracted from that delivered from the adsorbent filled vessel. This ensures that gas stored in ancillary piping etc. is not considered as being stored by the adsorbent [17]. In the evaluation of ANG adsorbents, this experiment is seldom carried out. Sometimes only a few grams of material are available, or the material is a powder of low density which makes it difficult to optimize its performance in this type of experiment.

The storage capacity of an ANG storage system is always greater than its delivered capacity, usually by about fifteen percent. For some carbons, however, it can be as high as thirty percent because of the large amount of methane which is held by the adsorbent at less than one bar, (0.1 MPa). Carbons which are very microporous, such as polyvinylidene chloride (PVDC) carbons, tend to have very steep initial slopes to their methane isotherm, and as much as thirty percent of their overall uptake occurs at less than 0.1 MPa. These carbons have a high storage capacity but a much lower deliverable V/V.

Isotherm measurements of methane at 298 K can be made either by a gravimetric method using a high pressure microbalance [31], or by using a volumetric method [32]. Both of these methods require correction for the non-ideality of methane, but both methods result in the same isotherm for any specific adsorbent [20]. The volumetric method can also be used for measurement of total storage. Here it is not necessary to differentiate between the adsorbed phase and that remaining in the gas phase in void space and macropore volume, but simply to evaluate the total amount of methane in the adsorbent filled vessel. To obtain the maximum storage capacity for the adsorbent, it would be necessary to optimally pack the vessel.

From isotherm measurements, usually carried out on small quantities of adsorbent, the methane uptake per unit mass of adsorbent is obtained. Since storage in a fixed volume is dependent on the uptake per unit volume of adsorbent and not on the uptake per unit mass of adsorbent, it is necessary to convert the mass uptake to a volume uptake. In this way an estimate of the possible storage capacity of an adsorbent can be made. To do this, the mass uptake has to be multiplied by the density of the adsorbent. This density, for a powdered or granular material, should be the packing (bulk) density of the adsorbent, or the piece density if the adsorbent is in the form of a monolith. Thus a carbon adsorbent which adsorbs 150 mg methane per gram at 3.5 MPa and has a packed density of 0.50 g/ml, would store 75 g methane per liter plus any methane which is in the gas phase in the void or macropore volume. This can be multiplied by 1.5 to convert to the more popular unit, V/V.

It is tempting to speculate on the storage capacity of a packed vessel by assuming that the density of the adsorbent can be increased to a higher value. In the above example, if the adsorbent density were increased to 0.70 g/ml, then 105 g of methane per liter (plus gas phase) would be stored. The quantity as gas phase in the vessel would decrease because of the increased volume of adsorbent. Care must be taken in speculating about increasing adsorbent density. Adsorption is dependent on the micropore volume of the carbon adsorbent. For example, Amoco PX-21, later known as Anderson AX-21 and now made by Kansai under license from Amoco and marketed as Maxsorb, has a micropore volume of about 1.20 ml/g. One gram of graphite, density 2.26 g/ml, occupies 0.44 ml. This would be the minimum volume occupied by a gram of carbon atoms in a porous carbon. The minimum volume of one gram of PX-21 would be $1.20 + 0.44$, 1.64 ml/g, hence a maximum density of 0.61 g/ml. If PX-21 could be packed to a greater density then this must be at the expense of micropore volume, which in turn would reduce the amount of methane adsorbed.

It is also interesting to speculate about the likely properties of an adsorbent carbon capable of delivering 150 V/V, which requires storing about 175 V/V or 117 g methane per liter. From the model of Tan and Gubbins [23], for the optimal pore with an effective wall separation of 0.78 nm, the methane density at 298 K and 3.5 MPa in this pore is 0.17 g/ml. At this density, the pore volume required to store 117 g methane will be 688 ml. In one liter of carbon with 688 ml of pores there will only be 312 ml of skeletal carbon atoms. This would be equivalent to 705 g carbon, (density 2.26 g/ml). Therefore the upper limit of density for a carbon adsorbent delivering 150 V/V will be about 0.7 g/ml, (it may be less if there is any "closed" pore volume present), with a minimum micropore volume of about 1.0 ml/g. The pore volumes shown in Fig. 6 suggest that the low temperature carbon has properties closer to this ideal value than the higher temperature carbon, which has too large a pore volume, (about 1.3 ml/g).

The above simplified and idealized argument does not take into account diffusion of methane in or out of a packed bed, or of heat transfer in large diameter packed cylinders. Barbosa-Mota et al. [33, 34] have described a model which predicts the filling times, capacities, temperature changes and heat transfer which occur with adsorption in cylindrical vessels packed with either monolithic or granular carbon used for natural gas storage. The AGLARG experience was that slow rates of diffusion and poor heat transfer substantially reduce the performance of the storage system.

3.5 Current Adsorbents

Parkyns and Quinn [20] showed a linear relationship between methane uptake at 25°C, 3.4 MPa and the Dubinin-Radushkevich micropore volume from 77 K nitrogen adsorption for porous carbons,

$$\text{Methane Uptake (25°C, 3.4 MPa)} = 0.120 * \text{Micropore Volume} + 0.021$$

where uptake is g methane per g carbon and micropore volume is ml micropore per g carbon.

McIntasty et al. [35] and others [13, 36] have measured methane uptakes on zeolites. These materials, such as the 4A, 5A and 13X zeolites, have methane uptakes which are lower than would be predicted using the above relationship. This suggests that either the zeolite cavity is more attractive to 77 K nitrogen than a carbon pore, or methane at 298 K, 3.4 MPa, is attracted more to a carbon pore than a zeolite. The latter proposition is supported by the modeling of Cracknell et al. [37, 38], who show that methane densities in silica cavities will be lower than for the equivalent size parallel slit shaped pore of their model carbon. Results reported by Ventura [39] for silica xerogels lead to a similar conclusion. Thus, porous silica adsorbents with equivalent nitrogen derived micropore volumes to carbons adsorb and deliver less methane. For delivery of 150 V/V a silica based adsorbent would require a micropore volume in excess of 0.70 ml per ml of packed vessel volume.

Porous polymers with large 77 K nitrogen surface areas also have inferior methane uptakes. For example Dow XV 43546, a porous polystyrene with a 77 K nitrogen BET area of 1600 m²/g has a methane uptake of 67 mg/g at 25°C, 3.4 MPa, whereas Takoda HGK 971 carbon of similar 77 K nitrogen surface area has an uptake of 116 mg methane per g. Rohm and Haas "Amberlite" porous polymers give similarly lower than expected methane uptakes.

High 77 K nitrogen surface area materials have been produced by Laine et al. [40], Jagtoyen and Derbyshire [41] and by Botha and McEnaney [42] using phosphoric acid activation of cellulosic materials at low heat treatment temperature, < 500°C. Using the same technique, MacDonald and Quinn [43] produced peach pit derived chars that had large 77 K nitrogen micropore volumes. These chars still contained large amounts of oxygen and hydrogen and so were not truly porous "carbons". Their methane uptake was considerably lower than that predicted from the Parkyns and Quinn [20] relationship for carbons.

Porous carbons are far from having a “clean” carbon surface but have many surface functional groups which for some applications and studies clearly alter the adsorbate / adsorbent interaction. Unless treated for specific functionality, most porous carbons have mainly oxygen complexes on their surface. To determine to what extent a modified surface altered methane uptake, a sample of Calgon BPL carbon, initially reduced by heating at 500°C for one hour under a flow of hydrogen, was then oxidized to varying degrees by nitric acid treatment, washed, dried and stored under vacuum [44]. Methane uptake at 25°C , 3.4 MPa was measured for each treatment. Unfortunately there did not seem to be a relationship between the exposure time to nitric acid and the extent of oxidation on the carbon surface. The results are listed in Table 1.

Nitric acid treatment lowered the methane uptake by about ten percent. This could be due to oxygen occupying sites within pores, but may be the result of weaker interaction between methane and an oxide surface as is observed for silica. Reduction of these treated carbons with hydrogen restored their original methane uptake. Clearly for methane storage, there is no advantage in modifying the carbon surface by nitric acid treatment.

Table 1. Surface Treatment of Calgon BPL Carbon with Nitric Acid

Sample	Treatment	Surface	Methane Uptake
		[O] mg/g	3.4 MPa, 298 K mg/g
(1)	As received	29	86
(2)	Hydrogen reduced	14	87
(3)	6M Nitric 80 min.	85	76
(4)	6M Nitric 120 min.	64	81
(5)	6M Nitric 240 min.	79	80
(6)	(3) Reduced	15	82
(7)	(4) Reduced	14	86
(8)	(5) Reduced	14	87

From the above data, it would appear that methane densities in pores with carbon surfaces are higher than those of other materials. In the previous section it was pointed out that to maximize natural gas or methane storage, it is necessary to maximize micropore volume, not per unit mass of adsorbent, but per unit volume of storage vessel. Moreover, a porous carbon filled vessel will store and deliver more methane than a vessel filled with a silica based or polymer adsorbent which has an equivalent micropore volume fraction of the storage vessel.

All commercial carbons have been made for uses other than natural gas storage. They are for the most part granular materials and pack into vessels with a substantial inter-particle void volume which results in low bulk densities. Some

also have a considerable macropore volume. These reasons alone detract from their potential as efficient ANG adsorbents. Additionally, these carbons have insufficient micropore volume for that required to give 170+ V/V storage at 3.5 MPa, 298 K. The micropores are also unlikely to have the correct dimensions for optimum ANG storage, 0.78 nm effective pore width.

Crushing, selective particle size packing or hydraulic compaction can be used to reduce interparticle void space and increase the bulk density within the storage tank to approach the particle density of the carbon. Even with these extreme methods of packing, the fraction of the vessel which is micropore is never greater than 0.50 for any commercial carbon, considerably short of the 0.70 which is necessary for 170 V/V storage.

Table 2. Fractional Volume Composition of Carbon Particle for some Commercial Carbons

Supplier	Type	Precursor	Hg Porosimetry Densities		Fractional Volume of Carbon Particle which is :		
			0.1 MPa g/ml	404 MPa g/ml	Carbon	Macro/meso	Micropore
Barneby- Sutcliffe	MI	CNS*	0.71	1.05	0.323	0.324	0.353
Calgon	BPL	Coal	0.75	1.11	0.341	0.324	0.335
California	GMS-70	CNS*	0.68	1.11	0.309	0.387	0.304
Kurcha	BAC	Pitch	0.90	1.08	0.409	0.167	0.424
Norit	R1	Wood	0.68	1.15	0.309	0.409	0.282
North American	G210	CNS*	0.69	0.96	0.314	0.281	0.405

* Coconut shell

Table 2 illustrates this point where, by using mercury porosimetry, carbon densities at 0.1 MPa and 404 MPa have been used to calculate the fractional volumes of macro/meso, micropore and skeletal carbon for some carbons based on the following:

$$\text{Fraction}_{\text{C atoms}} = \text{Density}[0.1 \text{ MPa}] / 2.2$$

$$F_{\text{micropore}} = \text{Density}[0.1 \text{ MPa}] * (1/\text{Density}[404 \text{ MPa}] - 1/2.2)$$

$$F_{\text{macro/mesopore}} = \text{Density}[0.1 \text{ MPa}] * (1/\text{Density}[0.1 \text{ MPa}] - 1/\text{Density}[404 \text{ MPa}])$$

where 2.2 g/ml is used for the density of non-porous carbon.

At 0.1 MPa the mercury surrounds the carbon particle but does not enter any pores. When the pressure on the mercury is increased to 404 MPa, it is considered to penetrate into all pores of wall separation greater than 3 nm. Pores of smaller dimensions can, for convenience, be regarded as micropores although this falls somewhat outside the IUPAC definition of a micropore. The fractional values for micropore given in Table 2 are more than optimistic since they are calculated assuming that the vessel is packed without any interparticle void space. There have been a number of attempts to increase the micropore volume of carbons for ANG by conventional activation methods, such as carbon dioxide on carbon fibers [45], phosphoric acid on wood monoliths [46], an air cycling method [47] and the enhancement of PVDC based carbons [64] to mention only a few which have showed promise. The method which seems to be most successful in creating a large micropore volume is by using a molten potassium salt, of which potassium hydroxide is the most popular, to activate carbon. The drawback to this method is that the highly activated product has a very low bulk (packed) density. When vessels are filled with these carbons at their normal bulk density, which is generally about 0.30 g/ml, they do not store sufficient gas to deliver 150 V/V from 3.4 MPa and 298 K.

Over the past ten years or so there have been several attempts to increase the bulk density of PX-21, AX-21 or Maxsorb, all basically the same carbon, made by activating petroleum coke with molten potassium hydroxide. This carbon can be compacted to densities about double its normal bulk density of 0.28 g/ml but when the constraining force is removed the carbon rebounds to a much lower density. Binders have been used to produce monoliths of higher density as a more practical solution compared to powder compaction. The penalty in using binders is a reduction in micropore volume and surface area as well as an associated decrease in methane uptake per unit mass of adsorbent. However, in some cases this penalty is more than offset by the density increase and results in greater overall methane storage. The most successful binding method reported for AX-21 is that of Bose et al. [16], who produced high density monoliths using only 2% polyvinyl alcohol as the binder at a compaction pressure of 136 MPa, which stored 186 V/V methane at 3.5 MPa, 298 K. Table 3 lists values of stored methane in a number of studies using Amoco type carbons.

Potassium hydroxide has been used as an activating agent for more than sixty years [54], but because it is a difficult process it was not used successfully until about ten years ago when Kansai started producing Maxsorb carbon. Although the original Amoco patent [55] used petroleum coke or coal coke as the feedstock, other feedstocks have been investigated recently. Kansai [56] have patented the use of KOH for coconut shell carbon (CNS) activation. Westvaco have several patents specifically for an ANG adsorbent [64] which use wood, CNS, and other ligno-cellulose based carbons activated using a two stage

Table 3. Some Studies on Methane Storage using Amoco Type KOH Activated Carbon Adsorbents

Study	Carbon Form	Density g/ml	BET Area sq m/g	Methane Uptake 3.4 MPa, 298K mg/g	Storage	Storage Conditions	
					Ads + Gas V/V	Pressure MPa	Temperature K
1983 Barton et al. [18]	Amoco GX-32 Extrudate	0.30	2500	164	98	3.4	298
1984 Remick et al [12]	Anderson AX-21	0.43			138	3.4	
1985 Notaro [6]	AX-21 Powder	0.27	2965				
	AX-21 Pellets	0.29	2342				
	AX-21 20% PVA	0.38		142		3.0	299
	AX-21 Diskstack	0.37			101	3.4	295
1987 Qunn et al. [48]	63% AX-21, 37% PVDC	0.70	1860	140	163	3.4	298
1989 Chaudron [49]	AK-AX Pellets	0.45	3000	153	105	2.0	293
	AK-AX Pellets	0.45	3000	180		3.5	293
1989 Pedersen [50]	Shell AX-21	0.33	3600	165		3.0	
1991 Bose et al. [16]	Anderson AX-21	0.30	2800	173	109	3.5	298
	AX-21 2% PVA	0.70		148	186	3.5	298
1992 Wegrzyn et al. [17]	Kansai Maxsorb	0.27	2690		98	3.5	298
	Maxsorb compacted	0.40			122	3.5	298
1993 Lin and Huff [51]	Amoco PX-21	0.26	3000		85 Delivered	3.4	298
	PX-21 Monolith	0.45			152 Delivered	3.4	298
1995 Chen & McEnaney [52]	Anderson AX-21	0.27	2909				
	AX-21 17% Phenolic	0.43	2432		127	3.4	298
	AX-21 31% Phenolic	0.59	2054		152	3.4	298
1997 Mansai et al. [53]	Kansai Maxsorb	0.28	3272	250 with gas phase	110	3.4	298
	Maxsorb Extrudate	0.32	2267	200 with gas phase	95	3.4	298
	Maxsorb Monolith	0.56	2043	180 with gas phase	155	3.4	298

method, firstly with phosphoric acid, followed by potassium hydroxide. Union Carbide [57] have also used KOH activation on a large variety of precursors but they indicate that on a volume basis more methane can be stored by conventionally steam activated carbons made from rayon or cotton. Recently, Kaneko and Murata [58] modified AX-21 by MgO impregnation and showed that the methane density in the micropore at pressures to 10 MPa at 303 K for the impregnated sample was increased considerably. However, the micropore volume from 77 K nitrogen per mass of carbon was dramatically reduced, thus on a V/V basis there would probably be no advantage. It may be that nitrogen adsorption at 77 K is more susceptible to MgO impregnation, resulting in reduced uptake rather than an increase in methane density at 303 K. The methane uptake per gram at 10 MPa would be approximately the same for both carbons. Very successful methane adsorbents have been produced by Chaffee and Pandolfo [59] using KOH to activate bituminous coal and lignite. Using their bulk density, the activated products were estimated to store 175 - 185 V/V methane at 4 MPa. Activation of the same precursors using steam resulted in clearly inferior adsorbents for methane storage. Verheyen et al.[60] have also shown the successful use of KOH in the production of activated carbons from coal.

In a recent study for the US Department of Energy [61], AGLARG have shown that suitable adsorbents for ANG can be produced from peach pit or coconut shell using KOH as the activating agent. These carbons, like all KOH produced carbons, were low in bulk density. Densities of greater than 0.6 g/ml were possible with compaction in small vessels (<50 ml) and deliveries of greater than 150 V/V methane could be obtained from 3.4 MPa at 298 K.

Brookhaven National Laboratory [62] has measured deliveries in excess of 150 V/V from small vessels of less than 100 ml, filled with compacted carbon, from a fill pressure of 3.5 MPa. Three different carbons, all made independently using potassium hydroxide as the activating agent [63-65], successfully delivered more than 150 V/V. With larger vessels these densities could not be obtained by compaction. To achieve a sufficiently high density, the AGLARG carbon was bound using a proprietary binder to produce monolithic pieces with densities based on their geometric volume in excess of 0.60 g/ml. In the laboratory, using a one liter cylindrically shaped vessel filled with 5 cm diameter cylindrically shaped monoliths, it was possible to deliver more than 150 V/V from 3.4 MPa, 298 K. However, with scale up to full size flat storage tanks (described elsewhere in this chapter) the delivery fell to 140-145 V/V. This was thought to be due to problems most probably associated with the complex shape of the monolith required for the extruded aluminum flat tank cells, see Fig. 4. Nonetheless, these tests have shown that storage in excess of

180 V/V and deliveries of more than 150 V/V are possible from a carbon adsorbent-filled vessel of realistic volume.

4 Adsorbent Fill-Empty Testing

Another criterion of importance to ANG systems is the long term deliverability of the adsorbent. In an ideal ANG system, the adsorption of methane on the adsorbent should be completely reversible. Indeed, this has been shown to be nearly the case for methane on carbon adsorbents. However, while methane is the chief component of natural gas, there are substantial amounts of other components, some of which are strongly adsorbed and thus tend to accumulate on the adsorbent over a period of many fill-empty cycles. Such strongly adsorbed gases cannot readily be desorbed except by heating the adsorbent and/or by evacuation, both of which present practical difficulties in a vehicle storage vessel. The net result is a decrease in the methane storage capacity. There is some evidence that this reduction may level off with repeated fill-empty cycling [66, 67]. An alternative, and perhaps better solution, to this problem is more fully discussed in the next section of this chapter, which considers preadsorption of non-methane species using guard beds.

Cyclic tests can be performed in just a few months to simulate years of fill and discharge cycles. The adsorbent filled ANG tank is repeatedly charged with natural gas to a preset pressure, then discharged through a flow meter to determine the quantity of gas delivered from each cycle.

The third property measured when testing the adsorbent filled storage vessel are the thermal changes which occur during the adsorption and desorption cycles. During adsorption, or a fuel fill, the exothermic adsorption causes the storage system temperature and pressure to rise. This results in an incomplete fill unless a slow fill is used, during which the tank is allowed to equilibrate with the surroundings. Depending on storage tank composition and design, this can take several hours. It should be noted that it is not the total heat of adsorption which is involved here. Since filling takes place from a pressure of 0.1 MPa, (1 bar), to the maximum fill pressure, usually 3.5 MPa, (35 bar), the carbon adsorbent already has most of the high energy sites occupied by methane adsorbed below 0.1 MPa. Conversely, during discharge, the endothermic desorption process causes a substantial temperature decrease within the tank along with a concomitant decrease in the tank pressure. Fig. 3 illustrates how dramatic this can be.

ANG tank design and the adsorbent materials chosen can help to minimize these problems. However, these alone may not provide a total solution to the

problems. Other means, such as multiple tanks with switching to provide a sufficient recovery time, or fuel booster compressors are worthy of consideration.

5 Guard Beds.

5.1 Storage System Protection

The application of ANG as a vehicular fuel storage system has also to address the variation in pipeline composition of natural gas from state to state within the USA, or from country to country in Europe and the rest of the world. The composition of natural gas varies widely and it often contains gases other than fuel gases e.g. nitrogen and carbon dioxide. Whereas the adsorption capacity for methane in ANG systems remains constant through many adsorption and desorption cycles, such cyclic operation using natural gas results in a gradual deterioration of capacity [67, 68]. This deterioration is the result of accumulation of the impurity gases on the adsorbent used in the ANG storage system because of preferential adsorption of the "heavier" hydrocarbon gases, which possess greater adsorption potentials on active carbon than that of methane. Recognition of this deterioration has been addressed by AGLARG using the addition of some form of preadsorption system, or "guard bed", to remove the "heavier hydrocarbon" gases prior to adsorption in the main storage tank [69, 70].

5.2 Target Gases for Guard Bed Systems

All hydrocarbon gases possess a higher adsorption potential than methane and it is often thought that these gases are targets for pre-adsorption in guard bed systems. In addition, most of the common odorant species, e.g. mercaptans, ethyl and methyl sulfide, etc., also possess adsorption potentials greater than that of methane. This is evidenced by the critical and boiling temperatures of such gases, as well as actual uptake measurements [71, 72]. Hence, one might think that all the gaseous minor components of natural gas should be targets for pre-adsorption because under equilibrium conditions all would be adsorbed in preference to methane. However, ANG storage systems are not equilibrium systems and therefore consideration must be given to the actual partial pressure of a specific minor component of natural gas and the influence of the dynamics of adsorption upon the target species. Adsorption data at high pressure are limited [71] and of high pressure mixtures even more so [72]. However, gas behavior at STP can be considered to establish an adsorption ranking because the adsorption potential of the gaseous components will increase in line with their molar composition in a pressurized mixture.

Table 4 shows the composition of a typical British natural gas, including the components as relative pressures, and their potential for adsorption on a coal based pellet (SSC 207EA 4mm).

Table 4. Typical Composition of British Natural Gas expressed as relative pressure and their potential for adsorption on a coal based carbon.

Bacton Terminal Gas Component	Concentration vol.%	Relative Pressure	Potential Uptake g/g
Carbon dioxide	0.25		
Nitrogen	3.17		
<u>Hydrocarbons</u>			
Methane	92.81		
Ethane	2.84	7.320E-04	
Propane	0.58	2.350E-04	0.019
Butane	0.20	9.480E-04	0.068
Pentane	0.067	1.370E-03	0.127
Hexane	0.032	2.240E-03	0.176
Heptane	0.017	3.970E-03	0.232
Octane	0.007	4.800E-03	0.259
Nonane	0.001	2.220E-03	0.262
Benzene	0.022	2.960E-03	0.127
<u>Odorants</u>			
Diethyl sulfide	7.00E-04	1.160E-04	0.143
Methyl ethyl sulfide	6.00E-05	4.260E-06	2.920E-02
Ethyl mercaptan	6.00E-05	1.180E-06	8.600E-04
Tert. butyl mercaptan	1.20E-04	8.500E-06	0.079

Comparison of the volume/volume composition data with the relative pressure data shows that although C2-C4 hydrocarbons are present to the greatest volume percent, their actual pressures are an order of magnitude lower than the C5 plus hydrocarbons. Hence, the C5 plus hydrocarbons would be adsorbed in preference to the C2-C4 hydrocarbons and would displace them over a number of cycles. It is apparent therefore that the C5 plus hydrocarbons must be considered the primary target gases for pre-adsorption in guard bed systems

The added odorants in natural gas require specific consideration. Table 4 shows that odorants are present at low partial pressures. Hence, adsorption of these odorants within a guard bed is likely to be small, especially when associated with the competitive adsorption of the hydrocarbon gases. It is probable therefore that some odorants e.g. ethyl mercaptan, will in fact pass through the guard bed and be present within the storage tank. Adsorption of odorants within the storage tank will be small because of their low partial pressures, and competitive adsorption of C4 and C5 hydrocarbons. Therefore, it seems unlikely that the odorant gases would accumulate within the storage vessel and thus would have an insignificant effect upon the storage performance. Indeed, their presence within the storage tank may be advantageous ensuring that the natural gas is odorized throughout the ANG storage system.

5.3 Guard Bed Adsorbent Characteristics

It is difficult to make generalizations regarding the desirable characteristics of active carbons for guard bed applications without consideration of specific guard bed designs, e.g., fixed or mobile, and method of operation, i.e., heated or non-heated. However, consideration of the target gases and their likely adsorption/desorption behavior, allows some generic classification to at least be intimated. The basic function of the guard bed is to adsorb C5 plus other hydrocarbons, preventing their accumulation within the main adsorbent storage bed. The relatively low partial pressures or relative pressures (relative to the pure substance vapor pressure) of these trace components suggests the need for an adsorbent of high adsorption capacity, i.e. containing a high proportion of micropores. However, probably more important than the adsorptive properties are the desorptive properties of the adsorbent. Facile desorption is required to prevent retention of the C5 plus gases on the guard bed, shortening its operating life and increasing the need for bed replacement. The importance of adsorbent desorptive properties are already widely appreciated in Evaporative Loss Control Devices (ELCDs), where the saturation uptake of butane under dynamic conditions, and weight desorbed in 200- 300 bed volumes of air passing through the adsorbent, are used to define the optimum adsorbent characteristics [73]. For ELCDs, it is generally accepted that adsorbents exhibiting a high proportion of pores at the upper end of the micropore range and the lower end of the mesopore range exhibit the desired adsorption/desorption behavior. Such carbonaceous adsorbents tend to be typically (but not exclusively) those from coal or wood based precursors. Since the guard bed is a specialized ELCD, adsorbents already optimized for these applications should be well suited to the guard bed application. However, the porous structure of the adsorbent and its adsorption/desorption properties are not the only features of importance in

defining the requirements of a guard bed adsorbent, the heat capacity and thermal conductivity of the adsorbent must additionally be considered.

The heats of adsorption and desorption need to be dissipated and subsequently returned if good cyclic efficiencies are to be gained. Indeed, the thermal effects of adsorption are critical factors for mobile guard beds, where heat load for desorption may place an additional electrical load on the vehicle systems. Adsorbents should possess high heat capacity and thermal conductivity values, properties which favor high density carbons. To some extent, desirable adsorptive and thermal properties are somewhat contradictory. Adsorbents possessing large inherent pore volumes will exhibit low thermal conductivity. Additionally, granular beds exhibit poor heat transfer characteristics. Thermal conductivity values in the range of 0.86 W/m.K have been calculated for single grains of SSC 208C, which reduced to 0.17 W/m.K for a bed of 208C used in ammonia adsorption studies [74]. However, good adsorptive and thermal properties can be combined in densified or immobilized adsorbents, provided the incorporation of binder phase is not deleterious to adsorptive capacity. A thermal conductivity of 0.33 W/m.K was reported for an immobilized 208C adsorbent used in ammonia studies [74]. Therefore, the desired guard bed adsorbent is one which combines high adsorptive capacity with low retentivity and which also has good thermal conductivity, a particularly difficult target to achieve.

5.4 Guard Bed Design

Two guard bed design concepts need to be considered, a large fixed unit present at the fuel source or filling point, or a small mobile pre-adsorption unit incorporated into the vehicle mounted ANG storage system. The fixed system has the obvious advantage of scale, making possible the use of conventional regeneration technologies e.g. hot gas or steam, with proper gas handling facilities for the enriched desorbed phase. However, the fixed system has the primary disadvantage that it produces a substantially deodorized gas stream to downstream pipework and the vehicle refueling point. This fact, in addition to the large fixed capital costs associated with the installation of such facilities at every filling station, has tended to rule out their use in favor of small vehicle mounted guard bed units in most ANG storage concepts. The smaller mobile unit suffers the disadvantage of scale, and would be less efficient in complete removal of undesirable gas species. However, it would offer the advantage of allowing some odorized gas throughout the storage system. Heat management in mobile guard beds also must be considered. Being relatively small units, with a high external surface to mass ratio, heats of adsorption can be relatively quickly dissipated. The heat of desorption needed to effectively purge mobile guard beds must come from an external source. This could be made available

via a thermal feed back loop from the vehicle cooling or exhaust systems. Such systems would be complex and possibly too heavy for practical application. However, the guard beds could be heated by internally mounted electrical cartridge heaters, powered from the vehicle electrical system. Such an approach has been shown to be successful [69, 70].

Data on the long term performance of guard bed systems has not been widely reported because of its proprietary nature. Work reported to Future Fuels Inc. [75], confirmed the observations above, i.e., that guard beds were effective in the removal of C5 plus hydrocarbons. The C2 - C5 hydrocarbons were shown to pass to the ANG storage vessel where they desorbed again on depressurization. C2 - C5 hydrocarbons were desorbed from the guard bed on flow through and the guard bed was as effective in desorbing these hydrocarbons when cold as it was when heated. However, the fate of the adsorbed C5 plus hydrocarbons was not discussed in this work and it is likely that a guard bed would require heating to desorb these species.

6 Summary.

In excess of one million vehicles worldwide presently use natural gas as their fuel. Predominantly, it is stored as CNG at about 20 MPa. An alternative which may be safer and more advantageous to use is an ANG storage system operating at considerably lower fill pressures. However, a successful adsorbent storage system for NGVs requires much more than a good adsorbent, but, without a high performance adsorbent, ANG can not become a commercial reality. With limited space available on-board a vehicle, storage performance must be based on the energy which can be stored within a given volume. The minimum acceptable level is considered to be 150 V/V, 6.2 lb./cubic foot, equivalent to about one gallon of gasoline. To achieve this level of performance the adsorbent has to adsorb about 120 mg gas per ml of adsorbent, where the adsorbent volume must be the practical packed volume. To date, porous carbons have yielded the best performance, but the micropore volume and pore size must be carefully controlled to make such an uptake possible.

The second essential element of an ANG system is the storage vessel itself. The high pressures (20+ MPa) used for CNG storage demand the use of a cylindrical vessel. The external envelope of large cylinders cannot easily be placed efficiently within a small vehicle structure. The lower ANG pressure (<5 MPa) provides for more versatility in vessel design compared to CNG. The AGLARG tank design helps solve the problem of efficient space utilization. Possibly, future vessels of a similar type can be integrated into the vehicle structure.

Good heat dissipation on adsorption (fueling) and good heat input during desorption (fuel use) are desirable features for maximizing capacity and use of an ANG system. The flat aspect and internal webs of the AGLARG tank design provides better heat transfer when compared to a cylindrical vessel, and greatly improve the overall performance of the ANG system.

Natural gas composition varies greatly. Although principally methane, it often contains components such as higher alkanes which are irreversibly adsorbed at ambient temperature, and gradually reduce the adsorbent uptake of methane, lowering the overall storage capacity. Currently, it is unlikely that natural gas will be "cleaned up" prior to delivery to a NGV. Consequently a vehicle's ANG storage system will have to be protected from the deleterious components in natural gas. The use of guard beds, which in themselves are adsorbent systems where the adsorbent has to be carefully selected for rapid preferential adsorption of the higher alkanes, pentanes and above, has been shown to be effective in maintaining the storage capacity of the ANG tank. Thus the "guard bed" is an essential component of a satisfactory ANG storage system. Finally, although a good adsorbent is key to the success of ANG, it must be integrated into a well designed system which must compensate for the weaknesses inherent in the adsorption process, deleterious poisoning and heat effects.

7 References

1. Stephenson, J., A Position Paper on Natural Gas Vehicles 1993, International Association of NGVs, (1993)
2. Darrow, K.G., Light Duty Vehicle Full Fuel Cycle Emissions Analysis Topical Report, Gas Research Institute Report GRI-93/0472 (1994)
3. European Natural Gas Vehicle Association Bulletin, April 1996
4. Hagen, M., "Clathrate Inclusion Compounds", Reinhold, New York, 1962
5. Dignum, M.J., Report 33259, Ontario Ministry of Transportation, 1982, 1201 Wilson Ave, Downsview, Ontario, Canada M3M 1J8
6. Notaro, F., "Enhancement of Automotive Compressed Natural Gas Fuel Storage Via Adsorbents" New York State Energy Research and Development Authority Report 85-11, 1985
7. Komodromos, C., Pearson, S. & Grint, A., "The Potential of Adsorbed Natural Gas for Advanced On-board Storage in Natural Gas Fueled Vehicles", International Gas Research Conference, Florida, 1992.
8. Fricker, N. and Parkyns, N.D., "Adsorbed Natural Gas for Road Vehicle Applications", 3rd Biennial International Conference and Exhibition of Natural Gas Vehicles, International Association for Natural Gas Vehicles, Gothenburg, Sweden, 1992
9. Komodromos, C., Fricker, N. & Slater, G., "Development of Novel Tanks for Low-Pressure Adsorbed Natural Gas Storage in Vehicles", International Association for Natural Gas Vehicles, Toronto, 1994
10. Bennett, P.G. & Tilley, G., Methamotion Conference, London, 1995

11. Mullhaupt, J.T., BeVier, W.E., McMahon, K.C., Van Slooten, R.A., Lewis, I.C., Grienke, R.A., Strong, S.L., Ball, D.R., and Steele, W.E., *Carbon* '92 p. 367 (1992)
12. Remick, R.J., & Tiller, A.J., Advanced Methods for Low Pressure Storage of CNG, Non-petroleum Vehicular Fuels Conference, Washington, April 1985
13. Otto, K., *Alternative Energy Sources IV*, Vol 6 p241, Ann Arbor Science, MI
14. Barton, S.S., Holland, J.A. & Quinn, D.F., "The Development of Adsorbent Carbon for Storage of Compressed Natural Gas, Report AF-85-01, Ontario Ministry of Transportation, 1985 1201 Wilson Ave, Downsview, Ontario, Canada M3M 1J8
15. Hayhurst, D.T. & Lee, J.C., *J. Coll. Interface Sci.* 1988, 122, 456
16. Bose, T., Chahine, R. and St Arnaud, J.M., US Patent 4999330, (1991)
17. Wegrzyn, J., Wiesmann, H. and Lee, T., Low Pressure Storage of Natural Gas on Activated Carbon, SAE Proceedings 1992 Automotive Technology, Dearborn, Michigan
18. Barton, S.S., Dacey, J.R. and Quinn, D.F., in "Fundamentals of Adsorption" 1st Engineering Foundations Conference, ed Belfort and Myers, p. 65, Engineering Foundation, New York 1983
19. MacDonald, J.A.F. and Quinn, D.F., *J. Porous Materials*, 1995, 1, 43
20. Parkyns, N.D. and Quinn, D.F., "Porosity in Carbons" Ed John Patrick, Ch 11, p. 291, Edward Arnold, London 1995
21. Lennard-Jones, J.E., *Trans. Farad. Soc.* 1932, 28, 333
22. Matranga, K.R., Myers, A.L. and Glandt, E.D., *Chem. Eng. Science*, 1992, 47, 569
23. Tan, Z. and Gubbins, K.E., *J. Phys. Chem.* 1992, 94, 6061
24. Dacey, J.R. and Thomas, D.G., *Trans. Farad. Soc.* 1954, 50, 740
25. Jagiello, J., Bandosz, T.J., Putyera, K. and Schwarz, J.A., in "Characterization of Porous Solids III" *Studies in Surface Science* 1994, 87, 679
26. Horvath, G. and Kawazoe, K., *J. Chem. Eng. of Japan* 1983, 16, 470
27. Stoeckli, H.F., "Porosity in Carbons" ed John Patrick, Ch 3, p67, Edward Arnold, London 1995
28. Kakei, K., Ozeki, S., Suzuki, T. and Kaneko, K., *J. Chem. Soc., Faraday Trans.* 1990, 86, 371
29. Sosin, K. and Quinn, D.F., *J. Porous Materials* 1995, 1, 111
30. Everett, D.H. and Powl, J.C., *J. Chem. Soc. Faraday Trans.* 1976, 72, 619
31. Staudt, R., Saller, G., Tomalla, M. and Keller, J.U, *Ber Bunsenges Phys. Chem.* 1993, 97, 98
32. Masters, K.J. and Gesser, H.D., *J. Physics E; Scientific Instruments* 1981, 14, 1043
33. Barbosa Mota, J.P., Saadjan, E. and Tondeur, D., *Adsorption*, 1995, 1, 17
34. Barbosa Mota, J.P., Rodrigues, A.E., Saadjan, E. and Tondeur, D., *Adsorption* 1997, 3, 117
35. Mentasty, L., Woestyn, A.M. and Zgrablich, G., *Adsorption Science and Technology* 1994, 11, 123
36. Ozawa, S., Kusumi, S. and Ogino, Y., *J. Coll. Interface Sci.* 1976, 56, 83
37. Cracknell, R.F., Gordon, P. and Gubbins, K.E., *J Phys. Chem.* 1993, 97, 494
38. Cracknell, R.F. and Gubbins, K.E., *J. Mol. Liquids* 1992, 54, 261

39. Ventura, S. C., Hum, G.P. and Narang, S.C., "Novel Strategies for the Synthesis of Methane Adsorbents with Controlled Porosity and High Surface Area", Gas Research Institute Report GRI-93/0018, 1993
40. Laine, J., Calafat, A. and Labady, M., *Carbon* **27** 191 (1989)
41. Jagtoyen, M. and Derbyshire, F., *Carbon* **31** 1185 (1993)
42. Botha, F.D. and McEnaney, B., *Adsorption Science and Technology* **10** 181 (1993)
43. MacDonald, J.A.F. and Quinn, D.F., *Carbon* **34** 1103 (1996)
44. Barton, S.S., Evans, M.J.B., and MacDonald, J.A.F., *Carbon* **29** 1099 (1991)
45. Alcaniz-Monge, J., de la Casa-Lillo, M.A., Cazorla-Amoros, D. and Linares-Solano, A., *Carbon* **1997**, **35**, 291
46. Lopez, M., Labady, M. and Laine, J., *Carbon* **1996**, **34**, 825
47. Quinn, D.F. and MacDonald, J.A.F., US Patent 5071820
48. Quinn, D.F. and MacDonald, J.A.F., "Natural Gas Adsorbents" Report to Ministry of Transportation, Ontario, 1987, 1201 Wilson Ave, Downsview, Ontario, Canada M3M 1J8
49. Chaudron, G., "Natural Gas for Vehicles Adsorption Storage Tanks" Intercom, Belgium 1989
50. Petersen, A.S. and Larsen, B., Riso National Laboratory Report M-2781, Denmark, 1989
51. Lin, Y.C. and Huff, G.A., "Adsorbed Natural Gas" SAE Future Transportation Conference, San Antonio, Texas, 1993
52. Chen, X. and McEnaney, B., *Carbon '95 Abstracts* p 504, San Diego 1995
53. Manzi, S., Valladares, D., Marchese, J. and Zgrablich, G., *Adsorption Science and Technology* **1997**, **15**, 301
54. Berl, E., *Trans. Farad. Soc.* **1938**, **34**, 1040
55. Wennerberg, A.N. and O'Grady, T.M., US Patent 4082694 (1978)
56. Otowa, Y., US Patent 5064805 (1991)
57. Lewis, I.C., Greinke, R.A. and Strong, S.L., *Carbon '93 Abstracts* p490, Buffalo, 1993
58. Kaneko, K. and Murata, K., *Adsorption* **1997**, **3**, 197
59. Chaffee, A. and Pandolfo, A., *Carbon '90 Abstracts* p246, Paris 1990
also presentation to Gas Utilisation Research Forum, London, 1990
60. Verheyen, V., Jagtoycn, M. and Derbyshire, F., *Carbon '93 Abstracts* p 474 1993
61. AGLARG Report to US Dept. of Energy, Contract 466590, 1997
62. Private Communication, J. Wegrzyn, Brookhaven National Laboratory
63. Allied Signal, US Patent 5292706, 5292707, 5308821 and 5461023
64. Westvaco, US Patent 5416056, 5626637, Euro Pat. Application 649815, Canadian Pat. Application 2134160
65. Quinn, D.F., Report to AGLARG, September 1993
66. Elliott, D. and Topaloglu, T., *Gaseous Fuels for Transportation I*, p489 B.C. Research, Vancouver (1986)
67. Golovoy, A. & Blais, E.J., SAE Conference Proc., Pittsburgh, p47, (1983)
68. Chaffee, A.L., Loch, H.J. and Pandolfo, A.G., "Methane Adsorption on High Surface Area Carbons" CSIRO, Division of Fuel Technology, Investigation Report FT/IR 031R (1989)

69. Getman, R. Atlanta Gas Light Co. R&D Report #91 4-10 (1991)
70. Fricker, R.N. and Parkyns, N.D., "Adsorbed Natural Gas Road Vehicle" NGV'92, Gothenberg, Sweden. Sept. 1992
71. Valenzuela, D. and Myers, A.L., "Adsorption Equilibrium Data Handbook", Prentice Hall, (New Jersey) 1989 ISBN 0- 13-003815-3
72. Ritter, J.A. and Yang, R.T., *Ind. Eng. Chem. Res.* 1987, 26, 1679
73. Urbanic, J.E. et al. Paper 890621 SAE Conf. Proc., Detroit, (1989)
74. Critoph, R.E. and Turner, L., *Int. J. Heat & Mass Transfer*, 1995, 38(9), 1577)
75. "Cyclic Test Unit & Filter Evaluations", Report to Future Fuels Inc., Oct. 1987, Alcohol Energy Systems, California.

CHAPTER 10

Adsorption Refrigerators and Heat Pumps

Dr. R.E. CRITOPH

*Engineering Department
University of Warwick
Coventry CV4 7AL, UK*

1 Why Adsorption Cycles ?

Active carbons can be used in both refrigeration and heat pumping cycles, but their potential for use in these applications does not necessarily merit the development of such systems. Before devoting research and development effort into active carbon-based thermodynamic cycles, the interest in both heat-driven cycles in general, and adsorption cycles in particular, must be justified.

A major reason for the interest in heat-driven cycles is that they offer better utilisation of primary energy. Conventional vapour compression cycles used for refrigeration, air conditioning and heat pumping use electricity to drive a mechanical compressor. The efficiency of conversion from mechanical work to cooling or heating can be high. For example, the COP (Coefficient of Performance, equal to cooling power divided by input power) may be 3 in an air conditioning application. However, the conversion of primary fuel (oil, gas, coal or nuclear) to electricity at the power station, followed by transmission losses on route to the consumer may only be 25% efficient. Thus the overall conversion of primary energy to cooling is about 75% efficient. A heat-driven air conditioner using gas as its energy source might have a COP slightly greater than 1.0, but this is the overall conversion efficiency from primary energy, which is considerably better than that of the conventional electrically driven machine.

The COP's of specific air conditioners will vary widely with both manufacturer and application. Electricity utility efficiencies will also differ between countries. However, the reason for the economic interest in heat-driven cycles remains clear. Given that primary fuels can cost the consumer approximately 25% of the cost of electricity and that electricity frequently costs more at times of peak demand, there is justification for considering alternative systems. The use of a primary fuel at the point of use can also reduce CO₂ and other emissions.

Another reason for the interest in heat-driven cycles is their ability to produce higher temperature outputs than vapour compression cycles. There are industrial

heat pump or thermal transformer applications where the ability to pump heat at several hundred degrees Celsius is required. This is generally beyond the capability of the refrigerants and compressors used in conventional vapour compression systems.

A further application of heat-driven systems is in places where there is no electrical energy supply available. An example is the refrigeration of vaccines and other medicines in remote areas of developing countries. The World Health Organisation has evaluated a number of solar adsorption refrigerators designed for this purpose. They have to compete with vapour compression refrigerators powered by photo-voltaic panels. The inherent simplicity of solar thermal-powered refrigerators makes them ideal in these applications. There is also a need for larger thermal refrigerators for food preservation in remote areas. There is a particular need for local ice production in fishing villages, where a large proportion of the catch is often spoilt before it can be transported to market or be preserved elsewhere. Machines of up to 1 tonne/day of ice production are required for this application. They need not be solar powered, which is an expensive option in this size range, but could be driven by heat derived from locally available fuels such as agricultural waste, wood, charcoal, etc.

Heat-driven cycles can be split into two broad categories: engine-driven cycles and sorption cycles. The former use some sort of engine to produce work which then powers a conventional refrigeration cycle. Stirling engines, gas turbines, and conventional reciprocating engines have all been used. The refrigeration cycle is normally a vapour compression cycle, but Brayton cycles and Ericsson cycles have both been used experimentally. Engine-driven cycles have been built and operated successfully but have potential problems with noise and maintenance requirements / reliability. These problems can be minimised in an industrial or large commercial environment and hence most of the successful applications have been in 100 + kW sizes.

Sorption cycles do not have a mechanical compressor and need little or no mechanical work input. Consequently they have few or no moving parts. This makes them particularly attractive for smaller applications, although it should be mentioned that the biggest existing market is for Lithium Bromide - Water absorption air conditioners which provide cooling in the MW range. All sorption (absorption and adsorption) cycles can be thought of as using a 'chemical compressor' rather than a mechanical one. In its simplest form an adsorption refrigerator consists of two linked vessels, both of which contain refrigerant and one of which is also filled with adsorbent as shown in Fig. 1.

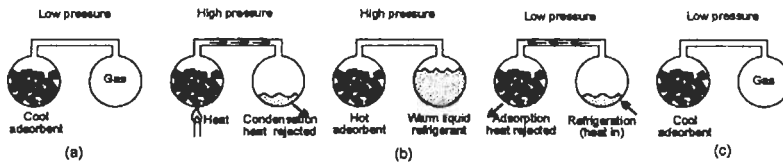


Fig. 1. Simplified adsorption cycle schematic

Initially the whole assembly is at low pressure and temperature, the adsorbent contains a large concentration of refrigerant within it and the other vessel contains refrigerant gas (a). The adsorbent vessel (generator) is then heated, driving out the refrigerant and raising the system pressure. The desorbed refrigerant condenses as a liquid in the second vessel, rejecting heat (b). Finally the generator is cooled back to ambient temperature, re-adsorbing the refrigerant and reducing the pressure. The reduced pressure above the liquid in the second vessel causes it to boil, absorbing heat and producing the refrigeration effect. The cycle is discontinuous since useful cooling only occurs for one half of the cycle. Two such systems can be operated out of phase to provide continuous cooling.

The above description is of an adsorption cycle which might well use an active carbon adsorbent. However, it applies equally well to liquid sorbents used in absorption cycles. The thermodynamics of liquid absorption and solid adsorption cycles are very similar, although the practicalities are very different. The major, and obvious, difference is that it is not possible to pump the solid adsorbents around the system. Given that the whole machine is a heat transfer device, it would clearly be advantageous to pump the sorbent through a heat exchanger. There are ways in which a bed of a solid sorbent can be made to behave as if it has been pumped through a counterflow heat exchanger, but it is more complicated than if it could be truly pumped like a liquid. Available methods are discussed in Section 5.2. Whilst the heat and mass transfer limitations imposed by the use of a solid adsorbent are a problem, there are a number of advantages that solid adsorbents have over liquid absorbents.

The first advantage of solid adsorbents is that they are totally non-volatile unlike most liquid absorbents. One of the two conventional liquid absorption cycle pairs uses ammonia as the refrigerant and water as the absorbent. In the generation phase a-b above, when a concentrated ammonia - water solution is heated, the ammonia is driven off but the vapour contains a few percent of water. This must be removed in a rectifier which preferentially condenses most of the water vapour and returns it to the generator. Unfortunately this reduces the energy efficiency as well as requiring an additional heat exchanger within the system. The other commonly used pair uses water as the refrigerant and Lithium

Bromide as the absorbent in air conditioning applications. It does not suffer from the same problem, since LiBr is effectively non-volatile. However, the pair does have limitations due to the crystallisation limits of LiBr in water. In very hot climates where heat rejection temperatures are higher than about 35°C the pair cannot be used unless additives are used to move the crystallisation boundary.

The major advantage that solid sorbents have over liquid systems is the large range of suitable materials available and the ability to engineer them for a particular application. The number of liquid absorbent - refrigerant pairs that give reasonable performance is very limited and governed by unalterable chemistry and physics. When using physical adsorption, almost any refrigerant may be used and in principle an adsorbent can be manufactured with the optimal pore size distribution for the particular application.

In summary, heat-driven cycles for cooling or heat pumping can have energy saving and environmental benefits. There are also niche applications in developing countries or remote areas. Adsorption cycles using active carbons are one of a number of approaches that might be economically viable.

2 The Basic Adsorption Cycle

2.1 Introduction

In order to understand the operation of the cycle and the ideas put forward later it is useful to look at the essential properties of adsorbent-adsorbate pairs and the way that they are used in the solar refrigerator.

Adsorbents such as active carbons, zeolites or silica gels can adsorb large quantities (c. 30% by weight) of many gases within their micropores. The most widely used combinations are active carbons with ammonia or methanol, and zeolites with water, but the choice of which adsorbent and which refrigerant gas to use depends on the application. The quantity of refrigerant adsorbed depends on the temperature of the adsorbent and the system pressure. A good approximation to the form of the function is given by the Dubinin - Astakhov (D-A) equation which is illustrated graphically in Fig. 2 and is commonly referred to as a Clapeyron diagram.

The following section may be omitted on first reading:

In its original formulation, the D-A equation is

$$V = V_0 \exp \left[-B \left(\frac{T}{\beta} \ln \frac{p^*}{p} \right)^n \right]$$

where :

- V is the micropore volume filled with the adsorbed phase.
- V_0 is the limiting micropore volume.
- B is a function of the micropore structure, decreasing as microporosity increases.
- T is the temperature (K).
- β is the affinity coefficient, which is a property of the adsorbate alone. It is approximated by the ratio of the adsorbate volume with the adsorbed volume of a reference substance (normally benzene) under the same conditions.
- n is a constant
- p is the system pressure.
- p^* is the pressure of the adsorbed phase within the micropores.

p^* will vary within the micropores and is impossible to measure directly. However, the assumption is made that the adsorbed phase is analogous to saturated liquid at the same temperature, and p^* may be replaced by p_{sat} the saturation pressure of the adsorbate at temperature T . At temperatures higher than the critical temperature, other estimates for p^* may be used (Smisak and Cerný[1]).

The mass concentration x can be related to the volume of adsorbed phase V by an assumed density of adsorbed phase r :

$$x = \rho V$$

The value of r can be estimated as that of saturated liquid at the same temperature or related to supercritical properties at temperatures above critical. Critoph [2] found that for the practical purposes of modelling ammonia - carbon adsorption cycles, using experimentally determined porosity data, that the complexity of estimating both r and p^* at sub and supercritical levels was not justified. The measured porosity data could be fitted to a much simpler version of the equation with no loss of accuracy, as follows:

$$x = x_0 \exp\left(-k\left(T \ln \frac{p_{sat}}{p}\right)^n\right)$$

where:

- x_0 is the limiting concentration,
- k is a constant.

Combining this with the relationship between saturation pressures and temperatures:

$$\ln p_{sat} = a - \frac{c}{T_{sat}} \quad \text{where } a \text{ and } c \text{ are constants,}$$

$$x = x_0 \exp\left(-K\left(\frac{T}{T_{sat}} - 1\right)^n\right)$$

K is a constant.

T_{sat} is the saturation temperature of the adsorbate at the system pressure (Kelvin).

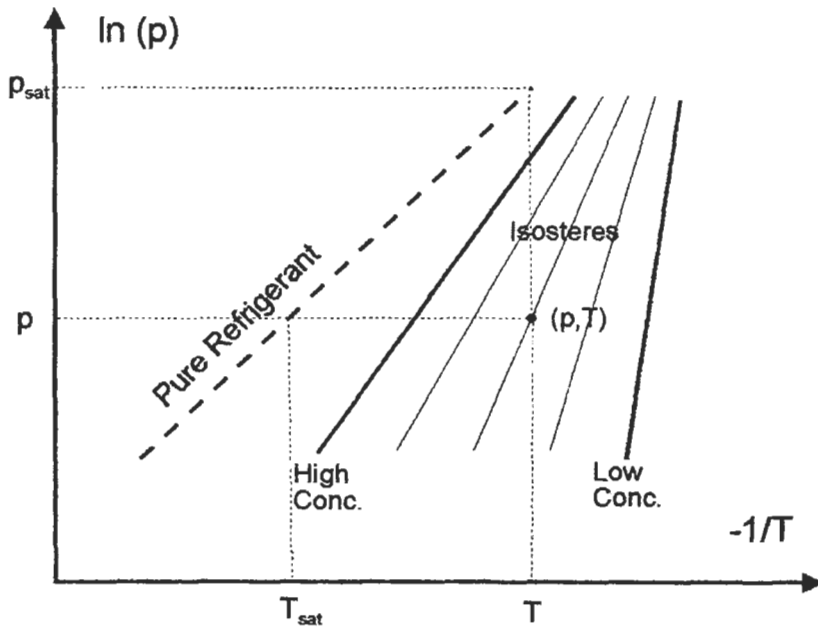


Fig. 2. Clapeyron diagram showing saturated refrigerant and isosteres

Lines of constant concentration (isosteres) are straight when the natural logarithm of pressure is plotted against the inverse of the absolute temperature. It is conventional to plot against $-1/T$ so that temperature still increases when moving from left to right. Since adsorbents hold less adsorbate when hot the low concentration isostere is on the right of the high concentration isostere. The line labelled 'pure refrigerant' shows the variation of the refrigerant's saturation pressure and temperature (i.e. the variation of its boiling/condensing temperature with its pressure). It takes energy (heat of desorption) to drive refrigerant from the pores and similarly, when gas is adsorbed into the pores heat is generated. This is analogous to the latent heat required or generated in boiling or condensation but is greater in size. The heat of desorption per mass of refrigerant is actually proportional to the slope of the isosteres.

2.2 The simple solar refrigerator

Now it is possible to understand the simple solar refrigerator illustrated in Fig. 3 below:

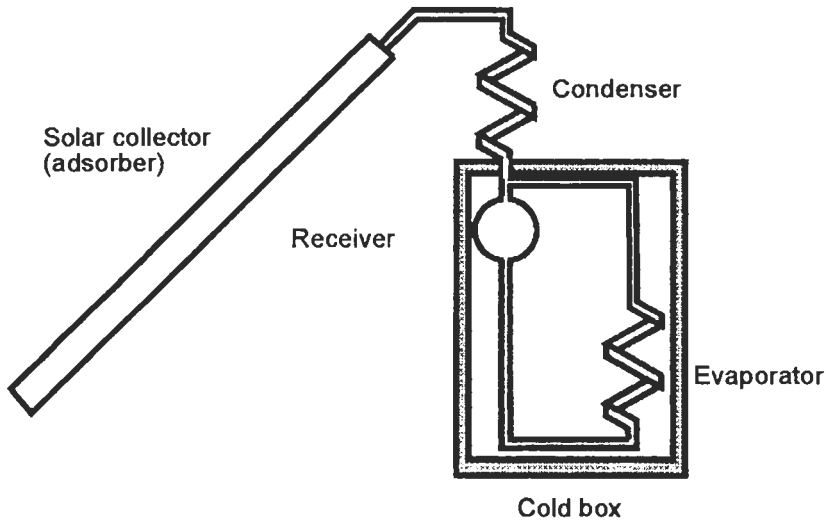


Fig. 3. Schematic solar refrigerator

Fig. 3 shows an idealised solar collector (generator) containing adsorbent which is connected to a condenser that rejects heat to the environment and an insulated box containing a liquid receiver and a flooded evaporator. Fig. 4 shows the p - T - x (pressure - temperature - concentration or Clapeyron diagram) for the adsorbent-adsorbate pair with typical temperatures.

The cycle begins in the morning with the generator (solar collector) at ambient temperature and the evaporator (but not the receiver) full of cold liquid refrigerant from the previous cycle. The adsorbent contains the maximum quantity of refrigerant at this time. As the sun heats the collector, the adsorbent temperature rises and some refrigerant is desorbed. Since it is desorbed into a system of fixed volume the pressure in the system rises. The gas does not condense because the saturation temperature corresponding to the system pressure is below ambient temperature. As more heat is transferred to the adsorbent, more gas is desorbed and the pressure rises further. Since the volume of the gas in the system is not large, the mass of gas desorbed is small compared to that still adsorbed and thus the reduction in mass concentration is small. Thus

the variation of pressure with adsorbate temperature approximates to that of an isostere as shown in Fig. 4.

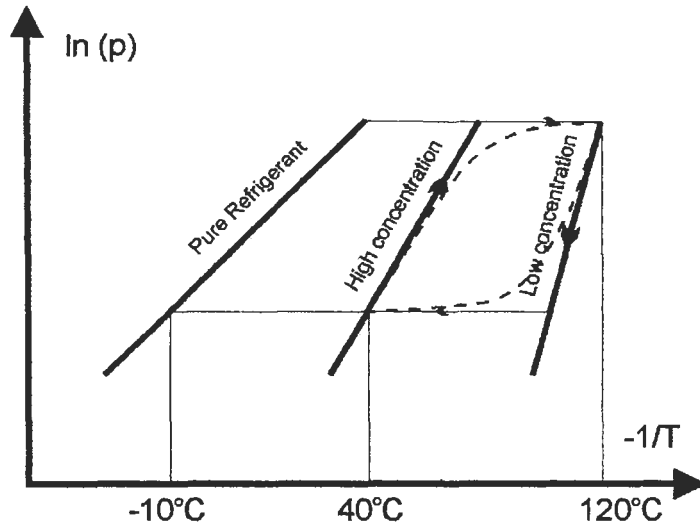


Fig. 4. Clapeyron diagram for a simple solar refrigerator

The situation changes when the system pressure becomes high enough for refrigerant to condense in the condenser and reject the resulting latent heat to the environment. Further addition of heat to the adsorbate desorbs more refrigerant which condenses in the condenser and trickles down into the receiver. The system pressure stays approximately constant as desorption and condensation proceed.

The rate at which refrigerant is desorbed is limited by heat transfer both into the adsorbent and out of the condenser. The minimum concentration of refrigerant in the generator / solar collector will be reached at some time during the day when it achieves its maximum temperature. The receiver will contain its maximum quantity of liquid refrigerant at this time.

As the incoming solar radiation decreases the collector will drop in temperature and so the adsorbent will now adsorb the surrounding gas, reducing the system pressure. Heat of adsorption is generated in the adsorbent which is rejected to the environment. At this stage it is beneficial if heat loss from the collector to ambient can be increased by means of removable insulation, flaps, or some other method. Since the pressure above the liquid refrigerant in the receiver is reduced, the liquid boils, replacing the gas adsorbed in the collector. The energy needed

for boiling is extracted from the liquid itself and so its temperature and pressure is reduced. For simplicity it is assumed that the insulation around the receiver is ideal and none of the energy to boil the liquid is taken from the environment. As the collector cools further during the late afternoon and evening the receiver liquid reaches the temperature of that remaining in the evaporator from the previous day's cycle. Usually the cooling is used to freeze water which then keeps the evaporator at a steady temperature despite heat leaking in from the environment through the insulation. Once the receiver and evaporator are at an equal temperature (approximately 0°C) a new source of heat becomes available.

The energy required for further boiling comes from the warmest source, which is now the water / ice jacket surrounding the evaporator. Since this results in the water freezing the evaporating temperature becomes stable and governed by heat transfer from evaporator to the ice front. As the night progresses the refrigerant desorbed during the day is resorbed and enough ice is formed in the cold box to maintain low temperatures for the following day. Since the rate of cooling is normally limited by the rate at which heat can be rejected from the adsorbent in the solar collector, it is not unusual for this to take many hours. The variation of pressure with temperature is shown on Fig. 4 both for an actual cycle (dotted line) and an idealised one consisting of two isosteres and two isobars.

2.3 The basic continuous adsorption cycle

The simple system above, with no moving parts, is appropriate to a solar refrigerator with a 1-2 m² collector on which the cooling load is only a few kilos of ice production each day. The adsorbent goes through one cycle per day and for each kilo of ice frozen about 5 kg of carbon is needed. However, if the cooling load is equivalent to one tonne of ice per day (A domestic air conditioner might be rated at three tons of refrigeration or about 10 kW) then the mass of carbon and refrigerant needed become impractically high. Obviously in such circumstances it would be preferable to have a rapid cycle in which the adsorbent were repeatedly heated and cooled every few minutes. The same adsorbent would be used several hundred times per day rather than once and the mass required could be reduced correspondingly. It is also sensible to have two adsorbent beds in which the heating and cooling processes are out of phase. When one bed is heated the other is cooled. This has the advantage of providing continuous cooling from the system. The beds and the check valves that route the adsorbing or desorbing gas to the condenser and from the evaporator become equivalent to the compressor in a conventional refrigerator except that they have a heat input rather than a work input. This is illustrated in Fig. 5a,b.

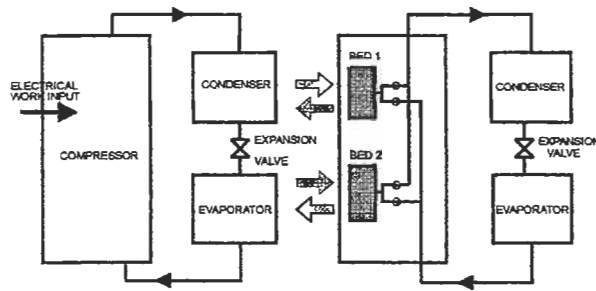


Fig. 5a. Vapour compression cycle

Fig. 5b. Basic adsorption cycle

In Fig. 5b the heat flows for one half of the cycle are shown with white filled arrows and for the other half are shown surrounded by shaded arrows.

The major difficulty in building a practical machine based on this principle is that in order to heat and cool the beds rapidly, good heat transfer is essential. Unfortunately, by their very nature, adsorbent beds are very poor conductors of heat. Their thermal conductivity is such that they would, in fact, make good building insulation. It is possible to improve the overall bed conductivity by incorporating metal fins within the bed. However, this increases the thermal mass of the bed, and every time it is heated, the heat that is used to raise the temperature of the fins is in effect wasted. This reduces the overall energy efficiency of the system significantly. Methods of improving the heat transfer within the beds are described in section 5.3.

Regardless of the problem of heating and cooling the bed from external sources and sinks, it is well known that the thermal efficiency of the system can be improved by transferring heat from one bed to another. Instead of directly using the heat of adsorption rejected by a bed (in the case of a heat pump) or throwing it away (in the case of a refrigerator) it is better to use it to pre-heat the other bed thus reducing the input of high grade heat needed from the gas flame or other source. Indeed, systems using more than two beds have been suggested, which by transferring heat between the various beds in an optimum manner would achieve large improvements in energy efficiency. The obvious drawback is in the increased complexity and capital cost. All of these proposed systems may be described as regenerative cycles since they use regenerated (or recovered) heat

from a bed which is cooling in order to assist the heating of another bed. Some of these multiple bed systems are described in section 5.2.

Before describing advanced cycles and improvements in heat transfer the thermodynamics of the basic cycle and the calculation of COP's must be explained.

3 Basic Cycle Analysis and Results

3.1 Thermodynamic analysis

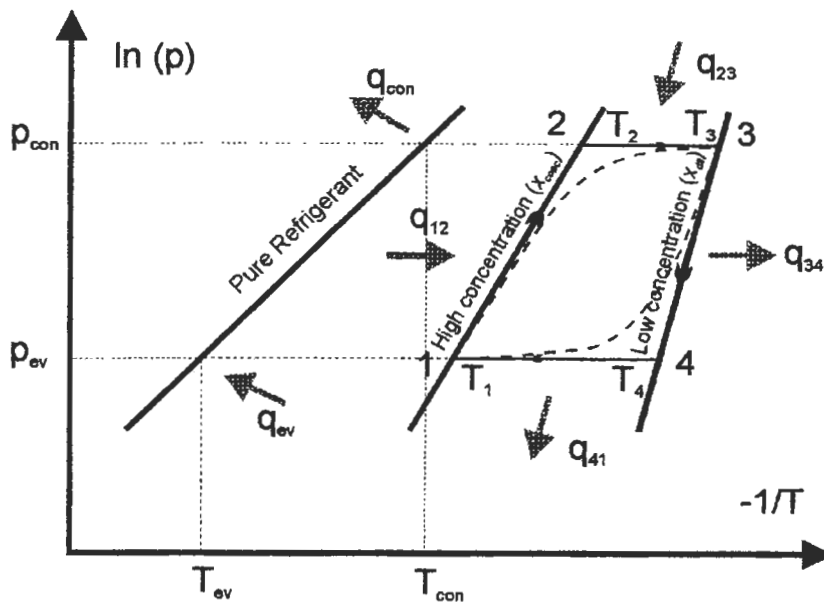


Fig. 6. Clapeyron diagram for analysis of the basic cycle

Fig. 6 shows both the actual cycle (shown in dashed lines) and the idealised cycle, which consists of two isosteres and two isobars. Heat flows in J/kg adsorbent (q) are shown as shaded arrows. For most purposes, analysis of the ideal cycle gives an adequate estimate of the COP and cooling or heating per kg of adsorbent. An accurate calculation of the path of the actual cycle needs information on the dead volume of the whole system and of the heat transfer characteristics of the condenser and evaporator. General trends are more apparent from an analysis of the idealised cycle.

The COP in cooling (COP_C) or heating (COP_H) is defined by:

$$COP_C = \frac{q_{ev}}{q_{12} + q_{23}}, \quad COP_H = \frac{q_{con} + q_{34} + q_{41}}{q_{12} + q_{23}}$$

Considering the processes occurring in Fig. 6 in sequence:

Process 1-2

The heat input per unit mass of adsorbent in the isosteric heating phase when the concentration is x_{conc} is given by:

$$q_{12} = \int_{T_1}^{T_2} (c_{pc} + x_{conc} c_{va}) dT$$

where :

- c_{pc} = Specific heat of adsorbent (carbon), possibly a function of temperature.
- x_{conc} = maximum concentration, obtained at point 1 by using the evaporating pressure and bed temperature T_1 in the Dubinin-Astakhov equation.
- c_{va} = Specific heat of adsorbed phase at constant volume.
- T_1 = minimum cycle temperature (K).
- T_2 = temperature at start of desorption (K).

The integrated terms are simply the specific heat of the unit mass of adsorbent and its associated adsorbate. The specific heat at constant volume has been used for the adsorbate since, theoretically, there is no expansion of the adsorbate volume and the heat required to raise the temperature is the change in internal energy. In practice there will be some expansion and a pessimistically high estimate could use the specific heat at constant pressure c_{pa} . The specific heat of the adsorbed phase is in any case difficult to estimate and it is common to approximate it to that of saturated liquid adsorbate at the same temperature.

T_2 is easily calculated, since the ratio of T/T_{sat} is constant along an isostere, giving:

$$\frac{T_1}{T_{ev}} = \frac{T_2}{T_{con}}$$

Process 2-3

The heat input per unit mass of adsorbent in the isobaric heating phase where the concentration varies is given by:

$$q_{23} = \int_{T_2}^{T_3} (c_{pc} + x c_{pa}) dT + \int_{x_{dil}}^{x_{conc}} H dx$$

where x_{dil} is the minimum concentration and H is the heat of desorption per unit mass of adsorbate. H at any point on 2-3 or 4-1 can be derived from the slope of the isostere on the Clapeyron diagram (A):

$$H = RA$$

where:

$$A = \left(\frac{\partial(\ln[p])}{\partial(1/T)} \right)_x$$

R = The gas constant at the system pressure and temperature.

Assuming the form of the Dubinin equation to be correct, or more generally that the ratio T/T_{sat} is constant along an isostere then H can be expressed as a multiple of the latent heat L of the refrigerant at the system pressure:

$$H = L \frac{T}{T_{sat}}$$

Process 3-4

The heat rejected per unit mass of carbon in the isosteric process 3-4 (q_{34}) is, by analogy with process 1-2 :

$$q_{34} = \int_{T_4}^{T_3} (c_{pc} + x_{dil} c_{va}) dT$$

where T_4 may be calculated from:

$$\frac{T_4}{T_{ev}} = \frac{T_3}{T_{con}}$$

Process 4-1

The heat rejected per unit mass of carbon in the isobaric process 4-1 (q_{41}) is similarly analogous to process 2-3:

$$q_{41} = \int_{T_i}^{T_4} (c_{pc} + x c_{pa}) dT + \int_{x_{dil}}^{x_{conc}} (H - [h_{gas\ bed} - h_{gas\ ev}]) dx$$

where:

$h_{gas\ bed}$ is the gas enthalpy evaluated at the bed temperature (J/kg),

$h_{gas\ ev}$ is the gas enthalpy evaluated at the evaporator (J/kg).

The first term in the second integral will not have the same magnitude as in the desorption process because the latent heat L will now be that at the evaporating

temperature rather than at the condensing temperature. The second bracketed term in the second integral takes account of the cooling effect on the bed of the cold gas entering from the evaporator.

Cooling (evaporation)

Finally, the cooling and the heat rejected in the condenser must be evaluated. The mass of refrigerant desorbed and then adsorbed per unit mass of adsorbent during every cycle is $x_{conc} - x_{dil}$. The useful cooling obtained from it is:

$$q_{ev} = (x_{conc} - x_{dil})(h_{gas\ ev} - h_{liquid\ con})$$

where:

$h_{gas\ ev}$ is the specific enthalpy of gas leaving the evaporator (J/kg),

$h_{liquid\ con}$ is the specific enthalpy of the condensed liquid (J/kg).

This formulation applies both to the use of a semi-continuous cycle with an expansion valve and to a discontinuous cycle (such as that in the solar refrigerator) using a flooded evaporator in which the warm condensate must first cool itself before it can cool the load.

Condensation heat

The heat rejected at the condenser is the sum of the condensation heat and that required to cool the gas down to the condensing temperature. Since the gas is desorbed at a range of temperatures between T_2 and T_3 , this should properly be evaluated as:

$$q_{con} = - \int_{x_{dil}}^{x_{conc}} h_{gas} dx - h_{liquid}(x_{conc} - x_{dil})$$

where:

h_{gas} is the gas enthalpy evaluated at the (varying) bed temperature,

h_{liquid} is the saturated liquid enthalpy in the condenser.

In practice there is only a small error if the hot gas is all assumed to leave the bed at the mean temperature of T_2 and T_3 .

3.2 Efficiency of the basic cycle

Whilst the above analysis is detailed and quite complex, there are general trends that become apparent relating to how both the carbon properties and the operating conditions affect the COP's of adsorption heat pumps and refrigerators. The cooling available from the cycle is approximately proportional to the difference between the high and low concentrations and to the latent heat of the refrigerant. The heat input to the cycle has three components: the sensible

heat load of the carbon, the sensible heat load of the adsorbed phase and the heat of desorption.

There is an obvious benefit if both x_{conc} is large (in order to minimise the effect of the carbon sensible heat load) and x_{dil} is small (to maximise the cooling effect). There would be an additional benefit if the isosteres were closely grouped in the region where desorption begins. This would correspond to a large concentration change over a small temperature rise, which reduces the peak cycle temperature and the heat input required. The ideal would be to drive out all of the refrigerant at one temperature. This would be similar to a chemical reaction and there are cycles based on reactions such as those between calcium chloride and ammonia or methanol. They have the advantage that many moles of refrigerant may be desorbed at one temperature but suffer problems due to swelling of the adsorbent and the dynamics of the reaction which are not present in physical adsorption. It is also clear that there will always be an optimum of the peak cycle temperature for the greatest COP. The bed must be heated to T_2 in order to desorb any refrigerant and achieve any cooling at all. As T_3 is increased the quantity of refrigerant desorbed increases, as does the COP initially. However, at higher temperatures the quantity of refrigerant desorbed per degree temperature rise is less. Eventually the benefit of the extra cooling derived by desorbing a little more refrigerant is offset by the disadvantage of the extra sensible heat load of the bed.

These effects are illustrated in Fig. 7 which shows a set of isosteres for a typical adsorbent with ammonia refrigerant. Fig. 7 shows a refrigeration cycle with evaporating temperature of -10°C and condensing temperature of 30°C . The adsorption heat is rejected down to 30°C and the maximum cycle temperature is 150°C . Raising this maximum to 200°C would result in the minimum concentration decreasing 3.5% and the cooling effect increasing 30%. However, the heat input required increases more rapidly and the COP drops from 0.375 to 0.366. The diagram also illustrates the effect of changing the cooling temperature and heat rejection temperatures. If the evaporating temperature goes down whilst the other temperatures remain the same then x_{conc} will be reduced since the minimum system pressure is lower. x_{dil} is unaltered and so the concentration change, the cooling per mass of carbon and the COP are all reduced. Increasing the condensing temperature will increase x_{dil} , also reducing the concentration change and COP. Raising the heat rejection temperature T_1 will reduce x_{conc} and hence the COP. These effects are as would be expected from a consideration of the global thermodynamic effect of lowering the evaporating temperature or raising heat rejection temperatures.

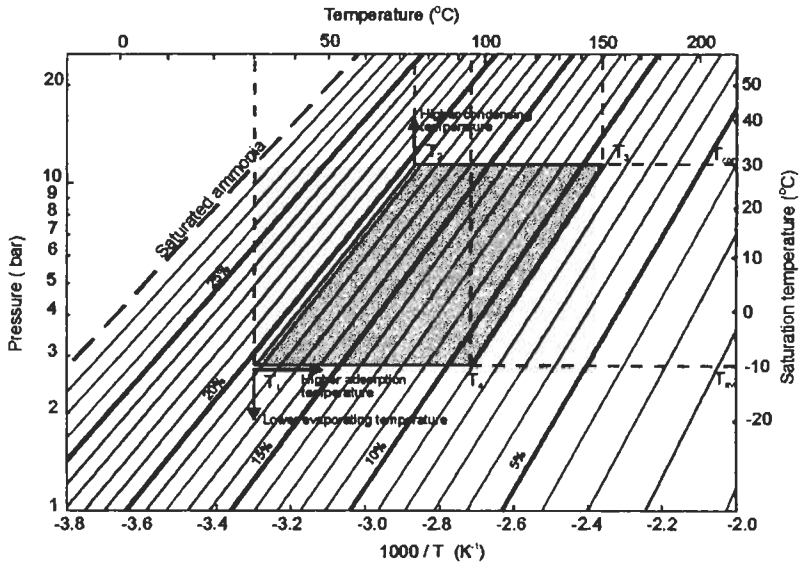


Fig. 7. Typical ammonia - carbon basic cycle

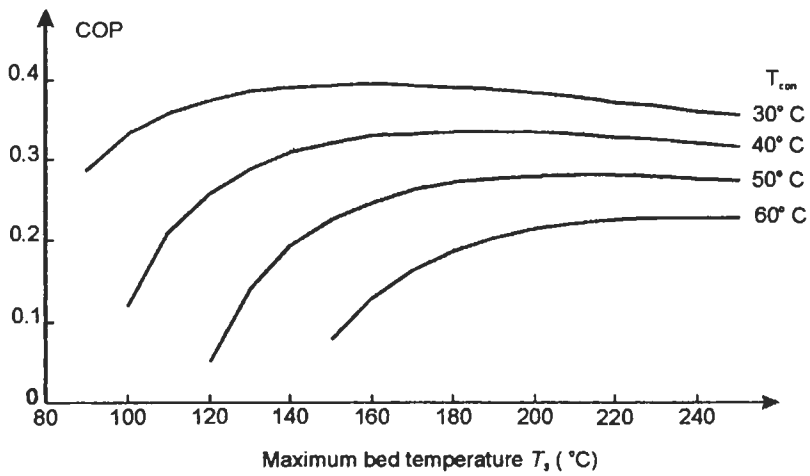


Fig. 8. Effect of heat rejection temperature and maximum cycle temperature on refrigeration COP

The variation of refrigeration COP with heat rejection temperature (final bed adsorption temperature and condensing temperature are assumed equal) and the maximum cycle temperature is illustrated for an evaporating temperature of -5°C in Fig. 8. Heat pump COP's follow similar trends but are higher.

4 Choice of Refrigerant - Adsorbent Pairs

The above discussion describes how cycle performance varies with the different external temperatures, but naturally the choice of adsorbent and refrigerant pairs used will also have a major effect. Most refrigerants can be adsorbed by carbons, but the most useful ones have a high latent heat. Any active carbon will have a maximum micropore volume which can contain the refrigerant in its adsorbed state. The maximum cooling that could possibly be achieved by totally desorbing and then adsorbing in a single cycle is the product of the liquid refrigerant's latent heat and the mass of adsorbed refrigerant that totally fills the micropores. Assuming some similarity between the adsorbed and liquid phases, refrigerants with high latent heat per unit liquid volume will give better performance.

Table 1 gives a selection of possible refrigerants with suitably high latent heats, all of which tend to have small polar molecules. The table is split into two groups: those with normal boiling temperatures above and below -10°C . The properties are taken at the normal boiling point. Attainable COP's correlate reasonably with the latent heat per unit volume. Of the high pressure refrigerants, ammonia is the best available. Although toxic and incompatible with copper and brass, it has no ozone depletion potential and is not a greenhouse gas. It is used widely as a refrigerant in industry and is being considered increasingly as an environmentally friendly refrigerant for other applications.

The best sub-atmospheric refrigerant is water. Unfortunately it is not strongly adsorbed by carbons, but refrigerators and heat pumps based on water - zeolite pairs have been built and tested in research laboratories. Methanol is adsorbed well by carbons and a solar refrigerator based on a carbon - methanol pair was marketed by Brissonneau et Lotz Marine in France. Methanol is environmentally friendly, but decomposes at temperatures around 150°C and so cannot be used for very high temperature cycles.

High pressure and sub-atmospheric cycles have different advantages and disadvantages. The choice between them will depend on the application. Low pressure cycles require perfect hermetic sealing against air ingress. Any air leaking into the system will migrate to the condenser, where it will impede the condensation process and eventually cause failure. Low pressure machines also

have to be designed to avoid pressure drops in pipework, which can reduce the performance significantly. However, low pressure machines do not need expensive and bulky pressure vessels. High pressure cycles can cope with low leakage rates to the atmosphere until the leak is rectified and they can easily be 'topped up' with refrigerant.

Table 1. Latent heat per unit liquid volume of useful refrigerants

Refrigerant		Normal Boiling Point (°C)	Mol Wt.	Latent heat L (kJ/kg)	Liquid density ρ (kg/m ³)	Latent heat per unit vol. $\rho L \times 10^{-3}$ (kJ/m ³)
Formula	Name					
NH ₃	Ammonia	-34	17	1368	681	932
HCHO	Formaldehyde	-19	30	768	815	626
C ₂ H ₃ F	Vinyl Fluoride	-38	64	389	1455	566
SO ₂	Sulphur Dioxide	-10	46	605	883	534
CH ₂ F ₂	R32	-52	52	382	1214	463
Cl ₂	Chlorine	-34	71	288	1563	450
CHClF ₂	R22 ¹	-41	86	235	1409	331
H ₂ O	Water	100	18	2258	958	2163
SO ₃	Sulphur Trioxide	45	80	508	1780	905
CH ₃ OH	Methanol	65	32	1102	791	872
C ₂ H ₅ OH	Ethanol	79	46	842	789	665
C ₂ H ₅ N	Ethylamine	57	43	746	833	621
CHN	Hydrogen Cyanide	26	27	935	688	643
NO ₂	Nitrogen Dioxide ²	21	46	415	1447	600
C ₂ H ₃ N	Acetonitrile	81	41	766	782	599
CH ₃ NH ₂	Methylamine	-7	31	836	703	588
Br ₂	Bromine ³	59	160	189	3119	588

1. Other chemicals not shown are superior to R22, but it is included as the best of the conventional refrigerants.

2. Freezes at -11°C.

3. Freezes at -7°C.

Other refrigerants, including CFCs R11 and R12, HCFC R22, HFC R32 and hydrocarbons such as butane have been evaluated in detail by Critoph [3,4] but are significantly worse in performance than methanol or ammonia. In 1996, these two refrigerants are the only ones used in the major laboratories working on carbon adsorption cycles.

Having chosen a suitable refrigerant, the best adsorbent must be found. Zeolites, silica gels and chemical adsorbents have been used as well as carbons, but this chapter will concentrate on the carbon adsorbents. An indication as to the range of COP's that can be expected and the influence of the type of carbon used can be obtained by modelling the performance of carbons with a range of adsorption parameters. For this purpose it is preferable to use the Dubinin-Raduschkevich

equation, in which the exponent n of the D-A equation is made equal to 2 for theoretical reasons. This reduces the adsorption parameters to x_0 the limiting concentration and K , which is related to pore size.

The range of the parameters which covers most carbons (and zeolites) is:

$$0.15 \leq x_0 \leq 0.75$$

$$1 \leq K \leq 17$$

Figs. 9 and 10 below show the COP's of refrigerators and heat pumps respectively in the basic cycle described in Section 2

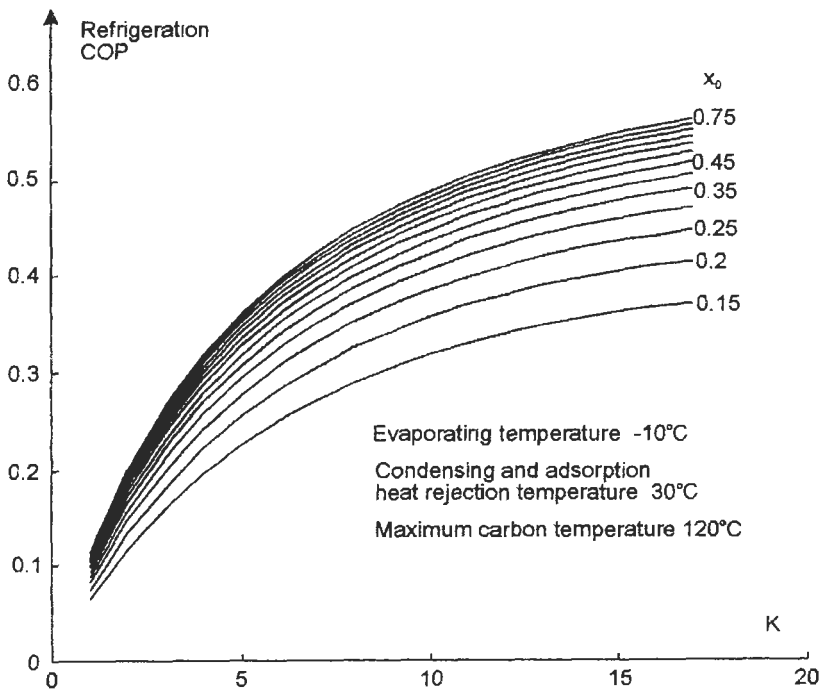


Fig. 9. Variation of refrigeration COP with carbon properties

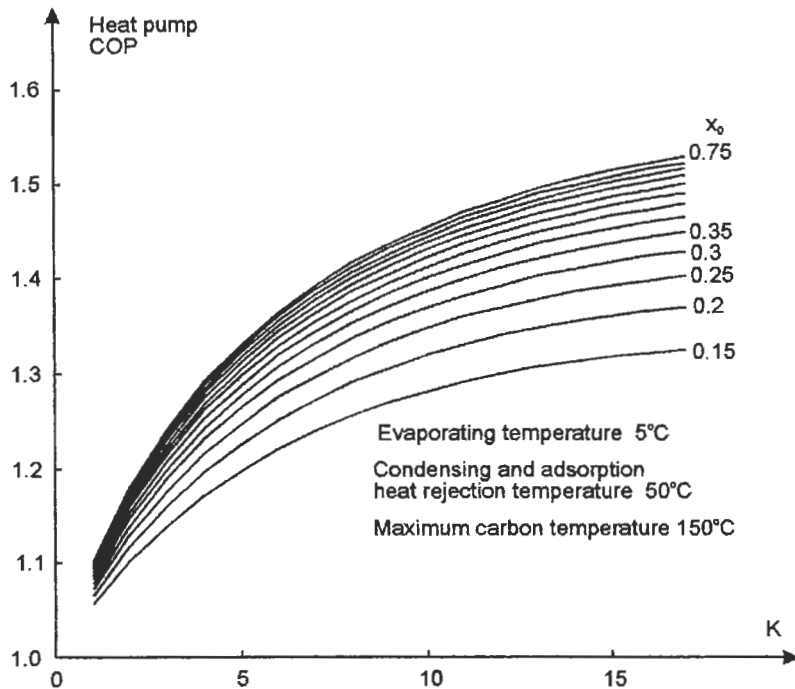


Fig. 10. Variation of heat pump COP with carbon properties

5 Improving Cost Effectiveness

The cost effectiveness of an adsorption cycle machine depends both on the COP, which will affect the operating costs and also on its size, which will influence the capital cost. The COP in a particular application will be both a function of the adsorbent properties and of the cycle used. Complex cycles described below can deliver high COP's but require more heat transfer area and are therefore larger, leading to a higher capital cost. There is a compromise between efficiency and complexity which determines the 'optimum' design.

In order to improve cost effectiveness, the following parameters must be considered. First, the limitations on improved porosity adsorbents will be explored and then a number of advanced cycles will be reviewed. All would benefit from improved heat transfer which leads to more compact and hence less costly machines.

5.1 Improved porosity adsorbents

The variation of COP with porosity characteristics x_0 and K was shown above in Figs. 9 and 10. There is an advantage in a large volume of pores since the sensible heat of the carbon is smaller compared to the sensible heat of the adsorbed phase and the desorption energy. For the example cycle temperatures there is also an advantage in having a high value of K . However, there will in general be an optimum value that leads to the maximum concentration change and maximum COP. A typical coconut shell based granular carbon used by the author has an x_0 of 0.25 with ammonia and other readily available carbons have an x_0 of 0.3. The current limit lies with a carbon such as Andersen AX-21 with an x_0 of 0.55. This material gives COP's that are 10-20% higher than conventional carbons, but the possible improvement is not so large as to radically improve the cost effectiveness. To achieve much higher performance, such as a doubling of the COP, new cycles which offer better regenerative use of heat are needed.

5.2 Advanced cycles

5.2.1 Multiple beds

In the basic continuous adsorption cycle illustrated previously in Fig. 5b two adsorbent beds are heated and cooled out of phase in order to provide continuous heating or cooling. It is possible to recover some of the adsorption heat rejected by each bed and use it to provide some of the heat required by the other bed. This might be done by the use of a circulating heat transfer fluid or a heat pipe. Meunier [5] first systematically looked at the potential gain in COP that might be obtained by such heat recovery, both as a function of the approach temperature of the beds donating and receiving heat and of the number of beds. The number of beds is not limited to two and the COP increases with the number of beds that it is possible to transfer heat between. There is of course a practical limitation, but it is possible to calculate the theoretical benefit of employing heat exchange between any number of beds.

Heat management within the cycle is best understood with reference to Fig. 11 showing the effective specific heat dQ/dT of one of the beds as a function of its temperature T as it completes a cycle. The top curve is the effective specific heat of a conventional bed during the heating phase. The heating phase is assumed to start with an isostere during which the bed increases in pressure from that of the evaporator to that of the condenser. Since there is no desorption, the effective specific heat of adsorbent plus adsorbate per unit mass of adsorbent (dQ/dT) is constant. The second part of the curve shows the effect of desorption occurring along an isobar. The pressure is maintained constant by the ideal condenser which rejects heat at a constant temperature. dQ/dT is high at lower temperatures

both because there is more adsorbate which imposes a sensible heat load and because the concentration change per unit temperature is higher giving a larger desorption heat load. As the temperature rises and the concentration falls dQ/dT will tend to the specific heat of the carbon.

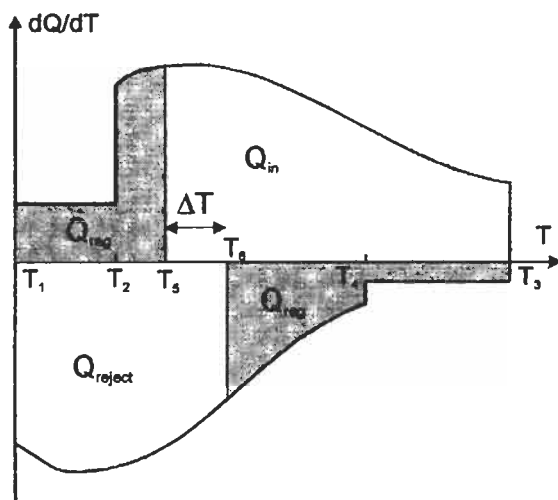


Fig. 11. Effective specific heat v. Temperature in a two-bed regenerative cycle

The lower curve shows the effective specific heat during adsorption. Since the process is one of cooling, the curve is negative. Meunier [5] showed how the two curves can be used to determine how much rejected heat from one bed can be used to heat another. The two rules guiding the calculation are: that the area under the curves between two temperature limits is equal to the total heat entering or leaving between those temperatures, and that heat can only flow from high to lower temperatures. In the two bed case illustrated, the heat rejected from the adsorbing bed between T_3 and T_6 , equal to Q_{reg} may be transferred across temperature difference ΔT to the adsorbing bed, which it heats from T_1 to T_5 . This reduces the total heat input from $Q_{in} + Q_{reg}$ to Q_{in} with a consequent improvement in COP. There is also a reduction in the rejected heat to Q_{reject} . A two-bed cycle with heat recovery across a ΔT of 10°C can increase the refrigeration COP by 50% or more as shown in Fig. 12.

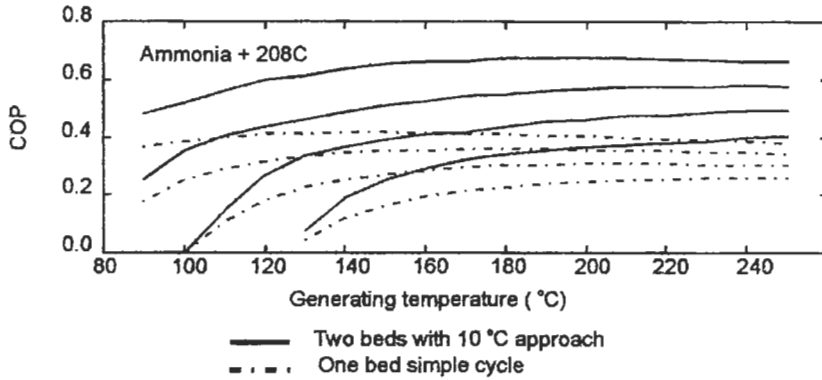


Fig. 12. Improvement in refrigeration COP possible with an idealised two-bed cycle

Greater numbers of beds allow more regeneration of heat but the benefit of increasing the number of beds drops off rapidly. Table 2 below taken from Meunier [5] shows how the COP changes with number of beds in a particular case.

Table 2. Variation in cooling COP of a zeolite - water regenerative cycle with evaporating, condensing, adsorption rejection and maximum desorption temperatures 0°C, 40°C, 50°C and 350°C respectively.

Number of beds	Cooling COP
1	0.425
2	0.684
4	1.008
6	1.293
∞	1.852

Considering the extreme case when there are an infinite number of beds (Fig. 13) and ideal heat transfer, the maximum amount of recovered heat is calculated by reflecting the lower curve in the upper half of the diagram, as is shown by the dashed line. The input heat that must be obtained from an external source is shown by the shaded area. The COP is the maximum that may be obtained from a single effect adsorption machine.

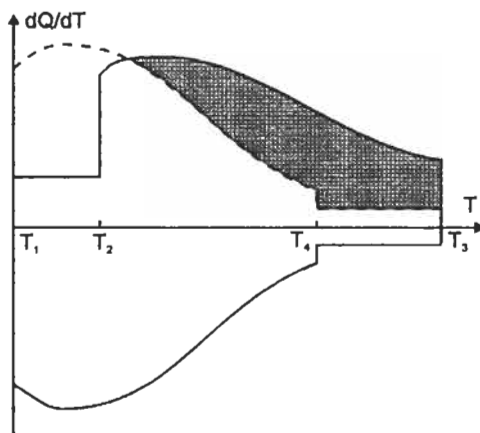


Fig. 13. Heat management with an infinite number of beds

5.2.2 Cascaded cycles

Another means of improving cycle efficiency is to combine two separate cycles such that the adsorption heat rejected by one is both sufficient in quantity and temperature to drive the other. This could be done with similar or totally different adsorbent - adsorbate combinations. Douss [6] experimented with a refrigerator in which a zeolite - water high temperature input cycle drove a carbon - methanol low temperature cycle. Critoph and Turner [2] carried out a theoretical analysis of a cascaded cycle using zeolite - ammonia and carbon - ammonia. These cycles and the multiple bed cycles all seek to input heat at higher temperatures only and to reject heat at lower temperatures only. Thermodynamic considerations imply that this will lead to higher theoretical COP's. Rockenfeller [7] has suggested triple cascaded chemical adsorption cycles in which theoretical refrigeration COP's as high as 1.2 are possible.

5.2.3 Thermal wave cycles

A practical means of approaching the performance of multiple bed cycles that only requires two beds is the thermal wave approach patented by Shelton [8] and illustrated in Fig. 14.

Heating and cooling of the adsorbent beds is no longer direct but via a heat transfer fluid such as a high temperature oil. The oil passes through special heat exchangers in each of the beds and through two conventional heat exchangers outside the beds. One of the external heat exchangers allows the oil to be heated by a gas flame, while the other removes heat, either to supply the heating load (in the case of the heat pump) or to be rejected (in the case of the refrigerator). A reversible pump circulates the oil in either direction round the loop.

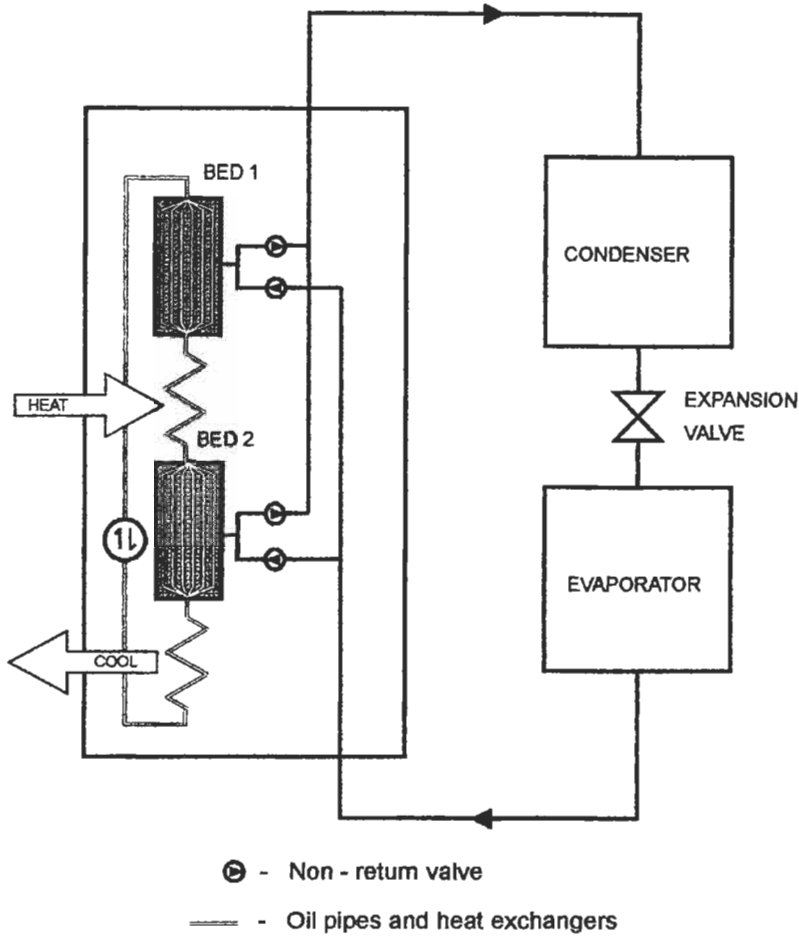


Fig. 14. The thermal wave cycle

The cycle consists of two phases. In the first, suppose pumping to be anticlockwise, and initially that bed 1 is cold (maximum adsorbent concentration) and bed 2 is hot (minimum adsorbent concentration). The oil recovers heat from bed 2, has a further heat addition from the gas heat exchanger and then proceeds to heat bed 1 via the special heat exchanger within it. Bed 1 desorbs refrigerant which passes to the condenser (giving a useful heat output in the case of a heat pump) and bed 2 adsorbs gas from the evaporator which

provides cooling. In the following phase of the cycle the pump is reversed, bed 1 is cooled and bed 2 is heated in a similar fashion until the original conditions are reached and the pump can again be reversed.

Thus far, the description could apply to simple but limited heat recovery between the beds. However the system achieves much better performance than this due to the combination of the design of the internal bed heat exchangers and the low oil flow rate. A hot slug of oil entering a cold region of the bed cools rapidly, before it has moved even a short distance through the cold portion and leaves the bed cold. If the oil has a very low thermal capacity flow rate and there is little conduction within the bed then a thermal wave will pass through the bed. The wave front will propagate through the bed, all of the carbon upstream of the wave being hot and that downstream cold. The wave velocity is much less than that of the oil flowing through the bed.

The oil emerging from the bed heat exchanger will be cold until the wave reaches the end of the bed, at which time a rapid temperature rise in the oil is observed as the wave 'breaks through'. At this stage the pump is reversed for the second half of the cycle and the bed is cooled as a cold wave front passes back down the bed in the opposite direction. This process is analogous to that in regenerators used in industrial high temperature gas furnaces or in Stirling engines. Its great merit is that it recycles the maximum amount of heat, giving the maximum thermal efficiency. Whilst the bed heat exchangers are thermally massive, the energy used to heat them is to some extent recycled along with the heat from the bed and the practical efficiency is high. Miles *et al* [9] have achieved a refrigeration COP based on gas input and under ARI conditions of 0.75.

5.2.4 Convective thermal waves

In the convective cycle proposed by Critoph [10] the thermally massive heat exchangers in the adsorbent beds are not required. Although the bed has very poor conductivity, the carbon (or other adsorptive) grains have a very high surface area which can be used for convective heat transfer. In the case of heating a carbon - ammonia bed, the ammonia can be heated external to the bed in a conventional heat exchanger and then pumped through the bed, where it rapidly gives up its heat to the carbon and, in the process, desorbs a little more ammonia. The cold ammonia issuing from the other end of the bed completes the circuit by returning to the gas heater via the pump. This is illustrated in Fig. 15. The flow of ammonia from the desorbing bed to the condenser and from the evaporator to the adsorbing bed is controlled by simple check valves.

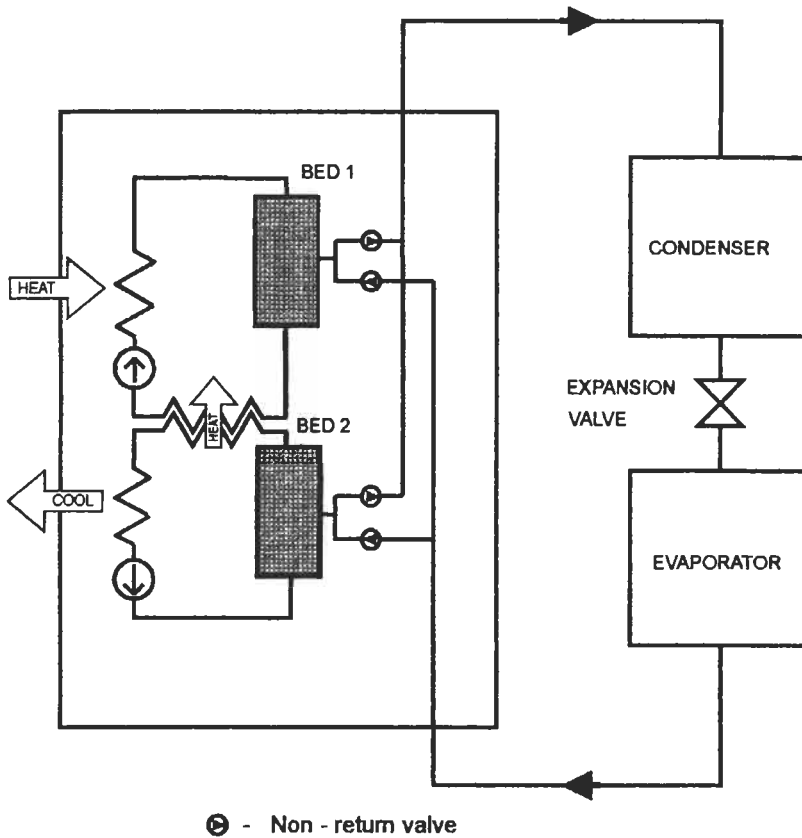


Fig. 15. The convective thermal wave cycle

Since the surface area of the grains is so high, the heat transfer per mass of bed is higher than with conventional heat exchangers within the bed. There is also the advantage that there is no heat exchanger within each bed which would add to its thermal mass. The external gas heat exchangers are in continuous use rather than being cyclically heated and cooled and so their thermal mass has no parasitic effect.

Additionally, a thermal wave is generated in the bed in a similar fashion to that of the thermal wave system. However it is more similar to existing gas

regenerators which also exhibit thermal waves. In order to use the recovered heat it is necessary to transfer it from the cooling bed loop to the heating bed loop. It was proposed to do this with a further gas-to-gas heat exchanger and is denoted by the vertical 'heat' arrow in Fig. 15.

Only one phase of the cycle is shown in Fig.15, in which bed 1 is heated and bed 2 is cooled. The clockwise flow of refrigerant through the bed 1 circuit takes the gas through the pre-heating heat exchanger where heat extracted from bed 2 is added, the external heat exchanger where heat from a gas flame is added and into bed 1. The refrigerant gas emerges cold from this bed until the thermal wave starts to break through.

In bed 2 the circulation of hot gas from the bed passes through the inter-loop heat exchanger, through the external cooler (which provides some of the useful output of a heat pump system) and back into bed 2. The gas emerging from the bed remains hot until the thermal wave starts to break through, at which time it undergoes a rapid drop in temperature.

When the two thermal waves start to break through, the opposite phase of the cycle begins. Valves are switched which effectively swap the two beds over so that bed 1 is cooled and bed 2 is now heated.

The advantages of this concept are :

1. The cycle is highly regenerative and hence highly efficient.
2. There is no complex and expensive heat exchanger within each bed.
3. There is no added thermal mass due to the use of heat exchangers.
4. The high heat transfer rate allows rapid cycle times which result in the plant being more compact and less expensive to produce.

One disadvantage of the system described is the need for the gas-to-gas heat exchanger required to transfer recovered energy between the fluid loops. As a conventional gas-to-gas heat exchanger, it could be both large and expensive and there might be matching problems when the heat rejected by one bed is not required at the same time by the other bed. Critoph and Thorpe [11] suggest the use of an inert packed bed regenerator to overcome both problems, as shown in Fig. 16.

Heat is no longer passed from loop 1 to loop 2 but instead the heat recovered from each active bed in desorption is stored in an inert bed before being passed back to the active bed in the next desorption phase. The inert bed could be as simple as a cylinder packed with steel balls.

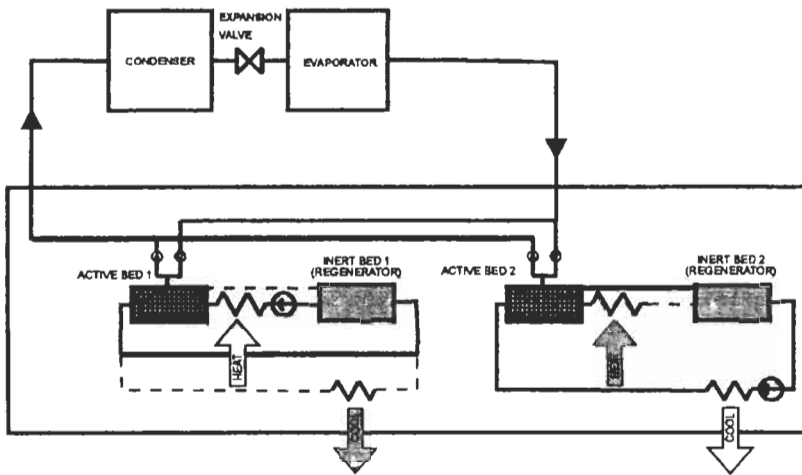


Fig. 16. Convective thermal wave cycle with inert bed regeneration

In Fig. 16, active bed 1 is being heated and active bed 2 is being cooled. Flow in loop 1 is anticlockwise with cold gas coming out of active bed 1, into inert bed 1 where it is pre-heated, through the heat exchanger where it is heated by a gas flame, and back into active bed 1 where it transfers heat to the adsorbent. The thermal waves in both beds ensure the optimum use of recycled heat and hence maximise the COP. Whilst active bed 1 is being heated it desorbs hot gas which passes through the check valve to the condenser. This produces part of the heat output of a heat pump or is simply rejected if the machine is a refrigerator. When hot gas starts to break out of active bed 1 the cycle enters the next phase. Whilst active bed 1 is being heated, active bed 2 is being cooled by a clockwise flow of gas. In an analogous process hot gas leaves active bed 2, passes to inert bed 2 where it is cooled (making a thermal wave progress down inert bed 2), passes through the external cooler where it is further cooled (and giving useful heat output in the case of the heat pump) and re-enters active bed 2 as cold gas. Whilst this process is occurring the active bed simultaneously adsorbs gas from the evaporator producing useful cooling.

When both of these processes (heating of active bed 1 and cooling of active bed 2) are complete, the other stage of the cycle takes place in which active bed 1 is cooled and active bed 2 is heated. This is achieved by switching valves so that the dotted flow paths replace the adjoining paths shown in full lines.

Work at Warwick funded by the Engineering and Physical Sciences Research Council and British Gas is underway to test the concept in a laboratory scale

system for air conditioning. A practical schematic is shown in Fig. 17. The two 'active' beds are packed with activated carbon and the two 'inert' beds are packed with non-reactive particles such as steel balls. The characteristic size of the carbon particles and steel balls is in the range 1-3 mm. The rest of the system contains ammonia refrigerant in either liquid or gaseous form. Fig. 17 shows the first half of the cycle, during which Active bed 1 is heated and desorbs ammonia and Active bed 2 is cooled, adsorbing ammonia.

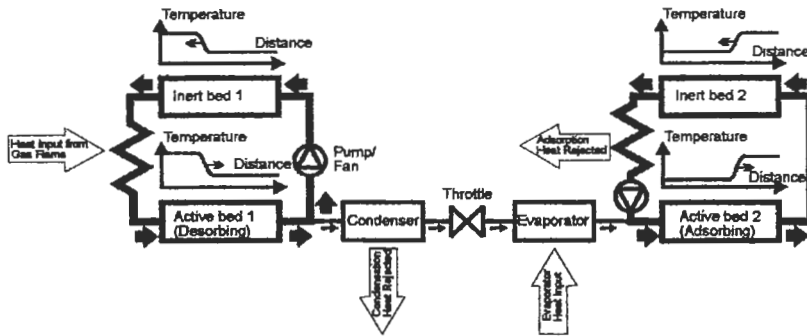


Fig. 17. Schematic layout of a convective thermal wave chiller

In the fluid circulation loop shown on the left, a low power pump or fan forces an ammonia stream through Inert bed 1 which is initially hot. The gas stream is heated by the bed and a 'cold' wave passes through the bed from right to left. Having been pre-heated by the inert bed the ammonia stream is heated to the maximum cycle temperature in a heat exchanger. This heat is supplied externally from, for example, a gas flame. The ammonia gas then passes to Active bed 1 where it heats the carbon, the resulting 'hot' thermal wave passing from left to right through the active bed. As the temperature of the active bed rises it desorbs ammonia which first increases the pressure in the left hand loop and then condenses in the condenser, rejecting heat to the environment. The mass flow rate of circulating ammonia is typically ten times that of the condensing stream of ammonia and it typically takes ten minutes for the two thermal waves to travel the length of their respective beds.

The condensed ammonia passes through a throttle and an evaporator in exactly the same way as in a standard vapour compression cycle and the useful cooling is obtained at the evaporator.

In the fluid circulation loop shown on the right the ammonia gas from the evaporator is adsorbed into Active bed 2 at low pressure. Heat must be removed

from the active bed, since it is hot initially and since heat is generated in the process of adsorption. This is achieved by pumping ammonia gas around the loop. Cold gas enters the active bed both from the loop and from the evaporator, resulting in a 'cold' thermal wave passing from left to right through the bed. As the bed cools, so ammonia is adsorbed. Until this wave breaks through the end of the bed the exit gas will be at a high temperature. Its heat is stored in Inert bed 2 which experiences a simultaneous 'hot' thermal wave from right to left. The ammonia gas leaving Inert bed 2 is warmer than ambient and a heat exchanger must reject its heat to the environment before the pump returns the gas back to the inlet of Active bed 2. As in the left hand loop the circulating flow might be ten times the adsorption flow from the evaporator.

At some time shortly before any of the four thermal waves break through the net effects are:

1. Active bed 1 and Inert bed 2 have been heated.
2. Active bed 2 and Inert bed 1 have been cooled.
3. Ammonia has been driven from one loop to the other achieving useful cooling between the two.

Now a system of valves is used which effectively transposes the positions of Active beds 1 and 2 and Inert beds 1 and 2. The transposition also results in each bed experiencing a reversal of flow direction. The state of the whole system is now as at the beginning and the whole process can be repeated indefinitely to achieve continuous cooling.

The advantages of this system are:

1. The four packed beds are in effect heat exchangers of very high surface area but of minimal cost and are very compact.
2. There are only four conventional heat exchangers and this is the minimum number allowed by thermodynamics. In addition to an evaporator and condenser, one is needed to get high grade heat in and one to reject the heat of adsorption to the environment.
3. The cycle is highly regenerative since the packed beds act like large counterflow heat exchangers. This results in good energy efficiency (i.e. high COP).

Thermodynamically, the concept is similar to thermal wave systems and predicted COP's are similar. A cooling COP of 0.9 (based on heat input to the cycle). is predicted for one design with modest regeneration efficiency, evaporating at 5°C and condensing at 40°C.

5.3 Improving heat transfer

Conventional beds of granular carbon have low thermal conductivity, typically 0.1 W/mK. This presents a problem, both in terms of the performance and cost of systems. Low power machines such as the diurnal cycle solar refrigerator can be economic even at very low power densities (Watts of cooling per kg adsorbent). The mean cooling power may be as little as 20 W and the adsorbent mass around 20 kg corresponding to a power density of 1 W/kg. However, this power density would be unacceptable in a 10 kW household air conditioning system since it would need 10 tonnes of carbon! In order to build a low cost compact machine, cooling power densities of 1000 W/kg are required. Increasing compactness by reducing the cycle time to minutes rather than hours demands high heat transfer coefficients. Additionally, the various regenerative cycles described above all demand heat transfer between beds in order to achieve competitive COP's. This also requires good heat transfer, and a low approach temperature between beds. The sections below consider both the fundamentals of thermal conductivity in conventional granular beds and some of the means available to achieve the required improvement.

5.3.1 Thermal conductivity in granular adsorbent beds

The preferred refrigerants for use with active carbons are methanol and ammonia. Methanol - carbon systems have been studied in depth by Meunier's team at LIMSI (Laboratoire d'Informatique pour la Mécanique et les Sciences de l'Ingénieur). Guilleminot, Meunier and Paklesa [12] modelled the two dimensional heat transfer in the methanol - carbon generator of a solar refrigerator. The generator was integrated into a flat plate solar collector with internal fins 90 mm high, 1 mm thick and with a pitch of 50 mm. The carbon was in the form of 1 mm extruded pellets of AC-35 manufactured by CECA. The heat transfer parameters (bed conductivity k and fin to bed heat transfer coefficient h) were calculated by varying their values within the model to match experimental results to be 0.19 & 0.07 W/mK and 16.5 & 0.6 W/m²K respectively. The model took into account the 'heat pipe effect' in which heat transfer may be enhanced by desorption of refrigerant at one location within the bed and simultaneous adsorption at a different location in the same bed. Any accurate model of a refrigerant - adsorbent bed must take account of this phenomenon during the closed isosteric heating and cooling phases, and of the varying effective specific heat of the bed which takes account of the enthalpy of sorption during the complete cycle.

Gurgel and Grenier [13] went on to make direct measurements of the bed thermal conductivity using the Bauer-Schlünder [14] model. This model is the most extensive and complete description of thermal conductivity within a granular bed. Previous models assumed either parallel isotherms perpendicular

to the heat flux (zero lateral resistance) or heat flux uniform in the direction of heat transfer (infinite lateral resistance). These are two extreme bounds of the correct solution. A variable contour particle shape with parallel heat flux lines is used which can successfully model packed cylinders, spheres and other shapes.

The model uses four parameters:

- A particle geometry factor.
- The relative grain contact area.
- A combined radiation length and emissivity term.
- The solid grain conductivity k_g .

Gurgel and Grenier's results showed the bed conductivity to increase from 0.14 to 0.17 W/mK as the pressure was raised from 4 mbar (evaporating pressure) to 110 mbar (condensing pressure). The principle reason stated for this small variation is the reduction in the gas conductivity with decreasing pressure (Knudsen effect) in the macropores. The solid grain conductivity varied linearly from 0.61 to 0.65 W/mK as the methanol concentration varied from 0 to 31%.

Critoph and Turner [15] carried out similar direct measurements for ammonia and 208C (coconut shell based) carbon manufactured by Sutcliffe Speakman Carbons. The bed conductivity was found to be around 0.165 W/mK at concentrations less than 20% and to rise to 0.19 W/mK at 25% concentration. The corresponding grain conductivities rose from 0.85 to 1.25 W/mK respectively. The higher grain conductivity than that found by Gurgel and Grenier may reflect the different structures present within the extruded and nut shell carbons.

The poor bed conductivities referred to above are typical. In order to achieve reasonable power densities, early attempts at improving heat transfer used finned heat exchangers with the adsorbent being packed between the fins. Zanife [16] obtained 200 W/kg of heat output in a 300 kW heat pump using finned tube exchangers. The design suffered from a lower than expected adsorbent packing density. The large fin area had the desired effect of reducing the bed conduction path length but the poorer grain packing near the fin surfaces reduced both the bed conductivity and the surface heat transfer coefficient. A further disadvantage of any such large or extended area heat exchanger is that the thermal mass of the heat exchanger itself will reduce the COP. However, it is possible to obtain good power density with large area heat exchangers. The Wave - Air gas fired heat pump prototype reported by Miles [9] uses a proprietary design heat exchanger within the granular carbon beds and has achieved 10 kW cooling with a total bed weight (including shell) of 226 kg. This corresponds to 44 W/kg cooling based on the total weight, and 217 W/kg based on the adsorbent weight.

Other ways that have been suggested to improve the bed conductivity are to use a bi-modal grain size distribution to increase the packing density, or to add

metallic powders to the bed. Both are of limited effectiveness since there is little direct contact between grains and the major thermal resistance is that of the gas filled voids.

5.3.2 Consolidated and composite carbons

The need for higher bed conductivity has led to research aimed at producing carbons that combine high packing density and improved conductivity. If a monolithic block of carbon adsorbent can be produced which eliminates void spaces there are several advantages:

- More carbon can be contained within a given pressure vessel.
- The surface heat transfer coefficient can be dramatically increased since the gas space between fin or tube and the adsorbent can be greatly reduced or eliminated.
- The 'bed' conductivity becomes that of the 'grain' since there is a continuous solid conduction path.

One such monolithic carbon has been produced by Sutcliffe Speakman Carbons and is described by Tamainot-Telto and Critoph [17]. Powdered activated carbon is mixed with a polymeric binder, compressed in a die and fired to produce a monolith of the desired shape, with a density of 713 kg/m^3 and conductivity of 0.33 W/mK . A heat transfer coefficient of $200 \text{ W/m}^2\text{K}$ has been measured between the blocks and aluminium fins.

Monolithic carbons may also be manufactured in finished form from PVDC as has been done by Quinn [18]. The porosity and density compare favourably with those of conventional granular carbons and the Sutcliffe Speakmann monoliths but the manufacturing process is not easy to scale up from the laboratory to commercial levels. The properties (including x_0 , K and n from the D-A equation) are compared in Table 3 below, taken from Critoph [4].

The 'grain density' given is based on a volume which is the envelope of the grain and is measured for 208C as in Turner [19]. The two other carbon volumes are obtained by direct measurement, both of them being supplied in the form of regular discs. The bulk density of the granular 208C carbon is lower since the particles cannot be packed perfectly, whereas the carbon monoliths can be manufactured to fill a vessel with negligible void space. The limiting concentration (x_0) per bulk volume gives an indication of the maximum mass of refrigerant that can be adsorbed in a given vessel. This is multiplied by the latent heat of the refrigerant at 0°C in the final column to reflect the cooling potential that this represents.

Table 3. Porosity test results

Carbon							PVDC
	208C	208C	208C	mono- lith	mono- lith	mono- lith	based monolith
Refrigerant	NH ₃	R32	butane	NH ₃	R32	butane	NH ₃
x_0	0.290	0.476	0.259	0.270	0.461	0.237	0.232
K	3.185	2.463	1.289	4.377	2.672	1.369	4.634
n	1.095	1.388	1.142	1.196	1.332	1.392	1.806
'Grain' density (g/cc)	0.740	0.740	0.740	0.713	0.713	0.713	1.011
Bulk density (g/cc)	0.500	0.500	0.500	0.713	0.713	0.713	1.011
Limiting conc. per unit vol. (g/cc)	0.145	0.238	0.130	0.193	0.329	0.169	0.234
Enthalpy of vaporisation per vol. (kJ/cc)	183	75	51	243	104	66	295

A brief inspection of the data implies:

1. The carbons are broadly comparable in terms of their maximum concentration and implied energy efficiency but the two monolithic forms offer the advantage of smaller pressure vessel sizes and improved heat transfer.
2. Despite very high adsorbed concentrations, R32 would appear to have a much lower adsorbed refrigeration capacity than ammonia. Butane has even less merit than R32.

The conductivity of any of the granular or monolithic carbons is low since the porous microstructure that is needed for high adsorption capacity is incompatible with the more ordered structure needed for good conduction. However, it is possible to produce composites which contain highly adsorptive particles within a conducting matrix. Groll [20] surveys some of the matrix - adsorbent combinations that have been tried. Copper or nickel foams have been used as conducting matrices for zeolite and metal hydride adsorbents and bed conductivities of between 1.7 and 9.3 W/mK have been measured. An anisotropic graphite matrix (IMPEX) combined with MnCl₂ developed by Spinner has a conductivity of 5-15 W/mK in the radial direction and < 1 W/mK

in the axial direction within a 150 mm radius vessel. A patented graphite matrix - zeolite adsorbent manufactured by LCL [21] has conductivity ranging from 5-15 W/mK and heat transfer coefficients from 200-3000 W/m²K. Similar heat transfer properties can be expected with graphite - active carbon composites and work is in progress to develop such materials.

There is a general consensus that power densities of at least 1 kW/kg for heating or 0.5 kW/kg for cooling are achievable using composite or monolithic materials.

5.3.3 Convective heat transfer

The convective wave cycle was described in 5.2.4 but its heat transfer properties not quantified. Critoph and Thorpe [22] and Thorpe [23] have measured the convective heat transfer coefficient between flowing gas and the grains within the bed. Preliminary results imply that the pressure drop through the bed can be expressed by a modified Ergun equation:

$$\frac{\Delta P}{L} = \frac{c(1-\varepsilon)^2}{d^2 \varepsilon^3} \mu u + \frac{m(1-\varepsilon)}{d \varepsilon^3} \rho u^2$$

where :

$\Delta P/L$ is the pressure drop per unit length (Pa/m)

ε is the void fraction of the bed.

r is the gas density (kg/m³).

m is the gas viscosity (Pa.s).

u is the gas free stream velocity (m/s).

d is the characteristic grain dimension (m).

c is a constant (317 for 208C granular carbon).

m is a constant (3.15 for 208C granular carbon).

The heat transfer coefficient is best based on the Reynolds-Colburn analogy using a modified friction factor f'_v :

$$\frac{j_h \varepsilon}{f'_v} = \frac{0.696}{Re^{1.02}}$$

$$f'_v = \frac{1}{36} \frac{\Delta P}{L} \frac{\varepsilon^3}{(1-\varepsilon)} \frac{d^2}{\mu u}$$

$$j_h = St Pr^{2/3}$$

where Re , St and Pr are the Reynolds, Stanton and Prandtl numbers respectively.

Using these correlations the number of transfer units (*NTU*) of a particular bed can be calculated together with its effectiveness as a heat exchanger for a particular mass flow. A sample calculation for a bed with a heating density of 1 kW/kg carbon, a power input of 12 kW and temperature difference between the hot gas and bed of 100°C has been carried out. The required bed would be 250 mm in diameter and 505 mm long and have a pressure drop of 1.17 kPa corresponding to a pumping power of 5 W. The total *NTU* is 120, giving an effectiveness of between 0.9 and 0.95. Predicted cooling COP's range from 0.8 to 1.0 depending on the condensing and evaporating temperature.

6 Summary and Conclusions

There is international interest in the use of active carbons within adsorption cycles to provide refrigeration or heat pumping. The benefits of heat-driven cycles range from reduction in primary energy demand within the developed countries to the ability to operate away from grid electricity supplies in developing countries. The technical feasibility of adsorption cycles has already been proven. The challenge is to make machines that are cost effective, which means that they must be both efficient and of high power density. This requires the use of adsorbents that have both optimised porosity characteristics and may be integrated into systems with high levels of heat transfer intensification.

7 References

1. Smisek M. and Cerný S., *Active Carbon - Manufacture, Properties and Applications*, Elsevier, Amsterdam - London - New York, 1970.
2. Critoph R.E. and Turner L., Performance of Ammonia-Activated Carbon and Ammonia Zeolite Heat Pump Adsorption Cycles. In *Proceedings of Pompes a Chaleur Chimiques De Hautes Performances*, Perpignan, Sept. 1989, Lavoisier, Paris, 1989, pp 202 211.
3. Critoph R.E., Performance limitations of adsorption cycles for solar cooling, *Solar Energy*, 1988, **41**(1), 21 31.
4. Critoph, R.E., Evaluation of alternative refrigerant - adsorbent pairs for refrigeration cycles, *Applied Thermal Engineering*, 1996,**16**(11), 891 900.
5. Meunier, F., Second law analysis of a solid adsorption heat pump operating on reversible cascade cycles: application to the zeolite-water pair. *Heat Recovery Systems*, 1985, **5**, 133 141.
6. Douss N. and Meunier F., Experimental study of cascading adsorption cycles. *Chemical Engineering Science*, 1989, **44**, 225 235.
7. Rockenfeller, U. *et al*, Advanced heat pump staging for complex compound chemi-sorption systems. In *proceedings of Solid Sorption Refrigeration*, Paris, IIR, 1992, pp.153 159.
8. Shelton, S., U.S. Patent No. 4,694,659, 1987.

9. Miles D.J. *et al*, Gas fired sorption heat pump development. *In proceedings of Solid Sorption Refrigeration*, Paris, IIR,1992, pp. 74 79.
10. Critoph, R.E., A forced convection regenerative cycle using the ammonia-carbon pair. *In proceedings of Solid Sorption Refrigeration*, Paris, IIR,1992, pp. 80 85.
11. Critoph, R.E. and Thorpe, R.N., U.K. Patent 9419202.8, 1994.
12. Guilleminot, J.J., Meunier, F. and Pakleza, J., Heat and mass transfer in a non-isothermal fixed bed solid adsorbent reactor: a uniform-pressure non-uniform temperature case. *International Journal of Heat and Mass Transfer*, 1987, 30(8), 1595 1606.
13. Gurgel J.M. and Grennier Ph., Mesure de la conductivité thermique du charbon actif AC-35 en présence de Gaz. *The Chemical Engineering Journal*, 1990, 44, 43 50.
14. R. Bauer, *VDI Forschungsh*, 1977, 582 .
15. Critoph R.E. and Turner L., *Int. J. Heat Mass Transfer*, **38**, 1577 (1995).
16. Zanife T.N., Etude de la regulation d'une pompe à chaleur à adsorption à deux adsorbants: cas zéolithe-eau. *In Proceedings of Pompes à Chaleur Chimiques De Hautes Performances*, Perpignan, Sept. 1989, Lavoisier, Paris, 1989, pp 212 221.
17. Tamainot-Telto, Z. and Critoph R.E, Adsorption refrigeration using monolithic carbon - ammonia pair. *International Journal of Refrigeration*, 1997, 20(2), 146 155.
18. Quinn, D., Royal Military College of Canada, Kingston, Canada. Private communication.
19. Turner, L., Improvement of activated charcoal-ammonia adsorption heat pumping/refrigeration cycles. Investigation of porosity and heat/mass transfer characteristics. Ph.D. Thesis, University of Warwick, UK ,1992.
20. Groll, M., Reaction beds for dry sorption machines. *In proceedings of Solid Sorption Refrigeration*, Paris, IIR,1992, pp.207 214.
21. SNEA-LCL, Patent WO 91/15292-11/04/1991.
22. Critoph, R.E. and Thorpe, R.N., Momentum and heat transfer by forced convection in fixed beds of granular active carbon. *Applied Thermal Engineering*, 1996, 16, 419 427.
23. Thorpe, R.N., Heat transfer by forced convection in beds of granular adsorbent material for solid adsorption heat pumps. Ph.D. Thesis, University of Warwick, UK, 1996.

CHAPTER 11

Applications of Carbon in Lithium-Ion Batteries

TAO ZHENG AND J.R. DAHN

*Department of Physics**Simon Fraser University**Burnaby, BC, Canada V5A 1S6***1 Introduction***1.1 Lithium-ion battery*

The rechargeable lithium-ion battery is one of a number of new battery technologies which have been developed in the last ten years. This battery system, operating at room temperature, offers several advantages compared to conventional aqueous battery technologies, for example,

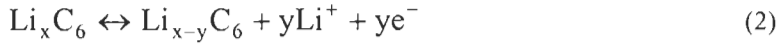
1. Higher energy density (up to 135 Wh/kg, 300 Wh/L);
2. Higher cell voltage (up to 4.0 V);
3. Longer shelf life (up to 5-10 years) and cycle life (1000 to 3000 cycles).

Lithium-ion batteries are presently the state-of-the-art rechargeable power sources for consumer electronics [1]. They are now produced by several Japanese and Canadian manufacturers, and many other firms worldwide are engaged in their development. This technology is based on the “rocking chair” concept, that is, using two suitable lithium intercalation compounds as cell electrodes. Thus, lithium ions are shuttled back and forth between the two intercalation hosts as the cell is charged and discharged. The cell voltage is then determined by the difference in the chemical potential of lithium in the two hosts, *i.e.*,

$$V = -\frac{(\mu_{\text{cathode}} - \mu_{\text{anode}})}{e}, \quad (1)$$

where μ_{cathode} is the chemical potential of lithium in the cathode material, μ_{anode} is the chemical potential of lithium in the anode material, and e is the magnitude of the electron charge. Obviously, a large chemical potential difference will lead to a high cell voltage. Presently, the lithium transition metal oxides LiNiO_2 , LiCoO_2 , or LiMn_2O_4 are chosen as the cathode and carbonaceous materials as the anode in the lithium-ion batteries. Figure 1 schematically shows a lithium-

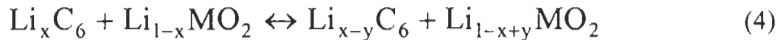
ion cell during both the discharge and charge processes. The electrode reactions which occur in the cell are:



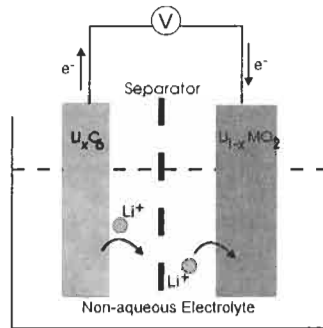
at the carbon anode, and



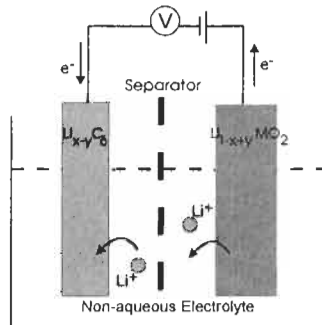
at the transition metal oxide cathode. Both equations lead to an overall cell reaction



where $\text{Li}_{1-x}\text{MO}_2$ represents the lithiated metal oxide intercalation compound. The forward direction of the reactions corresponds to the discharge of the cell. The recharge of the cell is accomplished by placing a power supply in the external circuit of the cell and forcing the electrons and ions to move in the opposite directions.



(a)



(b)

Fig. 1. Schematic drawing of a lithium-ion cell. (a) during discharge, (b) during charge.

1.2 Why is carbon a suitable candidate for the anode of a Lithium-ion Battery?

During the 1970's and 1980's, the search for high-energy-density batteries led to the use of lithium metal as the anode material for rechargeable lithium cells which had a reasonable cycle life. Lithium metal was later proven to be very difficult to make safe in a large scale cell, such as an *AA* size cell. The formation of dendrites on the surface of the lithium electrode, and changes in the shape of the lithium electrode, can lead to potential safety problems. When lithium is electroplated onto a metallic lithium anode during recharge, it forms a more porous deposit with a larger surface area than the original metal. Therefore, cell cycling causes the area of contact between the lithium metal and the electrolyte to get larger and larger. The thermal stability of the original lithium metal is good in many non-aqueous electrolytes. However, after a large number of cycles, the significant increase of the surface area of the metallic lithium leads to conditions which are very sensitive to thermal, mechanical and electrical abuse [2].

A possible solution to this problem is to use an electrolyte, such as a solid polymer electrolyte, which is less reactive with lithium metal [3]. Another simple solution is the lithium-ion cell.

In the lithium-ion approach, the metallic lithium anode is replaced by a lithium intercalation material. Then, two intercalation compound hosts, with high reversibility, are used as electrodes. The structures of the two electrode hosts are not significantly altered as the cell is cycled. Therefore the surface area of both electrodes can be kept small and constant. In a practical cell, the surface area of the powders used to make up the electrodes is normally in the $1 \text{ m}^2/\text{g}$ range and does not increase with cycle number [4]. This means the safety problems of *AA* and larger size cells can be solved.

One criterion for the anode material is that the chemical potential of lithium in the anode host should be close to that of lithium metal. Carbonaceous materials are therefore good candidates for replacing metallic lithium because of their low cost, low potential versus lithium, and wonderful cycling performance. Practical cells with LiCoO_2 and carbon electrodes are now commercially available. Finding the best carbon for the anode material in the lithium-ion battery remains an active research topic.

1.3 Introduction to this chapter

The work presented in this chapter involves the study of high capacity carbonaceous materials as anodes for lithium-ion battery applications. There are hundreds and thousands of carbonaceous materials commercially available. Lithium can be inserted reversibly within most of these carbons. In order to prepare high capacity carbons for lithium-ion batteries, one has to understand the physics and chemistry of this insertion. Good understanding will ultimately lead to carbonaceous materials with higher capacity and better performance.

The mechanism of lithium insertion in carbonaceous materials depends on the carbon type. The structure of carbons depends strongly on the type of organic precursors used to make them. Carbonaceous materials have historically been divided into two groups: soft and hard carbons. The soft carbons graphitize nearly completely upon heating to above $\sim 3000^{\circ}\text{C}$. Hard carbons never become graphite at any temperature unless a high pressure is applied. The reversible capacities of many carbons for lithium depend on both pyrolysis temperature and precursor type. Figure 2 shows the reversible capacities of many carbons prepared by the pyrolysis of organic precursors as a function of the heat-treatment temperature [5].

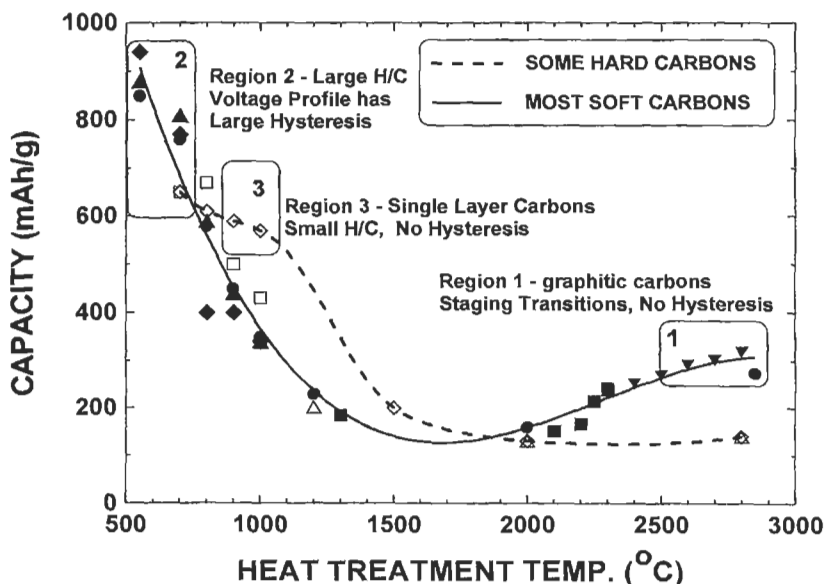


Fig. 2. The “master graph” of reversible capacity for lithium plotted versus heat treatment temperature for a variety of carbon samples. The three regions of commercial relevance are marked. Solid symbols are data for soft carbons, open symbols are data for hard carbons.

Carbons in the three highlighted regions of Fig. 2 are currently used or have been proposed for use in commercial lithium-ion batteries. Region 1 contains graphitic carbons prepared by heating soft carbon precursors to temperatures above 2400°C [6,7]. Region 2 contains both soft and hard carbons, heated to between 500 and 700°C, which have substantial hydrogen content [8,9,10]. Region 3 contains hard carbons made up predominantly of single graphene layers that include appreciable microporosity and are stacked more or less like a “house of cards” [8,11,12,13].

Figure 3 shows the voltage-capacity relation for lithium/carbon electrochemical cells made from representative materials from each of the three regions of Fig. 2.

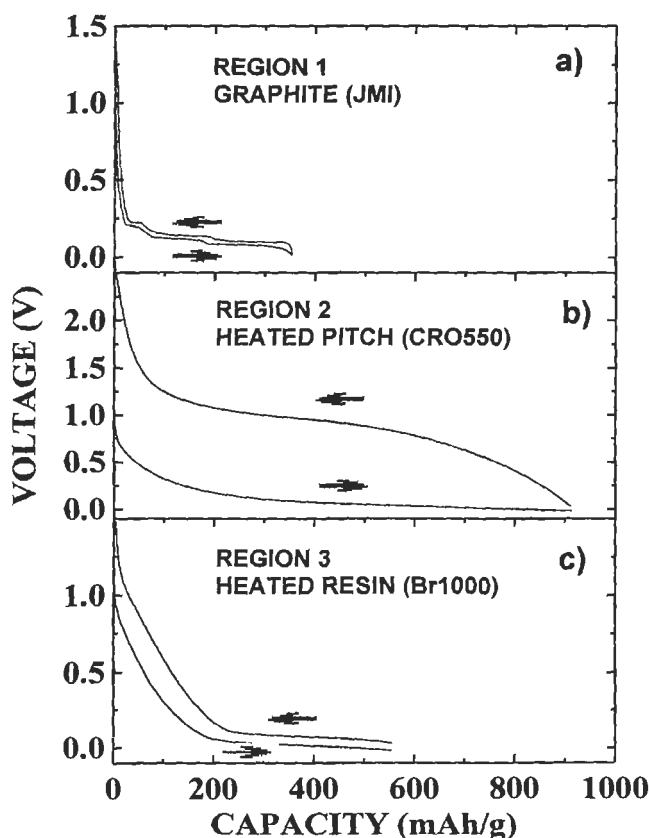


Fig. 3. Second cycle voltage profiles of carbons representative of regions (1), (2), and (3). a) JMI synthetic graphite, b) Crowley petroleum pitch heated to 550°C, and c) a resolec resin heated to 1000°C.

The synthetic graphite (Johnson-Matthey Inc.) sample [Fig. 3(a)] gives a reversible capacity of about 355 mAh/g [6]. Petroleum pitch heated to 550°C to get $H_{0.4}C$ [Fig. 3(b)] gives a reversible capacity of near 900 mAh/g [8]. The voltage profiles for all materials in region 2 show appreciable hysteresis; that is, the lithium is inserted near zero volts (versus lithium metal) and removed near one volt. Resole resin heated to 1000°C [Fig. 3(c)] contains less hydrogen and gives a reversible capacity of about 550 mAh/g [11]. The voltage profiles for each material in Fig. 3 are markedly different, which suggests that different reaction mechanisms are important in each of the three regions in Fig. 2.

To understand the mechanisms for the reaction of lithium with different carbons is the goal of this chapter. However, before we can do this, we need clear structural pictures for carbonaceous materials in each of the three regions.

Section 2 of this chapter describes the characterization of carbonaceous materials by powder X-ray diffraction, small-angle-X-ray scattering (SAXS), measurements of surface area, and by the carbon-hydrogen-nitrogen (CHN) test, a chemical analysis of composition. In this section, we also describe the electrochemical methods used to study carbonaceous materials.

Section 3 begins with synthesis, followed by structural models for graphitic carbons found in region 1 Fig. 2. The structural parameters for graphitic carbons are obtained from the structure refinement program for disordered carbons developed by Hang Shi, et al [14,15]. Turbostratic disorder, a random rotation or translation between adjacent graphene layers, determines the capacity for lithium intercalation and affects the staging phase transitions which occur during the intercalation of lithium.

Lithium insertion in hydrogen-containing carbons (region 2 of Fig. 2) is carefully studied in section 4. In all carbonaceous materials heated to $\sim 700^\circ\text{C}$, hydrogen is the largest constituent left except carbon, leading to hydrogen-containing carbons. Powder X-ray diffraction, SAXS, and Brunauer-Emmett-Teller (BET) surface area measurements show these hydrogen-containing carbons include both soft and hard carbons, with different amounts of micropores in the samples. Carbonaceous materials with high hydrogen content have high capacity for lithium insertion which shows large hysteresis. It is believed that the lithium atoms may bind to hydrogen terminated edges of hexagonal carbon fragments causing a change in the carbon bond from trigonal sp^2 to tetrahedral sp^3 .

Lithium insertion in microporous hard carbons (region 3 in Fig. 2) is described in section 6. High capacity hard carbons can be made from many precursors, such as coal, wood, sugar, and different types of resins. Hard carbons made from resole and novolac resins at temperatures near 1000°C have a reversible capacity of about 550 mAh/g, show little hysteresis and have a large low voltage plateau on both discharge and charge. The analysis of powder X-ray diffraction,

SAXS, and BET measurements shows that the high capacity hard carbons are made up of graphene monolayers, bilayers and trilayers stacked at arbitrary angles. Such a structure implicitly requires small pores between the oddly stacked groups of sheets. The structure resembles a “house of cards”. We believe that the lithium can be adsorbed on the internal surfaces of the graphene monolayers. The monolayers can adsorb lithium on both sides, leading to a large reversible capacity which may ultimately approach twice that of graphite for materials with the ideal disordered structure.

Carbons described in sections 3 and 5 have already been used in practical lithium-ion batteries. We review and briefly describe these carbon materials in section 6 and make a few concluding remarks.

2 Useful Characterization Methods

There are many ways to characterize the structure and properties of carbonaceous materials. Among these methods, powder X-ray diffraction, small angle X-ray scattering, the BET surface area measurement, and the CHN test are most useful and are described briefly here. To study lithium insertion in carbonaceous materials, the electrochemical lithium/carbon coin cell is the most convenient test vehicle.

2.1 Powder X-ray diffraction

Carbon samples used for powder X-ray diffraction were obtained by grinding the as-made carbons. If carbon samples are supplied in powder form, they can be measured directly. The powder consists of an enormous number of ten-micron-sized particles usually with completely random orientation.

2.1.1 Experimental methods

Powder X-ray diffraction patterns for each carbonaceous material were collected using a Siemens D5000 powder diffractometer equipped with a copper target X-ray tube and a diffracted beam monochromator. The divergence and antiscatter slits we normally used were 0.5° . For most disordered carbon samples, we selected a 0.6 mm receiving slit. These choices led to an instrumental resolution of about 0.15° in $2\theta_B$. However, for graphitic carbons, we selected a 0.2 mm receiving slit to obtain higher resolution. All the measurements were made between 10° and 120° in scattering angle.

2.1.2 Scherrer equation to estimate the size of organized regions

Imperfections in the crystal, such as particle size, strains, faults, *etc.*, affect the X-ray diffraction pattern. The effect of particle size on the diffraction pattern is one of the simplest cases and the first treatment of particle size broadening was made by Scherrer in 1918 [16]. A more exact derivation by Warren showed that,

$$L = \frac{K_s \lambda}{B \cos \theta_B} \quad (5),$$

now known as the Scherrer equation. Warren showed that the constant K_s is 1.84 [17], for two-dimensional peaks, and is 0.89 for three-dimensional peaks [18]. For carbonaceous materials, the lateral extent of the graphene layers and the number of stacked layers can be estimated using the Scherrer equation with the appropriate shape constant. Usually, the (002) or (004) reflection is used to estimate the carbon crystallite dimension perpendicular to the basal graphene layer, L_c , and the (100) or (110) reflection is used to estimate the lateral dimension of the graphene layers, L_a .

2.1.3 Structure refinement program for carbons

The X-ray diffraction pattern of carbon can be complex to interpret due to the complicated structural disorder of carbons. Recently, Shi *et al* [14,15] developed a structure refinement program for disordered carbons. The program is ideally suited to studies of the powder diffraction patterns of soft carbons heated between 2000°C and 3000°C. By performing a least squares fit between the measured diffraction pattern and a theoretical calculation, parameters of the model structure are optimized. For soft carbons heated above about 2200°C, the structure is well described by stacked two-layer packages in *AB* registry. The stacking of these packages is performed with the following probabilities:

- a) a turbostratic shift or rotation between adjacent packages with probability P' ;
- b) a registered shift between adjacent packages with probability, P'_1 , to describe local order *AB/CA/BC etc.*;
- c) no shift between adjacent packages to obtain the stacking *AB/AB/AB etc.* with probability $(1-P'-P'_1)$.

Thus, if $P'=0$ and $P'_1=0$, 2H graphite is obtained, if $P'=1$ and $P'_1=0$, turbostratic graphite (50%) is obtained, and if $P'=0$ and $P'_1=1$, 3R graphite is obtained. It is more convenient to use the stacking probabilities per layer, $P=P'/2$ and $P_1=P'_1/2$, and we will use these here.

In this chapter, the structure refinement program will be used to determine the structural parameters of graphitic carbons as shown in section 3.

2.2 Small-angle X-ray scattering

Small-angle X-ray scattering (SAXS) [19] has been widely used to investigate the inhomogeneous electron density in materials [20]. In carbonaceous materials, porosity is commonly encountered. The pores form and provide escape routes for gases produced during the pyrolysis process.

2.2.1 Experimental methods

SAXS data were collected on the carbon samples using the Siemens D5000 diffractometer. This diffractometer is generally used for flat-sample powder diffraction which performed in reflection geometry. In order to perform SAXS, it was necessary to make the measurement in transmission mode (see Fig. 4). To this end, the samples were filled in a rectangular frame with kapton (fluorinated polyamide) windows on both sides. The frame was held vertically. The incident and antiscatter slits were both 0.1° and the receiving slit was 0.1 mm. The empty frame with kapton windows showed negligible signal when there was appreciable scattering from the carbons. Therefore we neglected the background signal from the frame in our analysis of the SAXS data from pyrolyzed samples. The mass of sample held in the frame was recorded.

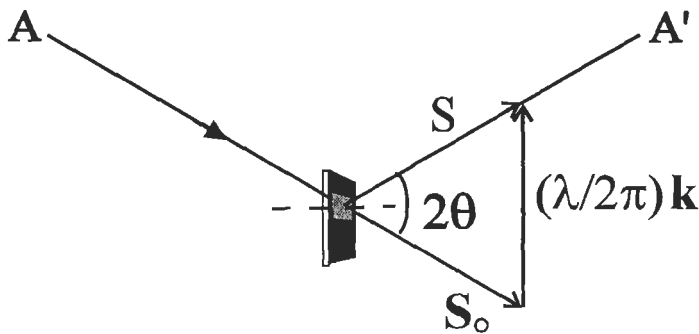


Fig. 4. Schematic showing the SAXS measurement on the Siemens D5000 diffractometer. The wave-vector, \mathbf{k} , is determined as $(2\pi/\lambda)(\mathbf{s}-\mathbf{s}_0)$, where \mathbf{s} and \mathbf{s}_0 are the unit vectors defining the directions of the scattered and incident radiation respectively.

2.2.2 Guinier's equation

Guinier's equation [19] was originally derived for a material with randomly positioned identical pores embedded in a uniform background. The intensity of small angle scattering, $I(\mathbf{k})$, from pores with volume V , is

$$I(\mathbf{k}) \propto NV^2 e^{-k^2 R_g^2/3} \quad (6),$$

where N is the number of pores, and R_g is the radius of gyration which is defined as

$$R_g^2 = \frac{\int d^3 r \cdot r^2 \rho(\vec{r})}{\int d^3 r \cdot \rho(\vec{r})} \quad (7).$$

Using eq. (7) for a spherical pore of radius R_0 , gives $R_g = \sqrt{\frac{3}{5}} R_0$.

2.3 Surface area measurements

The BET method is the most widely used procedure for determining the surface area of porous materials. In this chapter, BET results were obtained from single point measurements using a Micromeritics Flowsorb II 2300 surface area analyzer. A mixture of nitrogen in helium (30:70 mole percentage) was used. Although this simple method is not quantitative for the microporous materials studied in section 5, it still allows qualitative comparisons to be made.

2.4 CHN test

The CHN test determines the weight percentages of carbon, hydrogen, and nitrogen in the samples. Samples were combusted in pure oxygen in a quartz tube. Then the combustion products, including CO_2 , H_2O , and N_2 , *etc.*, were carried by a pure argon stream to a gas chromatograph and quantified. Small amounts (about 20 mg each) of our samples were sent to Canadian Microanalytical Service Ltd. (Delta, BC, Canada) for the CHN test. The accuracy of the test is $\pm 0.3\%$ by weight.

2.5 Electrochemical methods

For convenience and simplicity, the electrochemical study of electrode materials is normally made in lithium/(electrode material) cells. For carbonaceous materials, a lithium/carbon cell is made to study electrochemical properties, such as capacity, voltage, cycling life, *etc.*. Lithium/carbon coin cells use metallic lithium foil as the anode and a particular carbonaceous material as the

cathode. The purpose of using such cells rather than lithium-ion cells is that the chemical potential of lithium atoms in metallic lithium is fixed. Therefore, the cell voltage measures the chemical potential of lithium atoms within the carbonaceous material. In a lithium-ion cell, the chemical potential of lithium in both electrodes changes at the same time. This makes it difficult to study the carbon electrode alone.

Lithium/carbon cells are typically made as coin cells. The lithium/carbon coin cell consists of several parts, including electrodes, separator, electrolyte and cell hardware. To construct a coin cell, we first must prepare each part separately. Successful cells will lead to meaningful results. The lithium/carbon coin cells used metallic lithium foil as the anode and a carbonaceous material as the cathode. The metallic lithium foil, with a thickness of 125 μm , was provided by Moli Energy (1990) Ltd.. The lithium foil is stored in a glove-box under an argon atmosphere to avoid oxidation.

The cathode is made by coating a slurry. The slurry is a mixture of the carbon powder (90% by weight), Super S carbon black (Chemetals Inc.) (5% by weight), and a binder solution of 9.4% by weight of Polyvinylidene fluoride (PVDF) in 1-Methyl-2-Pyrrolidinone (NMP) (~50% by weight). Excess NMP is added to the mixture to obtain a syrupy consistency. The slurry is then spread in a 150- μm thick layer on a copper foil substrate using a doctor blade spreader. After coating, the electrode is dried in an oven overnight at a temperature of 105 to 110°C in air. The NMP evaporates and a flat and adhering film of the electrode material is obtained on the copper. The electrode is pressed between two flat plates at about 1000 kPa for about one minute before it is used for making cells. The pressure increases the connections between powder particles, leading to good conductivity of the electrode.

The electrolyte used is 1 molar LiPF_6 dissolved in a mixture of 30% ethyl carbonate (EC) and 70% diethyl carbonate (DEC) by volume. This electrolyte is easy to use because it will self-wet the separator and electrodes at atmospheric pressure. The electrolyte is kept under an argon atmosphere in the glove-box. The molecules of electrolyte solvents, like EC and DEC, have in-plane dimensions of about (4 \AA \times 5 \AA) to (6 \AA \times 7 \AA). These molecules are normally larger than the openings of the micropores formed in the region 3 carbons (Fig. 2) as described in section 5.

The carbon electrode is cut into unit squares 12 mm long \times 12 mm wide using a stainless steel ruler with 12 mm width, and a surgical blade. Then these squares are weighed. The weight of the copper substrate square is known to be 13.3 mg. The active electrode mass is finally obtained by correcting for the weight of the substrate, the weight of the binder, and the weight of the Super S carbon black (the so-called dead mass in the electrode). Typically, the active electrode mass is around 10 mg. Celgard 2502 microporous film is used for the separator. The

film is obtained from Moli Energy (1990) Ltd. and then is stamped into unit circles of 21 mm diameter with a brass cutter.

Electrochemical cells are assembled in the glove-box. The cell is a 2320-type coin cell (23 mm OD and 2.0 mm thickness) as schematically shown in Fig. 5. The cell includes the electrolyte, the cell cap and can which are stainless steel, a polypropylene gasket used to seal the cell, the two electrodes, the separator between the electrodes, as well as a stainless spacer and a mild steel disc spring which are used to increase the pressure on the electrodes. Once the cell is assembled in the right order, the cell is sealed by a pressure crimper inside the glove-box.

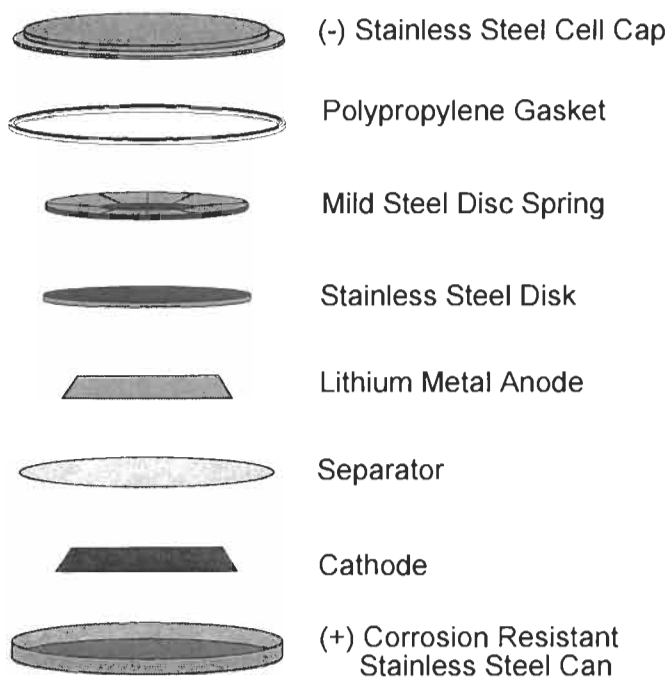


Fig. 5. Exploded view of a 2320-type coin cell.

Freshly assembled lithium/carbon coin cells typically have voltages between 2.8 and 3.4 volts. The cells are in their fully charged state which means that no lithium is inserted in the carbon anode. Then the coin cells are tested with computer-controlled constant-current cyclers having currents stable to $\pm 1\%$. The cells are placed in thermostats at a particular set temperature which is stable to $\pm 0.1^\circ\text{C}$ during the test. Most of our cells were tested at 30°C .

The current for charge and discharge is selected based on the active mass of the carbonaceous electrode. A 50-h-rate current applied to the cell corresponds to a change $\Delta x = 1$ in Li_xC_6 in 50 hours (for a typical cell with 14-mg active carbon mass, the current is $104 \mu\text{A}$). The parameter x is the concentration of lithium in the carbonaceous electrode.

3 Graphitic Carbons

Graphitic carbon is now used as the anode material in lithium-ion batteries produced by Moli Energy (1990) Ltd., Matsushita, Sanyo and A+T battery. It is important to understand how the structures and properties of graphitic carbons affect the intercalation of lithium within them.

3.1 Turbostratic disorder and structure of graphitic carbons

Graphitic carbons are the most crystalline of the carbonaceous materials of the three regions in Fig. 2. During the last 40 years, the structure of graphitic carbons has been carefully studied by many scientists [2,15,21,22].

Graphitic carbons can be readily obtained from soft carbons, such as petroleum coke, by heating. When the heat treatment temperature is limited to about 1000°C , coke-type materials are formed. These carbonaceous materials have graphene layers of relatively small extent (about 10 to 40 \AA) which are stacked in a roughly parallel fashion, but with random rotations and translations between every pair of layers. This type of disorder has been given the name “turbostratic disorder” [23]. As the carbons are heated from 1000 to 2000°C , the lateral extent of the layers grows and the stacking becomes quite parallel as evidenced by a sharpening of the (002) Bragg peak. However, at 2000°C there is still complete turbostratic disorder. Upon heating above 2000°C , the turbostratic disorder is relieved in a more or less continuous way, the amount of remaining turbostratic disorder decreasing to zero monotonically by 3000°C .

Graphitic carbon normally refers to soft carbon heated above about 2100°C . The probability of finding turbostratic disorder begins to decrease as the heat-treatment temperature increases to above 2100°C . When the heating temperature reaches above 3000°C , graphite forms. Conceptually, graphite is a graphitic carbon with no or very little turbostratic disorder.

In graphitic carbon, the in-plane structure of graphene layers is almost the same as in graphite except the lateral extent of the layers increases with heat-treatment

temperature. However, the distance between layers (d_{002}), where the turbostratic disorder occurs, is slightly larger than that in graphite.

3.2 Effect of turbostratic disorder on the intercalation of lithium

Several types of graphitic carbon were used for the studies presented here. These samples are from four different sources. First, mesocarbon microbeads (MCMB) were obtained from Osaka Gas Ltd. This carbon sample had been heat treated to about 1000°C. Further heat-treatment was done at Moli. We used a Centorr (series 10) graphitizing furnace to further heat the carbons under flowing nitrogen to 2300°C, 2400°C, 2500°C, 2600°C, 2700°C and 2800°C. Each sample was treated for one hour at the final temperature. These samples were called MCMB2300 through MCMB2800, respectively. Second, a petroleum coke sample (type XP, from Conoco, Houston TX, USA) was heat treated to 2250°C and 2300°C in a similar manner. These samples were called Conoco2250 *etc.*. Finally, a commercially available graphite powder (JMI) from Johnson Matthey Inc., and a natural graphite powder (IMP) from Industrial Mineral Park Mining Corporation (Vancouver, BC) were studied. Powder X-ray diffraction showed that the IMP sample contains large amounts of impurities and was not suitable for structural studies.

The structure refinement program for disordered carbons, which was recently developed by Shi *et al* [14,15] is ideally suited to studies of the powder diffraction patterns of graphitic carbons. By performing a least squares fit between the measured diffraction pattern and a theoretical calculation, parameters of the model structure are optimized. For graphitic carbon, the structure is well described by the two-layer model which was carefully described in section 2.1.3.

Figure 6 shows the changes which occur in the diffraction patterns of the heated MCMB samples, and the excellent description of these patterns by the structure refinement program. The structural parameters, P , P_t , a , d_{002} , L_c and L_a for all the carbon samples are listed in Table 1 [6].

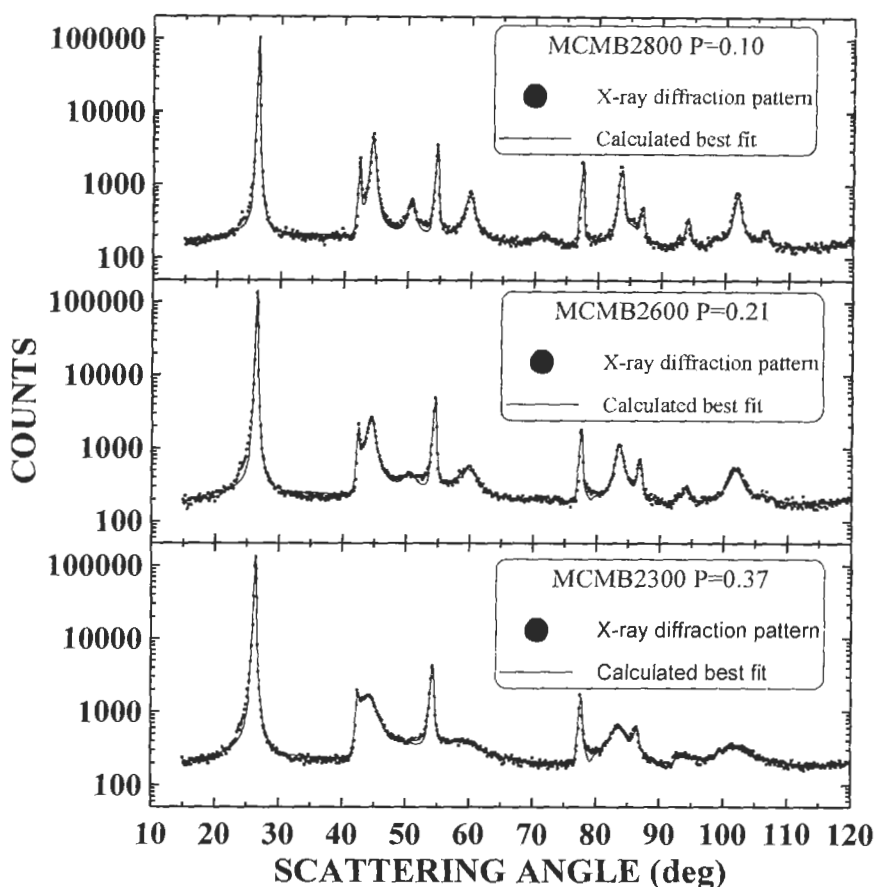


Fig. 6. The X-ray diffraction patterns and calculated best fits from the structure refinement program for the samples MCMB2300, MCMB2600 and MCMB2800.

P decreases as the heat-treatment temperature increases above 2200°C . The parameters which describe the size of the crystallite, L_c and L_a , also increase with the heat-treatment temperature. The capacity parameter x_{max} in Table 1 will be described and carefully discussed later in this chapter.

Two electrochemical coin-type cells were constructed for each of the graphitic carbons in Table 1. The cell construction and testing were described in section 2. All cells were tested in the same manner. The first cycle (discharge and charge) of the cells was made using a current which corresponds to a 50 hour rate. A passivating film formed during the first discharge [24,25] and created about 15-20% irreversible capacity. Once the growth of the passivating film

reaches completion, the irreversible reactions apparently stop. Therefore, all measurements were made on the second and third cycles of these cells.

Table 1. Structural parameters and capacity, x_{\max} , for the carbon samples studied.

Name	HTT(°C)	d_{002} (Å)	P	P_t	a(Å)	L_c (Å)	L_a (Å)	x_{\max}
Conoco2250	2250	3.382	0.42	0.03	2.457	340	294	0.579
Conoco2300	2300	3.376	0.37	0.04	2.457	350	320	0.645
MCMB2300	2300	3.369	0.37	0.04	2.456	440	310	0.657
MCMB2400	2400	3.363	0.29	0.06	2.456	490	310	0.684
MCMB2500	2500	3.359	0.24	0.07	2.456	550	330	0.729
MCMB2600	2600	3.358	0.21	0.07	2.456	560	350	0.788
MCMB2700	2700	3.357	0.17	0.06	2.457	610	360	0.814
MCMB2800	2800	3.352	0.10	0.04	2.457	670	420	0.859
JMI	?	3.356	0.05	0.04	2.460	380	330	0.924

Figure 7 shows voltage profiles, $V(x)$, for the second cycle of most of the graphitic carbon samples listed in Table 1. The curves have been sequentially offset by 0.1 V for clarity. Most striking is a reduction of the maximum reversible capacity, x_{\max} or Q_{\max} ($Q_{\max}=372 \cdot x_{\max}$), as P increases.

Figure 8 shows Q_{\max} , plotted versus P for all the carbons listed in Table 1 and for many others. There is a linear relationship between Q_{\max} and P which is well described by $Q_{\max}=372(1-P)$ mAh/g. This implies that little or no lithium is able to intercalate between randomly stacked parallel layers [2]. Therefore we call the space between these adjacent randomly stacked graphene layers, “blocked galleries”.

It is not surprising that it is difficult to insert lithium between parallel layers which are randomly stacked. When lithium intercalates between AB stacked layers, a shift to AA stacking occurs [26]. It is likely that the turbostratically stacked layers are pinned by defects (which can only be removed near 2300°C!) preventing the rotation or translation to AA stacking. Thus, we can understand why Q_{\max} varies as $372(1-P)$, the fraction of layers with AB registered stacking. More studies of the details of the voltage profiles in Fig. 7 can be found elsewhere [6,7,27].

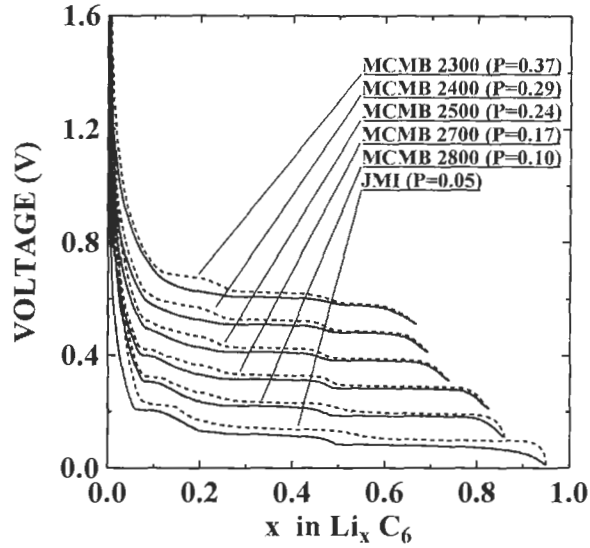


Fig. 7. The voltage profiles of the graphitic carbon samples as indicated. The curves have been shifted sequentially by 0.1 V for clarity. Solid lines are for discharge and dashed lines are for charge.

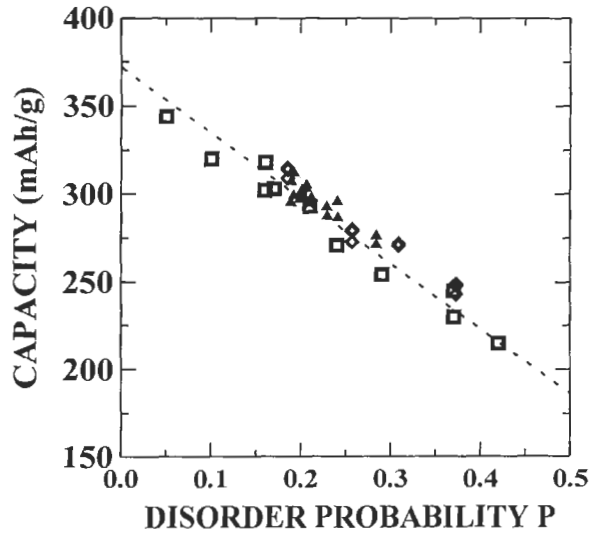


Fig. 8. Capacities versus P for graphitic carbons. \square included in Table 1 \diamond and Δ : other carbons not included in Table 1. The dashed line is a linear relationship described by $Q_{\max} = 372(1-P)$ mAh/g.

4. Hydrogen-Containing Carbons from Pyrolyzed Organic Precursors

A variety of materials have been pyrolysed at temperatures near 700°C which showed behavior similar to that in Fig. 2 for the CRO550 sample [28-30]. Yata *et al.* [28] and Mabuchi *et al.* [29] noticed that their carbons heated at these temperatures contained substantial hydrogen. However, they proposed that the large capacity and hysteresis was due to the storage of lithium in the pores of the materials. It was our idea that the hydrogen in these materials could be playing a crucial role. Therefore we synthesized several series of materials at different temperatures and studied them.

4.1. Preparation of carbonaceous materials heated at low temperatures

Petroleum pitch was obtained from Kureha Company, Japan (designated here as KS pitch). A second petroleum pitch was obtained from the Crowley Tar Company, U.S.A. (designated here as CRO pitch). Polyvinyl chloride (PVC) was obtained from the Aldrich Chemical Company (U.S.A.). These samples are all soft carbon precursors.

Oxychem phenolic resin (OXY) was supplied in powder form from Occidental Chemical Corp. (NY, USA). The powders were cured at 150 to 160°C for about 30 minutes in air to produce a solid lump. Epoxy novolac resin #DEN438 (poly[(phenyl glycidyl ether)-coformaldehyde]) was obtained from Dow Chemical Corporation (Midland, Michigan, U.S.A.). We used phthalic anhydride (Aldrich) as a curing agent to harden the epoxy samples prior to pyrolysis. Typically, between 15% and 30% curing agent by weight was added to the epoxy and mixed at 120°C. The samples were hardened by curing overnight at 120°C. We will call these samples ENR here. These samples are hard carbon precursors. These samples were all reduced to powder before pyrolysis.

Pyrolysis was performed in tube furnaces equipped with quartz or stainless steel tubes. The tubes were fitted with end caps through which argon could flow. Typically, about 10 grams of the precursor was placed in an alumina boat and inserted into the furnace tube. Argon was flushed through the tube for at least one hour to remove all air from the reaction tube. The samples were then heated at a rate of 16°C/min to the pyrolysis temperature which was maintained for one hour. An argon flow of 2 cc/sec was used during the pyrolysis. The samples were then cooled to room temperature under argon and weighed. The product yield is the ratio of the sample mass before pyrolysis to the mass obtained after the heating. All samples made were coded according to the starting material and pyrolysis temperature. For example, KS700 designates KS pitch

Table 2. Summary of the samples studied.

Sample	Heating temp (°C)	Weight Percentages (%)			H/C Atomic Ratio (± 0.03)	Yield (%)	BET surface area (m^2/g)	L_n (Å) (± 1)	(002) FWHM (deg.) (± 0.2)	Rev. Cap.* (mAh/g) (± 20)	Irrev. Cap. (mAh/g) (± 20)	Cap. Of one volt plateau* (mAh/g) (± 20)
		C	H	N								
CRO550	550	93.5	3.2	0.2	0.41	49		20	3.6	880	450	570
CRO700	700	93.3	1.8	0.3	0.23	46	4.2 \pm 0.2	20	5.2	810	140	560
CRO800	800	95.1	1.3	0.3	0.16	45		27	4.9	590	180	350
CRO900	900	96.4	0.7	0.6	0.09	46		29	4.8	440	130	200
CRO1000	1000	95.5	0.3	0.5	0.04	45	4.5 \pm 0.2	33	4.3	340	100	100
KS550	550	95.1	3.2	<0.1	0.40	90		18	3.4	850	390	600
KS700	700	95.7	1.7	0.6	0.21	88	7.6 \pm 0.5	23	5.2	760	250	500
KS800	800	95.4	1.4	0.4	0.17	88		27	5.2	580	80	340
KS900	900	97.1	1.0	0.2	0.12	87		29	5.5	450	120	200
KS1000	1000	98.0	0.5	<0.1	0.06	86	7.9 \pm 0.5	33	5.2	350	60	120

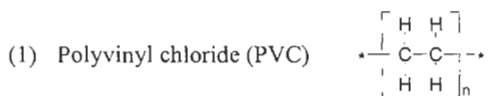
Sample	Heating temp. (°C)	Weight Percentages (%)			H/C Atomic Ratio (± 0.03)	Yield (%)	BET surfacc area (m^2/g)	L_a (Å) (± 1)	(002) FWHM (deg.) (± 0.2)	Rev. Cap.* (mAh/g) (± 20)	Irrev. Cap. (mAh/g) (± 20)	Cap. Of one volt plateau* (mAh/g) (± 20)
		C	H	N								
PVC550	550	93.9	2.8	0.6	0.36	10		20	4.0	940	340	670
PVC700	700	94.6	1.6	0.7	0.20	10	24 \pm 1	19	3.9	770	160	500
PVC800	800	96.7	1.1	0.2	0.14	9		29	4.5	560	80	320
PVC900	900	97.9	0.7	0.4	0.09	9		29	4.8	400	70	170
PVC1000	1000	97.9	0.4	<0.1	0.05	8	25 \pm 1	37	3.9	340	80	110
OXY700	700	94.7	1.8	0.4	0.22	58	250 \pm 10	27	9.5	630	260	400
OXY800	800	95.8	0.9	0.7	0.11	57		29	8.5	540	210	230
OXY900	900	94.8	0.5	0.5	0.06	57		30	9.0	410	300	100
OXY1000	1000	97.4	0.4	1.4	0.05	56	240 \pm 10	32	9.0	540	200	80
ENR800	800	91.7	0.9	<0.1	0.12	27		29	9.0	610	230	280
ENR900	900	93.4	0.5	<0.1	0.06	26		31	8.5	590	170	190
ENR1000	1000	93.1	0.2	0.6	0.03	26	220 \pm 10	31	9.0	570	150	150

Sample	Heating temp. (°C)	Weight Percentages (%)			H/C Atomic Ratio (±0.03)	Yield (%)	BET surface area (m ² /g)	L _a (Å) (± 1)	(002) FWHM (deg.) (±0.2)	Reversible Capacity* (mAh/g) (±20)	Irrev. Cap. (mAh/g) (±20)	Capa. Of One volt Plateau* (mah/g) (±20)
		C	H	N								
SUG600	600	92.5	2.3	0.1	0.30				760	380	540	
SUG700	700	93.8	1.4	0.2	0.18				720	270	430	
SUG800	800	95.2	0.9	0.3	0.11				620	200	300	
SUG900	900	95.5	0.6	0.4	0.07				570	180	190	
SUG1000	1000	97.0	0.5	0.7	0.06				530	130	130	
ASUG600	600	92.9	2.4	0.2	0.31				690	490	470	
ASUG700	700	91.4	1.5	0.3	0.20				580	380	330	
ASUG800	800	94.3	0.9	0.3	0.12				570	220	260	
ASUG900	900	95.4	0.5	0.4	0.06				600	190	170	
ASUG1000	1000	97.0	0.5	0.4	0.06				560	150	120	

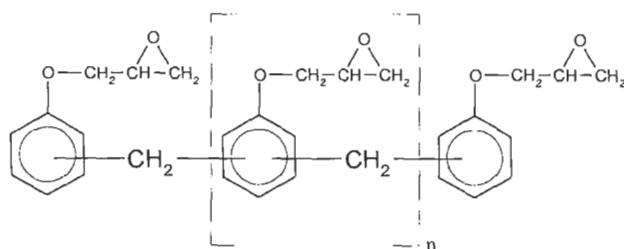
*obtained from the second cycles of voltage-capacity profiles.

pyrolyzed at 700°C, and ENR900 denotes epoxy novolac resin treated at 900°C. Table 2 lists the samples produced, and Table 3 shows the chemical structures for some of the precursors. In addition, hard carbon samples made from sugar (SUG) and sulfuric acid-washed sugar (ASUG) are also included in Table 2 [31].

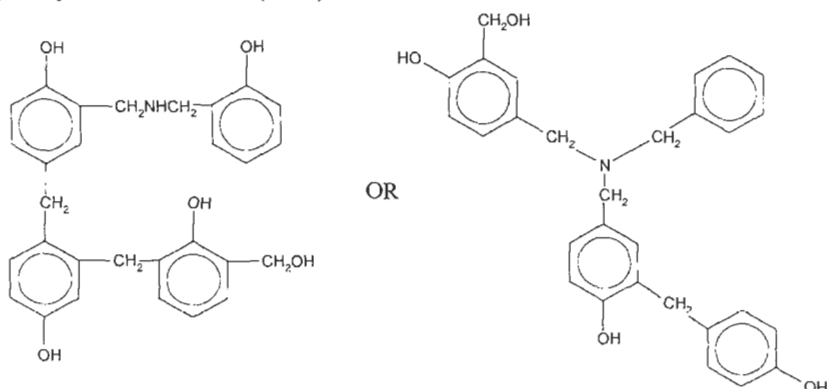
Table 3. Some precursors used



- (2) Epoxy Novolac Resin (ENR)
Poly[(phenyl glycidyl ether)-co-formaldehyde]
DEN438 has average $n=1.8$



- (3) Oxychem 29217 Resin (OXY)



4.2 Structure and properties

4.2.1 Results of CHN test and BET measurement

The results of the CHN Test are listed in Table 2. The quoted accuracy of the CHN test is $\pm 0.3\%$ by weight. The hydrogen to carbon atomic ratio was

estimated by taking the ratio of the hydrogen to carbon weight percentages and multiplying by 12. When precursors are pyrolyzed around 700°C, heteroatoms like oxygen and nitrogen are mostly lost but aromatic hydrogen is predominately left [32]. This is consistent with the results of the CHN test [33]. The aromatic hydrogen is eliminated continuously in carbonaceous materials as the temperature increases above 700°C

The single-point BET surface area measurement was used to check for open pores. The results for some soft and hard carbon samples heated at 700°C and 1000°C are presented in Table 2 for comparison. The hard carbon samples studied here have about ten times more open porosity than the soft carbons.

4.2.2 Structure and composition of most low-temperature heated samples

Figures 9 through Fig. 12 show the (002) Bragg peak region of some carbon samples studied. These figures give qualitative guidance about the differences between the samples. The lateral extent of the graphene sheets (L_a) was estimated from the (100) Bragg peak using the Scherrer equation, (refer to eq. 7 in section 2). The values of L_a for our samples are listed in Table 2. We did not use the structure refinement program for graphitic carbons for analysis of these very disordered materials. The (002) Bragg peak cannot be simply used to predict L_c for these highly disordered carbons [34]. This is because some of the samples made from hard carbon precursors have significant fractions of single graphene layers, which do not contribute to a peak in the (002) position, but add significantly to the background level (the structure of hard carbon will be carefully discussed in section 5). We have chosen therefore to simply report the (002) peak full width at half maximum, measured after subtraction of a linear background. This still allows the trends in the samples to be quantified (see Table 2).

The CRO pitch sample (Fig. 9) and the PVC samples (Fig. 10) show well formed (002) peaks which first broaden, and then sharpen, as the heating temperature is increased. The KS pitch sample shows a very similar result. Diamond [35] noticed this effect in his work on carbonization of coals. Figures 9 and 10 show that the width and position of the (002) peaks do not change dramatically upon heating in this temperature range for the pitch and PVC samples. These peak widths are consistent with stacks of order 5 to 7 layers according to the Scherrer equation assuming $d_{(002)}$ is about 3.5Å.

The OXY (Fig. 11), and ENR (Fig. 12) samples have very weak (002) peaks with widths which are almost twice those of the pitch and PVC samples. This

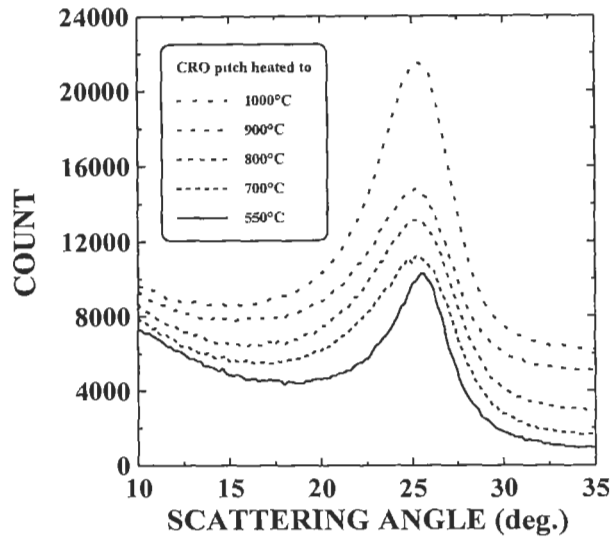


Fig. 9. Powder X-ray diffraction pattern for the (002) peak of CRO pitch samples as indicated. The data sets have been offset sequentially by 0, 500, 2000, 4400 and 5400 counts for clarity

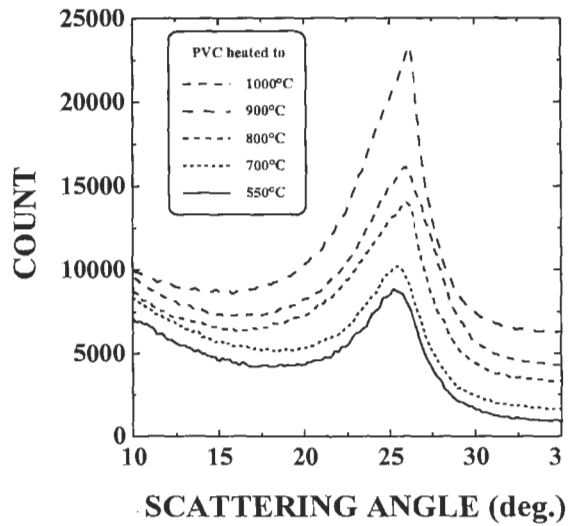


Fig. 10. Powder X-ray diffraction pattern for the (002) peak of samples made from PVC as indicated. The data sets have been offset sequentially by 0, 600, 2500, 3500 and 5500 counts for clarity.

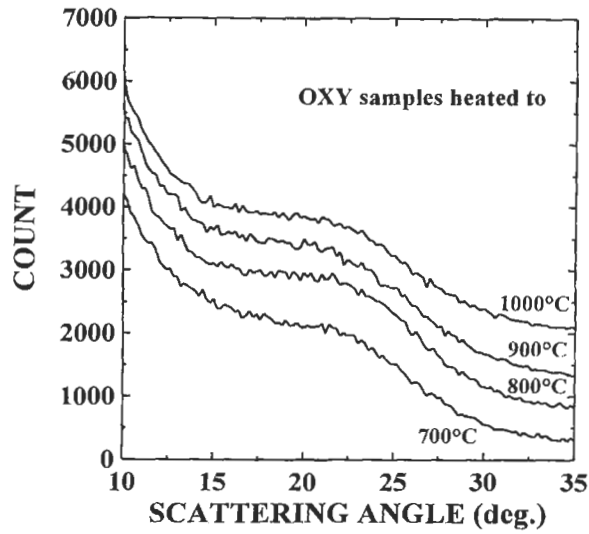


Fig. 11. Powder X-ray diffraction pattern for the (002) peak of samples made from Phenolic resin (OXY) as indicated. The data sets have been offset sequentially by 0, 500, 1000 and 1900 counts for clarity.

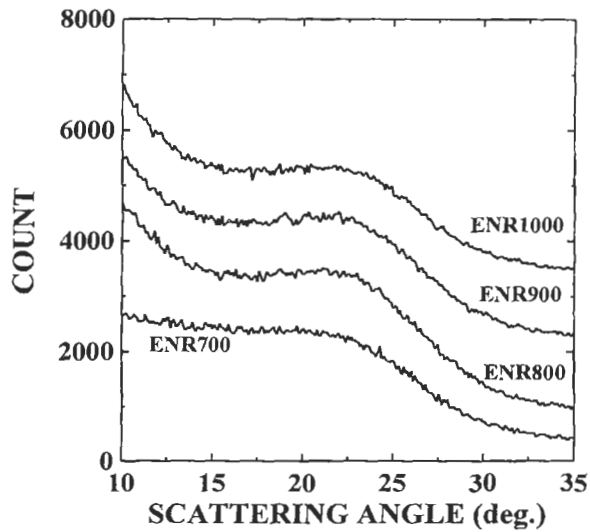


Fig. 12. Powder X-ray diffraction pattern for the 002 peak of samples made from epoxy novolac resin (ENR) as indicated. The data sets have been offset sequentially by 0, 500, 1900 and 3200 counts for clarity.

indicates that the samples contain significant fractions of single layer graphene sheets, which are stacked more or less like a “house of cards”, containing significant microporosity. Again, the (002) peak of these materials changes little as the temperature is increased. Figure 13 shows the (100) and (004) peak regions for samples made from each precursor heated to 1000 °C. The CRO1000, KS1000 and PVC1000 samples show some evidence for an (004) peak near 52° while the other samples do not. This is consistent with the behavior of the (002) peak for these samples. The (100) peaks do not differ greatly, indicating lateral layer extents of order 18 to 37Å for all samples (see Table 2).

Structurally, the materials are grouped into two main classes, those (soft carbons) with predominantly stacked layers (CRO, KS and PVC) and those (hard carbons) which have significant amounts of single layer sheets (OXY and ENR). All the samples show similar values of L_a when heated to a given temperature.

Figure 14 shows the SAXS measurements on the soft carbon samples CRO700 and CRO1000, and on the hard carbon samples OXY700 and OXY1000. All these samples were measured under the same conditions with about the same sample mass. Based on Guinier’s formula, materials with large pores have small angle scattering intensities which fall off rapidly with k or with scattering angle, while those with small pores show a slower decline. Materials with significant porosity have higher SAXS intensities, while those with less porosity show lower intensities.

Figure 14 shows that the hard carbons OXY700 and OXY1000 show evidence for significant microporosity, while the CRO700 and CRO1000 samples contain substantially less microporosity. The high counts at very low angle ($< 1.5^\circ$) in Fig. 14 are from larger pores which are typically larger than 30Å. We found that the hard carbon samples all have significant microporosity, but that the soft carbon samples do not. This result is consistent with the results of powder X-ray diffraction.

In Table 2, the H/C atomic ratio decreases monotonically for each of the samples as they are heated and all the samples approach pure carbon as the heating temperature is increased. Figure 15 shows the H/C atomic ratio plotted versus heat-treatment temperature for most samples in Table 2. Table 2 also gives the product yield for all the samples as a percentage of the starting weight of the precursor. The yields from the CRO, KS and OXY series are large, presumably because these precursors have large aromatic content and less heteroatoms. ENR shows intermediate behavior; it has less aromatic content and more heteroatoms. PVC shows the lowest yield of all presumably because it has no initial aromatic content.

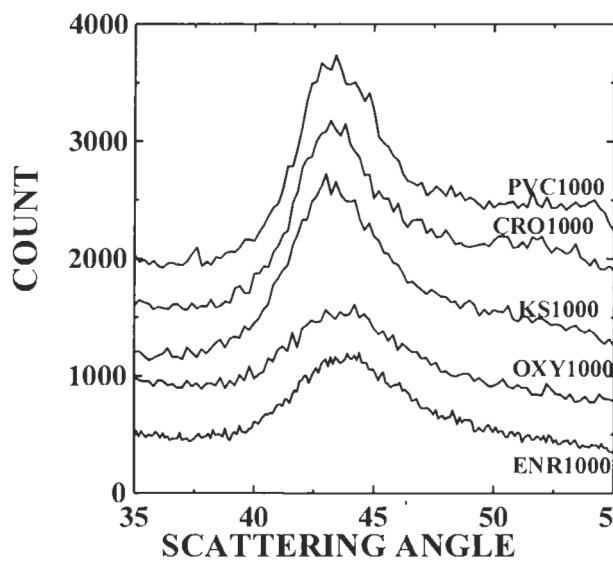


Fig. 13. Powder X-ray diffraction pattern for the (100) peak of all samples made at 1000°C as indicated. The data sets have been offset sequentially by 0, 400, 500, and 1200 counts for clarity.

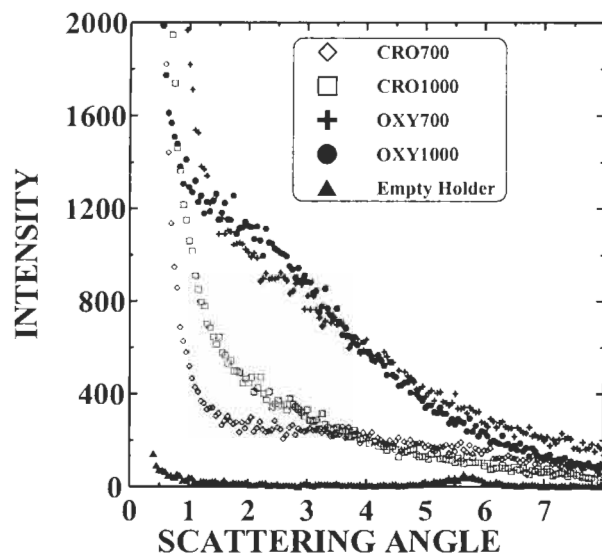


Fig. 14. The small angle scattering intensity versus scattering angle for samples CRO700, CRO1000, OXY700 and OXY1000.

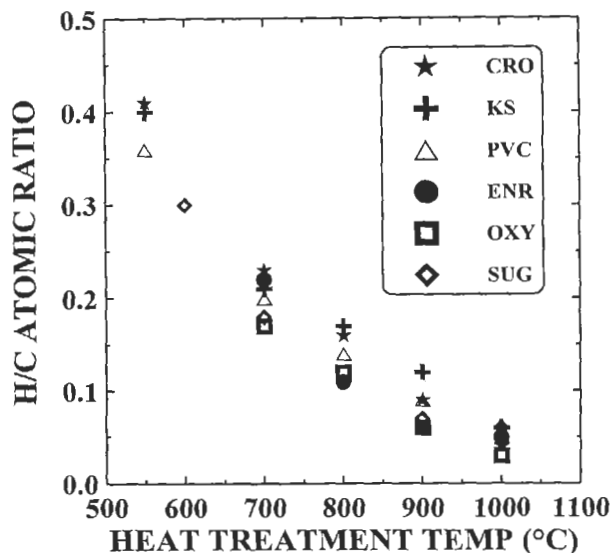


Fig. 15. The H/C atomic ratio versus heat-treatment temperature for samples as indicated

Figure 16 shows the second discharge and charge of cells using electrodes made from the CRO pitch. The CRO550 and CRO700 samples have first charge capacities of about 900 mAh/g. There is a large hysteresis between discharge and charge, of about one volt. As the samples are heated to 800°C and above, the reversible capacity is reduced dramatically. The majority of the capacity reduction is due to a shortening of the low voltage (near zero volts) plateau during discharge and the one volt plateau during charge. That is, the portion of the voltage profile which displays hysteresis and is responsible for the large capacity, is removed as the samples are heated above 700°C. The irreversible capacity during the first cycle (which is not shown here) is taken as the difference between the capacity of the insertion reaction measured during discharge and charge. Table 2 shows that the irreversible capacities for these samples are relatively small in comparison to the reversible capacity.

It is difficult to attribute the capacity reduction which occurs above 700°C to structural effects because the structure of the samples is not changed significantly, as indicated by our X-ray diffraction measurements on the CRO samples. On the other hand, the hydrogen content of the samples is dramatically reduced over this temperature range. To investigate the importance of the hydrogen content, we made a series of cells from the other samples.

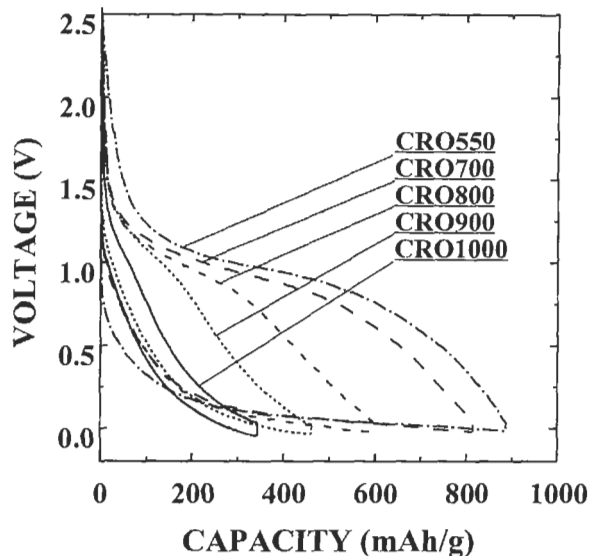


Fig. 16. Voltage versus capacity for the second cycle of the CRO pitch heated at different temperatures as indicated.

Figures 17 and 18 show the second cycles for the KS pitch samples and the PVC samples respectively. These materials show a trend with heating temperature which is almost identical to the CRO pitch samples. Again, the large capacity and hysteresis in the voltage profiles are eliminated as the samples are heated above 700°C, even though little structural change to the samples occurs. On the other hand, the hydrogen content of the samples drops dramatically over this temperature range. The OXY and ENR samples (hard carbons) show behavior similar to the CRO, KS and PVC samples (soft carbons) when their H/C ratio is large, but strikingly different behavior upon heating above 800°C.

Figures 19 and 20 show the second cycles for the OXY samples and the ENR samples respectively. The results for the OXY1000, ENR900 and ENR1000 samples are more striking. These samples will be discussed in section 5. Figures 19 and 20 show a long low voltage plateau on both discharge and charge caused by a reversible insertion process. These two Figs also show how the voltage profile changes with heating temperature. At 700°C, where the H/C ratio is large, the hard carbon samples show basically an identical capacity and voltage profile to the soft carbon samples, even though these materials have very different structures. However, after further heating, the hard carbon samples evolve into high capacity, low hysteresis materials. We believe that when substantial hydrogen is present it dominates the reaction with lithium. But, when the hydrogen is removed the structural differences between the samples play an important role.

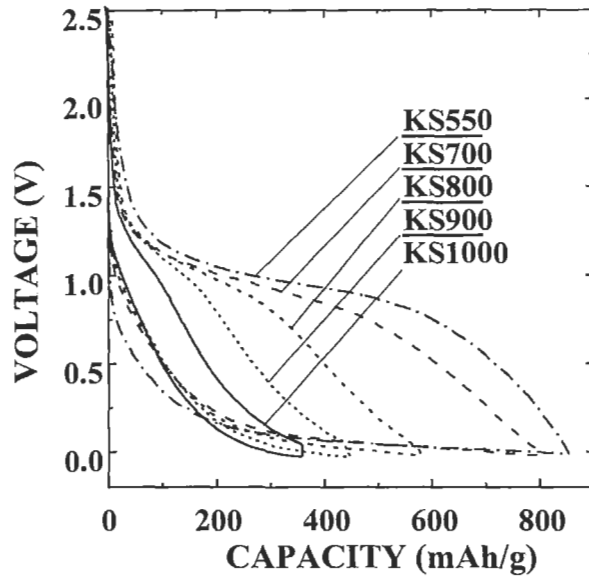


Fig. 17. Voltage versus capacity for the second cycle of the KS pitch samples heated at different temperatures as indicated.

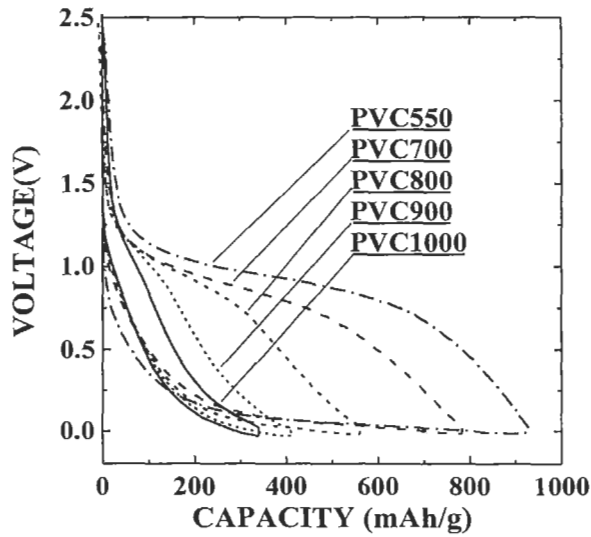


Fig. 18. Voltage versus capacity for the second cycle of the samples made from PVC heated at different temperatures as indicated.

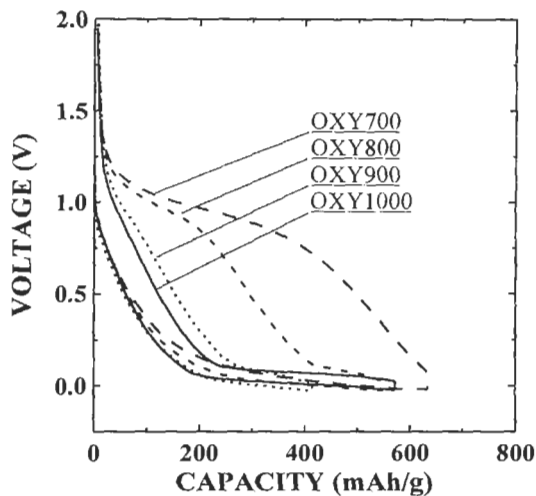


Fig. 19. Voltage versus capacity for the second cycle of the samples made from OXY resin heated at different temperatures as indicated.

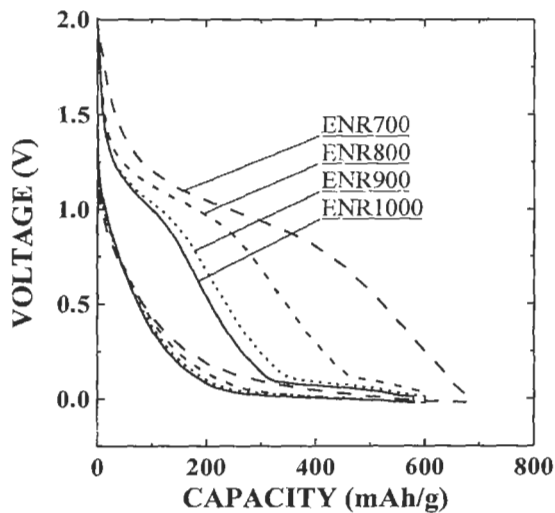


Fig. 20. Voltage-capacity profiles for the second cycles of lithium/carbon cells made from ENR resin heated at different temperatures as indicated.

4.3 Effect of hydrogen on the insertion of lithium

Figure 21 compares the voltage-capacity profiles for the second cycle of lithium/carbon electrochemical cells made from OXY, a representative hard carbon, and those for samples made from CRO, a representative soft carbon.

Significantly, there was a shortening of the one volt plateau during charge as the samples are heated above 700°C for both the soft and hard carbons. That is, the portion of the voltage profile which displays hysteresis is removed as the samples are heated above 700°C. The capacity of the one volt plateau (taken between 0.7 volts and 1.5 volts for all samples) is well correlated to the hydrogen to carbon atomic ratio of the samples as shown in Fig. 22. Changing the voltage limits of the one volt plateau to other values (e.g. 0.5 volts and 1.5 volts) does not significantly affect the correlation in Fig. 22. The solid line in Fig. 22 is expected if each lithium atom can bind near a hydrogen atom in the host and if a hydrogen-free carbon heated to higher than 1000°C does not have a one volt plateau. Mabuchi et al.'s data [29] have also been included and fit the trend well. The hydrogen contained in carbonaceous materials heated at low temperatures (below 800°C) is clearly important.

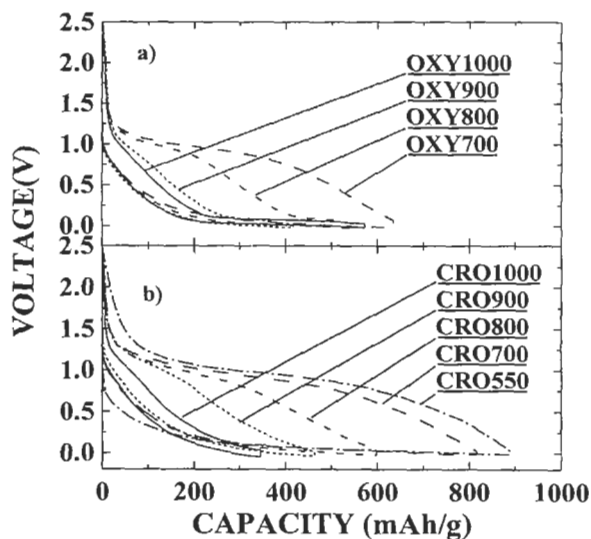


Fig. 21. Voltage-capacity profiles for the second cycles of lithium/carbon cells made from a) OXY resin and b) CRO pitch heated at different temperatures as indicated.

Hydrogen can affect lithium insertion in carbons. As an example, charge transfer from alkalis to hydrogen in carbons has been observed in ternary graphite-alkali-hydrogen materials [36]. In our hydrogen-containing samples, it is believed that the lithium atoms may bind on hydrogen-terminated edges of hexagonal carbon fragments, with local geometries analogous to the organolithium molecule $C_2H_2Li_2$ [37]. If this is true, then the capacity for the

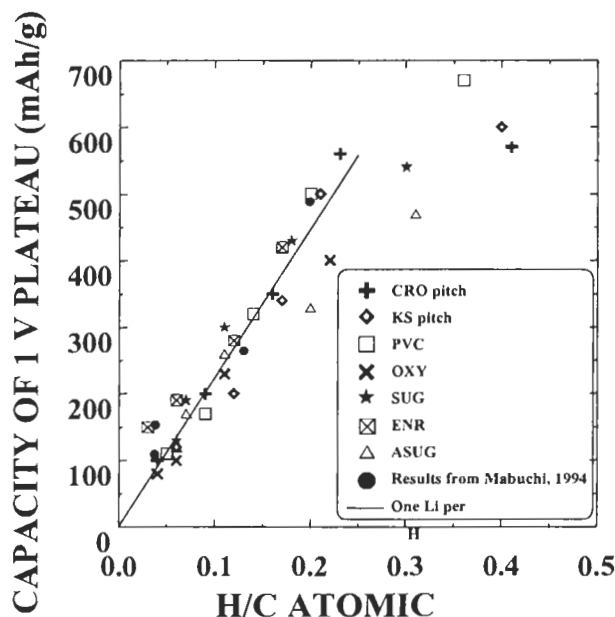


Fig. 22. The capacity of the one volt plateau measured during the second cycle of several series of samples versus the H/C atomic ratio in the samples. The solid line suggests that each lithium atom binds quasi-reversibly to one hydrogen atom.

insertion of lithium should strongly depend on the hydrogen content of the carbon materials as has been experimentally shown above. If the inserted lithium binds to a carbon atom which also binds a hydrogen atom, a corresponding change to the carbon-carbon bond from sp^2 to sp^3 occurs [37]. That is, the insertion and removal of the lithium atoms in carbons involves changes to the bonding in the host as shown schematically in Fig. 23 (obtained from reference 37). Bonding changes in the host have been previously shown to cause hysteresis in such electrochemical measurements. For example, hysteresis in lithium electrochemical cells was observed when Mo-S bonds in $LiMoS_2$ were broken due to the formation of Li-S bonds upon further insertion of lithium [38].

We do not believe that oxygen and nitrogen in the samples are important. When any precursor is heated near $700^\circ C$, the heteroatoms like oxygen and nitrogen are predominantly eliminated. Here we also point out that PVC contains no nitrogen or oxygen, nor does its pyrolyzed product. Since pyrolyzed PVC shows the same behavior in Fig. 22 as the other samples, we believe the effects of oxygen and nitrogen in these materials to be negligible. The presence of hydrogen is the only common factor in all these samples with a variety of microstructures prepared from a variety of precursors.

Although the hydrogen-containing carbons show higher capacities, they all display a large hysteresis with lithium insertion in these carbons near zero volts and removal at one volt. The hysteresis will affect the efficiency of a real lithium-ion cell during charge and discharge. For example, the cell may charge at four volts and discharge at three volts. The origin of the hysteresis has been explained in ref. 10 and will not be discussed here.

The cycle life of the hydrogen-containing samples also appears to be limited as shown in ref. 8. This is unacceptable for a practical application. The capacity loss is mostly due to the elimination of the excess capacity which exhibits hysteresis. Since this portion of the capacity appears related to the incorporated hydrogen, its elimination with cycling may not be unexpected. We do not understand this point fully yet, and further work would appear to be warranted.

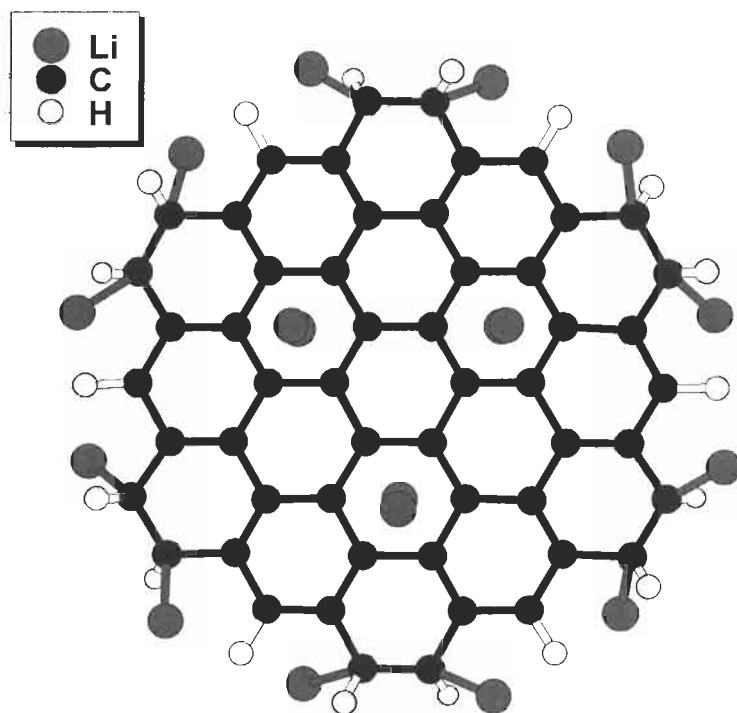


Fig. 23. When lithium inserts in hydrogen-containing carbon, some lithium atoms bind on the hydrogen-terminated edges of hexagonal carbon fragments. This causes a change from sp^2 to sp^3 bonding [37].

5 Microporous Carbons from Pyrolyzed Hard-Carbon Precursors

There have been a number of reports of carbons with voltage profiles similar to that of the region 3 material, microporous hard carbon, shown in Fig. 2. Omaru *et al.* [39], using pyrolyzed polyfurfuryl alcohol, Takahashi *et al.* [40], using unspecified precursors, Sonobe *et al.* [41], using pyrolyzed petroleum pitch and Liu *et al.* [12] using pyrolyzed epoxy novolac resin, have all prepared materials that show a low voltage plateau with a capacity of several hundred mAh/g, and little hysteresis. We believe that lithium can be adsorbed onto internal surfaces of nanopores formed by single, bi, and trilayer graphene sheets which are arranged like a “house of cards” [8,11,12] in the hard carbons (schematically shown in Fig. 24). Such hard carbons show promise for lithium-ion battery applications [8,11,12,39,40,40].

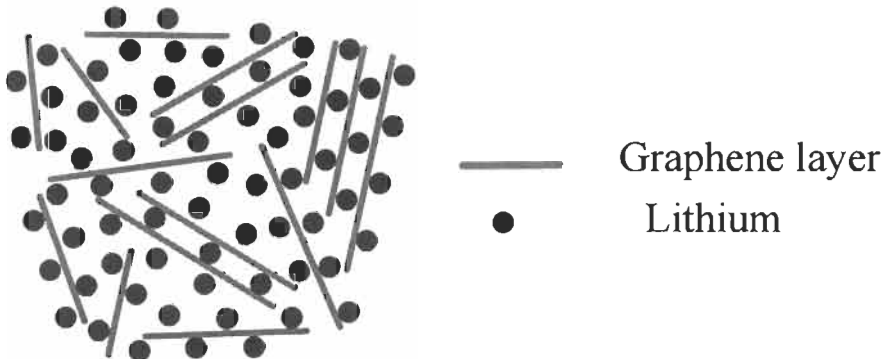


Fig. 24. Adsorption of lithium on the internal surfaces of micropores formed by single, bi, and trilayers of graphene sheets in hard carbon.

In lithium-ion battery applications, it is important to reduce the cost of electrode materials as much as possible. In this section, we will discuss hard carbons with high capacity for lithium, prepared from phenolic resins. It is also our goal, to collect further evidence supporting the model in Fig. 24.

5.1 Preparation of microporous carbons and their electrochemical testing

A hard carbon with high capacity can be made from epoxy novolac resin [12]. The epoxy resins used cost about US\$2.50 per pound and give pyrolysis yields between 20 and 30%. However, it is well known that phenolic (or phenol-formaldehyde) resins can be pyrolyzed to give hard carbons with a yield of over 50% [42]. In addition, these resins cost about US\$1.00 per pound. Phenolic resins therefore offer significant cost advantages over epoxy resins, so we

undertook a study of the electrochemical characteristics of hard carbons prepared by pyrolyzing both acid (novolac) and base-catalyzed (resole) phenolic resins [11]. The samples are described in Table 4.

Two electrochemical lithium/carbon cells were made for each of the pyrolyzed materials. We used currents of 18.5 mA/g (20-hour rate) for the first three charge-discharge cycles and 37 mA/g (10-hour rate) for the extended cycling test.

Table 4. Summary of the samples produced.

Sample	Heating temp (°C)	Weight			H/C Atomic Ratio (±0.03)	Yield (%) (± 2%)	Rev. Capacity (mAh/g) (±20)	Irrev. Capacity (mAh/g) (±20)
		Percentages						
		C	H	N				
Ar700	700	91.2	1.5	1.2	0.19	57	550	440
Ar800	800	93.1	1.0	1.3	0.13	55	510	280
Ar900	900	92.3	0.6	1.2	0.07	55	510	210
Ar1000	1000	94.2	0.4	1.9	0.05	54	450	160
Ar1100	1100	96.7	0.3	0.8	0.04	52	330	70
Br700	700	94.7	1.8	0.4	0.22	58	630	260
Br800	800	95.8	0.9	0.7	0.11	57	540	210
Br900	900	94.8	0.5	0.5	0.06	57	410	300
Br1000	1000	95.6	0.3	0.6	0.04	56	540	200
Br1100	1100	97.4	0.4	1.4	0.05	56	340	110
Cr800	800	95.7	0.9	0.6	0.11	64	530	210
Cr900	900	95.1	0.4	0.7	0.05	57	450	180
Cr1000	1000	96.5	0.3	0.8	0.04	58	450	130
Cr1100	1100	97.0	0.3	1.3	0.03	56	330	120
Arv1000	1000					58	520	270
Brv1000	1000					55	550	250
Crv1000	1000					57	550	220

Figure 25 shows the second cycle for the Br-series carbonaceous materials. The voltage profiles of the Ar and Cr-series samples were similar to those of the Br-

series samples [11,43]. The reversible capacity from the second cycle and irreversible capacities from the first cycle for all the samples are given in Table 4.

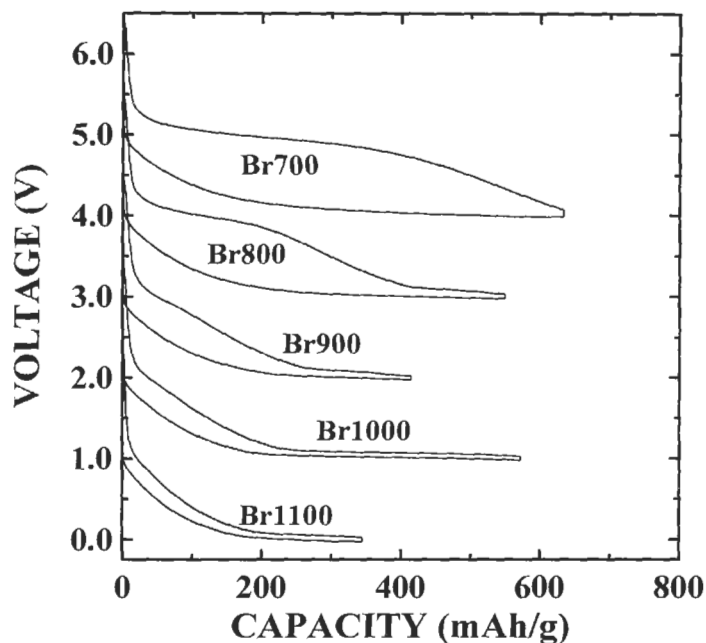


Fig. 25. Voltage versus capacity for the second discharge and charge of cells with lithium anodes and with cathodes made of Br-series samples. The curves have been sequentially offset for clarity. The shifts are: Br700, 4.0V; Br800, 3.0V; Br900, 2.0V; Br1000, 1.0V, and Br1100, 0.0V.

All samples heated at 700 and 800°C show significant hysteresis; that is, lithium is inserted in the materials near zero volts and removed at about one volt. We have shown that the amount of lithium which can be inserted in 700°C materials is directly proportional to their hydrogen (H) content. Table 4 shows that materials heated to 700 and 800°C retain substantial hydrogen. Upon heating to 900°C, the hydrogen is predominantly eliminated and so is the hysteresis. The samples then show substantial recharge capacity at low voltages.

The cell made from Br1000 appears most promising. Its reversible capacity is about 540 mAh/g and it has a long low voltage plateau. Similar results were found for the second cycles of samples made from Ar and Cr resins, except that the capacities were smaller.

The cycling behavior of sample Br1000 was tested. Figure 26 shows the capacity versus cycle number for one Br1000 cell. This cell was cycled with a current corresponding to 37 mA/g (10-hour rate) after the first three cycles.

There is little capacity loss upon cycling, and the materials show adequate rate capability.

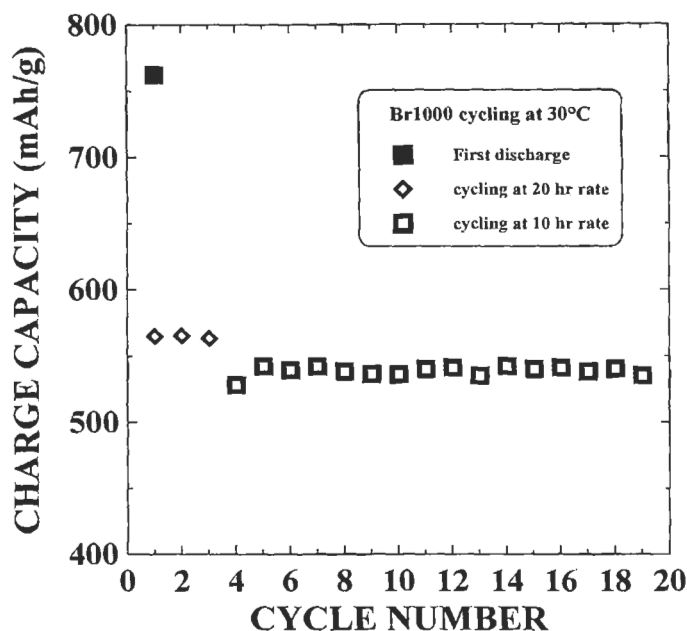


Fig. 26. Capacity versus cycle number for a cell containing Br1000 as the electrode material. The test was made at 30°C.

5.2 Sample Microporosity

Powder X-ray diffraction and SAXS were employed here to explore the microstructure of hard carbon samples with high capacities. Powder X-ray diffraction measurements were made on all the samples listed in Table 4. We concentrate here on sample Br1000, shown in Fig. 27. A weak and broad (002) Bragg peak (near 22°) is observed. Well formed (100) (at about 43.3°) and (110) (near 80°) peaks are also seen. The sample is predominantly made up of graphene sheets with a lateral extension of about 20-30Å (referring to Table 2, applying the Scherrer equation to the (100) peaks). These layers are not stacked in a parallel fashion, and therefore, there must be small pores or voids between them. We used SAXS to probe these pores.

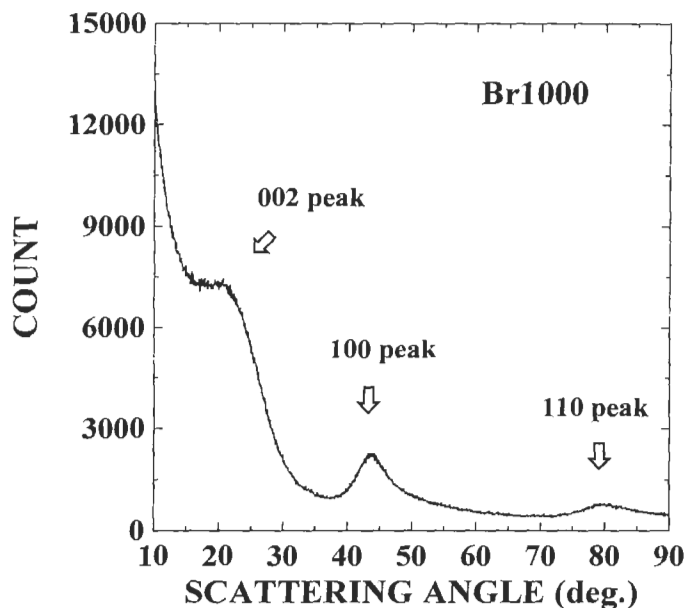


Fig. 27. Powder X-ray diffraction profile of the Br1000 sample.

Figure 28a shows the result of SAXS on sample Br1000. We used Guinier's formula (see eq. 6) for the small angle scattering intensity, $I(k)$, from randomly located voids with radius of gyration, R_g . Although Guinier's equation assumes a random distribution of pores with a homogeneous pore size, it fits our experimental data well. The slope of the solid line in Fig. 28b gives $R_g = 5.5 \text{ \AA}$ and this value has been used for the calculated curve in Fig. 28a. This suggests a relatively narrow pore-size distribution with an equivalent spherical pore diameter of about 14 \AA . Similar results were found for the other heated resin samples, except that the mean pore diameter changed from about 12 \AA for samples made at 700°C to about 15 \AA for samples made at 1100°C .

From Figs 27 and 28, we see a correlation between weak and broad X-ray (002) peak and large microporosity in the hard carbon samples. In our previous work [12], we showed that the amount of single graphene layers in hard carbon samples can be quantified by the empirical parameter, R , of the X-ray (002) peak. Figure 29 shows how we measure the parameter, R , defined to be the ratio of the peak count rate at the (002) peak divided by the background level (estimated by linear extrapolation) at the same angle. We now show the meaning and importance of R .

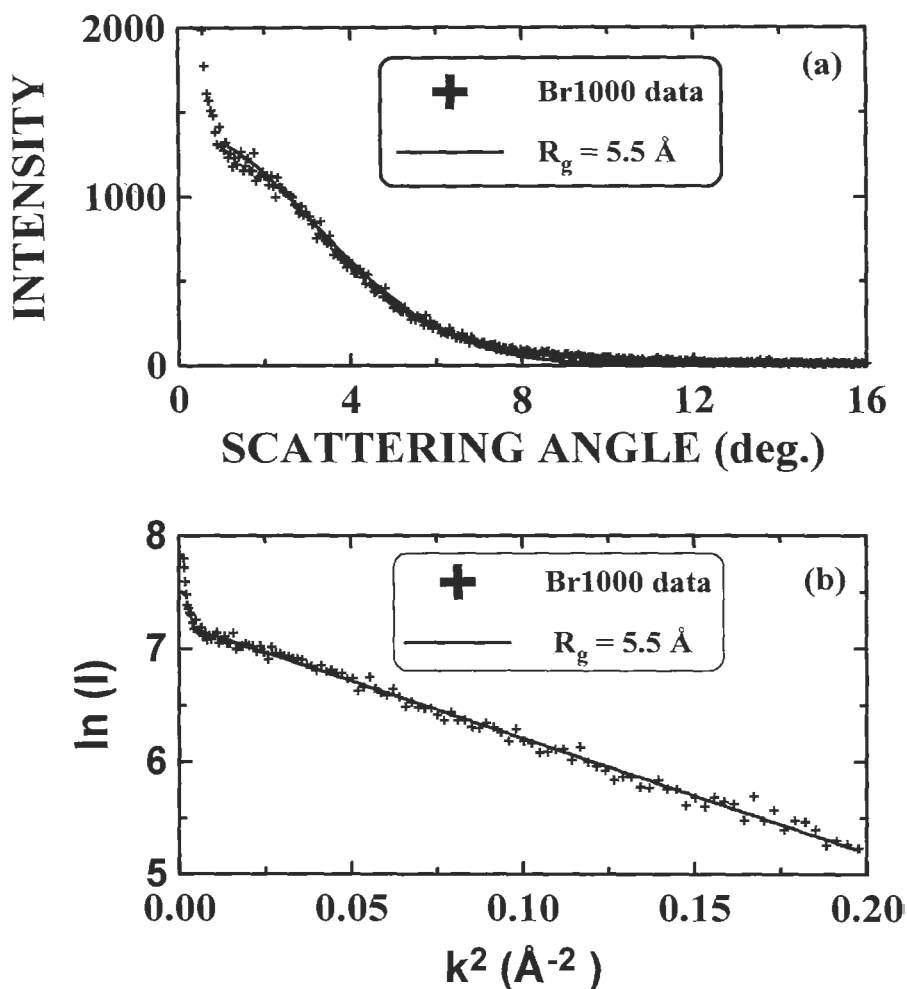


Fig. 28. (a) Small angle scattering intensity versus scattering angle for Br1000. The solid line is a fit using equation (6) with $R_g = 5.5 \text{ \AA}$. (b) Natural log of the scattered intensity versus k^2 . The straight-line fit allows R_g to be extracted from eq. (6). The large intensity at very small k is caused by the scattering from macropores or mesopores in the sample

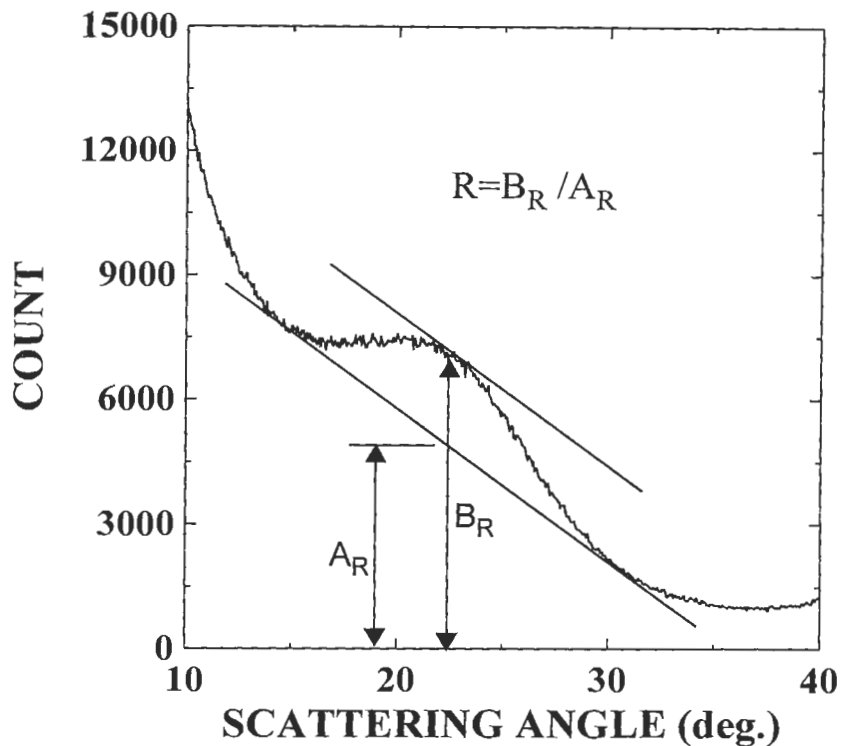


Fig. 29. Schematic graph showing the definition of the parameter, R , used to empirically estimate the fraction of single graphene layers in hard carbon samples.

Figure 30 shows a series of calculated patterns for carbon samples with a fraction, f , of carbon atoms in randomly oriented single layers, a fraction $2/3(1-f)$ in bilayers and a fraction $1/3(1-f)$ in trilayers [12]. These curves can be used to estimate the dependence of the ratio, R , defined by Fig. 29, on the single layer fraction. Figure 31 shows the dependence of R on single layer fraction for the calculated patterns in Fig. 30, and for another set of calculated patterns (not shown) where the fraction of carbon atoms in bilayers and trilayers was taken to be $1/2(1-f)$ [12]. Both curves in Fig. 31 clearly show that R decreases as the single layer content of the sample increases and is fairly insensitive to how the carbon is distributed in bilayers and trilayers.

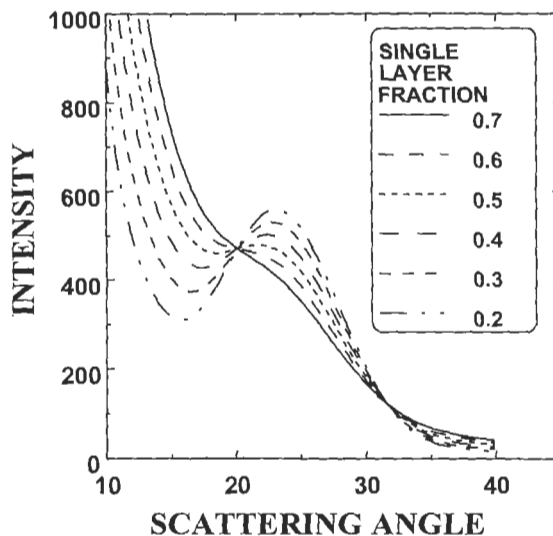


Fig. 30. Calculated (002) Bragg peaks for various single layer fractions of the sample from reference 12. The calculations assumed that a fraction, f , of the carbon was in single layers and that fractions $2/3(1-f)$ and $1/3(1-f)$ were included in bilayers and trilayers respectively.

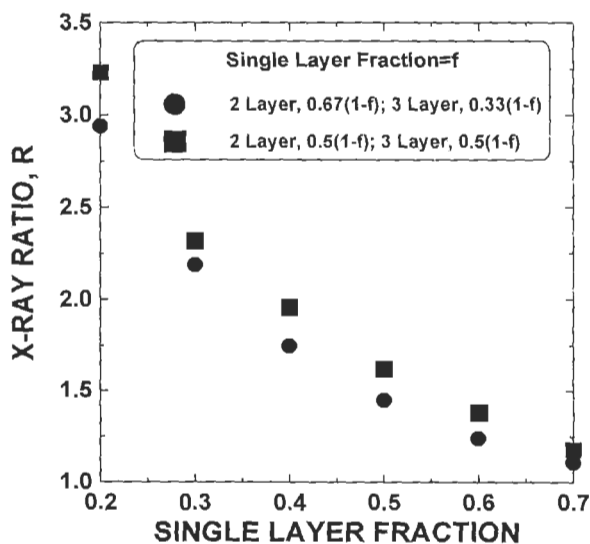


Fig. 31. The dependence of R on single-layer fraction for the calculated patterns of Fig. 30, and for a second set of calculations where the fraction of carbon atoms in bilayers and trilayers is equal [12].

5.3 Mechanism of lithium insertion

The materials made near 1000°C from the three resins have little hydrogen content. These materials show high capacity (up to 550 mAh/g), little charge-discharge hysteresis, and appear well-suited for application in lithium-ion batteries. The mechanism for lithium insertion on the low voltage plateau is believed to be the adsorption of lithium onto internal surfaces of nanopores formed by single, bi, and trilayer graphene sheets which are arranged like a “house of cards” as shown in Fig. 24.

Additional samples were prepared from the three resins and were heated at temperatures between 940° and 1100°, under different inert gas flow rate and with different heating rates. The samples have different microporosities and show different capacities for lithium insertion. The results for all the carbons prepared from resins are shown in Fig. 32, which shows the reversible capacity plotted as a function of R. The reversible capacity for Li insertion increases as R decreases. This result is consistent with the result reported in reference 12,

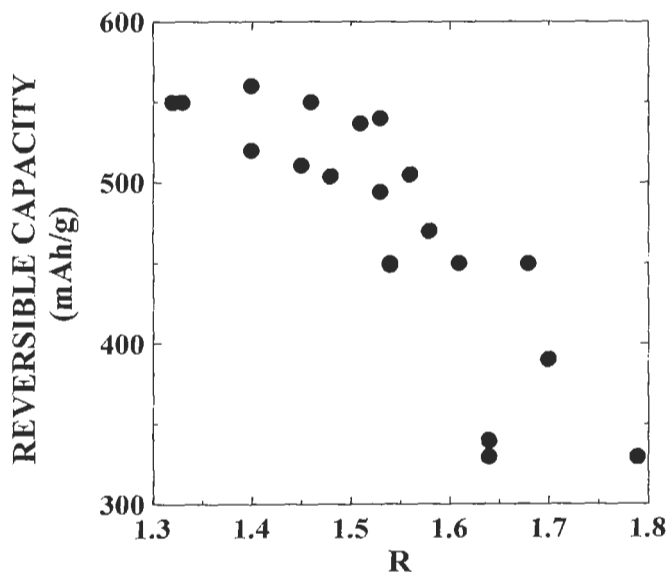


Fig. 32. Reversible capacity of microporous carbon prepared from phenolic resins heated between 940 to 1100°C plotted as a function of the X-ray ratio R. R is a parameter which is empirically correlated to the fraction of single-layer graphene sheets in the samples.

which suggests that Li atoms can be adsorbed onto the internal surface of micropores in the hard carbon samples as shown in Fig. 24. If there are more micropores (or small R for the sample), then the capacity is larger.

A lithium cluster in the micropores of the carbon sample has a very similar environment as lithium atoms in metallic lithium. Hence, we observe long low-voltage plateaus on both discharge and charge for lithium insertion in the microporous carbon.

Since these materials have significant microporosity, we expect their bulk densities to be low. For example, the tap density (100 taps) of Br1000 was measured to be 0.81 g/cc, compared to 1.34 g/cc for the synthetic graphitic carbon powder, MCMB2700, measured by the same method.

6 Carbons Used in Commercial Applications

Most commercial lithium-ion cells manufactured today use graphitic carbons from region 1 of Fig. 2. These are of several forms, with mesocarbon microspheres and natural graphites being the most commonly used. The specific capacity of these carbons is near 350 mAh/g.

Sony Energytec uses a disordered hard carbon of the type described in region 3 of Fig. 2. These carbons have been produced by a number of Japanese manufacturers including Kureha [41] and Mitsubishi Gas [40]. Our recent work [44], and other work in the patent literature shows how such carbons can be produced from natural precursors like sugar and wood. This suggests that it should ultimately be possible to prepare such carbons very cheaply. The specific capacity of region-3 carbons which are in commercial production are around 500 mAh/g.

There are numerous alternatives to pure carbons for use in Li-ion batteries. Wilson et al. [45] have shown how disordered carbons containing silicon nanoclusters can use the large alloying capacity of silicon for L_1 , in addition to the insertion capacity of the carbon itself. These materials can have reversible capacities up to 500mAh/g. They are prepared by chemical vapor deposition methods and hence are a lab curiosity at the moment. In an effort to make these materials more practical, Wilson et al. [46] examined the products of the pyrolysis of siloxane polymers and found they could have reversible capacities near 600 mAh/g. A recent patent filing by Seiko [47] showed that SiO (a mixture of nanometer sized amorphous Si and amorphous SiO₂ regions within particles) has a voltage of about 0.3V versus Li metal and a capacity for lithium near 1100mAh/g. Our preliminary experiments have confirmed this result, but

do not show good cycle life. In another recent patent filing, researchers at Fuji [48] have shown that SnO, SnO₂ and amorphous SiSnO₃ all have large reversible capacities (> 500 mAh/g) for lithium below about 0.8V. Fuji has even announced plans to commercialize a cell with one of the anodes described in ref. 48.

It is clear that there is enormous activity in the the search for better and cheaper anode materials for Li-ion batteries. In fact, it is not certain at this time whether carbon will remain the material of choice for this application. Nevertheless, large strides toward the optimization and understanding of carbons for Li-ion batteries have been made in the last 5 to 10 years. If continued progress is made, we can expect to see carbon materials in Li-ion batteries for a long time to come.

7 References

1. T. Nagaura and K. Tozawa, Prog. Batt. Solar Cells **9**, 209 (1990).
2. J.R. Dahn, A.K. Sleight, Hang Shi, B.W. Way, W.J. Weydanz, J.N. Reimers, Q. Zhong, and U. von Sacken, "Carbons and Graphites as Substitutes for the Lithium Anode", in *Lithium Batteries*, G. Pistoia, Elsevier, North Holland (1993).
3. S. Hossain, "Rechargeable Lithium Batteries (Ambient temperature)", in *Handbook of Batteries*, 2nd edition, D. Linden, McGraw-Hill Inc. (1995).
4. J.R. Dahn, U. von Sacken, M.W. Juzkow, and H. Al-Janaby, J. Electrochem. Soc. **138**, 2207 (1991).
5. J.R. Dahn, Tao Zheng, Yinghu Liu, J.S. Xue, Science **270**, 590 (1995).
6. Tao Zheng, J.N. Reimers, and J.R. Dahn, Phys. Rev. **B 51**, 734-741 (1995).
7. Tao Zheng and J.R. Dahn, Phys. Rev. **B53**, 3061-3071 (1996)
8. Tao Zheng, Yinghu Liu, E.W. Fuller, Sheilla Tseng, U. von Sacken, and J.R. Dahn, J. Electrochem. Soc. **142**, 2581 (1995).
9. Tao Zheng, J.S. Xue, and J.R. Dahn, Chemistry of Materials, **8**, 389 (1996)
10. Tao Zheng, W.R. McKinnon, and J.R. Dahn, J. Electrochem Soc., **143** (7), pp. 2137-2145 (1996).
11. Tao Zheng, Q. Zhong, and J.R. Dahn, J. Electrochem. Soc. **142**, L211 (1995).
12. Yinghu Liu, J.S. Xue, Tao Zheng, and J.R. Dahn, Carbon **34**, 193 (1996).
13. Tao Zheng, W. Xing and J.R. Dahn, *Carbons Prepared from Coals for Anodes of Lithium-Ion Cells*, Carbon, **34**(12), pp. 1501-1507 (1996).
14. Hang Shi, Ph.D. Thesis, Simon Fraser University (1993).
15. Hang Shi, J.N. Reimers, and J.R. Dahn, J. Appl. Cryst. **26**, 827 (1993).
16. P. Scherrer, Nachr Göttinger Gesell., 98 (1918).
17. B.E. Warren, Phys. Rev. **9**, 693 (1941).
18. B.E. Warren, *X-Ray Diffraction*, p. 254, Dover, N.Y. (1990).
19. A. Guinier, G. Fournet, *Small-Angle Scattering of X-Rays* (John Wiley & Sons, N. Y., 1955).

20. M. Kalliat, C.Y. Kwak and P.W. Schmidt, in *"New Approaches in Coal Chemistry"*, edited by B.D. Blaustein, B.C. Bockrath and S. Friedman, American Chemical Society, Washington, D.C., p. 3, (1981).
21. R.E. Franklin, *J. Chem. Phys.* **47**, 573 (1950).
22. For examples, see paper in volumes 1 and 2 in *Chemistry and Physics of Carbon*, edited by P.L. Walker, Jr., Marcel Dekker Inc., N.Y. (1965, 1966).
23. B.E. Warren, *Phys. Rev.* **9**, 693 (1941).
24. E. Peled, *J. Electrochem. Soc.* **126**, 2047 (1979).
25. R. Fong, U. von Sacken, and J.R. Dahn, *J. Electrochem. Soc.* **137**, 2009 (1990).
26. R.C. Boehm, and A. Banerjee, *J. Chem. Phys.* **96**, 1150 (1992).
27. Tao Zheng, and J.R. Dahn, *Synth. Met.* **73**, 1 (1995).
28. S. Yata, H. Kinoshita, M. Komori, N. Ando, T. Kashiwamura, T. Harada, K. Tanaka, and T. Yamabe, *Synth. Met.* **62**, 153 (1994).
29. A. Mabuchi, K. Tokumitsu, H. Fujimoto, and T. Kasuh, In Proc. 7th Int. Meeting on Lithium Batteries, May 15-20 (1994), Boston, USA, paper I-A-10, p. 207 of ext. abs.; also see H. Fujimoto, A. Mabuchi, K. Tokumitsu, and T. Kasuh, *ibid*, paper II-B-12, p. 540.
30. K. Sato, M. Noguchi, A. Demachi, N. Oki, and M. Endo, *Science* **264**, 556 (1994).
31. J.S. Xuc, A.M. Wilson, and J.R. Dahn, Canadian patent application, filed May 20 (1995).
32. B.R. Puri, "Surface Complexes on Carbons", in *Chemistry and Physics of Carbons*, edited by P.L. Walker, Jr., Vol. 6, Marcel Dekker Inc., N.Y. (1970)
33. For example, see Tao Zheng's Ph.D. Thesis, Simon Fraser University, Canada (1996).
34. R.E. Franklin, *Acta Cryst.* **4**, 253 (1951).
35. R. Diamond, in *Proc. Third Conf. on Carbon*, p. 367, Buffalo, New York (1957), published by Pergamon Press, New York (1959).
36. T. Enoki, S. Miyajima, M. Sano, and H. Inokuchi, *J. Mater. Res.* **5**, 435 (1990).
37. P. Papanek, M. Radosavljevic, and J.E. Fischer, *Chem. Mater.*, **8**(7), pp. 1519-1526 (1996).
38. L.S. Selwyn, W.R. McKinnon, U. von Sacken, and C.A. Jones, *Solid State Ionics* **22**, 337 (1987).
39. A. Omaru, H. Azuma, M. Aoki, A. Kita, and Y. Nishi, paper #25, 182nd meeting of the Electrochemical Society, Toronto, Canada. Extended Abstracts of Battery Division, p. 34 (1992).
40. Y. Takahashi, J. Oishi, Y. Miki, M. Yoshimura, K. Shibahara, and H. Sakamoto, 35th Battery Symposium in Japan, Nov. 14-16, Nagoya, Japan, paper 2B05, extended abstracts, page 39 (1994).
41. N. Sonobe, M. Ishikawa, and T. Iwasaki, 35th Battery Symposium in Japan, Nov. 14-16, Nagoya, Japan, paper 2B09, extended abstracts, page 47 (1994).
42. E. Fitzer, W. Schaefer, and S. Yamada, *Carbon* **7**, 643 (1969).
43. U. von Sacken, Q. Zhong, Tao Zheng, and J.R. Dahn, *Phenolic Resin Precursor Pregraphitic Carbonaceous Insertion Compounds and Use as Anodes in Rechargeable Batteries*, Canadian Patent Application #2,146,426 (1995).

44. Weibing Xing, J.S. Xue and J.R. Dahn, *Optimizing Pyrolysis of Sugar Carbons for Use as Anode Materials in Lithium-Ion Batteries*, J. Electrochem Soc., **143**, 3046 (1996); Weibing Xing, J.S. Xue, Tao Zheng, A. Gibaud and J.R. Dahn, *Correlation between Lithium Intercalation Capacity and Microstructure in Hard Carbons*, J. Electrochem. Soc., **143**, 3482 (1996).
45. A.M. Wilson and J.R. Dahn, J. Electrochem. Soc. **142**, 326 (1995).
46. A.M. Wilson, J.N. Reimers, E.W. Fuller and J.R. Dahn, Solid State Ionics, **74**, 249 (1994).
47. K. Tahara, H. Ishikawa, F. Iwasaki, S. Yahagi, A. Sakata, and T. Sakai, European Patent Application #93111938.2, (1993).
48. Y. Idota, M. Mishima, Y. Miyaki, T. Kubota and T. Miyasaka, Canadian Patent Application 2,134,052 (1994).

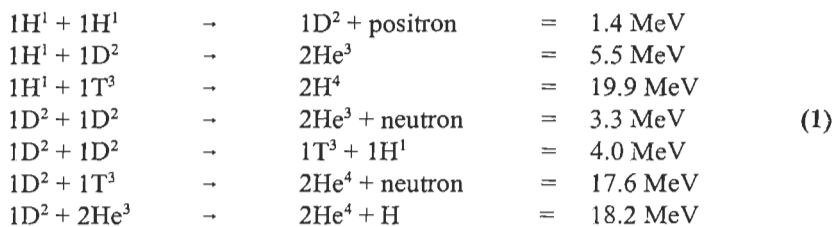
CHAPTER 12

Fusion Energy Applications

LANCE L. SNEAD

*Oak Ridge National Laboratory**P.O. Box 2008**Oak Ridge, Tennessee 37831-6087, U.S.A.***1 Introduction***1.1 Background*

When two light elements collide with sufficient energy they may "fuse" and form a third, heavier, element. A simple mass balance would show that there is a small mass loss in this process, corresponding to a significant energy release. Many light elements can undergo exothermic fusion reactions, but fusion of the isotopes of hydrogen and helium are the easiest reactions to induce. The most probable fusion reactions and their released energies are:



Fusion requires high temperature (energies) to cause the atoms to bind together. The likelihood of atoms fusing together is highly dependent on the individual isotopes and their temperature. It can be shown that the D+T reaction is the easiest reaction to drive. However, the inherent radioactivity and expense of tritium has restricted its use, while the lighter hydrogen isotopes have been extensively used. The gaseous temperatures required for D+T reaction are related to the kinetic energy of the ions, and are in excess of 50 million degrees Kelvin. While significant power has been produced from fusion systems, the total amount of power produced in any reactor is much less than the power added to the system to drive the fusion process. The current goal of fusion programs worldwide is to achieve "ignition," where the plasma begins a self-sustaining burn from which more power is generated than consumed in the fusion process.

Carbon materials in the form of graphite have played a major role in fusion systems as armor to keep higher atomic number elements from entering into, and extinguishing, the high temperature reactant gases known as the plasma. Although there are many benefits to the use of graphite in fusion systems, there are also significant design challenges and drawbacks. Significant progress has been made toward demonstrating self-sustaining, power-producing, fusion plasmas. Much of the progress can be attributed to the use of graphite and carbon-fiber composites (CFCs), as well as other low atomic number plasma-facing materials such as beryllium. With the use of advanced materials, it is possible that the next planned experiment, the International Thermonuclear Experimental Reactor (ITER), will demonstrate an ignited fusion plasma and provide a test bed for a demonstration fusion power reactor.

1.2 Current and planned fusion machines

The containment of very high-temperature, high-density plasmas and the maintenance of a near steady state plasma condition (thus enabling the fusion reaction) are the greatest challenges to fusion power. Many reactor concepts have been studied in the past and attention is now focused on the "tokamak" system. This toroidal confinement system was developed in the mid-1960s in Russia. The basic concept of the tokamak is to confine within, and couple the plasma ions to, continuous magnetic field lines which travel helically through a toroidal vacuum vessel. For a non-collisional plasma, the ions can therefore be heated by various external means to the extreme temperature necessary for the fusion reaction to take place. The tokamak concept is the basis for the four largest present day fusion machines (Table 1), and is the premise for the proposed ITER machine currently under design by the European Community, Japan, Russia, and the United States. The ITER design calls for a tokamak with an inner plasma chamber diameter (twice the minor radius) of about 6 meters, and a machine standing well over twenty meters.

1.3 Plasma-facing components

The greatest effort in the development of fusion energy has been in the enormously challenging area of plasma physics and plasma confinement. It is clear that perfect containment of a fusion plasma is impossible, and that interactions between the hot ionized plasma gas and their surroundings will take place. In confinement systems such as the tokamak, this interaction point is very close to, and in some cases defines, the edge of the plasma. The components which are in line of sight of the plasma, and therefore impacted by the hot gasses and particles, are called plasma-facing components (PFCs) or plasma-facing materials (PFMs). The reactions between the fusion plasma and the PFMs are severe and typically cause melting or sublimation, component mechanical failure due to high thermal stress, and

excessive surface erosion. The plasma ion flux and associated heat loading to the plasma-facing materials is highly non-uniform and quite dependent on the tokamak design.

The hot plasma gasses are made up of unburned hydrogen fuel, fusion byproducts such as helium, plasma electrons and impurity elements previously removed from PFCs, and plasma electrons. As can be seen in Eq. 1, the type of particles which may strike the PFMs are dependent on the fusion fuel. For the D+T fuel system, the plasma will contain not only the D+T fuel, but high energy alpha particles (3.5 MeV He) and neutrons (14.1 MeV). The partitioning of the reaction energy between helium and the neutron is both an advantage and a disadvantage for the D+T fuel system. Because the energetic helium nucleus quickly collides with the surrounding gasses, most of its energy remains in the plasma and helps to sustain a high plasma temperature. Conversely, the neutron has very little chance of collision in the low density plasma and loses its energy outside of the plasma (usually over meters of path length inside the structure of the reactor). Because less than 30% of the D+T reaction energy remains in the plasma, only this fraction is eventually distributed on the PFCs, thus reducing the heat load handling requirement and material erosion. However, as discussed in Section 3 of this chapter, the material damage associated with the 14.1 MeV neutron collisions is significant and offsets the reduced D+T heat loading.

Fusion devices can be characterized by how the plasma edge is defined and how the impacting flux and heat are handled. The classic approach is to define the plasma edge by placing a sacrificial component in contact with the plasma. This component, which intercepts the plasma edge particle flux, is known as a bumper or bumper limiter, and extends circumferentially around the torus. A second approach to defining the plasma edge is to magnetically capture and divert the edge plasma onto a divertor plate well removed from the central plasma. Once the plasma gasses are cooled they can be pumped away. The point on the "divertor" where the particle flux strikes experiences a significant ion heat loading, and many techniques such as magnetic sweeping to spread the loading and puffing of gas to "soften" the ion impact have been used to reduce the particle flux and energy. Regardless of whether the limiter or divertor design is employed, the majority of the particle and heat flux is intercepted by these components (Table 1). However, a significant flux also impacts the balance of the torus lining (generally referred to as the first wall). Because of cross field diffusion and other mechanisms (Table 1) the thermal loading and resulting thermomechanical requirements for the first wall are not as severe. A convenient comparison for the heat loadings given in Table 1 is the maximum output from a conventional propane torch, which is approximately 10 MW/m², or about the maximum heat flux seen in current fusion devices.

Table 1. Materials and heat loads for the major fusion machines world wide (see Section 1.3 for definitions of divertor and first wall)

Fusion Machine	Country	Fuel System	First Wall Heat Load (MW/m ²)	First Wall Material	Divertor or Limiter Heat Load (MW/m ²)	Divertor or Limiter Material
ITER (proposed)	International	D/D & D/T	0.6	TBD	15-30	TBD
DIII-D	U.S.A.	D/D	0.6	Poco ATJ	5.3	Poco ATJ
JT-60U	Japan			Dunlop DMS704		Hitachi HCB-18S Ibiden ETP-10 Showa-Denko CC312
JET	European Community (located in England)	D/D	Negligible	Dunlop DMS-704 Sepcarb N11 Sepcarb N11-s(3D)	18	Dunlop DMS-704
TFTR	U.S.A.	D/D & D/T		Poco AXF-5Q		FMI 4-D

1.4 Particle/matter interactions

The particles which collide with the plasma-facing components will be highly energetic and capable of inflicting severe damage to the bulk and near surface layer of the PFM. The greatest flux of particles in a steady state system will be from the plasma fuel. The energies of the impacting hydrogen depends on many variables, though will most likely be in the range of hundreds of electron volts (eV), which corresponds to ion speeds of hundreds of kilometers per second. Helium ash (burnt fuel) will likewise have high surface impact energies. Electrons, which are in number density equilibrium with the plasma ions, also travel along the plasma field lines, albeit in the opposite direction, and are lost to impacts with the PFMs. The high energy neutrons present in the D+T reaction (14.1 MeV), or those of the D+D reaction (2.4 MeV), have mean free paths of several centimeters in graphite, and so will typically not interact strongly with the first wall. However, these neutrons will be back scattered and slowed down behind the first wall resulting in a nearly isotropic flux of high energy neutrons throughout the first wall and first wall structure. The reaction of the plasma neutrons, ions, and electrons with graphite PFMs (which are discussed in some detail in the following sections) can cause a wide range of effects. Assuming that the PFM is capable of handling the heat loads generated by the plasma, these effects include physical and chemical erosion of the first wall and thermomechanical property degradation of the bulk and surface material.

The discussion thus far has been limited to the operation of tokamaks in the quasi-steady state (long pulse.) All present-day large tokamaks are pulsed machines with pulse lengths of no more than a few seconds, where the plasma discharge consists of a rapid heating phase, a steady state, and a cool down phase. In this case the heat flux is approximately uniform around the circumference of the machine and scales with the machine power. However, a significant number of these plasma shots end in an abrupt and somewhat violent fashion, referred to as a disruption. When this occurs the plasma becomes rapidly unstable and instantaneously "dumps" its entire energy onto the PFC. Disruptions cause significantly larger heat loads than normal operation, and in many cases defines the design limits for these components. In the ITER it is assumed that the plasma conditions can be controlled such that of the 10,000 or so 400 second pulses expected in the physics phase of the machine [1], the number of disruptions can be limited to about 500. In ITER a second assumption has been made regarding the disruption electrons. These electrons will have energies approximately the same as the plasma ions during normal operation, but because of their extremely fast reaction times can reach energies in the GeV range during disruptions. During such disruptive situations the electrons reach relativistic velocities and may focus on small areas of the tokamak which are totally incapable of handling the localized heat load. In some cases melting (or sublimation) of the PFC, as well as the underlying structure,

has occurred. For ITER, rather restrictive limits on the energy and energy deposition from these "runaway" electrons have been assumed.

2 The Advantages of Carbon as a Plasma-Facing Component

2.1 Plasma-facing materials as plasma impurities

A fusion reactor must first heat and confine the plasma. However, it must additionally maintain the plasma in an impurity free condition. Fusion plasmas are heated both internally by the fusion reaction products (*i.e.*, the 3.5 MeV helium nucleus from the D+T reaction) and externally, by means such as induction, radio frequency waves, or neutral particle injection. Plasma heating is balanced by plasma cooling mechanisms, of which electromagnetic radiation dominates. In a fully ionized plasma the radiative cooling comes from the Bremsstrahlung, or braking, radiation which occurs when the energetic ions interact with the plasma electrons. A fraction of the electromagnetic radiation released from this interaction is lost from the plasma. The energy lost from the plasma in this manner is significantly increased by low concentrations of impurities. The plasma power loss due to Bremsstrahlung radiation, P_{brem} , may be written :

$$P_{\text{brem}} \text{ (MW/m}^3\text{)} \approx 4.8 \times 10^{-43} Z_i^2 N_i N_e T_e^{1/2} \approx Z_i^2 N_i \quad (2)$$

where Z_i , N_i , N_e , and T are the atomic number of the radiating species, their density, the electron density, and the plasma temperature, respectively. It is apparent from Eq. 2 that low plasma impurity mass and density are beneficial. Because of the Z_i^2 dependence, plasma impurities greatly impact the amount of cooling. The choice of plasma-facing material, which is the source of many of the plasma impurities, is limited by the product $Z_i^2 N_i$. Ideally, plasma-facing materials should be light elements and have a low tendency to migrate into the plasma. Carbon and beryllium are two low atomic number elements which are commonly used in tokamaks. The next suitable element is aluminum, which would have almost a factor of five higher radiative loss on an atom per atom basis compared to carbon. On the same basis molybdenum, which has been used in many tokamak experiments, has a loss factor of 49 times that of carbon, and tungsten 150 times the radiative loss of carbon. However, this assumes that the same number of impurity atoms find their way into the plasma (*i.e.*, N_i) which, as is discussed later, is material dependent.

2.2 Normal thermomechanical loading

Under normal operating conditions the first wall must handle high plasma surface heat fluxes (Table 1), as well as volumetric heat loadings due to the penetrating neutron and electromagnetic radiation. The volumetric heat loading is dependent

on line-of-sight distance from the plasma, and can be as high as several MW/m^2 . These surface and volumetric heat loadings will induce a temperature gradient, and corresponding thermal stress, across the PFC, and stresses at the interface between the plasma-facing material and the heat sink. For example, if one assumes an ideal case of a 2.5-cm thick, infinitely wide graphite plate which is perfectly bonded to a 50°C copper heat sink, the thermal stress at the graphite-copper interface for a heat flux of $5 \text{ MW}/\text{m}^2$ has been shown to be 200 MPa [1]. The ability of the PFC to withstand this heat flux and thermal stress will depend both on the material properties and the component design. The two most significant design parameters are the thickness of the PFM and how it is attached to the heat sink. The material properties (which to some extent can be engineered to optimize thermal conduction to the heat sink, strength, and thermal expansion transverse to the interface) are strong functions of temperature. As discussed later in Section 3, these properties are also dependent on radiation displacement damage. A candidate design for the ITER divertor is shown in Fig. 1. In this design, the heat flux strikes the surface of carbon-fiber composite or graphite blocks and the heat flows into a water cooled copper tube which has been brazed inside the block. The PFC is bolted to a stainless steel support structure. This configuration of PFC is called the monoblock structure, as compared to the flat plate and saddle types inset into Fig. 1.

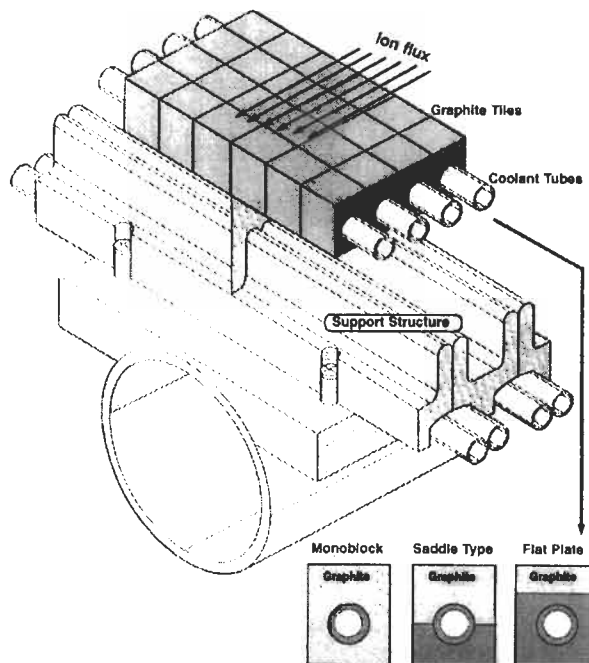


Fig. 1. Schematic diagram of the proposed first wall for the ITER reactor.

To provide a quantitative comparison of candidate PFMs, a number of figures of merit (Δ) have been derived. One of which may be written:

$$\Delta_{th} = \frac{K\sigma_y}{\alpha E(1-\nu)} \quad (3)$$

where K is the thermal conductivity, σ_y the yield strength, α the thermal expansion coefficient, E the Young's modulus, and ν the Poisson's ratio. High values of Δ_{th} indicate the best candidate material. Figure 2 shows a comparison of the three primary candidate PFMs: graphite, beryllium, and tungsten. Graphite has been further broken down into fine- and coarse-grained graphites (POCO and H451 respectively) as well as a high quality 1-D (MKC-1PH) and balanced 3-D (FMI-222) carbon-fiber composites (CFC). In Fig. 2 it has been assumed that the high thermal conductivity direction for the 1-D CFC is oriented normal to the surface of the PFC. From Fig. 2 it is apparent that the high quality graphites and composites, which possess high strength and thermal conductivity, exhibit Δ_{th} considerably higher than either beryllium or tungsten.

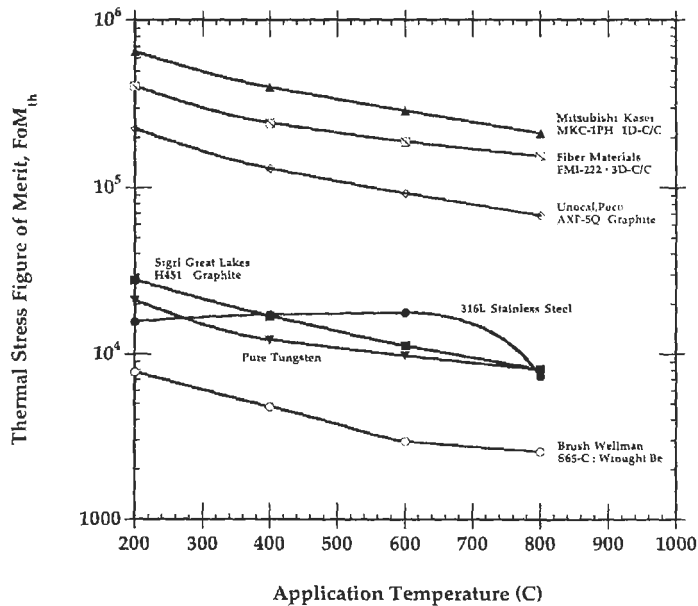


Fig.2. Thermal stress figure of merit for selected plasma facing materials

2.3 Thermal shock

As discussed in the introduction, disruptions cause the most severe thermomechanical loading experienced in a tokamak. In each of the 500 or so disruptions expected in ITER, approximately 10-20 MJ/m² will be deposited onto the first wall in 0.01 to 3 seconds. Such a disruption will cause very high thermal stresses and significant material erosion (Section 4). As these events are transient in nature, the ability of the PFC to withstand the disruption depends on the material's ability to both conduct and to absorb the deposited heat, before reaching a temperature or stress limit. For comparative purposes, a disruption figure of merit takes this into account :

$$\Delta_d = \frac{\sigma_u (C_p \rho K)^{1/2}}{\alpha E} \quad (4)$$

where σ_u is the ultimate tensile strength, C_p the specific heat, ρ the density, K the thermal conductivity, α the thermal expansion coefficient, and E is the Young's Modulus.

Figure 3 reports this disruption figure of merit to the materials in Fig. 2. Consistent with the results of the thermal Δ_{th} , high-quality, high-thermal conductivity composites and fine-grained graphites perform better than standard and larger grained graphites, and exhibit an order of magnitude better Δ_d than beryllium and tungsten. As discussed later in Section 4, the erosion of graphite and beryllium are very high and dictate the use of thick tiles in high flux areas. This is in contrast to tungsten, which has a relatively low erosion yield, allowing an armor thickness of only a few millimeters. Because the Δ are essentially calculated on a per unit tile thickness, it is somewhat misleading to compare tungsten with graphite. However, because graphite and beryllium are erosion-limited, the Δ and the melting temperatures are useful evaluation tools. While the sublimation temperature of graphite (~3350 °C) is comparable to the melting point of tungsten (~3400°C), it is clear that beryllium, which has a melting point of ~1300°C, is at a distinct disadvantage. Removal of beryllium, as well as other metallic PFCs, by melting has been seen in several large experimental devices.

Performance evaluations of graphite and CFCs have been conducted in both laboratory test stands and in operating tokamaks. Some experimental data generated using an electron beam facility are given in Fig. 4. The power is deposited by a rastered electron beam for approximately one second up to surface heat loads of 11 MW/m². The samples were 2.5 × 2.5-cm tiles facing the beam and were 1 cm in thickness. Each sample had a large notch machined into one edge (the highest stress area) to serve as a stress intensifier. It was noted that without the

notch, the graphites did not crack. Figure 4 gives the maximum heat flux at which each material was tested, and whether cracking of the tile occurred. The data indicate that CFC materials and higher thermal conductivity, high-density graphites are superior. Cracking did not occur in the three composites studied, nor in the two FMI graphites, to the maximum power density applied. The superior performance of the composite materials agrees with the performance of CFCs in the large tokamaks such as TFTR and JT-60U. The superior performance of the CFCs and the graphites is most likely because of their low thermal expansion coefficient and high strength. Also, the presence of the fibers in the CFCs may serve to blunt and arrest cracks, thus increasing toughness. All monolithic graphites shown in Fig. 4, with the exception of the two FMI-HDFG materials, cracked. It is interesting to note that this graphite possessed the highest Δ_d , even higher than that of the composites. However, strict correlation of improved performance with increased Δ_d was not seen, although a loose correlation was noted. As pointed out by Watson [2], the CTE may be the most dominant property, with the lowest CTE graphites showing the best resistance to thermal shock.

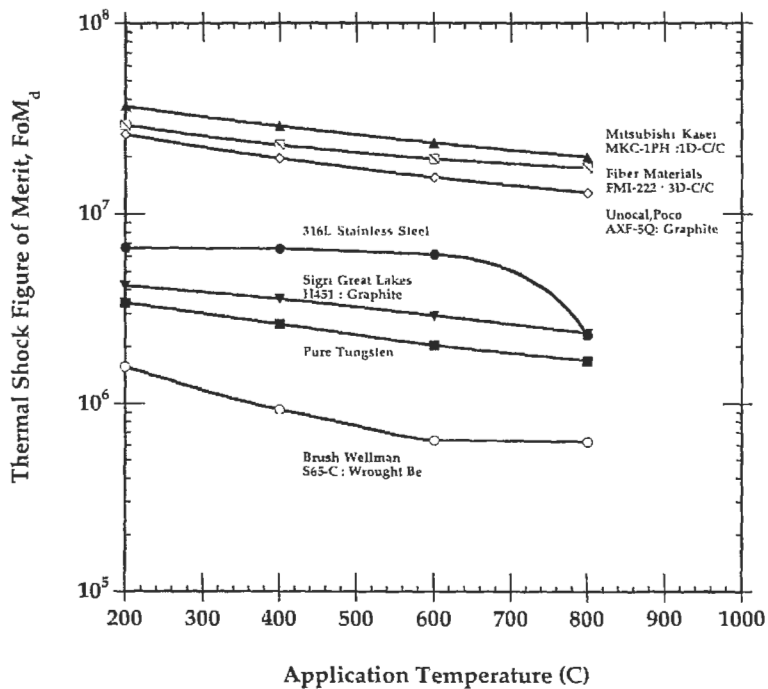


Fig. 3. Thermal shock figure of merit for selected plasma facing materials.

Finally, it should be noted that there are many issues regarding the selection of carbon materials as PFCs other than their thermal shock behavior. For example, the issues of radiation damage, erosion, and hydrogen retention are three leading drawbacks to the use of graphite as a PFC, and are discussed in the following sections. One issue, which will not be addressed in this chapter, is that of the attachment of the PFC to the heat sink. For most present day machines bolting or similar mechanical fastening is used. However, for next generation machines the anticipated heat loads are much higher, and physical bonding (*e.g.*, brazing) of PFCs to a water-cooled substrate will be required. One may appreciate the magnitude of this issue from the initial ITER design, which calls for many thousands of graphite or CFC tiles to be brazed to the heat sinks. When considering this large number of tiles, the anticipated large thermal and disruption loading, and the long repair time required if any one tile becomes detached, it is obvious that the robustness of the attachment is a critical issue.

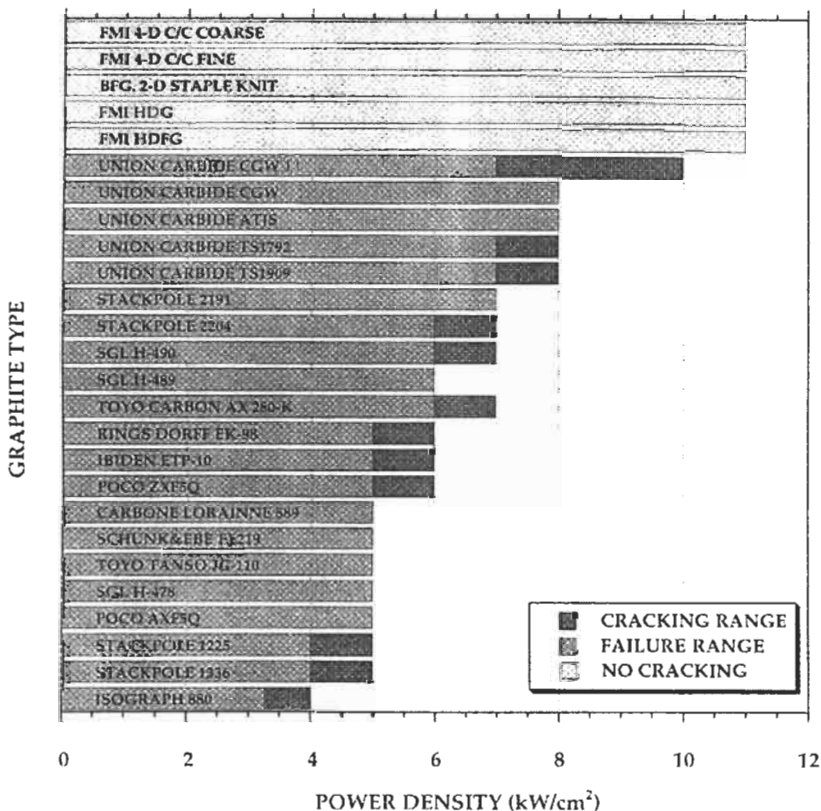


Fig. 4. The performance of several grades of graphite and graphite composites subjected to thermal shock loading.

3 Irradiation Effects on Thermophysical Properties of Graphite and Carbon Fiber Composites

3.1 Radiation displacement of atoms

Radiation effects in the graphite PFM can be categorized as near surface damage caused by interaction with the plasma, and/or bulk displacements caused by neutrons emanating from the plasma or back scattered by the surrounding structure. Amongst present day machines, only the TFTR has significant D+T fusion reactions and, therefore, experiences a damaging flux of fusion neutrons (see Eq. 1). However, because TFTR will undergo only a limited number of low power plasma "shots," the neutron dose will not be high enough for the PFCs and structural materials to experience appreciable neutron damage. In contrast, however, machines such as the ITER will experience significant neutron doses. Moreover, the next generation D+D machines such as the proposed TPX, will yield enough tritium to produce (D+T and D+D) fusion neutrons at levels sufficient to alter graphite properties.

High energy particles which travel through matter can interact with their surroundings. As the particles interact with matter they lose energy (per unit path length) in three ways: elastic collisions, electron excitations, and nuclear interactions. The interaction which is of primary interest from the materials point of view are the elastic collisions. If an ion or a neutron imparts sufficient energy to overcome an atom's binding energy (E_d carbon \approx 20 - 30 eV), the carbon is displaced from its original lattice position. If the energy transferred to the displaced atom (less its binding energy) is sufficient to displace further atoms, a series of displacement events or a "cascade" occurs. In the simplest interpretation, the Kinchin-Pease [3] model is used to calculate the total number of atoms displaced. For example, if a carbon atom were ejected by the plasma and re-impacted onto the carbon tile with a kinetic energy E of 1 KeV, the estimated number of atoms displaced (n) is estimated as follows :

$$n = (E/2 * E_d) = 25 \text{ atoms} \quad (5)$$

The interaction of high energy neutrons with matter is very similar to that of ions. The primary difference between the two being the amount of energy transferred in a single collision, and the distance over which the interactions take place. An ion, which has a relatively large radius and interacts coulombically, loses its energy over a short path length (typically less than a micron). In contrast, the comparatively small uncharged 14.1 MeV fusion neutron which undergoes only simple elastic or "billiard ball" collisions, has a mean free path of \sim 10 cm. So, on average, a fusion neutron will have an elastic collision with a carbon atom once in 10 cm of graphite. The amount of energy transferred to the carbon in this first

collision (E_c) is calculated by simple elastic theory as:

$$E_c = \left[\frac{4m_c m_n}{(m_c + m_n)^2} \right] E_0 \cos^2 \alpha = \left[\frac{4 \times 6 \times 1}{(6 + 1)^2} \right] (14.1 \text{ MeV}) \cos^2 \alpha \quad (6)$$

where m_c and m_n are the carbon and neutron mass (in amu), respectively, E_0 is the neutron energy, and α is the angle between neutron path before and after the collision. For a totally back scattered neutron (the maximum imparted energy) the energy transferred to the displaced carbon is 4 MeV. From Eq. 5, the number of displaced carbon atoms resulting from this 4 MeV neutron displacement event is approximately 80,000. The vast majority of these atoms do not stay "displaced," but diffuse back into the graphitic structure within a few picoseconds. To assess the effects such collision events have on a material, a convention has been adopted to compare irradiation doses. The displacement per atom, dpa, is the average number of times an atom has been knocked from its original lattice position. The dpa is an integrated average quantity and takes into account the density, the interaction cross section, and neutron energy spectrum. It has been estimated that lifetime displacement levels in TPX PFCs will be about 0.005 dpa, while the physics phase of ITER will accumulate approximately 1 dpa. In the second phase of ITER, which more closely represents a power producing system, as much as 30 dpa is expected.

3.2 Surface effects

In certain areas of a fusion machine the PFMs receive displacement levels much greater than 100 dpa, but only within the limited collisional range of the plasma ions, typically less than a few microns. The effect of this high damage level will be to reduce a well graphitized structure into one which appears amorphous. However, these near surface regions are subjected to erosion either by physical sputtering (caused by elastic collisions), or by chemical interactions. Both of these effects are addressed in Section 4. A second surface radiation damage issue (*i.e.*, the ability of the thin damaged surface layer to retain and transport hydrogen) is discussed in Section 5.

3.3 Effects of neutron displacements on graphite and carbon fiber composites

As discussed earlier, the first wall materials in next generation machines will receive from 0.005 to 30 displacements per atom. At the lower end of this range (<0.01 dpa) there are essentially no mechanical property changes expected in graphite materials. However, even at these low doses thermal conductivity and stored energy are of concern. For displacement levels >0.01 dpa other property

changes are significant: strength, elastic modulus, specific heat (C_p), CTE, Poisson's ratio (ν), and thermal conductivity. In addition, the dimensional stability under irradiation is important because the induced stresses may be significant, and because of the need for very tight dimensional tolerances at the plasma edge. It has been shown in fission neutron experiments that C_p [4] and ν [5] are not greatly affected by irradiation. Moreover, only moderate changes in the CTE occur, but the magnitude and nature of the CTE change is highly dependent on the type of graphite [4, 6-8].

The irradiation-induced graphite and CFC property changes which have received the most study by the fusion community are the dimensions, strength, elastic modulus, thermal conductivity, and hydrogen retention. A large body of data exists on the thermophysical changes in graphites, coming mainly from graphite moderated fission reactor development programs. A smaller body of data exists on CFCs, mainly from the same source, but with some additional data from fusion research. These data suggest that CFCs have similar irradiation behavior to graphite. In Chapter 13, Burchell discusses radiation damage mechanisms in graphite, and some of the specific property changes which occur. Because of their special significance to fusion energy, the remainder of this section will focus on the radiation effects in CFCs and on radiation-induced degradation in thermal conductivity in graphite and CFCs.

3.3.1 Dimensional changes in carbon fiber composites

As discussed in Chapter 13, irradiation-induced dimensional changes in graphite are highly anisotropic, and a strong function of irradiation temperature and neutron dose (dpa). The temperature range of interest for fusion applications varies from 100°C in areas well removed from the plasma, to over 1000°C for the surface of PFCs which experience appreciable plasma flux. The mechanism of graphite irradiation-induced dimensional change is described in detail in Chapter 13, and is a combination of intra- and inter-crystallite effects. Within the crystallites, displacement damage causes an a-axis shrinkage (within the basal plane) and a c-axis growth (perpendicular to the basal plane).

Similar dimensional change behavior has been observed in CFCs [9]. Figure 5 shows the dimensional change behavior of one-, two-, and three-directional composites. In this example, solid cylinders were irradiated at 600°C to doses ranging from 0-5 dpa and the resulting diameter and length measured. The behavior of each material can be explained by the accepted theory for dimensional change in graphite (Chapter 13) after taking into account the individual fiber architectures, and by observing that a graphite fiber, PAN-based in this example, is basically a filament of circumferential or radial basal planes running parallel to the fiber axis. The irradiation-induced dimensional change of such a fiber is therefore to shrink in length and grow in diameter, as observed for the

unidirectional composite of Fig. 5. At doses less than 1 dpa the dimensional change is relatively minor. As the dose is increased, the direction perpendicular to the fiber axis is more or less unchanged while a significant shrinkage along the direction parallel to the fiber axis occurs. At about 2 to 3 dpa swelling in the composite occurs in the perpendicular direction. The random fiber composite of Fig. 5 has a random orientation of chopped PAN fibers in the plane of the composite. The specimen diameter shows practically no change perpendicular to the fiber axis to about 4.5 dpa, though exhibits ~2% shrinkage parallel to the fiber axis. The 3-D balanced PAN-weave fiber has essentially isotropic shrinkage to a dose of ~2 dpa, at which point the diameter of the fibers, and hence the sample, begin to swell.

Also given in the 3-D composite plot in Fig. 5 is the radiation-induced dimensional change behavior parallel to the fiber axis of an Amoco P55 pitch fiber composite. This material was processed in an identical manner to the PAN fiber composite. From the plot it appears that the pitch fibers, and thus the composite, undergo slightly less shrinkage than the PAN fiber composite, possibly due to the higher fiber crystallinity. This hypothesis is also supported by the observation that fibers with higher final heat treatment temperatures tend to exhibit less dimension change [10] and is also consistent with the observation that elevating the heat treatment temperature of graphite reduces the irradiation-induced shrinkage [11].

3.3.2 Changes in strength and modulus

A marked increase in both strength and elastic modulus occurs in graphite and CFCs at dose levels as low as 0.01 dpa [6]. These increases continue to high displacement levels until volumetric expansion and extensive micro-cracking occur and the material begins to degrade. Structural degradation typically occurs at several to tens of dpa depending on the graphite type and irradiation temperature. The initial increase in modulus is a result of dislocation pinning by lattice defects produced by neutron irradiation. The magnitude of the increase is dependent on the perfection of the graphites. For most graphites a modulus increase of 2 to 2.5 times the unirradiated value is typical for irradiation temperatures less than 300°C, with the change becoming less pronounced at higher irradiation temperatures. Irradiation-induced increase in strength occurs in a similar fashion as the elastic modulus. The irradiated and unirradiated mechanical properties of some candidate ITER PFC materials are shown in Table 2. These materials were irradiated at approximately 1000°C to a dose of about 2 dpa [12]. The change in properties is relatively small because of the high irradiation temperature.

3.3.3 Thermal conductivity degradation

The irradiation-induced thermal conductivity degradation of graphites and CFCs will cause serious problems in fusion system PFCs. As with ceramics, the thermal conductivity of graphite is dominated by phonon transport and is therefore greatly

affected by lattice defects, such as those caused by neutron irradiation. The extent of the thermal conductivity reduction is therefore controlled by the efficiency of creating and annealing lattice defects and is, therefore, related to the irradiation temperature.

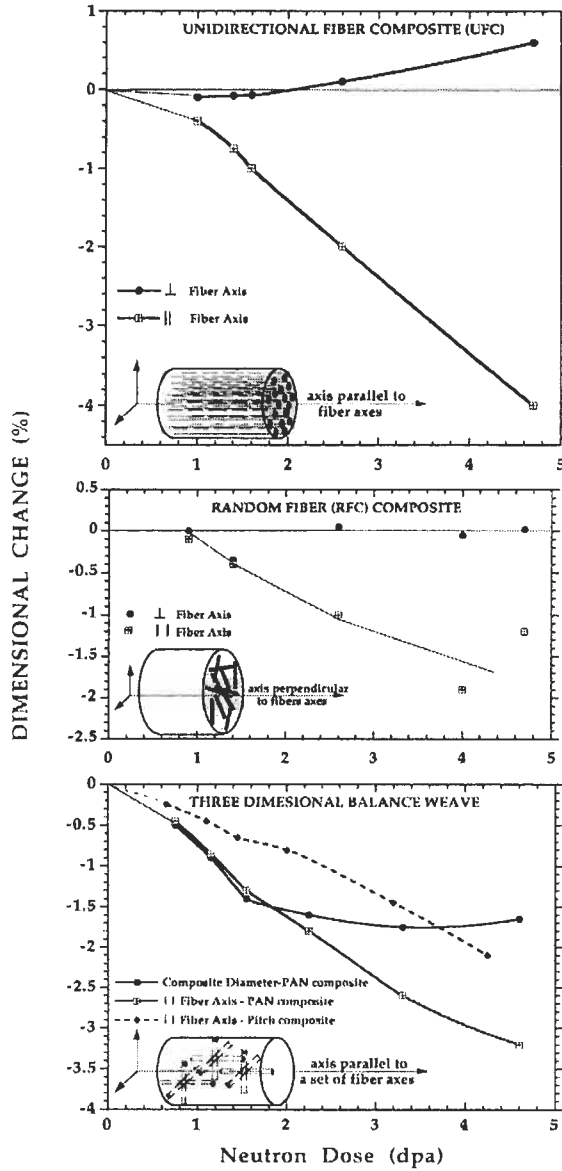


Fig. 5. Neutron irradiation induced dimensional changes in graphite composites.

The effect of neutron irradiation on the thermal conductivity of graphite has been widely studied. The majority of the literature [8, 10, 13-21] in this area has been in support of the gas-cooled, graphite-moderated, fission reactor program in the United States and United Kingdom and has focused on "nuclear" graphites as well as more fundamental work on pyrolytic graphite [6, 17, 22, 23]. In recent years, the emphasis of radiation effects research has switched to graphites used in plasma-facing components of fusion reactors [8, 24-27].

As discussed in Sections 2.2 and 2.3, composites with very high thermal conductivity are desirable because of the high heat flux present in certain areas of fusion devices. Because of the significant advances in processing of CFCs and fiber development, very high thermal conductivity materials have been recently demonstrated and become attractive for high heat flux applications. The highest thermal conductivities have been demonstrated for CFCs made from highly crystalline graphite fibers which have intrinsic conductivities approaching that of pyrolytic graphite. For example, vapor grown carbon fibers [28] have a thermal conductivity of 1950 W/m-K.

The physical processes governing the thermal conductivity of graphites, as well as the mechanisms responsible for the radiation-induced degradation in conductivity, are well established [6]. For all but the poorest grades of carbon, the thermal conductivity is dominated by phonon transport along the graphite basal planes and is reduced by scattering "obstacles" such as grain boundaries and lattice defects. For graphites with the largest crystallites (*i.e.* pyrolytic or natural flake graphite) the in-plane room temperature thermal conductivity is approximately 2000 W/m-K [29].

The thermal conductivity of graphite-based materials can be written as a summation of the thermal resistance due to scattering:

$$K(x) = \beta(x) \left[\frac{1}{K_u} + \frac{1}{K_{gb}} + \frac{1}{K_l} \right]^{-1} \quad (7)$$

where $\beta(x)$ is a coefficient which includes terms due to orientation (with respect to the basal plane), porosity, and some other minor contributors. This coefficient is, in most cases, assumed to be constant with temperature, with a value of around 0.6. The first two terms inside the parentheses are the contributions to the thermal conductivity due to Umklapp scattering (K_u) and the grain boundary scattering (K_{gb}). The grain boundary phonon scattering dominates the thermal resistance ($1/K_{gb}$) at low temperatures and is insignificant above a few hundred degrees celsius, depending on the perfection of the graphite. The Umklapp scattering, which defines the phonon-phonon scattering effect on the thermal conductivity,

Table 2. Effect of neutron irradiation on some graphite or CFC materials studied for fusion applications [12]

Property	Toyo-Tanso IG-110 Graphite	Showa-Denko CC-312 Felt CFC (\parallel to fibers)	Mitsubishi Kasei MKC-1PH CFC			Toyo Tanso CX- 2002U CFC (\parallel to fibers)
			X-direction	Y-direction	Z-direction	
Young's Modulus (GPa)						
Unirradiated	8.83	34.0	74.0	--	87.6	14.9
Irradiated	11.5	31.3	98.0	--	87.2	18.5
Bending Strength (MPa)						
Unirradiated	35.2+/-1.8	90.5+/-5.9	103.9+/-6.8	5.8+/-2.5	99.2+/-17.6	36.3+/-3.9
Irradiated	38.4+/-2.2	110.8+/-8.4	98.4+/-2.7	--	88.9+/-8.2	46.7+/-2.6
Compressive Strength (MPa)						
Unirradiated	85.0+/-2.6	65.1+/-2.5	59.8+/-6.8	76.7+/-14.0	59.6+/-6.7	33.3+/-8.7
Irradiated	82.0+/-3.2	93.7	55.9+/-3.1	--	51.0+/-7.3	41.2+/-9.2
Length Change 1/10(%)	-0.12	-0.30	-0.39	--	-0.97	-0.195

dominates at higher temperatures and scales nearly as T^2 [6]. The Umklapp scattering therefore defines the upper limit to the thermal conductivity for a "perfect" graphite. Following Taylor's analysis [30], the Umklapp-limited thermal conductivity of the graphite crystal would be ~ 2200 W/m-K at room temperature, in close agreement with the best pyrolytic graphites, or the vapor grown carbon fibers mentioned earlier.

The third term in Eq. 7, K_d , is the contribution to the basal plane thermal resistance due to defect scattering. Neutron irradiation causes various types of defects to be produced depending on the irradiation temperature. These defects are very effective in scattering phonons, even at flux levels which would be considered modest for most nuclear applications, and quickly dominate the other terms in Eq. 7. Several types of irradiation-induced defects have been identified in graphite. For irradiation temperatures lower than 650°C , simple point defects in the form of vacancies or interstitials, along with small interstitial clusters, are the predominant defects. Moreover, at an irradiation temperature near 150°C [17] the defect which dominates the thermal resistance is the lattice vacancy.

Due to its sensitivity to the presence of defects, the temperature at which graphite is irradiated has a profound influence on the thermal conductivity degradation. As an example, Fig. 6 shows one of the most complete sets of irradiation data on Pile Grade A (PGA) nuclear graphite [31]. PGA is a medium-grained, extruded, anisotropic material with a room temperature thermal conductivity of 172 W/m-K in the extrusion direction. Figure 6 presents the normalized room temperature thermal conductivity of this graphite at various irradiation temperatures. It is seen that as the irradiation temperature is decreased, the degradation in thermal conductivity becomes more pronounced. For example, following irradiation at 150°C , the thermal conductivity of this graphite appears to approach an asymptotic thermal conductivity of $\sim 1\%$ of original. As the irradiation temperature is increased, and the corresponding interstitial mobility becomes more significant, fewer defects remain in the structure and the thermal conductivity is reduced to a lesser extent. It is important to note that the data in Fig. 6 are from ambient temperature measurements and therefore underestimate the normalized thermal conductivity at the irradiation temperature, *i.e.*, $K_{\text{irr}}(T_{\text{irr}})/K_{\text{unirr}}(T)$.

Data have been published for CFCs whose thermal conductivities are similar to nuclear graphites, and show degradation similar to that expected from the graphite literature. For example, Burchell [24] has shown that the saturation thermal conductivity for a 3-directional composite (FMI-222, $K_{\text{unirr}} = 200$ W/m-K) is $\sim 40\%$ of the original room temperature conductivity following fast neutron irradiation at 600°C . Published data for the degradation of thermal conductivity in highly conductive CFCs have led to the conclusion that a higher initial conductivity results in a greater absolute conductivity reduction after irradiation [24, 32]. Figure 7

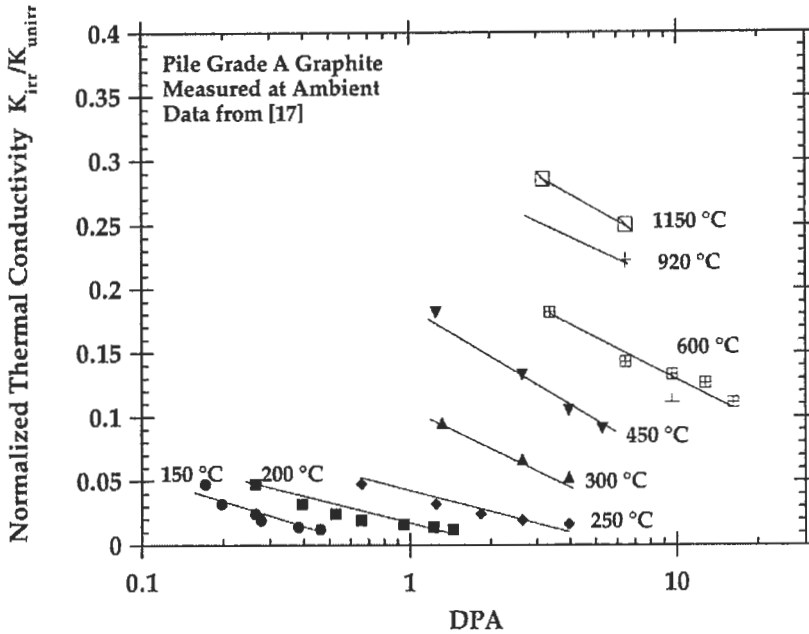


Fig. 6. Normalized thermal conductivity of neutron irradiated pile grade A graphite

demonstrates this point. For the extremely damaging irradiation temperature of $\sim 200^\circ\text{C}$, it is seen in Fig. 7 that the absolute reduction ($K_{unirr} - K_{irr}$) is substantially greater for the high thermal conductivity materials compared to the lower grade CFCs and graphite, although the normalized fraction (K_{irr}/K_{unirr}) is approximately the same for all of the carbon materials in Fig. 7. Moreover, a saturation in thermal conductivity degradation occurs, at a neutron dose of ~ 1 dpa. Data for higher irradiation temperatures [27] shows that the higher thermal conductivity materials have a slightly larger fractional change in thermal conductivity (K_{irr}/K_{unirr}) compared to lower conductivity materials, although the absolute value of the irradiated thermal conductivity is still greater for the higher conductivity materials.

An algorithm has been developed to predict the thermal conductivity degradation for a high thermal conductivity composite (~ 555 W/m-K at room temperature) as a function of radiation dose and temperature [33]. The absence of irradiation data on CFCs of this type required the use of data from intermediate thermal conductivity materials as well as pyrolytic graphite to derive an empirical radiation damage term [14, 17, 19, 25, 26].

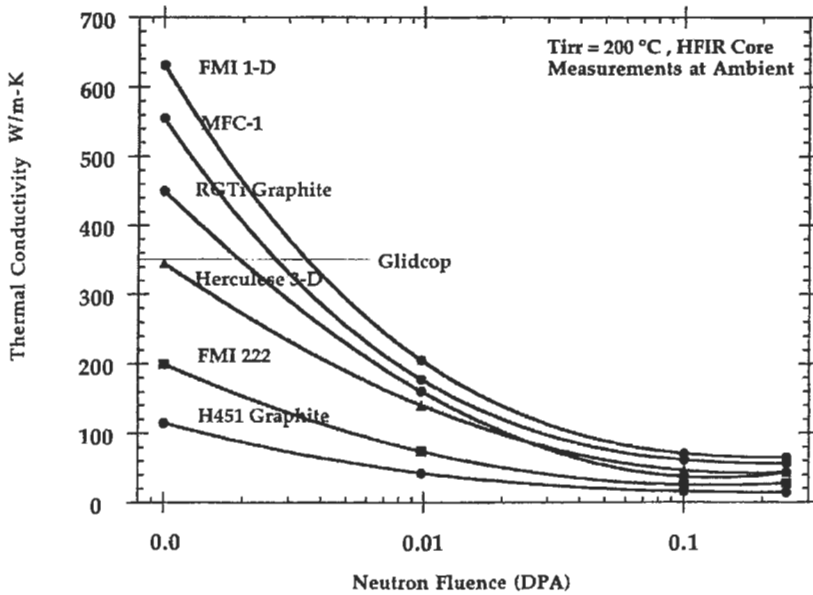


Fig. 7. Irradiation induced thermal conductivity degradation of selected graphite materials.

An analysis of the effects of temperature and neutron dose on the thermal conductivity is shown in Fig. 8. Specifically, the algorithm assumed the unirradiated properties of the unidirectional fiber composite, MKC-1PH, and is coupled with an empirical radiation damage term. As with the experimental data of Figs. 6 and 7, it is seen in Fig. 8 that an enormous loss in thermal conductivity occurs at low irradiation temperatures. Presently, only a few data points exist which are relevant to the validation of this algorithm, and these are also plotted on the Figure [25]. The data agree within the errors of irradiation temperature and thermal conductivity measurement with the algorithm predictions. However, they are insufficient to validate the algorithm and, clearly, the need exists for additional data for this purpose.

To illustrate the usefulness of such an algorithm, and the seriousness of the issue of thermal conductivity degradation to the design and operation of PFCs, the algorithm discussed above has been used to construct Fig. 9 [34], which shows the isotherms for a monoblock divertor element in the unirradiated and irradiated state and the "flat plate" divertor element in the irradiated state. In constructing Fig. 9, the thermal conductivity saturation level of 1 dpa given in Fig. 8 is assumed, and the flat plate and monoblock divertor shown are receiving a steady state flux of

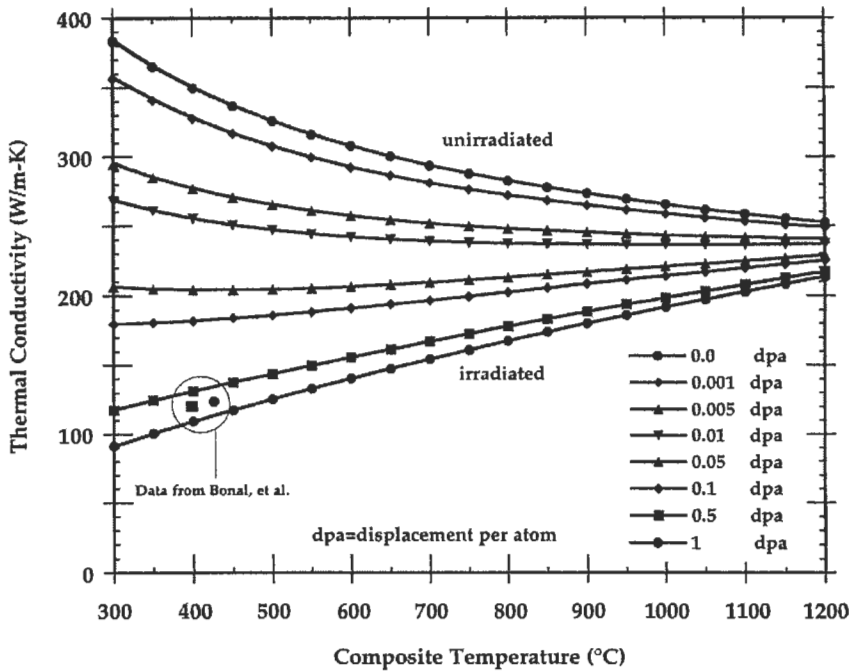


Fig. 8. Calculated thermal conductivity of neutron irradiated MKC-1PH composite.

15 MW/m². Both composite materials have been assumed to be in perfect contact with a copper coolant tube or plate. Figure 9 clearly illustrates two points. First, a very high conductivity composite is required to handle the extreme heat fluxes expected and to limit the surface temperature to < 1200°C (Section 4). Second, the effect of neutron irradiation on the conductivity is significant. For the case of the flat plate divertor the temperature rise (ΔT) changes from ~200 to ~500°C following irradiation, while for the monoblock it increases from ~350 to ~900°C. It should be noted that the larger temperature increase for the monoblock design is not due to the larger path length of graphite in that configuration, but rather to the larger amount of graphite material which is irradiated in the highly damaging low temperature regime (see Figs. 6 or 8). The larger temperature increase for the monoblock design could be unacceptable from an erosion standpoint as will be discussed in Section 4.

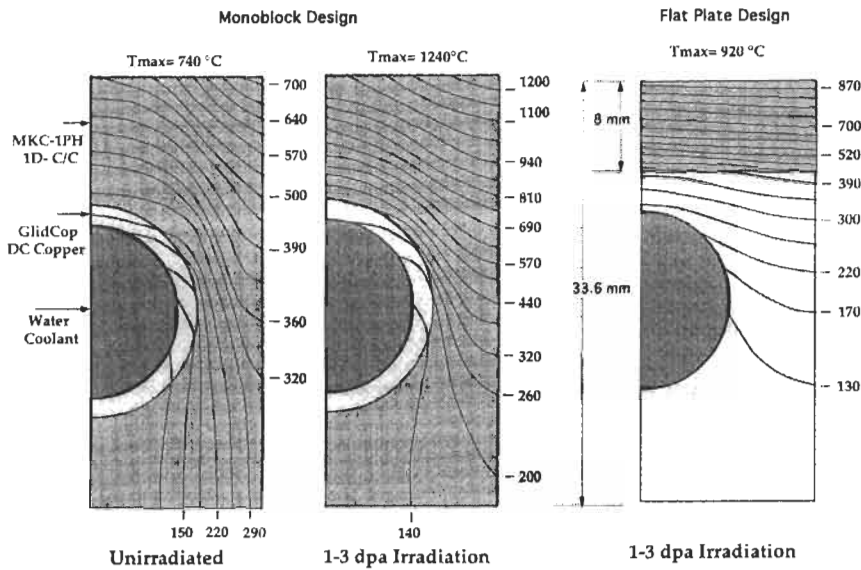


Fig. 9. Temperature contour for irradiated and unirradiated graphite divertor tiles.

Because of the serious thermal conductivity degradation in graphite, operating scenarios which limit this problem (such as baking the PFM) have been considered. Upon annealing above the irradiation temperature, interstitial atoms become mobile and can recombine with the vacancies, restoring the thermal conductivity of the lattice. It is, therefore, conceivable that intermittent annealing of the PFC could regain some of the irradiation-induced thermal conductivity degradation. Bake-outs are typically conducted between operating cycles of a fusion system for plasma impurity (usually oxygen) control. However, the wall conditioning temperatures are typically limited to less than 300°C and for various reasons can not be significantly increased. Inspection of data such as that given in Fig. 10 [33] indicates that little recovery in thermal conductivity is possible unless bake-out temperatures approach 1000°C. Thus, in-situ annealing can be of only marginal benefit.

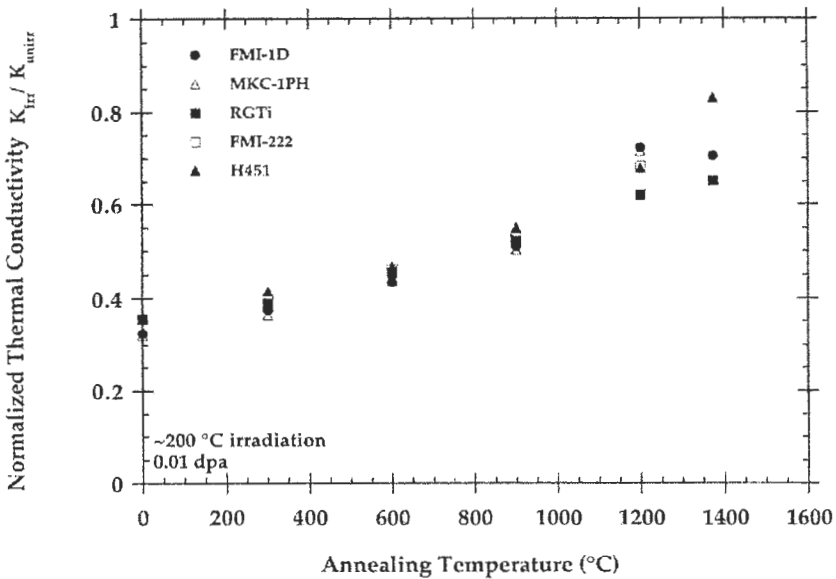


Fig. 10. The effect of annealing on the normalized thermal conductivity of irradiated graphite and graphite composites.

4 Plasma Wall Interactions

A range of particle types, fluxes, and energies strike the PFCs and interact in the near surface region. The most common interactions are with hydrogen fuel ions, which can range in energy from a few eV to hundreds of eV. In addition to hydrogen ions, fuel by-product ions such as helium and impurities from the first wall also impact the surface. Severe surface layer damage occurs because of such ion impacts, and significant erosion of surface material additionally occurs. Various mechanisms are responsible for erosion, depending on the surface temperature of the graphite. The mechanisms can be generally characterized in order of increasing temperature phenomenon as: physical sputtering, chemical erosion, and radiation enhanced sublimation (Fig. 11) [35]. Above 2000°C the vapor pressure of graphite dominates the erosion.

4.1 Physical sputtering

When an impacting particle transfers energy to a near surface carbon atom in an amount sufficient to overcome the lattice bond energy or surface binding energy, some carbon atoms may be displaced and move in a direction defined by the angle

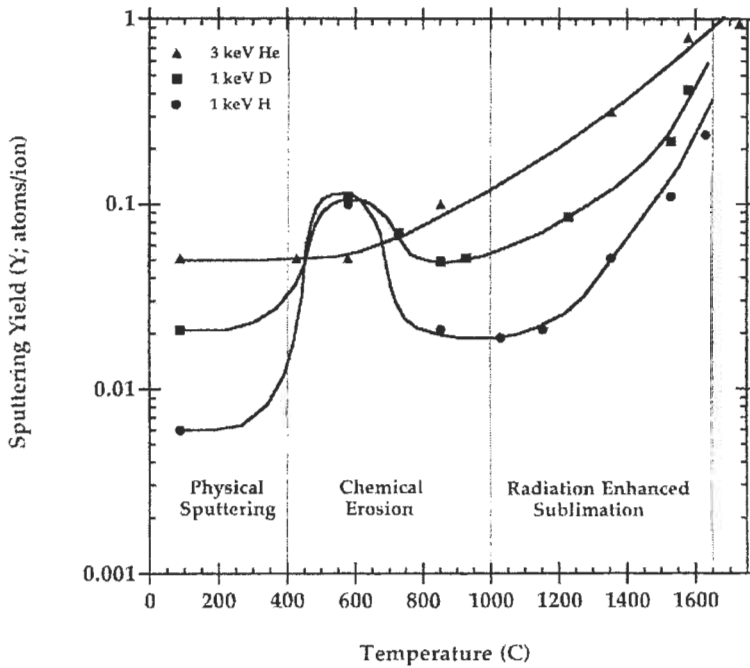


Fig. 11. Sputtering yield as a function of temperature for graphite.

between its path and the initial path of the impacting atom. Analogous to striking a billiard ball, this angle must be between 0 and 90° . The energy imparted to the displaced atom follows the same form as that given in Eq. 6. For an atom striking a surface normally, the recoiling atom can not be sputtered from the surface. However, for an off-normal angle of impact, or when considering displacement cascade events which occurs near the surface, some fraction of atoms will be emitted (physically sputtered) from the graphite surface. The amount of material lost from the surface is defined by the sputtering yield (Y), which is the number of target PFM atoms emitted per plasma ion impacting the surface. From Eq. 6 we see that the energy transferred, and thus the erosion yield, is a strong function of the impacting particle mass and the mass of the material being sputtered. The impact angle also has a large effect on the number of atoms which receive adequate kinetic energy normal to the PFM surface to be physically sputtered. The plasma ions travel along the magnetic field lines which are at a shallow (grazing) angle with the PFM, typically 1 to 5 degrees, and the ion impact angle will be modified by surface potentials and collisional processes.

The quantitative effect of the mass, energy, and angle of impact on the sputter yield for impacting deuterium ions is shown in Figs. 12a and b. As the kinetic energy

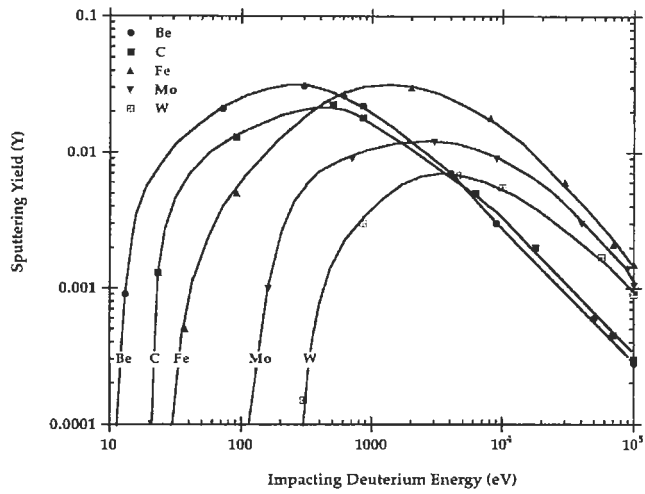
of the deuterium increases the total amount of energy transferred to the target atoms increases, as does the average amount of energy per collision, resulting in greater erosion. From Fig. 12a it may be seen that the physical sputtering yield of light target atoms is considerably greater than for the heavy atoms, primarily due to the reduced impact energy required to overcome the displacement energy of the higher-Z target atoms. For example, approximately 20 eV is required to displace an atom of carbon from the surface, while 220 eV is required for an atom of tungsten. In the sub-keV energy range of plasma fuels, the high yield materials are therefore carbon and beryllium. As the impacting ion energy increases, the sputtering yield for all materials decreases as the depth of interaction of the impacting ion becomes too great for displaced atoms to back scatter to the surface. In the case of graphite, the majority of the displaced material comes from the top few atomic layers [36].

With the correct combination of incident energy and target mass it is possible for the sputtering yield to exceed unity, *i.e.*, more than one atom leaves the surface for every particle impacting it. This quickly leads to what is called the catastrophic "carbon bloom," *i.e.*, self accelerating sputtering of carbon. As can be seen in Fig. 12b, this problem is worst for carbon self-impacts at grazing angles to the surface.

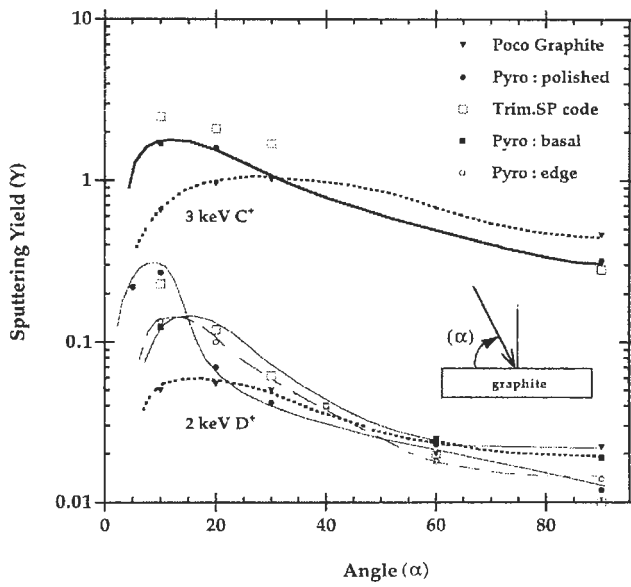
4.2 Chemical erosion

For intermediate temperatures from 400-1000°C (Fig. 11), the volatilization of carbon atoms by energetic plasma ions becomes important. As seen in the upper curve of Fig. 11, helium does not have a chemical erosion component of its sputter yield. In currently operating machines the two major contributors to chemical erosion are the ions of hydrogen and oxygen. The typical chemical species which evolve from the surface, as measured by residual gas analysis [37] and optical emission [38], are hydrocarbons, carbon monoxide, and carbon dioxide.

The interaction of hydrogen with graphite appears to be highly dependent on the ion species, material temperature, and on the perfection of the graphite. This is illustrated in Fig. 13 which shows typical bell shaped erosion yield curves for hydrogen and deuterium. The shape of the yield curve is influenced by the competition for hydrogenation from the sp^2 and sp^3 hybridization states [39-42], and for undamaged pyrolytic yields a relative maxima at ~280-330°C [43]. The lowest curve of Fig. 13 gives the total chemical erosion yield for pyrolytic graphite exposed to hydrogen plasma. The rate of formation of CH_2 , CH_3 , and complex hydrocarbons from atomic hydrogen in well graphitized material is fairly low, unless the material is altered (damaged) in the near surface layer. For pyrolytic graphite which has been pre-irradiated (*i.e.*, damaged) by high energy D^+ or H^+



(a)



(b)

Fig. 12. Sputtering yields for graphite as a function of (a) temperature and (b) incident angle.

ions, the total erosion yield following exposure to low energy hydrogen increases dramatically. This is illustrated in the upper curves of Fig. 13 which shows more than an order of magnitude increase in erosion yield over the undamaged case. This increased carbon loss has been attributed to the creation of active sites for H° attachment [44, 45]. This structurally dependent mechanism is supported by data due to Phillips *et al.* [46] showing a factor of two difference in erosion yield between high and low quality pyrolytic graphite.

Chemical erosion can be suppressed by doping with substitutional elements such as boron. This is demonstrated in Fig. 14 [47] which shows data for undoped pyrolytic graphite and several grades of boron doped graphite. The mechanism responsible for this suppression may include the reduced chemical activity of the boronized material, as demonstrated by the increased oxidation resistance of B doped carbons [48] or the suppressed diffusion caused by the interstitial trapping at boron sites.

Oxygen is the most damaging impurity in current tokamaks because of its presence in the molecular form, or as water vapor, and its tendency to be strongly adsorbed by carbon PFMs. Consequently, oxygen impurities have a large impact on the plasma performance, as well as erosion. It has been clearly demonstrated that the carbon flux away from the first wall is directly related to the evolution of oxygen. Typically, the oxygen enters the plasma from the PFMs in the form of CO or CO₂. Without special PFM surface treatment, such as plasma glow discharge and bake-out of the surface material, these fluxes dominate the surface erosion. For this reason, extensive research has been conducted into modification of graphite surfaces with impressive success in enhanced plasma performance [49]. These improvements are due less to suppressed carbon erosion, than to the decrease in the amount of oxygen released from the graphite. Towards this end, graphites have been modified to incorporate thermally and physically sputter resistant oxides through the formation of carbides with titanium [49], boron [50, 51], beryllium [52], and silicon [53]. A comprehensive review of the hydrogen and oxygen problem is given by Vietzke and Haaz [54], as well as a current article on the surface treatment of graphite wall by Winter [49].

Surface treatments, while extremely effective for the current day short pulse tokamaks (pulses typically less than a few seconds), are of limited value for the next generation (quasi-steady state) machines because of the significant surface erosion expected. However, if the entire graphite PFM were altered, rather than a surface layer, the beneficial effects would be gained regardless of how much erosion occurs. Promising results have been obtained by doping graphite with boron, which is a substitutional element in the graphite lattice and at higher concentrations forms stable carbides, and thus traps migrating interstitials and alters

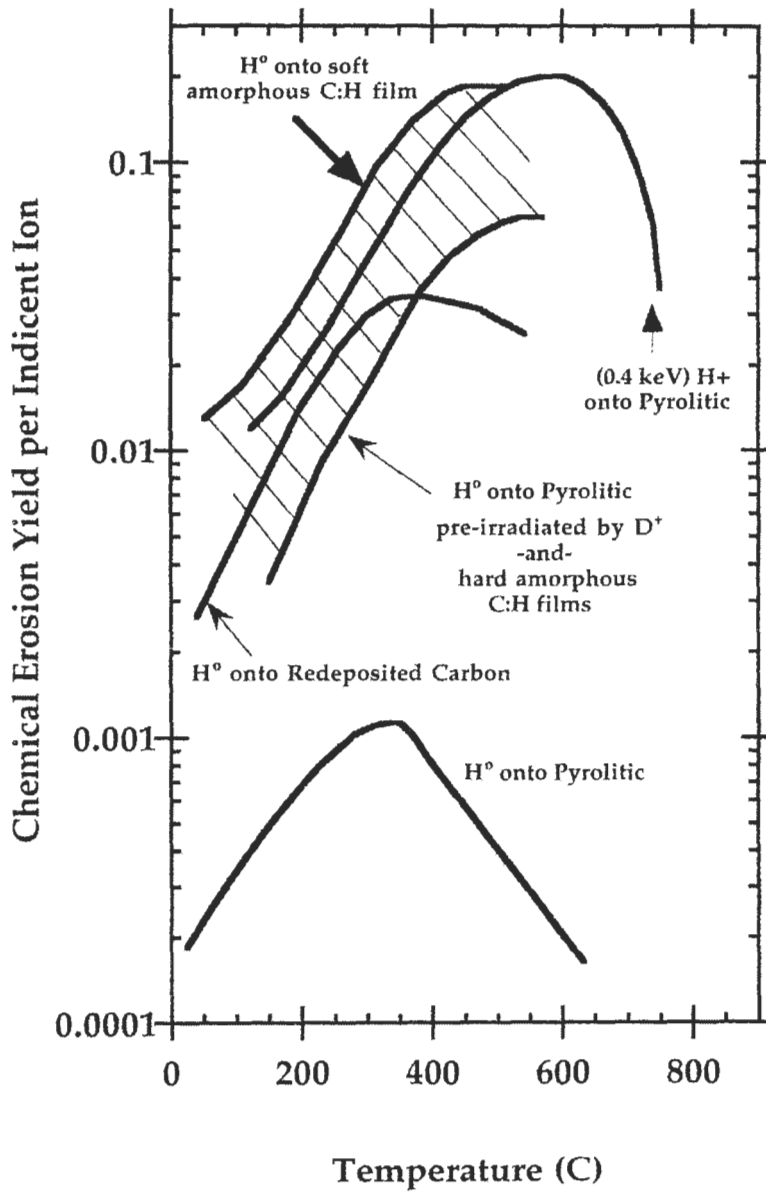


Fig. 13. Chemical erosion yield as a function of temperature for graphite.

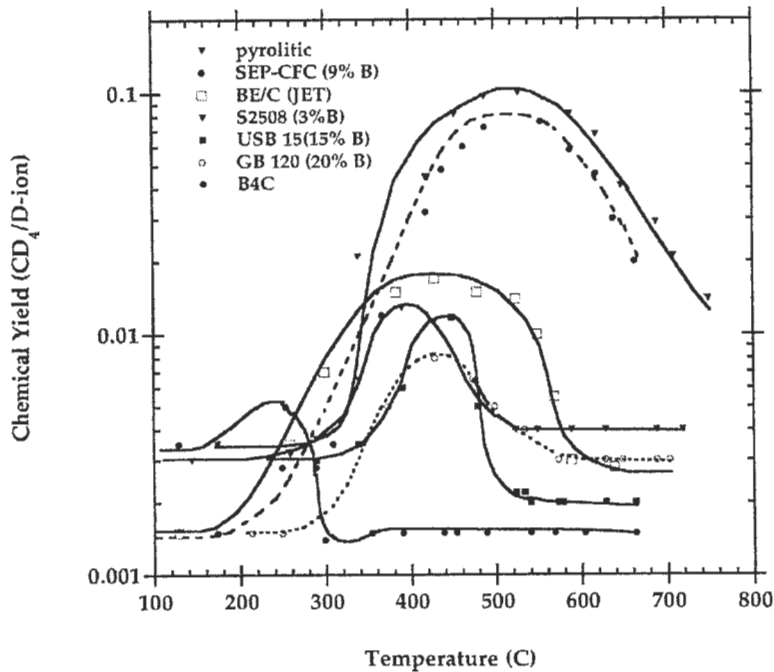


Fig. 14. Chemical yield as a function of temperature for boron doped graphites.

the electronic structure of the material. Boron doping [55] has been shown to both reduce the erosion due to oxygen and to significantly reduce the sputtering yield due to methane formation. However, other factors, such as the drastic reduction in thermal conductivity which occurs in boronized graphite, need to be factored into the overall picture.

4.3 Radiation enhanced sublimation

The limiting temperature for graphite use in fusion systems is defined by thermal sublimation ($\sim 1500\text{--}2000^\circ\text{C}$). However, a process which is very similar to thermal sublimation (in cause and in effect) appears to define the current temperature limit. This phenomenon, which is known as radiation enhanced sublimation (RES), is not clearly understood but dominates above a temperature of about 1000°C and increases exponentially with increasing temperature.

The process responsible for initiating RES follows from the earlier discussion of radiation damage in graphite. Specifically, in a displacement event a Frenkel pair

is created. The interstitial has a low (~ 0.5 eV) migration energy, is quite mobile between the basal planes, and thus diffuses readily. Some fraction of these interstitials recombine at vacancy sites, which are essentially immobile below about 600°C (migration energy ~ 4 eV). Other migrating interstitials can be trapped by microstructural defects or can coalesce into simple clusters, thus limiting their mobility. However, some fraction of the interstitials diffuse to the surface of the graphite and thermally sublime. The thermal sublimation of radiation-induced interstitials is essentially RES, and must be distinguished from both physical and chemical sputtering. Time of flight measurements have shown that the thermal energy of RES ions have a Maxwellian energy distribution, which is directly coupled to the mean surface temperature [56]. This clearly differentiates RES atoms from physically sputtered atoms, which exhibit highly anisotropic energy distributions. RES atoms are also distinguished from thermally sublimed species in that only single carbon atoms are detected, where as single atoms and molecules (C_2 , C_3 , ...) are found during thermal sublimation.

The effect of RES in the next generation of high surface particle flux fusion systems is presently unclear. Evidence suggests that the erosion yield does not scale linearly with flux, as physical sputtering does, but may in fact decrease significantly with increasing flux [57]. Moreover, as with chemical erosion, the inclusion of interstitial boron into the crystal lattice decreases RES and shifts the threshold to higher temperatures. Boron will volatilize above $\sim 1500^\circ\text{C}$, thus limiting the PFM temperature to $< 1500^\circ\text{C}$.

4.4 Erosion of graphite in simulated disruption events

The effect of plasma disruptions also needs to be considered. Section 2.3 discussed the thermomechanical response of the PFCs to the excessive plasma energy during a disruption. This large thermal energy dump can additionally cause enhanced erosion due to the increased particle flux, elevated surface temperature, or simply by exfoliation of the surface due to thermal shock. The latter two material losses are reduced for materials with high thermal conductivity. This has been demonstrated experimentally, and is shown in Fig. 15 [1], which gives the weight loss as a function of thermal conductivity for a number of graphites and composites of differing thermal conductivities subjected to one electron beam pulse at 4.1 MW/m^2 . As was discussed in Sections 2.3 and 2.4, and as seen in the data in Fig. 15, high thermal conductivity materials reduce the surface temperature and hence the overall erosion yield during a disruption.

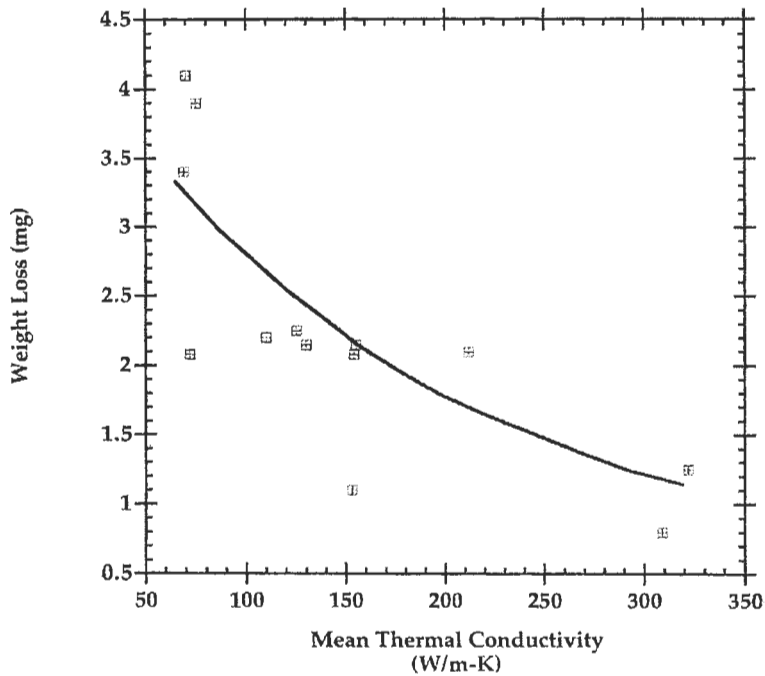


Fig. 15. Weight loss as a function of mean thermal conductivity of graphite.

5 Tritium Retention in Graphite

In the previous section the interaction of the plasma particle flux with the surface of graphite was discussed. However, the fate of the implanted particles (most importantly deuterium and tritium) following their impact with the graphite surface is also an important issue, and is seen by some as the major impediment to graphite's use as a PFM [58]. Quantification of the problem, and determination of possible mitigating steps, is complicated by experimental data which can vary by orders of magnitude [59-66] as reviewed by Wilson [67].

The physical process involved in the retention of hydrogen, as it corresponds to graphite PFMs, is fairly well understood. The energetic hydrogen isotopes are implanted to depths of less than a micron in the PFM surface. Once implanted, the hydrogen ions are either trapped, re-emitted, or diffused through the bulk graphite. At temperatures less than 100°C [68-72] the majority of ions are trapped near the end of their range. These trapped ions are not in solution in the graphite, but are

held [73] in the highly defective structure. The amount of hydrogen isotope which can be accommodated is largely dependent on implantation temperature [72, 74] and to a lesser extent by implantation depth [70, 71]. The total retained isotopic H can reach as much as 0.4-0.5 H/C in the implanted layer at room temperature [68, 71, 75].

As the amount of implanted hydrogen increases toward its saturation value, a larger fraction of ions are released from the graphite surface. None of these reemitted atoms become trapped in unsaturated regions. For intermediate and high temperatures ($>250^{\circ}\text{C}$) diffusion of hydrogen in the graphite lattice occurs. This in-lattice diffusion most likely occurs along internal surfaces, such as micro-pores and micro-cracks, while transgranular diffusion has been seen above 750°C [76, 77]. This bulk diffusion, along with the associated trapping of hydrogen at defect sites, has been studied widely with quite variable results. This variation is shown in Fig. 16 where the temperature dependence of the hydrogen diffusion coefficient is shown for several carbon and graphite materials.

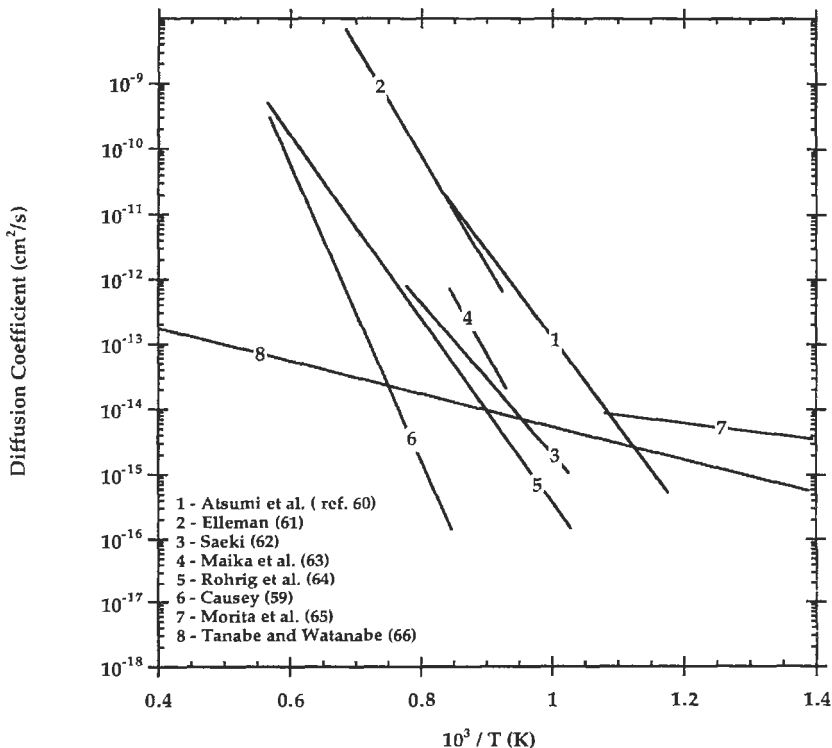


Fig. 16. Hydrogen diffusion coefficient as a function of inverse temperature.

It would be expected that the diffusion of hydrogen through graphite would be highly dependent on the graphite microstructure, which may explain the wide range of the data of Fig. 16. In any event, the transport of hydrogen through the bulk graphite and associated solubility limits, can significantly increase the hydrogen inventory. The effect of the perfection of graphitic structure on the solubility of hydrogen is shown by Atsumi's data [78] in Fig. 17 which indicates that the more defect-free, highly-graphitized material has a lower solubility limit. Further evidence for the role of structural perfection comes from the observation that material which has been disordered by neutron irradiation has significantly higher solubility for hydrogen [78,79].

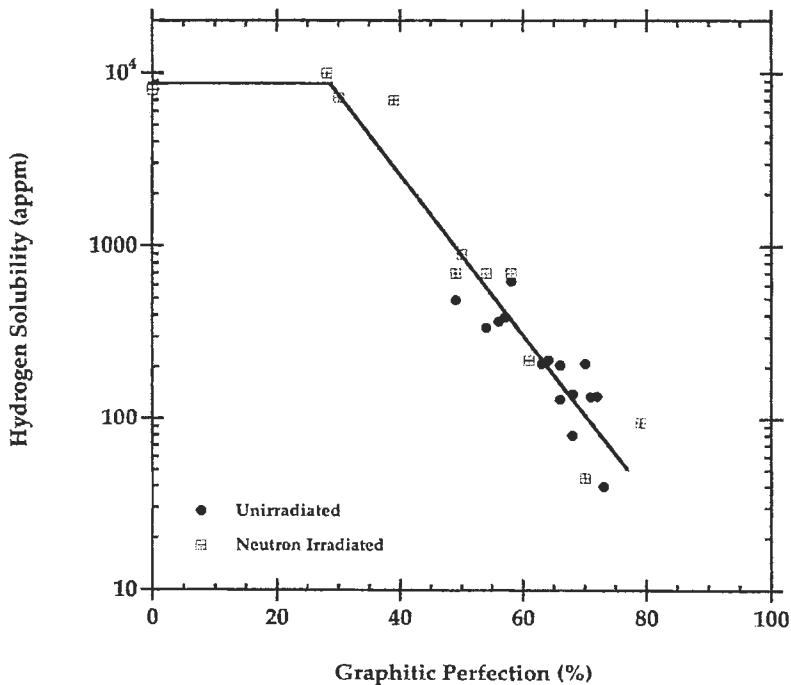


Fig. 17. Hydrogen solubility as a function of graphitic perfection.

The effect of atomic displacements on the hydrogen retention of graphite was first shown by Wampler using 6 MeV ion beams [80]. Wampler used four types of intermediate and high-quality graphites and irradiated with a high energy carbon beam at room temperature, followed by exposure to deuterium gas. Wampler's results indicated that the residual deuterium concentration increased by more than a factor of 30 to 600 appm for displacement doses appropriate to ITER. However, for reasons that are not yet clear, neutron irradiated high-quality CFCs retain

significantly less tritium than would be expected from the earlier work. This was reported by Atsumi [78] and is clearly shown by the recent work of Causey [81] (Fig. 18). Causey irradiated high thermal conductivity MKC-1PH unidirectional composite and FMI-222 3D composite at $\sim 150^\circ\text{C}$ (a particularly damaging irradiation temperature regime) to a range of displacement doses up to 1 dpa. As is seen in Fig. 18 the tritium retention is greater than one order of magnitude less than expected from earlier work on GraphNOL-N3M [82].

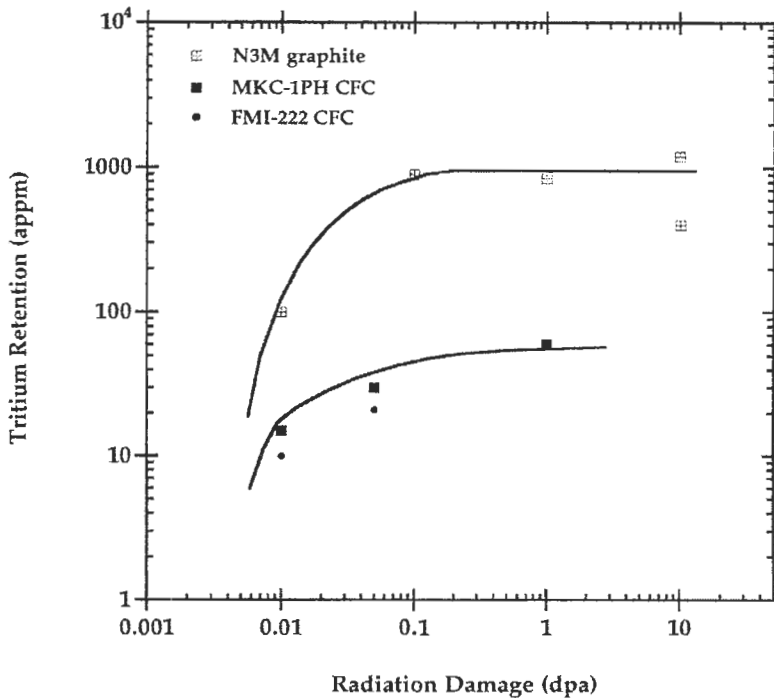


Fig. 18. Tritium retention as a function of neutron damage in graphite and graphite composite.

The primary concern related to fuel retention in the PFC is the inventory of hydrogen adsorbed into the graphite and subsequent release of near surface hydrogen (due to sputtering) as plasma discharge begins. The hydrogen sputtered from the wall oversupplies the plasma edge with fuel, causing instabilities and making plasma control problematic. Tritium inventory concerns are generally safety related, but can have significant economic consequences because of the high cost of tritium. The potential release to the environment in an accident situation has limited the allowed inventory in TFTR, and may have significant consequences

for the sighting of the ITER. It has been estimated [58] that as much as ~1.5 kg of tritium would reside in the graphite PFM of ITER, corresponding to an additional fuel cost of 1.5 to 3 million dollars.

A source of trapped hydrogen which has not been discussed to this point, and which may dominate the tritium inventory in ITER-like machines, is the "co-deposited layer" [58,83]. This layer is formed by the simultaneous deposition of carbon, which is eroded from the first wall, and hydrogen. Thick layers of carbon redeposited to low erosion areas are common, and have been seen in every large tokamak utilizing graphite PFMs. As this layer grows, the hydrogen contained therein cannot be liberated by surface sputtering and becomes permanently trapped. This problem is unique to graphite and will require continual surface conditioning to minimize the total inventory of trapped species.

6 Summary and Conclusions

Carbon and graphite materials have enjoyed considerable success as plasma-facing materials in current tokamaks because of their low atomic number, high thermal shock resistance, and favorable properties. However, their use is not without problems and their application in next generation fusion energy devices is by no means certain. Significant amongst the issues for carbon and graphite PFMs are: neutron irradiation damage, which degrades the thermal conductivity and causes increased PFC surface temperatures; physical sputtering, chemical erosion, and radiation enhanced sublimation, which results in surface material loss to the plasma, and redeposition of carbon; and tritium inventory, which poses both a safety problem and an economic impediment to the use of graphite. The high-heat loads and surface temperature that occur after plasma disruptions are also problematic for carbons. However, the same high temperatures make the use of Be, which has a significantly lower melting temperature, very unlikely.

Next generation machines will impose increasingly greater thermal loads on their PFCs. High thermal conductivity CFC materials may offer a solution to the high-heat loads, but further research is needed to overcome the problems noted above and to assure the place of carbon materials in future fusion power reactors.

7 Acknowledgments

Research sponsored by the U.S. Department of Energy under contract DE-AC05-96OR22464 with Lockheed Martin Energy Research Corporation at Oak Ridge National Laboratory.

8 References

1. M. Akiba and H. Madarame, *J. Nucl. Mat.*, 212-215, 90-96 (1994).
2. R.D. Watson, *et al.*, *High Heat Flux Testing of CIT First Wall Tiles*, 1988.
3. G.H. Kinchin and R.S. Pease, *Rep. Phys. Prog. Phys.*, 18 (1) (1955).
4. J.W.H. Simmons, *Radiation Damage in Graphite*, Pergamon Press, (1965).
5. C.R. Kennedy. In *Extended Abstracts for 14th Biennial Conference on Carbon*, 1979, Irvine, California.
6. B.T. Kelly, *Physics of Graphite*, Applied Science Publishers (1981).
7. G.B. Engle, *Carbon*, 12, 291-306 (1974).
8. T.D. Burchell and W.P. Eatherly, *J. Nucl. Mat.*, 179-181, 205-208 (1991).
9. T.D. Burchell, *Radiation Damage in Carbon Materials*. In *Physical Processes of the Interaction of Fusion Plasmas with Solids*, W.O. Hofer and J. Roth, Eds., 1996, Academic Press, pp. 341-382.
10. T.D. Burchell and T. Oku, *Materials Properties Data for Fusion Reactor Plasma Facing Carbon-Carbon Materials*. *Nuclear Fusion*, 1994 5(Suppl.), 77-128.
11. H.H. Yoshikawa, *et al.*, *Radiation Damage in Reactor Materials*, 1963.
12. M. Eto, *et al.*, *J. Nucl. Mat.*, 212-215, 1223-1227 (1994).
13. L. Ahlf, *et al.*, *J. Nucl. Mat.*, 171, 31 (1990).
14. L. Binkelc, *High Temp. High Pressures*, 4, 401 (1972).
15. J. Price, *Thermal conductivity of neutron-irradiated reactor graphites*, 1974, General Atomics.
16. B.T. Kelly, *et al.*, *J. Nucl. Mat.*, 20, 195-209 (1966).
17. R. Taylor, B.T. Kelly, and L.E. Gilchrist., *Chem Solids*, 30, 2251-2267 (1969).
18. R.W. Henson and W.N. Reynolds, *Carbon*, 3, 277-287 (1965).
19. B. Thiele, *et al.* In *ASTM. Proc. 16th Int. Symp. on Effects of Radiation on Materials*, 1992.
20. B.T. Kelly, P. Schofield, and R.G. Brown, *Carbon*, 28, 155-158 (1990).
21. B.T. Kelly, *Carbon*, 15, 117-127 (1977).
22. B.T. Kelly, *Carbon*, 5, 247-260 (1967).
23. B.T. Kelly and J.E. Brocklehurst, *Carbon*, 9, 783 (1971).
24. T.D. Burchell, W.P. Eatherly, and J.P. Strizak. In *Effects of Radiation on Materials 16th International Symposium ASTM, STP 1175*, eds. A. S. Kumar, D. S. Gelles, R. K. Nandstad, and E. A. Little. Philadelphia, 1993.
25. C.H. Wu, J.P. Bonal, and B. Thiele, *J. Nucl. Mat.*, 212-215, 1168 (1994).
26. T. Maruyama and M. Harayama, *J. Nucl. Mat.*, 195, 44-50 (1992).
27. J.P. Bonal and C.H. Wu, *J. Nucl. Mat.*, 228, 155-161 (1996).
28. J. Heremans and C.P. Beetz, *Phys. Rev. B*, 32, 1981 (1981).
29. A. DeCombarieu, *J. Phys. (France)*, 28, 931 (1968).
30. R. Taylor, *Phil. Mag.*, 13, 157 (1966).
31. B.T. Kelly, *Plot constructed from personally communicated data*
32. L.L. Snead and T.D. Burchell, *J. Nucl. Mat.*, 224, 222-229 (1995).
33. L.L. Snead and T.D. Burchell, *Carbon Extended Abstracts*, 774-775 (1995).
34. R.A. Vesey, *Unpublished Data*, 1995.
35. J. Roth, J. Bohdansky, and K.L. Wilson, *J. Nucl. Mat.*, 111-112, 775 (1982).
36. P. Sigmund, *et al.*, *Nucl. Instrum. Meth.*, B36, 110 (1989).
37. W. Poschenrieder, *J. Vac. Sci. Technol.*, A 5, 2265 (1987).
38. A. Pospiesznyk, . *Atomic and Plasma Material Interaction Processes in Controlled*

- Thermonuclear Fusion. Amsterdam, Elsevier (1993).
39. C. Lutterloh, *et al.*, *Surf. Sci.*, 316, L1039 (1994).
 40. J. Biener, *PhD Thesis*. 1994, University of Bayreuth.
 41. A. Horn, *et al.*, *Chem. Phys. Lett.*, 231, 193 (1994).
 42. A. Schenk, *et al.*, *Appl. Phys. Lett.*, 61 (1992).
 43. J.W. Davis, A.A. Haasz, and P.C. Stangeby, *J. Nucl. Mat.*, 155-157, 237 (1988).
 44. J. Roth, E. Vietzke, and A.A. Haasz, Erosion of Graphite Due to Particle Impact. In *Supplement of the Journal of Nuclear Fusion*, 1991, IAEA.
 45. A.A. Haasz, *et al.*, *J. Nucl. Mat.*, 128-129, 593 (1984).
 46. V. Phillips, K. Flashkamp, and J. Vietzke, *J. Nucl. Mat.*, 122-123, 1440 (1984).
 47. J. Roth, *et al.*, *J. Nucl. Mat.*, 191-194, 45-49 (1992).
 48. L.E. Jones and P.A. Thrower, *Carbon*, 29, 251 (1991).
 49. J. Winter, *Plasma Phys. Contr. Fus.*, 36, B263 (1994).
 50. J. Winter, *et al.*, *J. Nucl. Mat.*, 163-164, 713 (1989).
 51. G.L. Jackson, *J. Nucl. Mat.*, 196-198, 236 (1992).
 52. P.R. Thomas, *et al.*, *J. Nucl. Mat.*, 176-177, 3 (1990).
 53. J. Winter, *et al.*, *Phys. Rev. Lett.*, 71, 1549 (1993).
 54. E. Vietzke and A.A. Haasz, Chemical Erosion. In *Physical Processes of the Interaction of Fusion Plasmas with Solids*, W.O. Hofer and J. Roth, Eds., 1996, Academic Press, pp. 135-176.
 55. Y. Hirooka, *et al.*, *J. Nucl. Mat.*, 176-177, 473-480 (1990).
 56. E. Vietzke, *et al.*, *Nucl. Instrum. Meth.*, B2, 617 P.L. Andrew and M.A. Pict, *J. Nucl. Mat.*, 212-215, 111 117 (1994).
 57. W. Eckstein and V. Philipps, Physical Sputtering and Radiation-Enhanced Sublimation. In *Physical Processes of the Interaction of Fusion Plasmas with Solids*, W.O. Hofer and J. Roth, Eds., 1996, Academic Press, pp. 93-134.
 59. R.A. Causey, *J. Nucl. Mat.*, 162-164, 151 (1989).
 60. H. Atsumi, S. Tokura, and M. Miyake, *J. Nucl. Mat.*, 155-157, 241 (1988).
 61. T.S. Elleman, (General Atomics, San Diego, CA). Unpublished work, .
 62. M. Saeki, *J. Appl. Radiat. Isot.*, 43, 739 (1983).
 63. V. Malka, H.D. Rohrig, and R. Hecker. In *Tritium Technology in Fission, Fusion, and Isotope Application*, Proc. Conf., Dayton, OH (1980).
 64. H.D. Rohrig, P.G. Fischer, and R. Hecker, *J. Am. Ceram. Soc.*, 59, 316 (1976).
 65. K. Morita, K. Ohtsuka, and Y. Hasebe, *J. Nucl. Mat.*, 162-164, 990 (1989).
 66. T. Tanabe and Y. Watanabe, *J. Nucl. Mat.*, 176 (1990).
 67. K. L. Wilson, *et al.*, *Trapping, Detrapping and Release of Implanted Hydrogen Isotopes*, 1991, IAEA.
 68. R.A. Langley, R.S. Brewer, and J. Roth, *J. Nucl. Mat.*, 76-77, 313 (1978).
 69. P. Borgesen, P. Bottiger, and J. Möller, *J. Nucl. Mat.*, 49, 509 (1978).
 70. W.R. Wampler, D.K. Brice, and C.W. Magee, *J. Nucl. Mat.*, 102, 304 (1981).
 71. W.R. Wampler and C.W. Magee, *J. Nucl. Mat.*, 103-104, 509 (1981).
 72. M. Braun and B.J. Emmoth, *J. Nucl. Mat.*, 128-129, 657 (1984).
 73. W. Möller and B.M.U. Scherzer, *J. Appl. Phys.*, 64(10), 4860-4866 (1988).
 74. B.L. Doyle, W.R. Wampler, and D.K. Bryce, *J. Nucl. Mat.*, 103-104, 513 (1981).
 75. B.M.U. Scherzer, *et al.*, *J. Nucl. Mat.*, 63, 100 (1976).
 76. K.L. Wilson and W.L. Hsu, *J. Nucl. Mat.*, 145-147, 121 (1987).
 77. R.A. Causey, M.I. Baskes, and K.L. Wilson, *J. Vac. Sci. Tech.*, A4, 151 (1986).
 78. H. Atsumi, M. Iseki, and T. Shikama, *J. Nucl. Mat.*, 212-215, 1478-1482 (1994).

79. H. Kwast, *et al.*, *J. Nucl. Mat.*, 212-215, 1472-1477 (1994).
80. W.R. Wampler, *et al.*, *J. Nucl. Mat.*, 176-177, 983-986 (1990).
81. R.A. Causey, *et al.*, *Physica Scripta*, T64, 32-35 (1996).
82. R.A. Causey, *et al.*, *Fus. Tech.*, 19, 1585 (1991).
83. W.L. Hsu and R.A. Causey, *Vac. Sci. Tech.*, A5, 1768 (1987).

CHAPTER 13

Fission Reactor Applications of Carbon

TIMOTHY D. BURCHELL

*Metals and Ceramics Division**Oak Ridge National Laboratory**Oak Ridge, Tennessee 37831-6088, USA***1 The Role of Carbon Materials in Fission Reactors***1.1 Nuclear fission - basic concepts*

Nuclear (fission) reactors produce useful thermal energy from the fission (or disintegration) of isotopes such as ${}_{92}\text{U}^{235}$, ${}_{92}\text{U}^{233}$, and ${}_{94}\text{Pu}^{239}$. Fission of a heavy element, with release of energy and further neutrons, is usually initiated by an impinging neutron. The fission of ${}_{92}\text{U}^{235}$ may be written:



The two fission fragments "A" and "B" will vary over a range of mass numbers from about 74 to 160, there being a whole range of possible reactions. Although an integral number of neutrons is emitted for any one fission, the average yield per fission (when all possible methods of fission are considered) is about 2.5 neutrons. The neutrons emitted by the fission reactions can be described by a Maxwellian distribution in energy, with a mean value of about 2 MeV. The total amount of energy given up per atom fissioned is of the order of 200 MeV, which is distributed approximately as indicated in Table 1.

Table 1. Energy distribution from the fission of a U^{235} atom [1]

Nuclear Process	Energy (McV)
Kinetic energy of fission fragments	170
Instantaneous γ -rays	6
Kinetic energy of fission neutrons	6
Radioactive decay of fission fragments, β energy	5
Radioactive decay of fission fragments, γ energy	5

The exact distribution of energies will depend upon the actual fission fragments produced. However, it can be seen from Table 1 that the bulk of the energy is obtained as kinetic energy of the fission fragments, which is degraded to heat by successive collisions within the body of the uranium fuel mass in which the fission took place. Moreover, a significant fraction of the heat is produced outside the fuel. The fission neutrons give up their kinetic energy by elastic collisions, typically within the moderator, and the γ -ray energy is absorbed by the bulk of the reactor materials outside of the fuel (moderator, pressure vessel, and shielding). Finally, some of the energy release occurs slowly, through the radioactive decay of fission products. This heat release is not, therefore, instantaneously available in new fuel, but will build up with irradiation until the production of new fission products by neutron bombardment just balances their radioactive decay. Conversely, with irradiated fuel, there is a significant release of radioactive decay heat after irradiation is finished (after-heat).

Neutron reaction cross-sections (the probability of a given nuclear reaction taking place) are functions of neutron velocity (energy). Most cross-sections increase as neutron velocity (v) decrease, following a $1/v$ law, i.e., the longer a neutron dwells in the vicinity of a nucleus as it passes, the more probable it is that it will react with that nucleus. It is, therefore, advantageous in the operation of a nuclear reactor to slow the fission neutrons (referred to as "fast" neutrons) to lower (thermal) energies (~ 0.025 eV at room temperature), corresponding to a neutron velocity of 2.2×10^5 cm/s. The slowing down (or thermalization) process is also termed "moderation". In a thermal reactor the fission neutrons leave the fuel with high energy, i.e., they are fast neutrons, and are slowed down outside the fuel in a non-absorbing medium called a "moderator." The nuclear fuel is a mixture of ${}_{92}\text{U}^{238}$, ${}_{92}\text{U}^{235}$, and ${}_{92}\text{U}^{234}$. Natural uranium contains the isotopes ${}_{92}\text{U}^{238}$, ${}_{92}\text{U}^{235}$, and ${}_{92}\text{U}^{234}$ in the proportions 99.282, 0.712, and 0.006%, respectively. ${}_{92}\text{U}^{235}$ will undergo fission on capturing a neutron of any energy but, as discussed above, it is more likely to capture low-energy (slow) neutrons. ${}_{92}\text{U}^{238}$ will undergo fission with neutrons of energy > 1.1 MeV, and will capture (absorb) intermediate energy neutrons to form ${}_{94}\text{Pu}^{239}$. Once thermalized (moderated) the neutrons may be returned to the fuel, where they are unlikely to be captured by ${}_{92}\text{U}^{238}$, but will most probably cause fission in the ${}_{92}\text{U}^{235}$. Additionally, mixtures of fissile and fertile fuel have been utilized. In such cases, neutron absorption converts the "fertile" fuel (such as thorium) to a fissile fuel. A thermal reactor may, therefore, be fueled with natural uranium or, if the structural materials of the reactor absorb too many neutrons, slightly enriched (in ${}_{92}\text{U}^{235}$) uranium.

1.2 Requirements of a good moderator

A good moderator should possess the following properties:

- (i) The moderator must not react with neutrons because if they are captured in the moderator they are lost to the fission process, leading to an inefficient reactor.
- (ii) Neutrons should be slowed down over short distances and with few collisions in the moderator, i.e., the average neutron-moderator collision must lead to a large neutron energy loss. The chance of neutron capture by U^{238} resonances, moderator impurities, or by absorbing reactor structural materials is thus reduced. The resultant efficient neutron economy and physically small reactor help to minimize construction costs.
- (iii) The moderator should be inexpensive, yet must have satisfactory structural properties.
- (iv) The moderator must be compatible with the other structural materials used in the construction of the reactor. It should not corrode or erode, even under the influence of radiation.
- (v) The moderator must not undergo deleterious physical or chemical changes when bombarded with neutrons.

A good moderator must efficiently thermalize fast neutrons. This thermalization process occurs by neutron-nucleus elastic collisions. It can be shown from a simple consideration of Newton's laws that maximum energy loss per collision occurs when the target nucleus has unit mass, and tends to zero energy loss for heavy target elements. Low atomic weight (Z) is thus a prime requirement of a good moderator. The maximum energy is always lost in a head-on collision. However, elastic collisions occur at many scattering angles, and thermalization takes place over numerous collisions. Therefore, a useful quantity in characterizing the scattering properties of a moderator is the average logarithmic energy loss per collision, ξ , which is independent of energy. Values of ξ and n , the average number of collisions to thermalize a 2 MeV fast neutron to 0.025 eV, are given in Table 2.

Table 2. Scattering properties of some nuclei [1]

Element	Z	ξ	n
Hydrogen	1	1.000	18
Deuterium	2	0.725	25
Helium	4	0.425	43
Lithium	7	0.268	67
Beryllium	9	0.208	87
Carbon	12	0.158	114
Oxygen	16	0.120	150
Uranium	238	0.0084	2150

The parameter ξ gives a good indication of a material's moderating ability, but it is not entirely dependable. For example, as shown in Table 2, hydrogen is a good moderator based on its high ξ value yet, because it is a gas of low density, the chance of a collision between a neutron and a hydrogen nucleus would be small. Evidently, we must take account of the number of atoms per unit volume of moderator, and of the chances of a scattering collision taking place. Thus, when assigning orders of merit to moderators the *slowing-down power* is frequently used, which accounts for the average energy loss per collision, the number of atoms per unit volume, and the scattering cross section of a moderator. A complete picture of moderator nuclear performance requires a comparison of its *slowing-down power* (which should be large) with its tendency to capture neutrons (capture cross section) which should be small. Thus, the ratio of the *slowing-down power* to the macroscopic absorption cross section, which is referred to as the *Moderating ratio*, should also be considered when evaluating potential moderators. Table 3 reports the *slowing-down power* and *moderating ratio* of several potential moderators.

Table 3. Properties of good moderators [1]

Moderator	Slowing-down power, cm ⁻¹	Moderating ratio
H ₂ O	1.530	72
D ₂ O	0.370	12,000
Be	0.176	159
Graphite	0.064	170

In summary, it is evident that the only moderators of merit are based on elements of low atomic weight. Practically, this limits the choice to elements of atomic number less than sixteen. Gases are of little use as moderators because of their low density, but can be used effectively in chemical compounds such as H₂O and D₂O. The choice of potential moderators of practical use thus rapidly reduces to the four materials shown in Table 3. Comparing the candidate moderators in Table 3 with our requirements listed above we may note:

Water is low cost, easily contained, and is relatively unaffected by neutron irradiation. However, neutron absorption by the hydrogen reduces the moderating ratio. Consequently, water moderated reactors use enriched (in U²³⁵) fuel to achieve the required neutron economy. *Heavy water* or *deuterium oxide* is a particularly good moderator because ¹H² and ⁸O¹⁶ do not absorb neutrons. The slowing-down power is high and the moderating ratio is exceptionally high. *Heavy water* is easy to handle, but the cost of separating the heavy isotope of hydrogen from ordinary hydrogen is high. Thus, initial capital cost and leakage make-up costs are high. *Beryllium* or *beryllium oxide* are good moderators, but suffer from

the disadvantage that they are expensive, hard to machine and work, and are highly toxic. Finally, *carbon* is an acceptable moderator that has been used extensively in the form of graphite. It offers an acceptable compromise between nuclear properties, cost, and utility as a structural material for the reactor core. However, the use of graphite as a moderator is not without its problems. The structure and properties of graphite are greatly affected by neutron irradiation, as will be discussed in detail later in this chapter.

1.3 Graphite manufacture

Having established that carbon (in the form of graphite) is an acceptable nuclear moderator, it is appropriate to briefly describe the process by which graphite is manufactured. Detailed accounts of the manufacture of polygranular graphite have been published elsewhere [2-5]. The major processing steps in the manufacture of a conventional polygranular graphite are summarized in Fig. 1. Polygranular graphite consists of two phases: a filler material and a binder phase. The predominant filler material, particularly in the U.S.A, is a petroleum coke made by the delayed coking process. European nuclear graphites are typically made from a coal-tar pitch-derived coke. In the U.K., a Gilsonite coke derived from a naturally occurring bitumen found in Utah, U.S.A., has been used. The coke is usually calcined (thermally processed) at $\sim 1300^{\circ}\text{C}$ prior to being crushed and blended. Typically, the binder phase is a coal-tar pitch. The binder plasticizes the filler coke particles so that they can be formed. Commonly used forming processes include extrusion, molding, and isostatic pressing. The binder phase is carbonized during the subsequent baking operation ($\sim 1000^{\circ}\text{C}$). Frequently, engineering graphites are pitch impregnated to densify the carbon artifact, followed by rebaking. Useful increases in density and strength are obtained with up to six impregnations, but two or three are more typical.

The final stage of the manufacturing process is graphitization ($2500\text{-}3000^{\circ}\text{C}$) during which, in simplistic terms, carbon atoms in the baked material migrate to form the thermodynamically more stable graphite lattice. Nuclear graphites require high chemical purity to minimize neutron absorption. Moreover, certain elements catalyze the oxidation of graphite and must be reduced to an acceptable level. This is achieved by selecting very pure cokes, utilizing a high graphitization temperature ($>2800^{\circ}\text{C}$), or by including a halogen purification stage in the manufacture of the cokes or graphite. In its perfect form, the crystal structure of graphite (Fig. 2) consists of tightly-bonded (covalent) sheets of carbon atoms in a hexagonal lattice network [6]. The sheets are weakly bound with van der Waals type bonds in an ABAB stacking sequence with a separation of 0.335 nm. The crystals in a manufactured, polygranular graphite are less than perfect, with approximately one layer plane in every six constituting a stacking fault. The graphite crystals have two distinct dimensions, the crystallite size L_a measured parallel to the basal plane

and the dimension L_c measured perpendicular to the basal planes. In a coke-based nuclear graphite, values of $L_a \sim 80$ nm and $L_c \sim 60$ nm are typical [7].

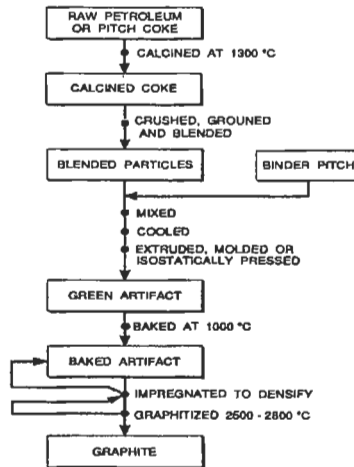


Fig. 1. The major processing steps in the production of a conventional polygranular graphite.

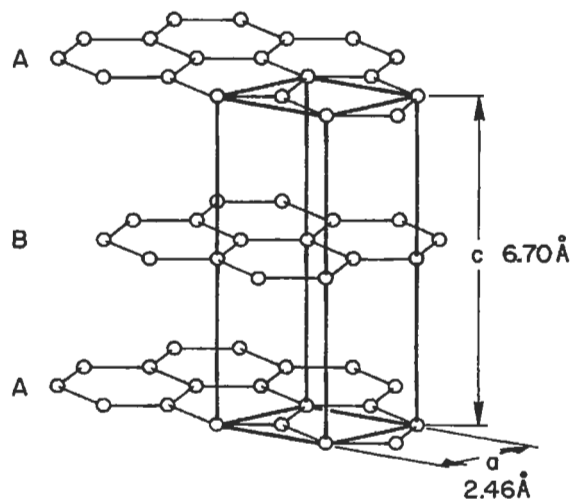


Fig. 2. The crystal structure of graphite.

Typical nuclear graphite microstructures are shown in Fig. 3. The Gilsonite filler coke used in IM1-24 graphite [Fig. 3(b)] is clearly visible. High density graphite (HDG) and pile grade A (PGA) graphites, (a) and (d) in Fig. 3 respectively, contain a needle coke filler, which takes its name from the acicular pores in the coke. The size of the needle coke particle is markedly different in the two graphites, as is the general structure of the material. Graphite (c) in Fig. 3 (grade SM2-24) has a mixture of needle and Gilso-coke fillers. As discussed by Heintz [8], the coke structure can have a major influence on the properties of a graphite artifact. Indeed, by careful selection and preparation of the coke, and forming method, it is possible to produce an isotropic graphite. Another striking difference in the structure of the graphites in Fig. 3 is the size and shape of the pores within the graphite. The pore structure has a significant effect on the behavior of a nuclear graphite during service. First, it provides accommodation for irradiation-induced crystal strain (see later discussion). Second, the pores transport the reactor coolant gas into the graphite where it (or the impurities in the coolant gas) may react and gasify the graphite (see later discussion of radiolytic oxidation). Finally, the pore structure controls the fracture behavior of a graphite [9,10]. The properties of some common nuclear grade graphites are given in Table 4.

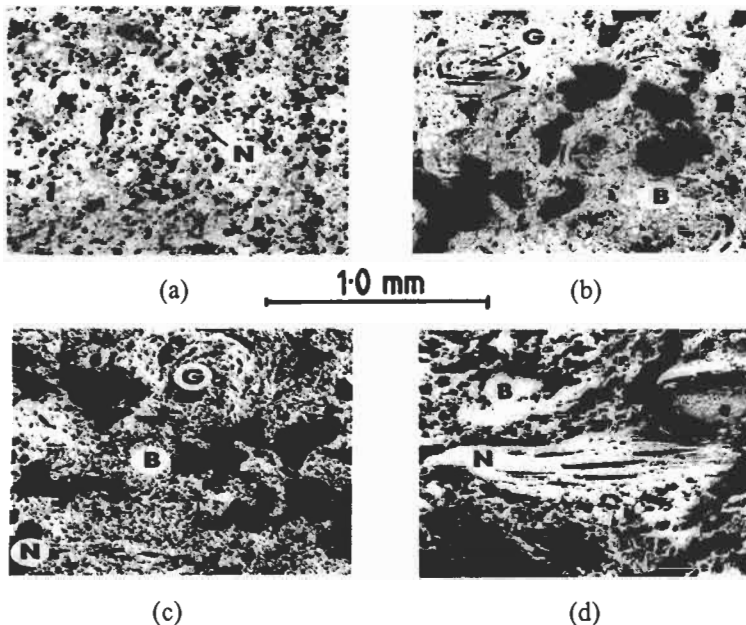


Fig. 3. Typical microstructures of four nuclear grade graphites: (a) high density graphite (HDG); (b) IM1-24, a Gilsonite coke graphite; (c) SM2-24, a Gilsonite and needle coke containing graphite; and (d) pile grade A (PGA), a needle coke graphite. In the figure G denotes Gilsonite filler coke, N denotes petroleum (needle) filler coke, and B denotes binder graphite.

Table 4. Physical and mechanical properties of some common nuclear graphites[11-19]

Grade	Source	Forming Method ^a	Bulk Density g/cm ³	Elastic Modulus ^b GPa	Strength ^b MPa			Thermal Cond. ^b W/m·K	CTE ^b 10 ⁻⁶ K ⁻¹
					Tensile	Bend	Comp.		
PGA	U.K.	E	1.74	12/5	17/11	19/12	27/27	200/109	0.9/2.8
SM2-24	U.K.	M	1.7	8/8.5	12	19	47	--	--
Pitch-coke	U.K./Fr.	E	1.8	13/10	25/17	32/26	70/63	130/135	4/3.8
IM1-24	U.K.	M	1.81	11	27.5	23	70	131	4.3
AGOT	U.S.A.	E	1.7	10/8	10/9	16/13	41/41	227/138	2.2/3.8
H-451	U.S.A.	E	1.75	11/9.6	15/13	20/24	60/60	150/135	3.5/4.5
ASR-1RS	Germany	M	1.78	9.9/9.2	15/14	26/232	67/63	125	4.7/4.9
IG-110	Japan	I	1.75	10	25	34	71	124/138	4/3.6
TSX	U.S.A.	E	1.7	14/3.8	--	25/7	--	--	1/4
GR-280	Russia	E	1.72	6.5/5	7.6/6	--	34/24	103/89	3.2/4.9
GR2-125	Russia	E	1.85	12/8.5	15/8	--	59/59	160/100	3.9/5.2

^aE-extruded, M-molded, I-isostatic pressing; ^b∥/⊥ to the forming axis

1.4 Historical use of graphite as a nuclear moderator

Graphite has been used as a nuclear moderator for over 50 years. The earliest reactors were comprised of stacks or "piles" of graphite blocks. In 1942, when a group of scientists led by Enrico Fermi [20] attempted to produce a self-sustaining nuclear chain reaction, graphite was chosen as the moderator because it was the only suitable material available. This first nuclear pile, designated CP-1, was constructed on a squash court under the stands of Stagg Field at the University of Chicago, and contained some 385.5 tons of graphite, the vast majority being grade AGOT manufactured by the National Carbon Company [20]. The world's first nuclear chain reaction was produced in CP-1 on December 2, 1942. The design of Fermi's reactor was based on data obtained from his earlier experiments at Columbia University aimed at determining the multiplication factor (k), the ratio of the number of neutrons in any one generation to the number of neutrons in the previous generation [21]. A sustained nuclear chain reaction will occur when $k > 1$. By the time CP-1 was being constructed in the spring of 1942, the value of $k_{\infty} = 1.007$ had been estimated for a uranium metal-graphite pile with sufficient accuracy to make a chain reaction in an infinite system a practical certainty [22]. However, control of the reaction, once initiated, was subject to considerable uncertainty.

CP-1 was assembled in an approximately spherical shape with the purest graphite in the center. About 6 tons of uranium metal fuel was used, in addition to approximately 40.5 tons of uranium oxide fuel. The lowest point of the reactor rested on the floor and the periphery was supported on a wooden structure. The whole pile was surrounded by a tent of rubberized balloon fabric so that neutron absorbing air could be evacuated. About 75 layers of 10.48-cm (4.125-in.) graphite bricks would have been required to complete the ~790-cm diameter sphere. However, criticality was achieved at layer 56 without the need to evacuate the air, and assembly was discontinued at layer 57. The core then had an ellipsoidal cross section, with a polar radius of 209 cm and an equatorial radius of 309 cm [20]. CP-1 was operated at low power (0.5 W) for several days. Fortuitously, it was found that the nuclear chain reaction could be controlled with cadmium strips which were inserted into the reactor to absorb neutrons and hence reduce the value of k to considerably less than 1. The pile was then disassembled and rebuilt at what is now the site of Argonne National Laboratory, U.S.A, with a concrete biological shield. Designated CP-2, the pile eventually reached a power level of 100 kW [22].

In early 1943, construction began on the X-10 reactor at what is now the Oak Ridge National Laboratory, U.S.A. The air-cooled X-10 reactor contained some 400 tons of moderator graphite, 274 tons of reflector graphite, and was rated at 3.5 MW(t). Criticality was achieved in November 1943 [22]. Also, construction commenced on the first reactors at the Hanford (U.S.A.) site in 1943. The mission of the Oak Ridge and Hanford reactors was the production of weapons grade U and Pu under the auspices of the U.S. Government's Manhattan Project. It is worth noting that the first irradiated fuel was discharged from the Hanford B reactor less than two years after the historic demonstration of a self-sustaining nuclear reaction in CP-1 [23]. The early Hanford reactors [23] were designed to operate at 250MW(t), significantly higher than the X-10 reactor. They had a core volume of 654 m³ and contained 1200 tons of moderator graphite and 600 tons of reflector graphite [22]. The reactors were surrounded by a CO₂/He gas mixture and were water cooled. In the U.K., two graphite moderated research reactors, the Graphite Low Energy Experimental Pile (GLEEP) and the British Experimental Pile Zero (BEPO), were built at Harwell. BEPO was rated at 6.5 MW(t), contained 310 tons of moderator graphite and 540 tons of reflector graphite, and was air cooled. BEPO went critical in July 1948 [22]. The construction of two graphite moderated production reactors at Windscale U.K. followed. The reactors were rated at 160 MW, were air cooled and went critical in 1950 and 1951. Both Windscale reactors were shutdown in 1957 [24]. Similar developments occurred in France, with the G1 reactor (criticality achieved January 1956), and in the U.S.S.R. [22].

2 Graphite Moderated Power Producing Reactors

A variety of graphite moderated reactor concepts have evolved since the first air-cooled reactors of the 1940s. Reactors with gas, water, and molten salt coolants have been constructed and a variety of fuels, and fissile/fertile fuel mixtures, have been used. The evolution and essential features of graphite moderated power producing reactors are described here, and details of their graphite cores are given.

2.1 Gas-cooled reactors

2.1.1 Magnox reactor (U.K.)

The *Magnox* reactor concept owes its origins to a design study conducted at Harwell, U.K., during the early 1950s. The reactor was designed with the dual role of plutonium and power production, and was known by the code word PIPPA

(pressurized pile producing power and plutonium) [26]. The inherently stable graphite-moderated gas-cooled reactor concept was adopted over the water-cooled, graphite-moderated design, which was used for the Hanford, U.S.A. reactors, because of the lack of remote sites in the densely populated U.K. [27]. Early in the design it was decided that the reactor would be fueled with natural-uranium, and thus the moderator had to be either graphite or heavy water. The latter option was dismissed on the basis of cost. Wasteful neutron capture occurs in the graphite, coolant gas, and fuel cladding. Therefore, considerable effort was expended in selecting appropriate materials for the PIPPA design. The moderator graphite, Pile Grade A (PGA), was manufactured from a particularly pure coke, thus reducing its neutron capture cross section substantially relative to the graphites used in earlier experimental reactors such as BEPO.

The choice of fuel canning materials was limited to those with low capture cross section, such as beryllium, magnesium, aluminum, and zirconium. Beryllium was hard to obtain, difficult to fabricate, and is highly toxic. Zirconium was impossible to obtain in the hafnium-free state essential for reactor applications. Therefore, only aluminum and magnesium were considered viable. Magnesium, at the time of the PIPPA design study, had not been used in reactor applications because its low neutron capture cross section only became known in 1948 [26]. One significant advantage that magnesium has over aluminum is its lack of reaction with the uranium fuel. After careful metallurgical investigation of various magnesium alloys, a Mg-0.8%Al-0.01%Be alloy which exhibited low oxidation was selected [28]. The use of this alloy for the fuel cladding led to the eventual adoption of the reactors familiar *Magnox* name (magnesium non-oxidizing).

The need to keep neutron absorbing metal out of the core led the designers away from the use of liquid metal coolant, or water coolant running through the core in metallic tubes. A gas chemically compatible with graphite, enabling it to flow directly through the moderator, thus appeared to be the only option. A study of potential cooling gases for PIPPA concluded that helium would be the most suitable gas because of its excellent heat transfer properties and chemical inertness. However, helium was unavailable in the U.K. in sufficient quantities, and import from the U.S.A. was restricted by the MacMahon Act. Other potential gases were rejected because of chemical incompatibility with graphite and metals, excessive neutron absorption, poor stability under irradiation, induced radioactivity, or poor heat transfer characteristics. Carbon dioxide emerged as the inevitable compromise. Although CO₂ is somewhat inferior to helium as a coolant, it had the

advantage of being plentiful, inexpensive, commercially pure, and easy to handle. Initial concerns that the reaction of CO₂ and graphite in the presence of radiation (Radiolytic Oxidation-Section 4) would be excessive were proved to be unfounded, and this cleared the way for the detailed design of a CO₂ cooled, graphite-moderated reactor.

In designing the graphite core several requirements had to be met. Stability and alignment had to be preserved in the core; the shape and linearity of the fuel and control rod channels had to be maintained; fracture of the graphite at the channel wall had to be avoided; irradiation-induced dimensional changes within each block, and across the core, could not adversely effect the safety or performance of the core; the graphite blocks had to possess sufficient strength to not fail under thermally induced stresses; transient and steady state temperature gradients across the blocks could not cause instability; coolant leakage from the fuel channels had to be minimized; neutron streaming and leakage from the core had to be minimized; and the core had to be economic in its use of graphite.

Prior to the PIPPA design study all of the graphite reactors built had the axis of the fuel and core horizontal. This concept was rejected for the PIPPA because support of the heavy graphite core from the surface of the pressure vessel proved to be an intractable problem [26]. While a vertical arrangement complicated the insertion, support, and removal of the uranium fuel elements, it allowed for a fail-safe gravity feed control rod/reactor shutdown system. Therefore, a vertical axis graphite pile was adopted, built up from individually machined blocks to produce a 24-sided prism about 36 ft (10.97 m) across, with a height of about 27 ft (8.23 m). The core consisted of some 32,000 graphite blocks each weighing about 100 lbs (45.4 kg) and measuring 25 in. (63.5 cm) in length and about 8 in. (20.3 cm) square. The core mass of about 1454 tonnes was supported on a steel grid framework about 4 ft (1.22 m) thick. The thermal expansion mismatch between the steel grid and the graphite core was accommodated by supporting the graphite on small steel rollers. Radial keyways located the stack in the pressure vessel.

By the end of 1952 it was certain that a PIPPA design had been produced which could and should be built. A summary report was prepared in January 1953, and soon after approval was granted for construction of the first two *Magnox* reactors at Calder Hall. Before the first reactor went critical in 1956 work had started on a further two reactors at Calder Hall, and all four were at power in 1959. Construction at Chapelcross, in the southwest of Scotland, began in 1955. The fist

reactor was at power in 1959 and all four at Chapelcross were in operation by early 1960. The first eight *Magnox* reactors were, therefore, designed, constructed, and commissioned within nine years. The construction of the eight dual-purpose *Magnox* reactors was followed by an expanded civil construction program in the U.K. and overseas (Latina, Italy and Tokai, Japan). Moreover, conceptually similar reactors were built in France (G2/G3, Chinon A1, A2 & A3, St. Laurent A1 & A2, and Bugey) and Spain (Vandellos) [29].

A total of nine commercial twin *Magnox* reactor/power plants were built in the U.K. (Table 5), culminating with the Wylfa reactors which began operation in 1971. The *Magnox* reactors at Wylfa each have a graphite core with a diameter of 18.7 m, a height of 10.3 m, a mass of 3740 tonnes, and contain 6150 fuel channels. Wylfa's net electrical output is 840 MW from two 1600 MW(t) reactors, substantially larger than the 150 MW(t) reactor with an electrical output of 35MW envisaged in the PIPPA design study! Table 6 shows key reactor parameters for several of the U.K. *Magnox* reactors, and illustrates the evolution of the *Magnox* reactor design.

Table 5. Commercial *Magnox* power plants in the U.K. [29]

Location	Commissioning Date	Coolant Pressure (MPa)	Reactor Vessel ^a	Rating ^b [MW(c)]
Berkeley	1962	0.9	Steel(c)	276
Bradwell	1962	0.9	Steel(s)	245
Hunterston A	1964	1.0	Steel(s)	300
Hinkley A	1965	1.3	Steel(s)	430
Trawsfynydd	1965	1.6	Steel(s)	390
Dungeness A	1965	1.8	Steel(s)	410
Sizewell A	1966	1.9	Steel(s)	420
Oldbury	1968	2.4	Concrete(c)	416
Wylfa	1971	2.7	Concrete(c)	840

^a (c) = cylindrical, (s) = spherical.

^b Continuous maximum, net from two reactors

Table 6. Key parameters of several U.K. Magnox reactors [30]

Parameters	Units	Reactors			
		Calder Hall	Berkeley	Trawsfynydd	Wylfa
<i>General</i>					
Output net	MWe	240	276	390	840
Output gross	Mwe		334.4	474.8	1001.6
No. of reactors		4	2	2	2
Heat output/reactor	MWth	272	--	860	1600
Inlet gas temp.	°C	150	167	180	230
Outlet gas temp.	°C	345	350	360	360
Net thermal effic. (1979/80)		--	21.83	24.34	25.78
<i>Pressure vessel</i>					
Material		steel	steel	steel	concrete
Geometry		cylindrical	cylindrical	spherical	spherical
Steel thickness	mm	51	76.102	89.0	19.5
Internal diameter	m	11.28	15.2	18.3	29.3
Internal height	m	21.24	24.2	--	--
Working pressure	bar	6.8	9.6	17.6	27.0
<i>Graphite moderator</i>					
Active core diameter	m	9.45	13.1	13.7	17.4
Active core height	m	6.4	7.4	7.9	9.1
Specific power	MW/m ³	0.61	--	0.76	0.74
Diameter over flats	m	10.97	14.6	14.6	18.7
Overall height	m	8.23	9.1	8.3	10.3
Overall weight	m	1158	1938	1900	3740
No. of fuel channels		1696	3265	3740	6150
Lattice pitch	mm	203	203	197	197
Max thermal flux	n/cm/s	--	1.7×10 ¹³	2×10 ¹³	2.0×10 ¹³
<i>Fuel</i>					
Weight of U/reactor	t	111	231.45	280	595
Specific power	kW/kg	2.4	2.4	3.11	3.16
Mean irradiation	MWD/t	3500	4300	4300	4755
<i>Turbo-alternators</i>					
No. per station		8	4	4	4
Capacity	MW	30	83	145	247.5

2.1.2 Advanced gas-cooled reactor, AGR (U.K.)

The large physical size of the later *Magnox* stations, such as Wylfa, led to the development of the more compact advanced gas-cooled reactor (AGR) design [31] that could utilize the standard turbine generator units available in the UK. Stainless-steel clad, enriched uranium oxide fuel can tolerate higher temperatures

than *Magnox* fuel, allowing higher coolant outlet temperatures in the AGRs. Like the *Magnox* reactors, the AGR has a graphite core and utilizes carbon dioxide gas coolant. The entire core, the boilers, and the gas circulators are enclosed in a prestressed concrete vessel. A typical AGR station in the U.K. [31] has twin 660 MW(e) nominal reactors with the major performance parameters listed in Table 7. Initial experience and confirmation of the operating characteristics of the AGR were gained from the 30 MW(e) prototype AGR at Windscale, U.K. (WAGR) [32]. Seven AGR stations have been constructed in the U.K.—Dungeness B, Hartlepool, Heysham I&II, Hunterston B, Hinkley Point B, and Torness.

Table 7. The major performance parameters of a typical AGR (Heysham II and Torness design) [33]

Parameter	Value
Reactor heat	1550 MW(t)
Number of fuel channels	332
Mean fuel channel power	4.7 MW(t)
Circulator gas outlet temperature	229°C
Mean fuel channel outlet temperature	635°C
Gas circulator total flow	4271 kg/s
Gas circulator pressure rise	0.2896 MPa
Gas circulator power consumption per reactor	42.6 MW(e)
Gas circulator outlet gas pressure	4.36 MPa abs
Steam generator steam flow	500 kg/s
Steam pressure at turbine inlet	16 MPa abs
Steam temperature at turbine inlet	538°C
Steam generator feedwater temperature	156°C

The AGR reactor core is a six-sided prism of stacked graphite bricks connected at the periphery to a steel restraint tank. Integral graphite and steel shields are incorporated into the graphite structure above, below, and surrounding the active core, thus reducing radiation levels and making it possible for personnel to enter the pressure vessel. The graphite moderator bricks are penetrated from the bottom to the top of the core by 332 channels containing fuel stringers. Interstitial channels, interspersed amongst the fuel channels, contain the control rods. Figure 4 shows the graphite moderator bricks from a typical AGR core (Hinkley Point B) under construction. The control rods consist of axially-linked, articulating tubular sections that contain boron-doped stainless steel. The graphite fuel bricks are additionally penetrated by axial holes which allow access of methane to the inner portions of the graphite brick. The methane is added to the carbon dioxide coolant as a radiolytic corrosion inhibitor (see Section 4).

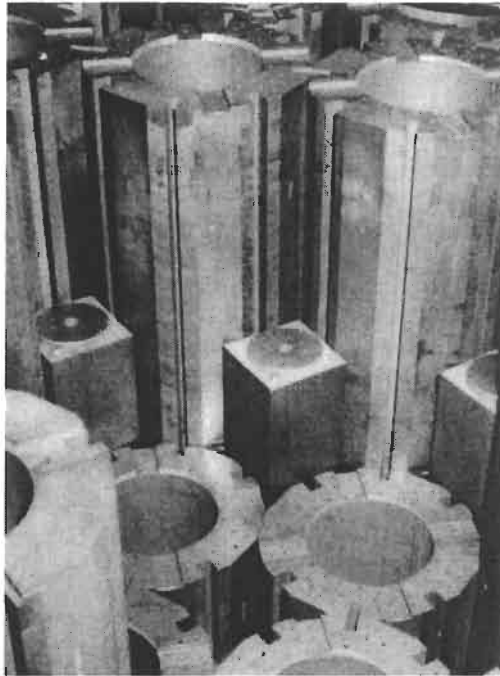


Fig. 4. A typical advanced gas-cooled reactor graphite core (Hinkley Point B under construction) [11].

The graphite core is located within a steel envelope called the gas baffle, which provides for reentrant cooling of the graphite structure (Fig. 5). Cooled carbon dioxide is drawn from the bottom of the steam generators by the gas circulators and discharged into the plenum below the core inside the gas baffle. About 30% of the gas flows directly into the fuel channel inlets, while the remainder (reentrant flow) passes up the annulus surrounding the core, returns down through the core in passages between the outer graphite sleeves of the fuel element assemblies and the graphite core bricks to the fuel channel inlets at the bottom of the core, where it combines with the cool gas flowing directly from the circulators (Fig. 5). The purpose of the reentrant flow is to cool the moderator bricks and the core restraint system. The gas baffle serves to contain the reentrant flow and isolate it from the fuel channel hot outlet flow. The hot gas passes up through the plenum above the graphite core in guide tubes which penetrate the thermally insulated top of the gas baffle, and then flows to the top of the steam generators. The entire core structure sits on a support grid (diagrid) which is itself supported by the skirt that forms the lower end of the gas baffle cylinder. The skirt is welded to the pressure vessel liner and includes an anchorage arrangement that ensures structural loads are transmitted to the concrete foundation of the pressure vessel bottom slab.

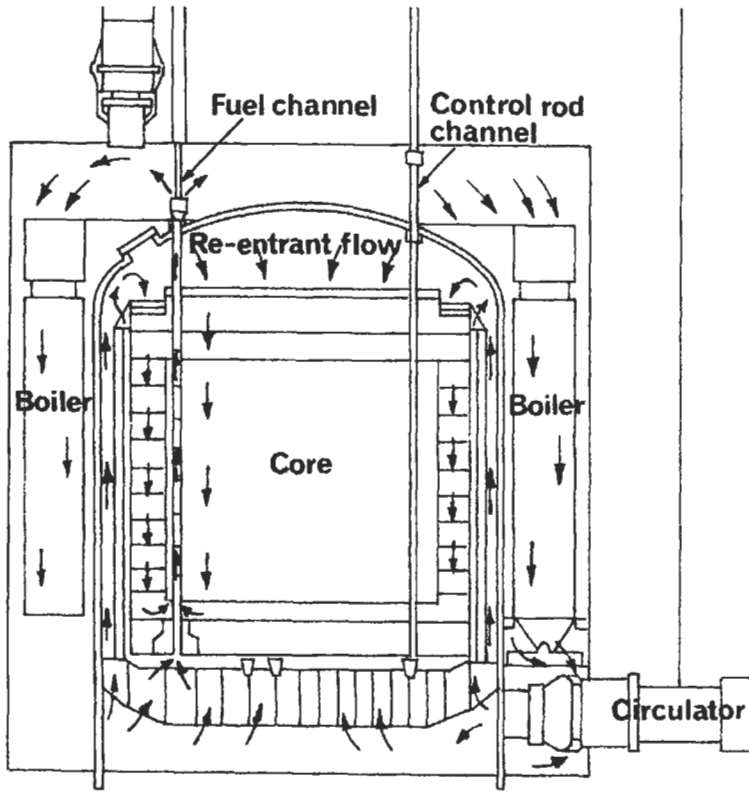


Fig. 5. The gas flow path of an AGR. Note the flow is reentrant, i.e., a fraction of the cool gas from the circulator flows up around the outside of the core entering the core from the top, then flows downward through the core, between the moderator and fuel element assembly, to the bottom where it mixes with the cool gas from the circulator and flows up the fuel channel inside the graphite fuel sleeves to the steam generators. Reprinted from [33], © 1977 Wilmington Business Publishing, Dartford, U.K., with permission.

Four steam generators, each consisting of three separate factory assembled units, are positioned in the annulus between the gas baffle and the inner wall of the pressure vessel. After passing down through a steam generator, the cooled carbon dioxide gas discharges into one of the quadrants of the circulator annulus which forms the entry plenum for eight 5.2 MW gas circulators mounted horizontally through the vessel side wall. This plenum is isolated from the boiler annulus by the main gas seal and is divided into four quadrants by division plates so as to form four reactor cooling circuits, each comprising one steam generator and two gas circulators in parallel. The steam generators supply two 660 MW(e) nominal turbines.

The fuel assembly consists of a fuel stringer and a fuel plug unit. The fuel stringer is comprised of eight 36-pin fuel elements stacked one above the other and suspended from the fuel plug unit by a tie bar. The fuel pins consist of enriched uranium oxide pellets clad in stainless steel and supported in steel grids mounted in a graphite sleeve. The fuel plug unit controls the coolant flow through the fuel stringer and also forms the shield and seal for the standpipe through which the fuel stringer is loaded into the reactor.

Several grades of graphite are used in the AGRs. The core bricks (Fig. 4) are machined from the isotropic nuclear grade IM1-24 (Section 1.3). Isotropy is achieved in IM1-24 graphite by utilizing the spherical Gilsonite coke and a molding process to form the graphite. The result is a moderator graphite with more than twice the strength of its predecessor, PGA. Moreover, the isotropic behavior of the graphite has significant advantages with respect to its response to radiation damage. The reflector region of the AGR core contains grade SM2-24, a molded graphite made from a blend of needle coke and Gilsonite coke filler. The AGR fuel sleeves are made from pitch-coke graphite, which is produced from coal-tar pitch-derived coke and formed by extrusion.

2.1.3 Dragon Reactor Experiment, DRE (Euratom)

The High Temperature Reactor Project, or Dragon Reactor Experiment (DRE) as it was more commonly known (located at Winfrith, Dorset, U.K.), went critical on August 23, 1964 [34]. Dragon was an experimental 20 MW(t) reactor with helium coolant at a working pressure of 2 MPa and an outlet temperature of $\sim 750^{\circ}\text{C}$, significantly hotter than the AGR coolant outlet temperature of 630°C . Although the DRE was not a power producing plant, its status as a first-of-its-kind high-temperature gas-cooled reactor (HTGR) makes it worthy of inclusion here. The DRE's mild steel pressure vessel was 17.8 m high with a maximum diameter of 3.4 m [29]. A reentrant jacketed coolant flow arrangement maintained the walls of the vessel and heat exchanger/circulator branches at their optimum temperature of $\sim 300^{\circ}\text{C}$. The helium flowed upwards through the core, entering at 370°C , and emerging at an average temperature of $810\text{--}830^{\circ}\text{C}$. A fraction of the total primary coolant flow, varying between 15 and 25%, bypassed the core and, therefore, the gas temperature at the primary heat exchangers was somewhat lower, typically 720°C .

The DRE core assembly consisted of 37 fuel elements 2.4 m in length, each comprised of a cluster of seven hexagonal section rods with ribs to separate them and provide a space for coolant flow. The central core section of each rod (1.4 m length) consisted of a graphite tube surrounding a stack of annular fuel compacts with a central graphite spine. The rod clusters were eventually replaced with a block type fuel element which was more representative of the core structures proposed for high temperature power reactors [34]. The radial graphite reflector

consisted of a fixed outer region of rigidly stacked blocks and two inner rings of vertical pillars which pivoted on a base plate. The thirty inner pillars were penetrated by channels, 24 of which served as control rod ducts. These inner columns were replaceable by means of the charge machine. The high neutron flow into the reflector, and the small core volume (1.4 m³), allowed the reactor to be controlled by absorbers outside the core-reflector interface. The DRE was fueled with 93% enriched uranium [34] and a fissile/fertile fuel mix. The latter was employed in only 10 of the 37 elements because of the heavy neutron loss. Initially the fertile component was thorium, but later ²³⁸U was utilized [29].

The Dragon reactor represented a departure from previous designs in that it did not have metallic clad fuel. Rather, a coated ceramic fuel bound in a carbon matrix (see Section 5) was clad in an entirely graphite structure. The initial Dragon design called for a fully emitting fuel from which the gaseous fission products freely escaped. The fuel design was changed to the fission product retaining coated particle type in May 1963. However, considerable effort had been expended on the development of low-permeability nuclear graphites as a consequence of the earlier fuel design. The gaseous fission products were to be purged from the fuel by a helium purge passing over the annular fuel bodies, through a location spike on which the fuel elements rested, to the fission product cleanup system. The purge flow was reduced to an acceptable level by using a low permeability fine-grained graphite. The selected graphite (Morganite Carbon Limited, grade EY-9) had to be subjected to additional processing to reduce its permeability to an acceptable level. This process, developed by the Royal Aircraft Establishment, Farnborough, U.K. [35], involved impregnation of the porous carbon with furfuryl alcohol, or a furan derivative to which a suitable polymerization catalyst had been added. The impregnant resin was cured in situ and pyrolyzed to 1000°C to leave a carbon deposit in the pore network. This process was carried out repetitively until the permeability was sufficiently reduced. Attaining grade EY-9 at nuclear purity proved to be problematic because the graphite picked up excessive boron during graphitization at the Morganite plant. Eventually, the material was purchased from Morganite in the baked stage and shipped to Compagnie Pechiney, France, for combined purification and graphitization at 2700°C. The graphite was then returned to the U.K. for impregnation, regraphitization, and outgassing at Winfrith.

The switch to coated particle fuel and the realization that the high temperature (>900°C) irradiation stability of EY-9 was unacceptable (EY-9 contained a significant portion of small crystallites due to the carbon black filler used), caused a change in the Dragon graphite development program away from fine-grained materials to coarser isotropic and near-isotropic graphites [34].

2.1.4 Peach Bottom (U.S.A.)

The HTGR designed by the General Atomic Company and constructed at Peach Bottom, Pennsylvania, U.S.A., was a 40 MW(e) experimental power plant which was similar in many respects to the Dragon reactor. Peach Bottom started commercial operation on June 1, 1967, and ceased operation on October 31, 1974 [36]. The major performance parameters of the Peach Bottom Reactor are shown in Table 8.

Table 8. The major performance parameters of the Peach Bottom Reactor [29]

Parameter	Value
Coolant	Helium
Pressure	2.4 MPa
Core inlet temperature	344°C
Core outlet temperature	728°C
Steam temperature	538°C
Steam pressure	10.00 MPa
Net thermal efficiency	34.6%
Reactor thermal output	115 MW(t)
Net electrical power	40 MW(e)
Pressure vessel	
Diameter	4.3 m
Height	10.8 m
Core	
Effective Diameter	2.8 m
Active height	2.3 m
Specific power	8.1 MW/m ³
Fuel element diameter	8.9 cm
Fuel element length	366 cm
Number of fuel elements	804
Reflector thickness	61 cm
Control rods	
Normal operating-rods	36
Shut-down rods	19
Fuel life at full power	900 days

The fuel for the Peach Bottom reactor consisted of a uranium-thorium dicarbide kernel, overcoated with pyrolytic carbon and silicon carbide which were dispersed in carbon compacts (see Section 5), and encased in graphite sleeves [37]. There were 804 fuel elements oriented vertically in the reactor core. Helium coolant flowed upward through the tricuspid-shaped coolant channels between the fuel elements. A small helium purge stream was diverted through the top of each element and flowed downward through the element to purge any fission products leaking from the fuel compacts to the helium purification system. The Peach

Bottom 1 prototype HTGR operated successfully in all respects under the auspices of the U.S. Atomic Energy Commission's Power Reactor Demonstration Program. However, its size (only 40 MW) was insufficient to justify continued commercial operation.

2.1.5 Fort St. Vrain (U.S.A.)

The 330 MW(e) Fort St-Vrain Nuclear Generating Station was the first commercial-size HTGR to employ the multihole fuel block design developed by Gulf General Atomic in the U.S.A. [38]. The construction permit for the plant was received in September 1968 [39] and construction was essentially complete in August 1971 [38], with initial criticality being attained on January 31, 1974. The major performance parameters of Fort St. Vrain are given in Table 9. The fuel was of the Triso particle type (see Section 5) with kernels of fissile uranium dicarbide (93% enriched) or fertile thorium dicarbide [40].

Table 9. The major performance parameters of the Fort St. Vrain HTGR [29,38-40]

Parameter	Value
Coolant	Helium
Pressure	4.83 MPa
Core inlet temperature	400°C
Core outlet temperature	770°C
Steam temperature	538°C
Steam pressure	16.5 MPa
Net thermal efficiency	38.5%
Reactor thermal output	842 MW(t)
Net electrical power	330 MW(e)
Concrete pressure vessel cavity	
Diameter	9.45 m
Height	22.9 m
Core	
Effective Diameter	5.94 m
Active height	4.75 m
Specific power	6.4 MW/m ³
Fuel element (distance across flats)	36.07 cm
Fuel element length	78.74 cm
Number of fuel elements	1482
Number of fuel columns	247
Reflector thickness (average)	118.9 cm
Number of refueling regions	37
Control rods	
Normal operating-rods	37 (pairs)
B ₂ C Reserve shut-down channels	37
Fuel life at full power	6 years

The reactor core was made up of stacks of hexagonal graphite blocks. Each fuel element block had 210 axial fuel holes and 108 axial coolant holes (Section 5, Fig. 14). The fuel particles were formed into a fuel compact (Section 5.3) and sealed into the fuel channels.

The core was divided into 37 regions, each containing 7 columns, except for the 6 regions at the core periphery which each contained 5 columns. The center column fuel elements and top reflector additionally contained three control rod channels, two for the operational rods and one for the B_4C reserve shutdown material. Each fuel region was centered beneath a refueling penetration in the prestressed concrete pressure vessel. During operation each of the penetrations contained a control rod drive and a controllable orificing assembly to control coolant flow. The coolant gas exited the bottom of the steam generators at 400°C and flowed around the core in the annulus between the inner surface of the concrete vessel's steel liner and the metallic core barrel. It entered the core from the top and flowed down through the fuel elements, mixing in the plenum beneath the bottom reflector before it entered the top of the steam generators at 770°C.

A conventional extruded needle-coke nuclear graphite, grade H-327, was selected for the fuel elements. Later, the fuel element graphite was changed to H-451, a near isotropic grade (Table 4). The radial reflector was composed of two parts. Immediately surrounding the core were replaceable reflector elements which were essentially identical to the fuel elements. The reflector elements were arranged in columns, but did not contain coolant or fuel channels. The reflector elements, along with those on the top and bottom of the core, were replaced when their associated fuel region was replaced. The second part of the radial reflector was the large permanent graphite blocks of irregular shape that surrounded the replaceable reflector and transitioned the hexagonal core brick shape to the cylindrical core barrel. The permanent reflectors were machined from grade PGX graphite.

The Fort St. Vrain HTGR was permanently shutdown in August 1988 [41]. The nuclear island performed well during the reactors 15-year life, although significant problems were encountered with some of the reactors non-nuclear support systems [29,38].

2.1.6 The AVR and THTR-300 (Germany)

The Arbeitsgemeinschaft Versuchsreaktor (AVR) and Thorium High-Temperature Reactor (THTR-300) were both helium-cooled reactors of the pebble-bed design [29,42,43]. The major design parameters of the AVR and THTR are shown in Table 10. Construction started on the AVR in 1961 and full power operation at 15MW(e) commenced in May 1967. The core of the AVR consisted of approximately 100,000 spherical pebble type fuel elements (see Section 5). The pebble bed was surrounded by a cylindrical graphite reflector and structural carbon

jacket [44]. The core bottom was conically shaped so as to funnel the fuel elements to the 0.5-m diameter pipe through which the fuel elements were discharged. The fuel elements were continuously added to the reactor core during reactor operation via five refueling pipes, passed through the core in about six months, and then entered the fuel element discharge pipe. Outside of the reactor the fuel elements were evaluated for their fuel burn-up and were either returned to defined regions of the core, or were removed for storage and reprocessing. Each element passed through the core, on average, ten times. Four graphite columns protruded into the reactor core, each containing a longitudinal bore hole for a shutdown control rod. For normal control the AVR made use of the negative temperature coefficient of reactivity, which allowed power level control exclusively by coolant gas flow rate variations. The helium coolant flowed upwards through the core and was heated from 275°C to 950°C, exiting through slits in the top reflector to the steam generator located above the core. The AVR reflector was constructed from grade AN2-500 graphite.

Table 10. The major design parameters of the AVR and THTR-300 [29]

Parameters	Units	Reactors	
		AVR	THTR
Net power output	MW(e)	15	300
Thermal power	MW	46	750
Mean power density	MW/m ³	2.6	6.0
Core height	m	2.47	6.0
Core diameter m	3	5.6	
Number of fuel elements		98000	675000
Helium pressure	MPa	1.09	3.9
Absorber rods			
In-core		0	42
In-reflector		4	36
No. of steam generators		1	6
Helium inlet temperature	°C	950	750
Superheated steam temperature	°C	505	550/535
Pressure vessel			
Material		Steel	Prestressed concrete
Outer diameter	m	5.8	24.8
External height	m	24.9	25.5

Construction of the THTR-300 began in 1972. Completion of construction was originally expected in 1977, but first criticality was not achieved until September 13, 1983 [29]. Nuclear trials continued until May 31, 1987, and power operation started with handover of the plant on June 1, 1987 [43]. The reactor was shut down

in mid 1989, predominantly for political reasons [45]. Unlike the AVR, the THTR had a prestressed concrete pressure vessel. The reactor core consisted of a bed of 675,000 spherical graphite fuel elements each containing almost 1 g of uranium at 93% enrichment, and 10.2 g of thorium-232. The fuel elements were contained in a cylindrical graphite vessel approximately 6 m in height and 5.6 m in diameter. The graphite vessel served as the neutron reflector. The bottom graphite reflector was conically shaped and tapered down to a central fuel element discharge pipe 80 cm in diameter. Reactor operating control and shutdown was achieved with 42 in-core rods which were inserted into the pebble bed, and 36 reflector rods which could be freely moved inside reflector control rod channels. Six electrically driven coolant gas blowers forced the helium to flow downward through the reactor core, where it was heated to 750°C by the spherical fuel elements. The coolant gas entered the hot plenum below the reactor core through holes in the bottom reflector and was then directed to the six steam generators via hot gas ducts. The helium exited the steam generators at 250°C and was redirected to the reactor core by the blowers. The fuel element handling system allowed continuous charging and discharging of the fuel. After discharge the fuel elements were automatically inspected for damage and those with unacceptable shape or dimensions were rejected. The elements were assessed for fuel burn-up and a process computer determined whether they were discharged or returned to the reactor core. The continuous refueling process assured that a uniform high burn-up was attained.

The nuclear graphites used in the THTR-300 core [46] were manufactured by Compagnie Pechiney, France. Grade PXA2N, a Gilsonite-coke graphite, was used for the core components close to the pebble-bed, including the bottom reflector (first layer), core support blocks, fuel element outlet tubes, layers No. 11 to 36 of the core chamber wall, the lower layer of the core chamber ceiling, and for dowels and thermal insulation cartridges in the core chamber wall. Grade PAN, a petroleum-coke containing graphite, was used for the remainder of the core except for the bottom layer of the lower reflector, which was an ungraphitized version of grade PAN and served as a thermal insulator.

2.1.8 High Temperature Test Reactor, HTTR (Japan)

The HTTR is an experimental helium-cooled 30 MW(t) reactor. The HTTR is not designed for electrical power production, but its high temperature process heat capability makes it worthy of inclusion here. Construction started in March 1991 [47] and first criticality is expected in 1998 [48]. The prismatic graphite core of the HTTR is contained in a steel pressure vessel 13.3 m in height and 5.5 m in diameter. The reactor outlet coolant temperature is 850°C under normal rated operation and 950°C under high temperature test operation. The HTTR has a primary helium coolant loop with an intermediate helium-helium heat exchanger and a pressurized water cooler in parallel. The reactor is thus capable of providing

nuclear heat for process applications such as hydrogen production [48]. The principal design parameters of the HTTR are given in Table 11.

Table 11. The principal design parameters of the HTTR [47,48]

Parameter	Value
Reactor thermal power	30 MW
Coolant	
Type	Helium gas
Outlet temperature	850°C/950°C
Inlet temperature	395°C
Primary pressure	4 MPa
Dir. of coolant flow	Downward-flow
Core	
Material	Graphite
Height	2.9 m
Diameter	2.3 m
Average power density	2.5 W/cm ³
Fuel	
Type	Low enriched UO ₂
Element type	Prismatic
Enrichment	3-10%
Average enrichment	6%
Pressure vessel	
Material	Steel (2 1/4 Cr-1 Mo)
Height	13.2 m
Diameter	5.5 m
Containment type	Steel containment
No. of coolant loops	1
Plant lifetime	20 years

The prismatic fuel elements are in the form of hexagonal blocks (similar to the Fort St. Vrain HTGR). The active core consists of 30 fuel element columns and 7 control rod guide columns. Each control rod column contains three control rod penetrations, and is surrounded by six fuel elements. The active core is surrounded by a replaceable reflector composed of a layer of hexagonal graphite blocks. The permanent reflector surrounds the replaceable reflector and consists of large irregular shaped blocks that are attached to the cylindrical pressure vessel. The fuel elements and replaceable reflectors are made from grade IG-110 graphite, and the permanent reflector blocks are made from grade PGX graphite. Reactivity control is provided by individually supported control rods which penetrate the hemispherical top head of the reactor pressure vessel and enter into the fueled region and replaceable reflector region. Hot shutdown is achieved by insertion of the nine pairs of reflector control rods, followed by the seven pairs of control rods

in the fueled region when the core temperature is $<900^{\circ}\text{C}$. Back-up shutdown capability is provided by boron carbide/graphite pellets that may be inserted into separate holes in the control rod guide blocks.

The fuel element is of the pin-in-block design and is 36 cm across the flats and 58 cm in height. The fuel consists of Triso coated particles of low enriched uranium oxide with a kernel diameter of 600 μm . The particles are bonded with a graphite powder to form the fuel annular compacts, which are contained in graphite sleeves with a 3.4 cm outside diameter and thus form the fuel rod. The fuel rods are located in vertical holes of 4.1 cm diameter in the fuel element block. The helium coolant flows downward through the 3.5-mm annular gap surrounding each fuel rod in the fuel element. The fuel rods, fuel elements, and replaceable reflector blocks are made from the fine-grained, high-strength, isotropic grade IG-110 graphite (Table 4).

2.2 *Water-cooled reactors*

2.2.1 N-Reactor (U.S.A.)

The N-Reactor was the only reactor constructed at the Hanford, Washington site which produced both electrical power and special nuclear materials. The previous eight reactors were all non-power producing, material production reactors [23]. N-Reactor was a pressure-tubed, light water-cooled, graphite moderated reactor which produced 3800 MW(t) and 860 MW(e) [49]. The N-Reactor started up in June 1964 and ceased operations in January 1987 [23,49]. The design and operating parameters of the N-Reactor are reported in Table 12. The fuel tubes (containing enriched uranium fuel) ran horizontally through the reactor from front to back, while the core water coolant pipes (zirconium) ran horizontally through the core from side to side, perpendicular to the fuel tubes. Additionally, the control rods were mounted horizontally and ran into channels in the graphite core. There were a total of 87 water-cooled control rods, which had a scram speed of 76 ft/s. Reserve shutdown capability was provided by 108 vertical channels into which balls of absorber material could be dropped. Initially, the absorber balls were samarium oxide, but they were subsequently replaced with B_4C .

The N-Reactor core was made up from a stack of interlocking grade TSX graphite blocks (Table 4). The core blocks had both keys and recesses machined into them such that when assembled an interconnected steam vent passage system running vertically and horizontally throughout the core was established. These passages gave sufficient cross-sectional area for steam and water dissipation to limit potential damage to a particular graphite block in which a tube burst might occur [49]. The active core was surrounded by a neutron reflector made from blocks of Speer nuclear grade 2 and Great Lakes Carbon nuclear grade 1 graphite, and was maintained under a low pressure, low flow, inert gas blanket. The entire core

assembly was contained within a steel thermal shield and a concrete biological shield, both of which were water cooled. The external dimensions of the reactor, including concrete biological shield, were 12 m in width, 14.55 m in depth, and 12.95 m in height [49].

Table 12. N-Reactor design and operating parameters [23,49]

Parameter	Value
Power output, MW(e)	860
Thermal power, MW(t)	3800
Core	
volume, m ³	495
specific power, MW/m ³	8.09
dimensions, m	12.01 length, 10.06 width, 10.16 ht.
pressure tubes (Zr-2)	1003 installed (16.15 m length 6.86 cm ID, 8.26 cm OD)
cooling tubes (Zr-2)	640 installed side to side (12.8 m len., 1.91 cm OD)
Graphite	
grade TSX	
mass, tonnes	1800
number of blocks	78,000 blocks; 17,000 sleeves
reflector graphite	Nuclear grade-2, grade R-1
operating temperature, °C	288 - 566
Control system	
normal operations	87 water cooled, B ₄ C hydraulically driven
emergency	108 vertical safety channels, B ₄ C balls 9.53 mm OD.

2.2.2 RBMK (Russia)

There are currently 11 uranium-fueled, graphite-moderated, light water-cooled RBMK reactors operating in Russia [50]. The graphite is both the nuclear moderator and the major core structural component. The core of an RBMK reactor contains 2488 vertical channels formed by stacks of rectangular section graphite bricks with an axial hole (11.4 cm in diameter) to accommodate the channel tube. There are 2044 fuel and control rods channels and 444 channels in the core periphery which are filled with graphite rods and act as the reflector [51,52]. The entire graphite stack has a mass of approximately 1700 tonnes [52]. Key design parameters of the RBMK graphite core are shown in Table 13. Radial displacement of the graphite stack is restrained by 156 water-cooled supporting tubes situated in the core periphery. The cooling tubes are free to move in vertical guides in the upper structure of the containment, and are welded to the core support

structure at their base. The core is contained above and below by the biological shield, and is surrounded by a 10% nitrogen/90% helium blanket and a water tank.

Table 13. The key design parameters of the RBMK-1000 reactor and graphite core [51,52]

Parameter	Value
Reactor power, MW	
thermal	3200
electrical	1000
Core	
Specific power, MW/m ³	2.67
Configuration	Cylindrical
Channel arrangement	Vertical
Number of channels	2488
Graphite grade	GR-280
Dimensions	
height, m	8
diameter, m	13.8
brick dimensions	
width, cm	24.88
breadth, cm	24.88
height, cm	20-60
Maximum graphite temperature, °C	750

The core cavity environment is maintained below atmospheric pressure. Each of the core brick columns is independent from its neighbors (no radial keying) and a gap (~1 mm) exists between adjacent bricks to accommodate radial thermal expansion and radiation-induced swelling. A cup and cone arrangement is used to join the bricks vertically. The top and bottom of the column consist of steel bricks. The bottom brick rests on a spigot, and the top of the column is aligned with the biological shield channel penetration by means of a telescopic joint. The brick to brick interfaces are staggered in adjacent channels to avoid horizontal planes of weakness. The fuel assembly is inserted in the channel tube hole in the center of each moderator column, and consists of a zirconium pressure tube into which the fuel element is inserted, and through which the water coolant flows. The fuel element assembly is removed before removing the pressure tube. The pressure tube is positioned in each moderator brick by a series of graphite split rings, which are alternately a close fit to the pressure pipe or the moderator brick fuel channel bore. Aligned slots in the graphite rings allow free flow of the gas blanket along the channels. Two types of graphite are used in the RBMK reactors. The moderator bricks are GR-280 grade graphite (Table 4) and the split rings are machined from grade GR2-125 graphite (Table 4). Both grades are anisotropic and have densities of 1.71 and 1.85 g/cm³, respectively [52].

2.3 Molten salt reactors

2.3.1 Molten Salt Reactor Experiment (U.S.A.)

While not a power producing reactor, the novelty of the Molten Salt Reactor Experiment (MSRE) makes it worthy of inclusion here. The MSRE concept was born out of the aircraft reactor experiment (ARE) which was successfully operated at the Oak Ridge National Laboratory in 1954. The fluid fuel in the MSRE consisted of UF_4 dissolved in fluorides of beryllium and lithium, which was circulated through a reactor core moderated by graphite [53]. The average temperature of the fuel salt was 1200°F (650°C) at the normal operating condition of 8 MW, which was the maximum heat removal capacity of the air-cooled secondary heat exchanger [54]. The graphite core was small, being only 54 in. (137.2 cm) in diameter and 64 in. (162.6 cm) in height. The fuel salt entered the reactor vessel at 1170°F (632°C) and flowed down around the outside of the graphite core in the annular space between the core and the vessel. The graphite core was made up of graphite bars 2 in. (5.08 cm) square, exposed directly to the fuel which flowed upward in passages machined into the faces of the bars. The fuel flowed out of the top of the vessel at a temperature of 1210°F (654°C), through the circulating pump to the primary heat exchanger, where it gave up heat to a coolant salt stream. All of the metal components in contact with molten salt were made of Hastalloy-N, a nickel-based superalloy. Details of the materials used in the MSRE are given in Table 14.

Table 14 . Molten salt reactor experiment materials [53,54]

Parameter	Value
Fuel salt	
Composition:	7LiF - BeF_2 - ZrF_4 - UF_4 (65.0-29.1-5.0-0.9 mole %)
Properties at 1200°F (650°C)	
Density	2.3 g/cm ³
Specific heat	2 kJ/kg.°C
Thermal conductivity	1.43 W/m.°C
Viscosity	29 kg/h.m
Vapor pressure	<1x10 ⁻⁴ bar
Liquidus temperature	434°C
Coolant salt	7LiF - BeF_2 (66-34 mole%)
Moderator	Grade CGB graphite
Specific power	3.3 MW/m ³
Salt containers	Hastalloy-N (68 Ni-17 Mo-7 Cr-5 Fe)
Cover gas	Helium

The circulating pump was maintained under a helium cover gas at a pressure of 5 psi. Approximately 50 of the 120 gal/min discharged by the pump was sprayed into the gas space above the pump, where ^{135}Xe and Kr escaped from the salt. A helium vent stream was bled to atmosphere through a clean-up system (see Section 5) and bottled helium was introduced to maintain system pressure. The control rods, which were flexible, consisted of hollow cylinders of $\text{Gd}_2\text{O}_3\text{-Al}_2\text{O}_3$ ceramic, canned in inconel, and threaded on a stainless-steel hose which also served as a cooling air conduit. An endless-chain mechanism raised and lowered the rods. When scrambled, the rods descended with an acceleration of $\sim 3.66 \text{ m/s}^2$. The core graphite, grade CGB, was specially produced for the MSRE, and had to have a small pore size to prevent penetration of the fuel salt, a long irradiation lifetime, and good dimensional stability. Moreover, for molten salt reactor moderators, a low permeability (preferably $<10^{-8} \text{ cm}^2/\text{s}$) is desirable in order to prevent the build up of unacceptable inventories of the nuclear poison ^{135}Xe in the graphite. At ORNL this was achieved by sealing the graphite surface using a gas phase carbon deposition process [53,55].

3 Radiation Damage in Graphite

3.1 Mechanism of neutron damage

The binding energy of a carbon atom in the graphite lattice is about 7 eV [56]. Impinging energetic particles, such as fast neutrons, can displace carbon atoms from their equilibrium lattice positions. There have been many studies of the energy required to displace a carbon atom (E_d), as reviewed by Kelly [57] and Burchell [58], and this topic is discussed here by Snead in his chapter on "Fusion Energy Applications." The value of E_d is not well defined but lies between 24 and 60 eV. The latter value has gained wide acceptance and use in displacement damage calculations, but a value of 30 eV would be more appropriate.

The primary atomic displacement [primary knock-on carbon atoms (PKAs)] produced by energetic particle collisions produce further carbon atom displacements in a cascade effect. The cascade carbon atoms are referred to as secondary knock-on atoms (SKAs). The displaced SKAs tend to be clustered in small groups of 5-10 atoms and for most purposes it is satisfactory to treat the displacements as if they occur randomly. The total number of displaced carbon atoms will depend upon the energy of the PKA, which is itself a function of the neutron energy spectrum and the neutron flux. Once displaced, the carbon atoms recoil through the graphite lattice displacing other carbon atoms and leaving vacant lattice sites. However, not all of the carbon atoms remain displaced. The displaced carbon atoms diffuse between the graphite layer planes in two dimensions and a high proportion will recombine with lattice vacancies. Others will coalesce to form C_2 , C_3 , or C_4 linear molecules. These in turn may form the nucleus of a dislocation

loop—essentially a new graphite plane. Interstitial clusters may, on further irradiation, be destroyed by a fast neutron or carbon knock-on atom (irradiation annealing). Adjacent lattice vacancies in the same graphitic layer are believed to collapse parallel to the layers, thereby forming sinks for other vacancies which are increasingly mobile above 600°C, and hence can no longer recombine and annihilate interstitials.

The neutron dose to graphite due to irradiation is commonly reported as a time integrated flux of neutrons per unit area (or fluence) referenced to a particular neutron energy. Neutron energies greater than 50 keV, 0.1 MeV, 0.18 MeV, and 1 MeV were adopted in the past and can be readily found in the literature. In the U.K., irradiation data are frequently reported in fluences referenced to a standard flux spectrum at a particular point in the DIDO reactor, for which the displacement rate was measured by the nickel activation [$^{58}\text{Ni}(\text{np})^{59}\text{Co}$] reaction [equivalent DIDO nickel (EDN)]. Early on, neutron irradiation doses to the graphite moderator were reported in terms of the burn-up (energy extracted) from unit mass of the adjacent nuclear fuel, i.e., MW days per adjacent tonne of fuel, or MWd/Ate.

Comparisons of irradiation data from different sources can only be made if conversions to a common displacement (damage) scale are available. Damage to the graphite occurs because of atomic displacements, the number of atomic displacements per atom, i.e., the average number of times each atom is displaced from its equilibrium lattice position, would thus appear to be the appropriate measure of graphite neutron damage dose. Table 15 gives displacements per atom (dpa) conversion factors for the most widely reported damage dose scales.

Table 15. Conversion factors for frequently reported damage dose units

Conversion	Multiplier
n/cm^2 [$E > 50$ keV] to dpa	6.8×10^{-22}
n/cm^2 [$E > 0.1$ MeV] to dpa	7.3×10^{-22}
n/cm^2 [$E > 0.18$ MeV] to dpa	8.9×10^{-22}
n/cm^2 [$E > 1.0$ MeV] to dpa	14.5×10^{-22}
n/cm^2 [EDN] to dpa	13.1×10^{-22}
Calder Equivalent Dose (MWd/Ate) to dpa	1.43×10^{-4}

If two irradiations are undertaken in similar neutron spectra to the same total number of atomic displacements and at the same temperature, but at different rates (i.e., over different time intervals), the graphite sample with the shorter exposure time will show more damage (i.e., a flux or rate effect). This is because the net observed damage is a function not only of the total damage produced (dependant on the neutron dose), but also on the extent of annealing of that damage, which is

dependent on temperature and *time*. This effect has been accounted for through the concept of equivalent temperature. If two irradiations are performed at different levels of fast neutron flux, ϕ_1 and ϕ_2 , identical damage will be caused if the two irradiation temperatures are related by

$$\frac{1}{T_1} - \frac{1}{T_2} = \frac{k}{A} \ln \left(\frac{\phi_2}{\phi_1} \right) \quad (1)$$

where k is Boltzmann's constant and A is an activation energy determined experimentally. Usually, one of the flux levels would pertain to a standard position in a materials test reactor. As discussed by Burchell [58] experimental evidence suggests that flux level or rate effects are significant only at low to moderate irradiation temperatures (<400°C).

3.2 Dimensional changes

A principal result of carbon atom displacements is crystallite dimensional change. Interstitial defects will cause crystallite growth perpendicular to the layer planes (c-axis direction), whereas coalescence of vacancies will cause a shrinkage parallel to the layer plane (a-axis direction). The damage mechanism and associated dimensional changes are illustrated in Fig. 6. Radiation-induced dimensional changes can be very large, exceeding 60% in well-ordered graphite materials. Pyrolytic graphite has frequently been used to study the neutron irradiation-induced dimensional changes of the graphite crystallite [57,59]. Price [60] conducted such a study. Figure 7 shows Price's data for crystallite shrinkage in the a-direction for neutron doses up to ~12 dpa. Price's samples were graphitized at a temperature of 2200-3300°C prior to being irradiated at 1300-1500°C. The a-axis shrinkage increased linearly with dose for all of the samples, but the magnitude of the shrinkage at any given dose decreased with increasing graphitization temperature. Similar trends were noted for the c-axis expansion. The effect of graphitization temperature on irradiation-induced dimensional change accumulation can be attributed to thermally induced improvements in crystal perfection. Higher graphitization temperatures reduce the initial number of lattice defect sites which are available to trap irradiation-induced vacancies, and thus reduce the rate of damage accumulation.

Polygranular graphites possess a polycrystalline structure, usually with significant texture resulting from the method of forming during manufacture. Consequently, structural and dimensional changes in polygranular graphites are a function of the crystallite dimensional changes and the graphite's texture. In polygranular graphite, thermal shrinkage cracks formed during manufacture and that are preferentially aligned in the crystallographic a-direction, initially accommodate the c-direction expansion, so mainly a-direction contraction will be observed. The

graphite thus undergoes a net volume shrinkage. With increasing neutron dose (displacements), the incompatibility of crystallite dimensional changes leads to the generation of new porosity oriented parallel to the basal planes, and the volume shrinkage rate falls, eventually reaching zero. The graphite then begins to swell at an increasing rate with increasing neutron dose because of the combined effect of c-axis growth and new porosity generation. The graphite thus undergoes a volume change "turnaround" into net growth which continues until the generation of cracks and pores in the graphite, due to differential crystal strain, eventually causes total disintegration of the graphite.

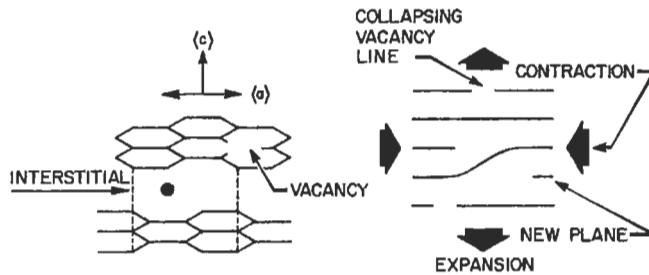


Fig. 6. Radiation damage in graphite showing the induced crystal dimensional strains. Impinging fast neutrons displace carbon atoms from their equilibrium lattice positions, producing an interstitial and vacancy. The coalescence of vacancies causes contraction in the a-direction, whereas interstitials may coalesce to form dislocation loops (essentially new graphite planes) causing c-direction expansion.

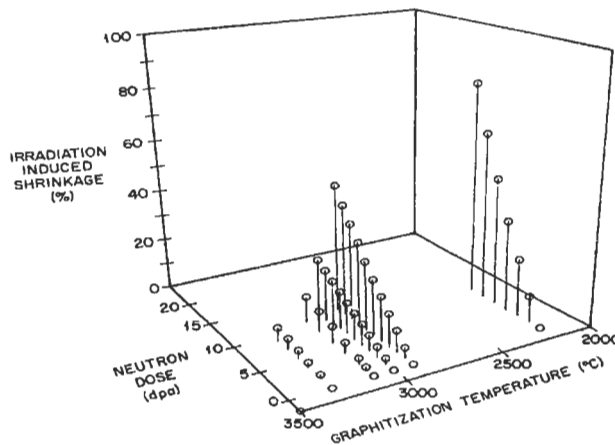


Fig. 7. High-temperature neutron irradiation *a*-axis shrinkage behavior of pyrolytic graphite showing the effects of graphitization temperature on the magnitude of the dimensional changes [60].

Irradiation-induced dimensional damage data for GraphNOL N3M are shown in Fig. 8. N3M is a molded graphite and thus the filler coke particles are preferentially aligned in the radial direction. Consequently, the crystallographic a-direction is predominantly aligned in the radial direction (perpendicular to forming) direction. Therefore, the a-direction irradiation-induced shrinkage is more apparent in the radial direction, as indicated by the radial data (both 600 and 875°C) in Fig. 8.

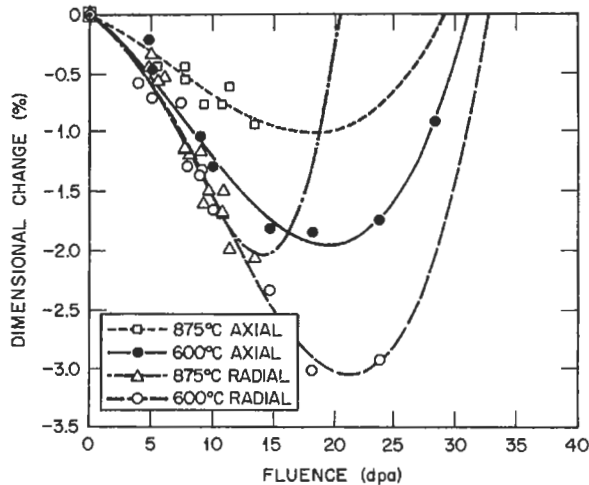


Fig. 8. Neutron irradiation induced dimensional changes for GraphNOL N3M graphite irradiated at 600 or 875 °C [61]. Note that the radial dimensional changes exceed the axial changes due to textural effects.

A general theory of dimensional change in graphite due to Simmons [62] has been extended by Brocklehurst and Kelly [17]. A detailed account of the treatment of dimensional changes in graphite can be found in Kelly and Burchell's analysis of H-451 graphite irradiation behavior [63].

3.3 Stored energy

The irradiation induced displacement processes previously described can cause an excess of energy (associated with the vacancy/interstitial pairs) in the graphite crystallites. The release of this stored energy (or Wigner energy, after the physicist who first postulated its existence [21]) was historically the first problem of radiation damage in graphite to manifest itself. When an interstitial carbon atom and lattice vacancy recombine, their excess energy is given up. If sufficient damage has accumulated in the graphite, the release of this stored energy can result in a rapid rise in temperature. Stored energy accumulation was found to be

particularly problematic in the early (air-cooled) graphite moderated reactors, which operated at relatively low temperatures. Figure 9 shows the rate of release of stored energy with temperature, as a function of temperature, for graphite samples irradiated at 30°C to three different doses (0.01, 0.1, and 0.6 dpa) in the Hanford K reactor. The release curves are characterized by a peak occurring at ~200°C which is associated with the recombination of single interstitials and vacancies. With increasing neutron dose, the 200°C peak becomes broader and the maximum release rate is reduced. The release rate exceeds the specific heat, thus under adiabatic conditions the graphite would rise sharply in temperature. For ambient temperature irradiations it was found that the stored energy could attain values up to 2720 J/g, which if released adiabatically would cause a temperature rise of some 1300°C [7]. The uncontrolled release of stored energy from graphite, causing a sharp rise in core temperature, was of great concern to the operators of the early air-cooled (low-temperature) graphite reactors. In order to limit the total amount of stored energy it became necessary to periodically anneal the graphite. The core temperature was raised sufficiently, by nuclear heating or inserted electrical heaters, to “trigger” the release of stored energy from the graphite. The release then self-propagated slowly through the core, raising the graphite moderator temperature and thus partially annealing the graphite core. It was during such a reactor anneal that the Windscale (U.K.) Reactor accident occurred in 1957 [24].

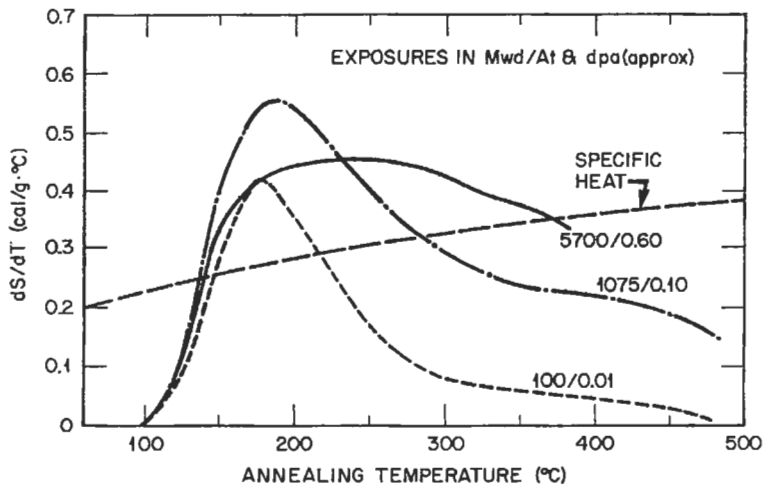


Fig. 9. Stored energy release curves for CSF graphite irradiated at ~30°C in the Hanford K reactor cooled test hole [64]. Note, the rate (with temperature) of stored energy release ($J/Kg\cdot K$) exceeds the specific heat and thus under adiabatic conditions self sustained heating will occur.

The accumulation of stored energy in a graphite is both dose and irradiation temperature dependent. With increasingly higher irradiation temperatures the total amount of stored energy and its peak rate of release diminish, such that above an irradiation temperature of $\sim 300^\circ\text{C}$ stored energy ceases to be a problem. Excellent accounts of stored energy in graphite can be found elsewhere [7,62,64,65].

3.4 Effects on mechanical and physical properties

The physical properties of carbon and graphite materials are drastically altered by irradiation damage. For example, low dose irradiation ($\ll 1$ dpa) can increase the strength of a graphite by up to 80% while simultaneously reducing the thermal conductivity by more than an order of magnitude. Graphite is a phonon conductor of heat. The temperature dependence of thermal conductivity is shown in Fig. 10 for various pyrolytic graphites in the unirradiated condition. The substantial improvements in thermal conductivity caused by thermal annealing, and/or compression annealing, are attributable to increased crystal perfection and size of the regions of coherent ordering (crystallites). This minimizes the extent of phonon-defect scattering and results in a larger phonon mean free path. With increasing temperature the dominant phonon interaction becomes phonon-phonon scattering (Umklapp processes). Therefore, the observed reduction of thermal conductivity with increasing temperature, and the convergence of the curves in Fig. 10, are attributed to the dominant effect of Umklapp scattering in reducing phonon mean free path.

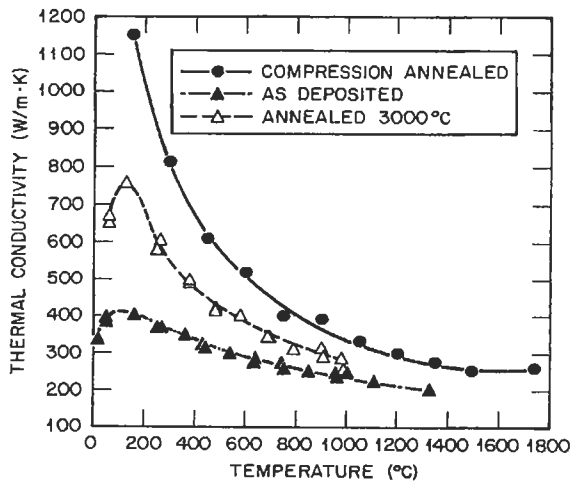


Fig. 10. The temperature dependence of thermal conductivity for pyrolytic graphite in three different conditions [66]. The reduction of thermal conductivity with increasing temperature is attributed to increasing Umklapp scattering of phonons.

The mechanism of thermal conductivity and the degradation of thermal conductivity have been extensively reviewed [57-59]. The increase of thermal resistance due to irradiation damage has been ascribed to the formation of [67]: (i) submicroscopic interstitial clusters, containing 4 ± 2 carbon atoms; (ii) vacant lattice sites, existing as singles, pairs, or small groups; and (iii) vacancy loops, which exist in the graphite crystal basal plane and are too small to have collapsed parallel to the hexagonal axis. The contributions of collapsed lines of vacant lattice sites and interstitial loops to the increased thermal resistance is negligible. The reduction in thermal conductivity due to irradiation damage is temperature and dose sensitive. At any irradiation temperature, the decreasing thermal conductivity will reach a "saturation limit." This limit is not exceeded until the graphite undergoes gross structural changes at very high doses. The "saturated" value of conductivity will be attained more rapidly, and will be lower, at lower irradiation temperatures. The effect of radiation damage on the thermal conductivity of carbon materials is discussed extensively here by Snead in his chapter on "Fusion Reactor Applications." In graphites, the neutron irradiation-induced degradation of thermal conductivity can be very large, particularly at low temperatures. Bell *et al.* [65] report that the room temperature thermal conductivity of PGA graphite (the *Magnox* core graphite) is reduced by more than a factor of 70 when irradiated at 155°C to a dose of ~0.6 dpa. At an irradiation temperature of 355°C the thermal conductivity of PGA was reduced by less than a factor of 10 at doses twice that obtained at 155°C. Above 600°C the reduction of thermal conductivity is less significant. For example, Kelly [7] reports the degradation of PGA at a high temperature. At an irradiation temperature of 600°C and a dose of ~13 dpa, the thermal conductivity was only degraded by a factor of ~6. Moreover, at a irradiation temperatures of 920°C and 1150°C the degradation was minimal (less than a factor of 4 at ~7 dpa).

The thermal expansion of polygranular graphites is controlled by the thermal closure of aligned internal porosity. Irradiation-induced changes in the pore structure (see earlier discussion of structural changes) can therefore be expected to modify the thermal expansion behavior of carbon materials. The behavior of GraphNOL N3M (Fig. 11) is typical of many fine-textured graphites [61], which undergo an initial increase in the coefficient of thermal expansion followed by a steady reduction to a value less than half the unirradiated value of $\sim 5 \times 10^{-6} \text{ }^\circ\text{C}^{-1}$. Similar behavior is reported by Kelly [7] for the AGR moderator graphite (grade IM1-24).

The electrical resistivity of graphite will also be affected by radiation damage. The mean free path of the conduction electron in an unirradiated graphite is relatively large, being limited only by crystallite boundary scattering. Neutron irradiation introduces: (i) scattering centers, which reduce charge carrier mobility; (ii) electron traps, which decreases the charge carrier density; and (iii) additional spin

resonance. The net effect of these changes is to increase the electrical resistivity on irradiation, initially very rapidly, with little or no subsequent change to relatively high fluence [58,61]. A subsequent decrease at very high neutron doses may be attributed to structural degradation.

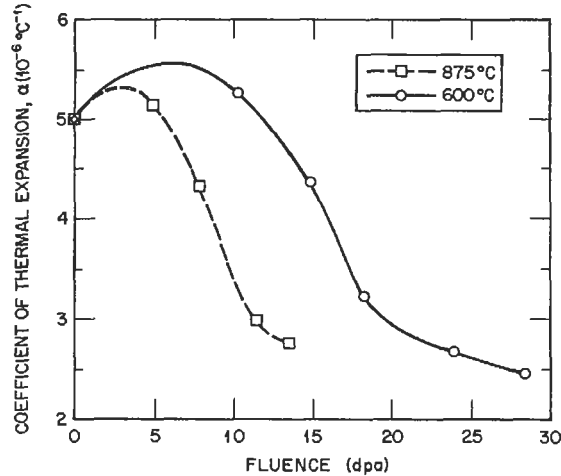


Fig. 11. Neutron irradiation-induced changes in the coefficient of thermal expansion of GraphNOL N3M at irradiation temperatures of 600 and 875°C [61].

The mechanical properties of graphites are substantially altered by radiation damage. In the unirradiated condition, polygranular graphites behave in a brittle fashion and fail at relatively low strains. The stress-strain curve is non-linear, and the fracture process occurs via the formation of sub-critical cracks, which coalesce to produce a critical flaw [9,10]. When graphites are irradiated the stress-strain curves become more linear, the strain to failure is reduced, and the strength and elastic modulus increased. As shown in Fig. 12, there is a rapid rise in strength attributed to dislocation pinning at irradiation-induced lattice defect sites. This effect has largely saturated at doses >1 dpa. Above ~ 1 dpa a more gradual increase in strength occurs due to structural changes within the graphite. For polygranular graphites the dose at which the maximum strength is attained loosely corresponds with the volume change turnaround dose, indicating the importance of pore generation in controlling the high-dose strength behavior.

The strain behavior of polygranular graphite subjected to an externally applied load is largely controlled by shear of the component crystallites. As with strength, irradiation-induced changes in Young's modulus are the combined result of in-crystallite effects, due to low fluence dislocation pinning, and superimposed

structural changes external to the crystallite. The effects of these two mechanisms are generally considered separable, and related by:

$$(E/E_0)_{\text{irradiated}} = (E/E_0)_{\text{pinning}} (E/E_0)_{\text{structure}} \quad (2)$$

Where E/E_0 is the ratio of the irradiated to unirradiated elastic modulus. The dislocation pinning contribution to the modulus change is due to relatively mobile small defects and is thermally annealable at $\sim 2000^\circ\text{C}$. Figure 13 shows the irradiation-induced elastic modulus changes for GraphNOL N3M. The low dose change due to dislocation pinning (dashed line) saturates at a dose < 1 dpa.

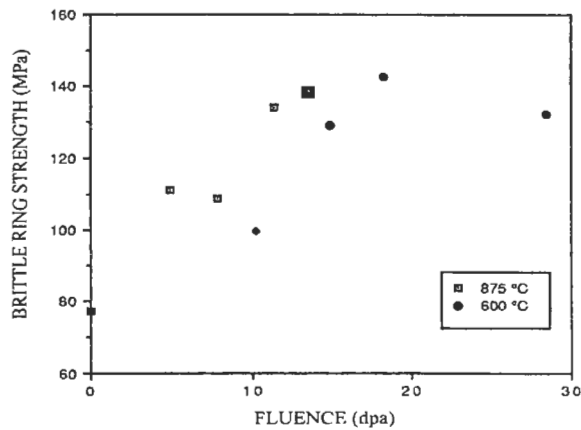


Fig. 12. Neutron irradiation-induced strength changes for GraphNOL N3M at irradiation temperatures of 600 and 875°C [61].

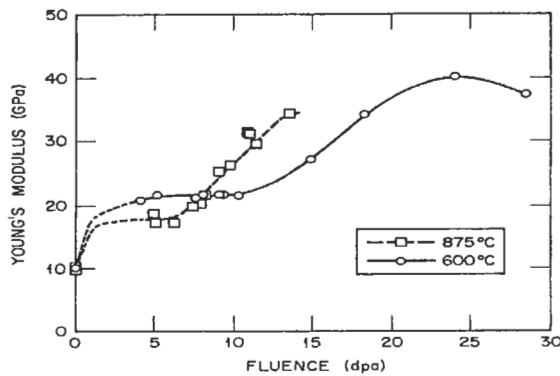


Fig. 13. Neutron irradiation-induced Young's modulus changes for GraphNOL N3M at irradiation temperatures of 600 and 875°C [61].

The elastic modulus and strength are related by a Griffith theory type relationship.

$$\text{strength, } \sigma = \left(\frac{GE}{\pi c}\right)^{1/2} \quad (3)$$

where G is the fracture toughness or strain energy release rate (J/m^2), E is the elastic modulus (Pa), and c is the flaw size (m). Thus, irradiation-induced changes in σ and E (in the absence of changes in $[G/c]$) should follow $\sigma \propto E^{1/2}$. High dose data reported recently by Ishiyama *et al.* [68] show significant deviation from this relationship for grade IG-110 graphite, indicating that changes in G and or c must occur.

3.5 Radiation creep

Graphite will creep under neutron irradiation and stress at temperatures where thermal creep is normally negligible. The phenomenon of irradiation creep has been widely studied because of its significance to the operation of graphite moderated fission reactors. Indeed, if irradiation induced stresses in graphite moderators could not relax via radiation creep, rapid core disintegration would result. The observed creep strain has traditionally been separated into a primary reversible component (ϵ_1) and a secondary irreversible component (ϵ_2), both proportional to stress and to the appropriate unirradiated elastic compliance (inverse modulus) [69]. The total irradiation-induced creep strain (ϵ_c) is thus:

$$\epsilon_c = \epsilon_1 + \epsilon_2 \quad (4)$$

or,

$$\epsilon_c = (\sigma/E_0)[1 - \exp(-b\gamma)] + (K/E_0)\sigma\gamma \quad (5)$$

where E_0 the unirradiated Young's Modulus, b is a constant, γ is the neutron dose, and K is the irradiation creep coefficient. Kelly [7] has reported that values of -4×10^{-20} for b and 0.23×10^{-20} for K apply to U.K. data taken over a range of irradiation temperatures (300-650°C). At high fluences Eq. (5) must be modified to account for structural changes occurring in the graphite:

$$\epsilon_c = \frac{\sigma}{E_0} + \left[\frac{d\epsilon_c}{d\gamma}\right]_0 \int_0^\gamma S^{-1}(\gamma) \cdot d\gamma \quad (6)$$

where $\left[\frac{d\epsilon_c}{d\gamma}\right]_0$ is the initial secondary creep rate and $S(\gamma)$ is the "structure factor" normally deduced from Young's Modulus changes ascribed to structural effects

(i.e., $S(\gamma) = (E/E_p)$ where E is the Young's Modulus at fluence γ and E_p is the Young's modulus after the initial increase due to dislocation pinning).

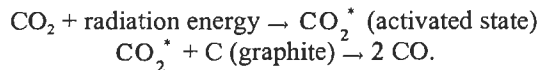
Oku *et al.* [70] have reported the creep coefficient of IG-110 graphite and shown it to be reasonably linear with temperatures over the range 300-1400°C at low to moderate fluences (< 2 dpa). Kennedy *et al.* [71] have reported the irradiation creep rate of a German graphite in tension and compression for creep strains in excess of 3.5%. Their data show the creep rate decreasing at higher fluences (>6 dpa) where the creep strain exceeds ~1%. Kelly and Burchell [72] attempted to rationalize the disparity between Kennedy *et al.*'s data indicating a reducing creep rate and the more commonly reported constant creep rate. They concluded that the reported reduction in creep rate was not a true reduction, but rather an artifact of changes in the properties in the stressed sample which modified their dimensional change under irradiation compared to the unstressed control samples. Based upon the success of their analysis at linearizing creep rate data, Kelly and Burchell proposed a redefinition of irradiation creep strain as "the difference in dimensions between a stressed sample and a sample with the same properties as the stressed sample irradiated unstressed" [72].

4 Radiolytic Oxidation

In reactor designs which utilize inert gas coolants (typically helium), the only process which alters the properties of the graphite is irradiation damage. However, in carbon dioxide-cooled reactors graphite properties are also changed by the process of radiolytic oxidation. Complete reviews of radiolytic oxidation and its effects on graphite properties may be found in the literature [73-75]. Here, radiolytic oxidation of graphite is briefly reviewed and its consequences for reactor design and operation discussed.

4.1 The mechanism of radiolytic oxidation

The simplest description of the reaction responsible for the radiolytic oxidation of graphite is:



In reality the situation is considerably more complicated. The exact nature of the activated stated (oxidizing species) has been the subject of intense study [73-75], but is now generally accepted to be the negatively charged ion CO_3^- [73,75,76]. The oxidation reaction occurs at temperatures far below those at which thermal oxidation becomes significant and, although the reaction is slow, it can lead to significant mass loss from the moderator during its lifetime. The oxidation reaction

takes place primarily in the graphite pores which are open to the gas. The reaction rate is proportional to the rate of energy deposition in the gas, and hence approximately to the coolant pressure. To a first approximation, the number of activated species (CO_2^*) produced in CO_2 for 100 eV of energy absorbed in the gas phase, G_o , is constant at $\sim 3/100$ eV. Therefore, the rate of production per unit volume of gas, \dot{X} ($\text{cm}^{-3}\text{s}^{-1}$), at pressure P , and temperature T , with an energy deposition rate E (eV/g.s), is given by:

$$\dot{X} = E \cdot \rho_g \cdot \left[\frac{G_o}{100} \right] \left(\frac{P}{P_o} \right) \left(\frac{T_o}{T} \right) \quad (7)$$

where ρ_g is the CO_2 density at standard pressure P_o and temperature T_o .

The oxidizing species, once created, can be deactivated in the gas phase by interaction with a number of molecules. The radiolytic oxidation rate of the graphite can, therefore, be reduced by gas phase inhibitors such as carbon monoxide (including that produced by the oxidizing reaction), hydrogen, water, and methane. Inhibition of the radiolytic oxidation reaction is achieved by adding, in the case of *Magnox* reactors, a few %CO to the coolant. In the AGR reactors, which have higher gas pressures and power density, additions of methane are additionally required to inhibit the oxidation reaction. The range (distance traveled between creation and deactivation) of the oxidizing species, L , depends on the coolant composition. It can be shown that in pores with linear dimensions less than L , essentially all of the oxidizing species reach the pore walls and gasify the graphite. In pores with linear dimensions greater than L , only a fraction of the oxidizing species reach the pore wall. Both the total porosity and the pore size distribution can thus be expected to influence the rate of radiolytic oxidation.

The mechanism of inhibition is rather complex. Simplistically, the oxidizing species created in the CO_2 react with molecules such as H_2 , H_2O , CO , or CH_4 and are deactivated in the process. A product of the gas phase reaction is a depositing carbon species which provides protection for the graphite surface by being sacrificially oxidized as the oxidizing species reaches the graphite surface. The presence of inhibitors in the coolant does not completely arrest graphite moderator oxidation, but reduces its rate to an acceptable level. The radiolytic oxidation process described results in both the production of CO at a rate proportional to the oxidation rate and the destruction of the added inhibitors. Polygranular graphite contains a complicated pore structure, with approximately half of the porosity being interconnected and open to the coolant gas. The coolant gas gains access to the inner parts of the graphite moderator bricks by permeating through the pores and graphite pore walls either by diffusion or under the influence of a pressure gradient. The local gas composition, and hence the oxidation rate, changes as it permeates the graphite. Thus, the gas composition in the pores depends upon the

diffusivity ratio and the permeability of the graphite, both of which are affected by the radiolytic weight loss and neutron irradiation-induced graphite structural changes.

4.2 Effects of radiolytic oxidation on properties

Radiolytic oxidation alters most of the important properties of graphite, including strength, elastic modulus, work of fracture, thermal conductivity, permeability, and diffusivity but does not affect the thermal expansion coefficient or Poisson's ratio. The effects of radiolytic oxidation on the properties of a wide range of graphites have been studied in the U.K. [7,73,74] where it was found that, to a first approximation, they can be described by similar relationships:

$$\text{Strength} \quad \sigma = \sigma_0 \exp(-4x) \quad (8)$$

$$\text{Elastic modulus} \quad E = E_0 \exp(-3.6x) \quad (9)$$

$$\text{Work of fracture} \quad \gamma = \gamma_0 \exp(-2.2x) \quad (10)$$

$$\text{Thermal conductivity} \quad K = K_0 \exp(-2.7x) \quad (11)$$

$$\text{Diffusivity} \quad \lambda = \lambda_0 + (\frac{1}{2} - \lambda_0)x^2 \quad (12)$$

where the zero subscript denotes initial values, and x is the fractional weight loss due to radiolytic oxidation. Property changes due to oxidation must also be corrected for the effects of radiation damage. The combination of these two effects is made using multiplicative rules. For example, the combined effect on thermal conductivity would be given by:

$$K(T) = K_0 (K/K_0)_i \exp(-2.7x) \quad (13)$$

where K_0 is the unirradiated value and $(K/K_0)_i$ is the effect of irradiation alone at the irradiation temperature. Similar rules apply to strength and elastic modulus and have been verified experimentally [77]. The interaction between radiolytic oxidation and dimensional change is complicated. As previously discussed, irradiation-induced dimensional changes are a consequence of both intracrystallite dimensional changes (a-axis shrinkage and c-axis growth) and intercrystallite dimensional changes (elimination and creation of cracks or pores), with the former dominating at lower neutron doses. Intracrystallite changes are unaffected by radiolytic oxidation and thus low neutron dose dimensional change is not modified. With increasing dose, however, intercrystallite effects (pore and crack generation) become dominant and the graphite dimensional changes begin to "turn around" or go into shrinkage reversal. Evidence from pre-oxidized samples, and samples doped with boron-11 to enhance the rate of radiation damage, indicate that shrinkage reversal is delayed in dose [7]. Presumably, this delay can be attributed

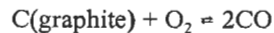
to the enlargement of porosity that accommodates the intercrystallite strains, thus reducing the strain mismatch and the rate of pore generation, and consequently delaying the onset of shrinkage reversal.

It is well known that for a given weight loss, thermal oxidation of graphite causes a larger reduction in strength and elastic modulus than radiolytic oxidation. Pickup *et al.* [78] showed the decrement in dynamic elastic modulus, E , due to thermal oxidation fitted an exponential relationship:

$$E = E_0 \exp(-7.0x) \quad (14)$$

where E_0 and x are the unoxidized modulus and the fractional weight loss, respectively. This equation has an identical form to Eq. 9, but the exponent is almost twice as large. Thus, for a 5% weight loss the modulus would be reduced by approximately 30% for thermal oxidation but only by 16% by radiolytic oxidation. Burchell *et al.* [79] examined the microstructure of thermally and radiolytically oxidized PGA graphite and noted that, in contrast to thermal oxidation which selectively develops slit-shaped pores, radiolytic oxidation was much less selective. They developed models for the effects of thermal and radiolytic oxidation upon elastic modulus and related the modulus decrement to the pore aspect ratio (a/c). Pore aspect ratios of 6 for radiolytic oxidation and 11 for thermal oxidation were predicted, in qualitative agreement with their microstructural observations. The more severe effects of thermal oxidation on modulus was attributed, therefore, to its preferential development of pores of high aspect ratio.

Thermal oxidation of graphite moderators is significant in several contexts. In the early air-cooled reactors the moderator temperature was low and hence the thermal oxidation rate was acceptable. However, the rate increased as the graphite became damaged by neutron irradiation. Moreover, the heat produced from the exothermic reaction



was easily removed by the coolant flow. However, under off-normal conditions, i.e., during stored energy anneals when the air flow was reduced to allow core heat-up, runaway air oxidation could cause uncontrolled heating. Rapid thermal oxidation of the moderator graphite was implicated as a contributing factor to the 1957 Windscale Reactor accident [24].

4.3 Implications for reactor core design and operation

Radiolytic oxidation is important to the design and operation of reactors because it adversely affects key graphite properties and, by removing moderator material, may bring about the need for increased fuel enrichment. As mentioned earlier, an inhibitor (methane) is added to the coolant to reduce radiolytic oxidation to acceptable levels. However, access of the inhibitor to the inner portions of the moderator brick must be assured. Two approaches have been adopted in the AGRs to provide this access. Vertical methane access holes are provided in the fuel bricks and in the later stations, Heysham II and Torness, a pressure drop from outside to inside the brick was established to cause an enhanced flow through the brick. The amount of inhibitor added must be restricted, however, because the carbon inhibition reaction product deposits on the fuel pin and restricts heat transfer to the coolant, thus reducing reactor efficiency.

Structural integrity of the graphite core has to be assured, and thus predictive core behavior models are required to account for property changes due to radiolytic oxidation and radiation damage [80,81]. Typically, these models incorporate core monitoring data for the extent and distribution of graphite weight loss throughout the core [76]. A further concern arises during air ingress accidents in graphite moderated reactors when heat, generated from the thermal oxidation of the graphite, must be removed. In this respect, the situation with a CO₂ cooled reactor is more complex because of the presence of the very reactive carbon deposits which arise from the gas phase inhibition reaction discussed in Section 4.1. Therefore, it behooves the reactor operator to have a reliable assessment of the amount and distribution of the reactive carbon deposit in the reactor core.

5 Other Applications of Carbon in Fission Reactors

The overwhelming majority of carbon utilized in nuclear reactors is in the form of graphite for the neutron moderator and reflector. However, several other applications of carbon are noteworthy, and are briefly discussed here.

5.1 Activated carbon

Gaseous fission products are produced during reactor operation, notably iodine (in elemental form and as methyl iodide), krypton, and xenon. Accidental leakage of these gasses could occur from the reactor core or primary coolant circuit during operation. Therefore, these gasses are trapped in activated carbon beds to reduce their concentration in the coolant gas. Because methyl iodide is less readily adsorbed than iodine under the conditions of high humidity frequently encountered in reactor, the carbon is impregnated with potassium iodide, potassium triiodide,

or triethylenediamine [82]. Nuclear grade activated carbons are prepared from coconut shell or coal-based precursors and are highly microporous. The adsorption beds have long contact time allowing the radioactive krypton and xenon gases opportunity to decay. In the DRE (see Section 2) the fission products were adsorbed in activated carbon delay beds housed in water-cooled tubes. The cooling was necessary to remove radioactive fission product decay heat so as to maintain the bed temperatures sufficiently low to retain the fission product gasses. Bed delay times were 15 hours for krypton and 200 hours for xenon [34]. Downstream of the delay beds a liquid nitrogen-cooled activated charcoal bed was provided to trap (adsorb) the stable Xe and ^{85}Kr and helium coolant gas impurities (N_2 , CH_4 , and Ar). Unlike the delay beds, which ran in continuous breakthrough mode, the cold trap was regenerated by purging with warm helium to desorb the impurities, which were vented to atmosphere in a controlled fashion. A similar system was utilized at the AVR in Germany [42] and at the Peach Bottom Reactor in the U.S.A. [29]. However, in the Peach Bottom Reactor a helium purge flow through the fuel element passed through a charcoal fission product trap at the base of the fuel element, and then to the external gas cleanup system [36].

In the MSRE, a helium cover gas stripped Xe and Kr from the fuel salt, and was bled at the rate of 4 l/min through a charcoal-based, clean-up system before being released to atmosphere. The gas passed through a holdup bed where the fission products decayed and gave up their heat. The gas then passed to beds which consisted of pipes filled with charcoal, submerged in a water-filled pit at $\sim 90^\circ\text{F}$. The beds operated on a continuous flow basis and delayed the Xe for ~ 90 days and the Krypton for ~ 7 days. Thus, only stable or long-lived gaseous nuclides were present in the helium that was discharged through the stack after passing through the beds [54].

5.2 High temperature fuel for HTGRs

The desire to operate nuclear reactors at higher temperatures and thus achieve greater efficiencies and economy, necessitated the development of high temperature fuels. The use of metal fuel and light alloy cladding limits the fuel temperature to $\sim 600^\circ\text{C}$. Although the use of oxide fuel and stainless-steel clad allows increased fuel temperatures, an all ceramic/carbon fuel and fuel element will tolerate substantially higher operating temperatures. Fission product retention within the fuel, or fuel element, must be assured in HTGRs. Several approaches to retaining or minimizing fission product migration to the primary coolant circuit of HTGRs were developed, but the approach that has enjoyed the greatest popularity and success has been the use of the coated fuel particle. The technology of coated fuel has been described elsewhere, for example see Ref. [83], Piccinini [84], or Nabilek *et al.* [85]; the key features of the fuel are briefly described here. The basic philosophy of coated particle fuel is that the fission products should be

retained in the fuel by the various overcoated layers. The fuel particle is a small spherical fuel element up to ~1 mm in diameter which is comprised of a fuel "kernel" of oxide, carbide, or oxycarbide, and several overcoating layers. The two coated particle types most commonly used have been those with the two-layer Biso coating (buffer and pyrolytic carbon) and the four layer Triso coating with its interlayer of SiC between two layers of high density isotropic pyrolytic carbon [86] over the buffer layer. The buffer layer of porous pyrolytic carbon overcoats the fuel kernel and provides sufficient pore volume for the adsorption of gaseous fission products. The overcoating process occurs via gas phase deposition. By varying the type of hydrocarbon gas, deposition temperature, flow rate, etc., pyrolytic carbon coatings can be deposited with the desired properties. SiC coatings are deposited by the decomposition of $\text{CH}_3\text{Cl}_3\text{Si}$ in the presence of hydrogen. A fluidized bed coating furnace is used for these processes [87,88]. Bokros [89] showed that the irradiation behavior of the pyrolytic carbon coatings is highly dependant upon deposition conditions, which control coating properties such as crystalline anisotropy and density. Both Biso and Triso particles are capable of retaining all gaseous fission products with properly designed and specified coatings. Moreover, intact Triso particles also provide near complete retention of metallic fission products at current peak fuel design temperatures [86].

5.3 HTGR fuel matrix materials

Once fabricated, the fuel particles are combined with a matrix material containing a pitch or resin binder, and graphite or carbon filler. Fuel element designs usually fall into two categories, referred to as prismatic fuel elements or spherical fuel elements. The former arrangement was used in the U.S.A. for the Peach Bottom and Fort St. Vrain HTGRs [Fig. 14(a)], and in Japan for the HTTR core. The latter design was developed in Germany and was used successfully in the AVR and THTR [Fig. 14(b)]. The reference HTGR (U.S.A.) fuel design [90] consists of coated fuel particles contained in a matrix formed into cylindrical shaped rods [Fig. 14(a)]. The matrix material, which bonds the coated particles together to form the rods, is primarily composed of a homogeneous mixture of pitch and graphite flour. During fuel element technology development in the U.S.A., both coal tar and petroleum binder pitches were evaluated, as well as various thermosetting resins. Numerous graphite flours were also evaluated, including natural-flake, artificial-flake, and near-isotropic graphites. The matrix is injected while in a fluid state (usually at elevated temperature) into a bed of close-packed particles constrained in a mold. The rods are then placed in a graphite block and are heated to high temperature to carbonize the binder pitch. Harmon and Scott [90] report typical fuel matrix compositions to be: 50% Ashland A240 petroleum pitch, 40% near isotropic graphite flour (Great Lakes Carbon Co. grade 1089); or 10% thermax powder or, 60% Ashland A-240 petroleum pitch, and 40% Airco-Speer grade RC4 near-isotropic graphite flour. Figure 14(b) shows a spherical fuel element typical

of those used in the THTR. About 10^4 coated fuel particles are dispersed in a graphitic matrix to form a fueled zone, which is surrounded by a fuel free shell composed of the same graphitic materials [91]. The overall diameter of the element is 6 cm, with a 0.5-cm thick fuel-free shell. Fuel element manufacture begins with the warm mixing of powdered graphitic materials and thermosetting resin to form a resinated powder, which is ground to the preferred size. A portion of the resinated powder is used to overcoat the coated fuel particles. A further portion of the resinated powder is mixed with the overcoated fuel particles and premolded to produce the fueled zone of the fuel sphere. In a second molding stage, the premolded fueled part is encased in the fuel-free shell, which is also made from the resinated powder. The final forming process is a high-pressure isostatic pressing operation. The fuel element is machined to the required dimension and heat treated in a two stage process (900/1950°C) to carbonize the resin binder and remove impurities [85,91].

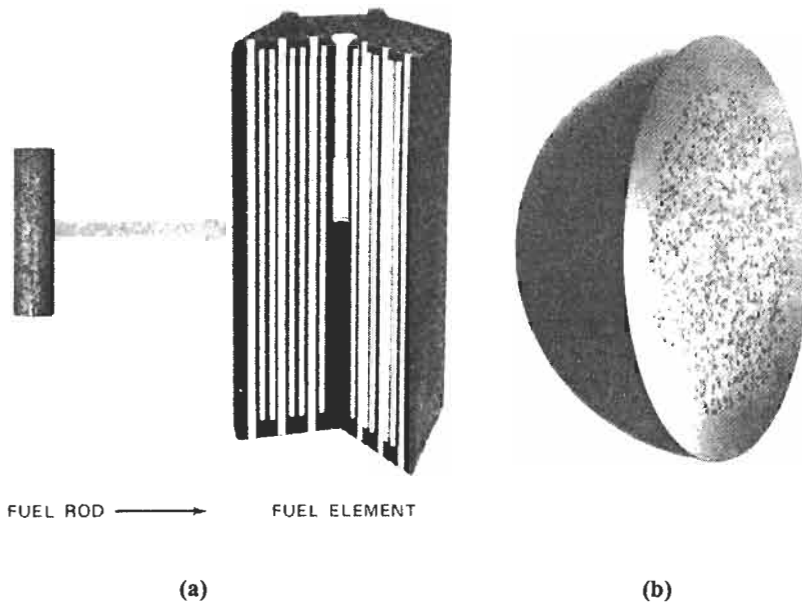


Fig. 14. HTGR fuel elements: (a) prismatic core HTGR fuel element (b) cross section of a spherical fuel element for the pebble bed HTGR. Reprinted from [88], © 1977 American Nuclear Society, La Grange Park, Illinois.

5.4 Carbon-carbon composites

Control of the nuclear chain reaction in a reactor is maintained by the insertion of rods containing neutron absorbing materials such as boron, boron carbide, or borated steel. In state-of-the-art high temperature reactor designs, such as the Gas

Turbine-Modular High Temperature Reactor (GT-MHR) and the HTTR, the reactor core temperature can approach 1600°C during severe loss of coolant accidents. A high temperature control rod is therefore desirable, and assures control rod availability under all conceivable reactor conditions. With this goal in mind, efforts have been directed in the U.S.A. [92] and Japan [93,94] toward the development of carbon-carbon (C/C) composite control rods. A C/C composite material comprises a carbon or graphite matrix that has been reinforced with carbon or graphite fibers. Multidirectionally reinforced C/C composites are substantially stronger, stiffer, and tougher than conventionally manufactured polygranular graphites, and are thus preferred over graphites for many critical applications, such as control rods.

5.5 Carbon insulation materials

Because of their low thermal conductivity, high temperature capability, low cost, and neutron tolerance, carbon materials make ideal thermal insulators in nuclear reactor environments. For example, the HTTR currently under construction in Japan, uses a baked carbon material (Sigril, Germany grade ASR-ORB) as a thermal insulator layer at the base of the core, between the lower plenum graphite blocks and the bottom floor graphite blocks [47].

6 Summary and Conclusions

The development of graphite moderated reactors has advanced substantially in the fifty years since Enrico Fermi's first exponential pile. Gas and water-cooled graphite moderated reactors have been constructed for experimental, production, or power generation purposes in numerous countries. In the U.K. and France, the CO₂/graphite reactors have operated economically and safely for greater than 40 years. Commercial HTGRs based on helium coolant have been operated in the USA and Germany, and experimental helium-cooled HTGRs are currently under construction in Japan and China.

In support of the development of graphite moderated reactors, an enormous amount of research has been conducted on the effects of neutron irradiation and radiolytic oxidation on the structure and properties of graphites. The essential mechanisms of these phenomena are understood and the years of research have translated into engineering codes and design practices for the safe design, construction and operation of gas-cooled reactors.

Gas-cooled, graphite moderated reactors have several significant advantages over other reactor designs by virtue of their inherent passive safety characteristics. These are the result of the large thermal mass of the graphite core, the high

temperature tolerance of the ceramic/graphite fuel system, a negative temperature coefficient of reactivity, and excellent retention of fission products [95]. Recent research and design activities in the U.S.A. have led to the evolution of a direct (Brayton) cycle HTGR design, known as the GT-MHR. This reactor concept has the advantage of high efficiency and a modular design, offering flexibility in meeting uncertainties in load growth [96].

Increasingly, national and world leaders are concerned about fossil-fueled power plant gas emissions (the so-called greenhouse gases) and the consequences of the ensuing global warming. Hence, there is reason to believe that the role of nuclear power may become more prominent in the future [97]. However, as highlighted by Fulkerson and Jones [98], the use of nuclear power will not expand significantly until a number of technical and institutional issues have been resolved to the satisfaction of the public and utilities. Inherently safe reactors (such as HTGRs) could play a vital role in the process of regaining public acceptance of nuclear power [98].

The author considers the long term prospect for the deployment of HTGRs to be good. Continued public and political awareness of global warming and the ultimate escalation of fossil fuels prices will necessitate the construction of inherently safe reactors. In the short term, however, the situation is less encouraging. There are currently no commercial HTGRs under construction, and only a handful of countries have active HTGR development programs. It is hoped that experienced and resourceful engineers and scientists will be available when the need for renewed nuclear construction arises.

7 Acknowledgments

Research sponsored by the U. S. Department of Energy under contract DE-ACO5-96OR22464 with Lockheed Martin Energy Research Corporation at Oak Ridge National Laboratory.

8 References

1. Nuclear Physics. In *Modern Power Station Practice*, Vol. 8, Nuclear Power Generation, 2nd edn, pub. for the Central Electricity Generating Board by Pergamon Press, Oxford, 1978, pp. 1-49.
2. Eatherly, W.P. and Piper, E.L., Manufacture. In *Nuclear Graphite*, ed. R.E. Nightingale. Academic Press, New York, 1962, pp.21-51.
3. Mantell, C.L., *Carbon and Graphite Handbook*, Interscience Publishers, New York, 1968.

4. Hutcheon, J.M., in *Modern Aspects of Graphite Technology*, ed. L.C.F. Blackman, Academic Press, London, 1970, pp. 49-78.
5. Ragan, S. and Marsh, H., Review: science and technology of graphite manufacture, *J. Mater. Sci.* 1983, 18, 3161-3176.
6. Ruland, W., X-ray diffraction studies on carbon and graphite, *Chem. Phys. Carbon*, 1968, 4, p. 1.
7. Kelly, B.T., Nuclear reactor moderator materials. In *Materials Science and Technology: Nuclear Materials*, Part 1 (VCH Weinheim, 1994) pp. 365-417.
8. Heintz, E.A., Influence of coke structure on the properties of the carbon-graphite artefact, *FUEL*, 1985, 64, 1192-1196.
9. Tucker, M.O., Rose, A.P.G., and Burchell, T.D., The fracture of polygranular graphites, *Carbon*, 1986, 24(5), 581-602.
10. Burchell, T.D., A microstructurally based fracture model for polygranular graphites, *Carbon*, 1996, 34(3), 297-316.
11. Burchell, T.D., Studies of fracture in nuclear graphite. Ph.D. thesis, University of Bath, U.K., 1986.
12. Strizak, J.P. The effect of volume on the tensile strength of several nuclear-grade graphites, In *Proceeding of the IAEA Specialists meeting on the Status of Graphite Development for Gas Cooled Reactors*, IAEA-TECHDOC-690, IAEA, Vienna, 1993, pp. 233-240.
13. Romanoski, G.R. and Burchell, T.D., The effect of specimen geometry and size on the fracture toughness of nuclear graphites, In *Proceeding of the IAEA Specialists meeting on the Status of Graphite Development for Gas Cooled Reactors*, IAEA-TECHDOC-690, IAEA, Vienna, 1993, pp. 241-247.
14. Sato, S., Kawamata, K., Kurumada A., Ugachi, H. and Awaji, H. Degradations of thermal shock resistance and the fracture toughness of reactor graphite subjected to neutron irradiation. In *Proceedings of the IAEA Specialist Meeting on Graphite Component Structural Design*, ed. K Sanokawa, JAERI-M-86-192, IWGGCR/11, Japan Atomic Energy Research Institute, 1987, 144-157.
15. Platonov, P.A., Karpukhin, V.I., Shtrombakh, Ya.I., Alekseev, V.M., Chugunov, O.K., Gurovich, B.A. and Trofimchuk, E.I., Specific behavior of reflector and matrix graphite under high temperature irradiation. In *Proceeding of the IAEA Specialists meeting on the Status of Graphite Development for Gas Cooled Reactors*, IAEA-TECHDOC-690, IAEA, Vienna, 1993, pp. 205-209.
16. Haag, G., Mindermann, D. and Wagner, M.H., Nuclear graphites on their way to their next application, In *Proc. 18th Biennial Conf. on Carbon*, 1987, 517-518.
17. Brocklehurst, J.E. and Kelly, B.T., Analysis of the dimensional changes and structural changes in polycrystalline graphite under fast neutron irradiation, *Carbon*, 1993, 31, 155-178.
18. Kennedy, C.R. and Woodruff, E.M., Irradiation effects on the physical properties of grade TSX graphite, WCH-EP-0211, Westinghouse Hanford Company, Richland, Washington, 1989.
19. Burchell, T.D. and Nelson, G.E., Thermal physical properties of H-451 graphite, ORNL/NPR-93/10, Oak Ridge National Laboratory, 1993.
20. Fermi, E., Experimental production of a divergent chain reaction, *Am. J. Phys.*, 1952, 20(9), 536-558.
21. Wigner, E.P., Theoretical physics in the metallurgical laboratory of Chicago, *J. Appl Phys.*, 1946, 17(11), 857-863.

22. Nightingale, R.E., Graphite in the nuclear industry, in *Nuclear Graphite*, ed. R.E. Nightingale, Academic Press, New York, 1962, pp. 1 20.
23. Morgan, W.C., Nuclear graphite development, operational problems, and resolution of these problems at the Hanford production reactors. In *Proceedings of the IAEA Specialists Meeting on Graphite Moderator Lifecycle Behavior*, IAEA-TECHDOC-901, IAEA, Vienna, 1996, pp. 69 77.
24. Arnold, L., *Windscale 1957, Anatomy of a Nuclear Accident* St. Martin's Press, New York, 1992.
25. Frost, B.R.T., *Nuclear Materials Part I*, Materials Science and Technology, Vol. 10A. VCH, New York, 1994.
26. Moore, R.V. and Goodlet, B.L., The 1951-53 Harwell design study, *J. Brit. Nucl. Energy Conf.* 1957, 2, 47 60.
27. Hinton, Sir C., The place of the Calder Hall type of reactor in nuclear power generation, *J. Brit. Nucl. Energy Conf.*, 1957, 2, 43 46.
28. Alexander, W., and Street A., *Metals in the Service of Man*, 7th edn, Penguin Books 1979, p. 326.
29. *Status of and Prospects for Gas-Cooled Reactors*, IAEA Tech Report No. 235, IAEA, Vienna, 1984.
30. Bindon, F.J.L., CEBG Magnox gas-cooled reactor operating performance 1962-1980, *Nucl. Energy*, 1981, 20, 127 132.
31. Southwood, J.M.R., The engineering development of thermal reactors in the U.K., *Proc. Instn. Mech. Engrs.*, 1978, 192, 311 323.
32. Gallie, R.R. and Hewitt, P.V., Eighteen years of operating and development experience with Windscale AGR, *Nucl. Energy*, 1982, 21, 21 28.
33. National Nuclear Corporation, New advanced gas-cooled reactors incorporate design improvements, *Nucl. Engr. Int.*, March 1981, 27 36.
34. Howard, R.M., Price, M.S.T. and Shepherd, L.R., *A Summary and Evaluation of the Achievements of the Dragon Project and its Contribution to the Development of the High Temperature Reactor*, Dragon Project Report 1000, AEE Winfrith, Dorset, 1978, pp. 2.17 2.24
35. Graham, L.W., Watt, W., Johnson, W., Arragon, P.A.P. and Price, M.S.T., The development of low permeability graphite for the Dragon Reactor Experiment. In *Proceeding of the Fifth Conference on Carbon*, Vol. 2, Pergamon Press, Oxford, 1963, pp. 387 404.
36. Malinauskus, A.P., de Nordwall, H.J., Dyer, F.F., Wichner, R.P., Martin, W.J. and Kolb, J.O., Fission product behavior during operation of the second Peach Bottom core. In *Proceeding of the Symposium on Gas-Cooled Reactors with Emphasis on Advanced Systems*, Vol. 1, IAEA-SM-200/50, IAEA, Vienna, 1976, pp. 237 249.
37. Goeddel, W.V., Tully Jr., G.R., and Meyer, R.A., The use of graphite in high temperature nuclear fuel elements. In *Proceeding of the Fifth Conference on Carbon*, Vol. 2, Pergamon Press, Oxford, 1963, pp. 347 386.
38. Cadwell, J.J., McEachern, D.W., Read, J.W., Simon, W.A. and Walker, R.F., Operational testing highlights of Fort St. Vrain. In *Proceeding of the Symposium on Gas-Cooled Reactors with Emphasis on Advanced Systems*, Vol. 1, IAEA-SM-200/58, IAEA, Vienna, 1976, pp. 151 163.
39. Walker, R.E. and Johnston, T.A., Fort Saint Vrain nuclear power station, *Nucl. Engr. Int.*, December 1969, 1069 1073.

40. Dahlberg, R.C., Turner, R.F. and Goeddel W.V., Core design characteristic, *Nucl. Engr. Int.*, December 1969, 1073 1077.
41. Nuclear Reactors Built, Being Built, or Planned 1994. DOE/OSTI-8200-R58, Pub. U.S. Department of Energy, Office of Scientific and Technical Information, 1995, p. 27.
42. Ziermann, E., Review of 21 years of power operation at the AVR nuclear power station in Julich, *Nucl. Engr. Des.*, 1990, 121, 135 142.
43. Theymann, W., Status and prospects of the HTR 500 based on the THTR 300 operation experience and recent R & D-work, *Nucl. Engr. Des.*, 1992, 136, 127 133.
44. Knufer, H., Preliminary operating experience with the AVR at an average hot-gas temperature of 950°C, *Nucl. Engr. Des.*, 1975, 34, 73 78.
45. Roedig, M., Status of HTR development in Germany. In *Proceedings of the Specialists Meeting on The status of graphite development for gas cooled reactors*, IAEA-TECDOC-690, Pub. IAEA, Vienna, 1993, 40 43.
46. G. Haag, Forschungszentrum Jülich GmbH, Jülich, Germany, personal communication to T. D. Burchell, Oak Ridge National Laboratory, Oak Ridge, Tenn., March 1997.
47. Saito, S., Status of the HTGR Program in Japan. In *Proceedings of the IAEA Specialists meeting on the Status of Graphite Development for Gas Cooled Reactors*, IAEA-TECHDOC-690, IAEA, Vienna, 1993. pp. 29 36.
48. Japan Atomic Energy Research Institute, High Temperature Engineering Test Reactor (HTTR), Technical Literature.
49. Woodruff, E.M., Graphite surveillance in N reactor. In *Proceedings of the IAEA Specialists meeting on the Status of Graphite Development for Gas Cooled Reactors*, IAEA-TECHDOC-690, IAEA, Vienna, 1993. pp. 273 280.
50. Platonov P.A., Chugunov. O.K., Manevsky V.N. and Karpukhin, V.I., Radiation damage and lifetime evaluation of RBMK graphite stack. In *Proceedings of the IAEA Specialists Meeting on Graphite Moderator Lifecycle Behavior*, IAEA-TECHDOC-901, IAEA, Vienna, 1996. pp. 79 90.
51. Rodchenkov, B.S., Platonov, P.A., Manevskij, V.N., Kashirin, B.A. and Chugunov, O.K., Strength analysis code for graphite structural components in uranium-graphite nuclear reactors. In *Proceedings of the IAEA Specialists meeting on the Status of Graphite Development for Gas Cooled Reactors*, IAEA-TECHDOC-690, IAEA, Vienna, 1993. pp. 225 230.
52. Jones, C.J., Davis, M.A., Marsden, B.J., Bougaenko, S.E., Baldin, V.D., Dermintievski, V.N., Rodtchenkov, B.S. and Sinitsyn, E.N., Assessment of the stress and deformation in an RBMK graphite moderator brick. In *Proceedings of the IAEA Specialists Meeting on Graphite Moderator Lifecycle Behavior*, IAEA-TECHDOC-901, IAEA, Vienna, 1996. pp. 137 149.
53. Rosenthal, M.W., Kasten, P.R., and Briggs, R.B., Molten-salt reactors—history, status and potential, *Nucl. Appl. Tech.*, 1970, 8, 107 117.
54. Haubenreich, P.N. and Engel, J.R., Experience with the molten-salt reactor experiment, *Nucl. Appl. Tech.*, 1970, 8, 118 136.
55. Kasten, P.R., Bettis, E.S., Cook, W.H., Eatherly, W.P., Holmes, D.K., Kedl, R.J., Kennedy, C.R., Kirslis, S.S., McCoy, H.E., Perry, A.M., Robertson, R.C., Scott, D.D. and Strehlow, R.A., Graphite behavior and its effects on MSBR experiments, *Nucl. Engr. Des.*, 1969, 9, 157 195.
56. Thrower, P.A. and Mayer, R.M., Review Article: Point defects and self-diffusion in graphite, *Phys. Stat. Sol. (a)*, 1978, 47, 11 37.

57. Kelly, B.T., *Physics of Graphite*, Applied Science Publishers, London, 1981.
58. Burchell, T.D., Radiation damage in carbon materials. In *Physical Processes of the Interaction of Fusion Plasmas with Solids*, ed. J. Roth and W.O. Hoffer, Academic Press, San Diego, 1996, pp. 341-384.
59. Engle, G.B. and Eatherly, W.P., Irradiation behavior of graphite at high temperature, *High Temperatures—High Pressures*, 1972, 4, 119-158.
60. Price, R.J., High temperature neutron irradiation of highly oriented carbons and graphites, *Carbon*, 1974, 12, 159-169.
61. Burchell, T.D. and Eatherly, W.P., The effects of radiation damage on the properties of GraphNOL N3M, *J. Nucl. Mater.*, 1991, 179-181, 205-208.
62. Simmons, J.H.W., *Radiation Damage in Graphite*, Pergamon Press, Oxford, 1965.
63. Kelly, B.T. and Burchell, T.D., Structure-related property changes in polycrystalline graphite under neutron irradiation, *Carbon*, 1994, 32, 499-505.
64. Nightingale, R.E., Stored energy. In *Nuclear Graphite*, ed. R. E. Nightingale. Academic Press, New York, 1962, pp. 325-353.
65. Bell, J.C., Bridge, H., Cottrell, A.H., Greenough, G.B., Reynolds, W.N. and Simmons, J.W.H. Stored energy in the graphite of power producing reactors, *Phil Trans. Roy. Soc. A*, 1962, 254, 361-395.
66. Roth, E.P., Watson, R.D., Moss, M. and Drotning, W.D., *Thermophysical properties of advanced carbon materials for tokamak limiters*, Sandia Report No. SAND 88-2057, UC-423, 1989.
67. Taylor, R., Kelly, B.T., and Gilchrist, K.E., The thermal conductivity of fast neutron irradiated graphite. *J. Phys. Chem. Solids*, 30, 1969, 2251-2267.
68. Ishiyama, S., Burchell, T.D., Strizak, J.P. and Eto, M., The effect of high fluence neutron irradiation on the properties of a fine-grained isotropic nuclear graphite, *J. Nucl. Mater.*, 1996, 230, 1-7.
69. Kelly, B.T. and Brocklehurst J.E., Dimensional changes of pyrolytic graphite at very high fast neutron doses. In *Proc. Fifth SCI Conf. on Industrial Carbons and Graphites*, SCI London, (1979), pp. 892-897.
70. Oku, T., Eto, M. and Ishiyama, S., Irradiation creep properties and strength of fine-grained isotropic graphite, *J. Nucl. Mater.* 1990, 172, 77-84.
71. C. R. Kennedy, M Kundy, and G. Kleist, The irradiation creep characteristics of graphite to high fluences. In *Proceedings of Carbon '88*, ed. B. McEnaney and T.J. Mays, IOP, London, 1988, pp. 443-444.
72. Kelly, B.T. and Burchell, T.D., The analysis of irradiation creep experiments on nuclear reactor graphites, *Carbon*, 1994, 32, 119-125.
73. Kelly, B.T., The radiolytic corrosion of advanced gas-cooled reactor graphite, *Progress in Nucl. Energy*, 1985, 16(1), 73-96.
74. Kelly, B.T., The effect of radiolytic oxidation on the graphite moderator brick strength in advanced gas-cooled reactors, *Nucl. Energy*, 1984, 24(3), 265-272.
75. Best, J.V., Stephen, W.J. and Wickham, A.J., Radiolytic graphite oxidation, *Progress in Nucl. Energy*, 1985, 16(2), 127-178.
76. Minshall, P.C., Saddler, I.A. and Wickham, A.J. In *Proceedings of the IAEA Specialists Meeting on Graphite Moderator Lifecycle Behavior*, IAEA-TECHDOC-901, IAEA, Vienna, 1996. pp. 181-191.
77. Birch, M., Schofield, P., Brocklehurst, J.E., Kelly, B.T., Harper, A. and Prior, H., The combined effects of fast neutron damage and radiolytic oxidation on the physical

- properties of Gilsocarbon graphite. In *Proceedings of Carbone '90*, Pub. Groupe Francais D'Etude Des Carbones, France, 1990, pp. 242 243.
78. Pickup, I.M., McEnaney, B. and Cooke, R.G., Fracture processes in graphite and the effects of oxidation, *Carbon*, 1986, 24, 535 543.
 79. Burchell, T.D., Pickup, I.M., McEnaney, B. and Cooke, R.G., The relationship between microstructure and the reduction of elastic modulus in thermally and radiolytically corroded nuclear graphites, *Carbon*, 1986, 24, 545 549.
 80. Judge, R.C.B., Application of a method for assessing probability of graphite core brick failure. In *Proceedings of the IAEA Specialists Meeting on Graphite Moderator Lifecycle Behavior*, IAEA-TECHDOC-901, IAEA, Vienna, 1996. pp. 117 124.
 81. McLachlan N., Reed, J. and Metcalfe M.P. In *Proceedings of the IAEA Specialists Meeting on Graphite Moderator Lifecycle Behavior*, IAEA-TECHDOC-901, IAEA, Vienna, 1996, pp. 125 136.
 82. Derbyshire, F., Jagtoyen, M. and Thwaites, M., Activated carbons - production and applications. In *Porosity in Carbons*, ed. J.W. Patrick, Halsted Press, New York, 1995, pp. 227 252.
 83. Coated Particle Fuels, *Nuclear Technology*, 1977, 35, 205 573.
 84. Piccinini, N., Coated nuclear fuel particles. In *Advances in Nuclear Science and Technology*, Vol. 8, ed. E.J. Henly and J. Lewins, Academic Press, New York, 1975, pp. 255 341.
 85. Nabielek, H., Kuhnlein, W., Schenk, W., Heit, W., Christ, A. and Ragoss, H., Development of advanced HTR fuel elements, *Nucl. Eng. & Des.* 1990, 121, 199 210.
 86. Gulden, T.D. and Nickel, H., Preface, Coated Fuel Particles, *Nuclear Technology*, 1977, 35, 206 213.
 87. Lackey, W.J., Stinton, D.P. and Sease, J.D., Improved gas distribution for coating high-temperature gas-cooled reactor fuel particles, *Nuclear Technology*, 1977, 35, 227 237.
 88. Lefevre, R.L.R. and Price, M.S.T., Coated nuclear fuel particles: the coating process and its models, *Nuclear Technology*, 1977, 35, 263 278.
 89. Bokros, J.C., Deposition, structure, and properties of pyrolytic carbon, *Chem. & Phys. Carbon*, 1969, 5, 1 118.
 90. Harmon, D.P. and Scott, C.B., Properties influencing high-temperature gas-cooled reactor coated fuel particle performance, *Nuclear Technology*, 1977, 35, 343 352.
 91. Heit, W., Huschka, H., Rind, W., and Kaiser, G.G., Status of qualification of high-temperature reactor fuel element spheres, *Nuclear Technology*, 1985, 69, 44 54.
 92. Strizak, J.P., Effects of oxidation on the strength of C/C composites for GT-MHR control rods. In *Proceedings of 22nd Biennial Conf. on Carbon* Pub. American Carbon Society, 1995, pp 760-761.
 93. Ishiyama, S. and Eto, M., Recent R&D of C/C Composite Control Rod for HTGRs In *Proceedings of 22nd Biennial Conf. on Carbon* Pub. American Carbon Society, 1995, pp 762-763.
 94. Eto, M., Ishiyama, S., and Ugachi, H., Status of the research and development at JAERI on the C/C composite control rod for the HTGR. In *Proceedings of the IAEA Specialists Meeting on Graphite Moderator Lifecycle Behavior*, IAEA-TECHDOC-901, IAEA, Vienna, 1996. pp. 205 214.
 95. Haag, G., Kugeler, K. and Philippen, P.-W., The high temperature reactor (HTR) and the new German safety concept for future nuclear power plants. In *Proceedings of the*

- specialists meeting on graphite moderator lifecycle behavior*, IAEA-TECDOC-901, IAEA, Vienna, 1996, 57 68.
96. Hoffman, D.P. and Mears, D.L., Outlook for MHTGR project development, *Nucl. Engn. Des.*, 1992, 136, 201 204.
 97. Maden, C. and Mole T., Nuclear energy: an option to keep open? *Energy Convers. Mgmt*, 1996, 37, 891 896.
 98. Fulkerson, W. and Jones Jr., J.E., CO₂ and the world energy system: the role of nuclear power, *Nucl. Engn. Des.*, 1992, 136, 23 28.

CHAPTER 14

Fracture in Graphite

GLENN R. ROMANOSKI AND TIMOTHY D. BURCHELL

*Metals and Ceramics Division
Oak Ridge National Laboratory
PO Box 2008, Oak Ridge, Tennessee 37831-6088, USA.*

1 Introduction

Graphites have numerous engineering applications. Coarse-grained, anisotropic, extruded graphites are used as electrodes in steel smelting arc furnaces. Molded isotropic graphites are used for continuous casting molds, electrical brushes, bearings and seals, tooling for electro-discharge machining, and in the semiconductor industry. Gas-cooled reactors such as the US designed Gas Turbine - Modular High Temperature Reactor (GT-MHR), the Japanese High Temperature Engineering Test Reactor (HTTR), and the British Advanced Gas Cooled Reactor (AGR) use near-isotropic or isotropic grade graphites as their nuclear moderator and for their major core structural components (see Chapter 13). Moreover, graphite has been extensively used in Fusion reactors as an armor material because of its low atomic number and attractive physical properties (see Chapter 12).

In the above applications, graphites are subjected to complex stresses, and thus a failure criterion which allows the prediction of the probability of failure at a given stress level would be particularly useful. Moreover, a fracture model capable of predicting changes in the strength of a graphite, resulting from changes in textural and process related parameters, would be useful to graphite manufacturers. Any assessment of the fracture behavior of graphite will recognize the nominally brittle nature of this material and the prominent role of the flaw structure in the fracture process. A failure criterion may be rationalized in terms of a dominant flaw (or ensemble of flaws) and local stress which results in the formation and extension of a macroscopic crack to failure. The dominant flaw generally develops from the larger of the intrinsic flaws. However, local stress concentrations and/or cyclic loads may initiate and propagate the dominant flaw from lesser flaws. The dominant flaw may be present as an anomaly from processing, or machining and handling damage. The dominant flaw becomes the critical flaw when its effective dimension and the local stress satisfy the prevailing failure criterion. It is evident that the appropriate failure criterion for graphite fracture may lie in the realm of

fracture mechanics formalisms developed for metals, ceramics, and other brittle materials.

Here, the dominant processes involved in the fracture of graphite are discussed. Fracture mechanics theories are reviewed and their applicability to graphitic discussed. The flaw tolerance of two nuclear grade graphites is reported and discussed, and linear elastic fracture mechanics in graphite is applied to define the critical flaw at differing stress levels. Finally, a full account of the Burchell model [1-4] of graphite fracture is presented. The physical basis and assumptions behind the model are reported and the necessary microstructural inputs for the model are discussed. The performance of the model in predicting the influence of changes in microstructural features on the failure probability is discussed. Finally, the model's performance is assessed in terms of its ability to predict the tensile strength distributions of several graphites with widely different textures.

2 Studies and Models of Fracture Processes in Graphite

2.1 Acoustic emission

When a graphite is stressed, micromechanical events such as slip, shear, cleavage or microcracking may be detected in the form of acoustic emission (AE). In early work Kaiser [5] found that graphite emitted AE when stressed, and upon subsequent stressing AE could only be detected when the previous maximum stress had been exceeded - a phenomena named the Kaiser effect. Krauss and Semmler [6] investigated the AE response of industrial carbon and polygranular graphites subject to thermal and mechanical stresses. They reported significant AE in the range 2000 - 1500°C on cooling from graphitization temperatures, the amount of AE increasing with the cooling rate. Although Krauss and Semmler offered no explanation for this, Burchell *et al.* [7] postulated that it was associated with the formation of Mrozowski cracks [8]. In an extensive study, Burchell *et al.* [7] monitored the AE response of several polygranular graphites, ranging from a fine textured, high strength aerospace graphite to a coarse textured, low strength electrode graphite. They confirmed the previous results of Pickup *et al.* [9], who had concluded that the pattern of AE is characteristic of the graphite microstructure. Burchell *et al.* [7] showed the development of AE was clearly associated with the micromechanical events that cause non-linear stress-strain behavior in graphites, and that post-fracture AE is indicative of the crack propagation mode at fracture. For different graphite, both the total AE at fracture and the proportion of small amplitude events tended to increase with increasing filler particle size (*i.e.*, coarsening texture). Ioka *et al* [10] studied the behavior of AE caused by microfracture in polygranular graphites. On the basis of their data they described the fracture mechanism for graphite under tensile loading. Filler

particles, whose basal planes were inclined at 45° to the loading axis deformed plastically, even at low stresses. Slip deformation along basal planes was detected by an increase in root mean square (RMS) voltage of the AE event amplitude. The number of filler particles which deform plastically increased with increasing applied tensile stress. At higher applied stress, slip within filler particles was accompanied by shearing of the binder region. Filler grains whose basal planes were perpendicular to the applied stress cleave, and surrounding binder must shear to accommodate the deformation. At higher stress levels, microcracks propagate into the binder region, where they may coalesce to form a critical defect and lead to the eventual failure of the graphite. The evidence produced through AE studies, suggests a fracture mechanism consisting of crack initiation, crack propagation, and subsequent coalescence to yield a critical defect resulting in fracture.

2.2 Microstructural studies of fracture

Graphite is a composite material consisting of a coke filler and a carbonized pitch or resin binder. The graphite structure is porous, typically containing between 15 - 25 % porosity. An account of the manufacture and properties of graphite may be found in Chapter 13. A microstructural study of fracture in graphite [11] has revealed the manner in which certain microstructural features influence the process of crack initiation and propagation in graphites; the principal observations are summarized below.

2.2.1. Porosity

Two important roles of porosity in the fracture process have been identified. First, the interaction between the applied stress field and the pores will cause localized stress intensification, promoting crack initiation from favorably oriented high aspect ratio pores at low applied stresses. Second, propagating cracks can be drawn toward pores in their vicinity, presumably under the influence of the stress field around the pore. In some instances such pore/crack encounters serve to accelerate crack growth; however, occasionally a crack will be arrested by a pore, and does not break free until higher applied stresses are attained. Pores of many shapes and sizes are observed in the microstructure of a graphite. The larger, more slit-shaped pores being more damaging to the graphite.

2.2.2. The binder phase

Two arbitrarily defined types of microstructure can be identified in the binder phase: (i) domains, which are regions of common basal plane alignment extending over linear dimensions greater than $100\mu\text{m}$, and (ii) mosaics, which are regions of small randomly-oriented pseudo-crystallites with linear dimensions of common basal plane orientation of less than about $10\mu\text{m}$. Cleavage of domains can occur at stresses well below the fracture stress, and such regions can act as sites for crack initiation, particularly when in the vicinity of pores. Fracture of mosaic regions is

usually only observed at stresses close to the fracture stress. At lower stresses, propagating cracks which encounter such regions are arrested or deflected.

2.2.3. Filler particles

Coke filler particles with good basal plane alignment are highly susceptible to microcracking along basal planes at low stresses. This cleavage is facilitated by the needle-like cracks which lie parallel to the basal planes, and are formed by anisotropic contraction of the filler-coke particles during the calcination process. Frequently, when a crack propagating through the binder phase encounters a well aligned filler particle, it takes advantage of the easy cleavage path and propagates through the particle. However, in contrast to the mechanism suggested by Ioki et al [10], the reverse process, *i.e.*, propagation of a crack initiated in the filler particle into the binder phase, was much less commonly observed.

2.3 Fracture models

There have been several probabilistic fracture models developed to predict the behavior of graphites. An early model was developed by Buch [12] for fine grained aerospace graphites. The Buch model was further developed and applied to nuclear graphites by Rose and Tucker [13]. The Rose and Tucker model assumed graphite to consist of an array of cubic particles representative of the materials filler particle size. Within each block or particle, the graphite was assumed to have a randomly oriented crystalline structure, through which basal plane cleavage may occur. When a load is applied, those cleavage planes on which the resolved shear stress exceeds a critical value, were assumed to fail. If adjacent particles cleaved, the intervening boundary was regarded as having failed also, so that a contiguous crack was formed extending across both particles. Pickup et al. [9], and Rose and Tucker, equated the cleavage stress with the onset stress for acoustic emission, *i.e.*, the stress at which acoustic emission was first detected. In applying the model to a stressed component, such as a bar in tension, cracks were assumed to develop on planes normal to the axis of the principal stress. The stressed component would thus be considered to have failed when sufficient particles on a plane had cleaved such that together they formed a defect large enough to cause fracture as a brittle Griffith crack. Pores were treated in the Rose and Tucker model as particles with zero cleavage strength, the number of these being chosen to give the correct pore volume fraction for a given graphite. Hence, the Rose and Tucker model takes into account the mean size of the filler particles, their orientation and the amount of porosity, but is relatively insensitive to the size and shape distributions of both microstructural features.

Rose and Tucker applied their fracture model to Sleeve graphite, an extruded, medium-grain, pitchcoke nuclear graphite used for fuel sleeves in the UK AGR (see Chapter 13). The performance of the model was disappointing; the predicted

strength distribution was a poor fit to the experimental data. In an attempt to improve the performance of the Rose and Tucker model, experimentally determined filler particle distributions were incorporated [14]. The model's prediction improved as a result of this modification and the higher strength of one pitch-coke graphite compared to the other was correctly predicted. Specifically, the predicted failure stress distribution was a better fit to the experimental data than the single grain size prediction, particularly at lower stresses. However, in order to correctly predict the mean stress (50% failure probability) it was found necessary to increase the value of the model's stress intensity factor (K_{Ic}) input to $1.4 \text{ MPa}\sqrt{\text{m}}$. Such a value is far in excess of the actual measured K_{Ic} of this graphite ($1.0 \text{ MPa}\sqrt{\text{m}}$). The inclusion of an artificially high value for K_{Ic} completely invalidates one of the Rose and Tucker model's major attractions, *i.e.*, that its inputs are all experimentally determined materials parameters. A further failing of the Rose and Tucker fracture model is its incorrect prediction of the build up of acoustic emission counts. Although the Rose and Tucker model considers the occurrence of subcritical damage when the applied stress lies between the cleavage and failure stress, the predicted build up of acoustic emission is markedly different from that observed experimentally [7]. First, the model fails to account for any acoustic emission at very low stresses. Second, at loads immediately above the assumed cleavage stress there is a rapid build up of damage (acoustic emission) according to the Rose and Tucker model, but very little according to the acoustic emission data. Moreover, the observation of acoustic emissions immediately as load is applied to a specimen [7] invalidates an assumption that is fundamental to the Rose and Tucker model, *i.e.*, that the acoustic emission onset stress can be equated with the cleavage stress of the graphite filler particles.

Recognizing the need for an improved fracture model, Tucker, Rose and Burchell [15] investigated the fracture of polygranular graphites and assessed the performance of several failure theories when applied to graphite. These theories included the Weibull theory, the Rose-Tucker model, Fracture Mechanics, Critical Strain Energy, Critical Stress and Critical Strain Theories. While no single criterion could satisfactorily account for all the situations they examined, their review showed that a combination of the fracture mechanics and a microstructurally based fracture criterion might offer the most versatile approach to modelling fracture in graphite. Evidently, a necessary precursor to a successful fracture model is a clear understanding of the graphite fracture phenomena. Several approaches have been applied to examine the mechanism of fracture in graphite, including both direct microstructural observations and acoustic emission monitoring as previously discussed and reported elsewhere [7,16-18].

2.4 Elements of a fracture model

While some of the direct observations discussed above are not in total agreement

with the mechanism postulated from AE data, there are a number of similarities. Both AE and the microstructural study show that failure is preceded by the propagation and coalescence of microcracks to yield a critical defect. However, based on the forgoing discussion of graphite fracture processes, it is evident that the microstructure plays a dominant role in controlling the fracture behavior of the material. Therefore, any new fracture model should attempt to capture the essence of the microstructural processes influencing fracture. Particularly, a fracture model should embody the following: (i) the distribution of pore/ flaw sizes; (ii) the initiation of fracture cracks from stress raising pores, and (iii) the propagation of cracks to a critical length prior to catastrophic failure of the graphite (*i.e.*, subcritical growth). The Burchell fracture model [1-4] reported here recognizes these aspects of graphite fracture, and applies a fracture mechanics criteria to describe steps (ii) and (iii) above. The model was first postulated [1] to describe the fracture behavior of the AGR fuel sleeve pitch coke graphite, and was successfully applied to describe the tensile failure statistics. Moreover, the model was shown to predict more closely the AE response of graphite than its forerunner, the Rose and Tucker model. Subsequently, the model was extended and applied to two additional nuclear graphites [2]. Again, the model performed well and was demonstrated to be capable of predicting the tensile failure probabilities of the two graphites (grades H-451 and IG-110). In an attempt to further strengthen the model [3], quantitative image analysis was used to determine the statistical distribution of pore sizes for grade H-451 graphite. Moreover, a calibration exercise was performed to determine a single value of particle critical stress intensity factor for the Burchell model [3]. Most recently, the model was successfully validated against experimental tensile strength data for several graphites of widely different texture [4,19].

Tucker and McLachlan [20] reported the performance of a model [21] developed from an earlier version [1] of the graphite fracture model reported here. Their purpose in extending the model was to describe stress related physical properties (other than fracture), such as strain hysteresis and acoustic emission more adequately, and thereby improve the physical basis of the fracture model. To achieve this, more sophisticated microstructural processes were proposed for the graphite polycrystals in the vicinity of stressed crack-like defects. Pores within the graphite were considered to be either active or passive according to whether or not they were likely to initiate cracks when the graphite body was stressed. The combination of the presence of porosity and the cleavage of close, suitably oriented, granular boundaries in highly stressed material near to an active pore was assumed to give rise to grain deformation through crystallite shear. This process relieved the stress intensification adjacent to the active pore - an effect not dissimilar to the spread of plasticity ahead of a notch in a metal. McLachlan [21] applied the method developed by Bilby et al [22], for describing dislocation mechanisms in metals, to model the stress relieving process in graphite which was

the basis for their new approach to graphite failure. While this new approach has been shown to yield an improved performance in some instances, it is significantly more complex than either the Rose and Tucker model, or the Burchell fracture model reported here. The model of Tucker and McLachlan required fourteen separate materials properties inputs, compared to nine inputs for the model reported here. Moreover, in the former case, many of the inputs were not derived experimentally, but rather were obtained by selecting initial values of the parameters and iteratively applying the model together with amending the values of the parameters until appropriate fits to experimental data were obtained. Therefore, the Tucker and McLachlan approach to fracture modeling has moved away from the simplicity and physical soundness embodied in the Burchell model, and consequently, the Tucker and McLachlan model is not considered further in this Chapter. The basis of the Burchell fracture model is discussed in a subsequent section of this Chapter. However, before introducing the basis of the model it is appropriate to review and discuss the application of Fracture Mechanics to graphite.

3 Linear Elastic Fracture Mechanics Behavior of Graphite

3.1 Basic concepts

Linear elastic fracture mechanics (LEFM) is based on a mathematical description of the near crack tip stress field developed by Irwin [23]. Consider a crack in an infinite plate with crack length $2a$ and a remotely applied tensile stress acting perpendicular to the crack plane (mode I). Irwin expressed the near crack tip stress field as a series solution:

$$\sigma_{ij}(r, \theta) = \frac{K_I}{\sqrt{2\pi r}} f_{ij}(\theta) + O(r^{1/2}) + \dots \quad (1)$$

where $K_I = \sigma^\infty \sqrt{\pi a}$, and (r, θ) are the cylindrical polar coordinates of a point with respect to the crack tip. In the near crack tip region ($r \rightarrow 0$) the first term of the series solution serves as an adequate approximation to the elastic stress field for most applications.

$$\sigma_{ij}(r, \theta) = \frac{K_I}{\sqrt{2\pi r}} f_{ij}(\theta) = \frac{\sigma^\infty \sqrt{\pi a}}{\sqrt{2\pi r}} f_{ij}(\theta) \quad (2)$$

K_I is the mode I stress intensity factor which serves as a scalar multiplier of the crack tip stress field.

The variation of the stress σ_y as a function of r at $\theta = 0$ is illustrated in Fig. 1. For large values of r in eq. 2, σ_y approaches zero, whereas in reality it can only fall to the remotely applied stress (σ^∞). As r approaches zero at the crack tip, σ_y approaches infinity, while it should not exceed σ_{UTS} . Hence, it is clear that eq. 2 is valid only for a limited region around the crack tip and is more accurate for low values of σ^∞ .

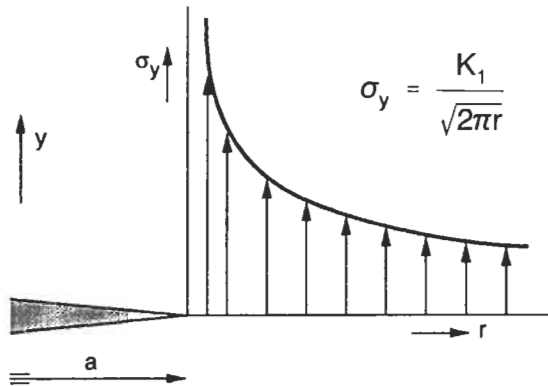


Fig. 1. Elastic solution for the crack tip stress field [24].

Rather than bearing an infinite stress at the crack tip, yielding occurs resulting in a volume of inelastically deformed material along the crack front called the process zone, as shown in Fig. 2. The size of the inelastic zone, r_{inm}^* , under a monotonic tensile stress, σ_{inm}^* , can be approximated by substituting $\sigma = \sigma_{in}$ into eq. 2 for the horizontal plane, $\theta = 0$

$$r_{inm}^* = \frac{1}{2\pi} \left[\frac{K_I}{\sigma_{in}} \right]^2 \quad (3)$$

where σ_{in} is the stress level required for inelastic deformation and microcrack formation. In reality, the stress above the inelastic zone exceeding σ_{in} is redistributed giving a somewhat larger monotonic inelastic zone. Hence, for monotonic loading, under conditions of small scale inelastic deformation, the crack driving force may be expressed in terms of

$$K_{max} = Y \sigma_{max} \sqrt{\pi a} \quad (4)$$

where Y is the combined flaw shape and free surface correction factors. Paris and Erdogan [25] extended the use of LEFM and K to correlating subcritical crack

growth rates under conditions of cyclic loading. The tensile range of the stress intensity factor is used to express the crack driving force according to:

$$\Delta K = K_{\max} - K_{\min} \quad (5)$$

for all $K_{\min} \geq 0$. The principal variables are K_{\max} and R-ratio (K_{\min}/K_{\max} or $\sigma_{\min}/\sigma_{\max}$).

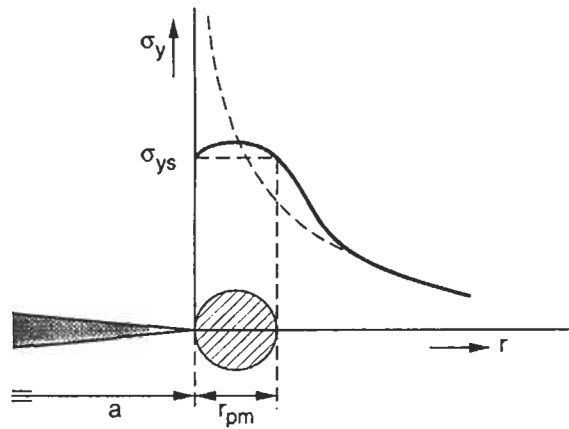


Fig. 2. Elastic solution for the crack tip stress field with small scale yielding [24].

3.2 Crack closure and K_{eff}

Crack extension is often observed to vary significantly at the same nominal value of $\Delta K (= Y \Delta\sigma_{\text{pos}} \sqrt{\pi a})$ for different values of R-ratio. Elber [26] was the first to explain this observation for metals in terms of the crack closure phenomenon. He determined, by measuring specimen compliance, that fatigue cracks open and close at the crack tip at positive values of stress due to contact between crack surfaces behind the crack tip. For elastic fatigue conditions it is generally found that $P_{\text{op}} = P_{\text{cl}}$ and $K_{\text{op}} = K_{\text{cl}}$, where P is the applied load.

The effective stress range was defined by Elber as:

$$\Delta\sigma_{\text{eff}} = \sigma_{\max} - \sigma_{\text{op}} \quad (6)$$

Correspondingly, the effective stress intensity factor range, K_{eff} , may be expressed as

$$K_{\text{eff}} = Y(\sigma_{\text{max}} - \sigma_{\text{op}}) \sqrt{\pi a} \quad (7)$$

According to Elber, crack closure occurs as a consequence of crack tip inelastic behavior. The growing crack generates a monotonic inelastic zone ahead of the crack tip. As the crack advances, there is residual inelastic deformation consisting of monotonically deformed material behind the crack tip due to prior inelastic zones. This material does not fit in the surrounding elastic body, therefore, the crack flanks make physical contact at a high positive value of load on unloading. A high positive load is also required to open the crack. Under elastic conditions crack opening and closure occur at approximately the same value of load. This mechanism of crack closure is generally referred to as inelasticity induced closure. Roughness induced closure is also possible. Roughness (or asperity) induced crack closure [27-31] is caused by fracture surface asperities making contact at positive loads on unloading. The crack opening load is also positive. This mechanism of closure depends on fracture surface morphology (therefore microstructure) and results in fracture surface mismatch.

3.3 Applicability of LEFM to small cracks in graphite

The basic assumptions of fracture mechanics are: (1) that the material behaves as a linear elastic isotropic continuum and (2) the crack tip inelastic zone size is small with respect to all other dimensions. Here we will consider the limitations of using the term $K = Y\sigma_{\text{pos}} \sqrt{\pi a}$ to describe the mechanical driving force for crack extension of small cracks at values of stress that are high with respect to the elastic limit.

The stress intensity factor is a first-term approximation to a series solution for the near crack tip elastic stress field. The accuracy of this approximation decreases with distance from the crack tip. Evans and Luxmoore [32] compared the approximation given by $K/\sqrt{2\pi r}$ to the full equations of the Westergaard stress function for a central crack in an infinite plate and found errors on the order of 10% in the local stress components when the near crack tip field was limited to $a/10$. Wilson [33] found the errors in local stress components exceeded 10% at the $a/10$ boundary when typical fracture mechanics specimens were considered. Consequently, K serves as a good parameter to estimate the near crack tip elastic field when its extent is limited to $a/10$. Smith [34] reasoned that for a global application of fracture mechanics (Fig. 3a) where σ_1 represents the stress applied to a structure or laboratory specimen, the near crack tip field ($a/10$) should be at least the size of the largest microstructural feature, that is, the grain size. Therefore, the crack length must be ten times the grain size if K_1 is to accurately represent stresses in the crack tip field. On the other hand, if σ_2 represents the

boundary stress applied to a single grain (Fig. 3b), the crack length would be half a grain size and the near crack tip field would extend over a distance of $0.1x$ (grain size/2), which is many orders of magnitude greater than the lattice spacing. However, for this localized application of fracture mechanics, the local material behavior is no longer an isotropic continuum for most graphites.

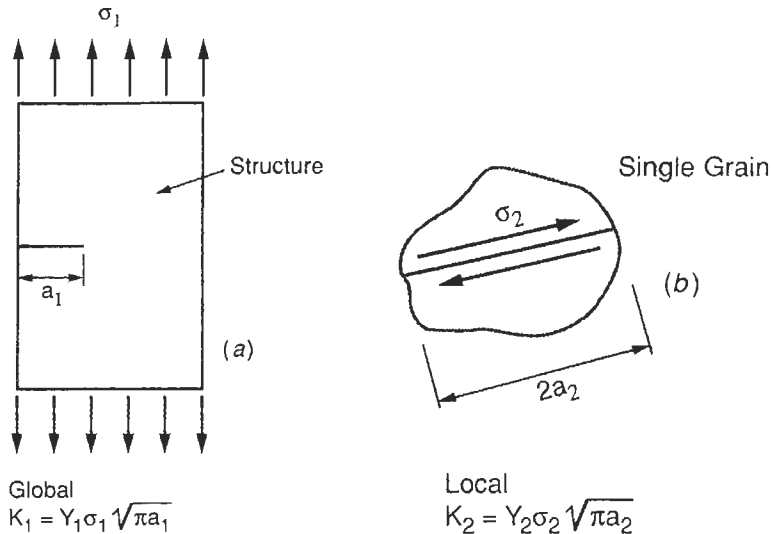


Fig. 3. Schematic of (a) global and (b) local application of fracture mechanics [34].

In metals, inelastic deformation occurs at the crack tip, yielding a plastic zone. Smith [34] has argued that the elastic stress intensity factor is adequate to describe the crack tip field condition if the inelastic zone is limited in size compared with the near crack tip field, which is then assumed to dominate the crack tip inelastic response. He suggested that the inelastic zone be $1/5$ of the size of the near crack tip elastic field ($a/10$). This restriction is in accordance with the generally accepted limitation on the maximum size of the plastic zone allowed in a valid fracture toughness test [35,36]. For the case of crack propagation, the minimum crack size for which continuum considerations hold should be at least $50 \times (r_{um})$.

The utility of K or any elastic plastic fracture mechanics (EPFM) parameter to describe the mechanical driving force for crack growth is based on the ability of that parameter to characterize the stress-strain conditions at the crack tip in a manner which accounts for a variety of crack lengths, component geometries and loading conditions. Equal values of K should correspond to equal crack tip stress-strain conditions and, consequently, to equivalent crack growth behavior. In such a case we have mechanical similitude. Mechanical similitude implies equivalent crack tip inelastic zones and equivalent elastic stress fields. Fracture mechanics is

based on the formulation of parameters which express crack tip similitude.

Mechanical similitude requires: (1) a small inelastic zone size with respect to all length dimensions, including crack front length, (2) a small inelastic zone size with respect to the distance over which the first term of the stress field solution is dominant, (3) equivalent K_{\max} and ΔK , (4) equivalent constraint, *i.e.*, plane stress or plane strain, and (5) equivalent crack closure fields. In addition, microstructural similitude requires that the crack tip be embedded in a microstructurally similar material. The material should be equivalent in terms of microstructural constituents and flaw size distribution. This condition is satisfied when the crack front is long with respect to microstructural features, particularly the grain size, and therefore encounters an average microstructural condition. The various factors which influence small crack behavior (*i.e.*, which influence similitude) will be discussed further and illustrated with examples from the literature in a later section. In spite of the potential which small cracks have for violating similitude conditions, the need to describe crack growth behavior in terms of fracture mechanics remains a requirement of defect tolerant design.

Brocklehurst [37] has written an exhaustive review of the early work (prior to 1977) on fracture in polycrystalline graphite. Much of this work focused on the fracture behavior of nuclear graphites. In most investigations considered, conventional fracture mechanics tests and analysis were performed for macroscopic cracks. LEFM provided an adequate criterion for failure. Additionally, results on work of fracture, strain energy release rate, and fatigue crack propagation were reported.

Since the Brocklehurst review, most investigations of the fracture behavior of graphites have focused on nuclear graphites and many have employed LEFM to characterize fracture behavior [38-47]. The following general conclusions can be drawn from this work:

1. The mode I fracture toughness, K_{Ic} , for nearly all nuclear graphites falls in the range $0.75 \text{ MPa}\sqrt{\text{m}}$ to $1.5 \text{ MPa}\sqrt{\text{m}}$.
2. Fracture toughness exhibited a significant dependence on specimen type and specimen size such that fracture toughness appears to increase for larger specimens which require greater crack extension.
3. Specimen size effects have been attributed to rising R-curve behavior for most graphites studied.
4. Rising R-curve behavior has been attributed to grain bridging tractions and microcrack dilatation in the crack wake region.

5. The few studies which addressed the fracture mechanics behavior of very small cracks generally revealed a quantitative departure from behavior determined at longer crack lengths. This result may be attributed to a departure from perfect mechanical and microstructural similitude between long and small cracks.

4 Elastic-plastic Fracture Mechanics Behavior of Graphite

As demonstrated in the previous section, LEFM has proven very useful in quantifying the fracture behavior of artificial graphites. Furthermore, engineering methodologies for employing LEFM in defect tolerant design are well established. There are, however, concerns related to applying LEFM to the fracture of graphite. The stress-strain relationship for most graphites deviates significantly from the simple linear relationship of Hook's Law. Many graphites exhibit anisotropic behavior as a result of extrusion processing. Individual coke grains can exhibit extreme anisotropic behavior. A further issue of concern is that the critical flaw size for fracture of graphite is generally small with respect to the process zone as the fracture stress is approached. Hence, it has been argued by a number of investigators [48,49] that EPFM provides a more appropriate framework for characterizing the fracture behavior of graphite.

Elastic-plastic fracture mechanics encompasses a number of quantitative approaches developed for characterizing fracture problems which lie beyond the applicability of LEFM. This class of problems generally involves: nonlinear material behavior, large scale crack tip inelasticity, small crack sizes, and net-section stresses approaching that required for irreversible deformation. We will not attempt here to re-derive the various approaches but will define the important parameters and provide a description of the physical basis for each approach. There are two basic approaches for quantifying elastic-plastic fracture of graphite. The first is an energy balance approach similar to Griffith's theory of brittle fracture [50] but extended to account for irreversible processes associated with deformation and fracture. The second general approach seeks to develop parameters, similar to K , which describe the crack driving force in a manner consistent with elastic-plastic material response.

A more general approach to quantifying the fracture criterion for a cracked body was first developed by Griffith [50] more than thirty-five years before the introduction of linear-elastic fracture mechanics. The Griffith criterion is based on conservation of energy and is illustrated in Fig. 4 for an infinite plate of unit thickness with a central transverse crack of length $2a$. The plate is subjected to a remotely applied stress and is fixed at its ends. The elastic energy in this stressed body is represented by the area under the load versus displacement diagram. As the crack extends over an increment, da , some elastic energy is released and is

equal in magnitude to the area OAC. The Griffith criterion states that crack propagation will occur if the energy released upon crack growth is sufficient to provide all the energy required for crack growth. The requirement for crack growth may be stated as follows:

$$\frac{dU_e}{da} = \frac{d\Gamma}{da} \quad (8)$$

where U_e is the elastic energy available for crack growth and Γ the energy required for crack growth. Following the stress field calculations by Inglis [51], Griffith calculated the condition for crack growth per unit plate thickness as:

$$\frac{dU}{da} = G = \frac{\pi\sigma^2 a}{E} \quad (9)$$

where E is the elastic modulus and G is a crack driving force or “strain energy release rate” per crack tip. The energy expended during crack growth is referred to as the “crack resistance,” $R = d\Gamma/da$. If R is constant for each increment of crack growth, crack growth occurs when G exceeds some critical value, G_{Ic} , the critical strain energy release rate.

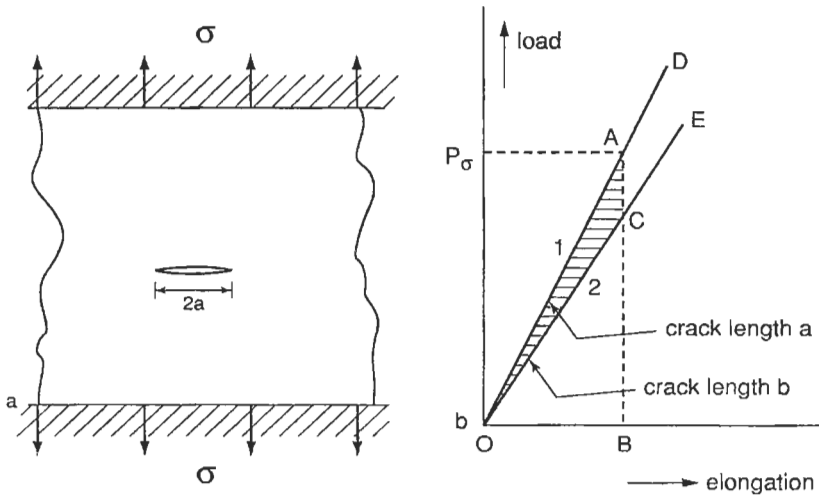


Fig. 4. The Griffith criterion for the fixed grip condition. (a) cracked plate with fixed ends; (b) schematic of elastic energy

Griffith derived his relationship for glass where R consists only of surface energy. In the case of metals, R is mainly plastic energy associated with the formation of a crack tip plastic zone. It is obvious from Eq. 9 that, for plane stress,

$$G_{Ic} = \frac{K_{Ic}^2}{E} \quad (10)$$

For the case of plane strain

$$G_{Ic} = (1 - \nu^2) \frac{K_{Ic}^2}{E} \quad (11)$$

A more general formulation of the energy approach to fracture of graphite has been reviewed by Sakai *et al.* [48]. Assume a graphite body containing a single crack of area A . Under conditions of stable crack growth, the global energy balance may be written as

$$\frac{\partial W}{\partial A} = \frac{\partial U_t}{\partial A} + \frac{\partial \Gamma}{\partial A} \quad (12)$$

where ∂A denotes the increment of the crack surface area, W is the work done by the applied force, U_t is the total internal energy, and Γ is the surface energy required to extend the crack. The internal energy consists of two terms

$$U_t = U_e + U_p \quad (13)$$

where U_e is the elastic stored energy and U_p is the plastic energy dissipation. Hence

$$\frac{\partial W}{\partial A} = \left(\frac{\partial U_e}{\partial A} + \frac{\partial U_p}{\partial A} \right) + \frac{\partial \Gamma}{\partial A} \quad (14)$$

That fraction of the applied work which is not consumed in the elastic-plastic deformation remains to create the new crack surface, *i.e.*, the crack driving force. Therefore, a nonlinear fracture toughness, \overline{G}_c , may be defined as follows:

$$\overline{G}_c = \frac{\partial}{\partial A} [W - (U_e + U_p)]_c \quad (15)$$

The difference between the work input and the elastic stored energy is the crack growth resistance, R ,

$$R = \frac{\partial}{\partial A} (W - U_e)_c = \frac{\partial}{\partial A} (U_p + \Gamma) \quad (16)$$

As with the purely elastic case, the energy values associated with elastic-plastic fracture may be ascertained from the load versus load-point deflection diagram for a cracked body as shown in Fig. 5.

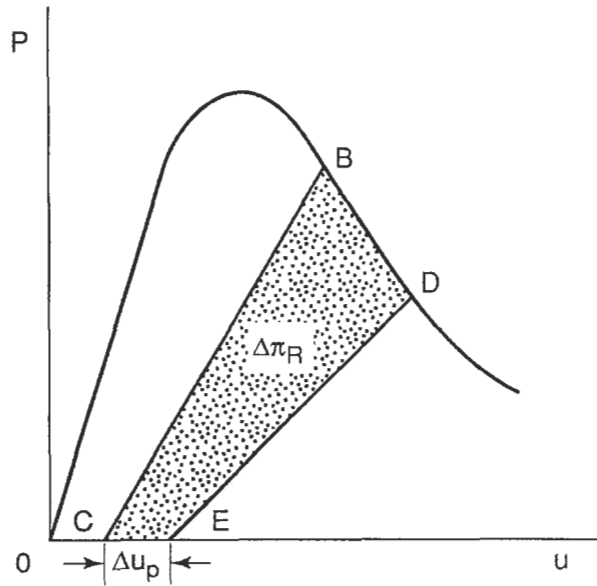


Fig. 5. Diagram of load versus load-point displacement for an elastic-plastic body experiencing stable crack extension [48].

For an increment of crack extension, ΔA is represented by a movement from B to D on the load versus deflection curve, the energy consumed may be represented by the area $\Delta\pi_R$. Hence the crack growth resistance may be expressed as

$$R = \frac{\Delta\pi_R}{\Delta A} = \frac{\Delta}{\Delta A} (W - U_e) \quad (17)$$

and similarly

$$\overline{G}_c = \frac{\Delta \pi_G}{\Delta A} = \frac{\Delta}{\Delta A} [W - (U_e + U_p)]_c \quad (18)$$

and

$$\phi_p = \frac{\Delta \pi_p}{\Delta A} = \frac{\Delta U_p}{\Delta A} \quad (19)$$

where $\phi_p \equiv \partial U_p / \partial A$ is the plastic energy dissipation rate.

The J value is defined as the elastic potential difference between the linear and nonlinear elastic bodies with the same geometric variables [52,53]. The elastic potential energy for a nonlinear elastic body is expressed by:

$$\pi = U_e - W \quad (20)$$

The J integral can be written as

$$J = \frac{-\partial \pi}{\partial A} \quad (21)$$

For elastic-plastic deformation [54]

$$\pi \approx U_t - W = (U_e + U_p) - W \quad (22)$$

or

$$J_c = -\left(\frac{\partial \pi}{\partial A}\right) = \frac{\partial}{\partial A} (W - U_t)_c \quad (23)$$

The graphical evaluation of J_c is presented in the load versus load point displacement diagram of Fig. 6.

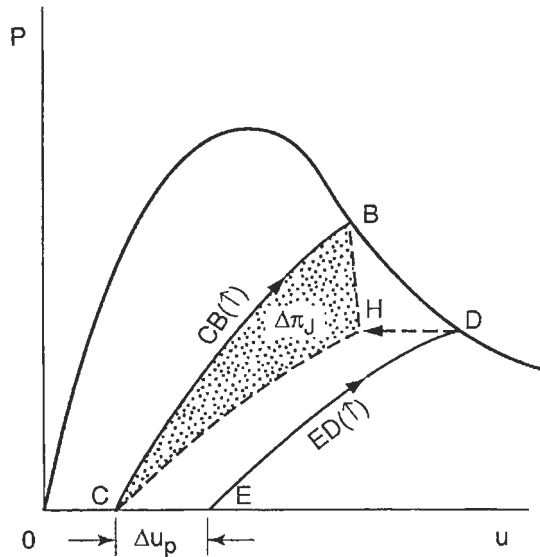


Fig. 6. Diagram of load versus load-point displacement illustrating a graphical determination of the J -integral [48].

Sakai *et al.* [48] investigated the fracture of an isotropic nuclear graphite, IG-11, using the chevron notched short bar specimen and found it to exhibit significant elastic-plastic behavior. Nonlinear fracture parameters \bar{G}_c , R , J_c , and ϕ_p were empirically determined from the load versus displacement diagrams. These nonlinear fracture parameters were found to be increasing functions of ϕ_p , and to converge to a constant value of G_c as $\phi_p \rightarrow 0$. The value of K_c calculated using the Irwin relation, Eq. 12, was only about one fourth the value measured using the ASTM E399 test method. This difference was attributed to significant inelastic deformation which occurred during fracture. It was estimated that approximately 38% of the total fracture energy was consumed as plastic energy dissipation.

Sakai *et al.* [48] further assessed the crack growth resistance (R-curve) behavior of IG-11 using compact tension specimens and found crack growth resistance to increase with increasing crack extension for a range of a/w values. This rising R-curve behavior was attributed to inelastic deformation and fracture in the process zone and crack wake region. In the crack tip region, significant inelastic material response was identified with basal slip and extension of pre-existing microcracks. Grain bridging tractions having a characteristic dimension of one filler coke grain, and compressive strains in the microcracking wake, contributed significantly to rising R-curve behavior.

5 Fracture Behavior of Small Flaws in Nuclear Graphites

As noted in the above discussion on fracture mechanics characterization of graphites, EPFM has many advantages over LEFM in accounting for the nonlinear deformation and fracture behavior of graphite. This is particularly true for laboratory specimens containing a single macroscopic, artificial flaw for which the measurement of load-point displacements is rather straight forward. Without a knowledge of local displacements, the work and energy terms used to calculate nonlinear fracture parameters can only be estimated. The application of EPFM to graphite is further complicated by a number of factors. Multiple flaws may act in unison as the critical flaw at fracture. Furthermore, the critical flaw may have a size which approaches microstructural features with a location and orientation unknown. Hence, for most fracture mechanics assessments of graphite, many investigators have employed a LEFM failure criterion as a workable solution to quantifying graphite fracture. The authors have addressed critical issues in graphite fracture by exploring the limits of LEFM while recognizing the nonlinear behavior of this unique material.

Graphite is used as a moderator and a structural material in the core of the Gas Turbine - Modular Helium Reactor (GT-MHR). Although the design is based on a maximum principal stress failure criterion, the need for applying fracture mechanics to component strength assessment becomes obvious when one considers the possible presence of significant flaws in nuclear graphites. An investigation was undertaken to determine the flaw sizes relevant to the fracture of graphite and to assess the applicability of fracture mechanics to defining an appropriate failure criterion for small macroscopic flaws in two grades of nuclear graphite, H-451 and IG-11.

5.1 Material

In our fracture mechanics studies and fracture model development we have utilized several grades of graphite. Three of the graphites examined are shown in Fig. 7. Grade H-451 graphite is an extruded, medium-grained, near isotropic, nuclear graphite which has been selected for use as the moderator and core structural material in the GT-MHR. Grade H-451 was manufactured by Sigri-Great Lakes Carbon Company in the USA. In addition to macroscopic pores and cracks, H-451 contains arrays of associated pores with trace lengths in the 1 to 5-mm range which are clearly visible on a machined surface of H-451 graphite. Individual spherical pores with diameters as large as 3 mm are common. Grade IG-110 graphite is an isostatically molded, fine-grained, isotropic, nuclear graphite which is used as the moderator and core structural material for the High Temperature Test Reactor (HTTR) which is currently under construction by the Japan Atomic Energy Research Institute. Grade IG-110 graphite is manufactured by Toyo-Tanso in

Japan and is a purified version of IG-11. Grade AXF-5Q is an isostatically molded, ultrafine-grained, isotropic, high strength graphite. Grade AXF-5Q is used for a variety of applications such as throats, nozzles, etc., in the aerospace industry, boats, crucibles and furnace parts in the semi-conductor industry and for other applications such as electrode discharge machining tools. Grade AXF-5Q is manufactured in the USA by the POCO Graphite Company. Grade AGX, (not shown in Fig. 7) is manufactured by UCAR Carbon Company, and is used for the production of arc-furnace electrodes for the steel industry.

The widely different textures of three of the graphites initially studied here are clearly shown in the photomicrographs in Fig. 7. Grade H-451 [Fig. 7(a)] contains relatively large filler coke particles, [F] in Fig 7(a), and pores, [P] in Fig 7(a). The microstructure shown in Fig. 7(a) reveals the presence of a large crack, [C] in Fig. 7(a), that has propagated between pores in the graphite. Microstructural evidence such as this supports the graphite fracture mechanism adopted in the Burchell fracture model (section 6). In contrast to H-451, grade IG-110 [Fig. 7(b)] contains much smaller filler coke particles, [F] in Fig. 7(b). The particles are typically 10-150 μm in length compared to the 0.5-1.5 mm filler particles found in H-451. Moreover, pores in IG-110, [P] in Fig. 7(b), are considerably smaller than in H-451, being in the range 10-250 μm . Grade AXF-5Q graphite [Fig. 7(c)] has an extremely fine texture. The filler particles are difficult to resolve in the photomicrograph. Typical pore sizes are $<10 \mu\text{m}$ and particle sizes appear to be $<5 \mu\text{m}$.

5.2 Test procedure

Four-point bend specimens of square cross-section measuring 25 mm \times 25 mm and 50 mm \times 50 mm were used in this investigation. Specimen corners were chamfered to minimize failure initiation there. A single artificial flaw was machined in the center of the tensile surface of most specimens. The flaw geometry perpendicular to the tensile axis was a circular section with a slot thickness of 0.25 mm and notch root angle of 45°. Crack depth ranged from $a = 0.025$ to 10 mm and the surface length ranged from $2c = 0.55$ to 22 mm. The surface flaw geometry is shown in Fig. 8. A number of specimens contained no artificial flaw, *i.e.*, contained only intrinsic flaws. Six specimens not containing artificial flaws were infiltrated under vacuum with a polyurethane bearing fluorescent dye to delineate surface connected porosity. Four-point bend tests were conducted in strict accordance with ASTM standard C651-91 [55]. All specimens were loaded in four-point bending to failure under displacement control. The peak load was measured and the fracture origin was noted as being at the artificial flaw or away from the flaw. Subsequent to testing, the flaw depth, a , and surface length, $2c$, were precisely measured in the fracture plane using an optical comparator.

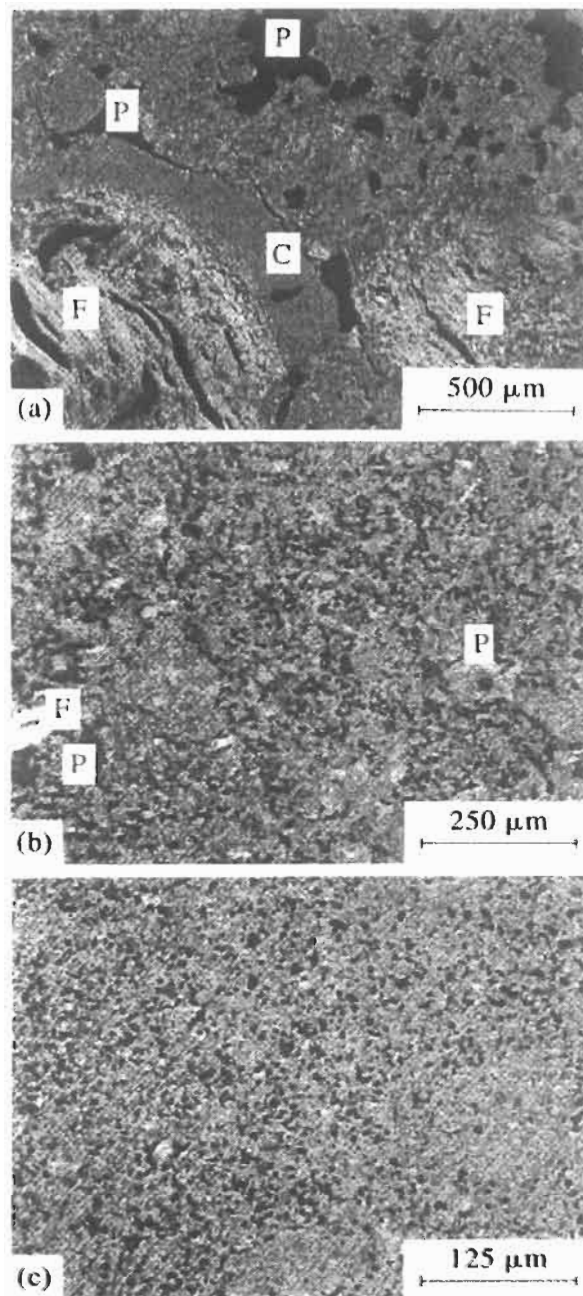


Fig. 7. Microstructures of the three primary graphites used in this work: (a) H-451, (b) IG-11, and (c) AXF-5Q. [F]-filler particles, [P]-pores and [C] cracks.

Specimen Dimensions
 $B = W \square 25.4 \text{ mm or } 50.8 \text{ mm}$

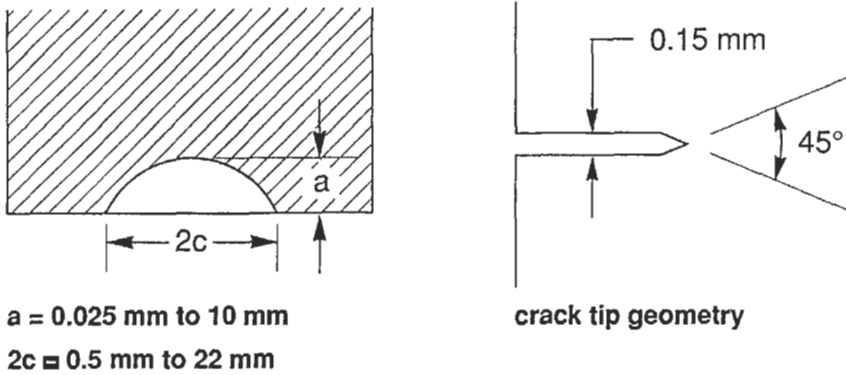


Fig. 8. Schematic of circular section flaws introduced in the tensile surface of IG-11 and H-451 graphites.

5.4 Results and discussion

Fracture at artificial flaws occurred by extending the plane of the flaw perpendicular to the tensile axis of the specimen. A typical fracture surface for specimens that failed at artificial flaws is shown in Fig. 9. Failure away from artificial flaws, *i.e.*, at intrinsic flaws, always occurred between the loading points in the region of constant tensile stress. Typical fracture surfaces for failure at intrinsic flaws are shown in Fig. 10 for an H-451 graphite specimen which had been infiltrated with fluorescent dye before testing. Near surface flaws with maximum dimensions around 1 mm appear to be the origins of failure. Origins of failure at intrinsic flaws in IG-11 graphite could not be identified on fracture surfaces even for specimens treated with fluorescent dye.

Test results for IG-11 graphite are given in Fig. 11 as a plot of fracture stress versus crack depth for specimens with and without artificial flaws. At longer crack lengths, the fracture stress is proportional to the square root of crack depth. The slope of fracture stress versus crack depth is approximately $-\frac{1}{2}$ on the logarithmic scale. As the artificial flaw size is reduced, failure occurs at higher stress levels until the fracture strength is equivalent to the unflawed specimens, *i.e.*, the mean flexural strength. At the transition crack depth, half of the specimens failed at the artificial flaw and half failed at intrinsic flaws. The transition crack depth is 0.050 mm for IG-11 graphite. It is notable that this value is comparable to the mean filler coke particle size for this graphite.

Test results for H-451 graphite are given in Fig. 12 as a plot of fracture stress versus crack depth for specimens with and without artificial flaws. The transition from artificial flaws controlling fracture strength to intrinsic flaws controlling strength occurs at 1 mm for this graphite. Although the mean filler coke particle size is around 0.5 mm, filler coke particles as large as 1 mm are common. Here again, at the transition crack depth, half of the specimens failed at the artificial flaw and half failed at intrinsic flaws.

The fracture stress for H-451 graphite exhibited greater variability than for IG-11 graphite in all tests, regardless of whether failure occurred at or away from artificial flaws. This greater variability may be attributed to a coarser microstructure for H-451 graphite. In the absence of artificial flaws, H-451 graphite presents a broader distribution of intrinsic flaw sizes from which failure may initiate. When artificial flaws are large enough to control strength, the microstructure along the front of an incipient crack was more variable for H-451 graphite, thus offering more varied resistance to crack extension.

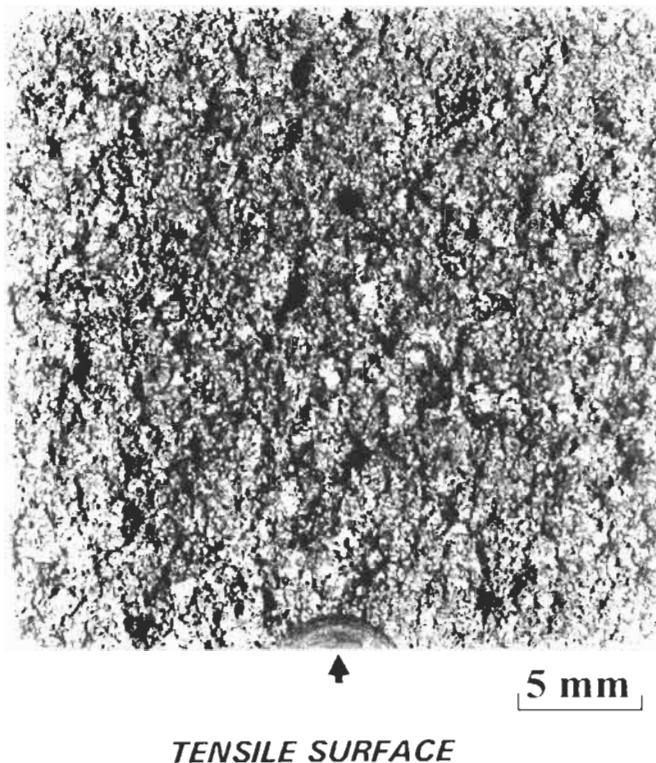


Fig. 9. Photograph of fracture surface of H-451 graphite bend specimen illustrating failure at artificial flaw.

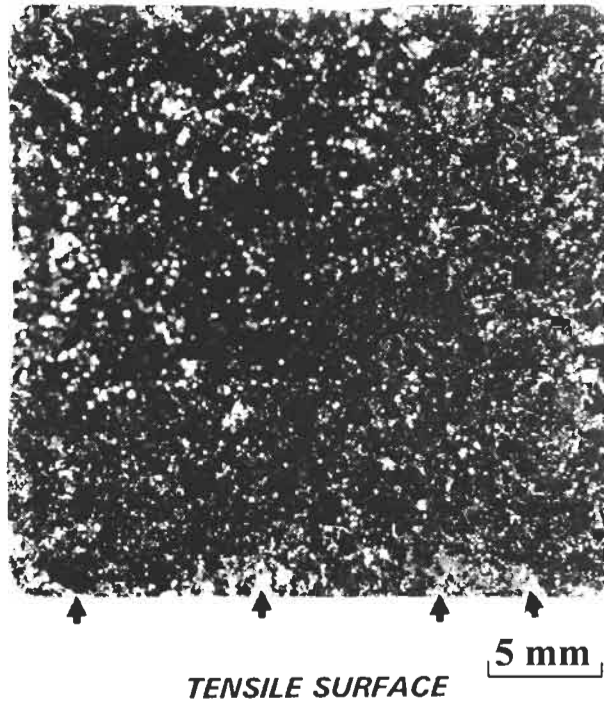


Fig. 10. Photograph of fracture surface of H-451 graphite bend specimen illustrating failure originating at natural flaws at the tensile surface.

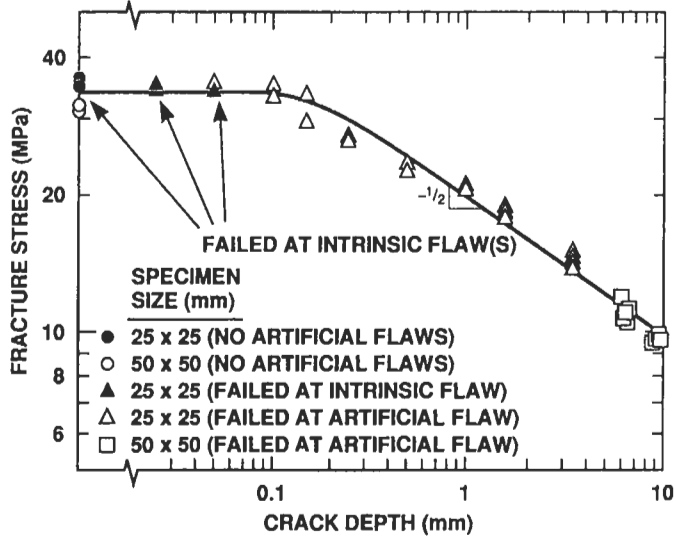


Fig. 11. Fracture stress versus crack depth for small flaw fracture tests in IG-11 graphite.

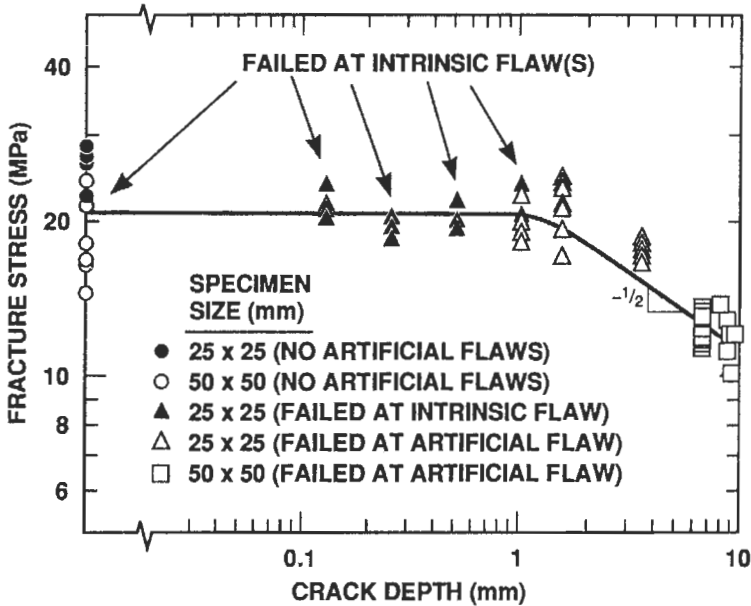


Fig. 12. Fracture stress versus crack depth for small flaw fracture tests in H-451 graphite.

Fracture mechanics analysis requires the determination of the mode I stress intensity factor for a surface crack having a circular section profile. Here the circular section flaw will be approximated by a semi-elliptical flaw.

Irwin [23] developed an expression for the mode I stress intensity factor around an elliptical crack embedded in an infinite elastic solid subjected to uniform tension. The most general formulation is given by:

$$K = \sigma \frac{\sqrt{\pi a}}{\Phi} \left[\sin^2 \theta + \frac{a^2}{c^2} \cos^2 \theta \right]^{1/4} \quad (24)$$

where Φ is an elliptical integral of the second kind and is given by

$$\Phi = \int_0^{\pi/2} \left[1 - \frac{c^2 - a^2}{a^2} \sin^2 \theta \right]^{1/2} d\theta \quad (25)$$

and the geometric variables a , c , and θ are defined in Fig. 8. Newman [56] has developed expressions for calculating the mode I stress intensity factor for a semi-elliptical surface flaw subject to uniform bending that incorporates correction

factors to account for: the free surface - M , the flaw shape - H , and the relative flaw size - S . Under bending with the nominal outer-fiber stress σ_b , the stress intensity factor at the deepest point on the crack periphery is given by

$$K_A = \sigma_b \frac{\sqrt{\pi a}}{\Phi} \times M \times H_2 \quad (26)$$

and at the intersection of the crack with the surface

$$K_B = \sigma_b \frac{\sqrt{\pi a}}{\Phi} \times M \times H_1 \times S \quad (27)$$

Empirical expressions for M , S , H_1 , and H_2 based on fitting results of finite element analysis are given elsewhere [55, 56]. The stress intensity factors, K_A and K_B , are plotted in Figs. 13 and 14 for small flaw tests on IG-11 graphite and H-451 graphite, respectively. Two regimes of behavior are observed for both graphites. Fracture behavior at longer crack lengths, greater than 1 mm, is characterized by a nearly constant value of stress intensity factor at failure. The measured fracture toughness in this regime is approximately $1.0 \text{MPa}\sqrt{\text{m}}$ for IG-11 graphite and $1.2 \text{MPa}\sqrt{\text{m}}$ for H-451 graphite. The fracture condition is likely the larger of K_A or K_B . At smaller crack depths, fracture occurs at decreasing values of K , and consequently the fracture stress begins to fall below that expected from extrapolating the longer crack regime, as can be seen in Figs. 11 and 12. Fracture at intrinsic flaws is presumed to occur at flaw sizes smaller than or equal to the transition crack lengths and at stress intensity values equivalent to those shown in Figs. 13 and 14 for an artificial flaw of comparable dimensions.

The value of K at fracture for IG-11 graphite decreased from $1.0 \text{MPa}\sqrt{\text{m}}$ to $0.5 \text{MPa}\sqrt{\text{m}}$ as the artificial flaw depth decreased more than an order of magnitude from 1 mm to 50 μm . The value of K at fracture for H-451 graphite decreased from $1.2 \text{MPa}\sqrt{\text{m}}$ to $0.8 \text{MPa}\sqrt{\text{m}}$ as the artificial flaw depth decreased to 1 mm, where intrinsic flaws comparable to this size are presumed to control strength. This observation is consistent with measurements of artificial flaw sizes for H-451 graphite specimens which had been infiltrated with fluorescent dye. Variability in the maximum intrinsic flaw size results in a corresponding variable strength for specimens without artificial flaws.

The variability in fracture stress when small artificial flaws were controlling strength was particularly pronounced for H-451 graphite, as can be seen in Fig. 12. Here the crack dimensions and crack tip process zone dimensions are comparable to the microstructural dimensions. Consequently, local variations in microstructure

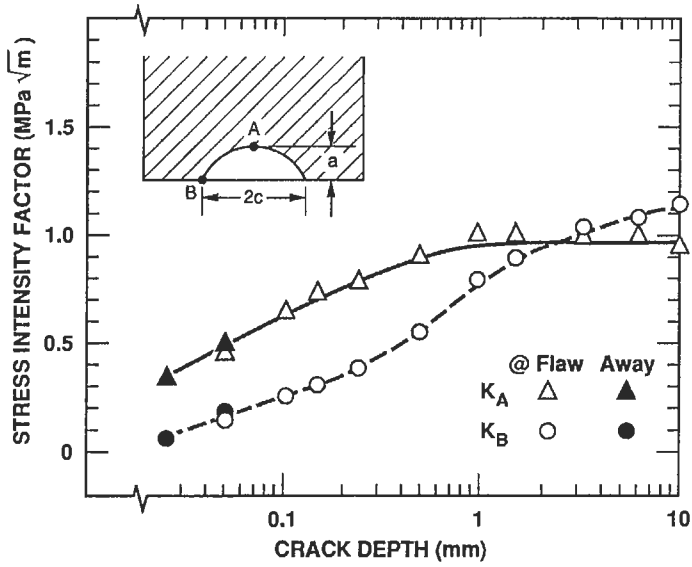


Fig. 13. Mode I stress intensity factor versus crack depth for small flaw fracture tests in IG-11 graphite.

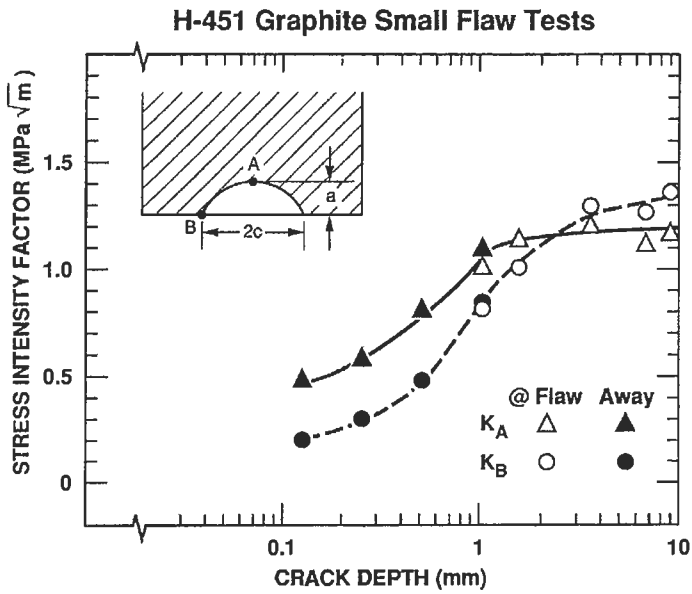


Fig. 14. Mode I stress intensity factor versus crack depth for small flaw fracture tests on H-451 graphite

present significant variation in crack growth resistance with attendant variation in fracture stress.

The decrease in K_{crit} with crack depth for fracture of IG-11 graphite presents an interesting dilemma. The utility of fracture mechanics is that equivalent values of K should represent an equivalent crack tip mechanical state and a singular critical value of K should define the failure criterion. Recall Eq. 2 where K is defined as the first term of the series solution for the crack tip stress field, σ_y , normal to the crack plane. It was noted that this solution must be modified at the crack tip and at the far field. The maximum value of σ_y should be limited to σ_{UTS} and that the far field stress should decrease only to the applied stress at increasing distance from the crack tip. The nominal fracture stress for IG-11 specimens with artificial flaws ranged from 28 to 100% of σ_{UTS} .

The decreasing value of K with decreasing flaw size for fracture of IG-11 graphite suggests that the near crack tip failure criterion would be better expressed by combining the near crack tip stress intensification estimated by K with the far field applied stress, S_{fract} (Eq. 28). Using simple superposition of the stress perpendicular

$$\sigma_{crit} = \frac{K_1}{\sqrt{2\pi r}} + S_{fract} \quad (28)$$

to the crack plane, it can be shown that σ_{crit} is the largest principal component of the local stress in the highly constrained volume near the crack tip. Here we may presume that σ_{crit} is a material constant and defines the near crack tip failure criterion. In applying Eq. 28 to the IG-11 graphite fracture data of Fig. 13, a value for r is found for which $r_{crit} = a$ constant such that $r = r_{crit}$ defines the critical crack tip process zone dimension. A simple iteration procedure was used to determine that $r = 90\mu\text{m}$ resulted in the minimum variance in σ_{crit} . The corresponding value of critical fracture stress, $\sigma_{crit} = 60.2 \text{ MPa}$ (Std. Dev. = 2.45 MPa) was determined for this data set. Figure 15 shows σ_{crit} plotted versus crack depth for IG-11 graphite data on the same scale as was used for Fig. 11. Note that the fracture condition can now be defined by a single parameter. It may seem physically inconsistent to define failure at a stress level nearly twice the nominal flexural strength of the bulk material. However, this high fracture stress may be related to the very small volume of the near crack tip field in which the requirements for failure are met. Graphite strength has been shown to be strongly volume dependent with small test section volumes exhibiting significantly higher strengths due to a lesser flaw content [57]. Within the critical crack tip volume, strength is likely controlled by a flaw content having a size regime significantly smaller than the artificial flaws

considered here.

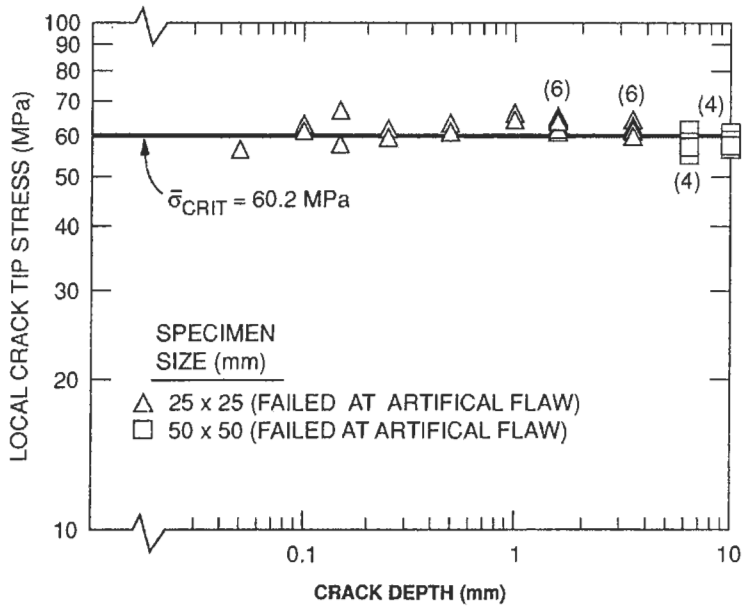


Fig. 15. Local crack tip stress versus crack depth for small flaw fracture tests on IG-11 graphite.

The second physical quantity of interest is, $r_{\text{crit}} = 90 \mu\text{m}$, the critical crack tip stress field dimension. Irwin's analysis of the crack tip process zone dimension for an elastic-perfectly plastic material began with the perfectly elastic crack tip stress field solution of Eq. 1 and allowed for stress redistribution to account for the fact that the near crack tip field would be limited to σ_{in} . The net result of this analysis is that the crack tip inelastic zone was nearly twice that predicted by Eq. 3, such that

$$r_{\text{inm}} = \frac{1}{\pi} \left(\frac{K}{\sigma_{\text{in}}} \right)^2. \quad (29)$$

If we take the nominal fracture toughness of IG-11 graphite to be $1 \text{ MPa}\sqrt{\text{m}}$ and the maximum stress in the process zone to be $\sigma_{\text{crit}} = 60.2 \text{ MPa}$ according to the above analysis, we find that $r_{\text{inm}} = 88 \mu\text{m}$. This value is virtually identical to $r_{\text{crit}} = 90 \mu\text{m}$, the process zone dimension determined using Eq. 3. To summarize, the above analysis strongly supports a hypothesis that the maximum critical stress

which defines the onset of failure for IG-11 graphite containing artificial flaws occurs at the boundary of the inelastic process zone. The magnitude of this critical fracture stress is twice the nominal fracture stress due to the small stressed volume there.

The experiments and analysis discussed above quantifies the fracture behavior of small flaws in two nuclear graphites for flaw sizes at and above intrinsic flaw dimensions. The fracture behavior of graphite in the regime where intrinsic flaws control fracture and, therefore, the nominal tensile strength, is the topic of the next section. In closing this discussion on the fracture behavior of small flaws, it is worthwhile reiterating the value of the stress versus crack length plot, as illustrated in Fig. 16, in assessing the failure/non-failure boundary for nuclear graphites. It is obvious that a single fracture criterion may not be adequate for the design of critical graphite components where there exists a significant probability of flaws greater than the transition dimension. In this regime, the maximum principal stress failure criterion based on tensile strengths overestimates graphite strengths. Consequently, care should be exercised when applying fracture mechanics below the transition crack length where the fracture toughness overestimates strengths.

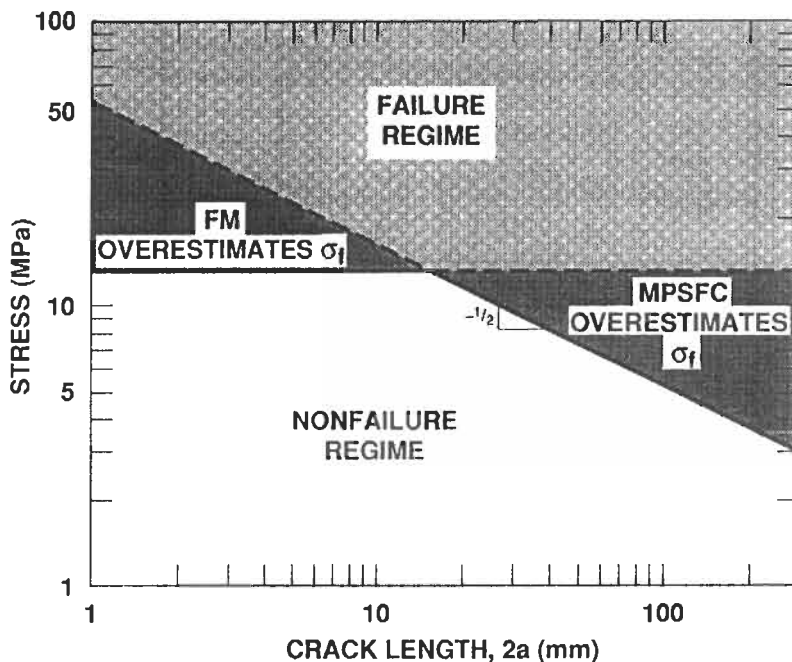


Fig. 16. Fracture strength versus crack length diagram illustrating the failure / non-failure boundary for fracture of a nuclear graphite.

6 The Burchell Fracture Model

6.1 Modelling the graphite microstructure

The microstructure of graphite is considered to be comprised of an array of cubic particles, each particle being equal to the mean filler particle size (a). Each of these particles is assumed to contain a plane of weakness oriented at some angle Θ to the applied stress (Fig. 17). Moreover, pores are randomly scattered about the microstructure, their size (cross-section) being log-normally distributed. Such pores have a stress intensification factor (K_i) associated with them, which is quantifiable in terms of the applied stress and the pore half length c according to the principles of linear elastic fracture mechanics (LEFM). Cracks are considered to initiate from these pores, and propagate by fracturing along the planes of weakness in the cubic particles of the graphite.

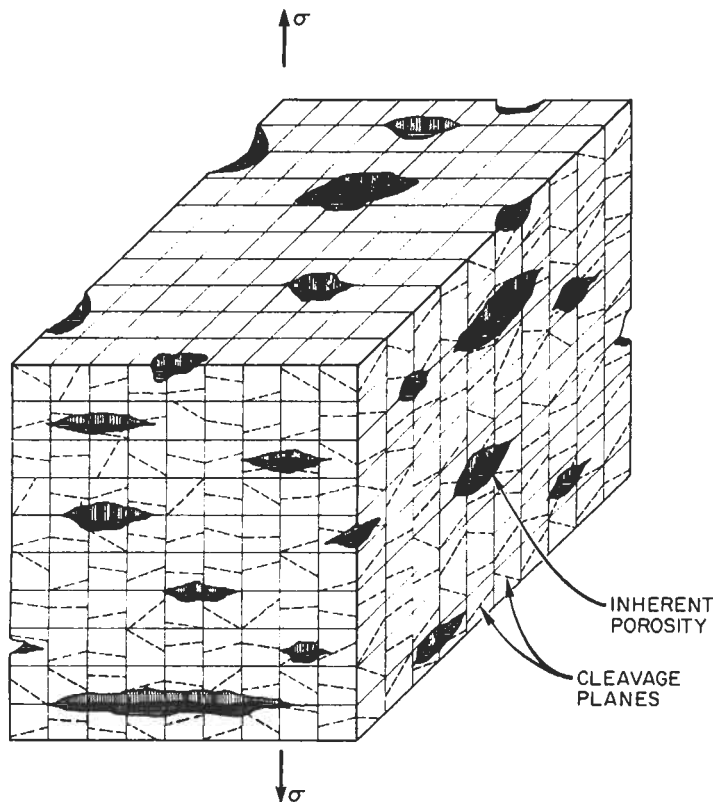


Fig. 17. Graphite microstructure as conceived in the Burchell fracture model.

A fracture mechanics criteria is developed to determine if fracture will occur on such planes in the vicinity of pores. A critical stress intensity factor (K_{Ic}) is ascribed to the particles, and when this is exceeded by the stress intensity factor (K_I) on the plane of weakness (K_I is a function of K_i and Θ) the particle is deemed to have failed. The initiating pore will then have grown from its original length c to $c+a$, where a is the particle size. In three dimensions the probability $P(n)$ that the crack will traverse all n of the particles in the row ahead of it is $P(n)=P(i)^n$. The probability $P(f)$ that the defect c will grow to length $c+ia$, fracturing i rows of particles may then be determined. Failure of the graphite is deemed to occur when the stress intensity factor (K_I) associated with the propagating defect, $c+ia$, exceeds a critical value which is related to the particle K_{Ic} . Moreover, there is a finite probability that the initiating defect (pore) exists, which is calculable from the pore size distribution. These two probabilities may be combined to determine the failure probability. The total failure probability that an inherent defect will initiate a crack which propagates to cause fracture, which is a function of the number of pores in the specimen and their size distribution, may then be defined for any applied stress.

6.2 A fracture criterion for particles in the graphite microstructure

The stress σ'_{yy} perpendicular to a plane x' at angle Θ to the x -axis at a point distance r from a crack tip (Fig. 18) may be written as [1]:

$$\sigma'_{yy} = \frac{K_i}{\sqrt{(2\pi r)}} \cos^3\left(\frac{\Theta}{2}\right) \quad (30)$$

where K_i is the stress intensity factor of the crack length $2c$ under applies stress σ . The stress σ'_{yy} may also be defined in terms of the stress intensity factor K_I of the plane x' at angle Θ from x :

$$\sigma'_{yy} = \frac{K_I}{\sqrt{(2\pi r)}} \quad (31)$$

where

$$K_I = K_i \cos^3\left(\frac{\Theta}{2}\right) \quad (32)$$

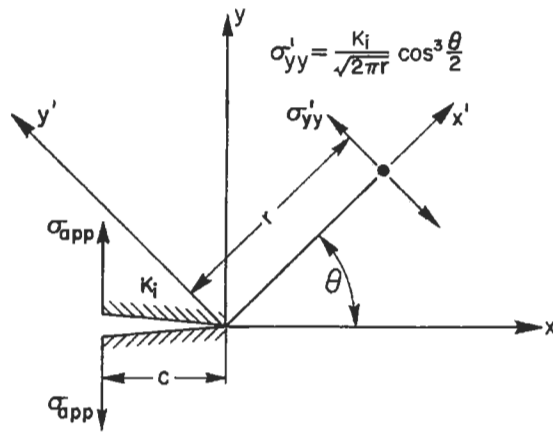


Fig. 18. The stress σ'_{yy} acting on a point distance r along a plane x' rotated through angle θ from the plane x .

At the moment of particle failure

$$K_I = K_I \cos^3\left(\frac{\theta}{2}\right) = K_{Ic} \tag{33}$$

where K_{Ic} is the critical stress intensity factor associated with fracture of the graphite particles. A criterion for the fracture of the particles may thus be defined. When K_I of a plane at angle Θ (which is a function of the K_I associated with the defect length c) exceeds K_{Ic} then all of the planes at angles less than Θ may be assumed to have failed (Fig. 19).

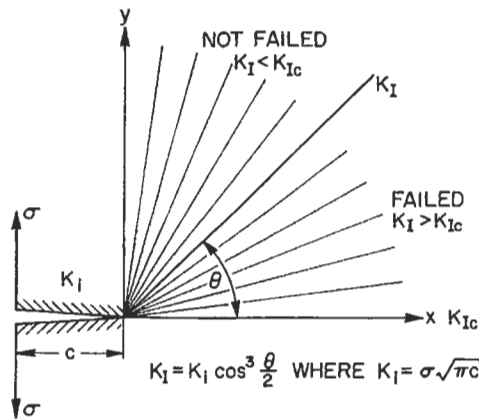


Fig. 19. Schematic illustration of the fracture criterion.

From equation (33), at fracture,

$$\left(\frac{K_{Ic}}{K_i}\right) = \cos^3\left(\frac{\theta}{2}\right) \quad (34)$$

thus,

$$\theta = 2 \cos^{-1} \left(\frac{K_{Ic}}{K_i} \right)^{1/3} \quad (35)$$

For a crack in tension K_i is defined as

$$K_i = \sigma_{app} \sqrt{(\pi c)} \quad (36)$$

substituting equation (36) in equation (35) we get

$$\theta = 2 \cos^{-1} \left[\frac{K_{Ic}}{\sigma \sqrt{(\pi c)}} \right]^{1/3} \quad (37)$$

From equation (37) above we see that Θ is a function of the applied stress, σ_{app} , and the crack half length c . For a given σ and c the angle Θ below which a particle may be assumed to have failed is given by equation (37). For simplicity the orientation of these planes about the x-axis (Fig. 18) is considered to be uniform. Therefore, the fraction of the particle that is potentially fractured is given by $2\Theta/180^\circ$ or $2\Theta/\pi$. This is also the probability, P_i , that the particle has failed. Thus we may write:

$$P_i = \frac{2\theta}{\pi} \quad (38)$$

Substituting for Θ from equation (35):

$$P_i = \frac{4}{\pi} \cos^{-1} \left(\frac{K_{Ic}}{K_i} \right)^{1/3} \quad (39)$$

The limits of probability of particle failure may now be defined:

$$(a) \quad \underline{P_i=0}$$

i.e., the particle cannot fail, this occurs when $K_i \leq K_{Ic}$.

(b) $\underline{P_i=1}$

i.e., particle cleavage is certain to occur. This happens when:

$$P_i = 1 = \frac{4}{\pi} \cos^{-1} \left(\frac{K_{Ic}}{K_i} \right)^{1/3} \quad (40)$$

that is when

$$\left(\frac{K_{Ic}}{K_i} \right)^{1/3} = \cos \left(\frac{\pi}{4} \right) = \frac{1}{\sqrt{2}} \quad (41)$$

or

$$\left(\frac{K_{Ic}}{K_i} \right) = \left(\frac{1}{\sqrt{2}} \right)^3 = \frac{1}{2\sqrt{2}} \quad (42)$$

Hence, when $K_i \geq 2\sqrt{2}K_{Ic}$ a particle ahead of the crack front is certain to fracture.

(c) $\underline{0 \leq P_i \leq 1}$

This corresponds to the condition $K_{Ic} \leq K_i \leq 2\sqrt{2}K_{Ic}$ when the probability of a particle failing in the row ahead of the crack front is given by equation (39).

6.3 Defining the probability that failure will occur from a pore of half length c

Equation (38) gives the probability that one particle has fractured. However there are $n=b/a$ particles in the entire row, therefore:

$$P(n) = (P_i)^n = \left(\frac{2\Theta}{\pi} \right)^{b/a} \quad (43)$$

now substituting for Θ from equation (37)

$$P(n) = \left[\frac{4}{\pi} \cos^{-1} \left(\frac{K_{Ic}}{\sigma\sqrt{\pi}c} \right)^{1/3} \right]^{b/a} \quad (44)$$

This is the probability that the initial pore of length c will grow from length c to length $c+a$, where a is the particle size, by fracturing all n particles. Similarly, the probability that the crack will grow from length $c+a$ to length $c+2a$ is:

$$P(n) = \left[\frac{4}{\pi} \cos^{-1} \left(\frac{K_{Ic}}{\sigma \sqrt{[\pi(c+a)]}} \right)^{1/3} \right]^{b/a} \quad (45)$$

Because the crack must extend from c to $c+a$ before it can extend from $c+a$ to $c+2a$ the probability that the crack will grow from c to $c+2a$ is given by the product of equations (44) and (45). Thus, the probability that the crack will grow from c to $c+ia$, fracturing i rows of particles can be written as:

$$P(n) = \prod_{i=0}^n \left[\frac{4}{\pi} \cos^{-1} \left(\frac{K_{Ic}}{\sigma \sqrt{[\pi(c+ia)]}} \right)^{1/3} \right]^{b/a} \quad (46)$$

This is shown schematically in Fig. 20, where $\prod(P_i)^n$ is given by Eq. 46. Taking logarithms

$$\ln P_f = \frac{b}{a} \sum_{i=0}^n \ln \left[\frac{4}{\pi} \cos^{-1} \left(\frac{K_{Ic}}{\sigma \sqrt{[\pi(c+ia)]}} \right)^{1/3} \right] \quad (47)$$

which may be approximated to

$$\ln P_f \approx \frac{b}{a} \int_0^n \ln \left[\frac{4}{\pi} \cos^{-1} \left(\frac{K_{Ic}}{\sigma \sqrt{[\pi(c+ia)]}} \right)^{1/3} \right] di \quad (48)$$

This is the probability that failure will occur due to the propagation of one tip of the initial defect c under stress σ , where K_{Ic} is the critical stress intensity factor of the filler particle and a is the filler particle size.

6.4 Defining the total probability of failure for the graphite specimen

The graphite microstructure is assumed to contain a log-normal distribution of pores. Under these circumstances, for a specific defect, the probability that its length falls between c and $c+dc$ is $f(c)dc$, with $f(c)$ defined as:

$$f(c) = \text{Constant.} \times \exp \left[-\frac{1}{2} \left(\frac{\ln 2c - \ln S_o}{\ln S_d} \right)^2 \right] \quad (49)$$

Where S_o is the mean pore size and S_d is a constant reflecting the spread of the distribution. The probability that one tip of a single defect will cause failure under applied stress σ may now be defined from equations (48) and (49) as:

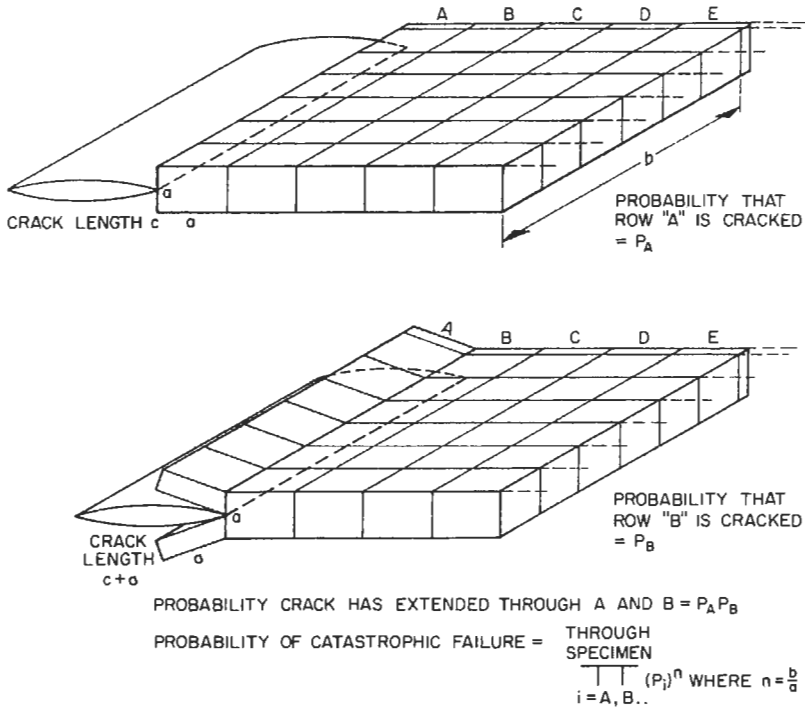


Fig. 20. The Burchell model, where crack extension occurs by successive fracture of rows of particles, from which the probability of fracture can be evaluated.

$$P_{fc} = \int_0^{\infty} f(c) \cdot P_f(\sigma, c) dc \tag{50}$$

However there are NV such defects in the specimen, where N is the number of pores per unit volume and V is the specimen volume. Each has a survival probability of one minus its failure probability, *i.e.*,

$$P_s = 1 - \int_0^{\infty} f(c) \cdot P_f(\sigma, c) dc \tag{51}$$

The total survival probability of the volume V under stress σ , containing $2NV$ crack tips, is thus $(p_s)^{2NV}$, and the total probability of failure of the specimen or stressed volume may be written as:

$$P_{tot} = 1 - (P_s)^{2NV} = 1 - \left[1 - \int_0^{\infty} f(c) \cdot P_f(\sigma, c) dc \right]^{2NV}. \tag{52}$$

6.5 Fracture model code and input parameters

Predictions of the tensile failure probabilities were made using the "**Stress Induced FracTure IN Graphite**" (SIFTING) code (Ver. 3.0, February 1994) of the Burchell fracture model. The following inputs are required to code the model for a particular grade of graphite: particle critical stress intensity factor, K_{Ic} ; mean filler particle size; bulk density; mean pore size and pore size distribution width; mean pore area; number of pores per cubic meter; specimen breadth and, specimen volume. The fracture code "SIFTING" is P.C. based and uses an iterative approach to calculate the failure probabilities as a function of stress. For a given stress, the minimum length of a defect that will yield a non-zero failure probability is calculated. The defect (crack) is assumed to propagate through the graphite, and the total probability that failure will occur is calculated from Eq. 52. The initial and final lengths of the propagating crack may thus be determined as a function of the applied stress. Fig. 21 shows initial and final defect lengths as a function of applied tensile stress for grade H-451 graphite, calculated from Eq. 46. Both the initial and final lengths of the defect decrease as the stress increases, *i.e.*, at higher stresses, smaller defects yield a non-zero failure probability, and the initial defect has to propagate to a much lesser extent before it reaches a critical length and causes failure. These observations are physically sound for brittle materials, and are in agreement with the principles of linear elastic fracture mechanics. Fig. 22 shows the probability of failure (P_{fc}) from equation 50, as a function of the applied stress for grade H-451 graphite. The probability that a single defect will exist and propagate to cause failure increases as the applied tensile stress increases, reaching a value of ~ 0.01 at the moment of certain failure, *i.e.*, when $P_{tot}=1$. The foregoing calculations (Figs. 21 and 22) indicate that the mathematical model and "SIFTING" code are sound and that the basis of the fracture model is physically correct.

6.6 The Burchell fracture model inputs

The model input parameters and the input values of the four graphites examined here are reported in Table 1. The mean pore sizes and pore size distributions of grades AGX, H-451, IG-110, and AXF-5Q were obtained using Quantitative Image Analysis (IA) and the data are reviewed elsewhere [19]. The mean pore sizes of the four graphites, taken from experimentally obtained log-normal distributions [19] were 188, 42, 16 and 1 μm for grades AGX, H-451, GI-110 and AXF-5Q, respectively. Moreover, the mean filler particle size (taken from manufacturers data) for the four graphites were 6350, 500, 20 and 4 μm for AGX, H-451, IG-110 and AXF-5Q, respectively. The number of pores per unit volume (N) was calculated from the pore area fraction, A_f , and the mean pore area P_a (μm^2) such that $N=A_f/P_a$. The pore area fraction, A_f , was calculated from $A_f = [(2.26-\rho)/2.26] \times 10^{12} \mu\text{m}^2/\text{m}^2$, where ρ is the bulk density and $2.26 \text{ g}\cdot\text{cm}^{-3}$ is the theoretical graphite crystal density. There are certain assumptions inherent in this approach

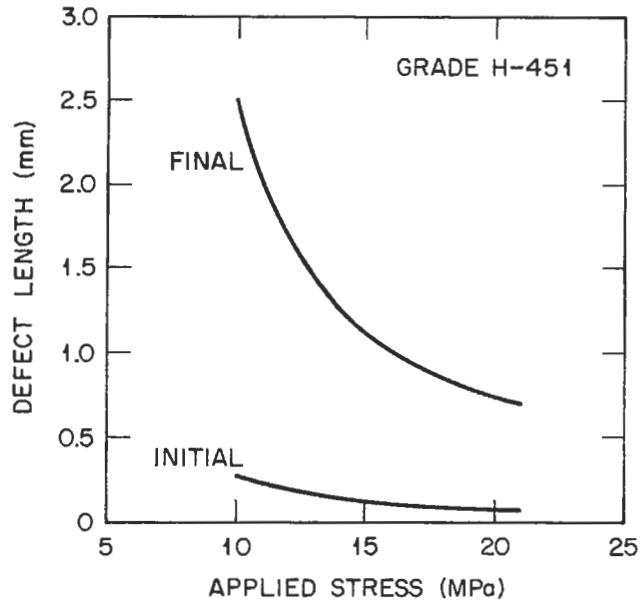


Fig. 21. Predicted initial and final defect lengths for H-451 graphite as a function of applied stress.

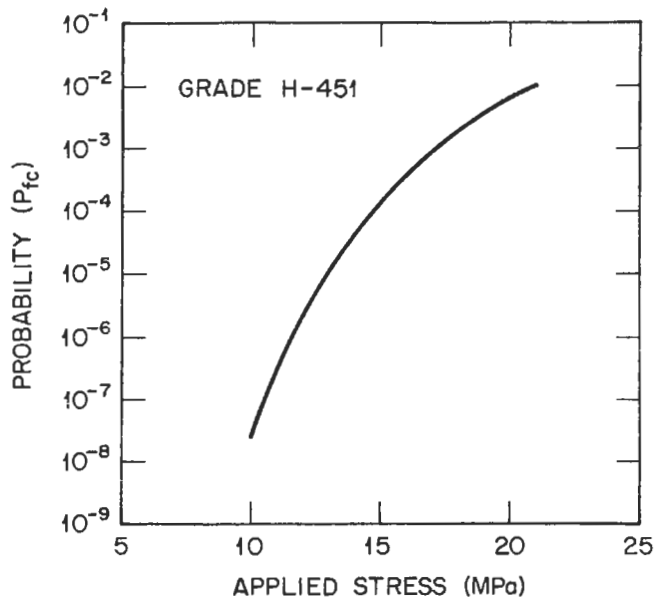


Fig. 22. The variation of probability, P_{fc} , with applied stress for H-451 graphite.

to calculating N . First, we assume that P_a is a true estimate of the mean pore area, which it is not, since we neglect many small pores, particularly in the coarser textured graphites. However, in the case of the AGX (for example), the graphite fracture process involves predominately the larger pores ($>2000\mu\text{m}^2$) and therefore a true estimate of the mean pore size would actually be substantially smaller than those pores that are responsible for the materials fracture behavior. Second, it is assumed that the pore area fraction is the same as the volume fraction of porosity. The final microstructurally related parameter required for the Burchell fracture model is the bulk density.

Several additional, non-microstructural, inputs are required for the fracture model: (i) Particle critical stress intensity factor, K_{Ic} . Here, the value determined in a previous study ($K_{Ic} = 0.285 \text{ MPa}\sqrt{\text{m}}$) [3] was adopted for all four graphites studied. This value is significantly less than the bulk K_{Ic} of graphites (typically ~ 0.8 - $1.2 \text{ MPa}\sqrt{\text{m}}$). However, as discussed in the previous section, when considering fracture occurring in volumes commensurate in size with the process zone a reduced value of K_{Ic} is appropriate; (ii) the specimen volume, taken to be the stressed volume of the ASTM tensile test specimens specimen used to determine the tensile strength distributions; and (iii) the specimen breadth, b , of a square section specimen. For cylindrical specimens, such as those used here, an equivalent breadth is calculated such that the specimen cross sectional area is identical, *i.e.*,

$$b = \sqrt{[\pi d^2/4]}$$

where d is the diameter of the ASTM C 749 [58] specimen used.

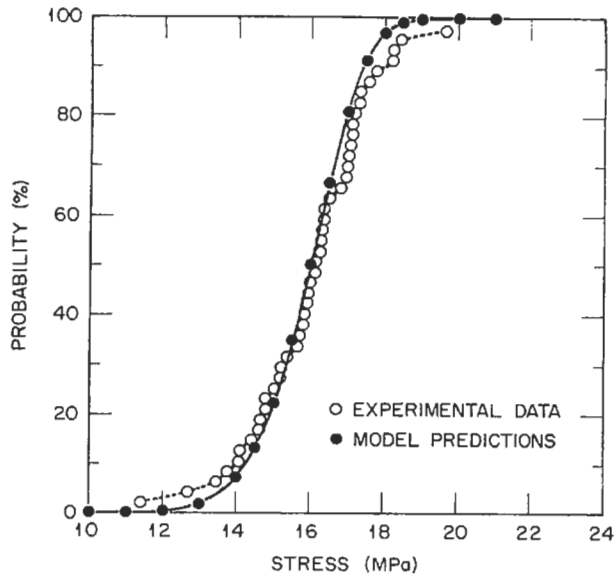
6.7 Burchell fracture model performance

The Burchell model's prediction of the tensile failure probability distribution for grade H-451 graphite, from the "SIFTING" code, is shown in Fig. 23. The predicted distribution (closed circles in Fig. 23) is a good representation of the experimental distribution (open circles in Fig. 23) [19], especially at the mean strength (50% failure probability). Moreover, the predicted standard deviation of 1.1 MPa compares favorably with the experimental distribution standard deviation of 1.6 MPa, indicating the predicted normal distribution has approximately the correct shape.

As described above, the code "SIFTING" requires several microstructural inputs in order to calculate a failure probability distribution. We are thus able to assess the physical soundness of the Burchell model by determining the change in the predicted distribution when microstructural input parameters, such as particle or pore size, are varied in the "SIFTING" code. Each microstructural input parameter

Table 1. Microstructural data from various graphites as used in the Burchell fracture model

Graphite Input Parameters	AGX	H-451	IG-110	AXF-5Q
Mean Part. Size, a , (μm)	6350	500	20	4
Bulk Density, ρ , ($\text{g}\cdot\text{cm}^{-3}$)	1.684	1.79	1.75	1.8
Mean Pore Size, S_o , (μm)	188	42	16	1
St.D. of Pore Size Dist., S_d	1.91	1.9	2.16	2.2
Mean Pore Area, P_a , (μm^2)	9862	700	100	0.44
Number of Pores per m^3 , N , (m^{-3})	2.585×10^7	2.97×10^8	2.26×10^9	4.63×10^{11}
Specimen Volume, V , (m^3)	51.48×10^{-6}	3.17×10^{-6}	3.17×10^{-6}	3.17×10^{-6}
Specimen Breadth, b , (mm)	22.51	8.44	8.44	8.44
Particle Critical Stress Intensity Factor, K_{Ic} ($\text{MN}\cdot\text{m}^{-3/2}$)	0.285	0.285	0.285	0.285

**Fig. 23.** Predicted and experimental tensile failure probability distributions for grade H-451 graphite.

was therefore systematically varied, while maintaining the others constant, to assess the individual impact on the predicted failure probability. Figure 24 shows the predicted tensile failure probabilities for H-451 graphite with three different mean filler particle sizes. The central distribution (closed circles in Fig. 24) represents the models prediction with the experimentally derived microstructural parameters, *i.e.*, $a = 0.5$ mm (Fig. 23). The remaining two curves in Fig. 24 are for mean filler particle sizes of 1 mm (open circles in Fig. 24) and 0.3 mm (open triangles in Fig. 24). Increasing the mean particle size in the Burchell fracture model clearly decreases the predicted strength of the graphite. In the case of H-451, a two-fold increase in the mean particle size (from 0.5 mm to 1 mm) decreased the mean tensile strength from 16 MPa to 12.4 MPa, a reduction of $\sim 23\%$. Conversely, a decrease in mean particle size from 0.5 mm to 0.3 mm causes an increase in the predicted mean tensile strength from 16 MPa to 19.7 MPa, a strength gain of $\sim 23\%$. The predicted trend of decreasing strength with increasing mean filler particle size is qualitatively correct [6,14] and is a further indication of the sound physical basis of the Burchell fracture model.

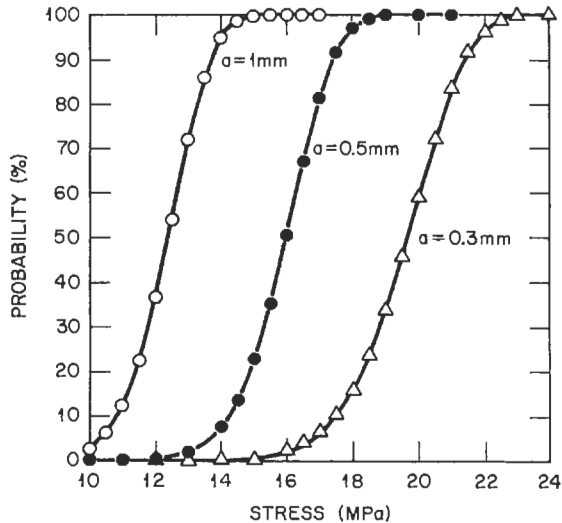


Fig. 24. The effect of particle size on the predicted tensile failure distribution of grade H-451 graphite.

The effect of varying the mean pore size and number of pores on the predicted strength distributions of grade H-451 graphite are shown in Fig. 25. In this instance, both the mean size (S_0) and number (N) of pores per unit volume was varied in the "SIFTING" code. This was necessary because the density was held constant, *i.e.*, the pore fraction remains unchanged, and therefore a decrease of the mean pore size must be accompanied by an increase in the number of pores per unit

volume of graphite. In Fig. 25 the central distribution (closed circles) is our "base case" for H-451, *i.e.*, experimentally determined microstructural inputs in the "SIFTING" code. The two additional curves in Fig. 25 are the predicted distribution for H-451 with a decreased mean pore size (open circles) and an increased mean pore size (open triangles). Clearly, the Burchell model's predictions are sensitive to mean pore size, predicting an increased strength for a graphite with finer pores. Again, this prediction is qualitatively correct. The trend for fine-textured graphites containing smaller pores and inherent defects to be stronger than coarser textured graphites is well known, and is readily explained in terms of the Griffith theory of fracture [50].

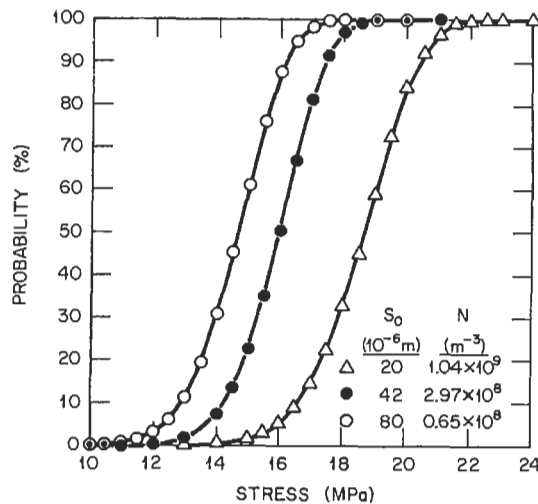


Fig. 25. The effect of mean pore size and number of pores per unit volume on the predicted tensile failure probability distribution for grade H-451 graphite.

The influence of the pore size distribution spread (S_d) on the predicted tensile strength of H-451 graphite is shown in Fig. 26. The central curve in Fig. 26 (solid circles) is our base case for H-451. Two additional curves are shown in Fig. 26, which are for $S_d = 2.2$ (open circles) and $S_d = 1.6$ (open triangles). An increased standard deviation results from a wider pore size distribution. Therefore, the probability of a larger, more damaging, flaw existing in the graphite is greater and a weaker graphite would be anticipated. Conversely, a smaller standard deviation would result from a narrower pore size distribution. The probability of the same damaging flaw existing in the graphite is thus less and a stronger graphite would be expected. The model's prediction of the effect of S_d on graphite strength is therefore qualitatively correct and is yet further evidence of the physical soundness of the Burchell fracture model.

The effect of varying the bulk density, which is used to calculate the pore fraction and hence the number of pores per unit volume, for H-451 graphite, is shown in Fig. 27. Again, the central curve is our base case for H-451, *i.e.*, the output from the "SIFTING" code with the input parameters given in Table 1. The two additional curves in Fig. 27 are for bulk densities of $1.65 \text{ g}\cdot\text{cm}^{-3}$ (open circles) and $1.90 \text{ g}\cdot\text{cm}^{-3}$ (open triangles). The Burchell model predicts only a weak dependency of tensile strength on density. While this is qualitatively correct, the actual dependency of strength on density for polygranular graphites is much stronger than is suggested by the predictions in Fig. 27. However, in reality, change in the density of a graphite would be accompanied by changes in the pore size distribution (mean and standard deviation), and might be expected to result from changes in the materials formulation, *i.e.*, filler particle size distribution, filler-binder ratio, and the forming process *e.g.*, extruded, molded or isostatic pressing. The data presented in Figs. 24-26 have clearly demonstrated that changes in microstructural parameters such as filler particle size, mean pore size, standard deviation of the pore size distribution and number of pores, strongly influence the predicted graphite strength. There is a strong tendency for high density graphites to possess finer texture, as evidenced by the microstructural data in Table 1. Consequently, the predicted weak dependency of graphite strength on density is not a consequence of a flaw in the Burchell model, but rather, results from the artificial nature of the input data sets used in the "SIFTING" code in this instance. Clearly, a better validation of the fracture model would be a test against strength data from several graphites, representing a wide range of textures.

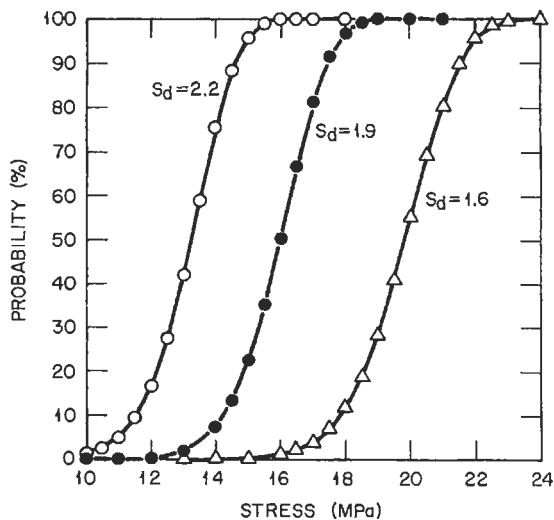


Fig. 26. The effect of pore size distribution spread (standard deviation) on the predicted tensile failure probability distribution for grade H-451 graphite.

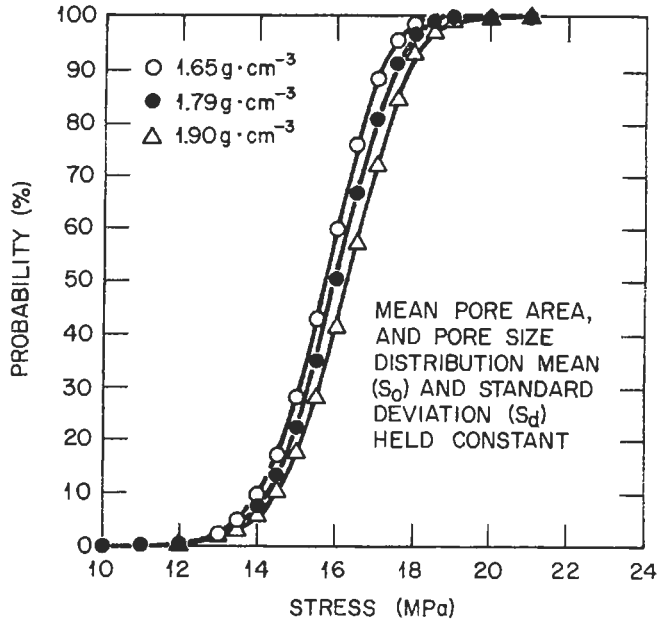


Fig. 27. The effect of density on the predicted tensile failure probability distribution for grade H-451 graphite.

Microstructural input data for the "SIFTING" code are reported in Table 1 for four graphites, AGX, H-451, IG-110 and AXF-5Q. The spread of texture represented by the graphites is clearly demonstrated by the mean filler particle size, which ranges from 6350 μm in the case of AGX, to 4 μm in the case of AXF-5Q. The model's predictions of the tensile failure probabilities for graphites examined here are in Fig. 28 along with the experimentally determined tensile strength data [19]. The Burchell model's predicted tensile strength distribution for IG-110 graphite is a reasonable fit to the experimentally determined distribution. The predicted mean tensile strength (26.3 MPa) compares favorably with the experimental strength (25.7 MPa). Moreover, the predicted and experimental standard deviations are in reasonably good agreement, *i.e.*, 1.9 and 2.5 MPa, respectively. The models predictions for the tensile strength of grade AXF-5Q graphite is a reasonable representation of the experimental data, the predicted mean and standard deviation (63.1 and 6.1 MPa) being comparable with the experimental values (65.1 and 5.5 MPa). The predicted AGX tensile failure probability obtained from the "SIFTING" code, with the inputs reported in Table 1, is in reasonable agreement with the experimental data. However, the predicted mean strength of 5.14 MPa is an over prediction of the experimental mean (4.61 MPa) [19], which is attributed to inaccuracies in the experimentally determined pore size distribution [19]. In all four cases the agreement between experimental and predicted strength is good,

demonstrating the flexibility of the fracture model, which is attributed to its sound physical basis. The Burchell fracture model has demonstrated considerable versatility, as indicated in Fig. 28, in successfully predicting the tensile failure probability distributions for graphite grades AXF-5Q, IG-110, H-451 and AGX.

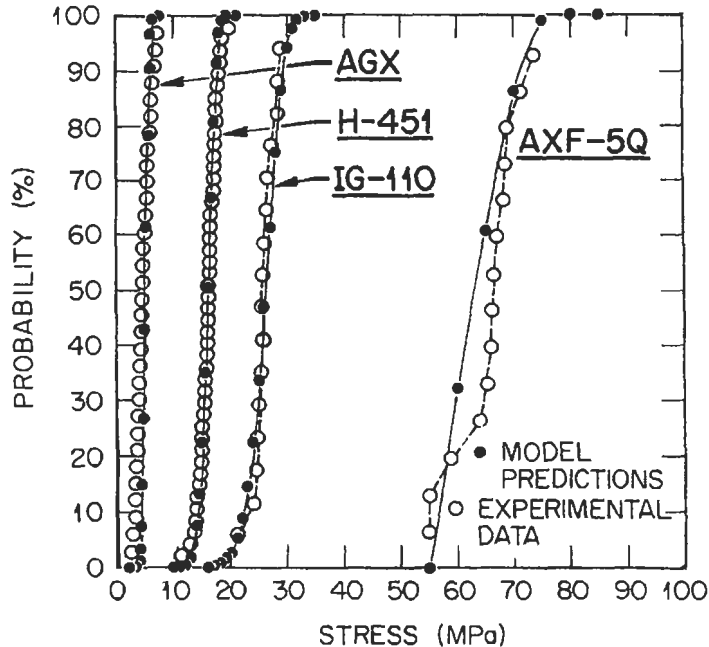


Fig. 28. A comparison of experimental and predicted tensile failure probabilities for four graphites with widely different textures: AGX, H-451, IG-110 and AXF-5Q.

7 Summary and Conclusions

Because of the important role of graphite in high temperature structural applications its fracture behavior has been extensively studied. Graphite behaves in a pseudo-brittle fashion, with a limited degree of plasticity within a process "zone". The extent of the process zone has been studied in numerous qualitative and quantitative studies of graphite fracture. The flaw structure within the graphite plays a prominent role in the fracture process. A failure criteria may be rationalized in terms of a dominant flaw (or ensemble of flaws) and local stress which result in the formation of a macroscopic crack, which subsequently extends to cause failure. The dominant flaw usually develops from the larger of the intrinsic flaws, although it may occur from lesser flaws due to local stress concentrations and/or cyclic loads. Moreover, the dominant flaw may be present

as an anomaly arising from processing, machining or handling damage. These fracture processes may be described and understood through the fracture mechanics formulations developed for metals, ceramics and other brittle materials. The principles of linear elastic fracture mechanics and elastic plastic fracture mechanics have been reviewed, and the former applied to describe the fracture behavior of small flaws in two grades of nuclear graphite. For both of the graphites studied a decreasing K_{Ic} value was noted for decreasing crack sizes.

A physically well based fracture model that combines a microstructural approach to fracture with a fracture mechanics failure criterion has been reported. Input data for the model has been acquired from four grades of graphite with widely varying texture. The model and code were successfully benchmarked against H-451 tensile strength data and validated against tensile strength data for grades AGX, IG-110 and AXF-5Q. Two levels of verification were adopted. Initially, the models predictions for the growth of a subcritical defect in H-451 as a function of applied stress was evaluated and found to be qualitatively correct. Both the initial and final defect lengths were found to decrease with increasing applied stress. Moreover, the sub-critical crack growth required prior to fracture was predicted to be substantially less at higher applied stresses. Both of these observations are qualitatively correct and are readily explained in linear elastic fracture mechanics terms. The probability that a particular defect exists and will propagate through the material to cause failure was also predicted to increase with increasing applied stress. Quantitative validation was achieved by successfully testing the model against an experimentally determined tensile strength distribution for grade H-451 graphite. Moreover, the model appeared to qualitatively predict the effect textural changes on the strength of graphite. This was subsequently investigated and the model further validated by testing against three additional graphites, namely grades AGX, IG-110 and AXF-5Q. The versatility and excellent performance of the Burchell fracture model was attributed to its sound physical basis, which recognizes the dominant role of porosity and flaws in the graphite fracture process.

8 Acknowledgments

Research sponsored by the U. S. Department of Energy under contract DE-ACO5-96OR22464 with Lockheed Martin Energy Research Corporation at Oak Ridge National Laboratory.

9. References

1. T. D. Burchell. Studies of Fracture in Nuclear Graphite, Ph.D Thesis, University of Bath, UK, 1986.
2. T. D. Burchell. A Microstructurally Based Fracture Model for Nuclear Graphites. In *Proc. IAEA Specialist's Meeting on Status of Graphite Development for Gas Cooled Reactors*, Toki-Mura, Japan, Sept 1991, IAEA TECDOC No. 690, Pub. IAEA, Vienna, 1993, pp. 49 58.
3. T. D. Burchell and J. P. Strizak. Modelling the Tensile Strength of H-451 Nuclear Graphite. In *Proc. 21st Biennial Conf. on Carbon*, Buffalo NY, USA.. Pub. American Carbon Society, 1993, pp. 687 688.
4. T. D. Burchell and J. P. Strizak. The Performance of a Fracture Model for Graphites. In *Proc. Carbon 94*, Granada, Spain. Published Spanish Carbon Society, 1994, pp. 128 129.
5. J. Kaiser. Untersuchungen uber das Auftreten von Gerauschen beim Zugversuch. Ph.D. Thesis, Technische Hochschule, Munich, Germany, 1950.
6. G. Kruass and J. Semmler. Die charakterisierung des mechanischenverhaltens von kohlenstoff - und graphitmaterialien mit hilfe der schallemissionsanalyse, *Carbon*, 16(3), 185 193.
7. T. D. Burchell, R. G. Cooke, B. McEnaney and I. M. Pickup, Acoustic emission from polygranular graphites, *Carbon* 1985, 23(6), 739 747.
8. S. Mrozowski. Mechanical strength, thermal expansion and structure of cokes and carbons. Proc. 1st and 2nd Conf. on Carbon., Waverley Press, Baltimore, MD, USA, 1956, p. 31.
9. I. M. Pickup, R. G. Cooke and B. McEnaney. Stress-induced acoustic emission from graphite In *Proc. 16th Conf. on Carbon*, University of California, San Diego, CA. USA, 1983, pp. 406 407.
10. I. Ioka, S. Yoda and T. Konishi. Behavior of acoustic emission caused by microfracture in polycrystalline graphites, *Carbon* 1990, 28(6), 879 885.
11. T. D. Burchell, M. O. Tucker and B. McEnaney. Qualitative and Quantitative Studies of Fracture in Nuclear Graphites, *Materials for nuclear reactor core applications. BNES*, London, 1987, pp. 95-103.
12. J. D. Buch. *A.S.T.M. STP 605*, pp. 124-144 (1972)
13. A. P. G. Rose and M. O. Tucker. A fracture criterion for nuclear graphites. *J. Nucl. Mater.* 1982, 110, 186 195.
14. T. D. Burchell, A. P. G. Rose and M. O. Tucker. The influence of grain size distribution on a fracture criterion for graphites. In *Proc. 17th Biennial Conf. on Carbon*, Lexington KY, USA. Pub. American Carbon Society, 1985, pp. 346 347.
15. M. O. Tucker, A. P. G. Rose and T. D. Burchell. The fracture of polygranular graphites. *Carbon* 1986, 24(5), 581 682.
16. I. Ioka and S. Yoda. Acoustic emission caused by reversed plastic deformation in polycrystalline graphites. *J. Nucl. Mater.* 1987, 148, 344 350.
17. G. Neighbour, B. McEnaney and M. Philips. Acoustic emission responses from cyclic loading of a nuclear graphite. *Carbon*, 1992, 30(3), 359 363.
18. T. D. Burchell, A. P. G. Rose and B. McEnaney. Acoustic emission from irradiated nuclear graphite. *J. Nucl. Mater.*, 1986, 140(1), 11 18.
19. Burchell T.D., A Microstructurally based Fracture Model for Polygranular Graphites, *Carbon* 34 (3) 1996, 297 316

20. M. O. Tucker and N. McLachlan. Fracture and microstructure of graphite. *J. Phys. D: Appl. Phys.*, 1993, 26(6), 893 907.
21. N. McLachlan. The Modelling of Polycrystalline Graphite Fracture and Deformation Properties, Ph.D. Thesis, University of Exeter, UK, 1992.
22. B. A. Bilby, A. H. Cottrell and K. H. Swindon. *Proc. R. Soc. A* 272, 304 (1963).
23. G. R. Irwin, *Journal of Applied Mechanics*, Trans. ASME, Vol. 24, 1957.
24. D. Broek, *Elementary Engineering Fracture Mechanics*, 3rd Revised Edition, Martinus Nijhoff Publishers, 1982.
25. P. C. Paris and F. Erdogan, "A Critical Analysis of Crack Propagation Laws", *Journal of Basic Engineering*, Trans. ASME, Vol. 85, 1963, p. 528-534.
26. W. Elber, "The Significance of Fatigue Crack Closure", *Damage Tolerance in Aircraft Structures*, ASTM STP 486, 1971, pp. 230 242.
27. S. Suresh and R. O. Ritchie, "A Geometric Model for Fatigue Crack Closure Induced by Fracture Surface Morphology", *Metallurgical Transactions*, 13A, 1982, pp. 1627 1631.
28. N. Walker and C. J. Beevers, "A Fatigue Crack Closure Mechanism in Titanium", *Fatigue of Engineering Materials and Structures*, Vol. 1, 1979, pp. 135 148.
29. C. J. Beevers, R. L. Carlson, K. Bell and E. A. Starke, "A Model for Fatigue Crack Closure", *Engineering Fracture Mechanics*.
30. K. Minakawa and A. J. McEvily, "Our Crack Closure in Near-Threshold Region", *Scripta Metallurgica*, Vol. 15, 1981, pp. 633 636.
31. R. O. Ritchie and S. Suresh, "Some Consideration on Fatigue Crack Closure Induced by Fracture Surface Morphology", *Metallurgical Transactions*, Vol. 13A, 1982, pp. 937 940.
32. W. T. Evans and A. R. Luxmoore, *Journal of Strain Analysis*, Vol. 11, 1976, pp. 177 185
33. W. K. Wilson, "Plane Strain Crack Toughness Testing of High Strength Metallic Materials", ASTM STP 410, American Society for Testing and Materials, Philadelphia, 1966, pp. 75 76.
34. R. A. Smith, "On the Short Crack Limitations of Fracture Mechanics", *International Journal of Fracture*, Vol. 13, 1977, pp. 717 720.
35. W. F. Brown and J. E. Strawley, "Plane Strain Crack Toughness Testing of High Strength Metallic Materials", ASTM STP 410, American Society for Testing and Materials, Philadelphia, 1966, pp. 1-65.
36. Plane Strain Fracture Toughness of Metallic Materials, 1982 *Annual Book of ASTM Standards*, Part 10, Standard No. E399.
37. J. E. Brocklehurst, Fracture in Polycrystalline Graphite, In *Chemistry and Physics of Carbon*, Vol. 13, ed. Philip L. Walker, Jr. and Peter A Thrower, Marcel Decker, New York, 1977, pp. 145 279.
38. S. Sato, H. Awaji and H Akuzawa, Fracture Toughness of Reactor Graphite at High Temperature, *Carbon*, 1978, Vol. 16, No. 2, pp 95 102
39. M. Birch, R. G. Brown and J. E. Brocklehurst, Defining the Effective Inherent Defect Size of Graphite for Fracture Mechanics Applications, Extended Abstracts and Program-16th Biennial Conference on Carbon, Pub. American Carbon Society, 1983, pp 404405.
40. E. P. Kennedy, Fracture Mechanics Analysis of Extruded Graphite, Extended Abstracts and Program-16th Biennial Conference on Carbon, Pub American Carbon Society, 1985, pp 287 288.

41. C. R. Kenedy, Fracture Toughness of Anisotropic Graphites, Extended Abstracts and Program - 17th Biennial Conference on Carbon, Pub American Carbon Society, 1985, pp 289 290
42. G. R. Romanoski and T. D. Burchell, Specimen Size Effect an Fracture Toughness of Nuclear Graphites, Extended Abstracts and Program - 20th Biennial Conference on Carbon, Pub. Electrochemical Society, 1991 pp 584 585
43. S. Sato, K. Hirakawa, A. Kurumada, S. Kimura and E. Yasuda, Degradation of Fracture Mechanics Properties of Reactor Graphite Due to Burn-off, Nuclear Engineering and Design, Vol 118, 1990, pp 227 241
44. T. D. Burchell, I. Oku and M. Eto, A Comparison of Fracture Toughness Measurement Techniques as Applied to Nuclear Graphites, Extended Abstracts and Program, International Carbon Conference, 1990, pp 278 279
45. Proceedings of a IAEA Specialists Meeting on Graphite Component Structural Design, JAERI TOKAI, Japan, Ed. Konomo Sanokawa, 1987
46. Proceedings of a IAEA Specialists Meeting on the Status of Graphite for GAS Cooled Reactors, Tokai-mura, Japan, 1993
47. M. Sakai, K. Urashima, and M. Inagaki, "Energy Principle of Elastic-Plastic Fracture and Its Application to the Fracture Mechanics of a Polycrystalline Graphite," *Journal of the American Ceramic Society*, 1983, 66(12), 868 874.
48. M. Sakai, J. I. Yoshimura, Y. Goto, and M. Inagaki, "R-Curve Behavior of a Polycrystalline Graphite: Microcracking and Grain Bridging in the Wake Region," *Journal of the American Ceramic Society*, 1988, 71(8), 609 616.
49. T.D. Burchell and T. Oku and M. Eto. A comparison of fracture toughness measurement techniques as applied to nuclear graphite. In *Proc. Carbone 90*, Paris, France. Pub. Groupe Francais D'etude des Carbones, 1990. pp. 278 279.
50. A. A. Griffith, "The Phenomena of Rupture and Flow in Solids," *Phil. Trans. Roy. Soc. of London*, 1921, A221, 163 167.
51. C. E. Inglis, "Stresses in a Plate Due to the Presence of Cracks and Sharp Corners," *Trans. Inst. Naval Architects*, 1913, 55, 219 241.
52. J. R. Rice, "A Path Independent Integral and the Approximate Analysis of Strain Concentration by Notches and Cracks," *J. Appl. Mech.*, 1968, 35, 379 386.
53. S. J. Burns, J. C. Pollet and C. L. Chow, "Non-Linear Fracture Mechanics," *Int. J. Fract.*, 1978, 14(3), 311 326.
54. J. Eftis, D. L. Jones and H. Liebowitz, "On Fracture Toughness in the Nonlinear Range," *Eng. Fract. Mech.*, 1975, 17, 491 503.
55. ASTM Standard C651-91, Standard Test Method for Flexural Strength of Manufactured Carbon And Graphite Articles Using Four-Point Loading at Room Temperature, American Society for Testing and Materials, 1991
56. J. C. Newman, Jr. "A Review and Assessment of the Stress Intensity Factors for Surface Cracks," Part-Through Crack Fatigue Life Prediction, ASTM STP 687, J.B. Chang, Ed, American Society for Testing and Materials, 1979, pp. 16 42.
57. J. P. Strizak, The Effect of Volume on the Tensile Strength of Several Nuclear Grade Graphites, Proceedings of a Specialists Meeting on The Status of Graphite Development for Gas Cooled Reactors. Tokai-mura, Japan, 1991
58. ASTM C 749-92, "Standard Test Method for Tensile Stress-Strain of Carbon and Graphite". ASTM Standards Vol. 15.01, pp. 196 207, Pub. American Society for Testing of Materials, Philadelphia, USA (1994).

Index

A

- Adsorbents 280, 287
 - see also* activated carbon, active carbon fibers
 - fractional pore volumes 289
 - methane storage data 194, 291
 - temperature effects 191, 198, 277, 293
- Adsorbent storage
 - for vehicles *see* natural gas vehicles
 - natural gas 105, 271, 274
- Advanced gas cooled reactor (AGR) 442
- Acoustic emission 486
- Activated carbon 98, 183, 239
 - automotive applications 235, 242, 276
 - canisters *see* carbon canisters
 - nuclear applications 429, 473
 - production methods 239
 - properties 243, 244
 - thermal conductivity 191, 297, 334
- Activation
 - chemical 99, 240
 - physical 99, *see also* thermal
 - thermal 239
- Active carbon fibers 95, 183
 - applications 101
 - adsorbed natural gas 105
 - adsorption and catalysis 102
 - emerging 109
 - medical 109
 - water purification 106
- Adsorbent monoliths 183, 290, 336-337
- Adsorption 183, 246, 274-294, 303
- Adsorption heat pumps *see* refrigerators and heat pumps
- Adsorption refrigerators *see* refrigerators and heat pumps
- AGOT graphite 436, 437

- AGX graphite 504
- AN2-500 graphite 451
- ASR-1RS graphite 436
- AXF-5Q graphite 504

B

- BEPO 438
- Beehive oven 207
- Bond length 11
- Bonding between carbon atoms 1
- Buckminsterfullerene *see* fullerenes
- Bulk modulus 11
- Burchell fracture model 515
 - performance 524
- Butane working capacity 244, 252-253

C

- Carbon
 - application in fission reactors 429, 473
 - coal derived *see* coal derived carbons
 - films 14
 - hard 15
 - soft 15
 - graphitic, in Li batteries 353
 - graphitizing 23
 - hard 344 *see also* carbon, non-graphitizing
 - hydrogen containing 358
 - insulation materials 477, *see also* carbon bonded carbon fiber
 - nanoparticles 18
 - nanocoons 19
 - non-graphitizing 23
 - onion 20
 - plasma facing components 394
 - properties of crystalline forms 11

- soft 344 *see also* carbon, graphitizing
 - spheres, multi-walled 19
 - Carbon anodes *see also* Lithium-ion batteries
 - manufacture 210
 - Carbon atom
 - binding energy 3, 458
 - displacement energy, 458
 - Carbon bloom 414
 - Carbon bonded carbon fiber 173
 - mechanical properties 175
 - optical properties 181
 - physical properties 175
 - structure 174
 - thermal properties, 176
 - Carbon canister
 - applications
 - onboard refueling vapor recovery 263
 - running loss emission control 257
 - design 252
 - Carbon composites 139, 169
 - fission reactor applications 476
 - fusion reactor applications 394
 - Carbon dioxide adsorption 194
 - Carbon fibers
 - active, *see* active carbon fibers
 - high performance 96, 119
 - from novel precursors 133
 - from mesophase pitch 123, 170
 - carbonization and graphitization 131
 - microstructure 132
 - melt-spinning 128
 - stabilization 131
 - from Polyacrylonitrile 119
 - microstructure 123
 - processing 119
 - isotropic 170, 186-188
 - mechanical properties 133
 - vapor grown *see* VGCF
 - Carbon fiber composite molecular sieve *see* CFCMS
 - Carbon nanotubes *see* nanotubes
 - Carbonization 21
 - Carbynes 6
 - CBCF *see* Carbon bonded carbon fiber
 - CFCMS 183, *see also* porous carbon-carbon composites
 - activation 186
 - adsorption behavior 194
 - applications 183, 199
 - mesoporous 188
 - microporous 186
 - physical properties 190
 - pore structure 184
 - thermal conductivity 191
 - CGB graphite 457, 458
 - Chemical erosion 414
 - Coal derived carbons 205
 - Coal derived graphite 229
 - Coated fuel 447, 448, 454, 474
 - Coke 206
 - battery 207
 - metallurgical 206
 - petroleum 207
 - from solvent extraction
 - characteristics 225-228
 - preparation 223
 - CP-1, CP-2 437
 - Critical strain energy release rate 498
- D**
- Diamond 4
 - crystal structure 4
 - Diamond films 16
 - Disruption electrons 393
 - Dragon reactor experiment (DRE) 446
- E**
- Electrical double-layer capacitor 109
 - Electrical resistivity 56-59, 144, 155, 190-191, 230-232, 465
 - Electrical swing adsorption 197-199
 - Engineered carbons 20
 - Erosion 419
 - Evaporative emissions 236

EY-9 graphite 447

F

Fast neutrons 430
 Fission reactor applications 429
 Fluence 459
 conversion factors 459
 Flux effect 459
 Fort St. Vrain HTGR 449
 Fracture processes in graphite 486
 Fuel matrix materials, 475
 Fuel particles *see* coated fuel
 Fullerenes 9, 35
 applications 84
 doping 37
 electrical transport 56
 electronic properties 46
 Hall effect 58
 optical properties 48
 Raman spectra 54, 55
 structure 9, 39, 41
 superconductivity 59
 synthesis 37
 vibrational properties 52
 Fullerites 37
 Fullerene based solids *see* fullerenes
 Fusion reactor applications 389

G

Gas cooled reactors 438-454
 Gas separation 194
 Gasoline working capacity 252-253
 General purpose heat source 173
 G_{lc} *see* critical strain energy release rate
 Glassy carbon 26
 GLEEP 438
 GR-280 graphite 436, 456
 GR2-125 graphite 436, 456
 Graphite 5
 coal derived
 preparation 229
 properties 229-233
 crystal structure 5, 433
 engineering applications 485

fibers *see* carbon fibers
 fracture 485, 503
 microstructural studies 487
 fracture models 488
 manufacture 210, 433
 microstructure 487, 505 *see*
 also nuclear graphite
 nuclear *see* nuclear graphite
 Griffith criterion 497
 Graphitization 25, 211, 433
 mechanism 28
 Guard bed 199, 294
 design 297
 target gasses 199, 294

H

H-327 graphite 450
 H-451 graphite 436, 450, 503
 Hall effect 58
 Hanford reactors 438, 454
 HDG graphite 435
 Heat pumps *see* refrigerators
 Helium cooled reactors 446-454
 High temperature fuel *see* coated fuel
 High temperature gas cooled reactors
 (HTGRs) 448-454
 High temperature test reactor (HTTR)
 452
 Hydrogenation 214
 Hydrogen sulfide separation 194

I

IG-110 graphite 436, 453, 454, 503
 IM1-24 graphite 435, 436, 446
 Irradiation annealing 459
 Irradiation effects 400 *see also*
 radiation damage

J

J-integral 501

K

Kaiser effect 486
 K_{Ic} *see* stress intensity factor

L

Linear elastic fracture mechanics 491
 Lithium insertion mechanism 383
 Lithium ion batteries 341
 commercial cells 384
 Liquid crystal behavior 129

M

Magnox reactor 438
 Mesophase 24
 formation 123
 rheology 129
 Methane adsorption 194, 274-294
 Microporous carbons 375 *see also*
 adsorbents
 Moderation 430
 Moderator requirements 430
 Molten salt reactor experiment 457

N

N-reactor 454
 Nanotubes 18, 35, 61
 applications 84
 electronic structure 69
 historical perspective 36
 mechanical properties 83
 Raman spectra 78, 79, 81, 82
 structure 66
 synthesis 62
 transport properties 75
 vibrational properties 76
 Natural gas
 composition 295
 energy density 271
 fuel 273
 storage
 adsorbed 105, 271, 274

 compressed 274
 liquified 274
 storage capacity, ANG 284
 theoretical maximum 281
 Natural gas vehicles 269, 276
 energy aspects 271
 Nuclear fission 429
 Nuclear fusion 389
 Nuclear graphite 433
 fracture behavior of small flaws
 503
 manufacture 433
 microstructures 435
 physical properties 436
 Neutron fluence *see* fluence
 Neutron irradiation effects *see*
 irradiation effects

O

Optical properties
 fullerenes 48
 CBCF 6, 13

P

PAN fibers *see* carbon fibers
 PAN graphite 452
 Particle-matter interactions 393
 Peach Bottom HTGR 448
 Pebble-bed reactors
 AVR 450
 THTR-300 450
 Pebble type fuel elements 450,
 452
 PGX graphite 453
 Pile grade A (PGA) graphite 435, 436,
 439
 Phase diagram
 carbon 12
 K_xC_{60} 45
 Physical sputtering 412
 Pitch
 coal derived 208
 ash reduction 221
 mesophase 123

pyrolysis 124
 Pitch-coke graphite, 436, 446
 Plasma disruption 393, 397, 419
 Plasma facing components 390
 Plasma facing material 394
 Plasma-wall interactions 412
 Porous carbon-carbon composites 169
 activation 172
 manufacture 169
 PXA2N graphite 452

R

Radiation damage
 annealing of 463
 dimensional change 402, 460
 effect on electrical resistivity
 465
 effects on graphite & C/C 401
 effect on mechanical properties
 403, 466-468
 effect on thermal conductivity
 403, 464
 effect on thermal expansion
 465
 mechanism 458
 surface effects 401
 Radiation displacement damage 400,
 459
 Radiation enhanced sublimation 418
 Radiation creep 468
 Radioisotope thermal electric
 generator 173
 Radiolytic oxidation of graphite 469
 effect on properties 471
 mechanism of 469
 RBMK reactor 455
 Refrigerant-adsorbent pairs 319
 Refrigerators and heat pumps 303
 advanced cycles 323-333
 basic cycle 306, 313
 cascaded cycles 326
 thermal wave cycles 326
 Runaway electrons *see* disruption
 electrons

S

Scattering
 phonon-defect 405
 phonon-phonon *see* Umklapp
 scattering
 Scherrer equation 348
 Slowing down power 432
 SM2-24 graphite 435, 436, 446
 Small angle x-ray scattering 349
 Solar refrigerator 309
 Solvent extraction
 of coal 211
 of mesophase 127
 Stored energy 462
 Strength 134, 144, 153, 157, 176,
 190, 406, 436, 471, 508-509, 525
 Stress intensity factor 491, 496

T

Thermal oxidation of graphite 472
 Thermal conductivity 11, 144,
 148-152, 155, 177-181,
 191-193, 334-338, 403-412,
 420, 436, 464, 471
 Thermal expansion 144, 152, 176,
 230-232, 436, 465,
 Thermal shock 396-399
 Thermalization *see* moderation
 Tokamak 390
 TRISO particle fuel *see* coated fuel
 particles
 Tritium retention
 in graphite 420
 in C/C composites 422
 role of structural perfection 422
 TSX graphite 436, 454
 Turbostratic carbon 23, 353

U

Umklapp scattering 405

v

- Vehicle fuel vapor system 244
- VGCF 139
 - environmental and safety 163
 - manufacture
 - fixed catalyst method 142
 - floating catalyst method 143
 - issues 160
 - microstructure 140
 - properties 144
- VGCF composites
 - applications 158
 - properties 146, 156
 - aluminum matrix 154
 - carbon matrix 147
 - polymer matrix 151
- VGCF reinforced concrete 157
- VOC removal 102

W

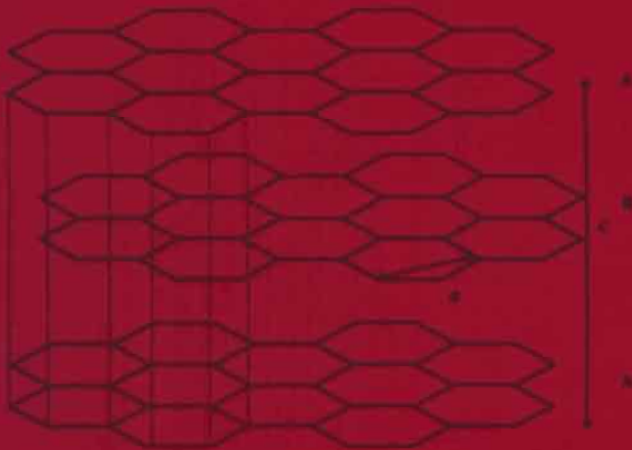
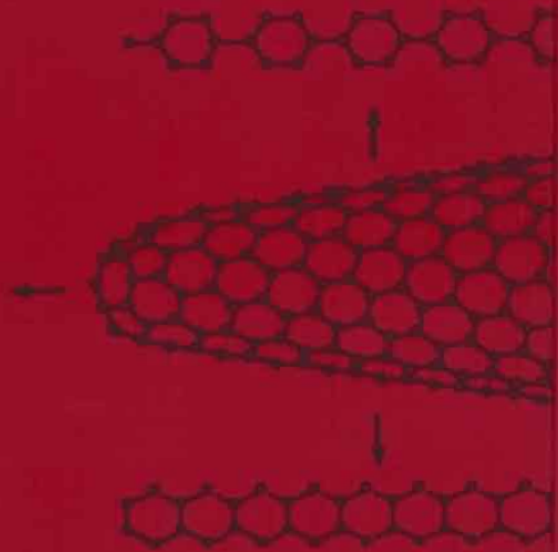
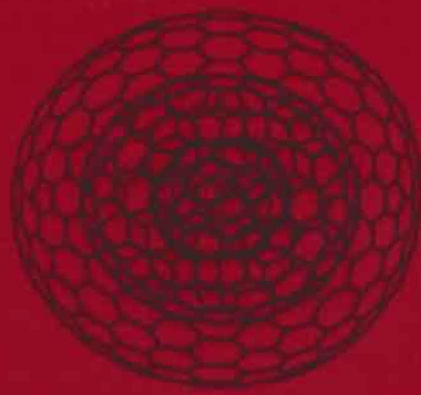
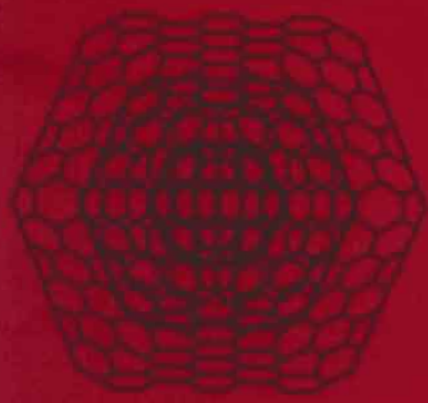
- Water- cooled reactors 454–456
- Water purification 106
- Wigner energy *see* stored energy

X

- X-10 reactor 438
- X-ray diffraction 25, 347

Y

- Young's modulus 11, 84, 134, 144, 153, 157, 406, 436, 471,



ISBN 0-08-042683-2



9 790080 426838